Forschungszentrum Karlsruhe
in der Helmholtz-Gemeinschaft

Wissenschaftliche Berichte
FZKA 7407

Migration of Actinides in the System Clay, Humic Substances, Aquifer

C.M. Marquardt (Editor)

Institut für Nukleare Entsorgung

in collaboration with:

Forschungszentrum Dresden-Rossendorf e.V., Institut für Radiochemie

Johannes Gutenberg-Universität Mainz, Institut für Kernchemie

Universität des Saarlandes, Institut für Anorganische und Analytische Chemie und Radiochemie

Institut für Interdisziplinäre Isotopenforschung e.V., Leipzig

Technische Universität München, Theoretische Chemie

Universität Potsdam, Institut für Chemie, Physikalische Chemie

September 2008

Forschungszentrum Karlsruhe

in der Helmholtz-Gemeinschaft

Wissenschaftliche Berichte

FZKA 7407

Migration of Actinides in the System Clay, Humic Substances, Aquifer

C.M. Marquardt (Editor)

Institut für Nukleare Entsorgung

in collaboration with:

Forschungszentrum Dresden-Rossendorf e.V., Institut für Radiochemie

Johannes Gutenberg-Universität Mainz, Institut für Kernchemie

Universität des Saarlandes, Institut für Anorganische und Analytische Chemie und Radiochemie

Institut für Interdisziplinäre Isotopenforschung e.V., Leipzig

Technische Universität München, Theoretische Chemie

Universität Potsdam, Institut für Chemie, Physikalische Chemie

Forschungszentrum Karlsruhe GmbH, Karlsruhe

2008

Forschungszentrum Karlsruhe GmbH
Postfach 3640, 76021 Karlsruhe

Mitglied der Hermann von Helmholtz-Gemeinschaft
Deutscher Forschungszentren (HGF)

ISSN 0947-8620

urn:nbn:de:0005-074070

The work described in this report has been financially supported by the German Federal Ministry of Economics and Technology (BMWi) under the Contract Numbers 02 E 9653, 02 E 9663, 02 E 9673, 02 E 9683, 02 E 9693, and 02 E 9924. The authors are responsible for the content of their contribution.

BMWi Project No.: 02 E 9673

Partner No. 1: Forschungszentrum Dresden-Rossendorf e.V.
Institut für Radiochemie
S. Sachs, A. Křepelová, K. Schmeide, A. Koban, A. Günther, J. Mibus, V. Brendler, G. Geipel, G. Bernhard

BMWi Project No.: 02 E 9653

Partner No. 2: Johannes Gutenberg-Universität Mainz, Institut für Kernchemie
S. Amayri, N. L. Banik, M. Breckheimer, R. A. Buda, S. Bürger, J. Drebert, A. Jermolaev, J. V. Kratz, B. Kuczewski, D. Kutscher, T. Ye. Reich, T. Reich, N. Trautmann

BMWi Project No.: 02 E 9683

Partner No. 3: Universität des Saarlandes, Institut für Anorganische und Analytische Chemie und Radiochemie,
R. Kautenburger, K. Nowotka, H. P. Beck

BMWi Project No.: 02 E 9663

Partner No. 4: Institut für Interdisziplinäre Isotopenforschung e.V., Leipzig
H. Lippold, K. Franke, M. Richter, H. Kupsch

BMWi Project No.: 02 E 9693

Partner No. 5: Technische Universität München, Theoretische Chemie
N. Rösch, S. Krüger

BMWi Project No.: 02 E 9924

Partner No. 6: Universität Potsdam, Institut für Chemie, Physikalische Chemie
S. Eidner, M. U. Kumke

External Partner without support

Forschungszentrum Karlsruhe GmbH, Institut für Nukleare Entsorgung
A. Bauer, M. Bouby, G. Buckau, Th. Fanghänel, H. Geckeis, C. M. Marquardt, Th. Schäfer, A. Seibert

Foreword

The present report summarises the progress and the results obtained within the BMWi[1]-Project "*Migration of actinides in the system clay, humic substances, aquifer* ". This project was conducted in the frame of a BMWi program directed towards the assessment of final repositories / underground disposal facilities in deep geological formations for high-level nuclear waste. The work presented in this report is a continuation of the work within a former BMWA[2] project performed in the years 1999 to 2003. These results are published in a Scientific Report of the Forschungszentrum Karlsruhe, Report FZKA-6999 (2004).

Eight partners have been concerned in this project; seven of them have received funding and one partner (FZK) has attended the project with its long experiences in the field of metal ion interaction with humic substances and of clay sciences, but without financial support. All the partners involved in this report are listed on page i.

The report contains an executive summary of the final reports prepared by the financially supported partners. These final reports are enclosed as Appendices A - F. The executive summary gives an overview of the covered topics and the obtained results without going into details. Especially, the relationships among the different studies are pointed out. The elaborated results are important contributions which can be introduced into safety assessments of nuclear waste disposal in deep geologic formations.

[1] German Federal Ministry of Economics and Technology (Bundesministerium für Wirtschaft und Technologie)

[2] German Federal Ministry of Economics and Labour (Bundesministerium für Wirtschaft und Arbeit)

Content

Executive Summary

1 Introduction

The present scientific report summarises the work of the project “Migration of actinides in the system clay, humic substances, aquifer”. The project presented here was supported by the Federal Ministry of Economics and Technology (BMWi) in the frame of a program focusing on future research & development studies on disposal of radioactive waste in deep geological formations. The project started in 2003 and ended in 2007. The results of this project are summarised by the final reports of the partners (see Appendices A - F).

Background of this project was that the working group Arbeitskreis Auswahlverfahren Endlagerstandorte (AkEnd), commissioned by the Federal Ministry for the Environment (BMU), has developed recommendations for criteria and procedures to be used in the site selection procedure. Based on that, the BMU wishes to compare the Gorleben site with other potential sites before a definite decision is taken. Among those, clay is one option beside salt formation or granite for disposal of radioactive waste.

The present project continues the work of a former project dealing with the influence of humic substances (HS) on the migration of actinides and heavy metal ions. The studies were extended in a new project to look on the role of clay on the immobilisation process of metal ions according to the program of BMU. In a first step the program has started with a model clay system. As a third component that mimics the mineral surface of the geological surrounding of a disposal, kaolinite was chosen as preferably homogeneous clay mineral. The kaolinite KGa-1b (IN 47907-2054) from the Clay Minerals Society Source Clays Repository (Washington County, Georgia) was used as model mineral within the framework of this joint project.

The basic approach of the present project was to provide fundamental process understanding. Along these lines it encompassed the synthesis and characterisation of humic acids (HA), complexation studies of metal ions, the role of phenolic OH groups in the redox process, studies on the sorption of metal ions on kaolinite in presence and absence of HA, characterisation of sorbed metal ions by EXAFS and time-resolved laser fluorescence spectroscopy (TRLFS), application of capillary electrophoresis coupled to ICP-MS (CE-ICP-MS) for speciation at very low metal concentrations and positron emission tomography (PET) for characterisation of pathways in the geomatrix. The chemical behaviour of the following metal ions has been considered: the actinides Th(IV), U(VI), Np(V), Pu(III,IV), Am(III) and the redox-stable trivalent analogues Eu(III), Tb(III), and Gd(III).

Regarding the so far not comprehended humate complexation, detailed studies of the fluorescence (luminescence) properties of HA, trivalent metal ions, and their humate complexes have been started. By measuring changes of luminescence during the complexation it was tried to elucidate binding mechanisms. This new approach can lead to the missing knowledge necessary to understand the interaction between HS and metal ions.

To support the experimental work on the humate complexation, modelling by quantum chemistry methods was introduced. In a first approach, actinide complexation by relevant organic functional groups was modelled to provide new insights at the atomic level. Modern quantum chemistry methods, e.g., those derived from relativistic density functional theory, were ap-

plied to provide accurate geometric, spectroscopic as well as energy data which are directly related to relevant and well-defined species. Thus, these data are useful for interpreting spectroscopic results, especially when geometric models are involved as in the interpretation of EXAFS measurements. The results of this project also provide insight into bonding mechanisms, solvation effects, and other detailed chemical and physical features that will foster an understanding of similarities and differences of actinide complexes.

Finally, migration experiments of metal ions in compacted clay have been performed to mimic the migration behaviour of metal ions in the natural geomatrix. Little is known about the migration behaviour of HS in clay formations which is supposed to be governed by diffusion processes. Since HA show a strong ability for complex formation, they can influence the migration of radioactive and non-radioactive toxic metal ions in environment of clay. The results of former studies on the migration of HA in clay systems and their influence on radionuclides migration are discussed controversially. Hence, these migration experiments should contribute to an understanding of transport mechanisms of metal ions in the presence of HS.

In the next chapters the scope of the project is summarised without being exhaustive, because details are given in the final reports of the partners in the Appendices A - F.

2 Experimental

2.1 Methods

As one of the most promising speciation methods for metal ions, capillary electrophoresis (CE) was established within the frame of this joint project. Recently, CE has been developed to be a powerful technique for the rapid and highly efficient separation of a variety of compounds, including metal species analysis. The objective of this project was to get more experiences with the method concerning metal speciation and to adopt the method for the purposes of this project. For that, studies have been performed on complexation and redox chemistry of metal ions. To get more information on involved species, especially on humic substances that are not amenable to ICP-MS, a second detector has been introduced and simultaneously applied. This second detector is a diode array detector, by which the absorption spectra of the separated species can be taken. As an alternative method, HA has been labelled with ^{127}I to be detectable by ICP-MS.

The following methods were used during in the project:

Speciation methods for free, complexed, and sorbed metal ions:

Direct methods:

- Stationary fluorescence spectroscopy
- Time resolved fluorescence (luminescence) spectroscopy

- X-ray absorption spectroscopy (XANES and EXAFS) at INE-Beamline, ANKA, Forschungszentrum Karlsruhe, and the Rossendorf Beamline (ROBL), European Synchrotron Radiation Facility (ESRF) in Grenoble (France)
- X-ray photoelectron spectroscopy (XPS)
- UV-VIS-NIR spectroscopy

Indirect methods to distinguish between free and complexed metal ion:

- Capillary electrophoresis coupled to ICP-MS (CE-ICP-MS)
- Ion focusing (IF) with capillary electrophoresis (CE) coupled to ICP-MS
- Anodic stripping voltammetry (ASV) for detection of Zn, Cd, Pb and Cu ions
- Ultrafiltration (UF) for separation of free metal ions from metal humate complexes
- Anionic and cationic exchange with Sephadex DEAE A-25 and Bio-Rad AG 50W-X2 to separate free metal ions from metal humate complexes
- Attenuated total reflection FTIR spectroscopy (ATR-FTIR)

Detection methods for metals:

- Radiometric methods like liquid scintillation counting, α- and γ-spectrometry
- Resonance ionisation mass spectrometry (RIMS) for measurements of very low amounts of plutonium
- ICP-MS, ICP-OES

Characterisation of humic material:

- FTIR spectroscopy
- Elemental composition of humic material
- Potentiometric titration, calcium acetate exchange for exchangeable protons, radiometric determination of phenolic/acidic OH groups
- ^{15}N-NMR spectroscopy

Miscellaneous methods:

- Diffusion cell for diffusion experiment of metal ions in compacted clay
- Positron emission tomography (PET) for 3D imaging of colloidal transport processes in geological matrices
- Stop-flow reaction measurements for kinetic experiments
- Liquid-liquid extraction with 2-thenoyltrifluoroacetone (TTA), 4-benzoyl-3-methyl-1-phenyl-2-pyrazolin-5-one (PMBP), (2-ethylhexyl) orthophosphoric acid (HDEHP) as extraction agents for neptunium and plutonium oxidation state speciation

- Glove boxes for oxygen free atmosphere (~1-10 ppm)
- Neutron irradiation at the TRIGA Mainz reactor to produce different radioactive tracers (^{160}Tb, ^{239}Np)
- Electrolysis at constant potential for the preparation of oxidation states of plutonium ions
- DOC (dissolved organic carbon) measurements for determining humic acid contents

2.2 Metal ions, humic material, and clay

Metal ions

Several metal ions have been probed in the frame of this joint project. These metal ions can be classified into two groups:

1. Actinide ions in different oxidation states:	Uranium (U(VI)), neptunium (Np(V)), plutonium (Pu(III,IV, V, VI)), americium (Am(III)),
2. Lanthanide ions used as model elements for trivalent actinides:	Neodymium (Nd(III)), europium (Eu(III)), gadolinium (Gd(III)), terbium (Tb(III))

Studies of the influence of environmental-relevant cations on the actinide humate complexation and actinide sorption onto kaolinite have been performed with Ca(II), Mg(II), and Fe(III).

Humic material

As humic substances, fulvic acid (FA) and humic acid (HA) fractions of ground and surface waters (FG1-FA, HO14-FA, HO13-HA, BS1-HA, Suwannee River-SR-FA, SR-HA, KFA), synthetic HS, as well as a commercial HA were used.

As in the previous project, commercially available natural humic acid from Aldrich (AHA) has been used by all project partners as reference material. To make some comparison between different humic acids, several other humic acids have been applied in the studies. All used humic substances have been characterised with many methods in the frame of this and the preceding projects. A list of the humic acids is given below.

A) Natural humic acids
   1) Aldrich humic acid (AHA)
      i. Purified AHA
      ii. ^{124}I- and ^{131}I-radiolabelled AHA
      iii. ^{18}F-radiolabelled AHA
   2) GoHy-573 HA and FA (purified) extracted from Gorleben groundwater 573.

3) Aquatic fulvic acid (KFA) and soil humic acid (bog soil HA) from the mountain bog “Kleiner Kranichsee” near Carlsfeld, Saxony, Germany

B) Synthetic humic acids

1) HA with different carboxylic/phenolic OH groups
   i. unmodified HA type M1 and M42
   ii. ^{14}C-labelled HA type M1 and M42 ([^{14}C]M1, [^{14}C]M42)
   iii. ^{15}N-labelled HA type M1 ([^{15}N]M1)
   iv. HA type M1 and M42 synthesised in presence of kaolinite (M1-K, M42-K)
2) Humic acid-like oxidation products with distinct redox functionalities (type Hyd-Glu, Cat-Gly)
   i. Unmodified HA type Hyd-Glu, Cat-Gly
   ii. HA with blocked phenolic OH groups prepared by methylating with diazomethane (type Hyd-Glu-PB)
3) Humic substance-kaolinite-sorbates M1-KS and M42-KS

Clay

All partners of the joint project have used the kaolinite KGa-1b (IN 47907-2054) from the Clay Minerals Society Source Clays Repository (Washington County, Georgia) as model mineral, which is well crystallized. Some physico-chemical characteristics are summarised in Table 1.

Synthesis of humic substances in presence of kaolinite and formation of humic substance-kaolinite-sorbates

Most natural clays are closely associated with natural organic matter. When organic compounds are mobilised from the clay rocks, they can influence the sorption behaviour of metal ions, such as actinides. The objective of this work was to study the influence of kaolinite on the formation of synthetic HA and their properties, and to prepare humic substance-kaolinite-sorbates as model compounds for natural organic matter-containing clays. It appears that such sorbates are suitable model compounds for organic rich clays. These sorbates have been used as well in sorption and diffusion experiments.

Table 1: Physico-chemical properties of kaolinite KGa-1b

Grain size	57.8% < 2 µm; 32.0% < 0.5 µm
ξ potential	-49.2 mV
Point of zero charge (p.z.c.)	6.0
Point of zero net proton charge (p.z.n.p.c.)	5.1 ± 0.2 4.99 ± 0.03
TOC	231 ppm
Cation exchange capacity (CEC)	1.2 - 1.8 meq/100 g
BET surface area	11.8 m^2/g

3 Interactions in binary systems

3.1 Complexation

The work of previous projects was continued to fill gaps in the database of complexation constants for metal humate complexes, or to introduce new methods like capillary electrophoresis to get more reliable data especially at lower metal concentrations that are not amenable to spectroscopic studies. All complexation constants are evaluated according to the charge neutralisation model that was stipulated by the partners in one of the previous joint projects. Within the frame of this joint research project the humate complexation of Eu(III), Gd(III), Tb(III), Pu(III), Pu(IV), and U(VI) has been examined. The obtained loading capacities (LC) and the complexation constants (log *K*, log *β*) are summarised in Table 2.

Complexation of U(VI) at neutral pH

The humate complexation of uranyl ion has been investigated by TRLFS at pH values where hydrolysis of U(VI) occurs. It was proposed that one UO_2OH^+ reacts with one proton exchanging group of the HA. The complexation constant of the mixed humate complex UO_2(OH)HA(I) for the reaction between UO_2OH^+ and HA(I) was determined to be log *K* = 6.95 ± 0.1 with a loading capacity of 0.76 ± 0.28. The complexation constant of the mixed humate complex is slightly higher than the constant for the pure UO_2HA(II) complex, indicating that the mixed complex is more stable than the pure one. The overall complexation constant of the reaction UO_2^{2+}, HA, and OH^- with formation of the mixed complex at pH 7 leads to the following value: UO_2(OH)HA(I); log *β* = 14.89 ± 0.54.

Tab. 2: Summary of loading capacities (LC) and stepwise complexation constants log *k* of metal humates determined in this work (log *β* is the overall complexation constant).

Complex	Method	pH	LC	log *K*
EuHA(III)	CE-ICP-MS	5.0	0.435	6.2 - 6.6
	Ultrafiltration (UF)	5.0	0.665	6.4 - 6.7
	Cation exchange (Schubert)	4.0	1.0[§]	8.2 - 8.5
GdHA(III)	CE-ICP-MS	5.0	0.44	6.3 - 6.4
	Ultrafiltration (UF)	5.0	0.687	6.2 - 6.6
UO_2(OH)HA(I)	TRLFS	7.0	0.76 ± 0.28	6.95 ± 0.1 log *ß* = 14.89 ± 0.54
PuHA(III)	Ultrafiltration (UF)	3.0	0.045 ± 0.005	6.21 - 6.86
		4.0	0.11 ± 0.005	6.57 - 6.87
$Pu(OH)_2$HA(II)	Ultrafiltration (UF)	1.8	0.033	6.5 - 7.9
		2.8	0.045	6.7 - 8.3
		3	0.09	6.4 - 8.4

[§] Assumption and not measured

U(VI) complexation of model compounds with nitrogen-containing functional groups

It has been discussed for many years whether nitrogen-containing functional groups are involved in the interaction between humic substances and actinides. This part of the project aims to the role of N-containing functional groups of humic substances in the complexation process of hexavalent uranyl cation. In a first attempt, model substances were used instead of humic substances, the L-phenylalanine (2-amino-3-phenylpropionic acid, C_6H_5-CH_2-$CH(NH_2)$-COOH) and the glycine (aminoacetic acid, $CH_2(NH_2)$-COOH). The complexation of U(VI) was investigated at acidic pH values by TRLFS (time-resolved laser-induced fluorescence spectroscopy) and ATR (attenuated total reflection)-FTIR spectroscopy. By comparison of the complex stability constant of uranyl L-phenylalanine complex (log *K* = 1.9 ± 0.2) and of uranyl 3-phenylpropionate complex (log *K* = 4.2 ± 0.2), it is obvious that the amino group is not involved in the complexation; but it rather destabilises the complex. From ATR-FTIR spectroscopy one can conclude that U(VI) is bound only on the carboxylate group and that the amino group is not involved directly in the binding.

Complexation of Pu(III) and Pu(IV)

Investigations of the plutonium humate complexation show that among the different oxidation states of plutonium only Pu(III) and Pu(IV) exist in contact with HS in aqueous solutions. The complexation constants of Pu(III) and Pu(IV) with Aldrich HA were determined by UF. Despite of huge imponderables like formation of Pu(IV) colloids and aggregation of Pu(IV) humate colloids that influence the results of UF, a complexation constant was estimated for trivalent and tetravalent Pu humates. For a pH range between 1.8 and 3.0 (pH 4.0 for Pu(III)) the following values were estimated: log $K_{Pu(III)}$ = 6.2 - 6.9; log $K_{Pu(IV)}$ = 6.4 - 8.4.

Complexation of Eu(III), Gd(III) and Tb(III)

The humate complexation was studied by capillary electrophoresis coupled to ICP-MS (CE-ICP-MS) and UF. CE-ICP-MS was applied as a new technique to determine complexation constants and the corresponding loading capacities (LC) for metal humate complexation. Separation is achieved by exploiting different mobility of species in an electric field. This technique has the advantage that speciation can be achieved at low metal concentration up to 10^{-9} M. Not only the migration of metal species in the electric field but also the migration of the ligand, here the HA, can be monitored by ICP-MS when it is marked with iodine-127. Direct correlation can be made between the signal of the metal ion and the ligand to assign the species.

The separation of the species has been achieved by 0.1 M acetic acid / 0.01 M sodium acetate as electrolyte. Despite overloading problems when measuring at higher concentrations, the loading capacities for europium and gadolinium at pH 5 have been estimated with CE-ICP-MS to be 43.5 and 44.0% (UF-values: 66.5% and 68.7%), respectively, and average complexation constants of log K_{Eu} = 6.44 ± 0.15 and log K_{Gd} = 6.33 ± 0.14 have been determined.

Investigations of the europium humate complexation by cation exchange (Schubert method) yield in much higher conditional complexation constants of 8.2 - 8.5 at [Eu(III)] = 10^{-11} - 10^{-8} M and pH 4. The competitive effects of other metal (Ca^{2+}, Fe^{3+}, Mg^{2+}, Al^{3+}) and ligand (SO_4^{2-}) ions on the europium humate complexation have been investigated, too. As a third trivalent metal ion, the complexation of Tb(III) with humic acid has also been studied. However, the LC and the complexation constant have not been determined from the experimental results.

3.2 Spectroscopic determination of thermodynamic and kinetic parameters of humate complexation

An important task of the joint project was the investigation of HA complexation with metal ions on a molecular level. For that the fluorescence and luminescence properties of trivalent metal ions and humic substances during the complexation reaction have been examined. Different time-resolved and steady-state luminescence spectroscopic techniques were applied to look in detail on the interactions between lanthanide ions (Ln^{3+}) and HS. Data of time-resolved fluorescence anisotropy, stopped-flow analysis and high resolution ultra-low temperature luminescence excitation spectra were evaluated to get specific information of the metal complexation on the structure (conformation, aggregation) of HS. From this work it appears, that FA and HA differ in size, association, or both due to metal complexation. By means of the principle of *Förster reso-*

nance energy transfer (FRET), a “spectroscopic ruler”, the mean distance between metal ions was calculated. Depending on the origin of HS and on the loading with metal ions distance in the range of ten ionic radii were found.

In order to access further structural details of metal-HS complexes high-resolution ultra-low temperature luminescence excitation spectra of Eu^{3+} complexes with model compounds and HS were recorded. A first comparison of the results of model ligands and of HS revealed that the major part of binding seems to be related to carboxylic acid type of ligands with no significant contribution from chelates.

It was also found that the photo-physical properties of the lanthanide ions (Ln^{3+}, Tb^{3+} and Eu^{3+}) are changed upon complexation from a mono-exponential to a non-exponential decay for Tb^{3+} and a decrease in decay time for Eu^{3+}. This change is discussed by formation of different complex species.

3.3 Quantum mechanical modelling of the complexation of actinides by humic substances

Quantum mechanical modelling (QMM) was introduced to support the mechanistic understanding of actinide complexation by humic acid on a molecular level. This activity was started with calculations on simple organic carboxylic molecules and extended to more complicated systems. Mainly actinyl interactions with carboxylic and alcoholic groups were examined with the help of relativistic density functional calculations that included a simulation of solvation effects. The results showed that in many ways small carboxylic acids and alcohols provide adequate models of pertinent complexation sites of HS.

The calculations focused on uranyl(VI), but neptunyl in the oxidation states (VI) and (V) was also examined. Results on mono-carboxylate complexes of uranyl with aliphatic and aromatic acids indicated somewhat stronger complexation interactions for aliphatic than for aromatic ligands. Monodentate structures where calculated to be energetically preferred due to a strong hydrogen bond between an aqua ligand of the first solvation shell of uranyl and the carboxyl group (pseudo-bridging geometry), but the bidentate complexation mode turned out to be favoured at the free energy level, due to stabilizing entropy effects. The latter findings are in line with crystal structures and common knowledge for carboxylate complexes, but are at variance with the prevailing interpretation of EXAFS results on actinyl humate complexes. The average bond length An-O_{eq} of equatorial ligands is a key parameter determined in EXAFS investigations. QMM showed that the value of An-O_{eq} is not sensitive to the detailed structure and the chemical nature of the oxygen donor site. Only the coordination number of the complex affects An-O_{eq} of solvated complexes - a finding that was corroborated by an appropriate re-evaluation of crystal structures. These results allowed one to rationalize also why blocking of phenolic OH groups of humic acids, which results in a change in the complexation behaviour, is not reflected in the lengths of the actinyl bonds and the An-O_{eq} data determined experimentally.

Summarising the consequences of these results on the interpretation of the atomistic structure and the energetic of actinyl humate complexation, it is proposed that these complexes, with a preferential coordination number of 5 for uranyl and neptunyl, should be assigned as

bidentate, mainly involving carboxylic groups, but likely also other oxygen donor sites, e.g., hydroxyl groups.

Appendix E provides further results, e.g., an accurate new determination of the heat of formation of uranyl(VI) and plutonyl(VI), one of the first applications of the density functional approach to actinide adsorption at mineral surfaces, as well as extensions of the Douglas-Kroll-Hess approach to relativistic density functional chemistry.

3.4 Redox reactions between humic acid and metal ions

The redox state of a metal ion is essential for its chemical behaviour in environmental aquatic systems. Especially the impact of humic substances on the redox behaviour of metal ions is one of the important questions that arise in the performance assessment of repositories of hazardous waste. To learn more about the redox mechanism of HS several experiments have been performed in the frame of this joint project. From many studies one assumes that phenolic and acidic OH groups play a dominant role, and therefore, humic acid-like synthetic compounds were synthesised with different redox functionalities. These synthetic HA-types were used for redox investigations with Np(V) under anaerobic conditions.

Np(V) reduction by various natural and synthetic humic substances

The reduction of Np(V) has been studied with two natural humic substances (AHA, KFA) and two synthetic humic acids with enlarged redox capacities (Hyd-Glu, Cat-Gly), and one synthetic HA with blocked phenolic OH groups (Hyd-Glu-PB).

The synthetic HA type Cat-Gly and Hyd-Glu show a stronger Np(V) reduction than the natural humic substances AHA and KFA. The strongest Np(V) reduction is found for the HA type Hyd-Glu at pH 9.0. After 865 h (36 d), 62% of the Np(V) are converted to Np(IV). Also in case of HA type Cat-Gly, the strongest Np(V) reduction is found at pH 9.0. After 961 h (40 d) of storage, 49% Np(IV) are detected in solution. In contrast to this, in the system with AHA only 15% Np(IV) are detected at pH 3.5 after 793 h. This shows that the pH-dependence of the reduction reaction differs between the natural and the synthetic HA.

It is to note that also in case of synthetic HA with enlarged redox capacities even after 1 year reaction time, Np(V) is still present in solutions and it seems that an equilibrium state is not reached and reduction proceeds with very slow kinetics. The higher reduction potential of synthetic HA-types can be correlated to higher phenolic/acidic OH group contents compared to natural HA. The phenolic OH groups might be involved in the electron transfer reaction of HS and metal ions.

Redox reaction of Pu with fulvic acid

The redox reactions of hexavalent Pu (Pu(VI)), trivalent Pu (Pu(III)), and a mixture of trivalent, tetravalent, pentavalent, and hexavalent Pu (Pu(III,IV,V,VI)) with fulvic acid at a pH range of 0 to 9 have been investigated. CE-ICP-MS and UV-VIS spectroscopy have been used as speciation methods. The experiments have shown that Pu(VI) is reduced by FA and HA to Pu(IV) and Pu(III) within a couple of weeks. The reduction of Pu(VI) with FA occurs faster with increasing pH values, and this has also been found for HA. The studies have

shown that the reduction of Pu(VI) to Pu(V) is fast compared to the reduction of Pu(V) to Pu(IV) and Pu(III).

3.5 Interactions in the binary clay systems: humic acid-kaolinite and metal ion-kaolinite

HA and kaolinite

The studies on the sorption of humic acid on kaolinite verifies information from literature that HA sorption decreases with increasing pH value due to electrostatic repulsion - the negative charge of binding sites of HA and kaolinite increases with pH. Furthermore, an effect of the ionic strength has been observed; the HA sorption increases with increasing ionic strength up to 0.1 M, that might be explained by screening of charges and steric effects due to coiling of HA molecules. However, the sorption of FA on kaolinite is lower than of HA. XPS characterisation of kaolinite with sorbed HA shows that the surface contains only about 5 atom % C. That indicates that HA does not cover the kaolinite in a homogeneous layer and that sufficient kaolinite sites should be available for metal interaction. That is supported by the fact that the surface composition of kaolinite with respect to Si, Al, and O is not changed by covering it with HA.

The observation has been made that the presence of U(VI) enhances the sorption of HA at pH values larger than 5.5. One explanation is that uranyl acts as a bridging metal ion between kaolinite surface and HA in the bulk solution and overcomes in this way the repulsion due to the negative charge of the two components.

Metal ion and kaolinite

The sorption of several metal ions (Eu^{3+}, Gd^{3+}, Tb^{3+}, Am^{3+}, Pu^{3+}, Th^{4+}, Pu^{4+}, NpO_2^{+} and UO_2^{2+}) on kaolinite was investigated in batch experiments. The results are summarised in Figure 1, where only one representative element is shown for each oxidation state (An(III), (IV), (V), (VI)). The tetravalent actinides are sorbed strongly over the entire pH range 1 - 10, the trivalent actinides show the same sorption strength at pH values larger than 6, but the sorption decreases significantly with decreasing pH values lower than 6. Only Np(V) is sorbed rather weakly at micro molar concentrations and has the maximum at about pH 9, but the sorption is significantly enhanced with decreasing concentration of the neptunyl ion. The sharp decline of the sorption at higher pH values is attributed to carbonate complexation, because the experiments have been performed under air conditions ($p_{CO2} = 10^{-3.5}$ atm). This carbonate influence vanishes in experiments under argon atmosphere, and the sorption remains at the same high level. At lower pH values the sorption behaviour of the metal ions is the same for both conditions, argon and air atmosphere.

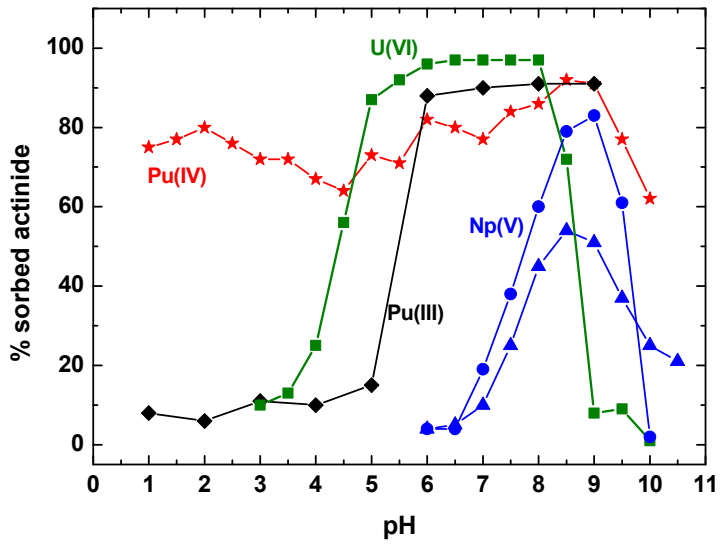

Figure 1: Sorption of tri-, tetra-, penta-, and hexavalent actinide ions on kaolinite as a function of pH. Experiments have been performed under air conditions (p_{CO2} = $10^{-3.5}$ atm). The sorption curve of Np is shown for two concentrations: ▲: $1 \cdot 10^{-6}$ M, ●: $7 \cdot 10^{-12}$ M.

The sorption of Eu(III) and Gd(III) was found to be very strong over the whole pH area and the drop in the sorption with decreasing pH value is not as pronounced as for Pu(III) and Am(III) for pH values lower than 5. Carbonate complexation has only minor effects in the high pH range. Desorption effects of Ca and Mg as competing cations were found to be very strong at the estimated concentration ranges. The following sorption ranking onto kaolinite was found: **Eu > Gd >> Ca > Mg.**

The batch experiments of Pu and Np sorption on kaolinite were concomitantly probed by EXAFS to get insight in the mechanism of metal sorption. Pu(III) is oxidised to Pu(IV) during the reaction with kaolinite, therefore only tetravalent Pu is sorbed onto the surface. Pu(IV) seems to be bound as polynuclear species by an inner-sphere sorption. Np(V) is bound on the kaolinite surface as a Np(V)-carbonato species at pH values >8 under ambient CO_2. The coordination is bidentate via two carbonate groups. Whether the binding is by inner- or outer-sphere complexes is unclear. At CO_2-free conditions the Np(V) is bound by inner-sphere sorption on the kaolinite surface.

As additional method to elucidate the binding mechanism, time-resolved laser-induced fluorescence spectroscopy (TRLFS) was applied to study the kind of U(VI) surface complexes onto kaolinite. The main conclusion is that U(VI) forms two surface species on kaolinite, which differ likely in the amount of water molecules in their coordination environment.

3.6 Utilisation of PET for visualising humic colloid-borne transport

Based on suitable radio-labelling techniques, positron emission tomography was successfully utilised for 3D imaging of colloid-borne transport processes by humic substances in geological matrices. The humic material was labelled with the positron-emitting nuclide ^{124}I. As a

result of first experiments with a sand column, a pronounced inhomogeneity in the mass flow distribution (channelling) was detected for a humic acid as compared to a conservative tracer. Studies on real geological barrier materials (clay rock, granite) planned in a follow-up project are promising.

3.7 Association of humic substances and low molecular-weight organic compounds

By means of radio-analytical measurements of octanol-water partition ratio $P_{O/W}$, different modes of interaction between humic substances and low molecular-weight organic compounds were identified on the basis of changes in the hydrophilic / hydrophobic properties of the colloids. Effects on sorption and metal binding turned out to be of minor importance. It can be concluded that the transport properties of organic colloids are not substantially affected by isolating them from the total inventory of organic matter. The absence of implications on size distribution suggests that humic colloids are macromolecules, rather than loose aggregates.

4 Interactions in the ternary system: kaolinite - humic acid - metal ion

This task focuses on the effect of humic acid on the sorption of metal ions. These investigations have been made with almost the same metal ions as the investigations for the binary system: Eu^{3+}, Gd^{3+}, Tb^{3+}, Pu^{3+}, Pu^{4+}, NpO_2^{+} and UO_2^{2+}. To understand binding mechanism, EXAFS and TRLFS have been applied to characterise the samples.

4.1 Batch experiments

Interaction among metal ion, humic acid and kaolinite

The sorption of metal ions in presence of HA generally follows the sorption of HA in the acidic pH range. Here, the HA enhances the uptake of metal ions compared to the system without HA. This is caused by the formation of additional binding sites due to sorption of HA onto the kaolinite. Then, the metal ions can be complexed to the sorbed HA. In the near neutral and alkaline pH range the metal humates do not sorb onto the mineral surface due to repulsion between negatively charged metal humate complex and negatively charged kaolinite surface. The binding mechanism via humate is not anymore available and only positively charged metal species are mainly sorbed on the mineral surface. But this sorption is somewhat reduced by a competition reaction with metal humate complexation in solution. The magnitude of metal sorption on kaolinite is inversely correlated to the strength of the humate complex. Consequently, HA can mobilise metal ions at environmental conditions and has in any case to be considered in performance assessment of repositories. But modelling seems not to be simple, because experiments with Tb(III) show that the composite distribution approach is not applicable to describe the metal adsorption on clay in presence of HA, according to findings from the literature.

In case of Pu(III) the sorption behaviour on kaolinite in presence of HA is rather unclear, because of overlaying redox reactions. This complex behaviour is also pronounced in experiments with various sequences of mixing of the three components (Pu, HA, kaolinite). Different sorption was observed by varying the equilibrium sequences (see Appendix B).

The batch experiments of uranyl ion sorption on kaolinite were concomitantly probed by EXAFS and TRLFS to get insight in the mechanism of metal sorption. The general conclusion is that U(VI) is preferentially bound to the kaolinite directly and not via the HA, otherwise no U-Si/Al interactions could be observed by EXAFS. The EXAFS structural parameters for the system U(VI)-HA-kaolinite are similar to values of the binary system U(VI)-kaolinite, and they are not influenced by the HA.

By TRLFS two adsorbed U(VI) species were identified on the kaolinite, that are similar for the binary system. Both surface species can be attributed to adsorbed bidentate mononuclear surface complexes, in which two oxygen atoms of the uranyl ion are bound to two Al, Si, or both atoms (aluminol octahedral, silanol tetrahedral). The two surface species differ probably in the number of water molecules in their coordination sphere. The uranyl ions are preferentially bound to the kaolinite and not to the HA, which is distributed between kaolinite particles. But it was also found that the hydrate shell of U(VI) is partly displaced with complexed HA.

Uranium(VI) sorption onto synthetic humic substance-kaolinite-sorbates

It is known that organic substances (OS) are very often embedded in natural clay. The question arises whether such clay-OS-sorbates show other sorption properties than clay without organics. For that synthetic humic substances-kaolinite-sorbates were prepared. Metal sorption experiments with the sorbates show that on one hand metal ion (U(VI)) can be immobilised by complexation with humic substances sorbed on the kaolinite. On the other hand, this substrate can enhance mobilisation due to release of humic substances from the kaolinite and subsequent formation of metal humate complexes in solution. The resulting process, immobilisation or mobilisation, is dependent on the pH value and the functional properties of the humic substances sorbed on the clay and in solution. These experiments show that synthetic humic substance-kaolinite-sorbates can be used as model compounds for organic matter-containing natural clay minerals.

4.2 Diffusion experiments

Diffusion experiments were carried out with compacted kaolinite to elucidate migration processes of humic colloids in clay and their influence on the U(VI) migration. Additionally, the diffusion of U(VI) in a compacted synthetic humic substance-kaolinite-sorbate was probed. It was found that the migration of HA in clay is governed by diffusion and influenced by its colloidal behaviour. The diffusion coefficient of HA (0.05 - $1.2 \cdot 10^{-10}$ m^2/s) is always smaller than the corresponding values of HTO diffusion (1.5 - $2.7 \cdot 10^{-10}$ m^2/s) and this effect is more pronounced at higher densities of the clay implying that the colloidal HA transport is attributed to steric hindrance. U(VI) is immobilised near the high concentration boundary in association with HA. However, a deeper penetration of U(VI) into the clay layer was observed for the humic substance-kaolinite-sorbate which exhibits more hydrophobic humic matter (see Appendix A). It is assumed that the experiment with the humic substance-kaolinite-sorbate

seems to mimic the behaviour of natural clay much better than pure kaolinite that is free of organic matter.

5 Conclusions and Outlook

Within this joint project significant new results have been obtained concerning the humate interaction of actinides and several lanthanides as redox-stable analogues, and the sorption of actinides/lanthanides on kaolinite in absence and presence of humic acids. These results are very important for some aspects of performance assessment of final repositories / underground disposal facilities in deep geological formations, e.g., they can be introduced into speciation modelling to describe the behaviour of actinide ions in environmental systems. Also some progress has been obtained concerning the understanding of reaction mechanism for humate complexation. This was achieved on one hand by a new approach using laser fluorescence spectroscopy and on the other hand by applying quantum chemistry in the framework of this the project.

The results of this joint project form a basis for the next step, investigations going from the model system kaolinite to the natural clay system. For that, a new joint project entitled “Interaction and transport of actinides in natural clay with consideration of humic substances and clay organics” has been launched, financially supported by BMWi[3].

[3] German Federal Ministry of Economics and Technology (Bundesministerium für Wirtschaft und Technologie)

6 Publications resulting from the project

The following list encompasses the publications resulting from the present joint project. The list is alphabetically indexed by authors.

Banik, N.L., Buda, R.A., Bürger, S., Kratz, J.V., Kuczewski, B., Trautmann, N., Speciation of the Oxidation States of Np and Pu in Aqueous Solutions by CE-ICP-MS and CE-RIMS, in: *Recent Advances in Actinide Science*, (I. May, R. Alvares, N. Bryan, eds.) The Royal Society of Chemistry, Cambridge, 2006, p 53

Banik, N.L., Buda, R.A., Bürger, S., Kratz, J.V., Trautmann, N., Speciation and Interactions of Plutonium with Humic Substances and Kaolinite in Aquifer Systems, *J. Alloys. Compd.* 444-445, 522 (2007)

Banik, N.L., Buda, R.A., Bürger, S., Kratz, J.V., Trautmann, N., Sorption of Tetravalent Plutonium and Humic Substances onto Kaolinite, *Radiochim. Acta* 95, 569 (2007)

Barkleit, A., Foerstendorf, H., Heim, K., Sachs, S., Bernhard, G., Complex formation of uranium(VI) with L-phenylalanine and 3-phenylpropionic acid studied by ATR FTIR spectroscopy, *Appl. Spectrosc.*, in press.

Bürger, S., Banik, N.L., Buda, R.A., Kratz, J.V., Kuczewski, B., Trautmann, N., Speciation of the Oxidation States of Plutonium in Aqueous Solutions by UV/VIS Spectroscopy, CE-ICP-MS, and CE-RIMS, *Radiochim. Acta* 95, 433 (2007)

Bürger, S., Buda, R.A., Geckeis, H., Huber, H., Kratz, J.V., Kunz, K., Lierse von Gostomski, Chr., Passler, G., Remmert, A., Trautmann, N., Isotope Selective Ultratrace Analysis of Plutonium for Environmental Studies by Laser Mass Spectrometry, in: *Radioactivity in the Environment* - Volume 8, (P.P. Povinec, J.A. Sanchez-Cabeza, eds.), Elsevier Ltd., 2006, p 581

Franke, K., Patt, J. T., Patt, M., Kupsch, H., Steinbach, J., A new technique for radiolabelling of humic substances, *Radiochim. Acta* 92, 359 (2004)

García-Hernández, M., Willnauer, C., Krüger, S., Moskaleva, L. V., Rösch, N., Systematic DFT Study of Gas Phase and Solvated Uranyl and Neptunyl Complexes [AnO2X4]n (An = U, Np; X = F, Cl, OH, n = 2-; X = H2O, n = 2+), *Inorg. Chem.* 45, 1356 (2006)

Grüning, C., Huber, G., Klopp, P., Kratz, J.V., Kunz, P., Passler, G., Trautmann, N., Waldek, A., Wendt, K., Resonance Ionization Mass Spectrometry for Ultratrace Analysis of Plutonium with a New Solid State Laser System, Int. *J. Mass Spectrometry* 235, 171 (2004)

Kautenburger, R., Beck, H.P., Complexation studies with lanthanides and humic acids analysed by ultrafiltration and capillary electrophoresis - inductively coupled plasma mass spectrometry, J. Chromatogr. A 1159, 75 (2007)

Kautenburger, R., Beck, H.P., Waste disposal in clay formations: Influence of humic acid on the migration of heavy metal pollutants, *ChemSusChem* (Chemistry & Sustainability, Energy & Materials) 1, 295 (2008)

Kautenburger, R., Nowotka, K., Beck, H.P., *Simultaneous analysis of free and humic acid complexed europium and gadolinium species by CE-ICP-MS*, Migration'05, 10th International Conference on Chemistry and Migration Behaviour of Actinides and Fission Products in the Geosphere, Avignon, 2005

Kautenburger, R., Nowotka, K., Beck, H.P., *Iodination of humic acid as ICP-MS marker in speciation studies with lanthanides analyzed by CE-ICP-MS*, Proceedings of the 13th Meeting of the International Humic Substances Society, Karlsruhe (Germany), 2006, 45, pp 937-940

Kautenburger, R., Nowotka, K., Beck, H.P., Online analysis of europium and gadolinium species complexed or uncomplexed with humic acid by capillary electrophoresis-inductively coupled plasma mass spectrometry, *Anal. Bioanal. Chem.* 384, 1416 (2006)

Kautenburger, R., Nowotka, K., Beck, H.P., Joint project: *Migration of actinides in the system clay, humic substance, aquifer - Kinetic investigations in the system humic acid - metal - clay*, BMWi Project No. 02 E 9683, Final report 2007, pp 49.

Kolokassidou, K.; Luschtinetz, F.; Eidner, S.; Paschalidis, I.; Kumke, M.U.: *Effect of metal ion complexation on humic acid conformation*, Technical Report - Svensk Kaernbraenslehantering AB, 2007, (TR-07-05), ISSN:1404-0344, pp 361-366,

Kratz, J.V., Trautmann, N., Huber, G., Passler, G., Wendt, K., Laser Mass Spectrometry, in: *Analytical Applications of Nuclear Techniques*, International Atomic Energy Agency, Vienna, ISBN 92-0-114703-1, 33 (2004)

Křepelová, A., *Influence of humic acid on the sorption of uranium(VI) and americium(III) onto kaolinite.* Wissenschaftlich-Technische Berichte, Forschungszentrum Dresden-Rossendorf, FZD-475, 2007

Křepelová, A., Brendler, V., Sachs, S., Baumann, N., Bernhard, G.: U(VI)-kaolinite surface complexation in absence and presence of humic acid studied by TRLFS, *Environ. Sci. Technol.* 41, 6142 (2007)

Křepelová, A., Reich, T., Sachs, S., Drebert, J., Bernhard, G.: Structural characterization of U(VI) surface complexes on kaolinite in the presence of humic acid using EXAFS spectroscopy, *J. Colloid Interf. Sci.* 319, 40 (2008)

Křepelová, A., Sachs, S., Bernhard, G.: Uranium(VI) sorption onto kaolinite in the presence and absence of humic acid, *Radiochim. Acta* 94, 825 (2006)

Krüger, S., Schlosser, F., Ray, S.R., Rösch, N.: Uranyl Complexation by Carboxylic Acids: A Relativistic Density Functional Model Study for Actinide Complexation by Humic Acids, in *Lecture Series on Computer and Computational Sciences* 7, 904 (2006)

Krüger, S., Schlosser, F., Rösch, N., Monocarboxylate Complexes of Uranyl: A Relativistic Density Functional Study, in: *Recent Advances in Actinide Science*, R. Alvarez, N. D. Bryan, I. May (Eds.), Proceedings of the Conference Actinides 2005, Manchester, 2005, The Royal Society of Chemistry, Cambridge, 2006, p. 252-254

Kuczewski, B., Marquardt, C.M., Seibert, A., Geckeis, H., Kratz, J.V., Trautmann, N., Separation of Plutonium and Neptunium Species by Capillary Electrophoresis - Inductively Coupled Plasma-Mass Spectrometry and Application to Natural Groundwater Samples, *Anal. Chem.* 75, 6769 (2003)

Kumke, M.U., Eidner, S., Fluorescence and energy transfer processes of humic substancesand related model compounds in terbium complexes, in: *Humic substances: molecular details and applications in land and water conservation*, E.A. Ghabbour and G. Davies (eds.), Taylor and Francis, Inc., 2005, pp 131-152

Kumke, M.U., Eidner, S., Krüger, T., Fluorescence quenching and luminescence sensitisationin complexes of Tb(III) and Eu(III) with humic substances, *Environ. Sci. Technol.* 39(24), 9528 (2005)

Kumke, M.U., Eidner, S., Marmodée, B., Primus, P., *Complexation of Lanthanide Ions by Humic Substances: New Aspects from Luminescence Sensitization and Photodynamics of Humic Substances*, Technical Report - Comissariat `a L'´ Energie Atomique (Rapport CEA-R-6122), 96-99, ISSN 0429-3460 (2006).

Lippold, H., Evans, N.D.M., Warwick, P., Kupsch, H., Competitive effect of iron(III) on metal complexation by humic substances: Characterisation of ageing processes, *Chemosphere* 67, 1050 (2007)

Lippold, H., Mansel, A., Kupsch, H., Influence of trivalent electrolytes on the humic colloid-borne transport of contaminant metals: Competition and flocculation effects, *J. Contam. Hydrol.* 76, 337 (2005)

Lippold, H., Müller, N., Kupsch, H., Effect of humic acid on the pH-dependent adsorption of terbium(III) onto geological materials, *Appl. Geochem.* 20, 1209 (2005)

Marmodée, B.; de Klerk, J.; Kumke, M.U.; Ariese, F.; Gooijer, C., Spectroscopic investigations of complexes between Eu(III) and aromatic carboxylic ligands, *J. Alloys Compd.* 451(1-2), 361 (2008)

Matveev, V., Majumder, S., Rösch, N., Efficient Treatment of the Hartree Interaction in the Relativistic Kohn-Sham Problem, *J. Chem. Phys.* 123, 164104, 1 (2005)

Mibus, J., Sachs, S., Pfingsten, W., Nebelung, C., Bernhard, G., Migration of uranium(IV)/(VI) in the presence of humic acids in quartz sand: A laboratory column study, *J. Contam. Hydrol.* 89, 199 (2007)

Moskaleva, L. V., Matveev, A. V., Dengler, J., Rösch, N., The Heat of Formation of Gaseous PuO22+ from Relativistic Density Functional Calculations, *Phys. Chem. Chem. Phys.* 8, 3767 (2006)

Moskaleva, L. V., Matveev, A. V., Krüger, S., Rösch, N., The Heat of Formation of the Uranyl Dication: Theoretical Evaluation Based on Relativistic Density Functional Calculations, *Chem. Eur. J.* 12, 629 (2006)

Moskaleva, L. V., Nasluzov, V. A. , Rösch, N., Modeling Adsorption of the Uranyl Dication on the Hydroxylated □-Al2O3 (0001) Surface in an Aqueous Medium. Density Functional Study, *Langmuir* 22, 2141 (2006)

Nowotka, K., *Untersuchungen zur Migration von Europium und Gadolinium in Kaolinit als Modellmineral für eine Endlagerstätte*, Dissertation, Universität des Saarlandes, 2007.

Nowotka, K., Kautenburger, R., Beck, H.P., *Speciation of europium and gadolinium complexes with humic acid by CE-ICP-MS*, European Winter Conference on Plasma Spectrochemistry, Budapest (2005)

Reich, T., Reich, T.Ye, Amayri, S., Drebert, J., Banik, N.L., Buda, R.A., Kratz, J.V., Trautmann, N., *Application of EXAFS Spectroscopy to Actinide Environmental Science*, AIP Conf. Proc. 882, 179 (2007)

Reich, T.Ye, Korshunov, M.E., Antonova, T.V., Ageev, A.L., Moll, H., Reich, T., *New Regularization Method for EXAFS Analysis*, AIP Conf. Proc. 882, 153 (2007)

Sachs, S., Bernhard, G., NIR spectroscopic study of the complexation of neptunium(V) with humic acids: influence of phenolic OH groups on the complex formation, *Radiochim. Acta* 93, 141 (2005)

Sachs, S., Bernhard, G., Sorption of U(VI) onto an artificial humic substance-kaolinite-associate, *Chemosphere*, in press

Sachs, S., Brendler, V., Geipel, G., Uranium(VI) complexation by humic acid under neutral pH conditions studied by laser-induced fluorescence spectroscopy, *Radiochim. Acta* 95, 103 (2007)

Sachs, S., Geipel, G., Mibus, J., Bernhard, G., Impact of humic acid on the uranium migration in the environment, in: *Uranium in the Environment. Mining Impact and Consequences,* B.J. Merkel, A. Hasche-Berger, (eds.), Springer, Berlin, 2005, pp 107-116

Sachs, S., Schmeide, K., Reich, T., Brendler, V., Heise, K.H., Bernhard, G., EXAFS study of the neptunium(V) complexation by various humic acids under neutral pH conditions, *Radiochim. Acta* 93, 17 (2005)

Schlosser, F., Krüger, S., Rösch, N., A Density Functional Study of Uranyl Monocarboxylates, *Inorg. Chem.* 45, 1480 (2006)

Schlosser, F., *A Relativistic Density Functional Study of Actinide Complexation in Aqueous Solution*, Dissertation, Technische Universität München, 2006

Schmeide, K., Geipel, G., Bernhard, G., Study of the neptunium(V) reduction by various natural and synthetic humic substances, in *Humic substances in performance assessment of nuclear waste disposal: actinide and iodine migration in the far-field,* G. Buckau (ed.), Wissenschaftliche Berichte, FZKA 7070, Forschungszentrum Karlsruhe, 2005, pp 19

Schmeide, K., Reich, T., Sachs, S., Bernhard, G., Plutonium(III) complexation by humic substances studied by X-ray absorption fine structure spectroscopy, *Inorg. Chim. Acta* 359, 237 (2006)

Schmeide, K., Reich, T., Sachs, S., Brendler, V., Heise, K.H., Bernhard, G., Neptunium(IV) complexation by humic substances studied by X-ray absorption fine structure spectroscopy, *Radiochim. Acta* 93, 187 (2005)

Trautmann, N., Passler, G. Wendt, K.D.A., Ultratrace Analysis and Isotope Ratio Measurements of Long-lived Radioisotopes by Resonance Ionization Mass Spectrometry (RIMS), *Anal. Bioanal. Chem.* 378, 348 (2004)

Wendt, K., Trautmann, N., Recent Developments in Isotope Ratio Measurements by Resonance Ionization Mass Spectrometry, *Int. J. Mass Spectrometry* 242, 161 (2005)

Appendix A - Institut für Radiochemie, Forschungszentrum Dresden-Rossendorf

Migration Behaviour of Actinides (Uranium, Neptunium) in Clays: Characterization and Quantification of the Influence of Humic Substances

Susanne Sachs, Adéla Křepelová, Katja Schmeide, Astrid Koban, Alix Günther, Jens Mibus, Vinzenz Brendler, Gerhard Geipel, Gert Bernhard

Final Report

Support Contract Number

02 E 9673

Forschungszentrum Dresden-Rossendorf e.V.
P.O. Box 510119
D-01314 Dresden
Germany

Content

Abstract

Objective of this project was the study of interaction processes between humic substances, U(VI), Np(V) and kaolinite KGa-1b. It contributed to the attainment of a better process understanding, the improvement of the knowledge on the interaction of humic substances and metal ions and the enhancement of the thermodynamic database.

With a synthetic humic acid (HA), N-containing functional groups of HA were characterized by ^{15}N-NMR spectroscopy. Based on these results, model studies of the influence of amino groups on the complexation behavior of HA were performed. Spectroscopic studies with amino acids show that the amino group do not contribute to the U(VI) complexation at pH 4.

The impact of kaolinite on the formation of HA and humic substance-kaolinite-sorbates was studied in model syntheses. The results exhibit, that the presence of kaolinite during the syntheses mainly influences the yields on HA and their elemental compositions. Synthetic humic substance-kaolinite-sorbates were isolated.

Under exclusion of CO_2, the U(VI) complexation by HA was investigated at pH 7 by means of the conventional time-resolved laser-induced fluorescence spectroscopy (TRLFS) and TRLFS with ultrafast pulses. Complexation parameters for the ternary complex UO_2(OH)HA(I) were determined ($\log\beta_{0.1M}$: 14.89 ± 0.54).

Studies of the Np(V) reduction in presence of HA with different functionalities under anaerobic conditions have shown that Np(V) is reduced to Np(IV) by HA. The redox capacity depends on the HA functionality. Applying a modified HA it was verified that phenolic/acidic OH groups play a dominating role in the Np(V) reduction.

The influence of HA on the U(VI) and Np(V) sorption onto kaolinite was investigated in batch experiments. In dependence on the experimental conditions, HA effects the sorption and consequently the mobility of U(VI) and Np(V). From studies of the U(VI) sorption onto synthetic humic substance-kaolinite-sorbates it was concluded that the structure and functionality of sorbed/associated humic substances considerably influence the sorption behavior of U(VI). The structure of U(VI)-kaolinite-surface complexes in presence of HA was studied by means of X-ray absorption spectroscopy and TRLFS and compared to those of U(VI)-kaolinite-complexes.

Investigations of the migration of HA and U(VI) in the laboratory system kaolinite-water were carried out in diffusion experiments. The migration of HA in compacted clay is governed by diffusion and influenced by its colloidal properties. Humic substances exert an immobilizing effect on the U(VI) transport in compacted kaolinite.

Zusammenfassung

Ziel des Projektes war die Untersuchung von Wechselwirkungsprozessen zwischen Huminstoffen, U(VI), Np(V) und Kaolinit KGa-1b. Es diente der Erzielung eines besseren Prozessverständnisses, der Erweiterung des Wissens über das Wechselwirkungsverhalten von Huminstoffen mit Metallionen sowie der thermodynamischen Datenbasis.

Am Beispiel einer synthetischen Huminsäure (HS) wurden N-haltige funktionelle Gruppen in HS mittels ^{15}N-NMR-Spektroskopie charakterisiert. Basierend auf diesen Ergebnissen wurden Modelluntersuchungen zum Einfluss von Aminogruppen auf das Komplexbildungsverhalten von HS durchgeführt. Spektroskopische Ergebnisse mit Aminosäuren zeigen, dass die Aminogruppe bei pH 4 nicht zur Komplexierung von U(VI) beiträgt.

Der Einfluss von Kaolinit auf die Bildung von HS und Huminstoff-Kaolinit-Sorbaten wurde in Modellsynthesen untersucht. Es wurde beobachtet, dass die Anwesenheit von Kaolinit bei der Synthese von HS vorwiegend deren Ausbeuten und Elementzusammensetzungen beeinflusst. Synthetische Huminstoff-Kaolinit-Sorbate wurden isoliert.

Unter Ausschluss von CO_2 wurde die U(VI)-Komplexierung mit HS bei pH 7 mittels konventioneller zeitaufgelöster laserinduzierter Fluoreszenzspektroskopie (TRLFS) und TRLFS mit ultrakurzen Pulsen untersucht und Komplexbildungsparameter für den ternären Komplex UO_2(OH)HA(I) bestimmt ($\log\beta_{0.1M}$: 14.89 ± 0.54).

Untersuchungen zur Np(V)-Reduktion in Gegenwart von HS unterschiedlicher Funktionalität unter anaeroben Bedingungen haben gezeigt, dass Np(V) durch HS zu Np(IV) reduziert wird. Die Redoxkapazität ist von der Funktionalität der HS abhängig. Durch Einsatz einer modifizierten HS konnte die dominierende Rolle phenolischer/acider OH-Gruppen für die Np(V)-Reduktion durch HS nachgewiesen werden.

Der Einfluss von HS auf die U(VI)- und Np(V)-Sorption am Kaolinit wurde in Batchexperimenten untersucht. In Abhängigkeit von den experimentellen Bedingungen beeinflusst HS die Sorption und folglich die Mobilität von U(VI) und Np(V). Untersuchungen zur U(VI)-Sorption an synthetisch hergestellten Huminstoff-Kaolinit-Sorbaten ergaben, dass Struktur und Funktionalität der sorbierten/assoziierten Huminstoffe einen wesentlichen Einfluss auf das Sorptionsverhalten von U(VI) ausüben. Mittels Röntgenabsorptionsspektroskopie und TRLFS wurde die Struktur von U(VI)-Kaolinit-Oberflächenkomplexen in Gegenwart von HS bestimmt und mit der von U(VI)-Kaolinit-Komplexen verglichen.

Studien zur Migration von HS und U(VI) im Laborsystem Kaolinit-Wasser erfolgten in Diffusionsexperimenten. Die Migration von HS im kompaktierten Ton wird durch Diffusion beherrscht und von ihren kolloidalen Eigenschaften beeinflusst. Huminstoffe üben eine immobilisierende Wirkung auf den Transport von U(VI) im kompaktierten Kaolinit aus.

1 Introduction

The long-term risk assessment and conception of a future nuclear waste repository requires detailed knowledge of the migration behavior of actinides. The migration of actinides in a potential host rock formation as well as their transport after a possible release from the repository in the aquifer has to be known for the selection of a suitable host rock. For that a comprehensive and reliable thermodynamic database is necessary. A substantial database is already available for salt as possible host rock formation, whereas for clay formations and granite studies are still necessary.

The behavior of actinides in an aquifer system can be strongly determined by humic substances, organic macromolecules ubiquitous found in natural environments. Because of their solubility in the pH range of natural waters, their ability for complex and colloid formation as well as their redox properties, they can considerably influence the transport of actinides. Most natural clays are closely associated with natural organic matter, e.g., humic acid- and fulvic acid-like compounds, which can be mobilized from the clay. Both, organic compounds associated with the clay as well as released from the clay are able to influence the migration behavior of metal ions, such as actinides.

Aim of this project was to study basic interaction processes of actinides in the system clay-humic substance-aquifer. The performed works tend to a better processes understanding as well as to a completion of the thermodynamic database, which allows the formulation of more realistic geochemical models and consequently, a more realistic long-term risk assessment. The main focus was on the generation of thermodynamic data on the influence of humic acids (HA) on the migration of uranium and neptunium in clay formations. For these studies kaolinite was chosen as model mineral. The performed investigations can be divided in the synthesis and characterization of HA model substances as well as complexation, sorption and migration studies.

In order to amend the thermodynamic database under environmentally relevant conditions, interactions in the system actinide-HA-water were investigated. To that belong studies of the U(VI) complexation by HA in the neutral pH range and of the redox stability of Np(V) in presence of different humic substances. The impact of HA on the U(VI) and Np(V) sorption onto kaolinite as well as the U(VI) migration in compacted kaolinite was studied in batch and diffusion experiments, respectively. For the future modeling of the U(VI) sorption onto kaolinite, U(VI)-kaolinite-surface complexes in presence and absence of HA were spectroscopically investigated.

A further aim of this project was the improvement of the knowledge of the interaction behavior of HA with metal ions, which contribute to the specification of existing thermodynamic models for the HA metal ion complexation. The influence of HA functional groups, other than oxygen-containing, on the metal ion complexation by HA is widely unclear. Nitrogen-containing HA model substances were synthesized and spectroscopically analyzed to identify nitrogen functional groups in HA. Based on these results first model investigations were performed to study the influence of nitrogen-containing functional groups on the U(VI) complex formation by HA. Furthermore, the impact of clay minerals on the formation of humic

substances and humic substance-kaolinite-sorbates and their properties was studied using synthetic HA.

This research project was performed in collaboration with the R&D projects of the Universities of Mainz (02 E 9653), Saarbrücken (02 E 9683), Potsdam (02 E 9924), München (02 E 9693), and Heidelberg (02 E 9703) and the Institute for Interdisciplinary Isotope Research Leipzig (02 E 9663) that were funded by Bundesministerium für Wirtschaft (BMWi). The project partners worked in cooperation with the Institute for Nuclear Waste Management (INE), Forschungszentrum Karlsruhe. Furthermore, the Institute of Radiochemistry (TU München) was an associated partner of the joint project.

2 Kaolinite

Within the framework of the joint project kaolinite KGa-1b (IN 47907-2054) from the Clay Minerals Society Source Clays Repository (Washington County, Georgia) was used as model mineral. Kaolinite KGa-1b is a well-crystallized kaolin, which was selected to replace the exhausted stock of kaolinite KGa-1. A comprehensive summary of the origin and analysis of kaolinite KGa-1b is given by Costanzo and Guggenheim (2001).

Kaolinite KGa-1b was characterized with regard to its structure, mineralogical and elemental composition, cation exchange capacity (CEC), and surface area within the project (Křepelová, 2006a) and the data were compared to literature. In the following some characteristics of kaolinite KGa-1b are summarized.

The grain size of KGa-1b amounts to 57.8% < 2 µm and 32.0% < 0.5 µm. The total organic carbon (TOC) content for unprocessed KGa-1b was determined to be 231 ppm (Pruett and Webb, 1993). Kaolinite KGa-1b is moderately hydrophilic and has a large negative ξ potential (-49.2 mV at pH 7.3-7.5, I: 0.015 M; Wu, 2001). The point of zero charge (p.z.c.) and point of zero net proton charge (p.z.n.p.c.) are reported to be 6.0 (Redden et al., 1998) and 5.1±0.2 (Sutheimer, et al., 1999) or 4.99 ± 0.03 (Schroth and Sposito, 1997), respectively.

Figure 2.1 shows the XRD spectrum of kaolinite KGa-1b which was measured with a Bruker-AXS D5005 powder diffractometer. The spectrum shows typical reflections for kaolinite. There is a peak at diffraction angle 25, which belongs to TiO_2 in the form of anatase. The spectrum is comparable with those reported in literature (e.g., Chipera and Bish, 2001). The measured FTIR spectrum of kaolinite KGa-1b (not shown) exhibits the typical spectrum for a well-crystallized kaolinite. The assignment of absorption bands (Křepelová, 2006a) matches the literature data very well (Madejová and Komadel, 2001).

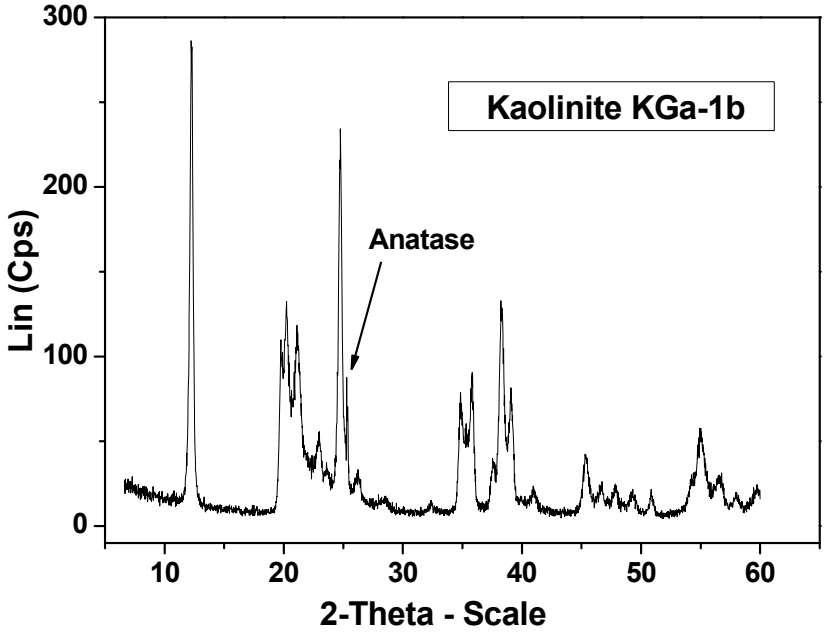

Fig. 2.1: XRD spectrum of kaolinite KGa-1b.

The chemical composition of KGa-1b was measured by ICP-MS (ELAN 6000, Perkin Elmer) after acidic digestion (HNO_3:HCl:HF = 3:1:1) in a microwave oven (Multiwave, Perkin Elmer). Table 2.1 summarizes selected data in comparison to literature values.

The cation exchange capacity (CEC) of kaolinite KGa-1b was determined by the compulsive exchange method (Sumner and Miller, 1996). The value determined in this work amounts to 1.8 meq/100 g. It is slightly lower than that reported with 3.0 meq/100 g by Borden and Giese (2001). This differences could be caused by the application of different method for the determination of CEC. Furthermore, due to the omnipresent impurities, it is generally difficult to determine true CEC values of clay minerals.

The surface area of kaolinite KGa-1b was determined by BET measurement (Oberflächenanalysator SA 3100, Beckman Coulter). It amounts to 11.8 m^2/g. This value agrees very well with the data reported by Pruett and Webb (1993).

Kaolinite KGa-1b was used without any pre-treatment for the experiments described in this report.

Tab. 2.1: Chemical composition of kaolinite KGa-1b (selected data) in comparison to literature.

Compound/Element (wt%)	This work Untreated KGa-1b	Literature (Pruett and Webb, 1993) < 44 μm
Al_2O_3	47.85	39.2
SiO_2	42.98	45.1
TiO_2	1.45	1.66
Fe_2O_3	0.27	0.21
CaO	< 0.06	0.03
K_2O	0.01	0.02
U (ppm)	3.69	1.96 (Kogel and Lewis, 2001)

3 Natural and synthetic humic acid reference materials

As in the previous projects (Pompe et al. 2000a, Sachs et al., 2004), commercially available natural HA from Aldrich (AHA; Aldrich, Steinheim, Germany) was used as reference material for natural HA. Before use, the sodium salt of AHA (Batch H1, 675-2) was purified by repeated dissolution with 0.1 M NaOH (0.01 M NaF) and precipitation with HCl according to the purification method described by Kim and Buckau (1998). AHA batch A2/98 was applied, whose purification is described in detail in (Sachs et al., 2004).

In addition to AHA, synthetic HA type M42 (batch M145) and ^{14}C-labeled HA type [^{14}C]M42 (batch M170 and M180) were used as synthetic HA reference materials (Pompe et al., 1998; Sachs et al., 2004). HA type M42 was synthesized starting from a mixture of xylose, glutamic acid and water. The ^{14}C-labeled HA type M42 was prepared according to the unlabeled product, however, applying ^{14}C-labeled glutamic acid as precursor substance. The synthesis of HA type M42 and [^{14}C]M42 is described in detail in (Sachs et al., 2004). Table 3.1 summarizes main properties of the applied HA. Further details on the HA characterization are given by Sachs et al. (2004).

Tab. 3.1: Main characteristics of the HA applied in this project according to Sachs et al. (2004).

HA	*Elemental composition* C (%)	H [a] (%)	N (%)	S (%)	O [b] (%)	Ash (%)	Moisture (%)
AHA (batch A2/98)	*58.6 ± 0.1*	*3.0 ± 0.1*	*0.8 ± 0.1*	*3.8 ± 0.1*	*23.5 ± 0.1*	*2.39*	*7.9*
M42 (batch M145)	*56.1 ± 0.3*	*4.1 ± 0.1*	*4.4 ± 0.1*	*-*	*26.8 ± 0.3*	*0.11*	*8.4*

HA	*Functional groups* COOH [c] (meq/g)	PEC [d] (meq/g)	Phenolic/acidic OH [e] (meq/g)
AHA (batch A2/98)	*4.49 ± 0.14*	*4.60 ± 0.08*	*3.1 ± 0.1*
M42 (batch M145)	*3.76 ± 0.09*	*3.51 ± 0.07*	*2.0 ± 0.2*
[^{14}C]M42 (batch M170)	*3.63 ± 0.03*	*3.55 ± 0.05*	*not measured*
[^{14}C]M42 (batch M180)	*3.59 ± 0.01*	*3.36 ± 0.53*	*not measured*

HA	*Specific Activity (^{14}C)*
[^{14}C]M42 (batch M170)	*2.38 MBq/g*
[^{14}C]M42 (batch M180)	*17.0 MBq/g*

[a] Corrected for the water content of the HA. [b] The oxygen content was calculated from the difference to 100% in consideration of the ash and moisture content of the HA. [c] Determined by calcium acetate exchange (Schnitzer and Khan, 1972). [d] PEC: Proton Exchange Capacity. Determined by potentiometric titration. [e] Radiometrically determined (Bubner and Heise, 1994).

In addition to AHA and M42, further natural and synthetic HA were used for the study of the Np(V) reduction in presence of HA as well as for some sorption studies. For the description of these humic materials see the corresponding chapters 9 and 11, respectively.

4 Nitrogen-containing humic acid model substances: synthesis and characterization by ^{15}N-NMR spectroscopy

Humic substances contain nitrogen, although in very different and occasionally very small amounts (e.g., 0.8-4.3% N in HA; Stevenson, 1994). It is very probable that the nitrogen in humic substances is derived from amino acids or peptides as biochemically induced fragments of proteins. Its fixation takes place during humification and occurs in several ways (Ziechmann, 1994). One possible way is the condensation of reducing sugars and α-amino acids (melanoidin formation), which is used for the synthesis of HA-alike substances (e.g., Pompe et al., 2000a). The nitrogen associated with humic and fulvic acids cannot be accounted for in known compounds. It occurs in different types of linkages such as in form of free amino groups (-NH_2), open chain groups (–NH-, =N-), and as part of heterocyclic rings (-NH- of indole and pyrrole, -N= of pyridine) (Stevenson, 1994).

To which extent nitrogen-containing functional groups contribute to the complexation process of HA with metal ions is widely unknown so far and not considered in thermodynamic models describing the HA-metal ion-complexation. Up to now the complexation behavior of humic substances is mainly attributed to their oxygen-containing functional groups. In order to elucidate the impact of nitrogen-containing functional groups on the HA complexation behavior, metal ion complexation studies with suitable nitrogen-containing model compounds has to be performed and the results of these studies have to be compared with those obtained with corresponding oxygen-containing substances. In order to get more detailed information on the kind of nitrogenous functionalities in HA, synthetic HA type M1 (Pompe et al., 1996; Pompe et al., 2000a) was ^{15}N-labeled and characterized by solid-state ^{15}N-NMR spectroscopy.

4.1 Synthesis of a ^{15}N-labeled humic acid

^{15}N-labeled HA type M1 ([^{15}N]M1) was synthesized from 3.4 g xylose (Merck), 1.0 g ^{15}N-L-phenylalanine (Berlin Chemie), 0.5 g glycine (Merck), and 8 mL water. This mixture was refluxed in a nitrogen stream for 10 h. The HA-like melanoidin fraction was separated from the reaction mixture as described in (Pompe et al., 1996), dialyzed against purified water (dialysis tubes Thomapor®, exclusion limit MWCO < 1000, Roth), and lyophilized. For comparison, an unlabeled HA type M1 was synthesized under identical conditions, however, using non-labeled L-phenylalanine (Merck) as starting material. Table 4.1 summarizes the elemental composition and the functional group content of the synthesized HA. The FTIR spectra (FTIR spectrometer Spectrum 2000 GX, Perkin Elmer; KBr method) are shown in Fig. 4.1.

Both batches of HA M1 and [^{15}N]M1 show comparable elemental compositions, functional group contents and FTIR spectra indicating a high reproducibility of the synthesis when L-phenylalanine or ^{15}N-L-phenylalanine are used as precursor substances.

Tab. 4.1: Characterization of HA M1 and [^{15}N]M1.

	Elemental composition				
	C (%)	H (%)	N (%)	S (%)	O (%) [a]
M1 (batch S1/05)	63.07 ± 0.08	5.69 ± 0.18	5.44 ± 0.01	-	25.81 ± 0.10
[^{15}N]M1 (batch S2/05)	62.76 ± 0.13	5.67 ± 0.17	5.43 ± 0.01	-	26.15 ± 0.30
	Functional groups				
	COOH (meq/g) [b]		PEC (meq/g) [c]		
M1 (batch S1/05)	1.50 ± 0.06		1.74 ± 0.22		
[^{15}N]M1 (batch S2/05)	1.49 ± 0.01		1.84 ± 0.12		

[a] The oxygen content was calculated from the difference to 100%. [b] Determined by calcium acetate exchange (Schnitzer and Khan, 1972). [c] PEC: Proton Exchange Capacity. Determined by potentiometric titration.

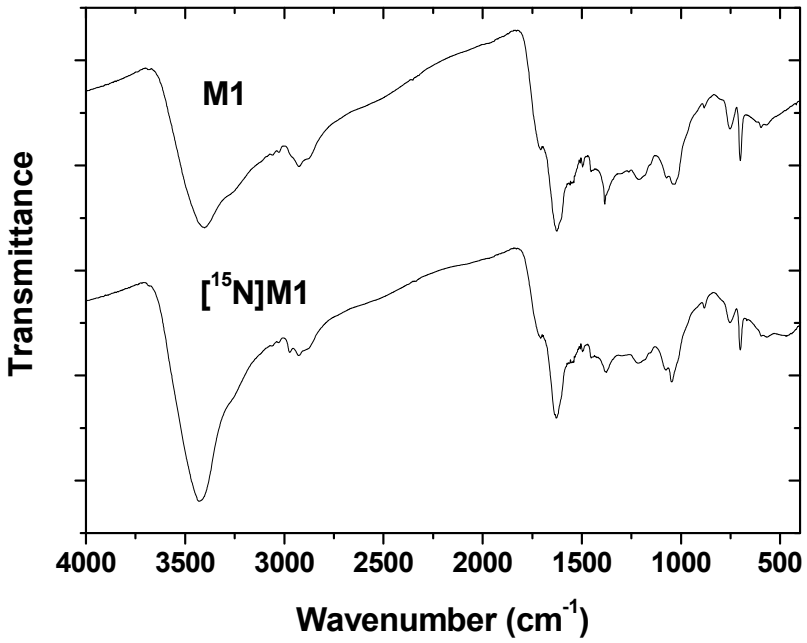

Fig. 4.1: FTIR spectra of synthetic HA type M1 and [^{15}N]M1.

4.2 NMR spectroscopic characterization of the ^{15}N-labeled humic acid type M1

To identify nitrogen-containing functional groups, HA type [^{15}N]M1 was analyzed by ^{15}N-NMR spectroscopy. Solid-state ^{15}N-NMR measurements were carried out by Dr. E. Brendler (Institute of Analytical Chemistry, TU Bergakademie Freiberg) using the technique of cross polarization with magic-angle spinning (CP/MAS). The ^{15}N-NMR spectra were recorded on a Bruker Avance 400 MHz WB spectrometer equipped with a 7 mm probehead. Contact times of 1 and 5 ms, repetition rates of 1 or 3 s, and rotation frequencies between 4 and 7 kHz were applied. The samples were filled into 7 mm ZrO_2 rotors. Chemical shifts were measured relative to nitromethane (= 0 ppm). For comparison, spectra of [^{15}N]-L-phenylalanine and unlabeled HA type M1 were recorded. The peak assignment is based on data collections for ^{15}N-NMR chemical shifts of organic compounds and humic substances (e.g., Berger et al., 1992; Bortiatynski et al., 1996).

Fig. 4.2 shows the ^{15}N-NMR spectrum of ^{15}N-L-phenylalanine. The spectrum shows one resonance signal at -336.3 ppm. This signal is attributed to the NH_2 group of phenylalanine. It agrees very well with literature data (neutral form of phenylalanine: -335.0 ppm; Berger et al., 1992).

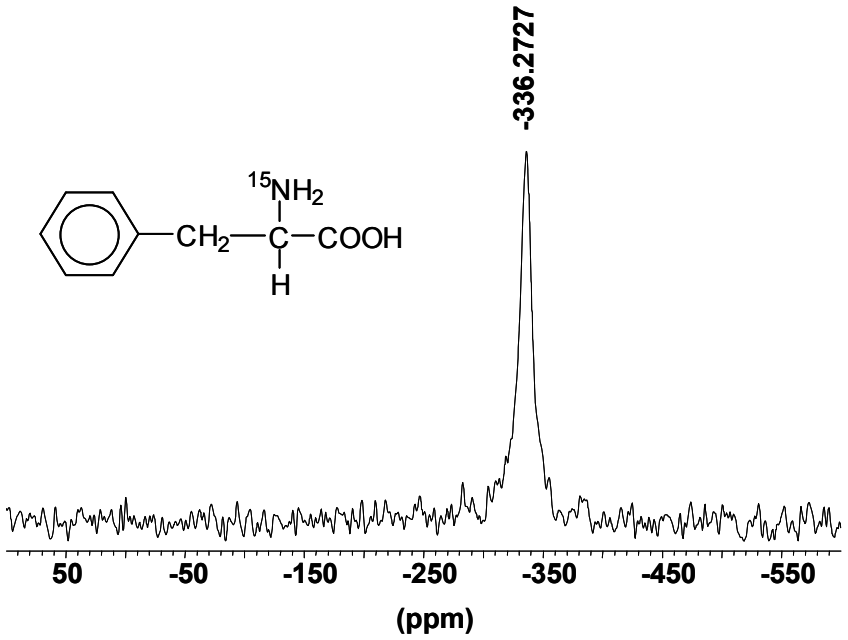

Fig. 4.2: ^{15}N-NMR spectrum of [^{15}N]-L-phenylalanine (4 kHz; contact time: 1 ms; repetition time: 3 s).

A ^{15}N-NMR spectrum of HA [^{15}N]M1 is depicted in Fig. 4.3. The spectrum shows different resonance signals between –150 and –350 ppm indicating the presence of various nitrogen-containing functionalities in the HA structure. It is dominated by signals at –223, –258, and -322 ppm.

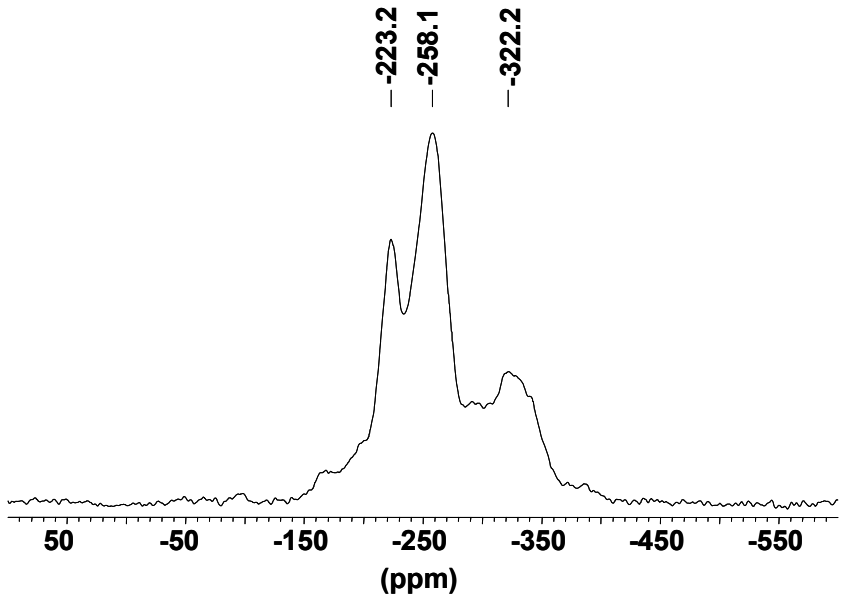

Fig. 4.3: ^{15}N-NMR spectrum of HA [^{15}N]M1 (5 kHz, contact time: 1 ms; repetition rate: 3 s).

In order to verify that the measured NMR signals are real resonance signals and no spinning side bands, the HA sample was measured at different rotation frequencies (Fig. 4.4). The main signals and shoulders in the spectra obtained with 5 and 7 kHz (contact time 5 ms) are nearly identical. Thus, it was concluded that the signals are real ^{15}N chemical shifts of the synthetic HA.

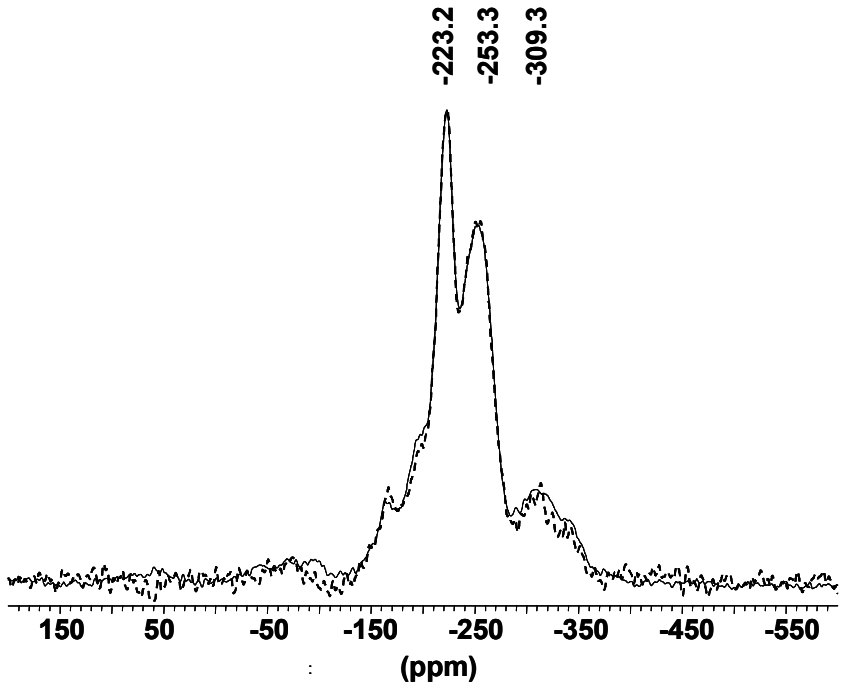

Fig. 4.4: ^{15}N-NMR spectra of HA [^{15}N]M1 measured at different rotation frequencies (solid line: 5 kHz, dashed line: 7 kHz; contact time: 5 ms; repetition rate: 3 s).

The recording of ^{15}N-NMR spectra is based on an indirect magnetization method. Thereby, the protons of a sample are excited and transfer their magnetization to the ^{15}N nuclei by irradiating the resonance frequencies of ^{1}H and ^{15}N during a contact time τ_{CP}, which results in an enhancement of the ^{15}N signal. In general, the enhancement maximum for proton free environments is found at longer τ_{CP} than for proton carrying groups. To distinguish between proton-free, heterocyclic and proton-rich nitrogen in the HA, the sample was measured with different contact times. Figure 4.5 shows the spectra of HA [^{15}N]M1 recorded with 1 and 5 ms contact time. The increase in the contact time results in an intensity increase of the signals between -150 and –200 ppm. In contrast to that, the signals at –255 ppm and about –315 ppm have higher intensity at shorter contact time. From that it can be concluded, that the chemical shifts up to –200 ppm are due to hydrogen-free heterocyclic structural elements, whereas the others can be ascribed to amide and/or amino groups.

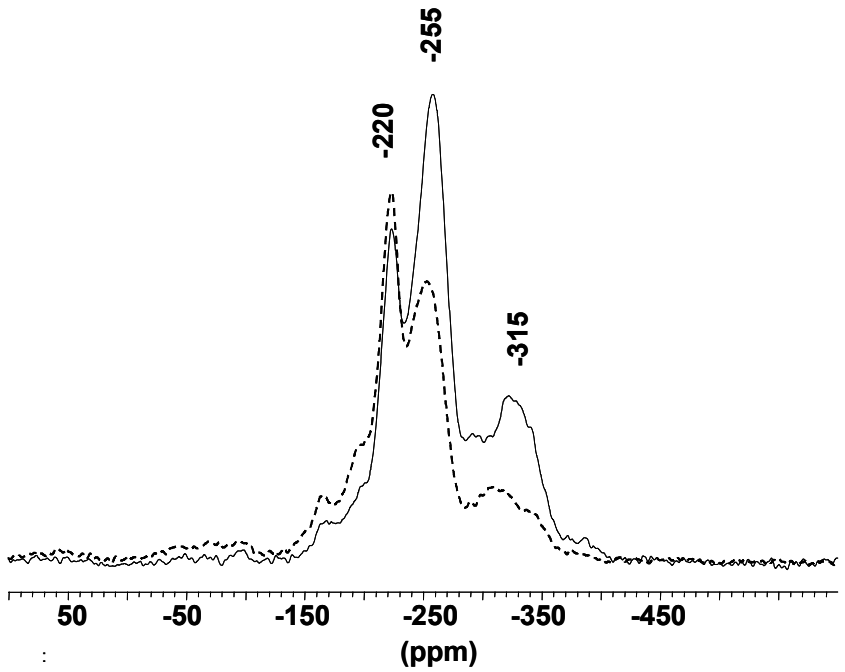

Fig. 4.5: ^{15}N-NMR spectra of HA [^{15}N]M1 measured at different contact times (solid line: 1 ms, dashed line: 5 ms; 5 kHz; repetition rate: 3s).

Based on the peak assignments given in the literature (Bortiatynski et al., 1996), the main resonance signals in the spectra of HA [^{15}N]M1 can be attributed to NH in pyrroles, indoles and/or amides (-220 ppm), NH in amide structures (–255 ppm), and to primary and secondary amines (NH, NH_2, -315 ppm). The shoulders between –150 and –200 ppm can be ascribed to N-substituted pyrroles and/or indoles or heterocyclic -N= sites in these compounds. Comparable types of nitrogen were already found for condensation products of xylose, glycine and water synthesized with varying reaction times (Benzing-Purdie and Ratcliffe, 1986).

Free NH_2 groups of amino acids exhibit resonance signals between –325 and –350 ppm (Bortiatynski et al., 1996). The ^{15}N-NMR spectra of [^{15}N]M1 show a broad unresolved signal in this spectral range, which is more intensive at lower contact time. This broad signal could be a result of overlapping chemical shifts of primary and/or secondary amines and terminal amino acid groups.

The ^{15}N-NMR spectrum of unlabeled HA M1 is shown in Fig. 4.6. Due to the low natural abundance of ^{15}N, the signal-to-noise ratio of this spectrum is very low, even after 36 h of measuring time. However, a resonance signal at –254 ppm with a shoulder at about -220 ppm was observed. These signals correspond to the main peaks in the spectrum of HA [^{15}N]M1 and can be attributed to NH in heterocyclic and amide structures.

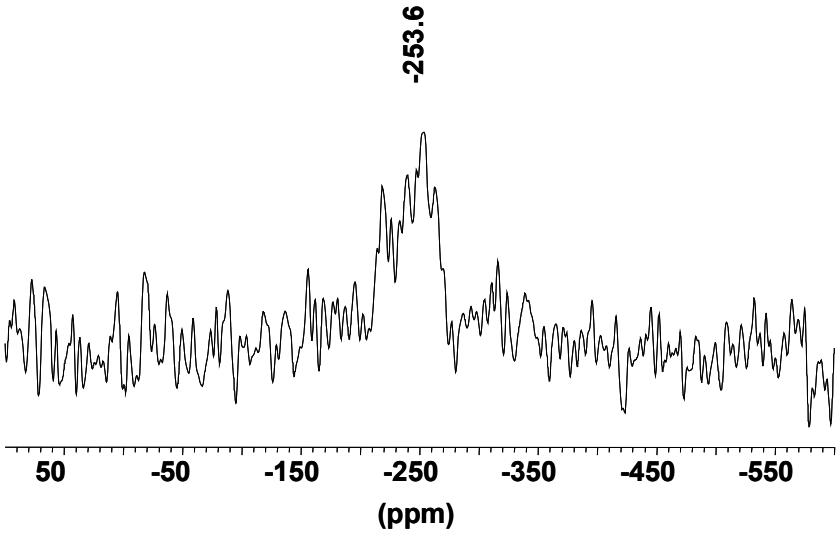

Fig. 4.6: ^{15}N-NMR spectrum of HA M1 (4 kHz; contact time: 1 ms; repetition rate: 1 s; measuring time: 36 h).

The ^{15}N-NMR spectra show that the amino groups of [^{15}N]phenylalanine are for the most part transformed into different heterocyclic and amide nitrogen functions. From the linewidth of the resonances can be concluded that no single, defined compound is formed but a heterogeneous, amorphous material.

Nevertheless the interpretation of the ^{15}N-NMR spectra is difficult and not clear in each case. The resonance signals are broad due to a distribution of bond length and angles at nitrogen in the above mentioned chemical environments. In addition to that, signals in one resonance range can be assigned to different nitrogen-containing structures. However, from our studies it can be concluded that the nitrogen in synthetic HA type M1 can be attributed to pyrrole and/or indole like N, amide N, primary and/or secondary amine N, and possibly N in terminal amino acid groups. Our obtained data agree well with nitrogen structures for natural organic matter discussed in the literature (e.g., Stevenson, 1994).

In conjunction with literature data for natural organic matter, these NMR results represent a base for the suitable selection of model ligands to elucidate the impact of nitrogen functionalities on the metal ion complexation behavior of HA.

5 Synthesis of humic substances in presence of kaolinite and formation of humic substance-kaolinite-sorbates

Clay minerals are able to bind manifold organic compounds at their outer surfaces or within the interlayers. Depending on the clay type, organic compounds are bound by intercalation, complexation, solvation, and ion exchange (Lagaly, 1993).

Most natural clays are closely associated with natural organic matter. If organic compounds are mobilized from the clay rocks, they can influence the sorption behavior of metal ions, such as actinides. Claret et al. (2003) described the generation of humic and fulvic acid-like compounds from Callovo-Oxfordian clay under alkaline conditions, which could be an important source of complexing mobile organic matter, which probably influences the mobility of actinide ions. In addition, clay minerals can catalyze the formation of humic substances. Taguchi et al. (1986) found that montmorillonite is able to promote the formation of humic substance-like melanoidins from glucose and glycine or alanine.

The objective of our work was to study the influence of kaolinite KGa-1b on the formation of synthetic HA and their properties. Furthermore, we investigated the formation of humic substance-kaolinite-sorbates as model compounds for natural organic matter-containing clays.

5.1 Synthesis of humic acid type M1 and M42 in presence of kaolinite

HA type M1 (Pompe et al., 1996) and M42 (Pompe et al., 1998) were synthesized in presence of kaolinite KGa-1b based on their standard synthesis methods. For synthesis of HA type M1 the following two methods were applied.

Method A): 17 g xylose (Merck), 5 g phenylalanine (Fluka), 2.5 g glycine (Merck), 2 g kaolinite, and 40 mL water were refluxed in a nitrogen stream for 10 h. The solid reaction product was separated by centrifugation and ground with ethanol and ether. The HA-like melanoidin fraction was extracted from the solid product with 2 M NaOH under nitrogen atmosphere and precipitated by 2 M HCl. The HA precipitate was dialyzed against purified water (dialysis tubes Thomapor®, exclusion limit MWCO < 1000, Roth) and lyophilized. The remaining NaOH insoluble solid fraction containing kaolinite and an alkaline less or not soluble melanoidin fraction was repeatedly washed with Milli-Q water and then lyophilized. A synthetic HA type M1-K(A) and a humic substance-kaolinite sorbate M1-KS(A) were obtained as synthesis products.

Method B): Method B starts with a diluted reaction mixture. 17 g xylose, 5 g phenylalanine, 2.5 g glycine, 2 g kaolinite, and 200 mL water were boiled under reflux in a nitrogen stream for 10 h. After separation, the solid reaction product was ground with ethanol and ether, washed with water, dialyzed (dialysis tubes Thomapor®, exclusion limit MWCO < 1000, Roth), and lyophilized. Then, synthetic HA M1-K(B) was isolated by alkaline extraction, however, using only 0.1 M NaOH, and acid precipitation with 2 M HCl. The remaining NaOH in-

soluble solid was neutralized, dialyzed, and lyophilized resulting in the humic substance-kaolinite-sorbate M1-KS(B).

The synthesis of HA type M42 in presence of kaolinite KGa-1b starts also from a diluted reaction mixture. 16.5 g xylose, 11 g glutamic acid monohydrate (Fluka), 2 g kaolinite, and 150 mL water were kept under reflux at 80 °C for 90 h. The isolation of HA type M42-K and of the synthetic humic substance-kaolinite-sorbate M42-KS was carried out according to method B.

Parallel syntheses were performed in absence of kaolinite resulting in HA type M1-A (method A), M1-B (method B), and M42.

The pH values of the reactions mixtures were measured at the start and the end of the syntheses. It was found that the presence of kaolinite exhibits no clear pH effect. This is in contrast to observations during the reaction of glucose with glycine or alanine in presence of montmorillonite (Taguchi et al., 1986). Due to reactions between exchangeable cations present in montmorillonite and the cation-exchange capacities of the melanoidins, montmorillonite caused an constant increased pH value in the reaction mixtures resulting in a promotion of the melanoidin formation. The different behavior of kaolinite and montmorillonite can be attributed to their different cation exchange capacities which amount to 1.8 and 70-120 meq/100 g for kaolinite KGa-1b (see chapter 2) and montmorillonite, respectively (Lagaly, 1993).

5.2 Characterization of humic acids synthesized in presence of kaolinite

The obtained HA were characterized with regard to their elemental composition (C, H, N, Al, Si), functionality (COOH) and structure (FTIR spectroscopy; FTIR spectrometer Spectrum 2000 GX, Perkin Elmer; KBr method). Results for three selected parallel syntheses in absence and presence of KG1a-1b are summarized in Tab. 5.1.

From Tab. 5.1 it becomes obvious, that for all HA syntheses in presence of kaolinite the yields on HA-like substances are lower than those of syntheses in absence of kaolinite. These differences could be attributed to the sorption of humic substances onto kaolinite, which probably promotes the formation of higher polymerized substances which are less or not at all soluble in alkaline solutions compared to the extracted HA. The decrease of the initial precursor concentrations for the synthesis of HA type M1 (method A $\rightarrow$ method B) results in a significant decrease in the yield on HA-alike substances as expected.

Tab. 5.1.: Characterization of selected HA type M1 and M42 synthesized in absence and presence of Kaolinite KGa-1b.

	HA Type M1					
	Method A		Method B		HA Type M42	
	M1(A)	M1-K(A)	M1(B)	M1-K(B)	M42	M42-K
Batch	M183	M182K	M191	M189K	M194	M192K
Yield (mg)	2530	2290	356	77	196	137
C (%)	61.5	61.5	60.3	56.3	55.5	55.2
H (%)	5.6	5.5	6.0	5.8	4.9	5.4
N (%)	5.2	5.2	5.8	5.8	4.7	5.5
Si (ppm)[a]	<40	<32	8	2948	<NWG	<600
Al (ppm)[a]	76	143	20	4688	<80	4377
COOH (meq/g)[b]	1.39 ± 0.03	1.45 ± 0.01	1.21 ± 0.22	1.30 ± 0.21	2.94 ± 0.15	2.34 ± 0.13

[a] Measured by ICP-MS after digestion of the HA with HNO_3 in a microwave oven. [b] Determined by calcium acetate exchange method (Schnitzer and Khan, 1972).

HA type M1(A) and M1-K(A) exhibit comparable elemental compositions and COOH group contents. Furthermore, they show nearly identical FTIR spectra (not shown). Therefore, it can be concluded that the presence of kaolinite has no significant influence on the properties of HA type M1 synthesized according to method A. However, after dilution of the reaction mixture, an influence of kaolinite on the formation of HA M1 becomes obvious. HA M1(B) and M1-K(B) show differences in their elemental compositions, especially in their carbon contents. The lower carbon content of M1-K(B) can be explained by an increase of the Si and Al content in the HA due to the presence of kaolinite. Both HA show similar amounts of COOH groups. Figure 5.1 presents the FTIR spectra of HA M1(B) and M1-K(B) in comparison to kaolinite KGa-1b.

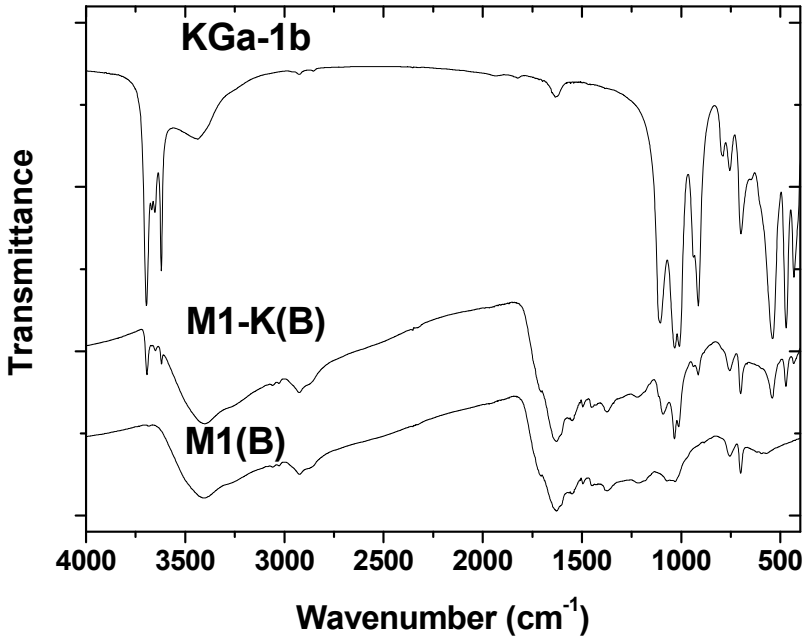

Fig. 5.1: FTIR spectra of HA type M1 synthesized in absence (M1(B)) and presence (M1-K(B)) of kaolinite KGa-1b according to method B in comparison to the spectrum of kaolinite KGa-1b.

Generally, FTIR bands of both HA are comparable. In the spectrum of HA M1-K(B), however, additional IR absorption bands were detected (e.g., at 3700, 3620, 1035, 1010, 905, 540, 470 cm^{-1}) that point to the occurrence of kaolinite residues in this HA. It can be concluded that the elemental composition of HA type M1 is influenced by kaolinite when the HA is synthesized according to method B.

HA M42 and M42-K possess no clear differences in their carbon, hydrogen and nitrogen contents. However, also HA M42-K shows an increased amount of Si and Al, pointing to an association of HA with kaolinite. Again, this is reflected in the FTIR spectrum of M42-K (Fig. 5.2), which exhibits absorption bands, as already found for HA M1-K(B), indicating the presence of kaolinite. The COOH group content of HA M42-K is slightly lower than that of HA M42 which is probably caused by the presence of kaolinite in HA M42-K.

The obtained results indicate that the presence of kaolinite during the HA synthesis mainly influences the yields on HA and their elemental compositions. Furthermore, a slight influence on the carboxyl group content of HA type M42 was observed.

In further syntheses, which are not subject of this report, comparable results were found. However, it was determined that the presence of kaolinite in the syntheses decreases the reproducibility of the product properties. A possible reason for that could be the heterogeneity of the reaction mixture.

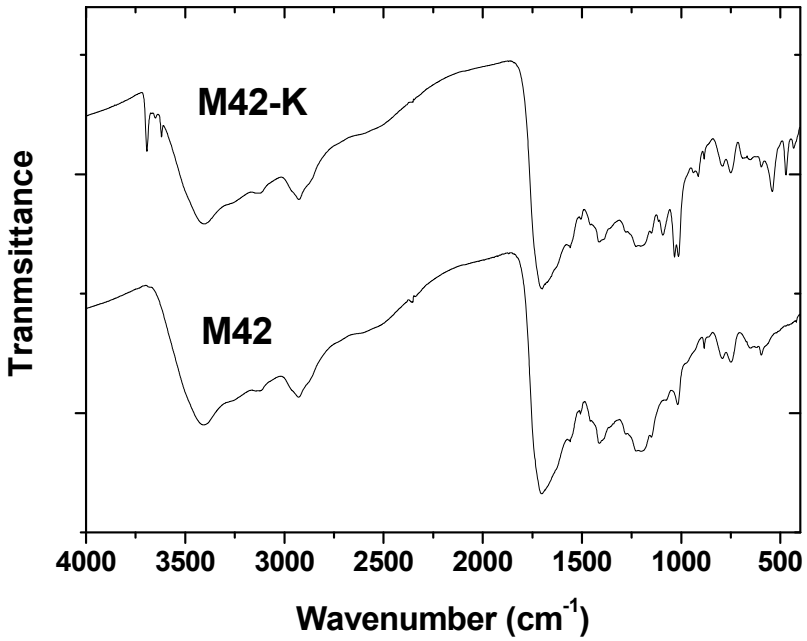

Fig. 5.2: FTIR spectra of HA type M42 synthesized in absence (M42) and presence (M42-K) of kaolinite KGa-1b.

5.3 Characterization of synthetic humic substance-kaolinite sorbates

The synthetic humic substance-kaolinite-sorbates were characterized with regard to their total organic carbon content (TOC) and structure as well as to the distribution of humic substances in the sorbate.

The TOC contents of the humic substance-kaolinite-sorbates were determined using a multi N/C analyzer with additional ELTRA high temperature oven (Analytik Jena). Table 5.2 summarizes the TOC contents of selected synthetic humic substance-kaolinite-sorbates and the derived amounts of humic substances. Comparing the TOC contents of M1-KS synthesized with method A and B (method B was started from a diluted reaction mixture), it can be seen that it is decreased with decreasing precursor concentrations. Consequently, the amount of humic substances associated with kaolinite is decreased. It is assumed that higher polymerized and more hydrophobic substances are associated with kaolinite after the alkaline extraction of the HA-like substances. As expected, the amount of these substances should be increased when a higher starting concentration on precursor substances is used for the synthesis. The TOC contents of the synthetic humic substance-kaolinite sorbates M42-KS that were synthesized under comparable experimental conditions exhibit variations. Batch M192KS shows a significant higher TOC content than the other batches. The lower reproducibility of the synthesis in the heterogeneous reaction mixture could be a reason for that observation.

Tab. 5.2: TOC and humic substance concentrations of selected synthetic humic substance-kaolinite sorbates.

	M1-KS(A)	M1-KS(B)	M42-KS [a]		
Batch	M182KS	M189KS	M192KS	R11/04KS	R1/06KS
TOC (mg/g)	10.4	3.9	24.1	4.9	5.1
HS [b] (mg/g)	17	7	44	9	9

[a] Different batches of synthetic humic substance-kaolinite-sorbates synthesized under comparable experimental conditions. [b] Estimated amount of humic substances (HS) in the sorbate. Calculated based on the carbon content of the corresponding HA.

The structure of the sorbates was analyzed by FTIR spectroscopy (FTIR spectrometer Spectrum 2000 GX, Perkin Elmer; KBr method). The FTIR spectra of the isolated synthetic humic substance-kaolinite-sorbates are dominated by the spectrum of kaolinite. Due to the low concentrations of humic substances in the sorbates (0.7-4 mass%), no or only very weak indications exist in the spectra that point to the occurrence of humic substances in the sorbates. For example, the FTIR spectrum of M42-KS (batch M192KS) in comparison to that of untreated kaolinite is plotted in Fig. 5.3. Both FTIR spectra are dominated by IR absorption bands of kaolinite. Only very small differences occur between 1700 and 1630 cm^{-1}. In this range, the intensity of the spectrum of M42-KS is slightly increased. This intensity increase is attributed to FTIR signals of aromatic structural elements and carbonyl groups of the humic substances associated with kaolinite. Generally, these bands are the most pronounced absorption bands in the spectra of humic substances (cf. Fig. 5.1 and 5.2). Therefore, it is not surprising that no other FTIR signals indicating the presence of humic substances in the sorbates could be detected. The FTIR signals of the original untreated kaolinite are identical to those of kaolinite in the sorbate. This indicates that no significant structural changes of kaolinite occur during the synthesis and the reprocessing procedure.

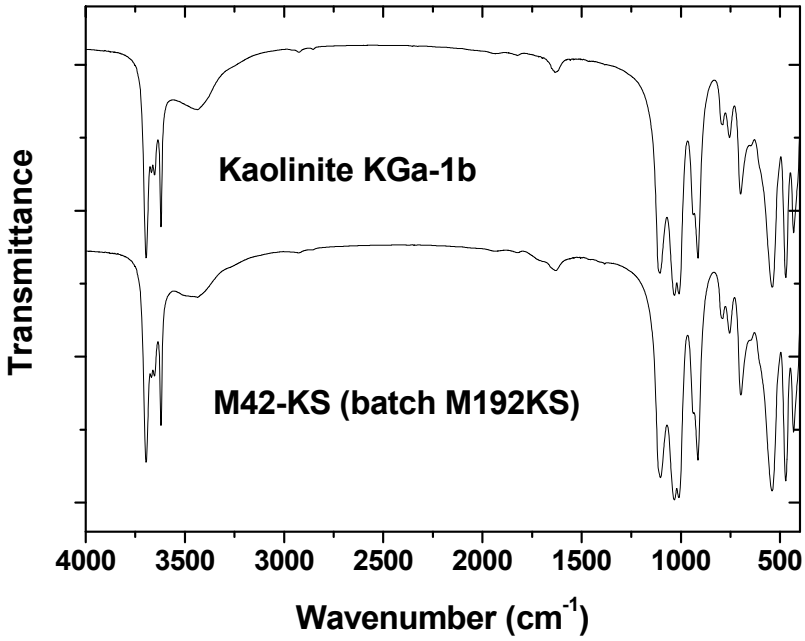

Fig. 5.3: FTIR spectrum of the synthetic humic substance-kaolinite-sorbate M42-KS (batch M192KS) in comparison to the spectrum of kaolinite KGa-1b.

The distribution of humic substances in a kaolinite sorbate type M42-KS (batch R11/04KS) was determined by X-ray photoelectron spectroscopy (XPS) in cooperation with the Institut für Kernchemie, Johannes-Gutenberg University Mainz (Reich et al., 2006a). The results were compared to those of untreated kaolinite KGa-1b as well as to two kaolinite samples with 1.2 and 2.4 mg/g of sorbed HA (Reich et al., 2006a). For the measurements, the powders were pressed into indium foil. Mg Kα radiation (1253.6 eV) was used for the excitation of XPS spectra. The measuring conditions are described in (Reich et al., 2006a). Figure 5.4 shows a section of the XPS spectrum. The main conclusions drawn from the XPS measurements of M42-KS are the following: At the untreated kaolinite surface relatively small amounts of adsorbed hydrocarbons (~1 atom%) were detected. The C1s/Al 2p intensity ratio of all humic samples with varying amounts of humic substances (1.2–9 mg/g) is nearly constant and does not show any correlation with the humic substance loading. Only approximately 5 atom% carbon were found on the surface of the samples. This shows that the surface of the clay particles is not covered by a homogenous layer of humic substances. A part of the humic substances must be distributed between the kaolinite particles. The surface composition of the synthetic humic substance-kaolinite-sorbate sample with respect to Si, Al, and O is comparable to the untreated kaolinite. This indicates that the chemical composition of the kaolinite surface was not altered during the synthesis and reprocessing procedure. A detailed summary of binding energies and XPS line intensities is given in (Reich et al., 2006a).

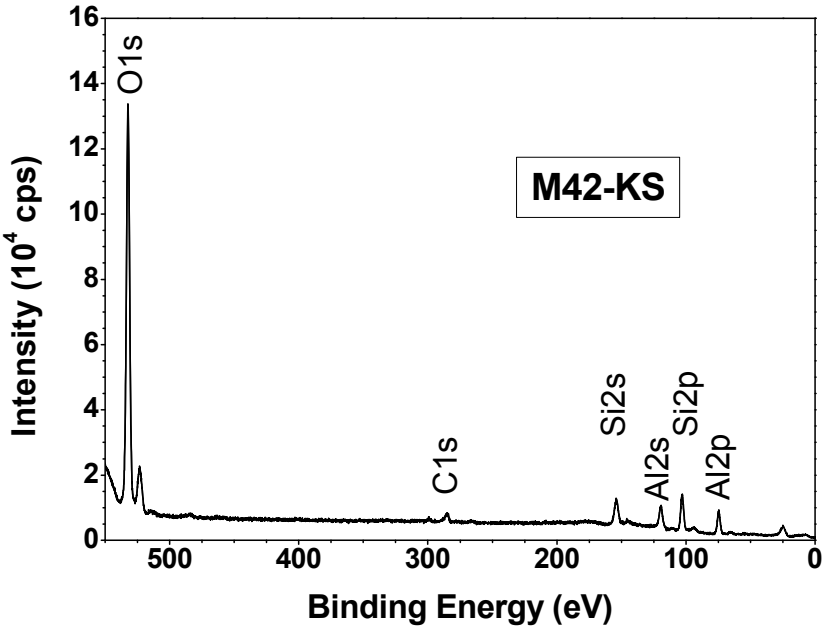

Fig. 5.4: XPS spectrum of a synthetic humic substance-kaolinite-sorbate M42-KS (batch R11/04KS, TOC: 4.9 mg/g).

It can be concluded that it is possible to synthesize humic substance-kaolinite-sorbates. Based on their synthesis this materials contain humic substances that are assumed to be more hydrophobic than synthetic HA-like substances extracted from the sorbates. Such sorbates are suitable model compounds for organic rich clays. Within the present project synthetic humic substance-kaolinite sorbates were used in batch sorption and diffusion experiments (see chapter 11 and 13). The results were compared to those obtained from untreated kaolinite and HA.

6 Studies of the influence of nitrogen-containing functional groups of humic substances of the complex behavior with model compounds

To receive an impression if nitrogen-containing functional groups can influence the interaction between humic substances and actinides even at acidic pH ranges, investigations with uranium(VI) (U(VI)) and some model compounds were done. As model substances were chosen L-phenylalanine (2-amino-3-phenylpropionic acid, C_6H_5-CH_2-$CH(NH_2)$-COOH), for comparison its equivalent without amino function 3-phenylpropionic acid (C_6H_5-CH_2-CH_2-COOH), and glycine (aminoacetic acid, $CH_2(NH_2)$-COOH). The complex behavior of these compounds toward U(VI) at acidic pH values has been studied by TRLFS (time-resolved la-

ser-induced fluorescence spectroscopy) and ATR (attenuated total reflection) FTIR spectroscopy.

6.1 Experimental

Solutions and reagents

The stock solutions of the ligands L-phenylalanine (Merck), 3-phenylpropionate (3-phenylpropionic acid, Aldrich) and glycine (Aldrich) were prepared freshly for each experiment. For TRLFS measurements the stock solution of UO_2^{2+} were made from $UO_2(ClO_4)_2 \cdot 6H_2O$ (Merck). For ATR FTIR measurements a UO_2Cl_2 stock solution was used. It was obtained from $UO_2(NO_3)_2$ (provided from VKTA Rossendorf), which was heated to get UO_3, and the nitrate free oxide was dissolved in 1M HCl. The ionic strength was kept constant by adding a $NaClO_4$ stock solution ($NaClO_4 \cdot H_2O$, Merck) for TRLFS measurements or a NaCl stock solution for ATR FTIR measurements. All stock solutions were prepared with deionized water. Necessary pH adjustments were made with $HClO_4$ (TRLFS), HCl (ATR FTIR) or NaOH with an accuracy of 0.05 units.

TRLFS measurements

The TRLFS measurements were performed at a total uranyl concentration of 10^{-5} M as a function of the ligand concentration (10 different concentrations between $1 \cdot 10^{-5}$ M to $2 \cdot 10^{-3}$ M each) at pH = 4.0 and an ionic strength of 0.1 M ($NaClO_4$).

The spectra were recorded at room temperature using a pulsed Nd:YAG laser system (minilite continuum Electro-Optics, Inc., Santa Clara, USA) with a digital delay/pulse generator (model DG535, Stanford Research systems, Inc., USA). The excitation wavelength of the uranyl fluorescence was 266 nm with pulse energy of 0.2 – 0.5 mJ. The TRLFS spectra were measured from 440 to 620 nm, averaging 3 spectra with 100 laser pulses each, and a gate time of 1 µs. The time-resolved fluorescence emission was detected using a digital triple grating spectrograph (EG&G Princeton Instruments, USA, model 1235). All functions of the laser spectrometer are computer controlled with the program WinSpec/32, version 2.5.19.6, Roper Scientific 2003 (Microsoft corporation).

ATR FTIR measurements

The ATR FTIR measurements were performed with aqueous solutions containing a uranyl-to-ligand ratio of 1 : 1, a concentration of 10^{-2} M, an ionic strength of 1 M (NaCl), and pH = 3.2. At higher pH values precipitation of a not yet defined uranyl compound (either hydroxide and/or complex) was observed.

The infrared spectra were recorded at room temperature with an FTIR spectrometer (Spectrum 2000 GX, Perkin Elmer) and a diamond ATR cell (crystal diameter: 4 mm, 9 reflections). For the experiments a flow cell (volume: 200 µL) with a constant flow rate of 200 µL/min was used. The spectra were calculated out of single beam spectra each co-added from 128

scans at a spectral resolution of 4 cm^{-1} in the wavenumber range from 5200 to 580 cm^{-1}. The results are presented as difference spectra between an aqueous solution of the free ligand and the related uranyl complex in the range from 1800 to 800 cm^{-1}.

6.2 Results and discussion

TRLFS measurements

Figure 6.1 shows the fluorescence spectra of the uranyl ion as a function of the ligand concentration of L-phenylalanine (left) and 3-phenylpropionate (right) at pH = 4.0. Both ligands caused a strong decrease of the fluorescence intensity with increasing concentration. We noticed no shift of the fluorescence peaks. This behavior is typical for static fluorescence quenching due to the complex formation.

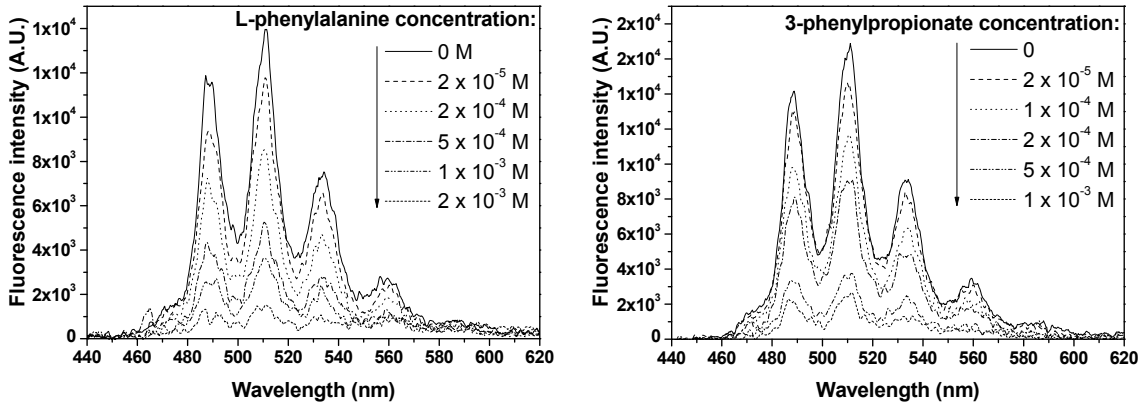

Fig. 6.1: Fluorescence spectra of U(VI) (10^{-5} M) at pH = 4.0 as a function of the ligand concentration of L-phenylalanine (left) and 3-phenylpropionate (right).

The complex formation reaction can be written as:

$$UO_2^{2+} + n\ HL \rightleftarrows UO_2L_n^{(2-n)+} + n\ H^+ \qquad (6.1)$$

Provided that the fluorescence intensity is straight proportional to the concentration of the free uranyl ion, with the following modified logarithmic form of the mass action law

$$\log\frac{[\{UO_2(L)_n\}^{(2-n)+}]}{[UO_2^{2+}]} = n\log[HL] + \log K' + pH \qquad (6.2)$$

the stoichiometry and the complex stability constant can be graphical determined via slope analysis, as demonstrated in Fig. 6.2. For both complex systems a slope (n) near 1 was cal-

culated, indicating a predominant 1 : 1 complex. The intersection offers the equilibrium constant log*K*', which can be converted under consideration of the pH and the pK_a of the ligand into the stability constant logK_{ML} (see Tab. 6.1).

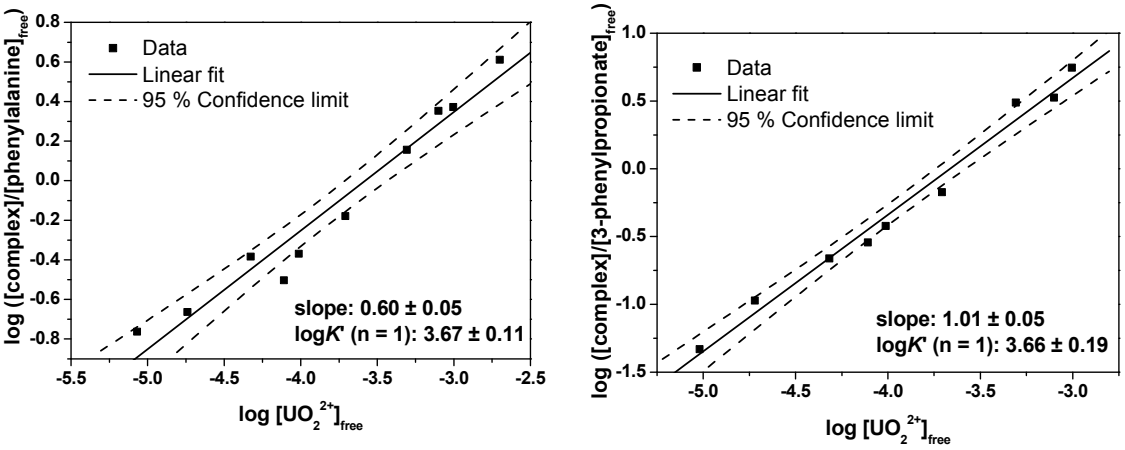

Fig. 6.2: Validation plot (slope analysis) of the complexation of U(VI) with L-phenylalanine (left) and 3-phenylpropionate (right) at pH = 4.0.

The fluorescence decay was mono-exponential in all samples. The lifetime, which belongs to the free uranyl ion, decreases with increasing ligand concentration, as to be seen in Fig. 6.3. This indicates additional dynamic fluorescence quenching, caused by the free ligand.

With the aid of the Stern-Volmer equation (Eq. (6.3)) the lifetimes likewise can be used to calculate the complex stability constants.

$$\frac{\tau_0}{\tau} = 1 + K_{SV} \cdot [Q] \qquad (6.3)$$

τ_0 represents the fluorescence lifetime of the uranyl ion without quencher, and τ is the lifetime with quenching substance Q (free ligand). The Stern-Volmer plots gave straight lines with an intersection of zero within the error limits. Their slope (K_{SV}) represents the complexation constant. Figure 6.4 shows the Stern-Volmer plots for both complex systems.

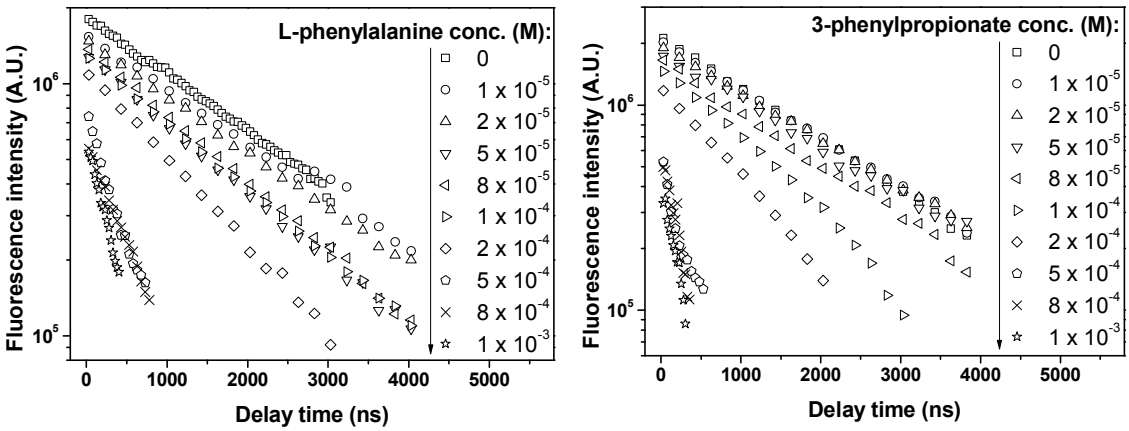

Fig. 6.3: Fluorescence decay of U(VI) as a function of the ligand concentration (dynamic quenching).

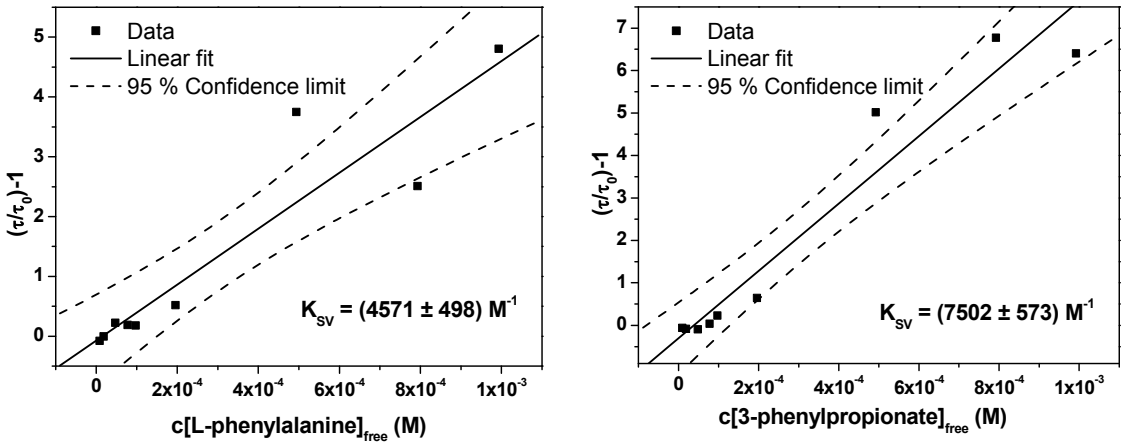

Fig. 6.4: Stern-Volmer plot (dynamic quenching) of U(VI) by L-phenylalanine (left) and 3-phenylpropionate (right).

The Stern-Volmer constant K_{SV} likewise can be converted into the complex stability constant $\log K_{ML}$, taking into account the pH and the pK_a values of the ligand (see Table 6.1).

Both methods to calculate the complex stability constants are well established and described detailed in the literature (e.g., Koban et al., 2003; Geipel et al., 2004; Vulpius, 2005). Table 6.1 summarizes the determined complex stability constants.

Tab. 6.1: Summary of the complex stability constants.

Complex	logK_{ML} (slope analysis)	logK_{ML} (Stern-Volmer plot)	logK_{ML} (average)
L-phenylalanine[a]: $UO_2[C_6H_5\text{-}CH_2\text{-}CH(NH_3)\text{-}COO]^{2+}$	1.91 ± 0.18	1.90 ± 0.07	1.9 ± 0.2
3-phenylpropionate[b]: $UO_2[C_6H_5\text{-}CH_2\text{-}CH_2\text{-}COO]^{+}$	4.06 ± 0.19	4.28 ± 0.08	4.2 ± 0.2

[a] pK_{a1}(COOH) = 2.24 ± 0.07; pK_{a2}(NH_3^+) = 9.16 ± 0.01 (pK_{a2} is not to be considered in the investigated pH range) (Ishimitsu et al., 1977).

[b] pK_a(COOH) = 4.40 ± 0.01 (Hasegawa et al., 1990).

The complex stability constant of the uranyl L-phenylalanine complex (log$K$ = 1.9 ± 0.2) is remarkable smaller than that of the uranyl 3-phenylpropionate complex (log$K$ = 4.2 ± 0.2). This indicates that the amino group, which appears in its protonated form R-NH_3^+ in acidic solution, is not involved in the complexation, but may rather destabilize the complex. This result is in accordance with other investigations (Fernandez-Botello et al., 2002; Moll et al., 2003; Koban and Bernhard, 2006).

ATR-FTIR measurements

Figure 6.5 shows the difference IR spectra of the uranyl L-phenylalanine system (left panel) and of the uranyl 3-phenylpropionate system (right panel). The bands below 1000 cm^{-1} represent the antisymmetric stretching vibration v_{as} of the uranyl cation. The bands at 959 and 957 cm^{-1} can be assigned to the free uranyl ion whereas the complexation of the uranyl cation causes a shift of the v_{as} mode to 928 cm^{-1} (L-phenylalanine) and 926 cm^{-1} (3-phenylpropionate).

In the region between 1600 and 1400 cm^{-1} stretching vibrations of the carboxylate groups are normally observed. Therefore, the absorption peaks at 1457 and 1531 cm^{-1} (L-phenylalanine), and 1458 and 1533 cm^{-1} (3-phenylpropionate) are assigned to the symmetrical (v_s) and antisymmetrical (v_{as}) stretching vibration of the uranyl coordinating carboxylate group, respectively. The spectral region above 1600 cm^{-1} is characterized by the strong absorption band of the water solvent and therefore can not be interpreted accurately.

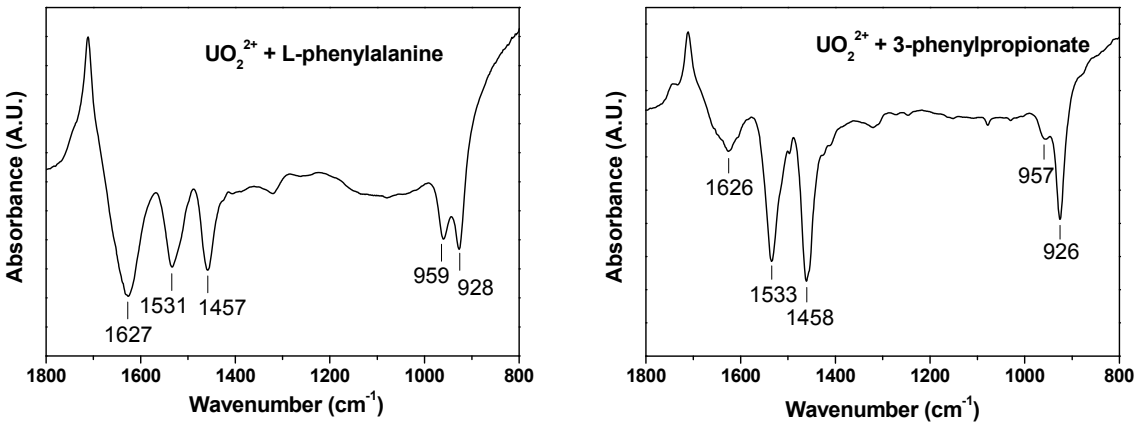

Fig. 6.5: FTIR difference spectra of solutions containing 10 mM UO_2^{2+} and 10 mM ligand at pH 3.2.

The spectra clearly demonstrate that the UO_2^{2+} cation is bound via the carboxylate groups to the ligands since the frequency of the uranyl band around 927 cm^{-1} is typically found for aqueous UO_2^{2+}-carboxylate complexes (Kakihana et al., 1987). Additionally the degree splitting between the v_{as} and v_s mode of the carboxylate group indicates a bidentate binding to the actinide cation (Kakihana et al., 1987).

In the uranyl L-phenylalanine mixture, the v_{as} mode of the free (959 cm^{-1}) and of the complexed (928 cm^{-1}) uranyl ion show nearly the same intensities. In contrast, in the uranyl 3-phenylpropionate complex the v_{as} mode of the complexed uranyl ion (926 cm^{-1}) shows a considerably higher intensity compared to the band of the free uranyl ion (957 cm^{-1}). This is in accordance with the findings by TRLFS, that the 3-phenylpropionate is the stronger complexing agent for the UO_2^{2+} cation.

In the FTIR spectrum of the uranyl L-phenylalanine complex system no bands can be assigned to a coordinating amino group. This underlines the conclusion made from TRLFS measurements, that the amino group is not involved in uranyl complexation under these experimental conditions, especially at acidic pH ranges. However, contributions from amino groups to the spectra might be hidden under the strong difference band of the water solvent above 1600 cm^{-1} and therefore can not be ruled out entirely.

In addition to fluorescence emission and UV-Vis absorbance studies (Günther et al., 2007) FTIR spectroscopic investigations of the U(VI) / glycine system were carried out.

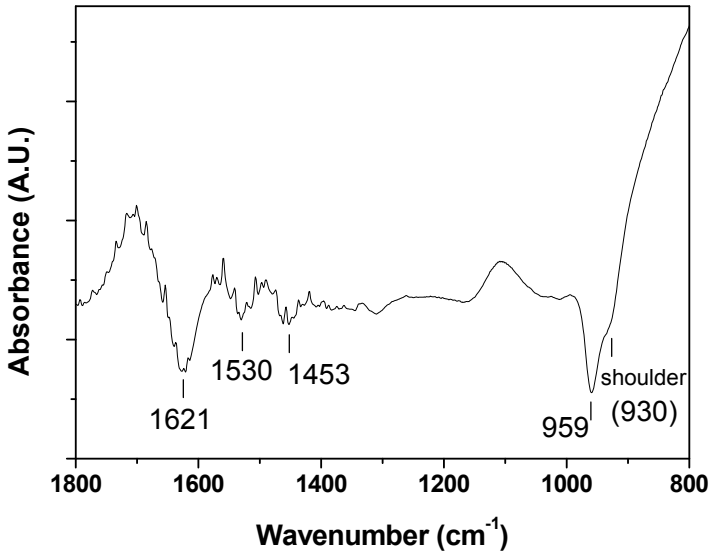

Fig. 6.6: FTIR difference spectra of U(VI) / glycine solution, initial solution contained 10 mM UO_2^{2+} and 10 mM glycine at pH 3.2.

A spectrum of the U(VI)/glycine system is shown in Fig. 6.6. Again, the relative intensities of the uranyl bands at 959 and around 930 cm^{-1} reflect the ratio of the $UO_2^{2+}{}_{aq.}$/UO_2^{2+}-ligand system. The detection of the shoulder indicates the formation of uranyl glycine species. The low intensity of the band of the UO_2^{2+}-glycine complex around 930 cm^{-1} confirms the low complex formation constant and only a small amount of complex species in the solution at a uranyl to ligand concentration ratio of 1:1 as it was found by TRLFS measurements (Günther et al., 2007). Consequently the symmetric and antisymmetric stretching vibration of the carboxylate anion of 1453 and 1530 cm^{-1} also show very low intensities (Fig. 6.6). In homology to the UO_2^{2+}-L-phenylalanine system no contributions of NH_3^+ or NH_2-groups can be identified in the spectra.

In conclusion, the complexation of uranyl with L-phenylalanine and 3-phenylpropionate was examined in acidic solution by TRLFS and FTIR spectroscopy to determine the influence of the amino function on the complexation. Both techniques showed very similar complex behavior of both ligands. The amino function seems not to be involved in the uranyl coordination, but it may rather destabilize the uranyl complex. The results of the investigated U(VI)/ glycine system using TRLFS, UV-Vis and FTIR spectroscopy supports the evidence that the uranyl cation is only bound on the carboxyl group of the amino acid in the acid pH range. To elucidate the impact of nitrogen functionalities on the metal ion complexation behavior of HA, further investigations with other model ligands, which represent alternative N-containing functional groups, should be done.

7 Uranium(VI) complexation by humic acid under neutral pH conditions

Thermodynamic complexation data for the interaction of U(VI) with HA have been determined applying different methods and complexation models (e.g., Shanbhag and Choppin, 1981; Czerwinski et al., 1994; Moulin and Moulin, 1995; Pompe et al., 2000b). These studies were predominantly performed under acidic pH conditions where competing reactions such as hydrolysis and carbonate complexation of the UO_2^{2+} ion are negligible. However, this does not hold for the environmentally relevant pH range. Thus, the formation of ternary U(VI) complexes with HA has to be taken into account for any trustworthy geochemical modeling.

There are only few works investigating the formation of such ternary U(VI) complexes in the presence of HA. Zeh et al. (1997) studied the sorption of the UO_2^{2+} ion onto humic colloids in Gorleben groundwater by ultrafiltration and anion exchange and fitted their data with a uranyl hydroxo humate complex UO_2(OH)HA(I). The solubility of $UO_2(OH)_2$ in presence and absence of HA was investigated by Pashalidis et al. (2006) resulting in complexation data for UO_2(OH)HA. Using the equilibrium dialysis-ligand exchange technique, Glaus et al. (1995) studied the formation of a mixed uranyl carbonato fulvate complex.

In order to improve the thermodynamic data base for the interaction of U(VI) with HA, we studied the complexation of U(VI) with HA at pH 7 in the absence of CO_2. These studies were performed in continuation of our previous work (Pompe et al., 2000a), however, the updated U(VI) complex formation constants compiled in Guillaumont et al. (2003) were used for calculation of the U(VI) speciation in solution. For the first time, two direct spectroscopic methods, the conventional time-resolved laser-induced fluorescence spectroscopy (TRLFS) and TRLFS with ultrafast pulses, were applied to study the formation of a ternary uranyl hydroxo humate complex (Sachs et al., 2006).

7.1 Experimental

Preparation of sample solutions

U(VI) humate solutions were prepared from Aldrich HA (AHA). The experiments were performed under N_2 atmosphere, excluding CO_2. The HA concentration was kept constant at 2 mg/L and the U(VI) concentration was varied between $1 \cdot 10^{-7}$ and $1 \cdot 10^{-5}$ mol/L. The ionic strength was set to 0.1 M $NaClO_4$ and the pH values were adjusted to 7.01 ± 0.02.

Reference samples without HA (1: $8.6 \cdot 10^{-6}$ M U, pH 6.61; 2: $5.6 \cdot 10^{-6}$ M U(VI), pH 6.69) were prepared to characterize the fluorescence behavior of the aqueous U(VI) hydroxo species present in solution. These samples were measured under the same experimental conditions as the humate solutions. The total uranium concentration in each sample was checked by ICP-MS analyses (Elan 6000, Perkin Elmer) to account for container wall adsorption. A detailed description of the sample preparation is given in (Sachs et al., 2006).

TRLFS measurements (U(VI) fluorescence)

The U(VI) fluorescence in solution was measured with a time-resolving fluorescence spectrometer. For that a Nd:YAG laser (Spectron, Laser Systems, Rugby, UK) was used as light source. The fourth harmonic oscillation of the Nd:YAG laser (266 nm) with laser energies of about 500 µJ was applied to excite the U(VI) fluorescence. The emission signal was focused into a spectrograph (Acton Research, Acton, USA) by a fiber optic cable. The fluorescence spectra were measured with an intensified CCD camera system (ROPER-Scientific, Ottobrunn, Germany). Using the internal delay generator time-resolved spectra were recorded during a gate width of 2000 ns. The first time step started 30 ns after the excitation pulse. In 76 delay steps, the gate was then shifted to delay times of 30.03 µs (series 1) or 56.28 µs (series 2). At each delay time, five accumulations of a spectrum were collected over 95 laser shots per spectrum. Fluorescence spectra were recorded in the wavelength range between 446 and 618 nm at a resolution of 0.168 nm (for more details see Sachs et al., 2006).

fs-TRLFS measurements (HA fluorescence)

For the measurement of the HA fluorescence as a function of the U(VI) concentration, a femtosecond-laser-pulse-based TRLFS system was applied (Geipel et al., 2004). A Nd:YVO_4 laser seeded amplifier system (Spectra Physics, Mountain View, USA) used as light source. The excitation of the HA fluorescence was generated by the third harmonic of the Nd:YVO_4 laser (266 nm) with laser energies of about 200 µJ. The emitted fluorescence was focused into a spectrograph (Acton Research, 300i, Acton, USA) and collected by an intensified CCD camera system (PICOSTAR, LaVision Inc., Göttingen, Germany). Applying a delay generator, time-resolved fluorescence spectra were recorded at delay times between 0 and 9 ns after application of the laser pulse, with time steps of 50 ps. The gate width for detection was set to 0.5 ns. Spectra were measured in the wavelength range between 330 and 524 nm at a resolution of 0.283 nm (for more details see Sachs et al., 2006).

7.2 Complexation model for neutral pH conditions

The U(VI) species distribution at pH 7 in absence of HA ($1 \cdot 10^{-7}$ – $1 \cdot 10^{-5}$ M U(VI), 0.1 M $NaClO_4$, no CO_2) was calculated with the code EQ3/6 (Wolery, 1992) based on the latest revision of the U(VI) complex formation constants (Guillaumont et al., 2003). Under the considered conditions, U(VI) occurs in form of various hydroxo species, mainly $(UO_2)_3(OH)_5^+$, $(UO_2)_4(OH)_7^+$, UO_2OH^+, and $UO_2(OH)_2(aq)$, with $(UO_2)_3(OH)_5^+$ dominating for U(VI) concentrations above 0.4 µmol/L (Fig. 7.1). In principle, HA can react with all the positively charged hydroxo species, whereas the neutral species $UO_2(OH)_2(aq)$ has a very low affinity to the negatively charged binding sites of HA at pH 7. Therefore, the presence of the different hydroxo species has to be taken into account in the spectra analyses and evaluation of the experimental data.

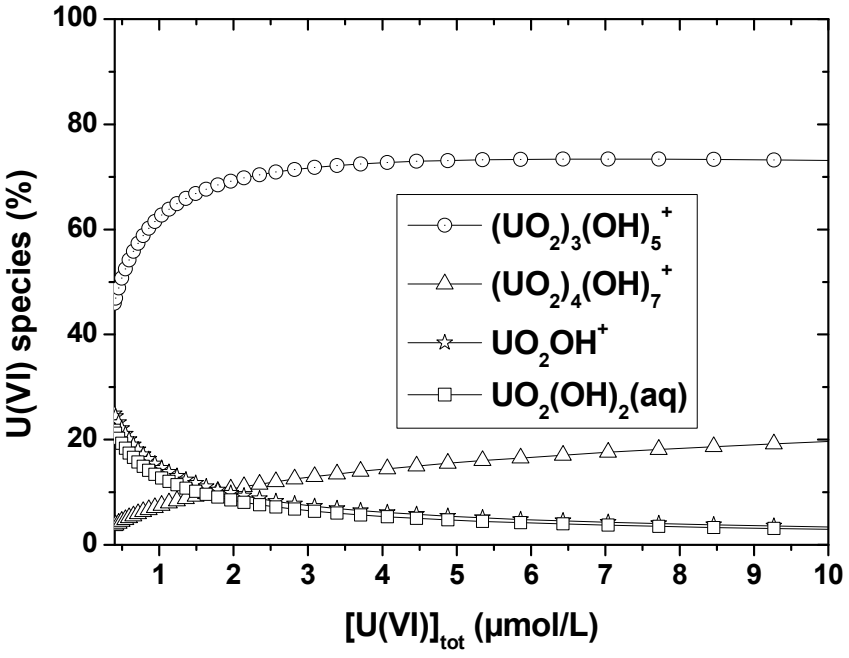

Fig. 7.1: U(VI) species distribution at pH 7 in absence of CO_2 and HA (I: 0.1 M $NaClO_4$). Species with a maximum concentration below 4% of the respective total U(VI) concentration are neglected.

Data analysis was based on the chemical model that UO_2OH^+ reacts with HA(I) as ligand forming a ternary uranyl mono hydroxo humate complex $UO_2(OH)HA(I)$ as shown in Eq. (7.1). HA(I) means that one proton exchanging functional group of the HA is taking part in the reaction.

$$UO_2OH^+ + HA(I)^- \rightleftarrows UO_2(OH)HA(I) \qquad (7.1)$$

Other possible chemical models involving $(UO_2)_3(OH)_5^+$ or $(UO_2)_4(OH)_7^+$ could be ruled out. The stability constant is described by Eq. (7.2), with square brackets denoting concentrations of the respective species:

$$K = \frac{[UO_2(OH)HA(I)]}{[UO_2OH^+]_{free} \cdot [HA(I)]_{free}} \qquad (7.2)$$

The free HA concentration in solution $[HA(I)]_{free}$ was determined based on two different models. Model A assumed that all proton exchanging functional groups of the HA are available for U(VI) complexation (subsequently identified by $[HA(I)]_{tot}$ = 100%; cf. Eq. (7.3)). In model B, $[HA(I)]_{free}$ was estimated according to the metal ion charge neutralization model (CNM, cf. Eq. (7.4); Kim and Czerwinski, 1996). CNM introduces the loading capacity (LC, Eq. (7.5)). There, $[UO_2(OH)HA(I)]_{max}$ is the maximum concentration of U(VI) mono hydroxo humate that can be formed under the same conditions.

A) [HA(I)]$_{tot}$ = 100%: $[HA(I)]_{free} = [HA(I)]_{tot} - [UO_2(OH)HA(I)]$ *(7.3)*

B) CNM: $[HA(I)]_{free} = [HA(I)]_{tot} \cdot LC - [UO_2(OH)HA(I)]$ *(7.4)*

$$LC = \frac{[UO_2(OH)HA(I)]_{max}}{[HA(I)]_{tot}} \qquad (7.5)$$

In both models, $[HA(I)]_{tot}$ was determined according to Eq. (7.6) (Kim and Czerwinski, 1996).

$$[HA(I)]_{tot} = \frac{[HA] \cdot PEC}{z} \qquad (7.6)$$

[HA] stands for the weight concentration of HA in g/L, PEC for the proton exchange capacity of HA in meq/g, and z for the nominal charge of the complexing metal ion, which is one in case of UO_2OH^+.

7.3 Results and discussion

7.3.1 Results of TRLFS measurements

U(VI) fluorescence in absence of humic acid

From the analysis of the fluorescence decay behavior of the reference samples (following Brendler et al., 1997), two decay constants (lifetimes) of τ_1 = 4.2 ± 0.4 µs and τ_2 = 19.8 ± 1.8 µs were obtained, pointing to at least two distinct fluorescent species. For the long-living fluorescence species a single emission spectrum was derived with peak maxima at 484, 498, 514, 534, 557, and 583 nm. Comparing lifetime and peak maxima of this species with those obtained for further reference samples containing various U(VI) hydroxo species (Brendler and Sachs, 2006) the long-living fluorescence species can be ascribed to the $(UO_2)_3(OH)_5^+$ complex which dominates the U(VI) speciation in the reference system. This assignment is supported by literature data of Moulin et al. (1998), who reported a fluorescence lifetime of 23 ± 3 µs and peak maxima at 479, 496, 514, 535, 556, and 584 nm for the $(UO_2)_3(OH)_5^+$ complex. The species with the shorter lifetime is assigned to $(UO_2)_4(OH)_7^+$ (Brendler and Sachs, 2006), the second largest contributor to the U(VI) speciation at pH 7. For more details see (Sachs et al., 2006)

U(VI) fluorescence in presence of humic acid

TRLFS spectra were measured at constant HA and varied U(VI) concentration. An example for a time-resolved fluorescence spectrum is shown in Fig. 7.2.

By analysis of the fluorescence decay behavior of the samples it was found that the fluorescence spectra of the uranyl humate solutions are clearly dominated by the HA-non-complexed $(UO_2)_3(OH)_5^+$ species. The proposed ternary U(VI) humate complex formed in

solution obviously does not contribute to the fluorescence signal during the time window of the measurements. Therefore, the first step in data processing was to calculate $[(UO_2)_3(OH)_5^+]_{free}$ for each sample as described in (Sachs et al., 2006). In a second step, the corresponding concentrations of free UO_2OH^+ ($[UO_2OH^+]_{free}$) and the total HA-uncomplexed U(VI) concentration ($[U(VI)]_{non\text{-}HA}$) were computed for each sample, assuming equilibrium conditions in solution and using the geochemical speciation code EQ3/6. In a third step, $[UO_2(OH)HA(I)]$ was determined according to Eq. (7.8).

$$[UO_2(OH)HA(I)] = [U(VI)]_{tot} - [U(VI)]_{non-HA} \qquad (7.8)$$

Finally, $[HA(I)]_{free}$ followed directly from Eq. (7.3) or Eqs. (7.4) and (7.5), and $\log K$ was calculated based on Eq. (7.2).

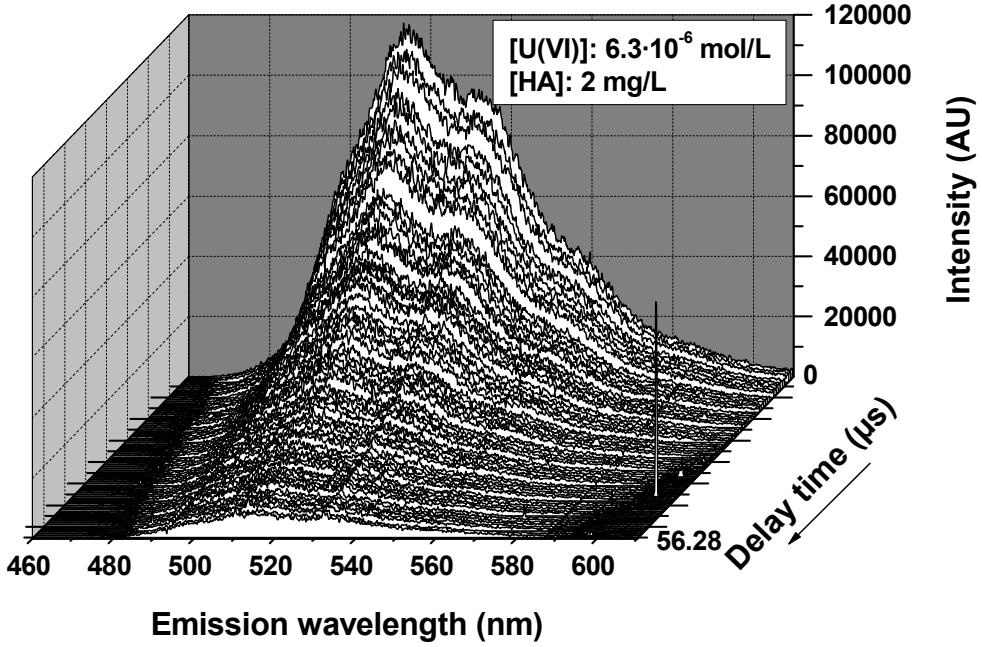

Fig. 7.2: Time-resolved fluorescence spectrum of a uranyl humate solution ([U(VI)]: $6.3 \cdot 10^{-6}$ mol/L, [HA]: 2 mg/L, pH 7, I: 0.1 M $NaClO_4$).

The complexation data resulting from the TRLFS measurements of series 1 and 2 as well as their weighted averages are summarized in Tab. 7.1. The two different definitions of $[HA(I)]_{free}$ give complexation constants that agree within their experimental errors for both series. In model B, applying the CNM, a LC value of 0.76 ± 0.28 was obtained. It indicates that at pH 7 about 80% of the HA proton exchanging sites are accessible for complexation of UO_2OH^+, which is quite close to the 100% assumed in model A. All other data processing steps are identical for both models. Thus, as expected, the $\log K$ values obtained by CNM are slightly higher than the ones for model A.

7.3.2 Results of fs-TRLFS measurements

Time-resolved fluorescence spectra of AHA were measured at varying U(VI) and constant HA concentration. Figure 7.3 shows a time-resolved fluorescence spectrum of AHA.

In all studied samples, AHA shows a comparable fluorescence decay behavior. It was best modeled by a bi-exponential decay function yielding two fluorescence decay times: τ_1 = 0.56 ± 0.16 ns and τ_2 = 2.52 ± 0.30 ns. These two lifetimes indicate the existence of a short and a long-living fluorescence species contributing to the HA fluorescence. The obtained lifetimes have the same order of magnitude as those reported by Kumke et al. (1998, 1999) for aqueous solutions of fulvic acid and natural organic matter. There, the authors reported further the occurrence of a third fluorescence contribution with a longer fluorescence lifetime τ_3 in the range from 11 to 24 ns. Our evaluation of the fluorescence decays of the AHA samples with a three-exponential decay yielded unacceptable strongly varying lifetimes with large errors, most likely due to the limited overall measurement duration of only 9 ns. An assignment of the two fluorescence lifetimes to distinct HA species or structural components of HA is not possible at the moment.

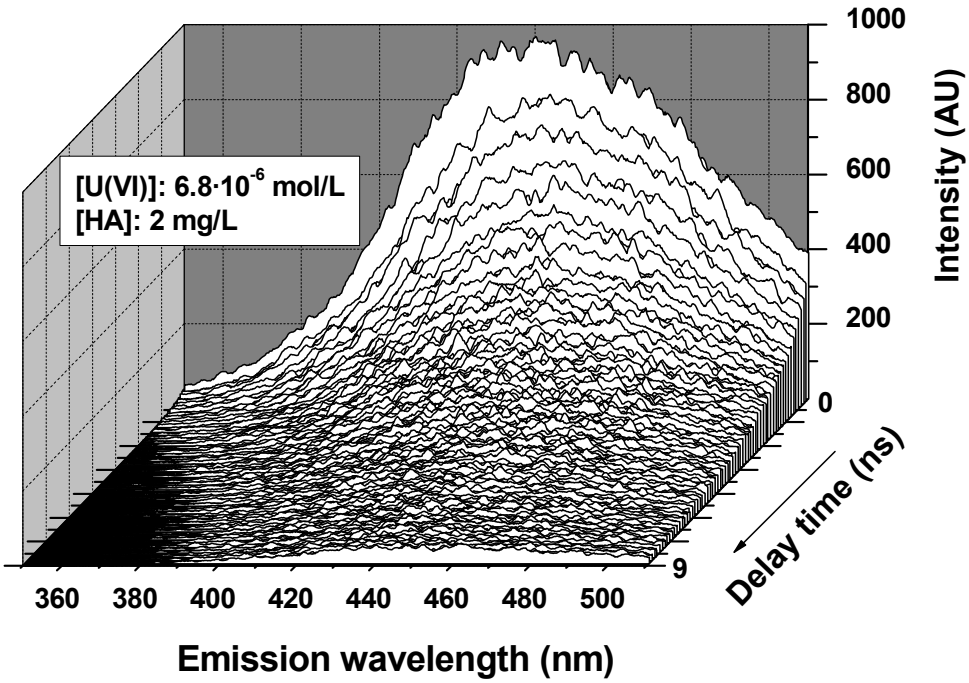

Fig. 7.3: Fs-time-resolved fluorescence spectrum of a uranyl humate solution ([U(VI)]: 6.8·10^{-6} mol/L, [HA]: 2 mg/L, pH 7, I: 0.1 M $NaClO_4$).

The observed fluorescence intensities decrease with increasing U(VI) concentration. This static fluorescence quenching results from the uranium binding by the HA, which was already

observed in synchronous fluorescence spectroscopic studies with fulvic acid in presence of UO_2^{2+} (Shin et al., 2001). From this quenching the amount of non-complexed HA in the U(VI) humate solutions could be derived as described in (Sachs et al., 2006).

The fs-TRLFS data were evaluated assuming that all proton exchanging functional groups of the HA contribute to the complex formation (cf. Model A: $[HA(I)]_{tot}$ = 100%). A direct evaluation of the fs-TRLFS data based on the CNM is not possible. Knowing the free and the total HA concentrations in solution, the difference gives the concentrations of $UO_2(OH)HA(I)$. Using Eq. (7.8), the total non-HA-complexed U(VI) concentrations $[U(VI)]_{non\text{-}HA}$ were calculated. Supposing chemical equilibrium in solution, the respective concentrations of uncomplexed UO_2OH^+ were then computed from $[U(VI)]_{non\text{-}HA}$ using EQ3/6.

Assuming $(UO_2)_3(OH)_5^+$ or $(UO_2)_4(OH)_7^+$ as reaction partner for HA would result in negative concentrations for non-HA-complexed U(VI), hence both can be excluded from further considerations. Finally, based on Eq. (7.2), the complexation constant was determined (Tab. 7.1).

Tab. 7.1. Parameters for the U(VI) complexation by Aldrich HA at pH 7 (I: 0.1 M $NaClO_4$).

Model	$[HA(I)]_{tot}$ = 100%	Metal Ion Charge Neutralization Model	
	log*K* [a]	LC [a]	log*K* [a]
	TRLFS measurements		
Series 1	6.69 ± 0.52	0.77 ± 0.36	7.14 ± 0.22
Series 2	6.47 ± 0.18	0.74 ± 0.40	6.76 ± 0.04
Weighted Average	*6.58 ± 0.24*	*0.76 ± 0.28*	*6.95 ± 0.10*
	fs-TRLFS measurements		
	6.33 ± 0.20	n.a. [b]	n.a. [b]

[a] ± 2σ. [b] n.a.: not applicable.

7.4 Discussion

Table 7.1 summarizes all parameters for the U(VI) complexation by AHA that were independently obtained by direct measurements of the U(VI) and HA speciation by TRLFS and fs-TRLFS, respectively. Based on the assumption that all HA functional groups contribute to

the U(VI) complexation ($[HA(I)]_{tot}$ = 100%), TRLFS and fs-TRLFS yield log*K* values that are comparable within their experimental errors. The agreement of the results of these two independent methods allows us to conclude that a U(VI) mono hydroxo humate complex is formed in the neutral pH range. Furthermore, the obtained data agree also with that from $UO_2(OH)_2$ solubility studies in presence of HA (Pashalidis, 2006), where a complex stability constant of 6.8 is reported for the formation of $UO_2(OH)HA$ starting from UO_2OH^+ (Eq. (7.1)).

Considering the first hydrolysis of UO_2^{2+}, the autoprotolysis of water (Cox, 1989) and the HA complexation by UO_2OH^+, an overall complex stability constant $\log\beta_{0.1M}$ of 14.89 ± 0.54 was calculated for the complexation process:

$$UO_2^{2+} + OH^- + HA(I)^- \rightleftarrows UO_2(OH)HA(I) \qquad (7.9).$$

This value is in very good agreement with $\log\beta_{0.1M}$ values of 14.7 ± 0.5 and 15.2 that were derived by Zeh et al. (1997) and Pashalidis et al. (2006), respectively, for the formation of $UO_2(OH)HA(I)$.

Comparing the data of $UO_2(OH)HA(I)$ with those of the binary complex $UO_2HA(II)$ (e.g., Aldrich HA $\log\beta_{0.1M}$ = 6.20 ± 0.56, evaluated based on the CNM (Pompe et al., 2000b) it becomes obvious that they are in the same order of magnitude. The complexation constant for $UO_2(OH)HA(I)$ determined based on the CNM in this work is about 0.8 log units higher than that of $UO_2HA(II)$ indicating a slightly stronger HA complexation by UO_2OH^+ than by UO_2^{2+}.

The formation of mixed actinide hydroxo humate complexes in the neutral pH range was also investigated for Am(III) and Cm(III) (Panak et al., 1996; Morgenstern et al., 2000). The formation of $An(OH)HA(II)$ and $An(OH)_2HA(I)$ complexes (An: $Cm^{3+}$and Am^{3+}) with Gorleben HA was reported in (Morgenstern et al., 2000) with stability constants evaluated to be $\log\beta_{111}$ = 12.82 ± 0.11 and $\log\beta_{121}$ = 17.53 ± 0.13 for Cm(III) and $\log\beta_{111}$ = 12.71 ± 0.17 and $\log\beta_{121}$ = 17.40 ± 0.21 for Am(III) in 0.1 M $NaClO_4$. Based on these overall stability constants, the first hydrolysis constants for Cm(III) (Wimmer et al., 1992) and Am(III) (Silva et al., 1995) as well as the autoprotolysis constant of water, the individual stability constants for the reaction of $CmOH^{2+}$ and $AmOH^{2+}$ with HA (cf. Eq. (7.10)) were recalculated and compared to that obtained for UO_2OH^+ in the present work.

$$AnOH^{2+} + HA(II)^{2-} \rightleftarrows An(OH)HA(II) \text{ with An: } Cm^{3+}, Am^{3+} \qquad (7.10)$$

The resulting stability constants amount to 6.37 and 5.78 for Cm(OH)HA(II) and Am(OH)HA(II), respectively. The data of Cm(III) and U(VI) agree very well. In contrast to that, $AmOH^{2+}$ shows a slightly lower tendency for HA complex formation. This dissimilarity in the Am(III) and Cm(III) complexation behavior may point to limitations of oxidation state analogues often used for trivalent actinides and lanthanides.

Above pH 8, Cm(III) and Am(III) form dihydroxo humate complexes ($An(OH)_2HA(I)$) by a charge neutralization process (Panak et al., 1996; Morgenstern et al., 2000). The formation of a comparable U(VI) complex is unlikely because of its lower charge and its tendency to form polynuclear hydroxo species at higher pH values.

To assess the impact of the binary and ternary U(VI) humate complex on the U(VI) speciation, the U(VI) distribution in the presence of HA was calculated for two U(VI) concentrations as a function of pH (Fig. 7.4). The calculations were performed based on U(VI) complex formation constants (Guillaumont et al., 2003), literature data for $UO_2HA(II)$ (Pompe et al., 2000a and 2000b; Montavon et al., 2000) and the data for $UO_2(OH)HA(I)$ from this work using the modified geochemcial speciation code EQ3/6 with integrated CNM (Sachs et al., 2004). At a U(VI) concentration of $1 \cdot 10^{-6}$ M in absence of CO_2, the U(VI) speciation is dominated by $UO_2HA(II)$ and $UO_2(OH)HA(I)$ between pH 4 and 8. $UO_2HA(II)$ exists in the acidic pH range between pH 3 and 6 with a maximum concentration around pH 4. Above pH 4.5 the U(VI) speciation is dominated by $UO_2(OH)HA(I)$, which occurs nearly quantitative in the pH range from 6.0 to 7.5, that is relevant for natural waters. This species distribution can significantly influence the mobility of U(VI). From U(VI) migration experiments in a laboratory quartz sand system, it is known that humic colloid-borne U(VI) is transported through the system and mobilized compared to U(VI) in a HA-free system (Mibus et al., 2007). The increase of the U(VI) concentration from $1 \cdot 10^{-6}$ to $1 \cdot 10^{-5}$ M at constant HA concentration causes a change in the species distribution. The hydrolysis of U(VI) and the formation of polynuclear U(VI) hydroxo species becomes more important. Nevertheless, in the pH region from about 6 to 8 the ternary $UO_2(OH)HA(I)$ complex is still dominating. An increase in the HA concentration promotes the formation of U(VI) humate complexes and consequently, a suppression of the U(VI) hydrolysis. It can be concluded that in the presence of HA the formation of the ternary $UO_2(OH)HA(I)$ complex significantly influences the U(VI) speciation under environmental conditions. Due to this the mobility of U(VI) can be enhanced.

8 Update of the database for humics complexation

Within the previous project a digital “Database for Humics Complexation – DHC” was developed covering so far published HA complexation data based on the metal ion charge neutralization model (Kim and Czerwinski, 1996) including the reported experimental conditions and data processing details (Sachs et al., 2004). This database provides an overview concerning investigated HA types, ligands, and parameter ranges (e.g., concentration of reaction partners, ionic strength, pH, …). In addition, it offers an extensive bibliography. Every stored data item is linked to both original citations and secondary literature references.

In the present project the database was updated. Data of ternary actinide hydroxo humate complexes from this study (see chapter 7) as well as from literature were added. In addition, actually complexation data generated based on the metal ion charge neutralization at the Institute of Interdisciplinary Isotope Research Leipzig were amended.

As of December 2006, the DHC database covers 12 different types of HA, contains 20 data records for proton exchange capacities and 92 complex formation constants with LC values.

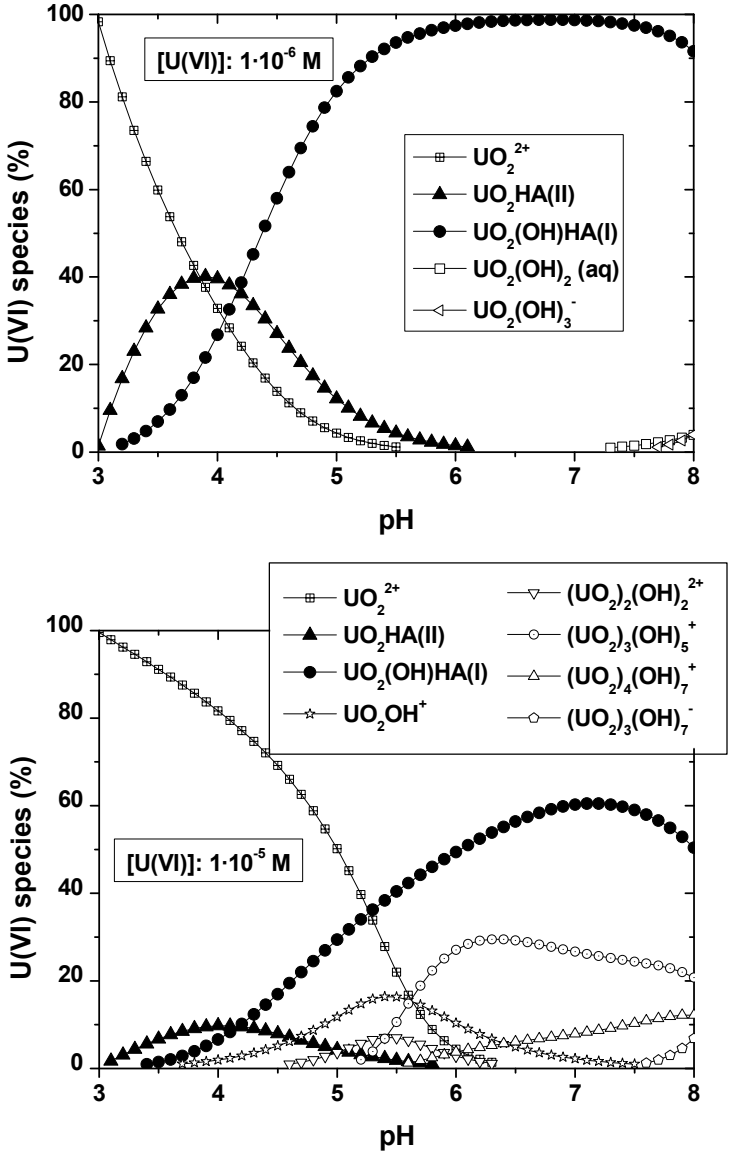

Fig. 7.4: Speciation of U(VI) in presence of HA as a function of the pH calculated with EQ3/6 ([U(VI)]: $1 \cdot 10^{-6}$ and $1 \cdot 10^{-5}$ mol/L, [HA]: 2 mg/L, I: 0.1 M $NaClO_4$, 0% CO_2). Data points below 1% are not plotted.

9 Neptunium(V) reduction by various natural and synthetic humic substances

The migration behavior of actinide contaminants in natural aquatic systems can be effected by humic substances due to their strong complexing and redox properties and their ability for colloid formation. Therefore, risk assessments, predicting the fate and transport of actinides in the environment, require basic knowledge of the interaction of humic substances with metal ions. The complexation of Np(V) by humic substances has been studied in a number of publications (e.g., Marquardt, et al., 1996; Marquardt and Kim, 1998; Seibert et al., 2001;

Sachs et al., 2005a). In a study of Np(IV) complexation by fulvic acid at pH 1 and 1.5, first values for conditional complexation constants were estimated (Marquardt et al., 2000). The redox behavior of humic substances of different origin towards Np and Pu in higher oxidation states (mostly hexa- or pentavalent) was reported in (André and Choppin, 2000; Artinger et al., 2000; Chen et al., 1993; Choppin, 1988; Marquardt et al., 1999 and 2004; Nash et al., 1981; Tan et al., 1993; Zeh et al., 1999).

Due to reduction of Np(V) to Np(IV), the migration behavior of the actinide changes strongly. Compared to Np(V), which shows a relatively weak interaction with HA, Np(IV) is generally stronger complexed by HA (Artinger et al., 2000). The humic colloid-borne Np(IV) species is known to remain stable in groundwater and to be easily mobile in porous aquifer systems (Artinger et al., 2000; Zeh et al., 1999).

Recently, synthetic HA with distinct redox properties were synthesized by oxidation of diphenolic compounds in the presence of amino acids in alkaline solution by Sachs et al. (2004). The most promising synthetic HA were the HA type Cat-Gly, which is an oxidation product of catechol and glycine, and the HA type Hyd-Glu, which is an oxidation product of hydroquinone and glutamic acid. These synthetic HA have shown significantly higher Fe(III) redox capacities (Sachs et al., 2004) and also higher U(VI) redox capacities than the natural Aldrich HA (Sachs et al., 2005b).

In this work, the stability of Np(V) in contact with various natural and synthetic aqueous humic substances was studied under anaerobic conditions between pH 3.5 and pH 9. For Np speciation in solution liquid-liquid extraction, NIR absorption spectroscopy and ultrafiltration were applied.

9.1 Experimental

Humic substances

Two natural humic substances and three synthetic HA were used in this study: The natural Kranichsee fulvic acid (KFA) was isolated from surface water of the mountain bog 'Kleiner Kranichsee' (Saxony, Germany) (Schmeide et al., 1998). The commercial Aldrich HA (AHA, charge A2/98) was purified before use (see chapter 3). The synthetic products were the HA type Cat-Gly (charge R1/03) and type Hyd-Glu (charge R13/02), as well as the HA with blocked phenolic/acidic OH groups type Hyd-Glu-PB (charge R20/02). Details to synthesis and characterization of the synthetic HA are given in (Sachs et al., 2004). The functional group contents of the humic substances are compiled in Tab. 9.1.

Sample preparation

The Np(V) stock solution was obtained by dissolving solid $^{237}NpO_2NO_3$ in 0.1 M HNO_3. The pentavalent oxidation state of Np in the stock solution was verified by NIR absorption spectroscopy and liquid-liquid extraction. Prior to the preparation of the various humic substance stock solutions, the humic material (50 mg each) was suspended in about 4 mL 0.1 M Na-

ClO_4 and degassed under vacuum. The Np(V) humate samples were prepared in a glove box under nitrogen atmosphere using carbonate-free solutions. The initial Np(V) and humic substance concentration was $1 \cdot 10^{-4}$ M and 100 mg/L, respectively. The ionic strength of the solutions was 0.1 M $NaClO_4$. The pH value of the samples (pH 3.5, 5, 7, 9) was adjusted applying diluted NaOH and $HClO_4$ solutions, no buffers were added. During the experiment, the pH value of the solutions was checked and readjusted repeatedly. Blanks without Np were prepared from each humic substance at pH 3.5 to pH 9. All samples were stored in the dark to minimize degradation of the organic material.

Tab. 9.1: Functional group contents of humic substances.

Humic substance	COOH [a] (meq/g)	Phenolic/acidic OH [b] (meq/g)
Cat-Gly (batch R1/03)	4.39 ± 0.13	6.6 ± 0.9
Hyd-Glu (batch R13/02)	3.65 ± 0.14	5.8 ± 0.2
Hyd-Glu-PB (batch R20/02)	2.67 ± 0.03	1.4 ± 0.1
KFA	6.05 ± 0.31	4.8 ± 0.7
AHA (batch A2/98)	4.49 ± 0.14	3.1 ± 0.1

[a] Determined by calcium acetate exchange (Schnitzer and Khan, 1972). [b] Radiometrically determined (Bubner and Heise, 1994).

Methods for Np speciation

The Np(V) reduction was determined by monitoring the Np(V) and Np(IV) concentrations in solution over time. For this, samples were taken after different time intervals and characterized by the redox speciation methods described in the following.

Liquid-liquid extraction

The separation of Np(V) and Np(IV) was performed by liquid-liquid extraction using 2-thenoyltrifluoroacetone (TTA) as complexing agent (Bertrand and Choppin, 1982). For this, 1.5 mL of the Np(V,IV) sample solution (pH 1) were shaken vigorously with 2 mL of 0.5 M TTA solution in xylene for 15 min. Under these conditions, Np(IV) is extracted into the organic phase, while Np(V) remains in the aqueous phase. After centrifugation, the Np content in the aqueous and organic phase was determined by liquid scintillation counting (Wallac system 1414, Perkin Elmer) using α-β discrimination. For this, 200 µL aliquots were mixed with 15 mL of a Ultima Gold™ scintillation cocktail (Packard BioScience Company).

NIR absorption spectroscopy

NIR absorption spectroscopy (CARY-5G, Varian) was applied for the direct spectroscopic detection of Np species in the sample solutions. Quartz cuvettes (Hellma) with 1 cm path-length were used and thermostated at 20°C. The sample solutions were measured directly, without any further preparations, in the spectral range from 920 nm to 1050 nm. For quantitative determination of uncomplexed Np^{4+} and NpO_2^+ aquo ions, the absorption bands at 960 nm and 980.4 nm with molar absorption coefficients of 162 L mol^{-1} cm^{-1} (Keller, 1971) and 395 ± 5 L mol^{-1} cm^{-1} (Marquardt et al., 1998), respectively, were used. For Np(IV) and Np(V) humate complexes, the absorption bands at 967.5 nm and 990 nm with molar absorption coefficients of 63 ± 8 L mol^{-1} cm^{-1} (Marquardt et al., 2000) and 230 ± 8 L mol^{-1} cm^{-1} (Marquardt et al., 1998), respectively, were used.

Ultrafiltration

For ultrafiltration experiments, MicroSep™ centrifugal concentrators (PallGelman Laboratory) of different pore sizes were used: 1 kDa, 10 kDa, 30 kDa, 100 kDa, 300 kDa, 1000 kDa.

9.2 Results and discussion

In Fig. 9.1, the Np(V) speciation in the starting solutions is shown for the experimental conditions applied in this study. It was calculated with the geochemical computer code EQ3/6 (Wolery, 1992) applying the Np(V) hydrolysis constants compiled in the NEA data base (Guillaumont et al., 2003), the Np(V) humate complexation constant $\log\beta$ = 3.6 and the pH function of the loading capacity (LC) with LC = -0.589 + 0.101 · pH (Sachs et al., 2004). The results show that the free neptunyl ion predominates the Np speciation in aqueous solution. The $NpO_2HA(I)$ species is formed increasingly in solution between pH 6 and pH 10. For the pH region higher than 9, the formation of the mixed complex $(NpO_2(OH)HA)_{coll.}$ is suggested by Marquardt et al. (1998). However, presently, this complex cannot be quantified thermodynamically. The formation of the neptunyl hydroxyl species $NpO_2OH_{(aq)}$ can be neglected in the considered pH range.

In contrast to Np(V), Np(IV) has a strong tendency to hydrolyze. In the absence of complexing ligands, at an Np(IV) concentration of $1 \cdot 10^{-4}$ M, amorphous NpO_2 can precipitate at pH values higher than pH 3.3. In the presence of complexing ligands such as humic substances, a strong complexation of Np(IV) already at low pH values is observed. The formation of mixed hydroxo fulvate complex species ($Np(OH)_2FA(II)$ and Np(OH)FA(III)) at pH 1 and 1.5 was proposed by Marquardt et al. (2000). Thus, it is assumed that the Np(IV) which is produced in the course of our reduction experiments occurs mainly as mixed Np(IV) hydroxo fulvate/humate complex species.

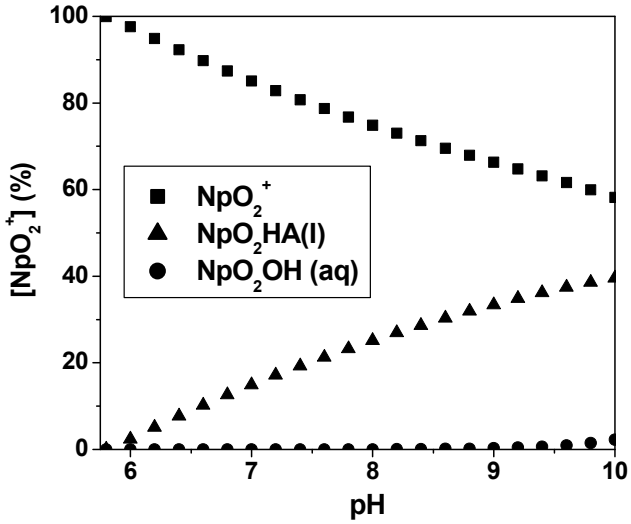

Fig. 9.1: Np(V) speciation at start of equilibration of the Np humic substance solutions. ($[NpO_2^+]$: $1 \cdot 10^{-4}$ M; [HA]: 100 mg/L; I: 0.1 M $NaClO_4$; N_2 atmosphere).

The reduction of Np(V), determined by TTA extraction, is shown in Figs. 9.2 and 9.3 as plot of the ratio of pentavalent Np to total Np versus equilibration time. It is obvious, that the Np(V) reduction is dependent on equilibration time, on the type of humic substances as well as on pH value of the sample solutions. In the initial phase of the equilibration of the Np humic substance solutions, the formation of Np(IV) is fast. With increasing equilibration time the rate of Np(IV) formation slows down. The synthetic HA type Cat-Gly and Hyd-Glu show a stronger Np(V) reduction in comparison to the natural humic substances AHA and KFA.

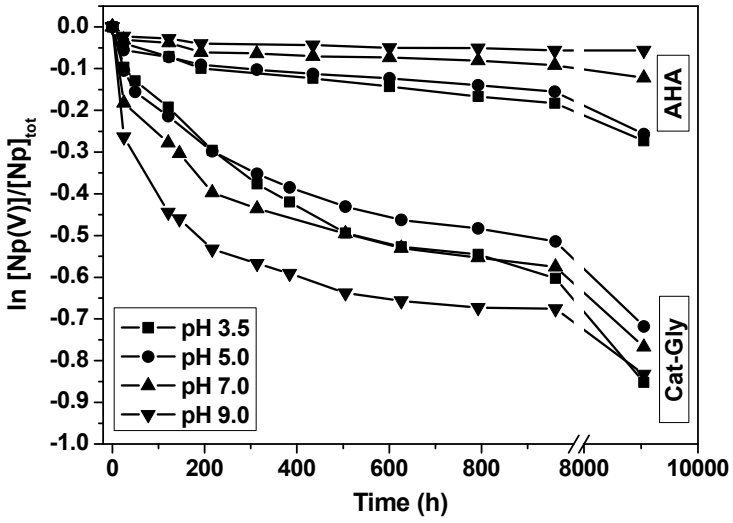

Fig. 9.2: Reduction of Np(V) to Np(IV) by HA type Cat-Gly and AHA between pH 3.5 to pH 9.0. Determination of Np(V) by TTA extraction.

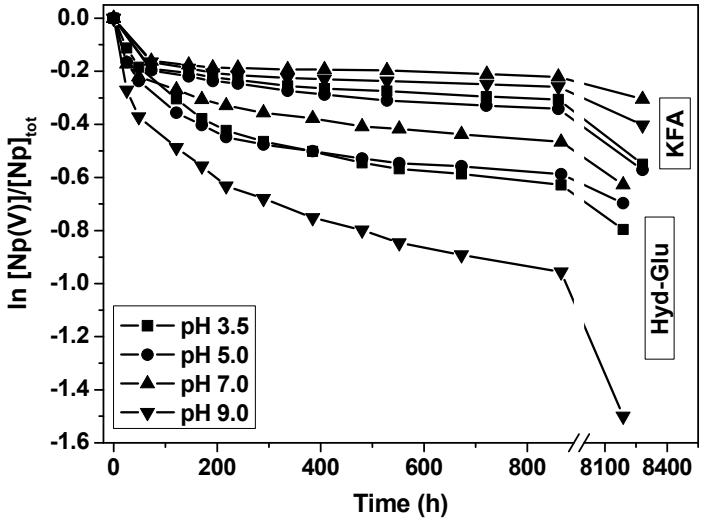

Fig. 9.3: Reduction of Np(V) to Np(IV) by HA type Hyd-Glu and KFA between pH 3.5 to pH 9.0. Determination of Np(V) by TTA extraction.

The strongest Np(V) reduction is found for the HA type Hyd-Glu at pH 9. After 865 h (36 d) 62% of the Np(V) is converted to Np(IV). Also in case of HA type Cat-Gly, the strongest Np(V) reduction is found at pH 9 (961 h (40 d), 49% Np(IV)). The pH dependency determined for the Np(V) reduction by AHA correlates with that found by Marquardt et al. (1996) for the same HA. Generally, however, no trend is observable for the pH dependency of the Np(V) reduction for the various humic substances. The samples taken about one year after starting the experiments (between 8200 h to 9050 h after start) show that Np(IV) is formed continually but with a comparatively slow rate.

The redox capacity, which decreases in the sequence synthetic HA > KFA > AHA, can be correlated to the phenolic/acidic OH group contents of the humic substances (cf. Tab. 9.1). A comparable correlation between the phenolic/acidic OH group content of various synthetic and natural HA and their Fe(III) and U(VI) redox capacities was observed in (Sachs et al., 2004 and 2005b).

Contrary to the partial reduction of Np(V) under the experimental conditions applied in this work, a nearly complete reduction of Np(V) was found in experiments applying the same Np concentration but the fourfold HA concentration (400 mg/L HA type Cat-Gly). After 1000 h only 4% Np(V) were detected.

As already mentioned, by liquid-liquid extraction with TTA as complexing agent, Np(IV) is extracted into the organic phase, while Np(V) remains in the aqueous phase. However, in case of the humic substance solutions studied here, the Np(IV) could not be extracted quantitatively into the organic phase but partly remained bound in the humic substance precipitate. Exemplary this is shown for HA type Hyd-Glu in Fig. 9.4. With increasing equilibration time, the amount of Np(V) determined in the aqueous phase decreases but the amount of Np(IV) determined in the organic phase does not increase to the same extent. This results in a decreasing Np recovery during TTA extraction. The part of Np that cannot be extracted represents a fraction of tetravalent Np which is strongly bound to the HA and which is not released from the HA even at pH 1. Np(V), however, would decomplex from the HA under these pH conditions and remain in aqueous solution as NpO_2^+ ion. This effect was even more pronounced in experiments applying the fourfold HA concentration (not shown here) which confirms again the strong complexation of Np(IV) by HA. Too low activity recoveries were also reported for liquid-liquid extraction of Pu species (Artinger at al., 2004).

To verify that no Np(IV) had precipitated during the reduction reaction the total Np content was also checked. Figure 9.4 shows, that the total amount of Np in the sample solutions remains constant in the course of the experiments. This also means, that the Np adsorption onto the vial walls is negligible, even at pH 9.0.

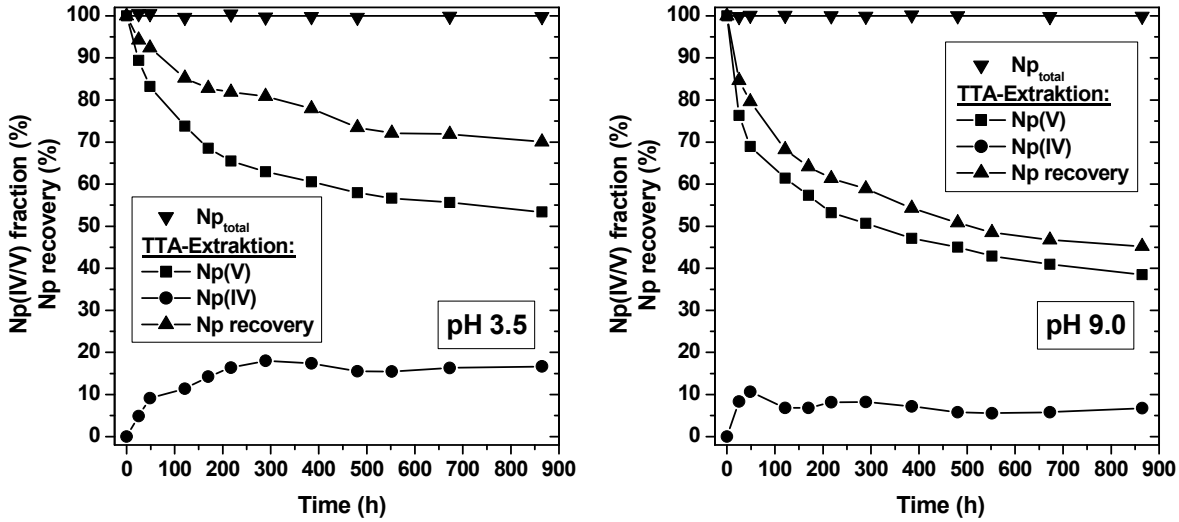

Fig. 9.4: Recovery of Np during TTA extractions in comparison to the total Np content for HA type Hyd-Glu equilibrated at pH 3.5 and pH 9.0.

To study influence of phenolic/acidic OH groups on the redox behavior of humic substances further, the synthetic HA with blocked phenolic/acidic OH groups of type Hyd-Glu-PB was equilibrated with Np(V) under the same experimental conditions as described above. Due to methylation with diazomethane (Pompe et al., 2000a; Schmeide et al., 2003), the phenolic/acidic OH group content of HA type Hyd-Glu-PB is 76% lower than that of HA type Hyd-Glu (cf. Tab. 9.1), which was used as starting material. The carboxylic group content of HA type Hyd-Glu-PB is also somewhat lower than that of HA type Hyd-Glu. Possible reasons are

a partial decomposition of HA molecules in acid-soluble components and/or leaching of smaller HA molecules with a higher carboxylic group content from the HA mixture (Pompe at al., 2000a) or an incomplete hydrolysis of the methyl ester groups that were previously formed during methylation with diazomethane. Nevertheless, Tab. 9.1 shows that the molar ratio of phenolic OH to carboxylic groups becomes significantly smaller due to the modification process.

The amount of Np(IV) formed by the modified HA with blocked phenolic/acidic OH groups type Hyd-Glu-PB is very small compared to the strong Np reduction by the unmodified HA type Hyd-Glu (Fig. 9.5). After 865 h (36 d) the amount of Np(IV) formed by HA type Hyd-Glu-PB is about 55% lower than the amount of Np(IV) formed by HA type Hyd-Glu (pH 9). This again shows that the phenolic/acidic OH groups play a major role for the redox behavior of humic substances. The slight Np reduction in the initial phase of the experiment can be attributed to the small amount of phenolic/acidic OH groups that could not be blocked by methylation (1.4 ± 0.1 meq/g).

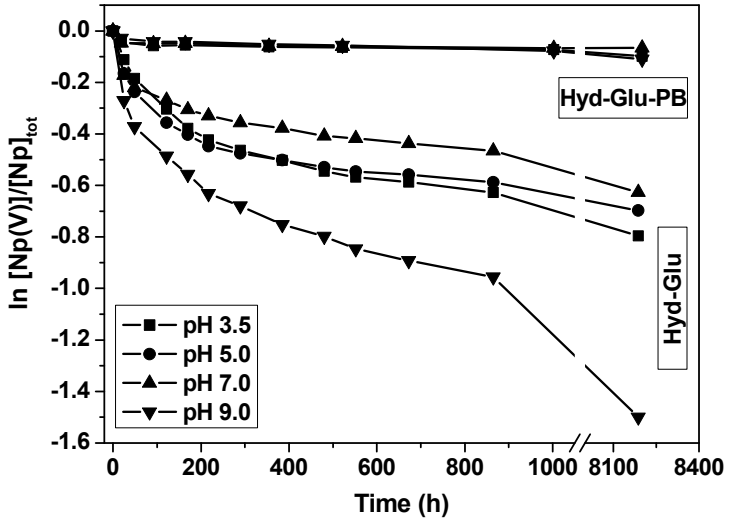

Fig. 9.5: Reduction of Np(V) to Np(IV) by HA type Hyd-Glu and HA type Hyd-Glu-PB between pH 3.5 to pH 9.0. Determination of Np(V) by TTA extraction.

By NIR absorption spectroscopy the gradual decrease of the Np(V) absorption peaks is observed, while the total Np concentration in the sample solutions remains constant in the course of the experiments (cf. Fig. 9.4). The formation of Np(IV) hydrolysis products besides the formation of Np(IV) humate cannot be excluded completely by this method since the various Np(IV) hydrolysis species and their mixed hydroxo fulvate or humate complex species cannot be distinguished by NIR absorption spectroscopy (Marquardt et al., 2000) or EXAFS (Schmeide et al., 2005).

The results of ultrafiltration of the Np(IV,V)/HA type Hyd-Glu sample solutions with membrane filters of pore sizes between 1 kDa and 1000 kDa are shown in Fig. 9.6. At pH 7 and pH 9, where 36.7% and 64.3% Np(IV) are detected by TTA extraction (after 1513 h), a Np fraction of 43.1% and 86.6%, respectively, is found to be retained on a 1 kDa filter, whereas at 1000 kDa, Np passes quantitatively through the filter. That means, that a fraction of about 43.1% or 86.6% of the Np is bound onto HA colloids, mostly as Np(IV) and but also as Np(V) (especially at pH 9, cf. Np(V) speciation given in Fig. 9.1). At pH 3.5 and pH 5, where 48.5% and 44.2% Np(IV) are detected by TTA extraction, a Np fraction of 49.2% and 45.8%, respectively, is found to be retained on a 1 kDa filter, showing the fraction of humic colloid-bound Np(IV). In this pH range, no Np(V) humate is formed (cf. Fig. 9.1), and the NpO_2^+ ion, detected by NIR absorption spectroscopy, passes through the filter. The Np humate solution at pH 3.5 shows the peculiarity that the amount of Np retained on the filters of pore sizes between 1 kDa and 1000 kDa is nearly constant. This is attributed to the precipitate and/or large aggregates that are formed by the humic colloid-bound Np(IV) in the sample solution at pH 3.5.

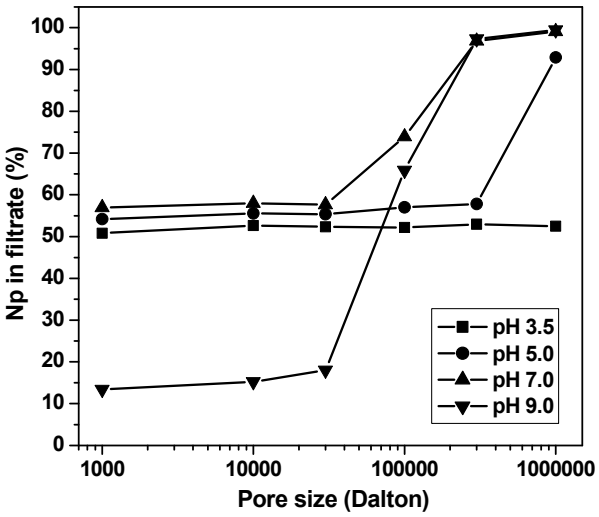

Fig. 9.6: Ultrafiltration of Np(IV,V)/HA type Hyd-Glu equilibrated at pH 3.5 to pH 9.0 for 1543 h (~64 d).

The results have shown that in comparison to the natural humic substances (AHA, KFA), the synthetic HA (type Hyd-Glu and Cat-Gly) lead to a stronger reduction of Np(V) to Np(IV). The Np(IV) formed in the course of the experiments is stabilized in form of Np(IV) humate complexes, whereas the remaining Np(V) occurs as NpO_2^+ ion or Np(V) humate depending on pH. The higher reduction potential of the synthetic HA can be attributed to their higher phenolic/acidic OH group contents compared to natural humic substances. This correlation could be verified applying a synthetic HA with blocked phenolic/acidic OH groups.

10 Influence of humic acid on the U(VI) sorption onto kaolinite

An important mechanism for retarding radionuclide migration in natural environment is sorption onto minerals present along the groundwater flow path. Due to their complexation, redox and colloidal properties, HA affects the speciation of actinide ions, and therefore, their sorption and migration in the environment. In the present study, we investigated the influence of HA on the U(VI) sorption onto kaolinite KGa-1b. Kaolinite is a main mineral component of clay-rich host rock formations considered as potential nuclear waste repositories. Batch sorption experiments were performed to study the U(VI) sorption onto kaolinite in absence and presence of HA under different experimental conditions. Furthermore, the HA sorption onto kaolinite was studied. Spectroscopic investigations were performed in order to identify U(VI)-kaolinite surface complexes in absence and presence of HA. These information are necessary for a future modeling of the U(VI) sorption onto kaolinite. The obtained results help to improve the understanding of the geochemical interactions of hexavalent actinides in the environment. The outcome of these studies is published in (Křepelová, 2006a and Křepelová et al., 2006b).

10.1 Batch sorption experiments

10.1.1 Experimental

Materials

Kaolinite KGa-1b (see chapter 2) was used without any pretreatment in all experiments. For the experiments, the ^{14}C-labeled synthetic HA type M42 (Batch M170, see chapter 3) was used. A HA stock solution of 5 g/L was prepared by weighting of 50 mg of HA, adding of 1720 μL of 0.1 M NaOH and filling the volume with 0.1 M $NaClO_4$ (Merck) up to 10 mL. A $1 \cdot 10^{-3}$ M $UO_2(ClO_4)_2$ was used as U(VI) stock solution for all experiments.

Batch experiments

The sorption experiments were performed under ambient atmosphere (pCO_2: $10^{-3.5}$ atm) or inert gas conditions (N_2-box). 40 mg of kaolinite were weighed into 15 mL polypropylene centrifuge tubes (Cellstar, Greiner Bio-One), 10 mL of 0.1 or 0.01 M $NaClO_4$ were added subsequently. The desired pH values were adjusted between pH 3 and 10. For studies at pH >7 in the presence of CO_2, a calculated amount of $NaHCO_3$ was added to accelerate the equilibrium process with atmospheric CO_2. For pre-equilibration the samples were continuously shaken on a horizontal shaker (mod. Promax 2020, Heidolph Instruments) and the pH values were controlled and readjusted. The conditioning time was 72 h and 4 – 5 weeks in the presence and absence of CO_2, respectively. After pre-equilibration, 9.26 or 92.6 μL U(VI) stock solution were added to the kaolinite suspension for the investigation of the U(VI) sorption onto kaolinite. The final concentration of U(VI) in the solution was $1 \cdot 10^{-6}$ M or $1 \cdot 10^{-5}$ M. To determine HA sorption onto kaolinite, 20 or 100 μL of the HA stock solution were added to

the kaolinite suspension. The final concentration of HA in the solution was 10 or 50 mg/L. For the investigation of U(VI) sorption onto kaolinite in the presence of HA, pre-equilibrated U(VI)-HA solution (equilibration time: 24 h, pH ~ 7) was added. The final concentrations of U(VI) and HA in the solution were $1 \cdot 10^{-5}$ M or $1 \cdot 10^{-6}$ M and 10 or 50 mg/L, respectively. After addition of U(VI), HA or U(VI)/HA solutions, the pH values were readjusted immediately. The samples were shaken on the horizontal shaker for 60 h to equilibrate. After shaking, the final pH values of the samples were measured and the samples were centrifuged (30 min, 4000 rpm, mod. Megafuge 1.0, Heraeus Sepatech). The supernatants of single samples were filtered (450 nm, Minisart N, Sartorius). Prior to filtering, the filters were rinsed with 1 mL of sample solution. The filtrates were analyzed for the final U(VI) and HA concentration. The U(VI) concentration in solution was determined by ICP-MS (ELAN 6000, Perkin Elmer) and the HA concentration in solution was measured by liquid scintillation counting (LSC, mod. LS 6000 LL, Beckman Coulter). A quantity of 1 mL of the filtered solution was mixed with 5 mL Ultima Gold (Perkin Elmer). Prior to the measurement of the U(VI) concentrations in the samples in presence of HA, HA was removed by digestion in a microwave oven (mod. mls 1200 mega, MLS) with HNO_3 (Riedel de-Haën) in order to avoid any disturbing effects of HA during ICP-MS measurements.

Finally, the U(VI) or HA sorption onto vial walls was investigated. The vials were washed with water and dried. Then, 7 mL 1 M HNO_3 or 1 M NaOH were added and the vials were shaken for 2 days. The maximal vial wall sorption of U(VI) was observed between pH 6 and 7.5 and reached values up to 5%. In the acidic pH range the vial wall sorption was maximal 3%, above pH 8 the vial wall sorption was negligible. HA vial wall sorption was negligible in the entire pH range.

The amount of U/HA adsorbed on the mineral surface was calculated as the difference between the initial U(VI)/HA concentration and the sum of the amounts of U(VI)/HA remaining in solution and U(VI)/HA adsorbed onto the vial walls.

Kinetic experiments

Kinetic experiments were conducted to evaluate the time required for the sorption equilibrium. The effect of equilibration of the suspensions as well as the influence of the sequence of the U(VI) and HA addition to the kaolinite suspension (a: addition of a 24 h pre-equilibrated U(VI)-HA solution, b: simultaneous addition of U(VI) and HA without pre-equilibration, c: U(VI) addition after 60 h contact time of HA with kaolinite) were studied. The experimental conditions were similar to those in the batch experiments (see above). The kinetic curves were obtained at two pH values: pH 5 and pH 7.5. Samples were shaken and taken after different contact times. The final U(VI)/HA concentrations were measured and the vial wall adsorption was determined. For more details see (Křepelová, 2006a; Křepelová et al., 2006b)

10.1.2 Results and discussion

10.1.2.1 Kinetic experiments

Figure 10.1 shows the results of the kinetic experiments for U(VI) and HA adsorbed onto kaolinite from the solution. It becomes obvious that both systems reach the sorption equilibrium quite fast. At pH 5 and pH 7.5, the amount of the adsorbed HA does not change significantly after 50 h; thus, 60 h are sufficient to establish the sorption equilibrium in the system. The kinetics of the U(VI) sorption onto kaolinite in the absence of HA is very similar. The amount of U(VI) adsorbed onto kaolinite is stable after 50 h at pH 5 and even earlier at pH 7.5.

Comparing the different sequences of U(VI) and HA addition to the kaolinite suspensions (not shown), no significant differences in the U(VI) sorption behavior were observed. Therefore, it can be concluded that the pre-equilibration of the U(VI)-HA solution before the addition to the kaolinite has no significant influence on the U(VI) sorption kinetic in the studied time scale, for more details see (Křepelová, 2006a; Křepelová et al., 2006b).

10.1.2.2 Humic acid sorption onto kaolinite

HA uptake onto kaolinite is shown in Fig. 10.2 as a function of pH and HA concentration. The observed results are comparable to those of natural HA described in the literature (e. g., Murphy et al., 1992; Kretzschmar et al., 1997; Samadfam et al., 2000). The sorption of HA decreases with increasing initial HA concentration and pH. More than 90% of 10 mg/L HA is adsorbed onto kaolinite at pH 3. However, there is a possibility that a part of HA precipitates at pH 3. There could be an overlapping of both processes, HA sorption and precipitation. The percentage of HA adsorbed decreases with increasing HA concentration due to a saturation of kaolinite binding sites. The observed decrease of the HA sorption with increasing pH is regarded as a result of the electrostatic repulsions between negatively charged deprotonated carboxyl groups of HA and negatively charged kaolinite surface (cf. p.z.c. and p.z.n.p.c. values in chapter 2).

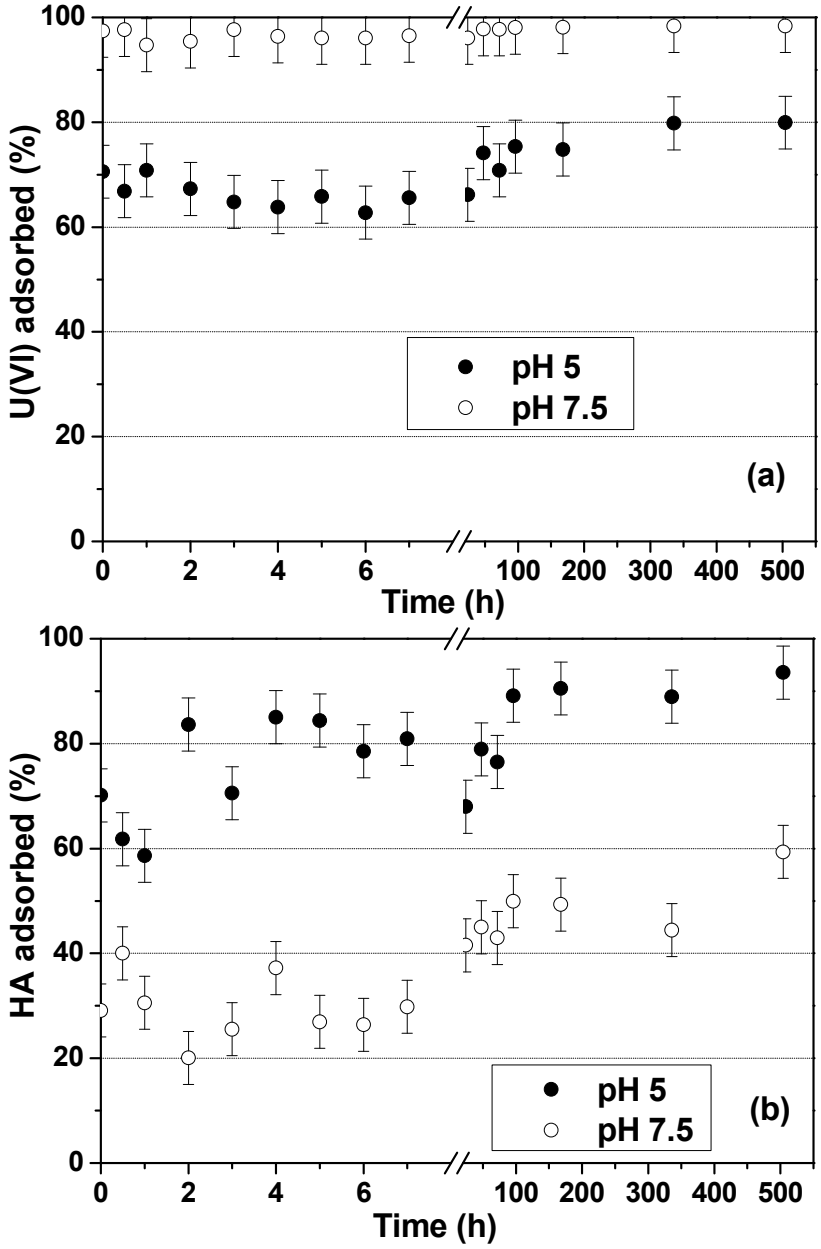

Fig. 10.1: Percentage of (a) U(VI) and (b) HA adsorbed from solution during kinetic experiments at pH 5 (filled symbols) and pH 7.5 (open symbols) ([U(VI)]: $1 \cdot 10^{-6}$ M, [HA]: 10 mg/L, I: 0.01 M $NaClO_4$, pCO_2: $10^{-3.5}$ atm).

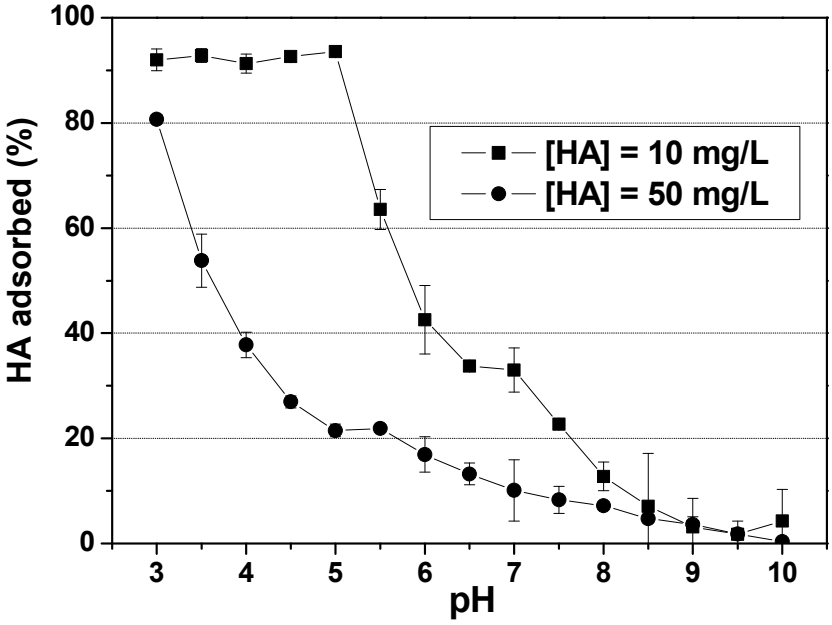

Fig. 10.2: HA sorption onto kaolinite as a function of pH and HA concentration (I: 0.01 M $NaClO_4$, pCO_2: $10^{-3.5}$ atm).

Figure 10.3 depicts the sorption of HA in 0.01 M and 0.1 M $NaClO_4$ solutions. Between pH 3 and pH 5, the HA adsorption at both ionic strengths reaches almost 95%. Strong differences in the amount of adsorbed HA occur at pH >5. The sorption of HA increased at higher ionic strength. The maximal difference in the adsorbed amount of HA between both ionic strengths (almost 60%) was achieved at pH 6.5. The changes in the macromolecular configuration of HA with the ionic strength can explain the observed phenomenon. At high ionic strength, the negative charges of HA macromolecules are well screened and consequently the HA wind up like random coils. Therefore, more HA can be adsorbed to the mineral surface (Kretzschmar et al., 1997). At low ionic strength, HA adopts a more linear and open configuration, therefore HA occupies a higher amount of kaolinite surface area (Murphy et al., 1992) resulting in lower HA adsorption on the surface.

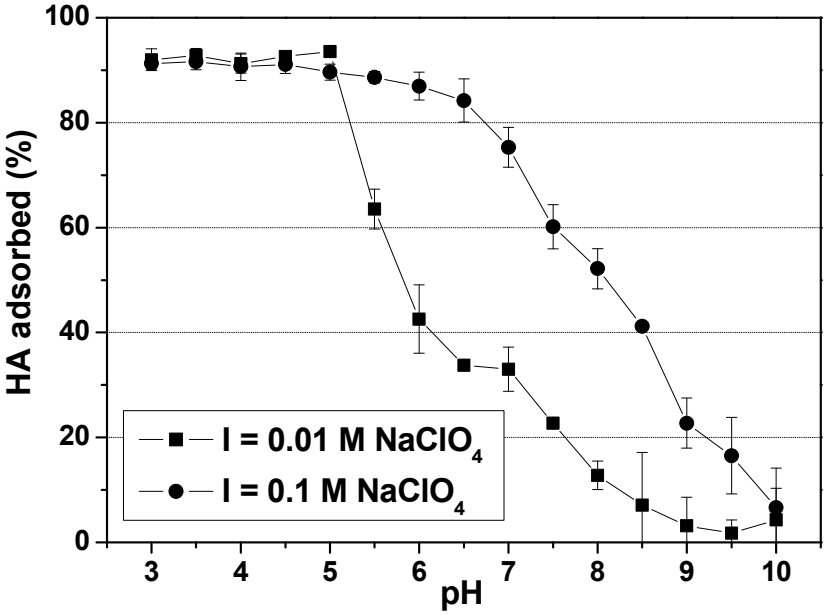

Fig. 10.3: Influence of the ionic strength on the HA sorption onto kaolinite ([HA]: 10 mg/L, pCO_2: $10^{-3.5}$ atm).

In the 0.01 M solution, the presence of U(VI) enhances the sorption of HA compared to the system without U(VI) at pH >5.5 (Fig. 10.4). This can be explained by the possible association between UO_2^{2+} and HA on the kaolinite surface, which is expected to be strongest in the pH range of increased U(VI) adsorption onto kaolinite (see chapter 10.1.2.4). Redden et al. (1998) reported that U(VI) enhances adsorption of citrate onto kaolinite, when the citrate concentrations are comparable to those of U(VI). Schmeide et al. (2000) explained a high HA sorption onto albite due to specific interactions of cations, released into the aqueous phase due to mineral weathering and cation exchange processes with carboxylate groups of HA. These cations are able to form bridges between negatively charged surface species and HA carboxylate groups thus increasing the number of sorption sites for HA.

XPS measurements were performed to study how HA is distributed on the kaolinite surface (Reich et al., 2006a). These XPS measurements in the system HA/kaolinite showed that the surface of the kaolinite particle is not covered by a homogenous HA layer. Part of the HA must be distributed between the particles. This implies that in the ternary system, U(VI) can interact with significant parts of the kaolinite surface that are not covered by HA.

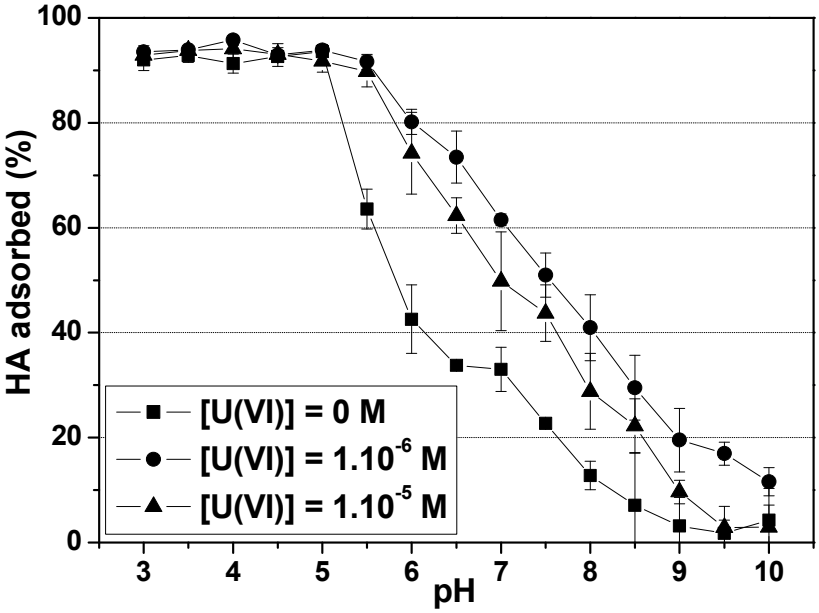

Fig. 10.4: Influence of the presence of U(VI) on the HA sorption onto kaolinite (I: 0.01 M $NaClO_4$, [HA]: 10 mg/L, pCO_2: $10^{-3.5}$ atm).

10.1.2.3 U(VI) speciation in solution

The sorption behavior of actinides is affected by their speciation in solution. Therefore, the aqueous distributions of U(VI) species for solutions in equilibrium with atmospheric CO_2 (pCO_2: $10^{-3.5}$ atm) and in the absence of CO_2 (N_2-atmosphere) were calculated using the code EQ3/6 (Wolery, 1992) based on the most recent compilation of U(VI) complex formation constants (Guillaumont et al., 2003). The results of speciation calculations for I: 0.1 M and [U(VI)]: $1 \cdot 10^{-6}$ M in the (a) absence and (b) presence of CO_2 shows Fig 10.5. Other calculations at I: 0.01 M are not shown because they do not differ significantly.

At pH <5, U(VI) prevails in solution as the free UO_2^{2+} cation. At pH >5 the U(VI) speciation is dominated by a series of hydrolyzed U(VI) species, e.g., UO_2OH^+, $(UO_2)_3(OH)_5^+$ and $UO_2(OH)_3^-$. In the presence of CO_2, uranyl carbonato complexes $(UO_2)_2CO_3(OH)_3^-$, $UO_2(CO_3)_3^{4-}$ and $UO_2(CO_3)_2^{2-}$ dominate at higher pH values (pH >6.5).

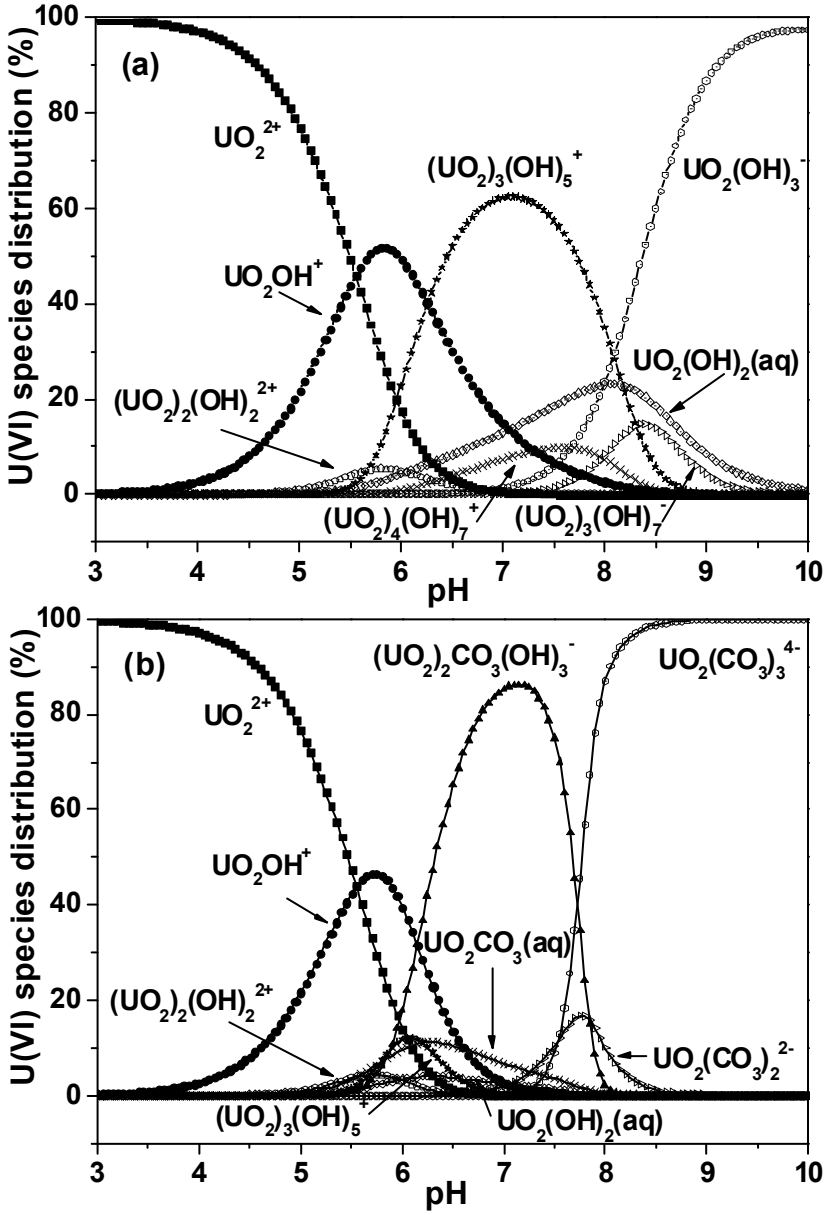

Fig. 10.5: U(VI) speciation in the (a) absence and (b) presence of CO_2 (I: 0.1 M $NaClO_4$, [U(VI)]: $1 \cdot 10^{-6}$ M).

HA affects the U(VI) speciation significantly. Figure 10.6 illustrates the U(VI) speciation in solution in the presence of HA. The computations were performed for solutions in equilibrium with atmospheric CO_2 and in its absence by means of EQ3/6 considering the metal ion charge neutralization model for the description of the HA complexation (Sachs et al., 2004). Within the calculations complexation data for two different U(VI)-humate complexes were considered: the binary $UO_2HA(II)$ complex (e.g., Pompe et al., 2000a and 2000b; Montavon et al., 2000) and the ternary complex $UO_2(OH)HA(I)$ (Sachs et al., 2006).

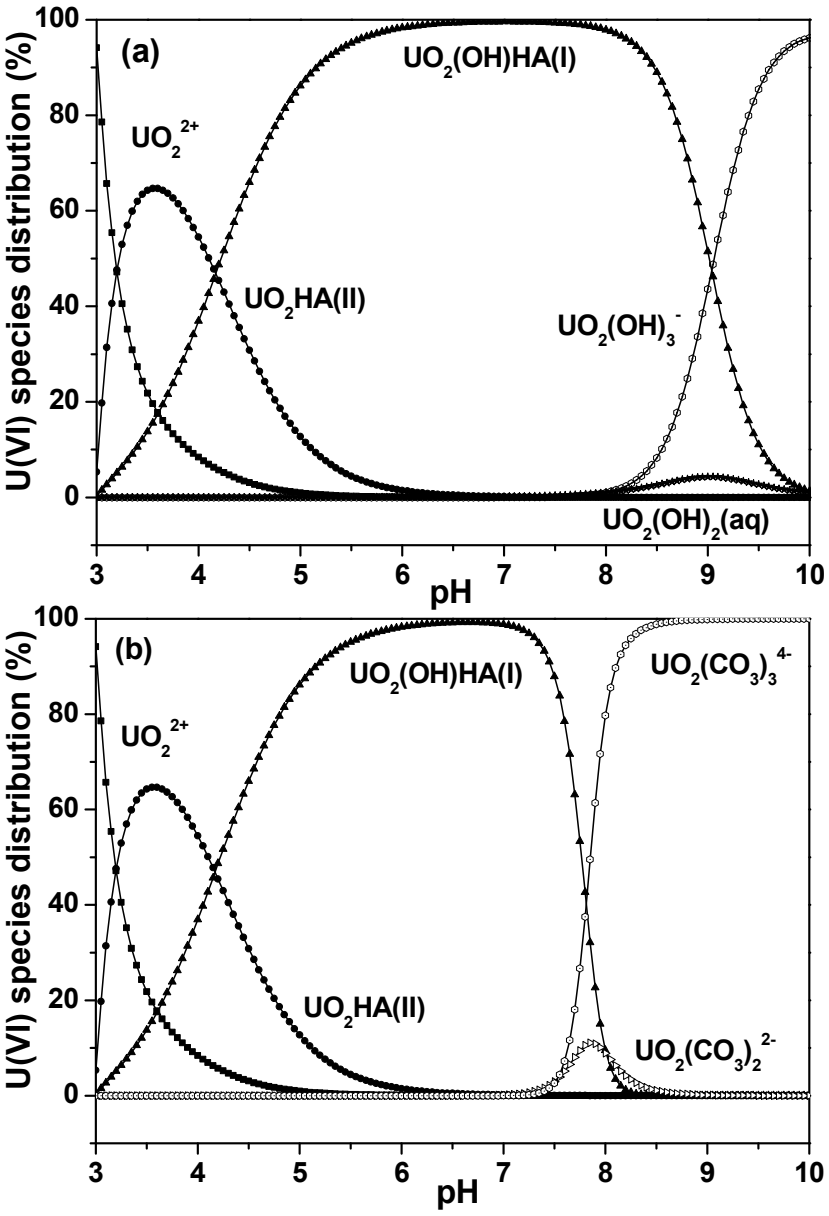

Fig. 10.6: U(VI) speciation in the presence of HA in the (a) absence and (b) presence of CO_2 (I: 0.1 M $NaClO_4$, [U(VI)]: $1 \cdot 10^{-6}$ M, [HA]: 10 mg/L).

In the presence of HA the free uranyl cation UO_2^{2+} predominates in the solution only at very low pH values. The $UO_2HA(II)$ complex dominates the speciation in solution below pH 4. Both uranyl humate species determine the speciation in solution in the pH range between pH 4.5 and pH 9 (absence of CO_2) and pH 4.5 and 7.5 (presence of CO_2). Then, the prevailing species in solution is the $UO_2(OH)HA(I)$ complex. At higher pH values uranyl carbonato and uranyl hydroxo complexes become dominant in the presence and absence of CO_2, respectively.

10.1.2.4 U(VI) sorption onto kaolinite in absence of humic acid

Results of batch experiments for kaolinite and U(VI) are depicted in Fig. 10.7. They are consistent with those data previously reported in the literature (e.g., Arnold et al., 1998; Kilislioglu and Bilgin, 2002; Payne et al., 2004).

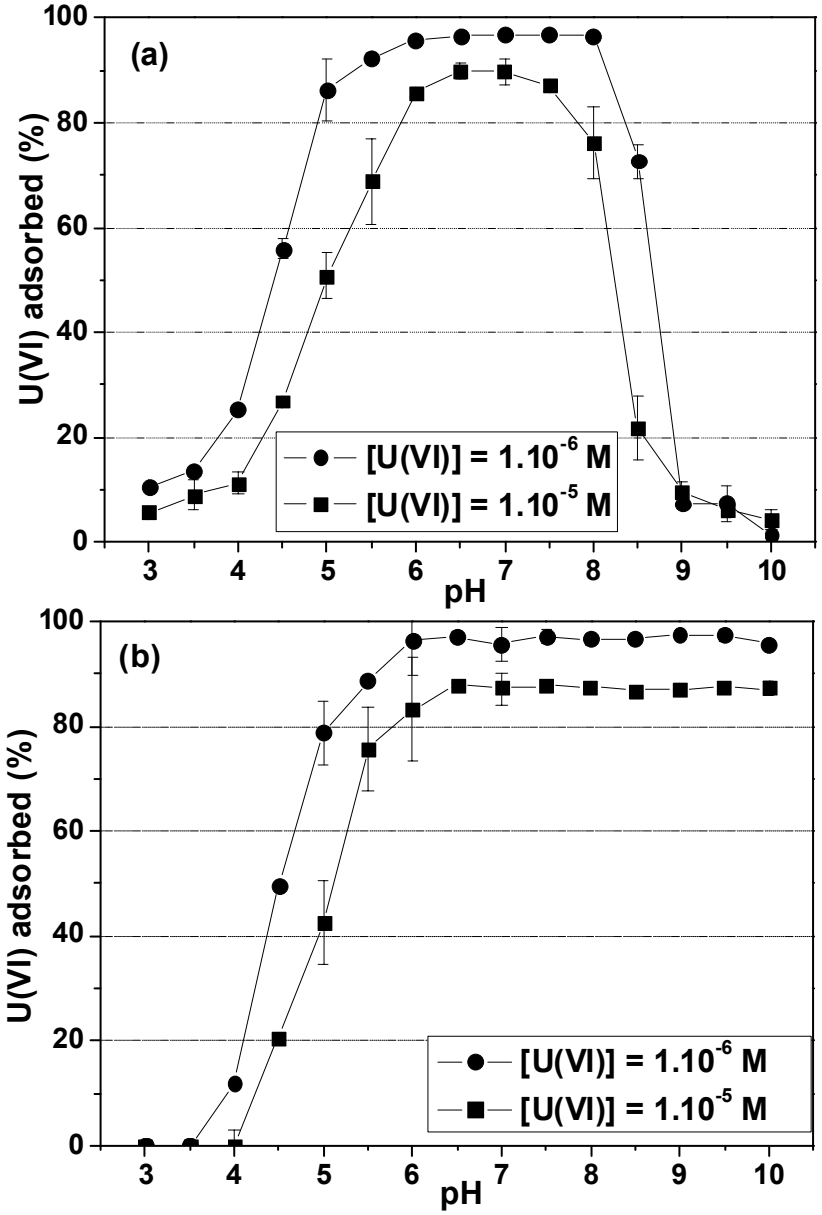

Fig. 10.7: U(VI) adsorption onto kaolinite as a function of pH and U(VI) concentration in the (a) presence and (b) absence of CO_2 (I: 0.01 M $NaClO_4$).

In the presence of CO_2, the percentage of the total U(VI) adsorbed onto kaolinite increases from nearly zero at pH 3 to 97% between pH 6 and pH 8. Above pH 8, the U(VI) sorption decreases. The highest U(VI) adsorption occurs in the pH range, where the U(VI) hydroxyl complexes are important. The positioning of the sorption edges at low pH values suggests the formation of relative strong actinide/surface site complexes. The U(VI) sorption behavior is comparable in the systems with and without CO_2 in the pH range between pH 3 and pH 8. At pH >8, however, no sorption decrease was observed in the absence of CO_2. This behavior is a result of the U(VI) speciation in the solution. In the presence of CO_2, U(VI) forms negatively charged uranyl carbonato complexes $UO_2(CO_3)_3^{4-}$ ($\log\beta = 21.0 \pm 0.3$, Pashalidis et al., 1997) and $(UO_2)_2CO_3(OH)_3^-$ ($\log\beta \approx 41$, Guillaumont et al., 2003). Under these conditions the kaolinite surface is also negatively charged. Therefore, the electrostatic repulsions between uranyl carbonato complexes and kaolinite result in the low U(VI) adsorption in this pH range.

An increase of the initial U(VI) concentration from $1 \cdot 10^{-6}$ M to $1 \cdot 10^{-5}$ M causes a shift of the sorption pH edge by one pH unit to higher pH values. The mass of adsorbed U(VI) in the maximum of sorption curves is higher in the case of $1 \cdot 10^{-5}$ M U(VI) concentration (e.g., pH 7: 532 μg U(VI)/ 1 g kaolinite is adsorbed) than in $1 \cdot 10^{-6}$ M U(VI) concentration (pH 7: 59 μg U(VI)/1 g kaolinite is adsorbed). However, the percentage of U(VI) adsorbed onto kaolinite decreases due to the higher initial U(VI) concentration. Varying the ionic strength from 0.01 M to 0.1 M has no (pH >6) or only a small (pH 3–5.5) influence on the U(VI) sorption (data not shown).

10.1.2.5 U(VI) sorption onto kaolinite in presence of humic acid

HA influences significantly the adsorption of U(VI) onto kaolinite in the entire studied pH range, see Fig. 10.8. The sorption curve can be divided into three parts. At pH <5, an enhancement in the U(VI) sorption was observed compared to the HA-free system. HA is almost 100% (10 mg/L) or 80% (50 mg/L) adsorbed on the kaolinite surface in this pH range (see Fig. 10.2), therefore reduction in the U(VI) uptake was expected due to the competition between HA and U(VI) for available binding sites on the kaolinite surface. However, the adsorbed HA features additional binding sites for U(VI), hence the U(VI) adsorption can increase in its presence.

In the near-neutral pH region, between pH 5 and pH 8.5, the U(VI) adsorption is lower in the presence of HA compared to the HA-free system. At pH 5, desorption of HA from the kaolinite surface starts (Fig.10.2). It leads to a decrease of the U(VI) adsorption onto kaolinite due to the formation of dissolved uranyl humate complexes. Binary complexes $UO_2HA(II)$ as well as mixed ternary uranyl hydroxo humate complexes $UO_2(OH)HA(I)$ can occur (see Fig.10.6). Although the HA concentration (10 mg/L $\approx 1.8 \cdot 10^{-5}$ mol/L HA(II), calculated according to Eq. (7.6)) exceeds the U(VI) concentration ($1 \cdot 10^{-6}$ M) in the solution, U(VI) uptake in the presence of HA is reduced only very slightly (about 10%) compared to the system free of HA.

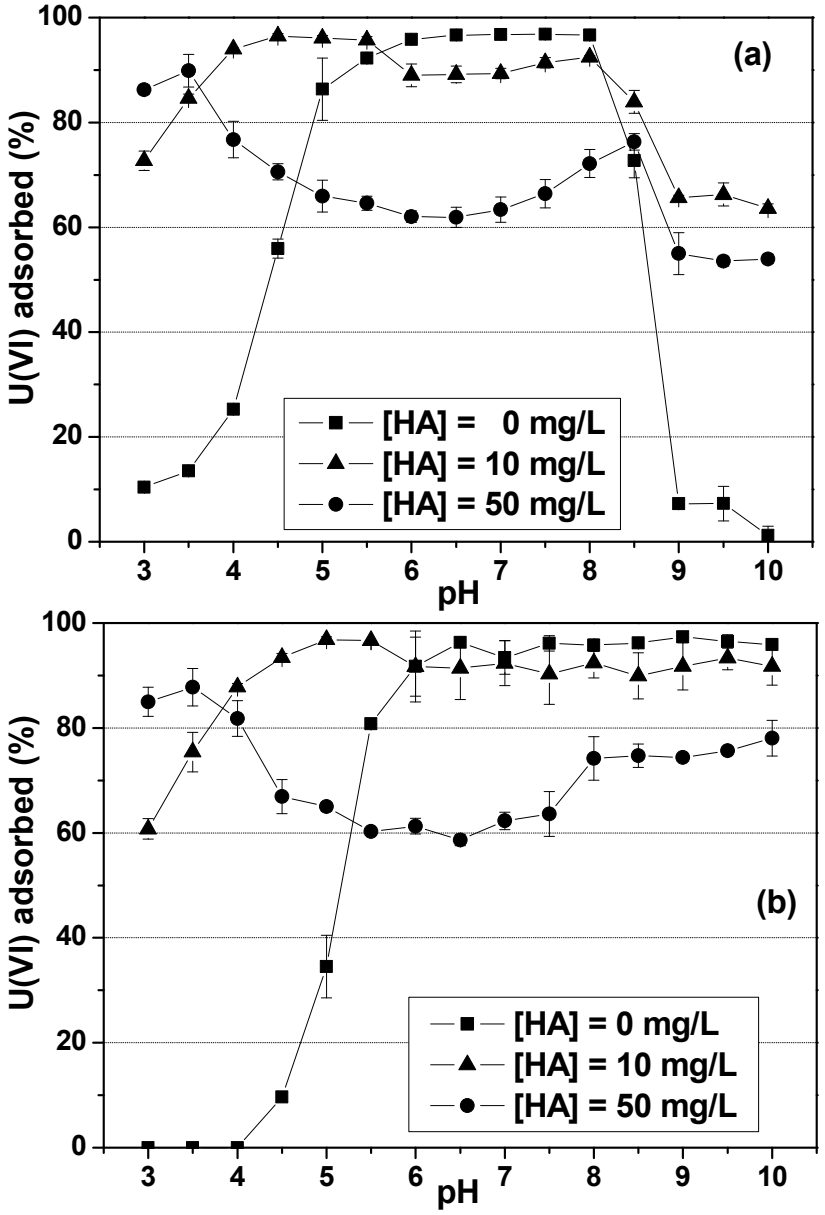

Fig. 10.8: U(VI) adsorption onto kaolinite as a function of pH and HA concentration in the (a) presence and (b) absence of CO_2 ([U(VI)]: $1 \cdot 10^{-6}$ M, I: 0.01 M $NaClO_4$).

It seems, that in spite of HA presence, U(VI) prefers sorption onto kaolinite than the complexation with HA in the solution. However, in the experiments carried out with higher HA concentration (50 mg/L) the U(VI) sorption is significantly lower than in the experiments conducted with only 10 mg/L. The lower U(VI) sorption at higher initial HA concentration results from a higher amount of dissolved HA forming aqueous complexes with U(VI). It can lead to an enhanced mobility of U(VI) in the environment. At pH >8.5, in the presence of CO_2, the sorption of U(VI) again increases in the presence of HA. As HA is nearly completely desorbed from the kaolinite surface (10% of HA remain adsorbed at pH 8.5), one should expect

reduced adsorption of U(VI) onto kaolinite in the HA presence. However, the U(VI) sorption is enhanced. From the comparison with the corresponding system without CO_2, where no decrease of U(VI) sorption was observed in the presence of 10 mg/L HA, one can conclude that carbonate must play a role in the U(VI) sorption onto kaolinite also in the presence of HA. It is possible that uranyl carbonato humate complexes are formed, which can interact with the kaolinite surface and, therefore, enhance the U(VI) sorption onto kaolinite in the presence of HA in the alkaline pH region. Glaus et al. (1995) reported the possible existence of the ternary uranyl carbonato humate complex $(UO_2CO_3)HA$ in waters containing humic substances, however its stability constant is low ($\log\beta \approx 5$). Such sorption behavior in the alkaline pH range seems to be specific for our system and experimental conditions used.

In conclusions, effects of different parameters on U(VI) sorption onto kaolinite were studied. U(VI) sorption onto kaolinite is influenced by pH, presence of CO_2, U(VI) concentration and HA presence. In the absence of CO_2, the U(VI) sorption increases up to pH ~ 6.5. Then, it remains unchanged. Formation of negatively charged uranyl carbonato complexes causes a decrease of the U(VI) sorption onto the negatively charged surface of kaolinite above pH 8 in the presence of CO_2. Increase of U(VI) concentration results in a shift of the sorption pH edge by one pH unit to higher pH, whereas the ionic strength has only a slight influence on the U(VI) sorption onto kaolinite. The adsorption of U(VI) closely follows the adsorption of HA. HA enhances the U(VI) uptake in the acidic pH range compared to the system without HA due to the formation of additional binding sites for U(VI) coming from HA adsorbed onto kaolinite. Formation of dissolved uranyl humate complexes reduces U(VI) sorption in the near-neutral pH range.

Finally, we conclude that the presence of HA can enhance the U(VI) migration under environmentally relevant conditions. Therefore, HA has to be involved in model calculations for the assessment of the long-term stability of nuclear waste repositories.

10.2 Structure of U(VI)-HA-kaolinite surface complexes studied by EXAFS

The structure of U(VI)-kaolinite-surface complexes in presence of HA was studied by extended X-ray absorption fine structure analysis (EXAFS). The influence of HA, pH and CO_2 presence was determined. Results of the system U(VI)-HA-kaolinite were interpreted and compared with the binary systems U(VI)-kaolinite (Reich et al., 2006b; Thompson et al., 1998) to obtain information on the influence of HA on the near-neighbor surrounding of U(VI) in kaolinite surface complexes.

10.2.1 Experimental

EXAFS samples were prepared in form of wet pastes. U(VI) and HA (unlabeled HA type M42, batch M145, see chapter 3) were adsorbed onto 200 mg of kaolinite, as described in chapter 10.1, under the following conditions: [U(VI)]: $1 \cdot 10^{-5}$ M, [HA]: 10 mg/L, S/L ratio: 4 g/L, pH: 5-8.5, $p(CO_2)$: $10^{-3.5}$ atm, I: 0.1 M $NaClO_4$. The supernatants were removed and meas-

ured by ICP-MS. The wet pastes (kaolinite with adsorbed U(VI) and HA) were immediately filled into special polyethylene sample holders. These sample holders were then sealed with Kapton polyamide tape and heat-sealed in two layers of polyethylene foil to avoid moisture loss during analysis and to provide several layers of containment of the radioactive sample.

EXAFS data were collected at the Rossendorf Beamline (ROBL) at the European Synchrotron Radiation Facility (ESRF) Grenoble, France. Uranium L_{III}-edge absorption spectra were recorded in fluorescence mode at room temperature. The ionization potential of the uranium L_{III}-edge was defined as 17 185 eV. Multiple scans (5–8) were measured for all samples. The EXAFS spectra were analyzed according to standard procedures including statistical weighting of the 13 fluorescence channels and their dead-time correction using the suite of programs EXAFSPAK (George and Pickering, 1995). Theoretical scattering phases and amplitudes were calculated with the scattering code FEFF 8.20 (Ankudinov et al., 2002).

The structural model for fitting the EXAFS oscillations was derived from the EXAFS investigations of the binary system U(VI)-kaolinite KGa-1b (Reich et al., 2006b). The best fits of the measured EXAFS oscillations in the studied ternary system were obtained considering two oxygen atoms in the axial (O_{ax}) and five oxygen atoms in the equatorial (O_{eq}) coordination shells coordinated to the uranyl ion, multiple scattering (MS) along the uranyl unit, and two coordination shells each with one Al/Si atom (for more details see Křepelová, 2006a).

10.2.2 Influence of different experimental conditions on the near-neighbor surrounding of U(VI) in kaolinite surface complexes

In this paragraph the influence of different parameters – pH, CO_2 and HA-presence – on the U(VI) surface complexation will be discussed (for details see Křepelová, 2006a) .

10.2.2.1 Effect of pH

Figure 10.9 shows the obtained U L_{III}-edge k^3-weighted EXAFS oscillations and the corresponding Fourier transforms (FTs) of the samples prepared at different pH values in the presence of HA.

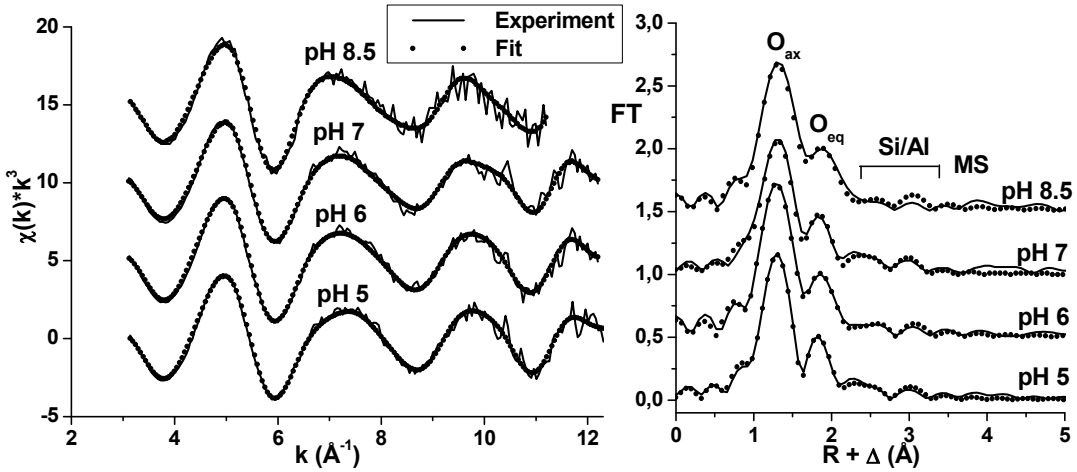

Fig. 10.9: EXAFS oscillations and FTs of the samples prepared at different pH values.

As it can be seen from the figure, all examined samples exhibit comparable EXAFS oscillations and FTs with no remarkable differences at different pH values. The results of the fitting procedure are summarized in Tab. 10.1.

Tab. 10.1: Obtained structural parameters for the samples prepared at different pH values.

		2 x O_{ax}		5 x O_{eq}		1 x Si_1/Al_1		1x Si_2/Al_2			
Sample	pH	R	σ^2	R	σ^2	R	σ^2	R	σ^2	ΔE	Red.
U4-134	5	1.76	0.0031	2.34	0.0144	3.10	0.0035	3.30	0.0036	-12.6	0.114
U4-135	6	1.77	0.0033	2.34	0.0140	3.10	0.0048	3.31	0.0056	-12.3	0.071
U4-136	7	1.77	0.0041	2.33	0.0145	3.08	0.0030	3.29	0.0032	-13.0	0.113
U4-137	8.5	1.78	0.0037	2.35	0.0130	3.08	0.0027	3.27	0.0036	-11.3	0.230

ΔR: ± 0.02 Å. $\Delta\sigma^2$: ± 0.001 Å

The obtained structural parameters show no significant differences. In the binary system, Reich et al. (2006b) observed an increase of U-O_{eq} bond distances with increasing pH value from 2.36 Å to 2.41 Å probably due to the formation of ternary surface uranyl complexes with carbonate. This effect was not found in the ternary system studied in this work, presumably because U(VI) forms uranyl hydroxyl humate complexes and the effect of carbonate on the U-O_{eq} atom distance is suppressed in the presence of HA.

10.2.2.2 Influence of CO_2

Two samples were prepared to study the effect of CO_2 at pH 8.5 on the U(VI) coordination environment in the surface complexes in the presence of HA. Also in this case the obtained U L_{III}-edge k^3-weighted EXAFS oscillations and corresponding FTs are comparable for both samples, see Fig. 10.10. It is obvious that the fit of the sample prepared on air is more problematic than that for the sample prepared in nitrogen atmosphere. It is due to the lower signal-to-noise ratio, which caused that the *k*-range had to be reduced to 11.2 $Å^{-1}$.

The resulted structural parameters for these two samples are given in Tab. 10.2. There is a small observable drop from 2.35 Å to 2.33 Å of the U-O_{eq} distance in the CO_2-free system. From this it could be derived that U(VI) adsorbed on the kaolinite surface interacts with carbonate, but the obtained difference is too small. Under consideration of the standard deviation it is not significant. However, Reich et al. (2006b) also observed such effect in the binary system U(VI)-kaolinite, where the decrease of the U-O_{eq} distance was more significant, from 2.41 Å to 2.36 Å. However, the U-O_{eq} distance in $[UO_2(CO_3)_3]^{4-}$ amounts to 2.44 Å, so it can not be concluded definitely that there is an influence of carbonate on the near-neighbor surrounding of U(VI) in the kaolinite surface complexes.

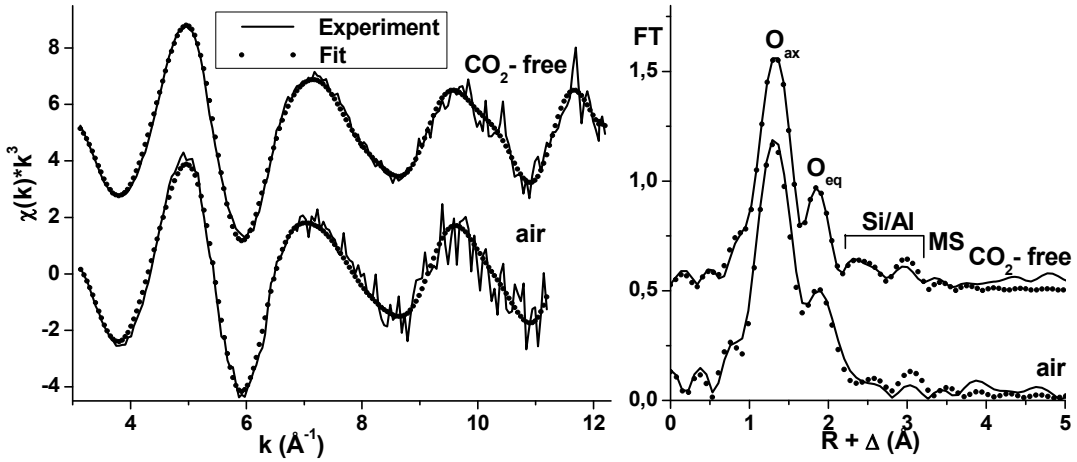

Fig. 10.10: EXAFS oscillations and FTs of the samples with different CO_2 concentration.

Tab. 10.2: Obtained structural parameters for the samples prepared in absence and presence of CO_2.

		2 x O_{ax}		5 x O_{eq}		1 x Si_1/Al_1		1x Si_2/Al_2			
Sample	pH: 8.5	R	σ^2	R	σ^2	R	σ^2	R	σ^2	ΔE	Red.
U4-137	Air	1.78	0.0037	2.35	0.0130	3.08	0.0027	3.27	0.0036	-11.3	0.230
U4-138	no CO_2	1.78	0.0040	2.33	0.0147	3.09	0.0035	3.30	0.0033	-11.8	0.097

ΔR: ± 0.02 Å. $\Delta\sigma^2$: ± 0.001 Å

10.2.2.3 Effect of humic acid presence

Figure 10.11 illustrates U L_{III}-edge k^3-weighted EXAFS oscillations and their corresponding FTs for the samples prepared at the same pH value (pH ~ 7) in absence and presence of HA. Again, the samples exhibit comparable EXAFS oscillations and FTs with no significant differences.

Also in this case, the obtained structural parameters (see Tab. 10.3) are very similar. The U-O_{ax} distances amount to 1.77 Å for both samples. The U-Si/Al distances are slightly shortened from 3.08 Å and 3.29 Å in the presence of HA to 3.06 Å and 3.26 Å in the absence of HA. The U-O_{eq} distances are almost identical: 2.33 Å for the sample with HA and 2.34 Å for the sample without HA. It leads to the conclusion that HA has no influence on the EXAFS structural parameters of U(VI)-kaolinite surface complexes.

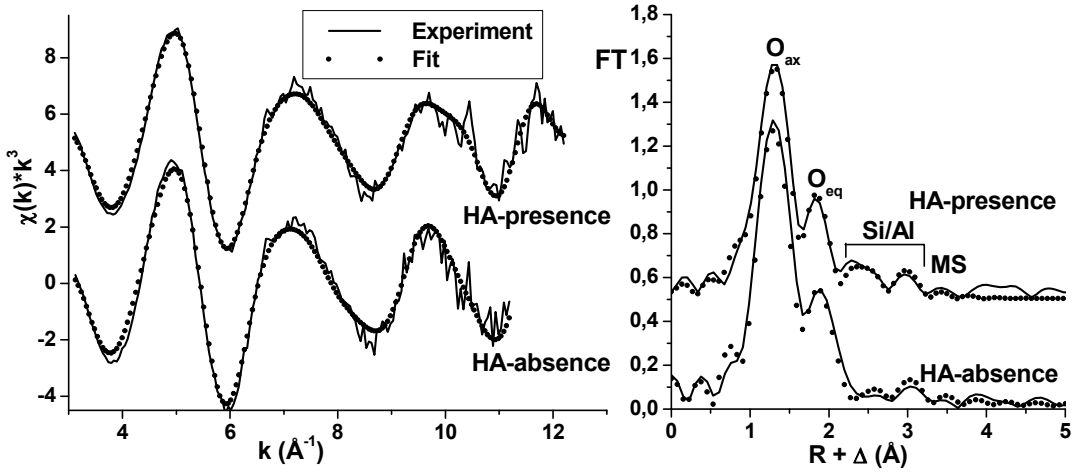

Fig. 10.11: EXAFS oscillations and FTs of the samples with and without HA.

Tab. 10.3: Obtained structural parameters for the samples prepared with and without HA.

Sample	pH ~ 7	2 x O_{ax} R	2 x O_{ax} σ^2	5 x O_{eq} R	5 x O_{eq} σ^2	1 x Si_1/Al_1 R	1 x Si_1/Al_1 σ^2	1x Si_2/Al_2 R	1x Si_2/Al_2 σ^2	ΔE	Red.
U4-136	HA-	1.77	0.0041	2.33	0.0145	3.08	0.0030	3.29	0.0032	-	0.113
U4-140	HA-	1.77	0.0030	2.34	0.0123	3.06	0.0040	3.26	0.0042	-	0.155

ΔR: ± 0.02 Å. $\Delta\sigma^2$: ± 0.001 Å

10.2.3 Comparison of EXAFS results of the binary and ternary systems

The EXAFS analysis of the ternary system was compared to the EXAFS analysis of the binary system U(VI)-kaolinite performed by Reich et al. (2006b). They studied the effect of pH, CO_2-presence and U(VI)-concentration on the U(VI) sorption onto kaolinite by means of combination of batch-type sorption experiments and EXAFS measurements.

For the EXAFS analysis they used two different tools. Firstly, the EXAFS analysis was performed using EXAFSPAK (George and Pickering, 1995). The following conclusions have resulted: No U-U interactions were observed, therefore U(VI) forms only mononuclear surface complexes. The U-O_{eq} distances increased with increasing pH values. U-Si/Al interactions at 3.1 Å and 3.3 Å were found, which points out to inner-sphere sorption of UO_2^{2+} by edge-sharing with SiO_4-tetrahedra and/or AlO_6-octahedra.

Secondly, the Tikhonov regularization method (Babanov et al., 1981) was used, which has been proposed for EXAFS analysis as an alternative to the analysis of EXAFS spectra by conventional shell fitting. An improved algorithm was developed and applied to the analysis of U L_{III}-edge EXFAFS spectra of U(VI) adsorbed onto kaolinite (Reich et al., 2006b). The U L_{III}-edge EXAFS spectrum calculated agreed well with experimental data. Two peaks at 1.79 Å and 2.35 Å with N equal 1.9 (O_{ax}) and 5.1 (O_{eq}), respectively, were obtained. Approximately 0.7 Si/Al atoms at 3.06 Å and 0.4 Å atoms at 3.26 Å were found to surround the U(VI) atom.

Table 10.4 shows the comparison of the structural parameters that were obtained from EXAFS analysis of the ternary and binary systems U(VI)-kaolinite (Reich, et al., 2006b; Thompson et al., 1998).

The U-O_{ax} distances obtained for both binary kaolinite systems KGa-1b and KGa-2 are the same, while in the presence of HA this distance was shortened. Reich et al. (2006b) observed an increase of U-O_{eq} with increasing pH from 2.36 to 2.41 Å, which did not occur in the ternary system. The system with kaolinite KGa-2 gave a value for the U-O_{eq} distance, which is comparable with that obtained for the binary system with kaolinite KGa-1b. The

value obtained for the ternary system is slightly lower. Thompson et al. (1998) obtained only one U-Si/Al distance, but this distance is the same as the longer U-Si/Al distance found for the systems with kaolinite KGa-1b.

Tab. 10.4: Comparison of the obtained structural parameters for the systems U(VI)-kaolinite and U(VI)-HA-kaolinite.

System	R(U-O_{ax}) (Å) N = 2	R(U-O_{eq}) (Å) N = 5	R(U-Si/Al) (Å) N = 1 or 2	Reference
Kaolinite KGa-1b	1.80	2.36 – 2.41	3.1/3.3	Reich et al., 2006
Kaolinite KGa-2	1.80	2.40	3.3	Thompson et al., 1998
Kaolinite KGa-1b-HA	1.77	2.34	3.1/3.3	this work

The obtained EAXFS structural parameters for the system U(VI)-HA-kaolinite studied are similar or they lie in the range of values that were obtained for the binary system U(VI)-kaolinite. Therefore, it can be concluded that HA has no effect on the EXAFS structural parameters in the system U(VI)-HA-kaolinite. Moreover, it seems that in spite of HA presence, U(VI) prefers to adsorb rather directly onto kaolinite than via HA, otherwise no U-Si/Al interactions could be observed. For more details about the EXAFS analysis and discussion see (Křepelová, 2006a).

10.3 TRLFS study of U(VI)-kaolinite surface complexes in absence and presence of humic acid

As additional method, time-resolved laser-induced fluorescence spectroscopy (TRLFS) was applied to study the kind of U(VI) surface complexes onto kaolinite. These investigations were performed at different pH values in the absence and presence of HA.

10.3.1 Experimental

The TRLFS data were collected for two systems. The binary system consists of U(VI) adsorbed onto kaolinite, whereas in the ternary system also HA was present. U(VI) or U(VI)/HA were adsorbed as described in chapter 10.1 under the following experimental conditions: [U(VI)]: $1 \cdot 10^{-5}$ M, [HA]: 10 mg/L (unlabeled HA type M42, batch M145, see chapter 3), I: 0.1 M $NaClO_4$, pH: 5-8, S/L: 4 g/L, $p(CO_2)$: $10^{-3.5}$ atm. After phases separation, the super-

natants were analyzed by ICP-MS for U(VI) final concentrations. For the spectroscopic investigation, kaolinite samples from the batch experiments were first re-suspended in 10 mL of a solution with pH and ionic strength being identical to the original solution (without U(VI) and HA). This ascertained that only fluorescence signals caused from originally adsorbed U(VI) would be detectable, eliminating the dissolved U(VI) fraction. Time-resolved spectra of these kaolinite suspensions were then recorded at permanent stirring.

The TRLFS system consisted of a Nd:YAG diode laser with subsequent 4th harmonic generation. The wavelength of 266 nm was used for the excitation of the samples with laser energies of about 0.3 mJ, providing a maximized signal-to-noise ratio. The delay time after the excitation laser pulse ranges from 0.03 μs to 10.03 μs (for details see Křepelová, 2006a).

The lifetimes of U(VI) fluorescence species were determined from bi-exponential fit analysis of obtained data indicating at least two surface species. An example for the sample of U(VI) adsorbed onto kaolinite at pH ~ 7 is shown in Fig. 10.12.

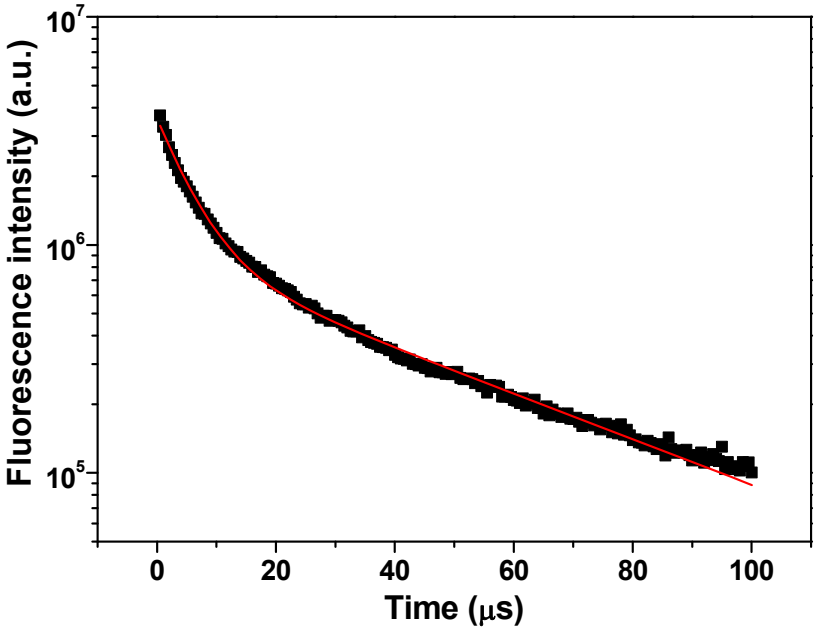

Fig. 10.12: Bi-exponential fluorescence decay behavior of a U(VI)-kaolinite (pH ~ 7).

The fluorescence lifetimes of two U(VI) surface species were calculated from Eq. 10.1:

$$y = y_0 + A_1 e^{-(x-x_0)/t_1} + A_2 e^{-(x-x_0)/t_2} \quad (10.1)$$

The lifetime analysis and the generation of the graphics utilized OriginPro 7.5G software (OriginLab Corp., Northampton, MA). For more details about the lifetime analysis and the spectra deconvolution see (Křepelová, 2006a).

10.3.2 Measurements in the binary system U(VI)-kaolinite

TRLFS measurements provide two kinds of characteristic information: the position of fluorescence emission bands and the fluorescence lifetimes. The positions of fluorescence bands are primary attributes of the TRLFS spectrum, whereas the fluorescence lifetime is a secondary feature, because of its dependence on the sample preparation and temperature of the experiment. The fluorescence lifetime varies depending on the number of neighboring water molecules surrounding the U(VI) atom (Geipel, et al., 2000). Such characteristic spectral information is useful for the identification of fluorescent aqueous uranium species, as well as U(VI) surface species adsorbed onto kaolinite.

Fig. 10.13 shows the dependence of the relative fluorescence intensity on the delay time. The original spectra of all samples with U(VI) adsorbed onto kaolinite at different pH values are comparable, thus only the TRLFS spectrum of U(VI) adsorbed onto kaolinite at pH ~ 7 is shown as an example.

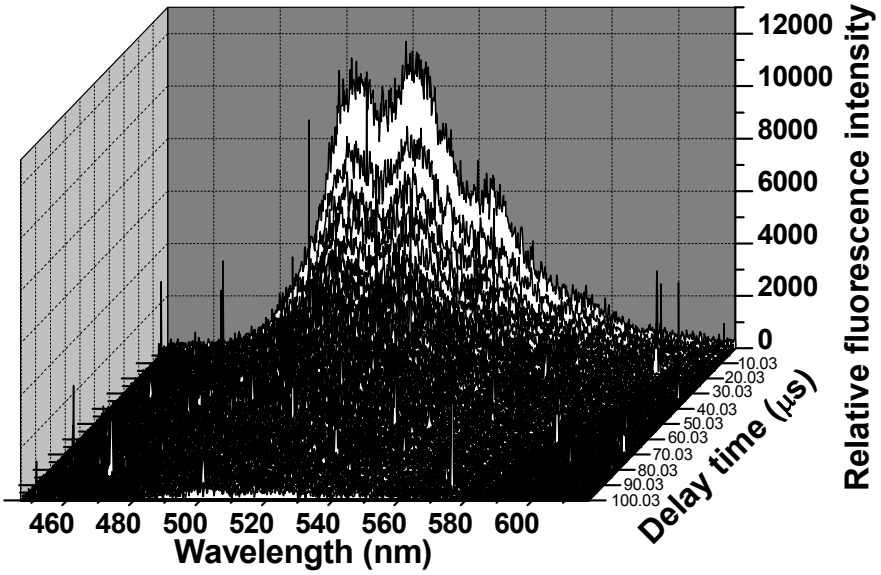

Fig. 10.13: TRLFS spectrum of U(VI) adsorbed onto kaolinite (pH ~ 7).

The TRLFS spectra of the adsorbed U(VI) surface species on kaolinite indicate at least two surface species with two different fluorescence lifetimes, i.e., one short- and one long-lived species. The results of the fluorescence lifetime determinations for all measured samples are summarized in Tab. 10.5. The values of the fluorescence lifetimes of both species demonstrate no dependence on pH value.

Tab. 10.5: Fluorescence lifetimes of the U(VI) species adsorbed onto kaolinite, errors represent 1σ.

Sample	pH	τ_1 (ns)	τ_2 (ns)
U5	5	5640 ± 150	40800 ± 440
U6	6	6880 ± 150	41300 ± 470
U7	7	5610 ± 120	44100 ± 630
U8	8	5330 ±160	43700 ± 730
Mean lifetime		5870 ± 690	42480 ± 1670

Six fluorescence emission bands were obtained for the fluorescence spectra of all measured samples, which can be described by a set of six absorption peaks similarly to the work of Bell and Biggers (1968). The deconvoluted fluorescence spectra revealed six characteristic fluorescence emission bands that are almost identical for both U(VI) surface species. The peak maxima are situated at 486.9 ± 0.9, 501.8 ± 0.6, 520.6 ± 0.9, 541.7 ± 0.7, 567. 8 ± 1.5, and 583.3 ± 0.6 nm. The positions of peak maxima are shifted significantly relative to the values for free uranyl ion in perchlorate medium (see Bell and Bigers, 1968). The shifts range from 16.8 nm for the first peak to 9.7 nm for the fifth one.

Due to coincidence of all the fluorescence peaks, the two adsorbed U(VI) surface species are assumed to be similar in coordination environment throughout the investigated pH range. Thus, they should have identical numbers of hydroxyl groups in their first coordination sphere, as different numbers of hydroxyl group cause changes in the spectral features (Baumann et al., 2005). Shorter fluorescence lifetimes indicate more water molecules in the coordination environment of the respective adsorbed U(VI) surface species, because water molecules quench the fluorescence lifetime (Arnold et al., 2006). On this basis, it can be concluded that U(VI) forms two surface species on kaolinite, which differ in the amount of water molecules in their coordination environment.

10.3.3 Measurements in the ternary system U(VI)-humic acid-kaolinite

The original TRLFS spectrum of U(VI) adsorbed on kaolinite in the presence of HA at pH ~ 7 is shown in Fig. 10.14 as representative of the original spectra of all samples with U(VI) adsorbed onto kaolinite in the presence of HA at different pH values.

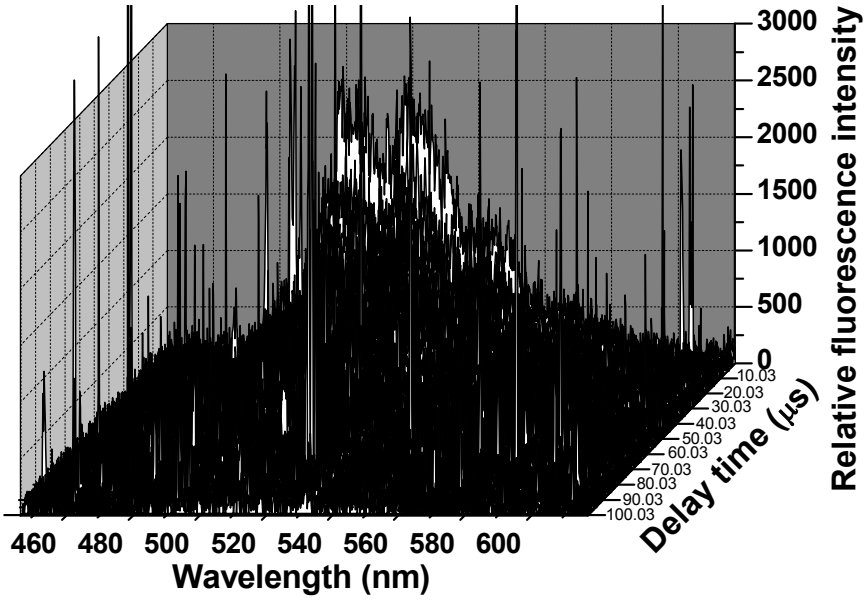

Fig. 10.14: TRLFS spectrum of U(VI) adsorbed onto kaolinite in the presence of HA (pH ~ 7).

It is obvious that, compared to the original TRLFS spectrum of U(VI) adsorbed onto kaolinite in the absence of HA at the same pH value, the spectrum has a lower quality due to the high signal noise because of the presence of HA. Therefore, the lifetime analysis and also the detection of the emission bands were more complicated and resulted in higher standard deviations.

The lifetimes of U(VI)-HA fluorescence species were determined from bi-exponential fit analysis of the obtained data. Comparable to the binary system, two different surface species with two different fluorescence lifetimes were indicated. Due to the high signal noise in the spectra the analysis was performed in the shortened wavelength range: 480 nm – 600 nm. The average fluorescence lifetimes were calculated from Eq. (10.1). The results of fluorescence lifetime determinations are summarized in 10.6. The obtained fluorescence lifetimes are not as consistent as in the binary system.

Tab. 10.6: Fluorescence lifetimes of the U(VI) species sorbed onto kaolinite in the presence of HA.

Sample	pH	τ_1 (ns)	τ_2 (ns)
U-HA5	5	3540 ± 490	26300 ± 410
U-HA6	6	4770 ± 370	31400 ± 1400
U-HA7	7	4540 ± 220	32700 ± 450
U-HA8	8	4680 ± 450	34700 ± 2980
Mean lifetime		4380 ± 570	31300 ± 3580

Due to the lower quality of the spectra and the shortening of the evaluated wavelength range, the detection of the fluorescence emission bands was limited. As in the binary system, six peaks were assumed to describe satisfactorily the measured spectra. However, the position of the last peak was very uncertain and thus, only the positions of the first five peaks were found. The peaks maxima are situated at 486.6 ± 1.1, 501.1 ± 2.2, 520.5 ± 1.5, 542.2 ± 2.6, and 566.7 ± 3.6. Two different obtained lifetimes indicate, as in the binary system, the formation of at least two different surface complexes. The interpretation of these two complexes is, however, more complicated due to the presence of HA. Uranyl humate itself does not show fluorescence under the applied experimental conditions (Sachs et al., 2006). So if U(VI) would be bound on kaolinite via HA, no U(VI) fluorescence should be measured for the prepared U(VI)-HA-kaolinite samples. This leads to the conclusion that U(VI) is not bound to kaolinite via HA.

10.3.4 Comparison of TRLFS measurements in the binary and ternary systems

Table 10.7 shows the comparison of the fluorescence intensities and the amounts of U(VI) adsorbed onto kaolinite of the samples prepared at pH ~ 7 in the presence and absence of HA. It can be seen that the U(VI) adsorption onto kaolinite is comparable in both cases. The difference in the adsorbed amounts is only 7%, while the fluorescence intensity is almost five times lower in the presence of HA than in its absence. It is obvious that HA decreases the measured fluorescence intensity of the samples. This points out to differences in surface speciation in both compared systems.

Tab. 10.7: Comparison of the relative fluorescence intensity and the amount of U(VI) adsorbed onto kaolinite of the samples prepared at pH ~ 7 in the absence and presence of HA.

pH ~ 7	U(VI)adsorb. (%)	RFI[a]
HA absence	91	12000
HA presence	98	2500

[a] Relative fluorescence intensity

Table 10.8 shows the comparison of the mean values of the fluorescence lifetimes of both species obtained in the presence and absence of HA. In the presence of HA, the fluorescence lifetimes of both species are significantly shorter. Shorter fluorescence lifetimes indicate HA in the coordination environment of the adsorbed U(VI) surface species, because HA

quenches the fluorescence lifetime. This means that in the presence of HA the hydrate shell of uranyl ions is partly displaced with HA.

Tab. 10.8: Comparison of fluorescence lifetimes in the absence and presence of HA.

pH 5 - 8	τ_1 (ns)	τ_2 (ns)
HA absence	5900 ± 700	42500 ± 1700
HA presence	4400 ± 600	30900 ± 3600

In Fig. 10.15 the obtained lifetimes of the surface species identified in the presence and absence of HA as a function of pH values are depicted. It becomes evident that pH values have no significant influence on the fluorescence lifetimes of U(VI) surface species in the binary as well as in the ternary system.

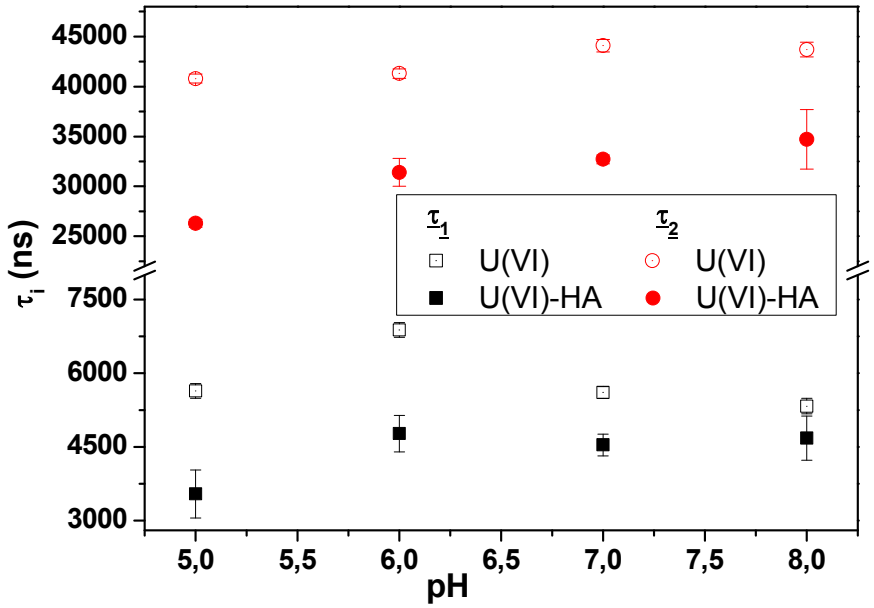

Fig. 10.15: Fluorescence lifetimes as a function of pH values.

Six fluorescence emission bands were obtained for the fluorescence spectra of all measured samples of U(VI) adsorbed onto kaolinite in the absence of HA. In the presence of HA, only five peaks were found due to the lower quality of the spectra. The comparison of the mean values of identified peak positions for the samples in the absence and presence of HA is

given in Tab. 10.9. No differences in peak positions were observed. Therefore, it can be concluded that HA does not influence the peak positions of both surface species.

Tab. 10.9: Comparison of absorption peak positions in the absence and presence of HA.

pH 5 – 8	1st peak	2nd peak	3rd peak	4th peak	5th peak	6th peak
HA absence	486.9 ±	501.8 ± 0.6	520.6 ± 0.9	541.7 ± 0.7	567.8 ± 1.5	583.3
HA presence	486.6 ±	501.1 ± 2.2	520.5 ± 1.5	542.2 ± 2.6	566.7 ± 3.6	-

10.3.5 Comparison with model systems

Spectroscopic techniques were used to obtain detailed information about the U(VI) interaction with kaolinite. They should help to identify, on which of possible binding sites of kaolinite (silanol, aluminol groups) U(VI) prefers to adsorb. Unfortunately, in EXAFS it is not possible to distinguish between Al and Si atoms. To decide between aluminol and silanol groups, TRLFS measurements of the system U(VI)-kaolinite were compared with U(VI)-gibbsite (Křepelová et al. 2006c) and U(VI)-silica gel (Trepte, 2006) systems. Gibbsite, $Al(OH)_3$, was chosen as a model mineral for aluminol sites and silica gel, SiO_2, represents silanol binding groups. Tab. 10.10 shows the comparison of mean values of fluorescence lifetimes obtained for the U(VI)-kaolinite system and for both model systems. In all systems, at least two fluorescence lifetimes were identified.

Tab. 10.10: Comparison of mean values of fluorescence lifetimes obtained for the systems studied in this work with those of the model systems UO_2-gibbsite and UO_2-silica gel.

System	τ_1 (ns)	τ_2 (ns)	Reference
UO_2-gibbsite	2360 ± 220	13200 ± 2500	Křepelová et al. 2006c
UO_2-silica gel	138400 ± 52900	361800 ± 103200	Trepte, 2006
UO_2-kaolinite	5900 ± 700	42500 ± 1700	this work
UO_2-HA-kaolinite	4400 ± 600	30900 ± 3600	this work

It becomes evident that the values of fluorescence lifetimes of both fluorescence species on kaolinite lie in the range between values obtained for gibbsite and for silica gel, however, the

fluorescence lifetimes of species on kaolinite are closer to those on gibbsite than on silica gel. It seems that U(VI) adsorbs on both kinds of available sites but not equal. It is not easy to identify, in which ratio they are represented or which binding sites are more occupied by U(VI). Aluminol binding sites are assumed to control the sorption of U(VI). In untreated kaolinite, the excess of Al_2O_3 was found by chemical analysis (cf. Tab. 2.1). From electron scanning microscopy of kaolinite particles, the ratio between planes and edges of kaolinite particles was calculated to be about 0.72, which indicates a higher amount of edges relative to basal planes. Similarly, Brady et al. (1998) reported higher percentage of edges relative to basal plane of the kaolinite KGa-1 resulting from scanning force microscopy. They also reported elevated reactivity of Al edge sites, relative to Si, and the weak sorption on basal planes resulting from their molecular modeling.

In conclusion, two adsorbed U(VI) species on kaolinite were identified in the binary (U(VI)-kaolinite) as well as in the ternary (U(VI)-HA-kaolinte) system. Both surface species can be attributed to adsorbed bidentate mononuclear surface complexes, in which two equatorial oxygen atoms of the uranyl ion are bound to two Al and/or Si (preferentially to Al) atoms of aluminol octahedra and/or silicon tetrahedra. Both surface species differ likely in the amount of water molecules in their coordination environment. In the ternary system, U(VI) prefers direct binding to the kaolinite than via HA, which is distributed between kaolinite particles. The hydrate shell of U(VI) is partly displaced with complexed HA.

11 Uranium(VI) sorption onto synthetic humic substance-kaolinite sorbates

Batch experiments in the ternary system U(VI)-HA-kaolinite showed that HA affects the U(VI) sorption onto kaolinite (chapter 10.1). However, natural clays are closely associated with a mélange of natural organic matter. Therefore, a more complex interaction is expected in contrast to the ternary system. The synthetic humic substance-kaolinite sorbates developed within this project contain a mixture of humic-like materials, especially humic substances that are assumed to be more hydrophobic than synthetic HA-like substances that were extracted from these sorbates directly after their syntheses (chapter 5). These sorbates can be used as model compounds for natural organic rich clays. They offer the possibility to approach natural conditions.

Within the project the U(VI) sorption onto two different types of synthetic humic substance-kaolinite-sorbates was studied. The results were compared to those of the ternary system U(VI)-HA-kaolinite and the binary system U(VI)-kaolinite.

During the syntheses of humic substance-kaolinite-sorbates, kaolinite is heated at 80 °C for 90 h in aqueous solution and is subjected to an alkaline and acidic treatment during the isolation of the sorbates. In order to study the influence of these treatments on the sorption properties of kaolinite, a pure kaolinite sample underwent the whole synthesis procedure described in chapter 5, however, without addition of further precursor substances. The U(VI)

sorption behavior of the resulting product was measured in comparison to that of original kaolinite KGa-1b.

11.1 Experimental

The batch experiments described in this report were performed with synthetic humic-substance-kaolinite sorbates type M1-KS(B) and M42-KS (see chapter 5.3). The sorption experiments were carried out under ambient atmosphere according to the sorption experiments described in chapter 10. However, slightly changed experimental conditions were applied.

U(VI) sorption onto synthetic humic substance-kaolinite-sorbates

Humic-substance-kaolinite sorbates M1-KS(B) (batch M189KS, TOC: 3.9 mg/g) and M42-KS (batch R11/04KS, TOC: 4.9 mg/g) were pre-equilibrated with 0.01 M $NaClO_4$ solution for 96 h between pH 3 and pH 10. The solid-to-liquid ratio (S/L) was 4 g/L. The resulting TOC content in the samples amounts to about 16 and 20 mg/L for M1-KS(B) and M42-KS, respectively. For the studies at pH >7, a calculated amount of $NaHCO_3$ was added to the suspensions to accelerate the equilibration with atmospheric CO_2. After pre-equilibration, a $UO_2(ClO_4)_2$ stock solution was added to the suspensions with a final U(VI) concentration of $1 \cdot 10^{-6}$ M. The pH values of the samples were readjusted immediately and the samples were shaken for 72 h. After shaking, the final pH values were measured and the samples were centrifuged for phases separation (30 min at 4000 rpm; model Megafuge 1.0, Heraeus Sepatech). The supernatants were removed from the solids and the U(VI) concentrations of the solutions were measured without further filtration by ICP-MS (ELAN 6000, Perkin Elmer). As humic substances were extracted from the humic substance-kaolinite-sorbates, the dissolved humic material was digested with HNO_3 in a microwave oven (model mls 1200 mega, MLS) before ICP-MS analyses. The U(VI) sorption onto the vial walls was investigated. For that, the vials were washed with water and dried. Then, 7 mL 1 M HNO_3 were added, the vials were shaken for 2 days and the U(VI) concentration in the HNO_3 solution was measured by ICP-MS. The amount of uranium adsorbed on the surface of the humic substance-kaolinite sorbates was calculated as the difference between the initial uranium concentration in solution and the sum of the amounts of uranium remaining in solution and adsorbed onto the vial walls.

In order to assess the amount of humic material released from the sorbates after the end of the experiments, UV-vis measurements (CARY-5G, Varian) were performed. The amount of humic substances in solution was estimated from the absorption intensities at 254 nm. Calibration curves were used from experiments where the pH dependent TOC release from synthetic humic-substance-kaolinite sorbates was studied.

U(VI) sorption onto original and treated kaolinite in absence of humic acid

The U(VI) sorption onto the original kaolinite and the kaolinite sample that was subjected to the synthesis procedure for humic substance-kaolinite-sorbates (see above) was studied under comparable experimental conditions: S/L: 4 g/L, pH 3-10, I: 0.01 M $NaClO_4$, [U(VI)]:

$1 \cdot 10^{-6}$ M. After the contact time of 72 h, the sample phases were separated by centrifugation (4000 rpm, 30 min) and the U(VI) concentration in the supernatants was mesured by ICP-MS without prior filtration step. The U(VI) sorption onto the vial walls was determined as described above.

U(VI) sorption onto original kaolinite in presence of humic acid

In order to compare the U(VI) sorption onto the humic substance-kaolinite-sorbates type M1-KS(B) and M42-KS with that of U(VI) onto kaolinite in presence of separately added HA, sorption experiments with HA type M1 or M42 were carried out applying comparable TOC contents in solution. For that the basic experimental conditions were kept constant (S/L: 4 g/L, pH 3-10, I: 0.01 M $NaClO_4$, [U(VI)]: $1 \cdot 10^{-6}$ M). HA concentrations of 29 and 35 mg/L HA type M1 and M42, respectively, were applied. These concentrations correspond to about 19 and 20 mg/L TOC. For the experiments, HA type M1 (batch M100A, Sachs et al. 2003) and type M42 (batch M145) were used. The HA solutions were spiked with ^{14}C-labeled HA type M1 (batch M130/4, 54.8 MBq/g) and type M42 (batch M180, 17.0 MBq/g) in order to determine the HA sorption onto kaolinite.

After pre-equilibration of kaolinite KGa-1b, uranyl humate solutions equilibrated for 24 h were added to the samples resulting in final U(VI) concentrations of $1 \cdot 10^{-6}$ M and the HA concentrations given above. The pH values of the suspensions were readjusted and the samples were shaken for 72 h. Then, the final pH values were measured, solutions and solids were separated by centrifugation (4000 rpm, 30 min). The remaining U(VI) concentrations in solution were analyzed by ICP-MS after digestion of the HA (see above). The HA concentrations were measured by liquid scintillation counting (LSC; Wallac System 1414, Perkin Elmer). Finally, the vial wall sorption of U(VI) and HA was determined using 1 M HNO_3 and 1 M NaOH, respectively, as described above.

11.2 Results and discussion

11.2.1 U(VI) sorption onto original and synthetic treated kaolinite KGa-1b

Figure 11.1 shows the results of the U(VI) sorption onto original kaolinite KGa-1b in comparison to that of U(VI) sorbed onto kaolinite that was treated by the synthesis procedure for humic substance-kaolinite-sorbates.

The sorption data obtained for U(VI) onto original kaolinite KGa-1b are in good agreement with those depicted in Fig. 10.7, where the sample solutions were subjected to an additional filtration step. The untreated and treated kaolinite samples exhibit a comparable sorption capacity for U(VI) between pH 3 and 10 within the experimental errors. From that it can be concluded that the synthesis procedure, i.e., the heating as well as the alkaline and acidic treatment of kaolinite, during the preparation of humic substance-kaolinite-sorbates has no significant influence on the sorption properties of KGa-1b.

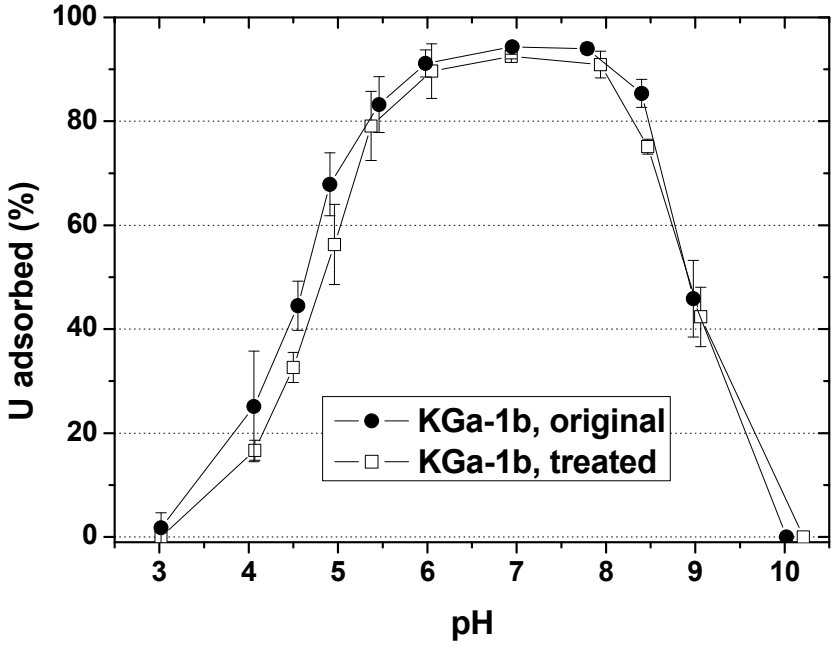

Fig. 11.1: U(VI) sorption onto original and treated kaolinite KGa-1b ([U(VI)]: $1 \cdot 10^{-6}$ M, I: 0.01 M $NaClO_4$, S/L: 4 g/L).

11.2.2 U(VI) sorption onto synthetic humic substance-kaolinite-sorbates in comparison to that of U(VI) onto kaolinite in presence of humic acid

Figure 11.2 illustrates the results of the U(VI) sorption onto the synthetic humic substance-kaolinite-sorbate type M1-KS(B) in comparison to that of U(VI) onto kaolinite in absence and presence of HA. The sorbed/bound amounts of humic matter in the studied systems as a function of pH are plotted in Fig. 11.3.

As already discussed in chapter 10.1, it can be concluded from Fig. 11.2 that humic substances influence the U(VI) sorption onto kaolinite. Compared to the HA-free system, the U(VI) sorption onto kaolinite is increased in the acidic pH range between pH 3 and 5, whereas it is decreased in the ternary system (U(VI)-HA M1-KGa-1b) between pH 6 and 8. The increase is attributed to the sorption/association of humic substances onto/with kaolinite which provides additional binding sites for U(VI). The amount of sorbed humic matter onto kaolinite is decreased with increasing pH value (see Fig. 11.3). As a result of this release, soluble binary and ternary uranyl humate complexes can be formed resulting in the decrease of the sorbed amount of U(VI). However, despite of similar initial TOC concentrations, the effect of humic material on the U(VI) sorption onto M1-KS(B) differs significantly from that onto KGa-1b in presence of HA type M1. In presence of 28 mg/L HA type M1, significantly less U(VI) is sorbed onto KGa-1b than in the system M1-KS(B).

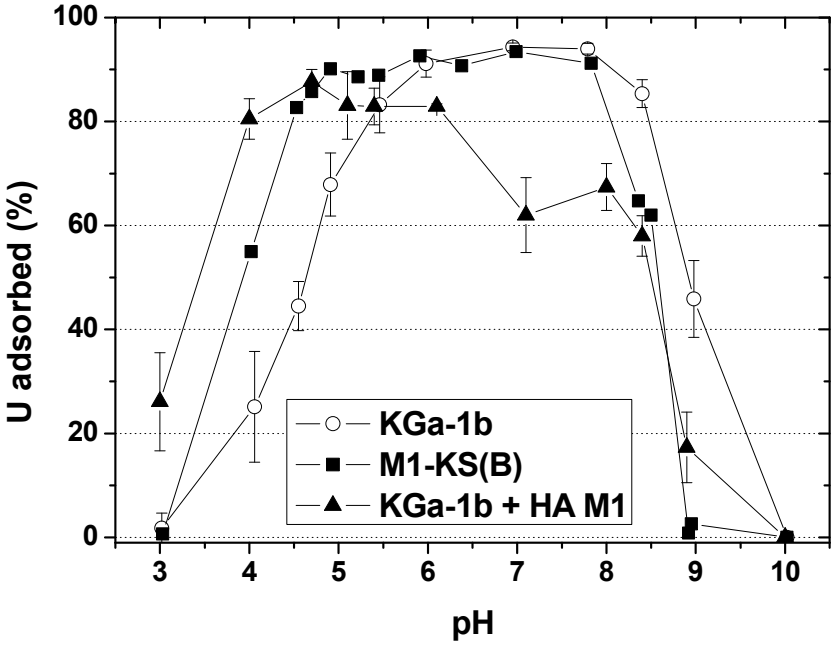

Fig. 11.2: U(VI) sorption onto M1-KS(B) in comparison to the U(VI) sorption onto KGa-1b in absence and presence of 29 mg/L HA type M1 ([U(VI)]: $1 \cdot 10^{-6}$ M, I: 0.01 M $NaClO_4$, S/L: 4 g/L, TOC: 16 mg/L (M1-KS(B)) and 19 mg/L (HA M1)).

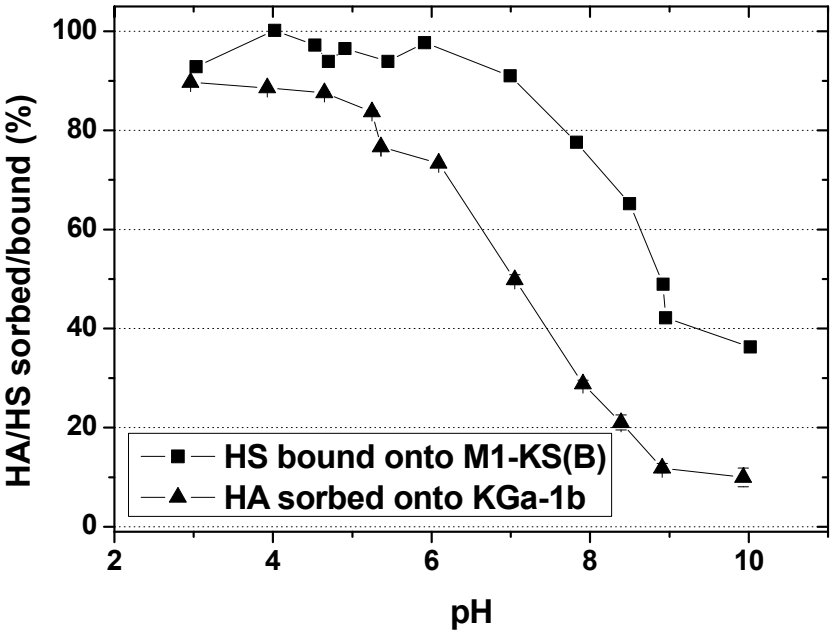

Fig. 11.3: Estimated amount of humic substances (HS) sorbed onto M1-KS(B) in comparison to the amount of HA type M1 sorbed onto KGa-1b.

The amount of sorbed/bound humic substances is decreased with increasing pH value in both systems (see Fig. 11.3). However, the HA in the ternary system is more mobile than the organic matter in the humic substance-kaolinite-sorbate. It is not clear if the material liberated from M1-KS(B) represents HA slowly released from the sorbate and not extracted during the isolation of the sorbate or if this material is produced by chemical transformations of non-HA-like substances during the batch experiments. Balcke et al. (2002) reported that the adsorption affinity of humic substances onto clays correlates directly with their aromaticity and inversely with their polarity. Based on that it is supposed that the humic matter associated with M1-KS(B) represents more hydrophobic humic substances with a higher aromaticity and a lower polarity than HA type M1. Probably, the humic material released from M1-KS(B) is a weaker complexing agent for U(VI) and keep less U(VI) in solution.

In all three systems, a further strong reduction of the U(VI) sorption can be observed between pH 8 and 10 (see Fig. 11.2). This behavior can be attributed to two overlapping and competing processes: (i) the formation of soluble U(VI) humate complexes and (ii) the formation of U(VI) carbonates which dominates the U(VI) sorption in the HA-free system in this pH range (see chapter 10.1).

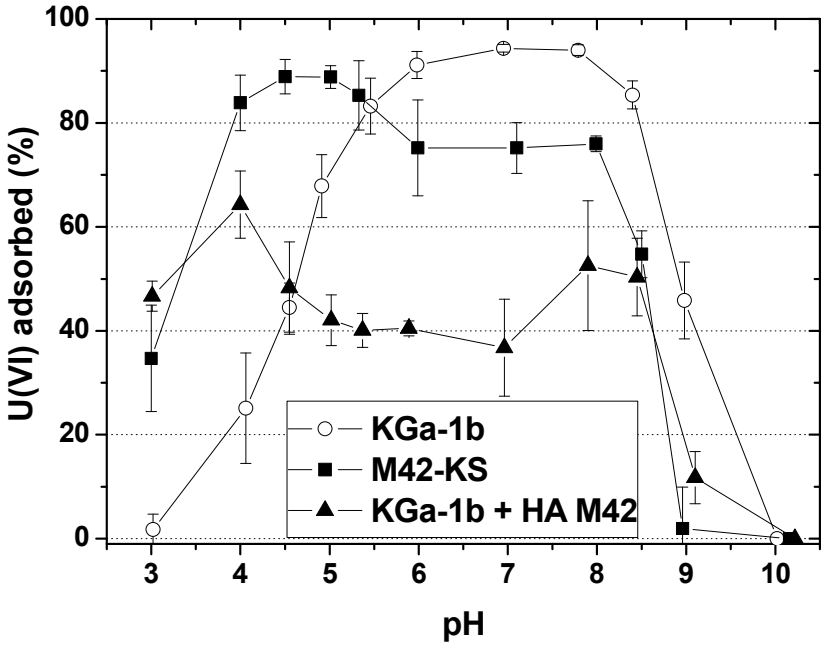

Figure 11.4 depicts the U(VI) sorption onto M42-KS in comparison to that onto kaolinite in absence and presence of HA type M42. The amounts of sorbed humic matter onto M42-KS and kaolinite are shown in Fig. 11.5.

Fig. 11.4: U(VI) sorption onto M42-KS in comparison to the U(VI) sorption onto KGa-1b in absence and presence of 35 mg/L HA type M42 ([U(VI)]: $1 \cdot 10^{-6}$ M, I: 0.01 M $NaClO_4$, S/L: 4 g/L, TOC: 20 mg/L (M42-KS) and 20 mg/L (HA M42)).

In general, the humic matter bound in M42-KS as well as HA type M42 influences the U(VI) sorption in a similar way as discussed in the systems with M1-KS(B) and HA type M1. However, the mobilizing effect in the neutral pH range is stronger pronounced. In the acidic pH range (pH 3-5: M42-KS; pH 3-4.5: KGa-1b + HA M42) the U(VI) sorption in presence of humic materials is increased. At higher pH values (pH ≥5-8) the U(VI) sorption is significantly reduced. Again, both systems differ significantly in their mobilizing properties on U(VI) which is attributed to their different release behavior of humic matter in the solutions (see Fig. 11.5). The reasons for that are the same as described above, namely differences in the aromaticity and the polarity of the humic materials.

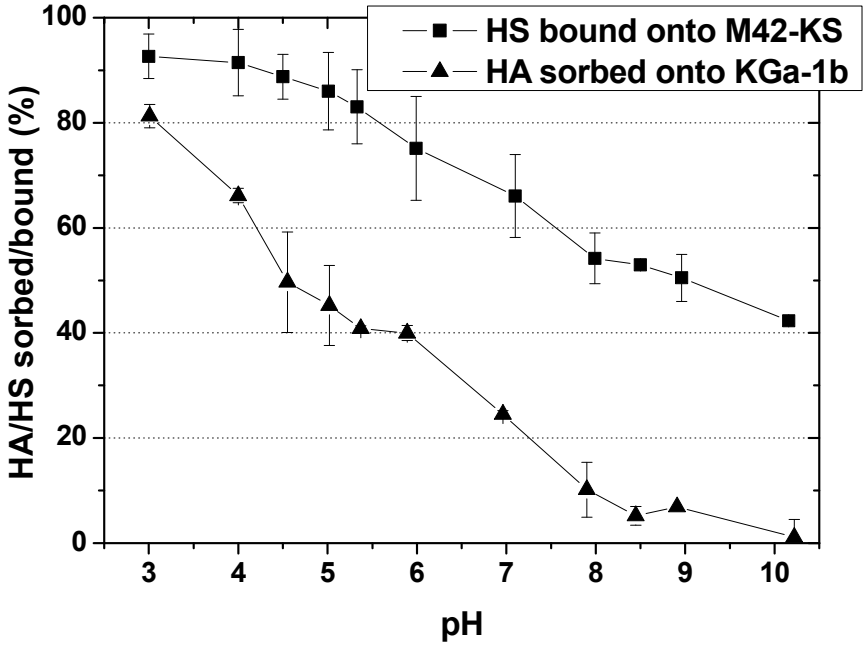

Fig. 11.5: Estimated amount of humic substances (HS) bound onto M42-KS in comparison to the amount of HA type M42 sorbed onto KGa-1b.

Comparing the sorption data shown in Fig. 11.2 and 11.4 it becomes obvious that the humic substances released from M42-KS as well as desorbed HA type M42 exhibits a stronger mobilizing effect on U(VI) than those released from M1-KS(B) and HA type M1. One possible reason for that is found in the slightly higher TOC concentrations in the system U(VI)-M42(KS) and U(VI)-HA M42-KGa-1b. This results in higher humate concentrations in solution and consequently in an increased uranyl humate complex formation. Nevertheless, differences in the aromaticity and the polarity influencing the sorption properties of the humic matter can also cause the observed dissimilarities. Previously, in own NMR studies it was found that HA type M1 is characterized by a higher aromaticity than HA type M42.

Compared to the studies of Křepelova et al. (2006b) differences in the sorption behavior of U(VI) in the ternary system with HA type M42 were found in the basic pH range. Křepelova et al. (2006b) found a higher U(VI) sorption due to a possible interaction of uranyl carbonato

humate complexes with the kaolinite surface. This behavior cannot be confirmed by these studies. Differences in the sample preparation (analysis of the supernatant solutions after centrifugation without filtration) could be the reason. Probably, the applied centrifugation is not able to remove U(VI)-HA-kaolinite colloids at such high HA concentrations from the solutions. Hence, the amount of U(VI) in solution was slightly overestimated, resulting in lower sorption rates.

The formation of humic matter-kaolinite colloids will be subject of future studies. Additionally, the structural and functional properties of humic matter released from the sorbates will be studied in more detail and compared to those of HA.

Humic substances associated with clay minerals can influence the migration behavior of U(VI). On the one hand, immobilization of U(VI) can occur due to humic matter associated with the clay. On the other hand, the release of humic substances from the clay and the formation of U(VI) humate complexes in solution can mobilize U(VI). The impact of humic substances on the migration behavior of U(VI) is controlled by the pH value and the structural and functional properties of the humic matter in the clay and in the aquifer systems. It was shown that HA separately added to the system can cause a stronger immobilizing effect on U(VI) than humic matter associated with clay.

These experiments show that synthetic humic-substance-kaolinite sorbates can be used as model compounds for organic matter-containing natural clay minerals. Processes influencing the migration behavior of actinide ions in clay formations can be identified by the use of these materials.

12 Neptunium(V) sorption onto kaolinite in the absence and presence of humic acid

In this work, the sorption of Np(V) onto kaolinite is studied under aerobic conditions as a function of pH, ionic strength and Np concentration in a series of batch equilibrium experiments. Furthermore, the effect of HA on the Np sorption is studied in order to determine whether humic material is likely to significantly influence Np sorption on kaolinite.

12.1 Experimental

Materials

For the sorption experiments the kaolinite standard KGa-1b from the Clay Minerals Society Source Clays Repository (Washington County, Georgia) was applied. The material is described in detail in chapter 2.

For preparation of a Np(V) stock solution, solid $^{237}NpO_2$ was dissolved in HNO_3. The Np solution was purified by anion exchange (Dowex 1X8) according to the procedure described in (Seibert, 1999). The effluent was evaporated repeatedly to dryness with addition of $HClO_4$ and redissolved in 1 M $HClO_4$. The hexavalent Np thus obtained was reduced electrolytically to Np(V).

As HA the ^{14}C-labeled synthetic HA type M42 (charge M180, specific activity: 17 MBq/g) and the inactive HA type M42 (charge M145) (see chapter 3) were used for the experiments.

Sorption experiments

40 mg kaolinite was weighed into 15 mL centrifuge tubes (PP, Nalgene). For sorption experiments in the absence and presence of HA, 10 mL and 9 mL 0.01/0.1 M $NaClO_4$ solution, respectively, were added. Then, the desired pH values (pH 6 to pH 10.5) were adjusted by addition of diluted $HClO_4$ or NaOH. For studies at pH values higher than 7, a calculated amount of $NaHCO_3$ was added to accelerate the equilibrium process with atmospheric CO_2. During pre-equilibration of the samples (60 h), the samples were shaken continuously and the pH values were readjusted.

The HA stock solutions were prepared by dissolving 2.5 mg ^{14}C-labeled synthetic HA type M42 (charge M180) and 10 mg inactive HA type M42 (charge M145/00) in 25 mL 0.01/0.1 M $NaClO_4$. The Np(V) stock solutions were prepared prior to each sorption run by passing the solutions through Dowex-50 to separate the ^{233}Pa daughter from ^{237}Np, so that the determination of the β-active nuclide ^{14}C of the ^{14}C-labeled HA by liquid scintillation (LS) counting was not interfered from the beta decay of ^{233}Pa. The oxidation state of Np in the stock solutions was spectroscopically confirmed to be pentavalent. Different dilutions of the Np(V) stock solutions were prepared.

The sorption experiments in the absence of HA were started by adding about 60 µL Np(V) stock solution to the preconditioned kaolinite. The sorption experiments in the presence of HA were started by adding 1 mL HA stock solution and instantly after this about 60 µL Np(V) stock solution to the preconditioned kaolinite. The initial Np and HA concentrations in the sample solutions were $1 \cdot 10^{-5}$ M or $1 \cdot 10^{-6}$ M and 50 mg/L, respectively. The solid solution ratio was 4 g/L. The pH values were readjusted immediately after addition of the stock solutions. Then, the samples were shaken at room temperature for about 72 h during which the Np and HA sorption onto the solids reached equilibrium. After centrifugation of the samples (4000 rpm, 30 min), the equilibrium pH values were measured. The final Np and HA concentration was determined by analyzing the LS spectra recorded with an LS counter (Wallac system 1414, Perkin Elmer) using α-β discrimination. For this, 1 mL of the sample supernatant was mixed with 15 mL of a Ultima Gold™ scintillation cocktail (Packard BioScience Company). The amount of Np and HA adsorbed to the mineral surface was calculated as the difference between the initial Np and HA concentration and the sum of the final Np and HA concentration in the sample solutions and the amount of Np and HA adsorbed onto the vial walls.

12.2 Results and discussion

The Np speciation, calculated for the experimental conditions applied in this study, is shown in Fig. 12.1. It was calculated with the geochemical computer code EQ3/6 (Wolery, 1992) applying the Np(V) complexation constants compiled in the NEA data base (Guillaumont et al., 2003), the Np(V) humate complexation constant logβ = 3.6 and the pH function of the loading capacity (LC) with LC = -0.589 + 0.101 · pH (Sachs et al., 2004). The results show that the free neptunyl ion predominates the Np speciation in aqueous solution up to pH 8.3 both in the absence and in the presence of HA. Starting at about pH 7.3, the neptunyl carbonate species are formed increasingly in solution and dominate the Np speciation above pH 8.3. In the presence of HA, $NpO_2HA(I)$ is formed between pH 6 and pH 9 with a maximum of 11.2% near pH 8. For the higher pH region, the formation of the mixed ternary neptunyl carbonate humate complex is expected. Presently, however, this complex cannot be quantified thermodynamically. The Np speciation calculated for the lower initial Np concentration applied in this study ($1 \cdot 10^{-6}$ M) is not shown because it differs only slightly.

In Fig. 12.2, the pH-dependency of the Np sorption onto kaolinite in the absence of HA is shown as a function of the initial Np concentration. The results obtained for sorption experiments applying $1 \cdot 10^{-5}$ M Np show that the Np sorption increases with pH up to pH 9 and decreases again at higher pH values. At pH 9, $NpO_2CO_3^-$ dominates the Np speciation in solution (cf. Fig. 12.1). Between pH 9 and pH 10, neptunyl carbonate complexes with a higher negative charge are formed in solution ($NpO_2(CO_3)_2^{3-}$, $NpO_2(CO_3)_2(OH)^{4-}$ and $NpO_2(CO_3)_3^{5}$). The surface charge of kaolinite in the considered pH range is also negative (p.z.c. = 6.0 (Redden et al., 1998), p.z.n.p.c. = 5.1±0.2 (Sutheimer et al., 1999), 4.99±0.03 (Schroth and Sposito, 1997)). Thus, the electrostatic repulsion between these neptunyl carbonate complexes and kaolinite decreases the Np sorption onto kaolinite above pH 9.

The decrease of the initial Np concentration from $1 \cdot 10^{-5}$ M to $1 \cdot 10^{-6}$ M leads to a shift of the Np adsorption edge to lower pH values by a half pH unit.

Figure 12.3 shows the influence of HA on the Np sorption onto kaolinite as a function of pH. In experiments with $1 \cdot 10^{-5}$ M Np the Np sorption is slightly enhanced by HA between pH 6 and pH 7.5. A slightly enhanced Np sorption onto kaolinite in the presence of HA and EDTA between pH 6 and pH 8 was also found by Niitsu et al. (1997) and Kohler et al. (1992), respectively. In experiments with $1 \cdot 10^{-6}$ M Np no effect of HA on the Np sorption is detectable in this pH range. At higher pH values up to pH 10.5 the amount of Np adsorbed onto kaolinite is decreased by HA. On the one hand, this can be attributed to the formation of dissolved neptunyl humate complexes which are formed in solution between pH 6 and pH 9 with a maximum of 11.2% near pH 8 (cf. Fig. 12.1). On the other hand, the mixed ternary neptunyl carbonate humate complex (mentioned above) would explain the reduction of the Np sorption by HA at pH values higher than 9. The mobilizing effect of HA on Np is more strongly pronounced in sorption experiments with the higher initial Np concentration ($[NpO_2^+]$: $1 \cdot 10^{-5}$ M).

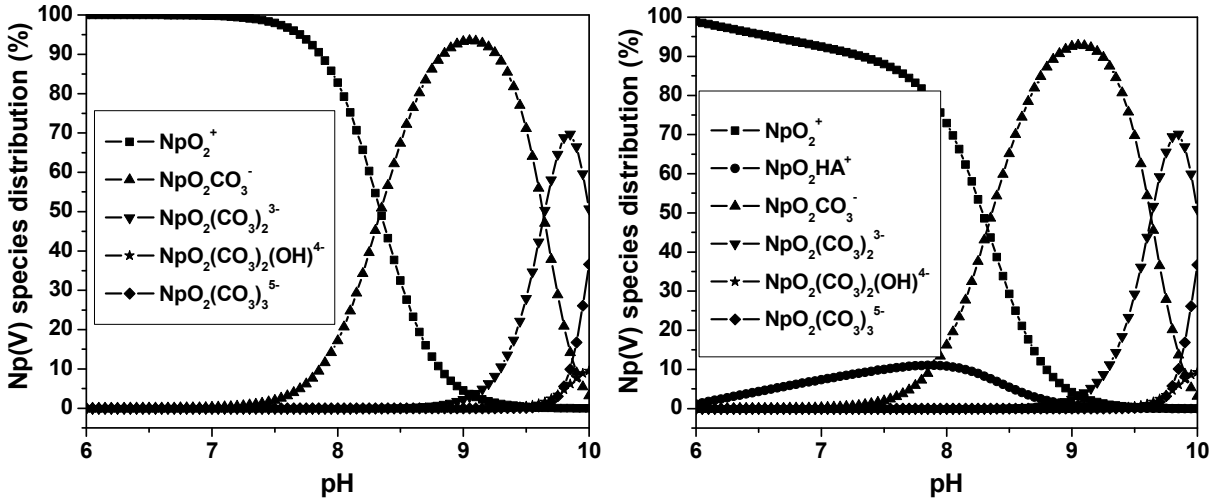

Absence of HA Presence of HA

Fig. 12.1: Np speciation in solution in the absence and presence of HA ($[NpO_2^+]$: $1 \cdot 10^{-5}$ M; [HA]: 0 or 50 mg/L; I: 0.01 M $NaClO_4$; pCO_2: $10^{-3.5}$ atm).

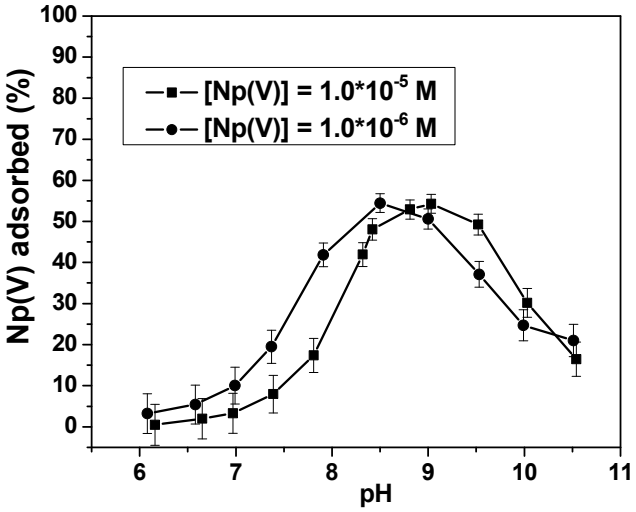

Fig. 12.2: Np sorption onto kaolinite in the absence of HA ($[NpO_2^+]$: $1 \cdot 10^{-5}$ or $1 \cdot 10^{-6}$ M; I: 0.01 M $NaClO_4$; pCO_2: $10^{-3.5}$ atm).

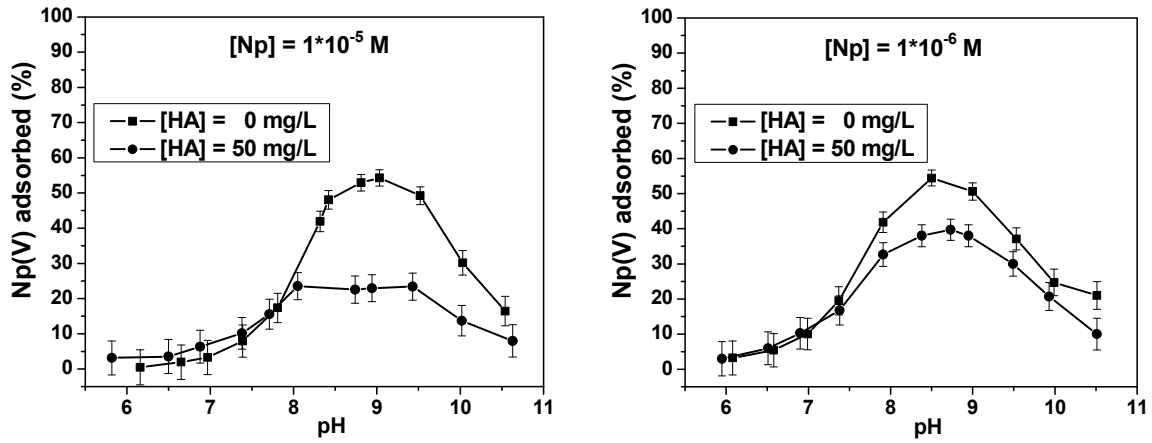

Fig. 12.3: Influence of HA on the Np sorption onto kaolinite ([NpO_2^+]: $1 \cdot 10^{-5}$ or $1 \cdot 10^{-6}$ M; [HA]: 0 or 50 mg/L, I: 0.01 M $NaClO_4$; pCO_2: $10^{-3.5}$ atm).

The HA sorption onto kaolinite as a function of pH in the absence and presence of Np is shown in Fig. 12.4. The HA sorption decreases with increasing pH. This can be attributed to electrostatic repulsion between negatively charged carboxyl groups of HA and the negative surface charge of kaolinite in the considered pH range. The influence of Np on the HA sorption is small for both initial Np concentrations.

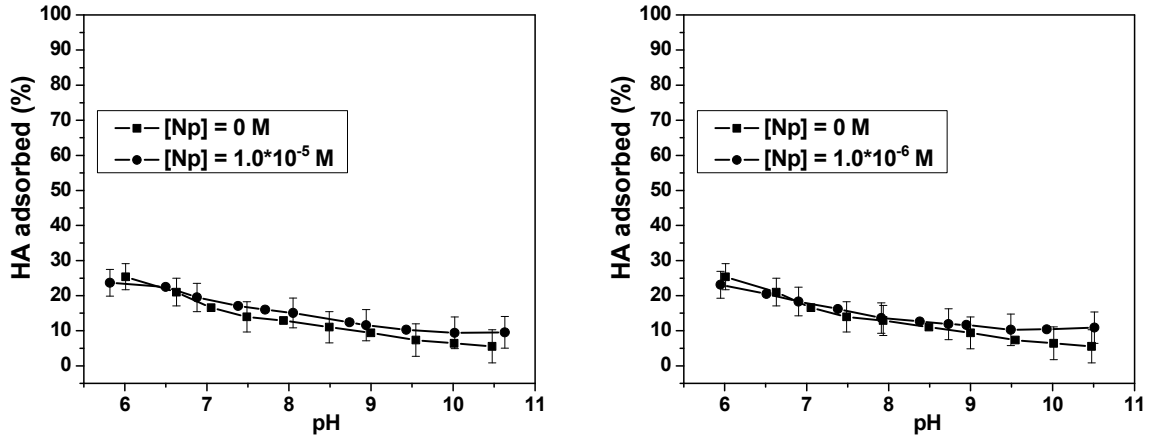

Fig. 12.4: HA sorption onto kaolinite in the absence and presence of Np ([NpO_2^+]: $1 \cdot 10^{-5}$ or $1 \cdot 10^{-6}$ M; [HA]: 50 mg/L, I: 0.01 M $NaClO_4$; pCO_2: $10^{-3.5}$ atm).

The influence of the ionic strength on the Np sorption onto kaolinite in the absence of HA is shown in Fig. 12.5. Compared to the sorption experiments performed with an ionic strength of 0.01 M ($NaClO_4$) the Np sorption is increased between pH 7.4 and pH 10 when a higher ionic strength of 0.1 M ($NaClO_4$) is applied. This result is consistent with the results obtained

by Amayri (2006). The effect of the ionic strength on the Np sorption onto kaolinite in the presence of HA is relatively small (not shown here).

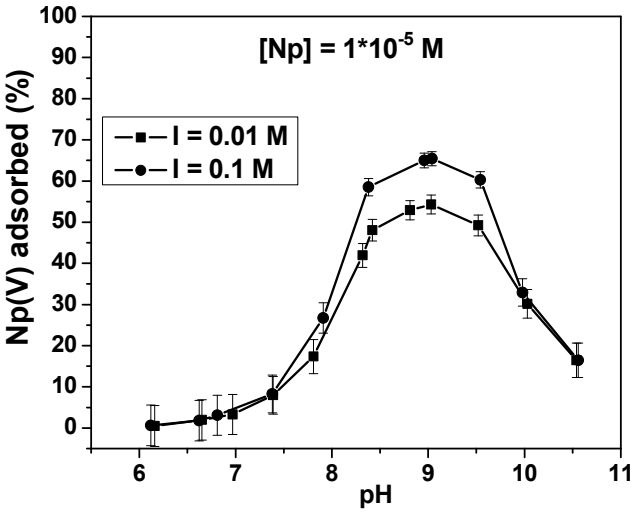

Fig. 12.5: Influence of ionic strength on the Np sorption onto kaolinite ($[NpO_2^+]$: $1 \cdot 10^{-5}$ M; I: 0.01 or 0.1 M $NaClO_4$; pCO_2: $10^{-3.5}$ atm).

The study showed that the Np(V) sorption on kaolinite under aerobic conditions is effected by pH, ionic strength, Np concentration and the presence of HA. HA influences significantly the Np sorption onto kaolinite. Between pH 7.5 and pH 10.5 the mobility of Np(V) is increased due to HA. This is attributed to formation of dissolved neptunyl humate complexes and/or neptunyl carbonate humate complexes.

13 Studies of the migration behavior of humic acids in compacted clay and of the influence of humic acids on the uranium(VI) transport

Little is known on the migration behavior of humic substances in clay formations which is supposed to be governed by diffusion processes. Since HA show a strong ability for complex formation, they can influence the migration of radioactive and non-radioactive toxic metal ions in clayey environments.

The results of former studies on the migration of HA in clay systems and their influence on radionuclide migration are discussed controversially. Wold and Eriksen (2005) found that humic colloids are able to diffuse through compacted bentonite without strong physical hindrance and to mobilize metal ions such as Co(II). Likewise, a nearly unhindered diffusion of

lignosulfonate has already been reported by Wold and Eriksen (2003). Wang et al. (2005), however, found a significant immobilization of Eu(III) by humic substances in compacted bentonite.

Maes et al. (2006) studied the migration of radionuclides in Boom Clay and gave information that the bulk of Am(III) dissociates nearly instantaneously from complexes with mobile organic matter and is bound to the clay and immobile organic matter. Only a small part of Am(III) has been transported over short distances. The reversibility of the interaction between radionuclide, organic matter and clay governs the migration of actinides in the organic-rich Boom Clay.

Field studies from Hendry et al. (2003 and 2005) substantiate a diffusive transport through a clay-rich till aquitard. Only the smallest molecular fraction of the dissolved organic matter proved mobile in the field and laboratory tests.

In the present study, we investigated the diffusion behavior of humic colloids in compacted clay as a function of the dry bulk density and of the pH. Furthermore, the impact of HA on the uranium transport was studied at pH 5 and 7. The U(VI) diffusion was measured in absence and presence of HA type M42. Additionally, the diffusion behavior of U(VI) was studied in a synthetic humic substance-kaolinite-sorbate (see chapter 5), representing a model substance for clays containing organic matter.

13.1 Experimental

The diffusion of humic colloids and its impact on the U(VI) migration was studied in a laboratory model system at room temperature and ambient air. The schematic set-up of the experiments is shown in Fig. 13.1.

In order to study the HA diffusion as a function of the porosity, kaolinite KGa-1b was compacted to bulk dry densities of 1.32, 1.56 and 1.67 g/cm^3 and fixed between two filter plates in the diffusion cell. For the experiments with U(VI), the kaolinite as well as the synthetic humic substance-kaolinite-sorbate (batch R1/06KS, see chapter 5.3) were compacted to bulk dry densities of 1.56 g/cm^3. Subsequently, the clay plugs were equilibrated for 3 to 4 weeks with 0.01 M $NaClO_4$ solution (1 mM NaN_3) at pH 5 and pH 7 in case of the experiments with kaolinite and at pH 7 for the study with the synthetic humic substance-kaolinite-sorbate.

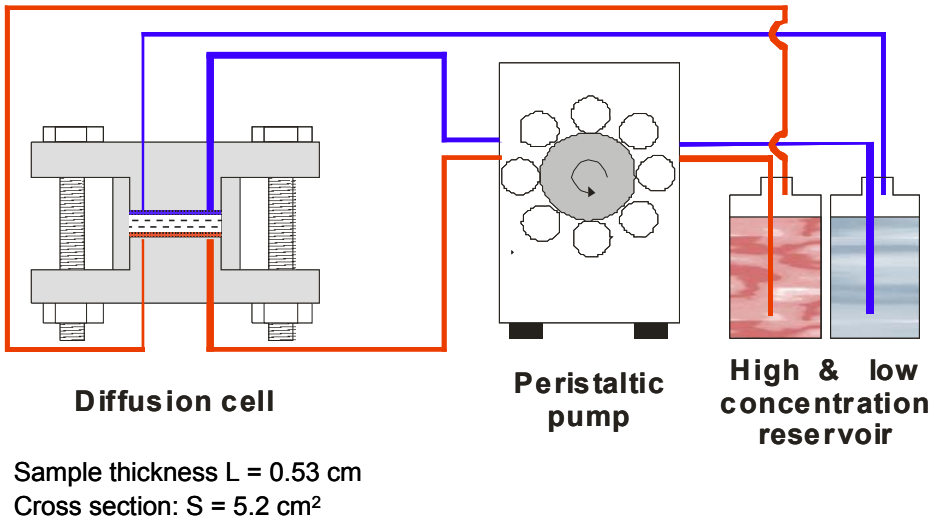

Fig. 13.1: Schematic set-up of the diffusion experiments (Van Loon and Soler, 2004).

The effective porosity of the clay plugs and the effective diffusion coefficient for the non-retarded transport through the cell were measured using tritiated water (HTO) as a conservative tracer. The HA diffusion was studied using ^{14}C-labeled synthetic HA type M42 (batch M180; see chapter 3) at a concentration of about 12 mg/L. For the experiments involving U(VI), the UO_2^{2+} concentration was $1 \cdot 10^{-6}$ M (^{238}U). ^{234}U was used as tracer in the experiments with humic substances. A steady state through-diffusion technique (Shackelford, 1991; Van Loon and Soler, 2004) with constant concentration gradient was applied. For that, the tracer concentrations at the boundaries (^{14}C and/or ^{234}U, ^{238}U) have been kept constant. The tracer activities in the high (x = 0) and low (x = L) concentration reservoirs were periodically analyzed by liquid scintillation counting (LSC; Wallac System 1414, Perkin Elmer) with α-β-separation (^{14}C, ^{234}U) and by ICP-MS (^{238}U; Elan 6000, Perkin Elmer). In case of ^{234}U, the α-LSC spectra were deconvoluted to determine the activity contribution of ^{232}U (contamination of ^{234}U) and its daughter nuclides (Nebelung, 2002).

To give an example, Fig. 13.2 shows the ^{14}C and ^{234}U tracer concentration at the high concentration boundary for a diffusion experiment with HA and U(VI) as a function of time.

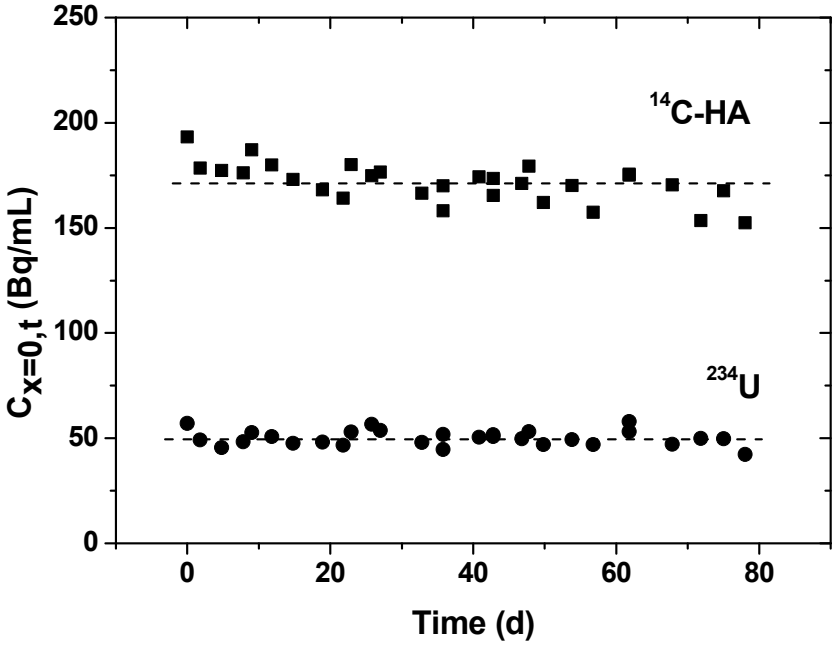

Fig 13.2: ^{14}C and ^{234}U tracer concentration at the high concentration boundary $C_{x=0,t}$ ($\rho_{bulk:}$ 1.56 g/cm^3, pH 5).

In one experiment (HA diffusion, pH 5, ρ_{bulk} = 1.56 g/cm^3), the high-concentration reservoir has been exchanged with a tracer-free solution after completing the through-diffusion experiment and out-diffusion has been started. The amount of tracer released from the clay to the external reservoirs has been monitored as a function of time.

To determine the tracer concentration within the clay plug, the cells were opened and the clay was cut into slices of 0.5 or 1 mm. After drying, HA and U were extracted from the clay by 1 M NaOH and 1 M HNO_3, respectively, and analyzed as described above.

The HA particle size distribution in the high and low concentration reservoir was measured by ultra centrifugation using filters of pore width of 1 to 1000 kD (Microsep Centrifugal Devices, Pall).

13.2 Data processing

The data evaluation of the through-diffusion experiments is based on Fick's second law (cf. Shackelford, 1991):

$$\frac{\partial C}{dt} = D_a \frac{\partial^2 C}{\partial x^2} \qquad (13.1)$$

with $$D_a = \frac{D_e}{\alpha} \qquad (13.2).$$

C represents the activity (Bq/m^3), t is the time (s), D_a is the apparent diffusion coefficient (m^2/s), x is the distance (m), D_e is the effective diffusion coefficient (m^2/s), and α is the rock capacity factor (-) according to Eq. (13.3).

$$\alpha = \varepsilon + \rho K_d \qquad (13.3)$$

In Eq. (13.3), ε represents the effective porosity (-), ρ is the bulk dry density (g/m^3) and K_d is the distribution coefficient (m^3/g). For a non-sorbing tracer, e.g., HTO, $K_d = 0$, thus, α is equal to ε, the porosity accessible for diffusion.

The results of the steady state part of the experiments were fitted to an analytical solution of the diffusion equation (Van Loon et al., 2003). Once steady state is reached, the accumulated activity A (Bq) becomes a linear function of t:

$$A(t) = \frac{-SLC_0\alpha}{6} + \frac{SC_0D_e}{L}t \qquad (13.4)$$

with S the cross sectional area (m^2), L the layer thickness (m), and C_0 the initial tracer concentration at the high concentration boundary (Bq/m^3). According to Eq. (13.4), D_e and α can be obtained by linear regression. The out-diffusion process can be modeled by a nonlinear equation presented in Van Loon and Soler (2004) not shown here.

In order to describe the transient diffusion profiles, the tracer concentrations in the clay plug were interpreted by Eq. (13.5) according to Crank (1975):

$$\frac{C_{S(x,t=t_{end})}}{C_{B(x=0,t=t_{end})}} = erfc\left(\frac{x}{2\sqrt{D_a t}}\right) \qquad (13.5)$$

where $C_{S\,(x,\ t=tend)}$ is the resident concentration in the solid (mol/g) normalized to the concentration at the high concentration boundary $C_{B\,(x=0,t=tend)}$ (mol/g).

13.3 Results and discussion

13.3.1 Diffusion of HTO

In all experiments, the diffusion of HTO was studied to determine the effective porosity ε of the kaolinite and the effective diffusion coefficient D_e for the non-reactive tracer diffusion through kaolinite. Figure 13.3 illustrates the diffused activity (A_{HTO}) and the diffusive flux in a through-diffusion experiment with HTO.

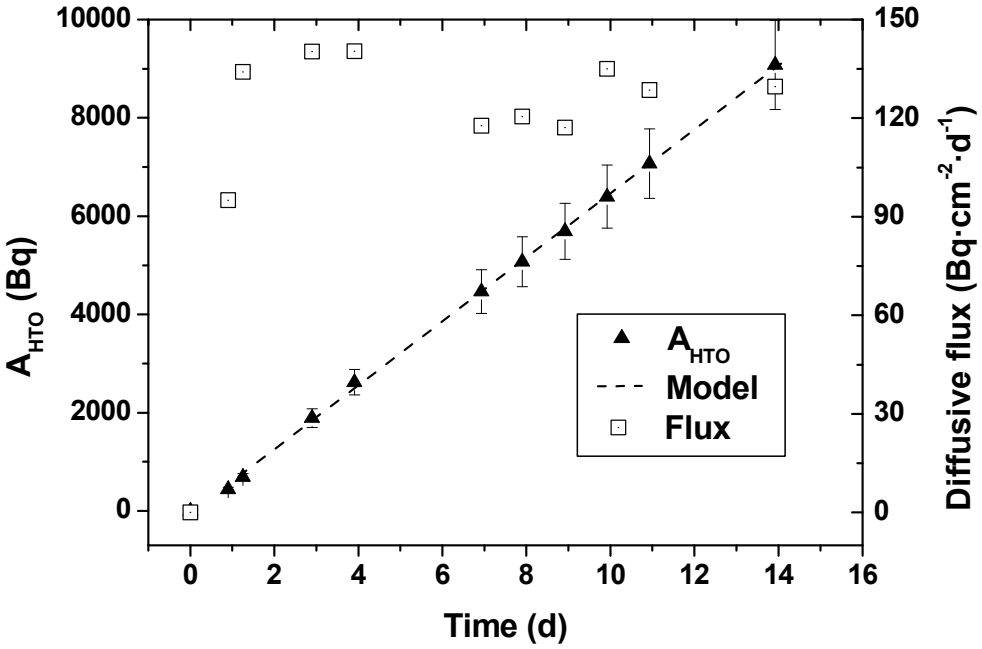

Fig. 13.3: Diffused activity and diffusive flux of HTO vs. time (ρ_{bulk}: 1.56 g/cm^3).

The effective porosities and the effective diffusion coefficients of the conservative tracer of all experiments are summarized in Fig. 13.9 and Tab. 13.1.

13.3.2 Humic acid diffusion in compacted clay

Figure 13.4 depicts the amount of HA diffused through the clay and the diffusive flux as a function of time in an experiment at a dry bulk density of 1.56 g/cm^3 and pH 5.

The flux steadily increases over a transient period of 20 d. Then it achieves values scattering between 0.02 and 0.06 µg·cm^{-2}·d^{-1}. In steady-state, the amount of diffused HA increases linearly with time.

Figure 13.5 illustrates the particle size distribution of HA in the high and low concentration reservoir of the same experiment. In the high concentration reservoir, the HA shows a particle size distribution with a mean particle size of about 50 kD. The mean particle size of HA shifts to less than 1 kD in the low concentration reservoir. From the filtration results, it can be concluded that only small HA particles are able to pass the narrow pores indicating a fractionation of colloidal particles in the clay system. Comparable results were found in all diffusion experiments with HA also in presence of U(VI).

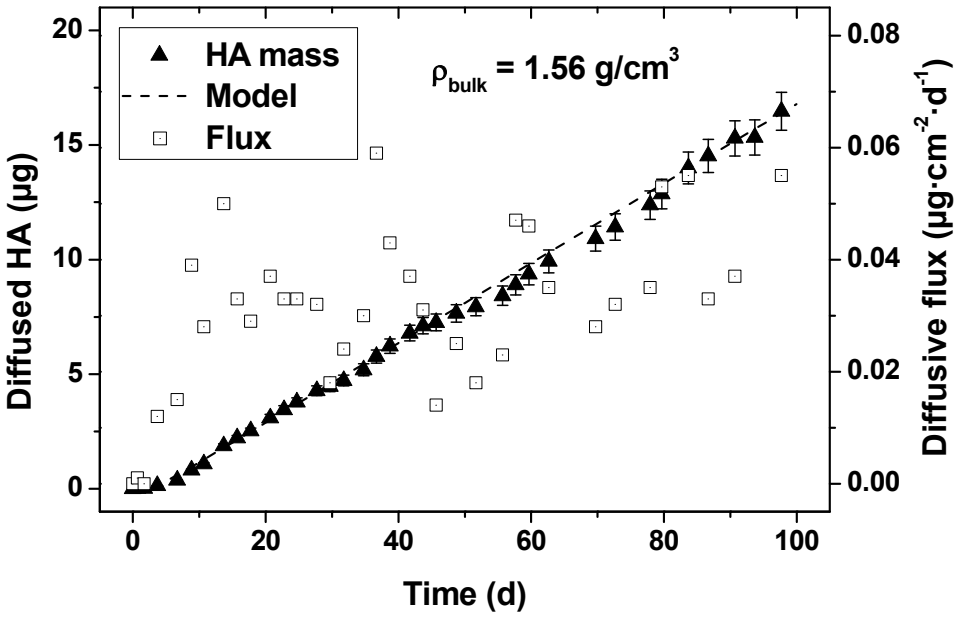

Fig. 13.4: Cumulative mass and diffusive flux of HA as a function of time (ρ: 1.56 g/cm^3, pH 5, [HA]: 12.6 mg/L, I: 0.01 M $NaClO_4$, 1 mM NaN_3).

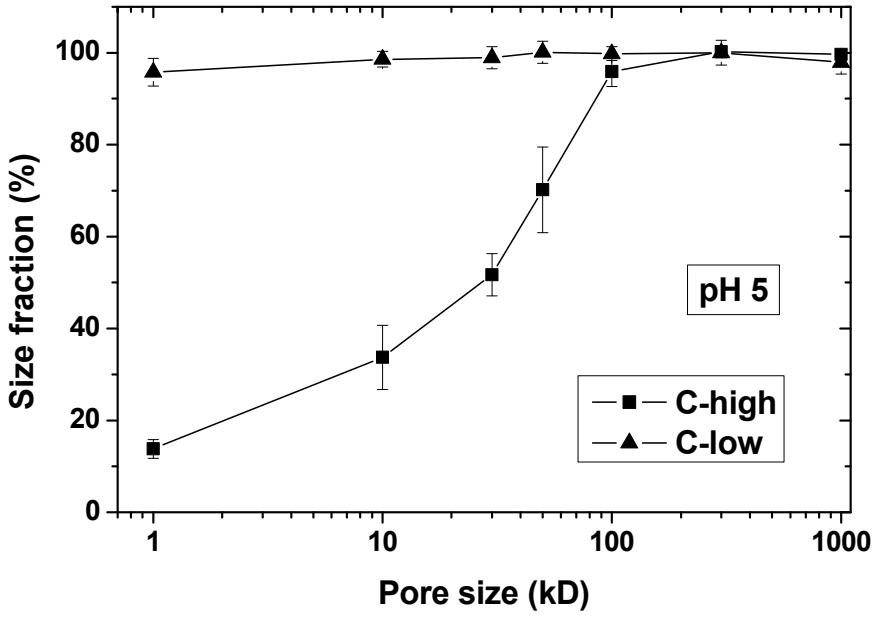

Fig. 13.5: Size distribution of humic colloids in the high and low concentration reservoir.

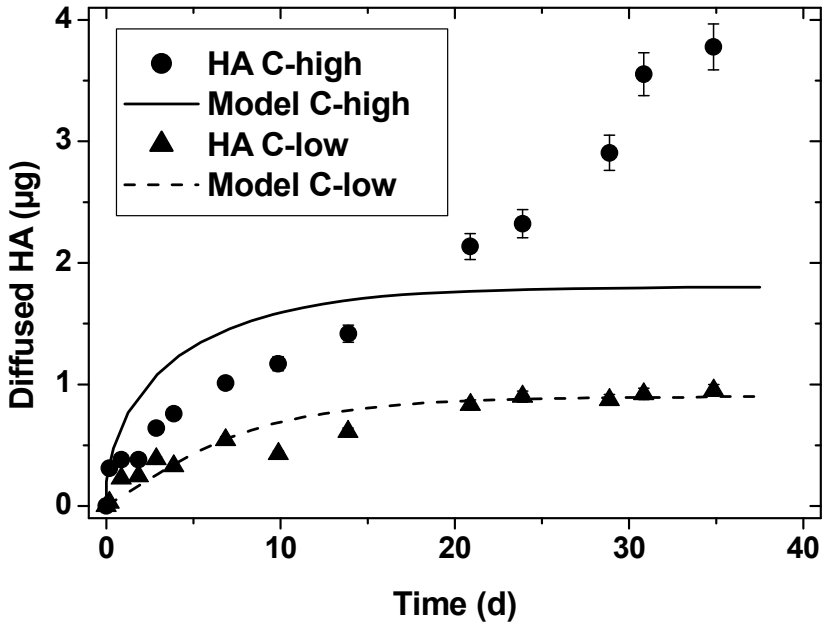

Fig. 13.6: Out-diffusion: cumulative mass vs. time (ρ: 1.56 g/cm^3, pH 5), model parameters (D_e = 6·10^{-12} m^2/s and α = 1.15) estimated from the low concentration side.

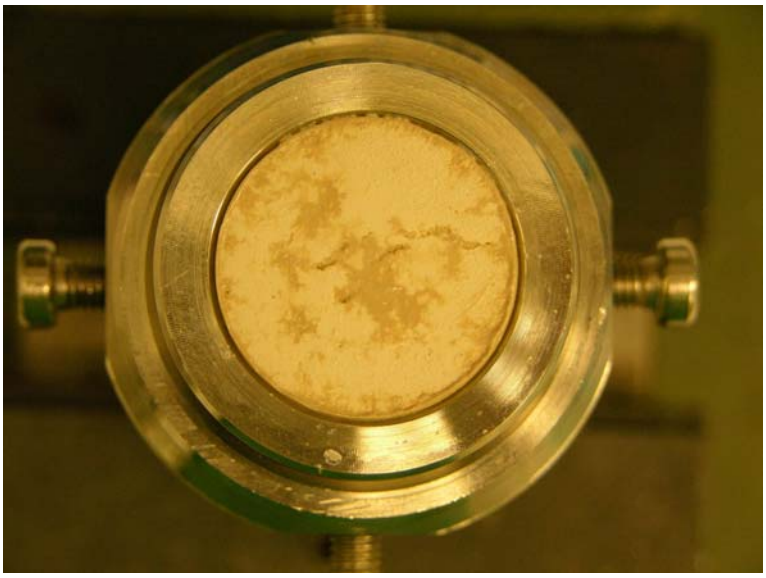

Fig. 13.7: Front view to an opened diffusion cell (ρ: 1.56 g/cm^3, pH 5), diameter of the clay plug 25.7 mm.

The out-diffusion of HA from the clay plug (pH 5, ρ = 1.56 g/cm^3) is demonstrated in Fig. 13.6. The accumulated tracer amounts in the external reservoirs of the high and low concentration side are plotted as a function of time. At the low concentration side, the tracer amount reaches a plateau after about 30 d. This behavior is describable by the model equation in

Van Loon and Soler (2004) and the parameter set $D_e = 6 \cdot 10^{-12}$ m^2/s and α = 1.15 could be estimated. This is comparable with the parameter from the corresponding through-diffusion experiment ($D_e = 1.2 \cdot 10^{-11}$ m^2/s and α = 0.78) within a deviation of 50% of the higher value. In contrast to the expected behavior, the high concentration side continuously released HA, not reaching a plateau in the accumulated concentration diagram over the experimental duration. The model assumes a linear tracer distribution within the clay plug when reaching the steady-state through-diffusion. Probably the distribution was non-linear. This was checked after terminating the out-diffusion by analyzing the residual profile. Figure 13.7 presents a view to the high concentration side after opening the cell. The dark areas indicate the accumulation of HA at the boundary between clay and external solution (filterplate).

The HA distribution as a function of the distance is shown in Fig. 13.8. The bulk of HA has been accumulated near the high concentration boundary entering the clay to a depth of ca. 1 mm. This accumulation is in accordance with the strong size fractionation.

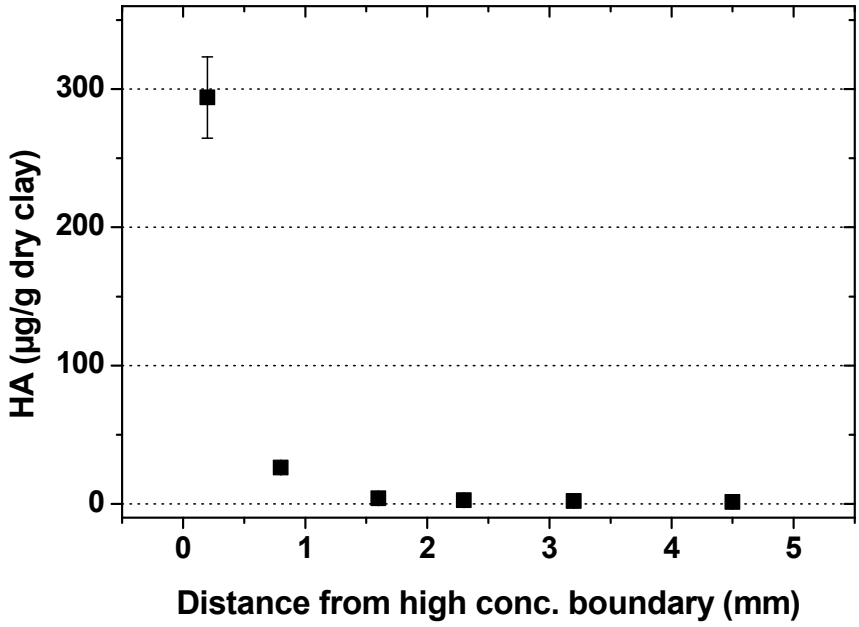

Fig. 13.8: Residual mass of HA in the clay plug after out-diffusion (t: 35 d, ρ: 1.56 g/cm^3, pH 5).

Based on Eq. (13.4), the effective diffusion coefficients D_e and the rock capacity factors α of HA were deduced from the steady-state periods of the experiments. Figure 13.9 illustrates the obtained data as a function of the bulk dry density in comparison to those of HTO. Furthermore, the data are summarized in Tab. 13.1.

Tab. 13.1: D_e, and α for HTO and HA as a function of the bulk dry density.

Parameter	Bulk dry density (g/cm^3)		
	1.32	1.56	1.67
	pH 5		
$\alpha_{, HTO}$ (-)	0.45 ± 0.14	0.37 ± 0.11	0.39 ± 0.12
$D_{e, HTO}$ (m^2/s)	$(2.70 \pm 0.27) \cdot 10^{-10}$	$(1.80 \pm 0.18) \cdot 10^{-10}$	$(1.57 \pm 0.16) \cdot 10^{-10}$
$\alpha_{, HA}$ (-)	31.96 ± 9.59	0.78 ± 0.23	0.35 ± 0.10
$D_{e, HA}$ (m^2/s)	$(1.23 \pm 0.12) \cdot 10^{-10}$	$(1.20 \pm 0.12) \cdot 10^{-11}$	$(5.13 \pm 0.51) \cdot 10^{-12}$
	pH 7		
$\alpha_{, HTO}$ (-)	n.m. [a]	0.26 ± 0.08	(0.910 ± 0.27)
$D_{e, HTO}$ (m^2/s)	n.m.	$(2.68 \pm 0.27) \cdot 10^{-10}$	$(1.95 \pm 0.20) \cdot 10^{-10}$
$\alpha_{, HA}$ (-)	n.m.	11.56 ± 3.47	13.59 ± 4.08
$D_{e, HA}$ (m^2/s)	n.m.	$(4.08 \pm 0.41) \cdot 10^{-11}$	$(3.01 \pm 0.30) \cdot 10^{-11}$

[a] n.m.: not measured.

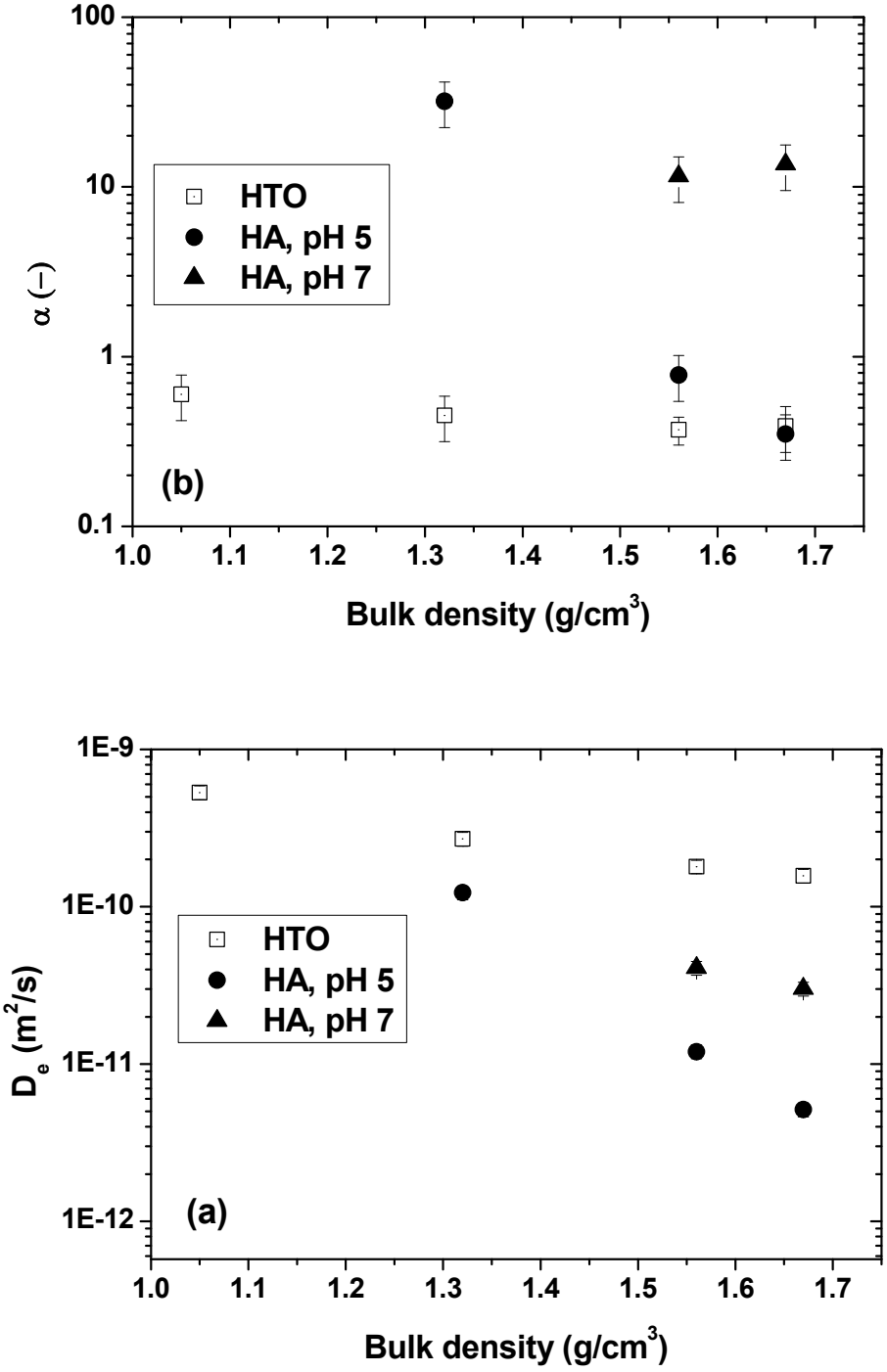

Fig. 13.9: Diffusion parameters D_e (a) and rock capacity factors α (b) for HTO and HA as a function of the bulk dry density.

At pH 5 and pH 7, HTO and HA show decreasing D_e values with increasing density. The D_e values of HA are always smaller than the corresponding values of HTO. This effect becomes

stronger with increasing density and points to an increased steric hindrance of the colloidal HA transport in the narrow pore space of kaolinite. This result is in agreement with the size distribution shown in Fig. 13.5, from which a fractionation of HA molecules in the clay plug could be concluded. The effective diffusion coefficients of HA were found to be higher at pH 7 compared to pH 5 (see Tab. 13.1). As the effective diffusion coefficients apply for the steady state, differences in the equilibrium interaction between HA and clay due to changes in the protonation state of the functional groups are not expected. Rather, variations in the free diffusion coefficients D_0 of the macro molecules are assumed. Lead et al. (2000) observed an increase in the D_0 of Suwannee river HA by a factor of about 1.2 when increasing the pH from 5 to 7. This effect has been attributed to an aggregation of humic colloids at pH <7.

The effective porosity ε of the system is represented by α_{HTO}. With the exception of the obtained value at ρ = 1.67 g/cm^3 (pH 7), it decreases slightly with increasing bulk density. The rock capacity factor α for HA depends stronger on the bulk density. At pH 5 an increase of α was observed with decreasing density. At pH 7 similar results were found at both studied densities. Based on the applied diffusion model, α_{HA} describes the sum of the accessible pore space for the HA diffusion as well as the sorption (K_d) of the HA in the system. From the data at pH 5 it can be concluded that sorption processes seem to be less effective at high densities. However, at low densities, these processes obviously become more important, which can be concluded from the increased α_{HA} values. The capacities obtained at pH 7 are not consistent with that. The observed trend at pH 7 is opposite to that at pH 5. Unfortunately, there exist data at only two different bulk densities and pH 7 not enabling a confirmation of the trend.

The rock capacity factors of HA at pH 5 are significantly lower than those at pH 7, pointing to a stronger sorption at pH 7. This is in contrast to the results of the batch sorption experiments with HA (cf. chapter 10.1) where a lower amount of sorbed HA was found at pH 7. The batch experiments were performed with the entire non-fractionated size spectrum of the HA and the data set represents the sorption behavior of the whole HA. In contrast to that, the rock capacity factor α applies only for the diffused part of HA, i.e., only for the low-molecular HA fraction that is able to pass the pore system. It might be possible that this HA fraction shows a different sorption behavior than the entire HA, resulting in the different diffusion behavior. Furthermore, the used K_d approach is possibly not able to describe the interaction sufficiently. Former studies on HA transport in quartz sand (Mibus et al., 2007) suggested a kinetic interaction of HA with the quartz surface which were definitely not describable by K_d.

13.3.3 Influence of humic acid on the uranium(VI) migration

13.3.3.1 Uranium(VI) diffusion in absence of humic acid

The U(VI) diffusion in absence of HA was studied at pH 5 and 7 at U(VI) concentrations of $1 \cdot 10^{-6}$ M. By the termination of the experiment (70 d at pH 5, 64 d at pH 7), no U(VI) breakthrough was observed. Because of that the cells were opened and the kaolinite plugs were cut into slices, which were analyzed on their U(VI) content. Figure 13.10 shows the U(VI)

distribution in the kaolinite after the experiments.

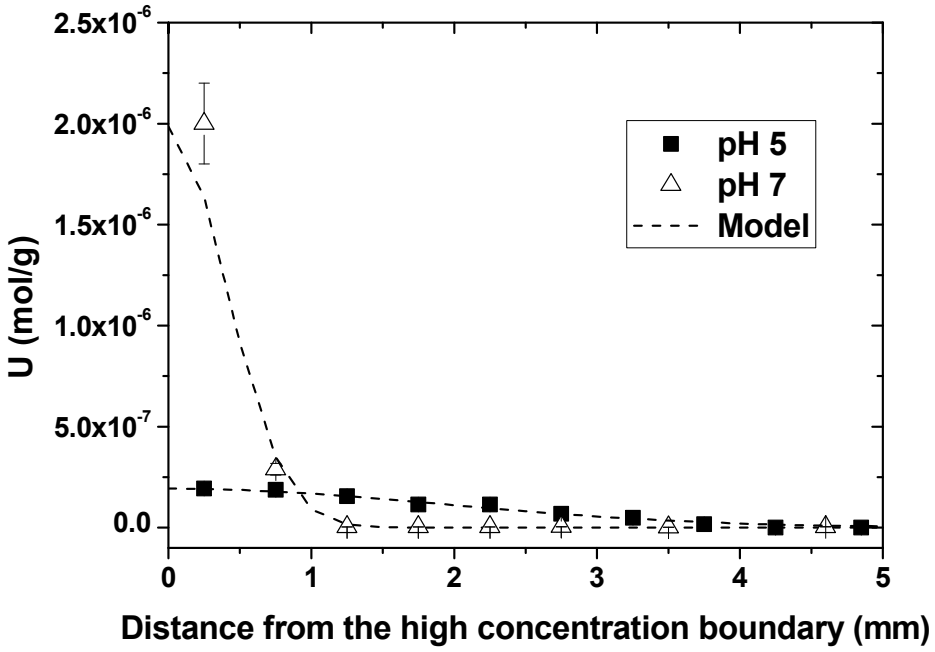

Fig. 13.10: U tracer concentration in the clay plug after 70 d (pH 5) and 64 d (pH 7).

At pH 5 and 7, U(VI) shows the typical behavior of a strong sorbing tracer. However, there are differences in the diffusion behavior at pH 5 and 7. At pH 5 the diffusion profile of U(VI) stretches across the clay plug. The U(VI) concentration decreases with increasing distance from the high concentration boundary. At pH 7, in contrast, U(VI) is accumulated at the high concentration boundary. Only a small part of U(VI) is able to enter the first layer of the clay plug. This behavior is attributed to the stronger U(VI) sorption onto KGa-1b at pH 7 (Křepelová et al., 2006b) preventing a deeper penetration of U(VI) into the clay compared to pH 5. This diffusion behavior is reflected in the apparent diffusion coefficients D_a of U(VI) at both pH values which amount to $1.5 \cdot 10^{-13}$ and $6.0 \cdot 10^{-15}$ m^2/s at pH 5 and 7, respectively.

13.3.3.2 Uranium(VI) diffusion in presence of humic acid

The low molecular fraction of HA diffusing through the clay plug was not found to convey uranium within the experimental duration. Possibly the uranyl humate complexes formed in solution dissociates in the pore system due to competition between humate and surface complexes. Alternatively, the mobile low molecular HA fraction is not able to complex U(VI) due to structural and functional dissimilarities.

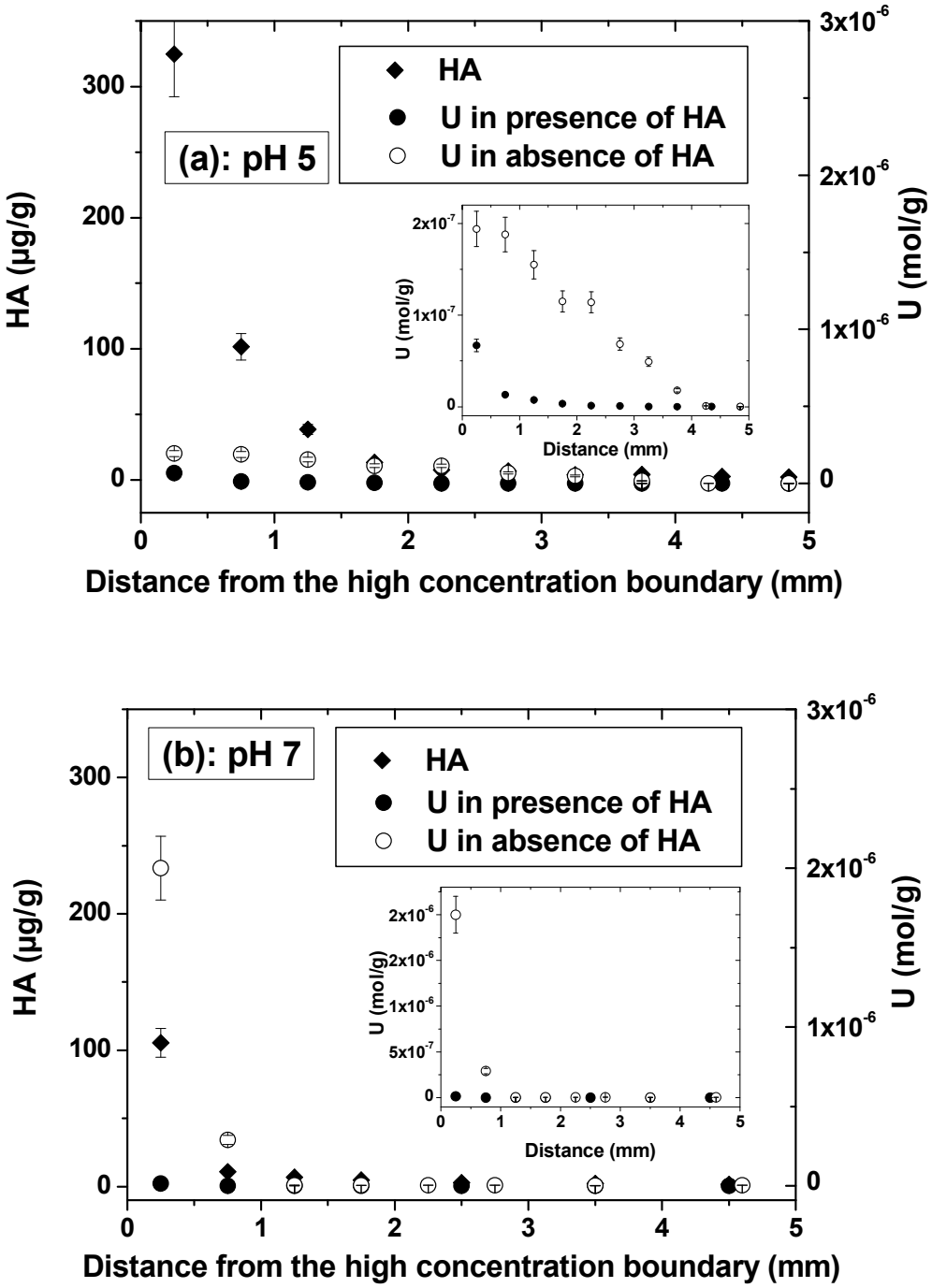

Fig. 13.11: U and HA distribution in the clay plug at pH 5 (a) and pH (7) (b). Reaction time in absence of HA: 70 d (pH 5), 64 d (pH 7), in presence of HA: 78 d (pH 5 and 7)

The in-diffusion profiles of both tracers are illustrated in Fig. 13.11. As in the experiments on HA diffusion, HA is immobilized at the high concentration boundary. In presence of HA, the U(VI) concentration is permanently lower compared to the HA-free system. The bulk of U(VI) is immobilized associated with HA at the solution clay boundary. Comparing pH 5 and pH 7,

a deeper penetration of U(VI) was observed at pH 5. This is in concordance with the penetration depth of HA, the complexing agent, and U(VI) in absence of HA. From the diffusion profiles of U(VI) in presence of HA it becomes clear that HA penetrates the clay deeper than U(VI) (see Fig. 13.11). This is in agreement with the observed through-diffusion behavior of the low molecular HA fraction.

In general, HA has a clearly immobilizing effect on the migration of uranium in the studied system.

13.3.3.3 Uranium(VI) diffusion in a synthetic humic substance-kaolinite-sorbate

Figure 13.12 presents the U(VI) distribution in the synthetic humic substances-kaolinite-sorbate after 79 d in comparison to that of U(VI) in kaolinite in absence of HA. From Fig. 13.12 it becomes clear that U(VI) is not able to migrate deep into the humic substance-kaolinite sorbate. It is immobilized at the solution clay boundary most likely in association with humic substances. However, the comparison of the results of this experiment with those of the experiment with kaolinite and HA in solution (Fig. 13.13.) shows that U(VI) penetrates slightly more into the humic substance-kaolinite-sorbate. There are different processes that can effect these differences in the migration behavior.

At the start of the experiment with the synthetic humic substance-kaolinite-sorbate, U(VI) exists in a HA-free solution. With access to the sorbate, U(VI) can interact with the immobilized humic material as well as with the kaolinite surface. From XPS measurements it is known that the surface of the kaolinite particles is not covered by a homogeneous humic substance layer (see chapter 5.3 and Reich et al, 2006a). Simultaneously, HA-like substances diffuse from the clay layer into the high and low concentration reservoir solutions, whose total organic carbon (TOC) concentrations steadily increase during the experiment. After the end of the experiment, the TOC content in the high and low concentration reservoir amounted to about 1.8 and 0.8 mg C respectively, representing about 3.2 and 1.5 mg of mobilized HA-like substances. These HA-like substances are able to complex increasing amounts of U(VI) in form of the ternary uranyl mono hydroxo humate complex. Thus, the diffusion of U(VI) is increasingly influenced by this complex and U(VI) is probably immobilized at the solution clay boundary in association with HA.

The deeper penetration of U(VI) into the kaolinite-humic substance-sorbate (see Fig. 13.13.) may be attributed to the first stage of the experiment, when no HA-like substances were present in solution and U(VI) was allowed to diffuse as non-HA-complexed species (see Fig. 13.10).

As many natural sediments and soils contain considerable amounts of organic matter, this model system is expected to reflect migration processes in the environment more realistically than the pure clay system originally free of organic matter.

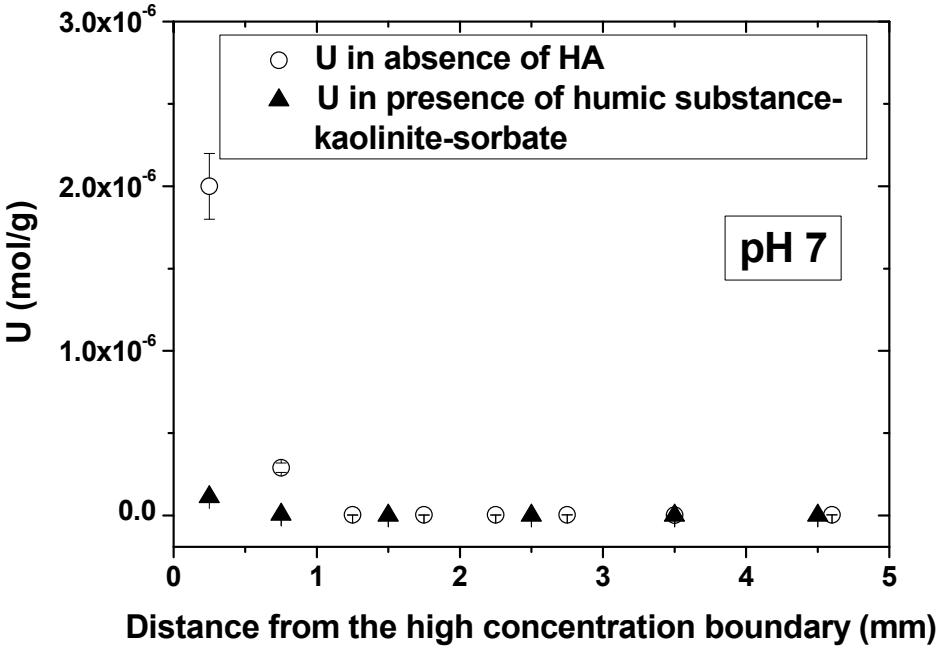

Fig. 13.12: U distribution in the kaolinite-humic substance-sorbate after 79 d in comparison to the U distribution in absence of HA (ρ_{bulk}: 1.56 g/cm^3).

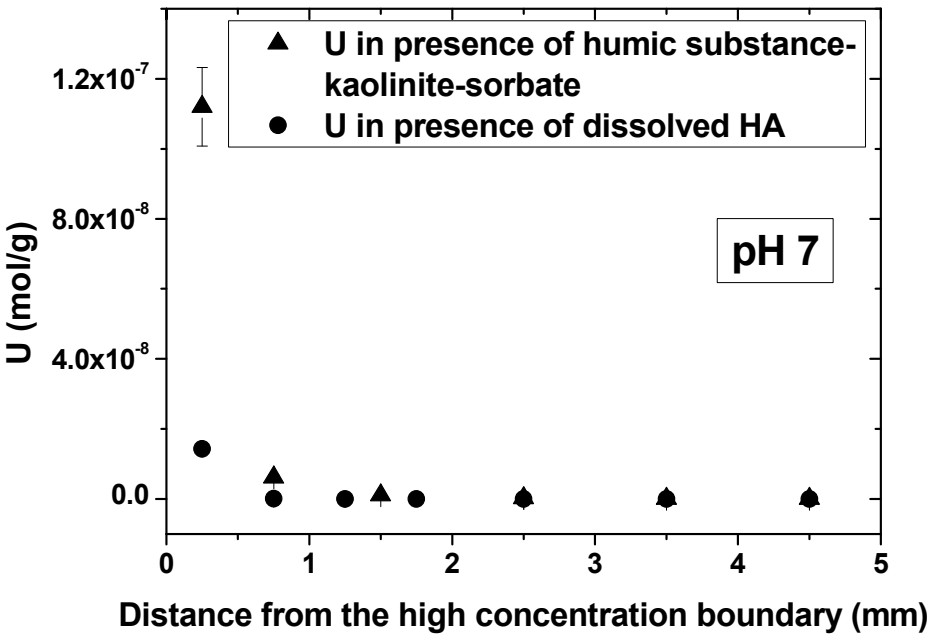

Fig. 13.13: U distribution in the clay plug after the experiment with the kaolinite-humic substance-sorbate and with kaolinite and HA in solution (pH 7, ρ_{bulk}: 1.56 g/cm^3).

The migration of HA in clay is governed by diffusion. It is influenced by the colloidal behavior of HA. At higher clay bulk densities, size fractionation affects the diffusion parameters. In presence of HA colloids U(VI) is immobilized in association with HA near the high concentration boundary.

In the advective quartz sand system, HA exhibits an ambivalent influence on the uranium transport (Mibus et al., 2007). Depending on the environmental conditions, an accelerating or a retarding moment could become effective. In the clay system, the retarding moment, i.e., the settlement of colloids and associated U(VI), clearly dominates, whereas the acceleration (humic colloid borne transport of U) could not be demonstrated.

14 Summary and outlook

The aim of this project was the study of basic interaction processes in the system clay-humic substance-aquifer to obtain a better process understanding, to improve the knowledge of the interaction behavior of HA with metal ions and to amend the thermodynamic database. Within the project kaolinite KGa-1b was used as model mineral.

In order to identify nitrogen-containing functional groups in HA, a ^{15}N-labeled HA type M1 was synthesized and characterized by ^{15}N-NMR spectroscopy. It was concluded, that the nitrogen forms in HA type M1 can be attributed to different types of linkages (pyrrole- and/or indole-like N, primary and/or secondary amine N, N in terminal amino acid groups), which agrees with literature data for natural HA. Based on these results, first U(VI) complexation studies with organic model ligands (phenylalanine, 3-phenylpropionic acid, glycine) were carried out to get an impression on the influence of NH_2 groups on the metal ion complexation by HA. It was found that the amino function seems to be not involved in the uranyl complexation at pH 4. A rather destabilizing effect on the complex was observed. To elucidate the impact of nitrogen-containing functional groups on the HA-metal ion-interaction further investigations are necessary under different experimental conditions using other model ligands representing alternative nitrogen functionalities in HA.

The impact of kaolinite on the formation of humic substances and humic substance-kaolinite-sorbates was investigated. Within these studies it was found that the presence of kaolinite during the HA synthesis mainly influences the yields on HA and their elemental compositions. Besides HA, it was possible to obtain humic-substance-kaolinite-sorbates that contain humic materials, which is assumed to be more hydrophobic than HA. The obtained sorbates are suitable model compounds for organic rich clays and were already used in batch and diffusion experiments.

To amend the thermodynamic database for the system actinide-HA-water, the U(VI) complexation by HA in the neutral pH range as well as the redox stability of Np(V) in presence of HA with different functionalities were studied. For the first time, two independent laser induced spectroscopic methods were applied to study the formation of the ternary U(VI) mono hydroxo humate complex UO_2(OH)HA(I) by reaction of UO_2OH^+ with HA. Assuming that all

proton exchanging functional groups of the HA are able to contribute to the complex formation, a mean stability constant of 6.58 ± 0.24 was derived for UO_2(OH)HA(I). Alternatively, the analytical data were evaluated based on the metal ion charge neutralization model resulting in a complexation constant of 6.95 ± 0.10 (LC: 0.76 ± 0.28). An overall complexation constant of $\log\beta_{0.1M}$ = 14.89 ± 0.54 was calculated for the total reaction of U(VI) with HA starting from the non-hydrolyzed UO_2^{2+} ion. Taking the UO_2(OH)HA(I) complex into account, the speciation of U(VI) in presence of HA was recalculated. The calculations indicate, that the formation of UO_2(OH)HA(I) can significantly influence the U(VI) speciation in the environmentally relevant pH region. As a consequence, the mobility of U(VI) in natural aquifer systems could be enhanced. The digital database for humics complexation based on the metal ion charge neutralization model was updated.

The redox properties of various natural and synthetic humic substances towards Np(V) were determined under anaerobic conditions between pH 3.5 and pH 9. In comparison to the natural humic substances (AHA, KFA), the synthetic HA (type Hyd-Glu and Cat-Gly) lead to a stronger reduction of Np(V) to Np(IV) and to a stabilization of the tetravalent oxidation state in form of Np(IV) humate complexes. The stronger reduction behavior of the synthetic HA in comparison to the natural humic substances can be attributed to their higher amount of phenolic/acidic OH groups. The influence of phenolic/acidic OH groups on the redox behavior of humic substances was verified applying a synthetic HA with blocked phenolic/acidic OH groups. By application of the synthetic HA with distinct redox properties actinides can be stabilized in lower oxidation states, e.g. in complexation and sorption studies.

Sorption experiments were performed to determine the influence of HA on the U(VI) and Np(V) sorption onto kaolinite. For comparison, the U(VI) sorption onto synthetic humic substance-kaolinite-sorbates was studied. For U(VI) a pH dependent sorption behavior onto kaolinite, which is affected by its concentration and the presence of CO_2 and HA, was observed. The adsorption of U(VI) closely follows the adsorption of HA. In the acidic pH range, HA enhances the U(VI) uptake compared to the HA-free system, whereas in the near-neutral pH range the formation of dissolved uranyl humate complexes reduces the U(VI) sorption, therefore, the presence of HA can enhance the U(VI) migration under environmentally relevant conditions. The structure of U(VI) kaolinite surface complexes in presence of HA was investigated applying spectroscopic methods (EXAFS, TRLFS) and compared to that in absence of HA. From EXAFS results it was concluded that HA has no effect on EXAFS structural parameters in the system U(VI)-HA-kaolinite. In presence of HA, U(VI) seems to adsorb directly onto kaolinite than via HA. Both in the absence and in the presence of HA, two adsorbed U(VI) species on kaolinite were identified by TRLFS spectroscopy. These surface complexes differ likely in their amount of coordinated water molecules. The TRLFS measurements confirmed, that in presence of HA U(VI) prefers to bind directly onto kaolinite than via HA. In the ternary system the hydrate shell of sorbed U(VI) is partly displaced by HA molecules.

From the U(VI) sorption experiments with synthetic humic substance-kaolinite-sorbates representing model substances for organic rich clays it was concluded, that humic matter associated with clay can exhibit an immobilizing as well as an mobilizing effect on U(VI). Due to structural and functional differences of the humic matter, the sorption behavior of U(VI) onto synthetic humic substance-kaolinite sorbates differs from that of U(VI) in the system U(VI)-

HA-kaolinite. HA separately added to the system can cause a stronger mobilizing effect on U(VI) than humic matter associated with clay.

In case of Np(V) it was found that the sorption behavior of Np onto kaolinite is effected by pH, ionic strength, Np concentration and the presence of HA. HA exhibits a significant influence on the Np sorption onto kaolinite. Between pH 7.5 and pH 10.5 the mobility of Np(V) is increased due to HA, which is attributed to formation of dissolved neptunyl humate complexes and/or neptunyl carbonate humate complexes.

Diffusion experiments were carried out to determine processes influencing the migration of humic colloids in compacted clay and its influence on the U(VI) migration. Additionally, the U(VI) diffusion in a compacted synthetic humic substance-kaolinite sorbate was measured. It was found that the migration of HA in clay is governed by diffusion and influenced by its colloidal behavior. Generally it was shown that in presence of humic matter U(VI) is immobilized near the high concentration boundary in association with HA. However, a deeper penetration of U(VI) into the clay layer was observed for the humic substance-kaolinite-sorbate which exhibits more hydrophobic humic matter.

The results of these studies improve the knowledge on basic interaction processes of actinides (U(VI), Np(V)) in the system clay humic substance-aquifer. Important results were obtained on the characterization of humic material and its complexation properties, the complexation of U(VI) under neutral conditions, the redox stability of Np(V), as well as on the influence of humic matter on the U(VI) and Np(V) sorption onto kaolinite and the U(VI) migration in compacted clay. Within the project data were generated that extent the thermodynamic database under environmentally relevant conditions. Furthermore, a better process understanding was obtained. In their combination the results contribute to a more realistic description of the migration behavior of actinides in clay formations and to an improved risk assessment for potential nuclear waste repositories.

Future studies should focus on interaction processes of actinides with natural clay rocks and the determination of the impact of natural organic matter present in the clay on the actinide migration. At first Opalinus clay will be investigated. Further studies on the actinide complexation by HA have to be performed. This includes model investigations on the influence of HA functional groups, other than oxygen-containing (nitrogen- and sulfur-containing), on the metal ion complexation by HA and studies on the formation of ternary actinide carbonato humate complexes. The thermodynamic database of the actinide humate complexation under near-natural conditions has to be completed. Besides tetravalent actinides (e.g. U(IV)), environmentally relevant temperature and concentration dependencies has to be considered.

15 References

Amayri, S. (2006). Wechselwirkung von Neptunium und Plutonium mit Huminstoffen und Kaolinit. 6. Workshop des Verbundprojektes 'Migration von Actiniden im System Ton, Huminstoff, Aquifer'. Mainz, 28.-29.03.2006.

André, C., Choppin, G.R.: Reduction of Pu(V) by Humic Acid (2000). Radiochim. Acta 88, 613.

Ankudinov, A. L., Bouldin, C.E., Rehr, J.J., Sims, J., Hung, H. (2002). Parallel Calculation of Electron Multiple Scattering Using Lanczos Algorithms. Phys. Rev. B 65, 104107.

Arnold, T., Zorn, T., Bernhard, G., Nitsche, H. (1998). Sorption of Uranium(VI) onto Phyllite. Chem. Geol. 151, 129.

Arnold, T., Utsunomiya, S., Geipel, G., Ewing, R.C., Baumann, N., Brendler, V. (2006). Adsorbed U(VI) Surface Species on Muscovite Identified by Laser Fluorescence Spectroscopy and Transmission Electron Microscopy. Environ. Sci. Technol. 40, 4646.

Artinger, R., Marquardt, C.M., Kim, J.I., Seibert, A., Trautmann, N., Kratz, J.V. (2000). Humic Colloid-borne Np Migration: Influence of the Oxidation State. Radiochim. Acta 88, 609.

Artinger, R., Kuczewski, B., Marquardt, C.M., Schäfer, Th., Seibert, A., Fanghänel, Th. (2004). Comparison of Humic Colloid Mediated Transport of Plutonium Studied by Column Experiments with Tri- and Tetravalent Actinide Experiments. In: FZKA 6969, Wissenschaftliche Berichte (G. Buckau, ed.). Forschungszentrum Karlsruhe, Karlsruhe, p. 47.

Babanov, Yu.A., Vasin, V.V., Ageev, Al.L, Ershov, N.V. (1981). A New Interpretation of EXAFS Spectra in Real Space . 1. General Formalism. Physica Status Solidi B-Basic Research 105, 747.

Balcke, G.U., Kulikova, N.A., Hesse, S., Kopinke, F.-D., Perminova, I., Frimmel, F. (2002). Adsorption of Humic Substances onto Kaolin Clay Related to Their Structural Features. Soil Sci. Soc. Am. J. 66, 1085.

Baumann, N., Brendler, V., Arnold, T., Geipel, G., Bernhard, G. (2005). Uranyl Sorption onto Gibbsite Studied by Time-resolved Laser-induced Fluorescence Spectroscopy (TRLFS). J. Coll. Interf. Sci. 290, 318.

Bell, J.T., Biggers, R.E. (1968). Absorption Spectrum of the Uranyl Ion in Perchlorate Media. III. Resolution of the Ultraviolet Band Structure; Some Conclusions Concerning the Excited State of UO_2^{2+}. J. Mol. Spectr. 25, 312.

Benzing-Purdie, L.M., Ratcliffe, C.I. (1986). A Study of the Maillard Reaction by ^{13}C and ^{15}N CP-MAS NMR: Influence of Time, Temperature, and Reactants on Major Products. Developments in Food Science 13, 193.

Berger, S., Braun, S., Kalinowski, H.-O. (1992). *NMR-Spektroskopie von Nichtmetallen. Band 2: ^{15}N-NMR-Spektroskopie.* Thieme Verlag, Stuttgart.

Bertrand, P.A., Choppin, G.R. (1982). Separation of Actinides in Different Oxidation States by Solvent Extraction. Radiochim. Acta 31, 135.

Borden, D., Giese, R.F. (2001). Baseline Studies of the Clay Minerals Society Source Clays: Cation Exchange Capacity Measurements by the Ammonia-Electrode Method. Clays Clay Miner. 49, 444.

Bortiatynski, J.M., Hatcher, P.G., Knicker, H. (1996). NMR Techniques (C, N, and H) in Studies of Humic Substances. In: *ACS Symposium Series 651 (Humic and Fulvic Acids)*, American Chemical Society, p. 57.

Brady, P.V., Cygan, R.T., Nagy, K.L. (1998). Surface Charge and Metal Sorption to Kaolinite. In: *Adsorption of Metals by Geomedia: Variables, Mechanisms, and Model Applications* (Jenne, E.A., ed.). Academic Press, San Diego, p. 371.

Brendler, V., Brachmann, A., Geipel, G. (1997). Software to Compute Lifetimes from Time-Resolved Laser-Induced Fluorescence Spectroscopy (TRLFS) Studies, Exploiting the Full Spectrum. In: *Institute of Radiochemistry, Annual Report 1996*. Wissenschaftlich-Technische Berichte, FZR-180 (H. Nitsche, ed.), Forschungszentrum Rossendorf, Dresden, p. 13.

Brendler, V., Sachs, S. (2006). Aqueous Uranium(VI) Hydrolysis Species Characterised by TRLFS. Spectrochim. Acta, in preparation.

Bubner, M., Heise, K.H. (1994). Characterization of Humic Acids. II Characterization by Radioreagent-derivatization with [^{14}C]Diazomethane. In: *Institute of Radiochemistry, Annual Report 1993*. Wissenschaftlich-Technische Berichte, FZR-43 (H. Nitsche and G. Bernhard, eds.), Forschungszentrum Rossendorf, Dresden, p. 22.

Chen, Y.Z., Tan, B.M., Lin, Z.J. (1993). A Kinetic Study of the Reduction of Np(VI) with Humic Acid. Radiochim. Acta 62, 199.

Chipera, S.J., Bish, D.L. (2001). Baseline Studies of the Clay Minerals Society Source Clays: Powder X-ray Diffraction Analyses. Clays Clay Miner. 49, 398.

Choppin, G.R.: Humics and Radionuclide Migration (1988). Radiochim. Acta 44/45, 23.

Claret, F., Schäfer, T., Bauer, A., Buckau, G. (2003). Generation of Humic and Fulvic Acid from Callovo-Oxfordian Clay Under High Alkaline Conditions. Sci. Tot. Environm. 317, 189.

Costanzo, P.A., Guggenheim, S., guest editors (2001). Baseline Study of the Clay Minerals Society Source Clays. Clays Clay Miner. 49, 371-453.

Cox, J.D., Wagman, D.D., Medvedev, V.A. (1989). *CODATA Key Values for Thermodynamics*, Hemisphere, New York.

Crank, J. (1975). *The Mathematics of Diffusion*, 2nd ed., Pergamon Press Oxford.

Czerwinski, K.R., Buckau, G., Scherbaum, F., Kim, J.I. (1994). Complexation of the Uranyl Ion with Aquatic Humic Acid. Radiochim. Acta 65, 111.

Fernandez-Botello, A., Gomez-Coca, R.B., Holy, A., Moreno, V., Sigel, H. (2002). Metal-ion Binding Properties of O-phosphonatomethylcholine (PMCh-). Effect of the Positive Charge of a Distant Trimethylammonium Group on the Coordinating Qualities of a Phosph(on)ate Group. Inorg. Chim. Acta 331, 109.

Geipel, G., Bernhard, G., Rutsch, M., Brendler, V., Nitsche, H. (2000). Spectroscopic Properties of Uranium(VI) Minerals Studied by Time-resolved Laser-induced Fluorescence Spectroscopy (TRLFS). Radiochim. Acta 88, 757.

Geipel, G., Acker, M., Vulpius, D., Bernhard, G., Nitsche, H., Fanghänel, Th. (2004). An Ultrafast Time-resolved Fluorescence Spectroscopy System for Metal Ion Complexation Studies with Organic Ligands. Spectrochim. Acta Part A 60, 417.

George, G.N., Pickering, I.J. (1995). EXAFSPAK: *A Suite of Computer Programs for Analysis of X-ray Absorption Spectra*. Stanford Synchrotron Radiation Laboratory, Stanford, CA, USA.

Glaus, M.A., Hummel, W., Van Loon, L.R. (1995). Stability of Mixed-Ligand Complexes of Metal Ions with Humic Substances and Low Molecular Weight Ligands. Environ. Sci. Technol. 29, 2150.

Guillaumont, R., Fanghänel, T., Fuger, J., Grenthe, I., Neck, V., Palmer, D.A., Rand M.H. (2003). *Update on the Chemical Thermodynamics of Uranium, Neptunium, Plutonium, Americium and Technetium*. *Chemical Thermodynamics Vol. 5* (OECD Nuclear Energy Agency, ed.), Elsevier, Amsterdam.

Günther, A., Geipel, G., Bernhard, G. (2007). Complex Formation of Uranium(VI) with the Amino Acids L-glycine and L-cysteine: A Fluorescence Emission and UV-vis Absorption Study. Polyhedron 26, 59.

Hasegawa, Y., Yamazaki, N., Usui, S., Choppin, G.R. (1990). Effects of Phenyl Groups on Thermodynamic Parameters of Lanthanoid(III) Complexation with Aromatic Carboxylic Acids. Bull. Chem. Soc. Jpn. 63, 2169.

Hendry, M.J., Ranville, J.R., Boldt-Leppin, B.E.J., Wassenaar, L.I. (2003). Geochemical and Transport Properties of Dissolved Organic Carbon in a Clay-rich Aquitard. Water Resour. Res. 39, 1194.

Hendry, M.J., Wassenaar, L.I. (2005). Origin and Migration of Dissolved Organic Carbon Fractions in a Clay-rich Aquitard: C-14 and Delta C-13 Evidence. Water Resour. Res. 41, 2021.

Ishimitsu, T., Hirose, S., Sakurai, H. (1977). Microscopic Acid Dissociation Constants of 3,4-Dihydroxyphenylpropionic Acid and Related Compounds, and 3,4-dihydroxyphenylalanine (DOPA). Talanta 24, 555.

Kakihana, M., Nagumo, T., Okamoto, M., Kakihana, H. (1987). Coordination Structures for Uranyl Carboxylate Complexes in Aqueous Solution Studied by IR and ^{13}C NMR Spectra. J. Phys. Chem. 91, 6128.

Keller, C. (1971). The Chemistry of the Transuranium Elements (K.H. Lieser, ed.). Verlag Chemie GmbH, Weinheim, p. 294.

Kilislioglu, A., Bilgin, B. (2002). Adsorption of Uranium on Halloysite. Radiochim. Acta 90, 155.

Kim, J.I., Czerwinski, K.R. (1996). Complexation of Metal Ions with Humic Acids: Metal Ion Charge Neutralization Model. Radiochim. Acta 73, 5.

Kim, J.I., Buckau, G. (1998). *Characterization of Reference and Site Specific Humic Acids.* RCM-Report 02188, TU München.

Koban, A., Geipel, G., Bernhard, G. (2003). Complex Formation Between Uranium(VI) and α-D-glucose 1-phosphate. Radiochim. Acta 91, 393.

Koban, A., Bernhard, G. (2006). Uranium Complexes with Phospholipid Model Compounds – A Laser Spectroscopic Study. J. Inorg. Biochem., submitted.

Kogel, J.E., Lewis, S.A. (2001). Baseline Studies of the Clay Minerals Society Source Clays: Chemical Analysis by Inductively Coupled Plasma-mass Spectroscopy (ICP-MS). Clays Clay Miner. 49, 387.

Kohler, M., Wieland, E., Leckie, J.O. (1992). Metal-ligand-surface Interactions During Sorption of Uranyl and Neptunyl on Oxides and Silicates. Water-Rock Interaction. Kharaka & Maest, eds., Balkema, Rotterdam, 51.

Křepelová, A. (2006a). *Influence of Humic Acid on the Sorption of Uranium(VI) and Americium(III) onto Kaolinite.* PhD Thesis, TU Dresden, in preparation.

Křepelová, A., Sachs, S., Bernhard, G. (2006b). Uranium(VI) Sorption onto Kaolinite in the Presence and Absence of Humic Acid. Radiochim. Acta 94, 825.

Křepelová, A., Brendler, V., Sachs, S., Baumann, N., Bernhard, G. (2006c). New TRLFS Measurements of U(VI) Sorption onto Gibbsite. Annual Report 2006, in preparation.

Kretzschmar, R., Hesterberg, D., Sticher, H. (1997). Effects of Adsorbed Humic Acid on Surface Charge and Flocculation of Kaolinite. Soil Sci. Soc. Am. J. 61, 101.

Kumke, M.U., Tiseanu, C., Abbt-Braun, G., Frimmel, F.H. (1998). Fluorescence Decay of Natural Organic Matter (NOM)-Influence of Fractionation, Oxidation, and Metal Ion Complexation. J. Fluorescence 8, 309.

Kumke, M.U., Zwiener, C., Abbt-Braun, G., Frimmel, F.H. (1999). Spectroscopic Characterization of Fulvic Acid Fractions of a Contaminated Groundwater. Acta Hydrochim. Hydrobiol. 27, 409.

Lagaly, G. (1993). Reaktionen der Tonminerale. In: *Tonminerale und Tone. Struktur, Eigenschaften, Anwendung und Einsatz in Industrie und Umwelt* (K. Jasmund, G. Lagaly, eds.), Steinkopff, Darmstadt, chapter 3.

Lead, J.R., Wilkinson, K.J., Starchev, K., Canonica, S., Buffle, J. (2000). Determination of Diffusion Coefficients of Humic Substances by Fluorescence Correlation Spectroscopy: Role of Solution Conditions. Environ. Sci. Technol. 34, 1365-1369.

Madejová, J., Komadel, P. (2001). Baseline Studies of the Clay Minerals Society Source Clays: Infrared Methods. Clays Clay Miner. 49, 410.

Maes, N., Wang, L., Hicks, T., Bennett, D., Warwick, P., Hall, T., Walker, G., Dierckx, A. (2006). The Role of Natural Organic Matter in the Migration Behaviour of Americium in the Boom Clay-Part I: Migration Experiments. Physics and Chemistry of the Earth 31, 541.

Marquardt, C., Herrmann, G., Trautmann, N. (1996). Complexation of Neptunium(V) with Humic Acids at Very Low Metal Concentrations. Radiochim. Acta 73, 119.

Marquardt, C., Kim, J.I. (1998). Complexation of Np(V) with Humic Acid: Intercomparison of Results from Different Laboratories. Radiochim. Acta 80, 129.

Marquardt, C., Artinger, R., Zeh, P., Kim, J.I. (1999). Redoxchemistry of Neptunium in a Humic Rich Groundwater. In: FZKA 6324, Wissenschaftliche Berichte (G. Buckau, ed.). Forschungszentrum Karlsruhe, Karlsruhe, p. 21.

Marquardt, C.M., Pirlet, V., Kim, J.I. (2000). Initial Studies on the Complexation of Tetravalent Neptunium with Fulvic Acid. In: FZKA 6524, Wissenschaftliche Berichte (G. Buckau, ed.). Forschungszentrum Karlsruhe, Karlsruhe, p. 45.

Marquardt, C.M., Seibert, A., Artinger, R., Denecke, M.A., Kuczewski, B., Schild, D., Fanghänel, Th. (2004). The Redox Behaviour of Plutonium in Humic Rich Groundwater. Radiochim. Acta 92, 617.

Mibus, J., Sachs, S., Pfingsten, W., Nebelung, C., Bernhard, G. (2007). Migration of Uranium (IV)/(VI) in the Presence of Humic Acids in Quartz Sand: A Laboratory Column Study. J. Contam. Hydr. 89, 199.

Moll, H., Geipel, G., Reich, T., Bernhard, G., Fanghänel, T., Grenthe, I. (2003). *Uranyl(VI) Complexes with Alpha-substituted Carboxylic Acids in Aqueous Solution.* Radiochim. Acta 91, 11.

Montavon, G., Mansel, A., Seibert, A., Keller, H., Kratz, J.V., Trautmann, N. (2000). Complexation Studies of UO_2^{2+} with Humic Acid at Low Metal Ion Concentrations by Indirect Speciation Methods. Radiochim. Acta 88, 17.

Morgenstern, M., Klenze, R., Kim, J.I. (2000). The Formation of Mixed-Hydroxo Complexes of Cm(III) and Am(III) with Humic Acid in the Neutral pH Range. Radiochim. Acta 88, 7.

Moulin, V., Moulin, C. (1995). Fate of Actinides in the Presence of Humic Substances under Conditions Relevant to Nuclear Waste Disposal. Appl. Geochem. 10, 573.

Moulin, C., Laszak, I., Moulin, V., Tondre, C. (1998). Time-Resolved Laser-Induced Fluorescence as a Unique Tool for Low-Level Uranium Speciation. Appl. Spectroscopy 52, 528.

Murphy, E.M., Zachara, J.M., Smith, S.C., Phillips, J.L. (1992). The Sorption of Humic Acids to Mineral Surfaces and their Role in Contaminant Binding. Sci. Tot. Environ. 117/118, 413.

Nash, K., Fried, S., Friedman, A.M., Sullivan, J.C. (1981). Redox Behavior, Complexing, and Adsorption of Hexavalent Actinides by Humic Acid and Selected Clays. Environ. Sci. Technol. 15, 834.

Nebelung, C. (2002). Correction of Sorption Data of ^{234}U Contaminated with ^{232}U. In: Institute of Radiochemistry, Annual Report 2001. Wissenschaftlich-Technische Berichte, FZR-343 (Th. Fanghänel, ed.), Forschungszentrum Rossendorf, Dresden, p. 32.

Niitsu, Y., Sato, S., Ohashi, H., Sakamoto, Y., Nagao, S., Ohnuki, T., Muraoka, S. (1997). Effects of Humic Acid on the Sorption of Neptunium(V) on Kaolinite. J. Nuclear Materials 248, 328.

Panak, P., Klenze, R., Kim, J.I. (1996). A Study of Ternary Complexes of Cm(III) with Humic Acid and Hydroxide or Carbonate in Neutral pH Range by Time-Resolved Laser Fluorescence Spectroscopy. Radiochim.Acta 74, 141.

Pashalidis, I., Czerwinsky, K., R., Fanghänel, Th., Kim, J.I. (1997). Solid-Liquid Phase Equilibria of Pu(VI) and U(VI) in Aqueous Carbonate Systems. Determination of Stability Constants. Radiochim. Acta 76, 55.

Pashalidis, I., Kim, J.I., Buckau, G. (2006). U(VI) Mono-Hydroxo Humate Complexation. J. Radioanal. Nucl. Chem., accepted.

Payne, T.E., Davis, J.A., Lumpkin, G.R., Chisari, R., Waite, T.D. (2004). Surface Complexation of Uranyl Sorption on Georgia Kaolinite. Appl. Clay Sci. 26, 151.

Pompe, S., Bubner, M., Denecke, M.A., Reich, T., Brachmann, A., Geipel, G., Nicolai, R., Heise, K.H., Nitsche, H. (1996). A Comparison of Natural Humic Acids with Synthetic Humic Acid Model Substances: Characterization and Interaction with Uranium(VI). Radiochim. Acta 74, 135.

Pompe, S., Brachmann, A., Bubner, M., Geipel, G., Heise, K.H., Bernhard, G., Nitsche, H. (1998). Determination and Comparison of Uranyl Complexation Constants with Natural and Model Humic Acids, Radiochim. Acta 82, 89.

Pompe, S., Bubner, M., Schmeide, K., Heise, K.H., Bernhard, G., Nitsche, H. (2000a). *Influence of Humic Acids on the Migration Behavior of Radioactive and Non-Radioactive Substances under Conditions Close to Nature. Synthesis, Radiometric Determination of Functional Groups, Complexation.* Wissenschaftlich-Technische Berichte, FZR-290, Forschungszentrum Rossendorf, Dresden.

Pompe, S., Schmeide, K., Bubner, M., Geipel, G., Heise, K.H., Bernhard, G. Nitsche, H. (2000b). Investigation of Humic Acid Complexation Behavior with Uranyl Ions Using Modified Synthetic and Natural Humic Acids. Radiochim. Acta 88, 553.

Pruett, R.J., Webb, H.L. (1993). Sampling and Analysis of KGa-1b Well-crystallized Kaolin Source Clay. Clays Clay Miner. 41, p. 514.

Redden, G.D., Jinhe, L., Leckie, J. (1998). Adsorption of U(VI) and Citric Acid on Goethite, Gibbsite, and Kaolinite. Comparing Results for Binary and Ternary Systems. In: *Adsorption of Metals by Geomedia*. *Variables Mechanisms Model Appl.* (Jenne, E. A, ed.). Academic Press, San Diego, p. 291.

Reich, T., Drebert, J., Křepelová, A., Sachs, S. (2006a). XPS Study of Humic Acid/Kaolinite Interaction. In: *Institute of Radiochemistry, Annual Report 2005.* Wissenschaftlich-Technische Berichte, FZR-443 (G. Bernhard, ed.), Forschungszentrum Rossendorf, Dresden, p. 46.

Reich, T. Ye., Kokrshunov, M.E., Antonova, T. V., Ageev, A.L., Moll, H., Reich, T. (2006b). New Regularizaton Method for EXAFS Analysis. AIP Proceedings XAFS13, in press.

Sachs, S., Heise, K.H., Bernhard, G. (2003). Synthetic Humic Acid Model Substances with Specific Functional Properties for the Use in Complexation and Sorption Experiments with Actinides. In: FZKA 6800, Wissenschaftliche Berichte (G. Buckau, ed.). Forschungszentrum Karlsruhe, Karlsruhe, p. 51.

Sachs, S., Schmeide, K., Brendler, V., Křepelová, A., Mibus, J., Geipel, G., Heise, K.H., Bernhard, G. (2004). *Investigation of the Complexation and the Migration of Actinides and Non-radioactive Substances with Humic Acids under Geogenic Conditions.* Wissenschaftlich-Technische Berichte, FZR-399, Forschungszentrum Rossendorf, Dresden.

Sachs, S., Bernhard, G. (2005a). NIR Spectroscopic Study of the Complexation of Neptunium(V) with Humic Acids: Influence of Phenolic OH Groups on the Complex Formation. Radiochim. Acta 93, 141.

Sachs, S., Geipel, G., Bernhard, G. (2005b). Study of the Redox Stability of Uranium(VI) in Presence of Humic Substances. In: FZKA 7070, Wissenschaftliche Berichte (G. Buckau, ed.). Forschungszentrum Karlsruhe, Karlsruhe, p. 11.

Sachs, S., Brendler, V., Geipel, G. (2006). Uranium(VI) Complexation by Humic Acid under Neutral pH Conditions Studied by Laser-induced Fluorescence Spectroscopy. Radiochim. Acta, in press.

Samadfam, M., Jintoku, T., Sato, S., Ohashi, H., Mitsugashira, T., Hara, M., Suzuki, Y. (2000). Effects of Humic Acid on the Sorption of Am(III) and Cm(III) on Kaolinite. Radiochim. Acta 88, 717.

Schmeide, K., Zänker, H., Heise, K.H., Nitsche, H. (1998). Isolation and Characterization of Aquatic Humic Substances from the Bog 'Kleiner Kranichsee'. In: FZKA 6124, Wissenschaftliche Berichte (G. Buckau, ed.). Forschungszentrum Karlsruhe, Karlsruhe p. 161.

Schmeide, K., Pompe, S., Bubner, M., Heise, K.-H., Bernhard, G., Nitsche, H. (2000). Uranium(VI) Sorption onto Phyllite and Selected Minerals in the Presence of Humic Acid. Radiochim. Acta 88, 723.

Schmeide, K., Sachs, S., Bubner, M., Reich, T., Heise, K.H., Bernhard, G. (2003). Interaction of Uranium(VI) with Various Modified and Unmodified Natural and Synthetic Humic Substances Studied by EXAFS and FTIR Spectroscopy. Inorg. Chim. Acta 351, 133.

Schmeide, K., Reich, T., Sachs, S., Brendler, V., Heise, K.H., Bernhard, G. (2005). Neptunium(IV) Complexation by Humic Substances Studied by X-ray Absorption Fine Structure Spectroscopy. Radiochim. Acta 93, 187.

Schmeide, K., Reich, T., Sachs, S., Bernhard, G. (2006). Plutonium(III) Complexation by Humic Substances Studied by X-ray Absorption Fine Structure Spectroscopy. Inorg. Chim. Acta 359, 237.

Schnitzer, M., Khan, S.U. (1972). *Humic Substances in the Environment* (A.D. McLaren, ed.). Marcel Dekker, Inc. New York.

Schroth, B.K., Sposito, G. (1997). Surface Charge Properties of Kaolinite. Clays Clay Miner. 45, 85.

Seibert, U.A. (1999). Wechselwirkung von neptunium mit Huminstoffen unter naturnahen Bedingungen. PhD Thesis, Johannes Gutenberg-Universität Mainz.

Seibert, A., Mansel, A., Marquardt, C.M., Keller, H., Kratz, J.V., Trautmann, N. (2001). Complexation Behaviour of Neptunium with Humic Acid. Radiochim. Acta 89, 505.

Shackelford, C.D. (1991). Laboratory Diffusion Testing for Waste Disposal-A Review. J. Contam. Hydrol. 7, 177.

Shanbhag, P.M., Choppin, G.R. (1981). Binding of Uranyl by Humic Acid. J. Inorg. Nucl. Chem. 43, 3369.

Shin, H.-S., Hong, K.-H., Lee, M.-H., Cho, Y.-H., Lee, C.-W. (2001). Fluorescence Quenching of Three Molecular Weight Fractions of a Soil Fulvic Acid by UO_2(II). Talanta 53, 791.

Silva, R.J., Bidoglio, G., Rand, M.H., Robouch, P.B., Wanner, H., Puigdomenech, I. (1995). *Chemical Thermodynamics, Volume 2: Chemical Thermodynamics of Americium.* North-Holland, Amsterdam.

Stevenson, F.J. (1994). *Humus Chemistry. Genesis, Composition, Reactions.* 2nd ed., J. Wiley, New York.

Sumner, M.E., Miller, W.P. (1996). Cation Exchange Capacity and Exchange Coefficients. In: *Methods of Soil Analysis*. *Part 3: Chemical Methods.* Soil Science Society of America, Inc., USA, p. 1201.

Sutheimer, S.H., Maurice, P.A., Zhou, Q. (1999). Dissolution of Well and Poorly Crystallized Kaolinites: Al Speciation and Effects of Surface Characteristics. Am. Mineral. 84, 620.

Taguchi, K., Sampei, Y. (1986). The Formation, and Clay Mineral and $CaCO_3$ Association Reactions of Melanoidins. Org. Geochem. 10, 1081.

Tan, J.X., Chen, Y.Z., Lin, Z.J. (1993). A Kinetic Study of the Reduction of Plutonium with Humic Acid. Radiochim. Acta 61, 73.

Thompson, H.A., Parks, G.A., Brown, Jr., G.E. (1998). Structure and Composition of Uranium(VI) Complexes at the Kaolinite-Water Interface. In: *Adsorption of Metals by Geomedia*. *Variables Mechanisms Model Appl*. (Jenne, E. A, ed.). Academic Press, San Diego, 349.

Trepte, P. (2006). Sorption von Radionukliden an Tongestein: Spektroskopische Referenzdaten. Diplomarbeit, HTW Dresden.

Van Loon, L.R., Soler, J.M., Bradbury, M.H. (2003). Diffusion of HTO, $^{36}Cl^-$ and $^{125}I^-$ in Opalinus Clay Samples from Mont Terri. Effect of Confined Pressure. J. Contam. Hydrol. 61, 73.

Van Loon, L. R., Soler, J. M. (2004). Diffusion of HTO, $^{36}Cl^-$, $^{125}I^-$ and $^{22}Na^+$ in Opalinus Clay: Effect of Confining Pressure, Sample Orientation, Sample Depth and Temperature. PSI Report 04-03, Villigen.

Vulpius, D. (2005). Zur Komplexbildung von Actiniden (U, Np) mit Hydroxybenzoesäuren. PhD Thesis, TU Dresden.

Wang, X., Chen, C., Yu, S., Zhou, X., Xu, D., Ren, A. (2005). Effect of pH and Fulvic Acid on the Sorption and Diffusion of Europium Ions in Compacted Bentonite as Studied by the Capillary Method. Ads. Sci. Technol. 23, 801.

Wimmer, H., Klenze, R., Kim, J.I. (1992). A Study of Hydrolysis Reaction of Curium(III) by Time Resolved Laser Fluorescence Spectroscopy. Radiochim. Acta 56, 79.

Wold, S., Eriksen, T.E. (2003). Diffusion of Lignosulfonate Colloids in Compacted Bentonite. Appl. Clay Sci. 23, 43.

Wold, S., Eriksen, T.E. (2005). Diffusion of Humic Colloids in Compacted Bentonite. Proceedings of the 2nd International Symposium "Clays in natural and engineered barriers for radioactive waste confinement", Tours, France, 14-18 March 2005, p. 547.

Wolery, T.J. (1992). *EQ3/6, a Software Package for the Geochemical Modeling of Aqueous Systems.* UCRL-MA-110662, Part 1, Lawrence Livermore National Laboratory.

Wu, W. (2001). Baseline Studies of the Clay Minerals Society Source Clays: Colloid and Surface Phenomena. Clays Clay Miner. 49, 446.

Zeh, P., Czerwinski, K.R., Kim, J.I. (1997). Speciation of Uranium in Gorleben Groundwaters. Radiochim. Acta 76, 37.

Zeh, P., Kim, J.I., Marquardt, C.M., Artinger, R. (1999). The Reduction of Np(V) in Groundwater Rich in Humic Substances. Radiochim. Acta 87, 23.

Ziechmann, W. (1994). *Humic Substances.* BI Wissenschaftsverlag, Mannheim.

16 Acknowledgements

The authors thank R. Ruske, M. Meyer and S. Heller for their valuable help with synthesis and characterization of humic materials, performance of batch experiments and sample preparation. We thank Dr. H. Foerstendorf and K. Heim for recording of FTIR and ATR FTIR spectra and for their help in the spectra interpretation. For technical support we thank C. Eckardt (BET and TOC analyses), K. Muschter (FTIR measurements), U. Schaefer and M. Leckelt (ICP-MS analyses), H. Görner (elemental analyses) and A. Scholz (XRD measurements). Thanks are given to Dr. N. Baumann for the performance of TRLFS measurements with kaolinite samples. We thank Ch. Müller for their technical assistance in the performance of diffusion experiments and C. Nebelung for evaluation of LSC spectra.

We thank Dr. E. Brendler (Institute of Analytical Chemistry, Faculty for Chemistry and Physics, TU Bergakademie Freiberg) for recording of ^{15}N-NMR spectra and for her support in the interpretation of these spectra.

We gratefully acknowledge Prof. Dr. T. Reich (Institut für Kernchemie, Johannes-Gutenberg University Mainz) for his support and the very good cooperation in the analysis and discussion of EXAFS spectra and for the performance and evaluation of XPS measurements.

EXAFS measurements were performed at BM20 at the European Synchrotron Radiation Facility in Grenoble (France). Thanks are given to Dr. A. Scheinost, Dr. H. Funke, Dr. H. Hennig, and Dr. A. Roßberg for their support during the EXAFS measurements.

The studies of the Np(V) reduction were partly supported by the EC Commission under contract No. FIKW-CT-2001-00128.

We would like to thank all colleagues who contributed to the success of this work.

Appendix B - Institut für Kernchemie, Universität Mainz

Interaction of Neptunium and Plutonium with Humic Substances and Kaolinite

S. Amayri, N. L. Banik, M. Breckheimer, R. A. Buda, S. Bürger, J. Drebert, A. Jermolaev, J. V. Kratz, B. Kuczewski, D. Kutscher, T. Ye. Reich, T. Reich, N. Trautmann

Final Report

Support Contract Number
02 E 9653

Institut für Kernchemie
Joh.-Gutenberg Universität Mainz
Fritz-Straßmann-Weg 2
55099 Mainz
Germany

Content

Abstract

The objective of this project was the study of the processes responsible for the mobilization or immobilization of neptunium and plutonium in the environment after an accidental release from a nuclear waste repository. The interaction of neptunium and plutonium with humic substances (HS) and kaolinite KGa-1b has been studied in detail. Furthermore, experiments with thorium, uranium, and americium were performed for comparison.

It could be shown that among the different oxidation states of plutonium only Pu(III) and Pu(IV) exist in contact with HS in aqueous solutions. The complexation constants of Pu(III) and Pu(IV) with Aldrich humic acid were determined using the method of ultrafiltration ($\log ß_{Pu(III)}$ = 6.2–6.9; $\log ß_{Pu(IV)}$ = 6.4–8.4).

The sorption of NpO_2^+, UO_2^{2+}, Pu^{3+}, Am^{3+}, Pu^{4+}, and Th^{4+}on kaolinite and of NpO_2^+ on hematite was investigated in batch experiments, and the speciation of U, Np, and Pu on the mineral surface was determined by means of XAFS spectroscopy. The binary system HS–KGa-1b was investigated in batch experiments and by means of XPS.

The influence of HS on the sorption of Pu(III) and Pu(IV) on kaolinite was investigated as a function of pH, concentration of HS, nature of HS (humic acid or fulvic acid), and the sequence in which the components were added to the system. It was found that HS enhances the sorption of Pu(III) and Pu(IV) on kaolinite at pH < 6 and decreases it at pH > 6.

New methods have been explored for the speciation of ultra-trace amounts of plutonium (CE-RIMS), as well as for the determination of the complexation constants of plutonium with humic and fulvic acids (CE-DAD-ICP-MS).

1 Introduction

The safety assessments of long-term nuclear waste repositories require detailed knowledge on the interaction processes that could lead to the migration of radioactive substances into the environment. Plutonium (Pu) and the minor actinides such as and neptunium (Np) contribute mainly to the radiotoxicity of spent nuclear fuel in a radioactive waste repository after storage times of more than 1000 years [1, 2].

Therefore, detailed studies of interaction processes of actinides, which might be released from the repository into the aquifer, with the engineered barriers and the host rock formation of a nuclear waste repository are needed for its performance assessment. An important factor, which determines the mobility of radionuclides in the environment, is their interaction with water and their migration behavior, which depends on the complexation and redox chemistry. To predict the radionuclide mobility, it is necessary to have fundamental knowledge about the retardation and mobilization phenomena and the underlying basic processes and interactions.

Although neptunium can exist in aqueous solution in the oxidation states III–VII, the pentavalent cation, NpO_2^+, dominates the aqueous speciation under a wide range of environmental conditions [3].

Plutonium occurs in aqueous solutions in four oxidation states (Pu^{3+}, Pu^{4+}, PuO_2^+, and PuO_2^{2+}) at the same time. The humic substances are organic matter ubiquitously found in ground water as a result of the biomass decomposition and have a reducing effect on the redox equilibrium of plutonium. Thus, Pu(III) and Pu(IV) are the species of most interest with respect to the migration of this element in the environment.

In our investigations clay minerals are considered as a geological barrier. These minerals are rather complex with respect to structural and chemical characteristics. In the framework of our project “Migration von Actiniden im System Ton, Huminstoff, Aquifer” (Migration of Actinides in the System Clay, Humic Substance, Aquifer), kaolinite KGa-1b was chosen as a model for clay minerals due to its relative simplicity in comparison with other minerals and because its physical and chemical properties are very well characterized [4-7]. In rock systems, iron oxides such as hematite (α-Fe_2O_3) are expected to play an important role for the migration of radionuclides because of their widespread distribution, high surface areas, and high sorptive capacities [8, 9].

The aim of this project was to study the basic interaction processes of NpO_2^+, Pu^{3+}, Pu^{4+}, and UO_2^+ in the aqueous system clay-humic substances. Thus, the redox chemistry as well as the complexation of plutonium with humic substances in aqueous solution was investigated.

Also, detailed investigations of the sorption of NpO_2^+, Pu^{3+}, Pu^{4+}, and UO_2^{2+} on kaolinite were conducted by combining batch experiments with techniques such as X-ray absorption fine structure (XAFS) spectroscopy to study the speciation of the metal ions on the surface of the kaolinite and hematite. In addition, the ternary systems Pu(III)/Pu(IV)–HS–kaolinite were investigated.

The development of new methods for the speciation of ultra-trace amounts of plutonium by means of capillary electrophoresis-resonance ionization mass spectrometry (CE-RIMS) and for the determination of the complexation constants of plutonium with humic substances by means of capillary electrophoresis-diode array detector-inductively coupled plasma-mass spectrometry (CE-DAD-ICP-MS) was also part of this work.

The work was performed in collaboration with the universities of Saarbrücken, Potsdam, München, and Heidelberg, the Institute for Interdisciplinary Isotope Research Leipzig, the Institute for Nuclear Waste Management (INE) at the Forschungszentrum Karlsruhe, the Institute of Radiochemistry at the Forschungszentrum Dresden-Rossendorf, and the Institute of Radiochemistry (TU München) as an associated partner of this joint project.

2 Chemicals and analytical techniques

Chemicals: All chemicals were of p.a. quality or better and were obtained from Merck (Darmstadt, Germany) or Riedel de Haen (Seelze, Germany). Milli-Q deionized water was used to prepare the solutions.

Humic and fulvic acids: The commercially available Aldrich humic acid (sodium salt, charge no. 01816-054) was purified as described by Kim and Buckau [10]. The proton exchange capacity (PEC) of Aldrich humic acid is 4.6×10^{-3} eq/g [10]. The Gorleben fulvic acid (GoHy-573) was isolated and purified in a similar manner; its PEC value is 6.82×10^{-3} eq/g [11].

Kaolinite: The reference clay kaolinite KGa-1b (Washington County, Georgia, USA) was obtained from the Clay Mineral Society Source Clays Repository. The chemical and mineralogical properties of this kaolinite are reported in the literature [12, 13]. Kaolinite suspensions were prepared in a solution of 0.1 M $NaClO_4$. All experiments were conducted at room temperature according to the batch procedure described below and were performed in 15 mL polypropylene (PP) centrifuge tubes sealed with screw caps.

Thorium solution: ^{234}Th was separated by ion chromatography from its mother, ^{238}U, in 8 M HCl following the procedure by Albinsson et al. [14]. After the purification step, the thorium stock solutions were prepared by fuming with $HClO_4$ and setting the $HClO_4$ molarity to 0.1 M. The purity of ^{234}Th was verified by γ spectroscopy.

Uranium solution: The 0.1 M U(VI) stock solution used in the sorption experiments was prepared by dissolving U_3O_8 in 0.5 M $HClO_4$. The concentration of uranium in solution was determined by ICP-MS.

Neptunium solution: For the sorption experiments, stock solutions of 0.8 nM $^{239}Np(V)$ and 8 mM $^{237}Np(V)$ in 0.03 M $HClO_4$ were used. The $^{237}Np(V)$ stock solution was purified from traces of ^{239}Pu and ^{233}Pa by anion-exchange chromatography. After fuming with concentrated $HClO_4$, a small amount of $NaNO_2$ was added to reduce Np(VI) to Np(V) in 0.03 M $HClO_4$. The pentavalent oxidation state of Np was verified by UV-vis spectroscopy (980 nm, ε = 395 M^{-}

$^{1}cm^{-1}$). The concentration of ^{237}Np was determined by γ spectroscopy using the γ lines at 29.4 and 86.5 keV. The isotope ^{239}Np was produced by irradiation of $^{238}UO_2(NO_3)_2 \cdot 6H_2O$ at the research reactor TRIGA Mainz. Following the irradiation, ^{239}Np was separated from U and its fission products by anion-exchange chromatography. The concentration of Np in solution was determined by γ spectroscopy using the γ lines at 103.8 and 106.1 keV.

Plutonium solution: For all sorption studies, a 99.1 wt % ^{239}Pu stock solution, with small amounts of other isotopes (0.888 wt % ^{240}Pu, 0.014 wt % ^{241}Pu) and known specific activity was used. The plutonium solutions were prepared by diluting aliquots of the stock solution with 1 M $HClO_4$. The resulting solutions consisted of different oxidation states of plutonium. The trivalent and tetravalent oxidation states of Pu were obtained by potentiostatic electrolysis and the purity was verified by UV-vis spectroscopy at the characteristic absorption bands of Pu(IV) and Pu(III) between 500 and 900 nm and 400 to 870 nm, respectively [15, 16].

Americium solution: A solution of ^{241}Am in 1 M $HClO_4$ was prepared after evaporating the initial 1 M HCl Am solution and fuming it with $HClO_4$. The purity of the ^{241}Am stock solution was checked by α spectroscopy.

pH measurements: The pH was measured by means of a pH meter (φ-310, Beckman, Germany) with a combined electrode (Beckman, Germany). The pH-meter was calibrated daily with certified commercial buffers at pH = 2, pH = 4, pH = 7, and pH = 9 (Merck, Darmstadt, Germany).

UV-vis spectroscopy: For absorption spectroscopy, a high-resolution UV-vis/NIR spectrometer Cary 50 (Varian, USA) was used. The samples were measured in 1 cm quartz cuvettes or polystyrene semimicrocuvettes.

Liquid scintillation counting (LSC): ^{239}Pu and ^{241}Am in solutions were determined by LSC using the scintillation cocktail Ultima Gold XR (Packard) and a home built scintillation counter.

γ spectroscopy: An HPGe spectrometer was used to determine the activity and purity of ^{234}Th, ^{237}Np, and ^{239}Np.

ß-delayed neutron activation analysis (DNAA): The total amount of sorbed plutonium on kaolinite was determined for part of the samples by applying DNAA [17]. The ^{239}Pu samples were irradiated with a thermal neutron flux of 1.7×10^{12} n/(s cm^2) for two minutes at the research reactor TRIGA Mainz and the ß-delayed neutrons were counted after a delay time of one minute with a helium-3 detector array using the $^{3}He(n,p)$ reaction.

Liquid-liquid extraction: Liquid-liquid extraction in combination with LSC was used to monitor the redox behavior of plutonium in aqueous solutions.

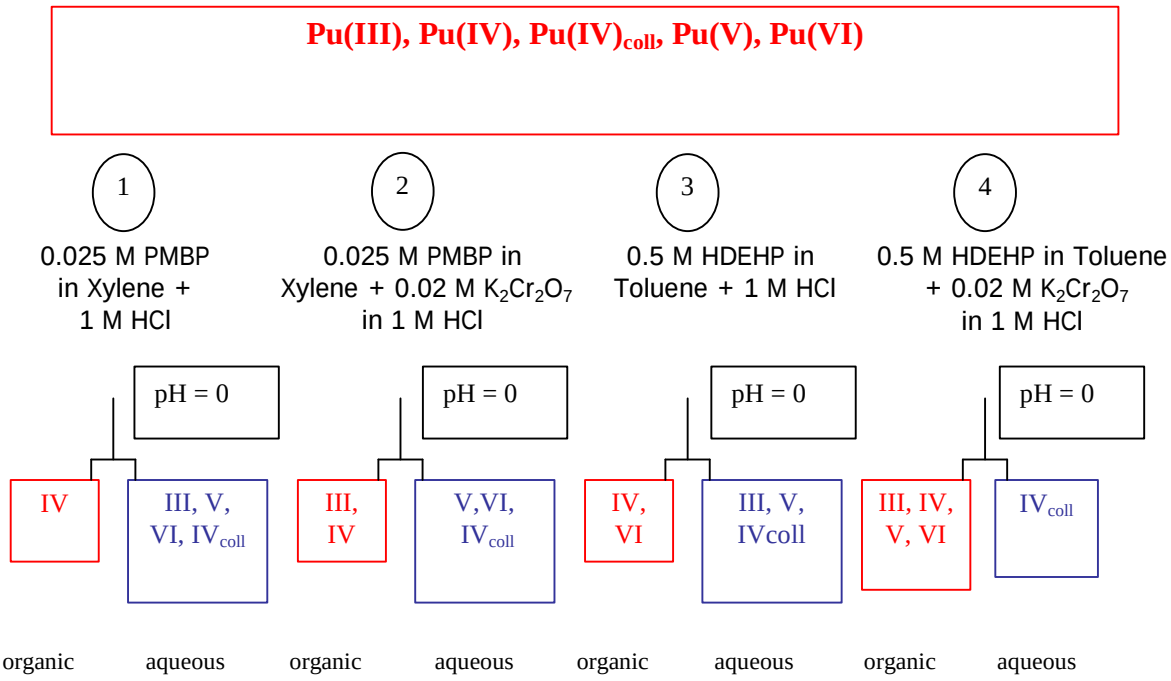

Pu^{3+} = (2) organic - Pu^{4+},

Pu^{3+} = (1) aqueous - (2) aqueous

Pu^{4+} = (1) organic

$Pu^{4+}_{colloids}$ = (4) aqueous

$Pu^{5+} = Pu_{total} - Pu^{6+} - Pu^{4+} - Pu^{4+}_{colloids} - Pu^{3+}$,

Pu^{6+} = (3) organic - Pu^{4+}

Figure 1: Liquid-liquid extraction procedures for the speciation of plutonium III, IV, V, and VI; $Pu(IV)_{coll}$ represents Pu^{4+} colloids [18].

Several extraction steps are needed for a complete characterization of the different oxidation states of a plutonium solution. We used as extracting agents a solution of 0.025 M 4-benzoyl-3-methyl-1-phenyl-2-pyrazolin-5-one (PMBP) (from Aldrich, 99% purity) dissolved in xylene and a solution of 0.5 M di(2-ethylhexyl) orthophosphoric acid (HDEHP) (Aldrich) dissolved in toluene.

The four extraction steps were carried out independently as indicated in Fig. 1. The extraction experiments were performed in less than 30 min in order to avoid redox reactions due to the acidic character of the solutions. For the extractions 400 µL of 1 M HCl and 400 µL 0.02 M $K_2Cr_2O_7$ dissolved in 1 M HCl were used for the steps 1 and 3, respectively 2 and 4. To each of these solutions, 200 µL of the samples to be analyzed were added. Then, 100 µL of the mixture were taken out and transferred in a vial containing 10 mL of LSC cocktail, and the activity was determined. These samples were used as references. Afterwards the solutions were mixed with the extraction agents. The solutions were centrifuged after mixing for about one minute at 2500 rpm and 200 µL from the organic and aqueous phases were transferred into vials and analyzed by LSC. The composition of the analyzed samples was determined as indicated in Fig. 1 bottom.

Capillary electrophoresis (CE): The CE system used is an improved version of the previously described home made system [19]. A high-voltage power supply (0 to ±30 kV) was developed and manufactured in our electronic workshop. Standard LSC vials (20 mL), or for small sample volumes 300 µL PE vials were used for the buffer and sample solutions. Hydrodynamic injection was applied to introduce the solution into the capillary with a pressure between 50 and 1000 mbar. For the sample injection, 50 to 100 mbar were used for 5–10 s. A fused-silica capillary with an inner diameter of 50 µm (PolyMicro Technologies, Phoenix, AZ) and 60 to 70 cm length was deployed. Before use, the capillary was purged for 5 min at 1 bar with 0.1 M HCl, 0.1 M NaOH, and for 10 min at 1 bar with Milli-Q deionized water and the electrolyte solution (1 M acetic acid at pH ≈ 2.4).

ICP-MS: The ICP-MS measurements were performed with a quadrupole HP 4500 (Agilent) or the recently purchased Agilent 7500ce.

Resonance ionization mass spectrometry (RIMS): The RIMS set-up consists of a high repetition rate solid-state laser system and a reflectron time-of-flight (TOF) mass spectrometer [20]. The plutonium atoms are excited into a Rydberg state by a three-step laser resonant excitation with λ_1 = 420.76 nm, λ_2 = 847.28 nm, and λ_3 = 767.53 nm and are subsequently field ionized. Three titanium-sapphire lasers pumped by a pulsed Nd:YAG laser (Clark-MXR ORC-1000) with a repetition rate of 6.6 kHz are used. In order to excite and ionize plutonium (ionization potential IP = 6.02 eV) in a three-step three-color excitation scheme, the frequency of the titanium-sapphire laser light for the first excitation step is doubled in a special crystal (BBO). To obtain a good spatial overlap with the atomic beam, the three laser beams are guided by a quartz fiber to the interaction zone. The line-width of the titanium-sapphire lasers is about 3 GHz, the isotope shifts for the isotopes ^{238}Pu to ^{244}Pu are between 5 to 20 GHz for the first and the second step, therefore, the wavelengths of the lasers 1 and 2 have to be adjusted for each isotope in order to attain the resonance conditions. The ions are mass-selectively separated in a reflectron TOF mass spectrometer and counted by channel plates. The TOF mass resolution of $m/\Delta m \approx 600$ is sufficient to discriminate the different iso-

topes of plutonium. The overall efficiency of the RIMS apparatus is $\geq 10^{-5}$, resulting in a detection limit of ~10^6 atoms of plutonium.

X-ray absorption fine structure (XAFS) spectroscopy: For XAFS measurements at room temperature, the sorption samples were centrifuged and loaded as wet pastes into Perspex sample holders with Kapton windows. For low temperature measurements at 13 K or 28 K, the solid residues were loaded after drying into polyethylene sample holders. Uranium and Np L_{III}-edge absorption spectra were collected in fluorescence mode at the Rossendorf beamline ROBL [21] at ESRF using a 13-element Ge solid-state detector. Since kaolinite KGa-1b contains traces of Zr, several XAFS spectra were collected at the Np L_{II} edge instead of the L_{III} edge. A Si(111) double-crystal monochromator (DCM) was used for tuning the energy of the incident X-ray beam. For recording the Np L_{III}-edge absorption spectra of the hematite samples, Cr foils were used to reduce the Fe Kα fluorescence background signal. Pu L_{III}-edge absorption spectra were measured in fluorescence mode using the 5-element Ge solid-state detector and Ge(422) DCM at the ANKA beamline of the Institute of Nuclear Waste Management (INE) [22].

Yttrium and zirconium foils were used for calibrating the X-ray energy. The raw L_{III}-edge data were analyzed using the programs AUTOBK [23] and EXAFSPAK [24]. Backscattering phase and amplitude functions required for data fitting were calculated with FEFF 8.20 [25, 26] using crystal structures of $(UO_2)_2SiO_4 \cdot 2H_2O$ [27], $NaNpO_2CO_3$ [28] and, $UFe^{III}O$ [29], respectively. For modeling possible interactions of Np or Pu with Si, Fe, etc., U was replaced in the crystal structures by Np or Pu. The shift in threshold energy, ΔE_0, was allowed to vary as a global parameter in the fits.

X-ray photoelectron spectroscopy (XPS): XPS spectra were measured using a UNI-SPEC ESCA System with a PHOIBOS 100 energy analyzer. Dry powders of humic acid sorbed on kaolinite were pressed into indium foils without further treatment. XPS spectra were excited by Mg Kα radiation (1253.6 eV). The analyzer pass energy was 50 eV. The vacuum during the measurements was $2 \cdot 10^{-8}$ mbar. The electrostatic charging of the sample surface was corrected by setting the C1s binding energy to 285.0 eV.

3 Development of speciation techniques

3.1 Speciation of plutonium by CE-RIMS

In order to improve the sensitivity of the speciation method for plutonium, off-line coupling of CE to RIMS has been successfully tested. Parallel to the on-line coupling of CE to ICP-MS, samples for RIMS measurements were collected off-line and RIMS filaments [30, 31] were prepared by electrodeposition. In comparison with CE-ICP-MS, the detection limit for Pu could be improved by at least two orders of magnitude with CE-RIMS. The principle of coupling CE to RIMS is based on collecting fractions of the different oxidation states of plutonium eluted from the capillary at different, known retention times [19, 32]. The fractions of the different oxidation states are collected in separate vials and subsequently analyzed by RIMS. A

schematic diagram for the off-line coupling of CE to RIMS is illustrated in Fig. 2 top. The separation conditions for the different oxidation states of plutonium have been determined by CE-ICP-MS (Fig. 2, bottom, upper part).

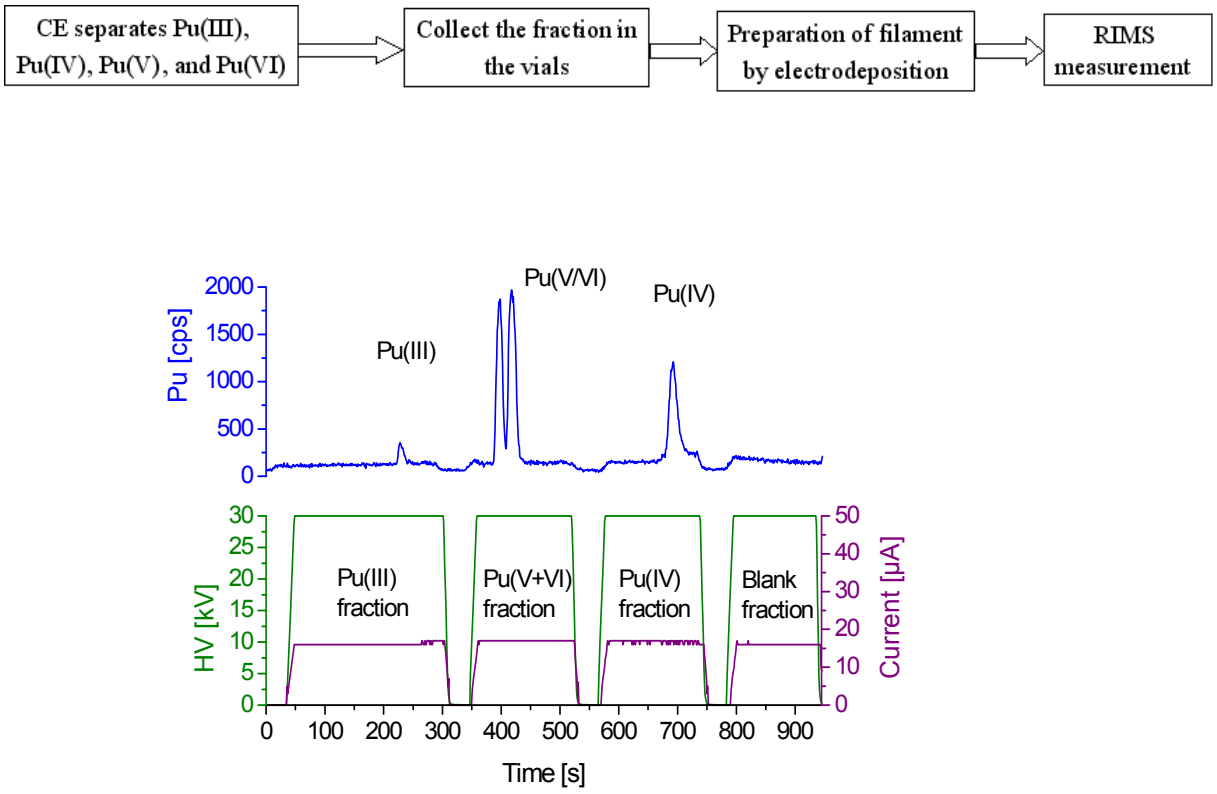

Figure 2: Schematic diagram for the off-line coupling of CE to RIMS (top); Separation of the plutonium oxidation states with short high-voltage breaks for the collection of the fractions of the oxidation states Pu(III), Pu(V+VI), and Pu(IV) in different vials and detection by RIMS (bottom).

For the RIMS measurements, the high voltage must be switched off for several seconds in order to change the collecting vial at the end of the capillary. Pu(VI) and Pu(V) fractions are collected in one vial due to their similar migration times. Fig. 2 (bottom, lower part) represents the separation of the plutonium oxidation states with short high-voltage breaks.

Before measuring the separated fractions by RIMS, the fractions have been analyzed by α spectroscopy to verify the method. The coupling of CE to RIMS was tested by determining the speciation of a mixture of Pu(IV), Pu(V), and Pu(VI) by CE-ICP-MS at a plutonium concentration of approximately 4×10^{-6} mol/L and by comparing it to the results obtained by RIMS for the same mixture with a concentration of ca. 2.5×10^{-7} mol/L Pu after separation

by CE. Tab. 1 gives the results obtained by the on-line coupling CE-ICP-MS and the CE off-line coupling to RIMS.

The detection limit of CE-RIMS is at least two orders of magnitude lower compared to the one with CE-ICP-MS. Thus, speciation of the oxidation states of plutonium at concentrations of 10^{-9} to 10^{-11} mol/L appears to be possible. The absolute detection limit of the CE-RIMS remains to be determined.

Table 1: Comparison between the determinations of the oxidation states of plutonium by CE-ICP-MS (ca. 4×10^{-6} mol/L plutonium) and by RIMS (ca. 2.5×10^{-7} mol/L) after separation by CE in different fractions (CE-RIMS off-line).

Coupling method	Pu(V+VI) [%]	Pu(IV) [%]
CE-ICP-MS (on-line)	19.2(2.0)	80.8(3.0)
CE-RIMS (off-line)	15.2(5.0)	84.8(5.0)

3.2 Development of CE-DAD-ICP-MS coupling

The ultrafiltration technique cannot be used for the investigation of the complexation of plutonium with fulvic acid, because of the reduced size of the organic molecules. Hence, the on-line coupling of CE with a diode array detector (DAD) and ICP-MS has been explored as an alternative method. Based on the experience achieved in the routine work with the CE-ICP-MS coupling, a Knauer Wellchrom K2800 DAD has been added as an additional detector.

By use of CE, the positively charged species (metal ions) are separated from the negatively charged ones (humic substances, humate-metal ions complexes) and possible neutral species (humate-metal complexes resulting from charge neutralization reactions). All the species are obtained at the end of the capillary, where the metal-containing species are measured by ICP-MS, as a result of a laminar flow of the electrolyte in the capillary, obtained by applying a slight pressure at the entrance of the capillary. The DAD enables the detection of humic substances in the CE capillary based on their spectral properties. In this way, it is possible to detect and quantify the metal species as well as the humic substances enabling the study of the complex formation between the two species, as schematically illustrated in Fig. 3.

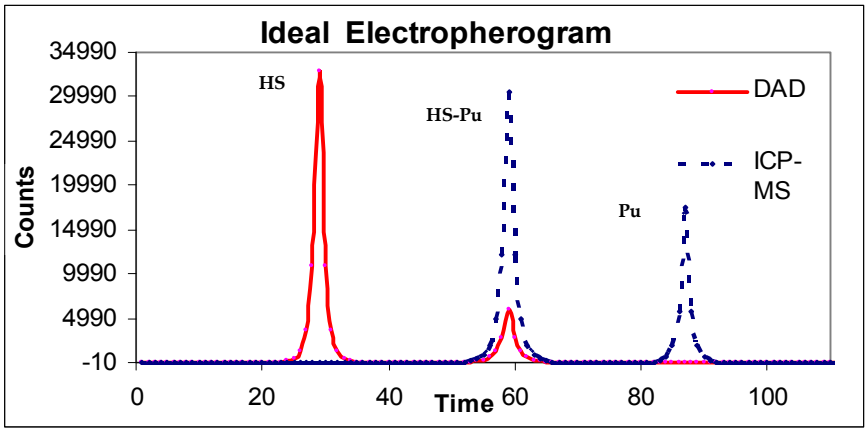

Figure 3: Schematic, hypothetic description of the analysis performed with CE-DAD-ICP-MS for determining the ratio humic substances/humate-plutonium complexes/free plutonium ions.

The detection of the humic substances is rather delicate as the UV-vis light path through the capillary is relatively short (50–75 µm). Using a series of adjustments at the DAD detection cell, it is possible to detect Aldrich humic acid with a concentration as low as 20 mg/L. The detection limit of the ICP-MS for the plutonium species is as low as 20 ppb. As a first step, in order to verify the applicability of the method, the timely synchronization of the two detectors was investigated using a highly concentrated solution of iodine and iodide, as they can be easily detected by both detectors. Two separate peaks were obtained with the DAD, as shown in Fig. 4. The separation was monitored at the same time by ICP-MS set on mass 127. Two different peaks corresponding to iodine carrying species were obtained with this method, too. The electropherogram obtained with the DAD using the optimal wavelength compared to the one obtained with the ICP-MS in order to evaluate their time correlation are shown in Fig. 4.

It was proven that there is a time correlation between the two detectors. Further, the complexation of lanthanides with Aldrich humic acid was investigated. The lanthanides were chosen as models for trivalent actinides. Many authors have already investigated the complexation of lanthanides with humic substances. In order to facilitate the identification of the registered signals on the two detectors, a solution containing iodine marked Aldrich humic acid ([AHA] = 250 mg/L) and holmium ([Ho] = 75 µg/L) was injected, separated by CE, and analyzed. The separation conditions are summarized in Tab. 2. The data are shown in Fig. 5.

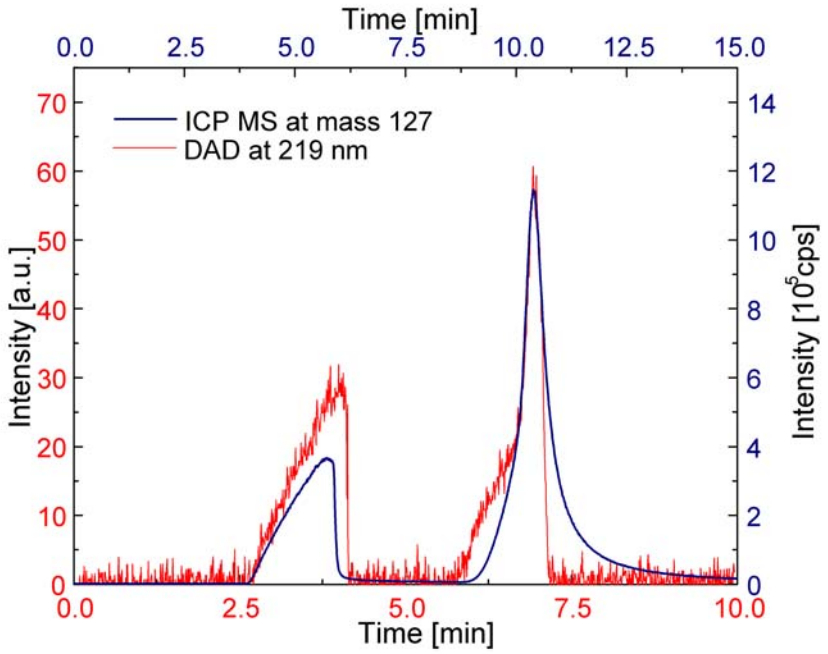

Figure 4: Equivalence of the DAD with ICP-MS. The peaks are obtained by monitoring simultaneously the separation of the iodine/iodide solution with the DAD set on wavelength 219 nm and ICP-MS on mass 127. The tailing of the peaks is caused by the high concentration of the solution.

Table 2: Conditions used in the investigation of the complexation of holmium with iodine marked Aldrich humic acid.

Mode	Anionic
Voltage	-25 kV
Pressure	250 mbar
Electrolyte	1 M acetic acid
Capillary	Fused-silica
Length	80 cm
Diameter	50 µm
DAD rating	2 Hz full spectra (180–1024 nm)

The overlapping of the peaks corresponding for the iodine species, humic substances, and holmium indicated clearly the presence of the metal-humate complex in the particular region (marked in brown in Fig. 5). The electro osmotic flow in the capillary was identified by use of DAD and is marked in red in Fig. 5. The relatively long tailing of the signal observed with the ICP-MS on the mass of holmium was attributed to the holmium metal ions that are dissoci-

ated from the complex during the separation by the high voltage used in the CE. Maybe this is the result of the formation of the so called “weak binding sites complexes”, which in comparison with the “strong binding sites complexes” are easier to dissociate. The formation of weak binding sites complexes was discussed by other authors too [33]. The identification of the correct position for the integration times of the peak corresponding to the free metal ion in solution is thus a rather delicate procedure.

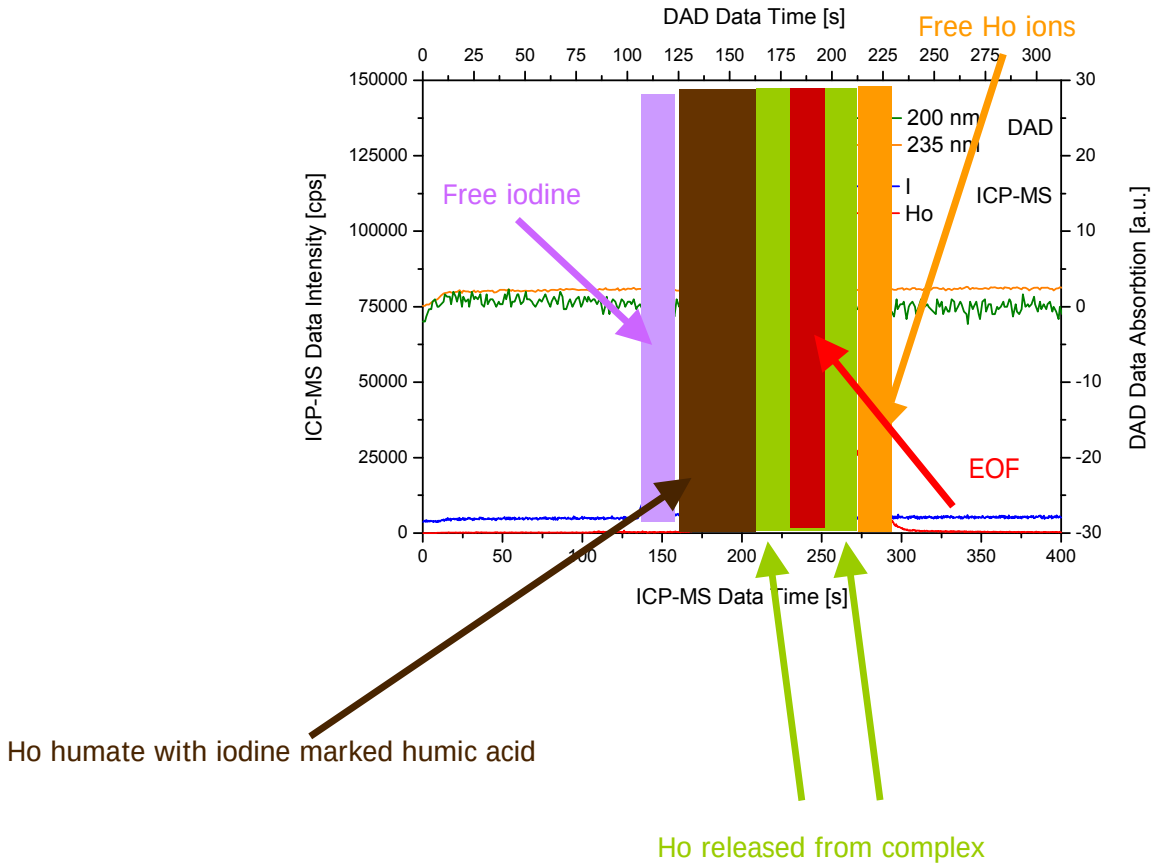

Figure 5: Electropherograms obtained for a solution containing holmium and iodine-marked Aldrich humic acid.

The first peak obtained by ICP-MS set on the mass of the metal, is definitely delivered by the metal complexed with AHA, as confirmed by the simultaneous signals registered by ICP-MS on the mass of iodine (from the iodine-marked humic acid) and by DAD for the AHA; it was assumed that the tailing of the first peak is generated by the metal ions which were dissociated from the weak binding sites during the CE separation (the minimum encountered in this region is attributed to a dilution effect caused by the concentration of the CE electrolyte induced by the EOF at this point); the last peak corresponds to the free, positively charged metal ion. It is noticeable that the peak corresponding to the metal ions dissociated from the weak binding sites interferes with the one attributed to the free metal ions, making it difficult to integrate precisely the two signals. Using the above described settings, a series of solutions containing a fixed concentration of Aldrich humic acid (100 mg/L) mixed with varying

concentrations of europium, samarium, and gadolinium, respectively, were prepared, mixed, and after a period of one week in which the vials containing the solutions were continuously agitated, the complex formation constant logß was determined by CE-DAD-ICP-MS. The concentration of the metal in solution varied between 0.0001–2 mg/L, which are rather high concentrations. Fig. 6 presents, as an example, the alteration of the form of the electropherogram obtained by ICP-MS while investigating the complexation of europium with Aldrich humic acid using varying Eu concentrations. It is observed that a small peak appears in front of the one corresponding to europium complexed with humic acid. This was not understood so far, but due to its diminutive size it was neglected in the calculation of logß. The peak of the complexed metal is increasing up to a certain point where the loading capacity of the humic acid is reached. Meanwhile, the peaks attributed to the species dissociated from the metal-humate complex during the separation and to the free metal, are rising with increasing concentration of europium. Based on the obtained data, the complex formation constants logß were calculated for all the three series after the model of Kim and Czerwinski [34].

The values obtained for logß were in all three cases too low in comparison with published data [34], varying between 4.98 and 5.28. This can be caused by the fact that the signal for the dissociated Eu from the weak binding sites tails into the peak of the free metal ion so that the free metal ion concentration is systematically overestimated. It is noticeable that the high concentrations of metal disturb the correct interpretation of the results due to formation of weak binding site complexes. It is anticipated that once the concentrations of metal as well as of the humic substances will decrease, the separation of the peaks will be much clearer, facilitating thus the proper assessment of the data. A new coupling technique of the CE to ICP-MS will be tested. The MiraMist coupling was used successfully by Ambard et al. [35] resulting in a decrease of the detection limit for plutonium by minimum three orders of magnitude.

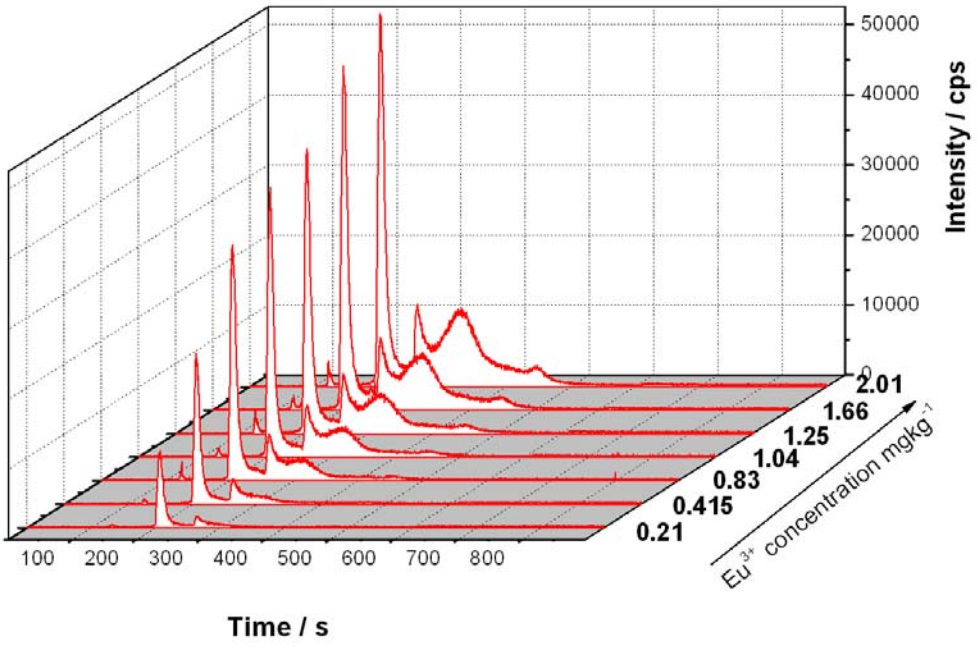

Figure 6: Electropherograms obtained by ICP-MS on the mass 153 during the investigation of the complexation of Eu with Aldrich humic acid. The humic acid concentration was constant at 100 mg/L.

4 Interaction of plutonium with humic substances

4.1 Experimental

Redox experiments

For the Pu(VI) reduction experiments, Pu(VI) solutions were brought in contact with Gorleben fulvic acid (FA) at different pH values. The concentration of the Pu(VI) solution in contact with FA (0.5 mg/L) was ~ 2.5×10^{-6} mol/L Pu at an ionic strength I ≈ 1 mol/L (1 M $HClO_4$) and pH values of 1, 2.5, 5, and 9. The reduction of the oxidation states of Pu in solution was measured by CE-ICP-MS and UV-vis spectroscopy at different time intervals. The experimental conditions of the reduction experiments with FA are summarized in Tab. 3.

For the redox kinetics experiments, a plutonium cocktail (~5% Pu(III), ~39% Pu(IV), ~22% Pu(V), and ~34% Pu(VI)) was brought into contact with FA at ionic strength I ≈ 1 mol/L and pH ≈ 1.

Table 3: Experimental conditions for the reduction experiments of Pu(VI) with Gohy-573 fulvic acid.

Parameter	Reduction of Pu(VI) with Gohy-573 FA (Expt. 1)	Reduction of a Pu mixture with Gohy-573 FA (Expt. 2)
Pu oxidation state	VI	III, IV, V, VI
pH	1, 2.5, 5, 9	1
Ionic strength	1 M $NaClO_4$	1 M $NaClO_4$
[Pu]	2.5×10^{-6} mol/L	6×10^{-5} mol/L
[FA]	0.5 mg/L	0–36 mg/L stepwise
Detection	CE-ICP-MS	CE-ICP-MS
Conditions	All experiments were performed in contact with air and light, under room temperature, and atmospheric pressure.	

Stabilization of Pu(III)

In order to obtain data on Pu(III), it had to be assured that the oxidation state remains unchanged under the conditions that would be used later on in the experiments. The stability of a solution of Pu(III) with a concentration ~8×10^{-5} M in 0.1 M $NaClO_4$ was investigated. In an attempt to stabilize Pu(III), a freshly electrolyzed solution of Pu(III) in 0.1 M $NaClO_4$ was contacted with GoHy-573 FA, hydroxy-ammonium hydrochloride, ß-alanin, and ascorbic acid at various concentrations. The speciation was performed by CE-ICP-MS, UV-vis spectroscopy, or by liquid-liquid extraction indicating that hydroxy-ammonium hydrochloride is best suited for the stabilization of Pu(III) up to pH = 6.

Table 4: Concentrations and conditions used in the experiments for determining the complexation constant of Pu(III) with Aldrich humic acid (AHA).

[Pu] mol/L	[AHA] mg/L	pH	Conditions
$1x10^{-6}$	0, 1, 2.5, 5, 7.5, 10, 15 20, 25, 40, 55	3, 4	air and argon
$1x10^{-7}$	0, 1, 2.5, 5, 7.5, 10, 15 20, 25, 40, 55	3, 4	air and argon
$1x10^{-8}$	0, 1, 2.5, 5, 7.5, 10, 15 20, 25, 40, 55	3	air

Complexation experiments

For the complexation experiments, Aldrich humic acid (HA) and Pu(III)/Pu(IV) were brought into contact at different pH values and the mixtures were shaken continuously. After equilibration times of one week, aliquots of the solutions were filtrated using ultrafiltration (1 k Dalton pore size), and the free Pu ion concentration was determined by LSC. The loading capacity (LC) was determined from plots of $[MHA(z)] / [HA(z)]_t$ vs. $[M^{z+}]_t / [HA(z)]_t$ for the different pH values as discussed in detail by Kim and Czerwinski [34]. The experimental conditions used for the investigation of the complexation of Pu(III) with Aldrich HA are shown in Tab. 4.

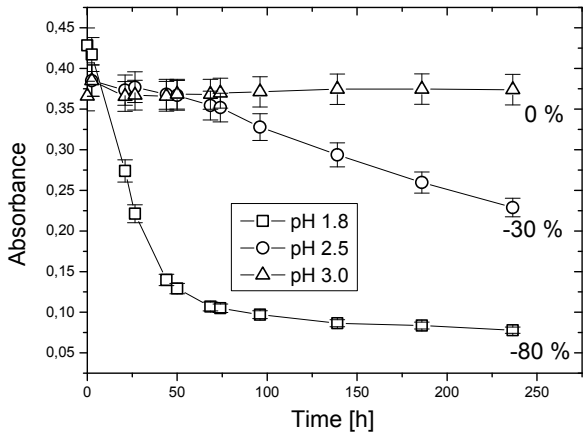

Figure 7: Decrease in the concentration of Aldrich humic acid (AHA) in solution at different pH-values (1.8, 2.5, and 3.0) as a function of time (values in percent define the decrease after 10 d) for a starting AHA solution of 25 mg/L.

Precipitation of Aldrich humic acid (AHA) as a function of pH

The influence of the pH value on the precipitation of AHA at pH 1.8, 2.5, and 3.0 was studied by UV-vis spectroscopy by measuring the change in concentration of AHA in solution. AHA was used at concentrations of 1, 10, and 25 mg/L. A precipitate of AHA at the bottom of the cuvette was easily observable at lower pH values.

A reduction of the AHA concentration in solution (original concentration 25 mg/L) by 80% at pH 1.8, 30% at pH 2.5 and almost 0% at pH 3.0 was found for the Aldrich humic acid after 240 h (Fig. 7).

Limitation of the ultrafiltration method for the determination of the complexation constants with humic substances

FA is soluble in all pH ranges whereas HA precipitates at pH < 3 as shown in Fig. 7. Therefore, FA is better suited for determining the complexation constants of metal ions at low pH values, where adsorption effects on filter materials are almost negligible.

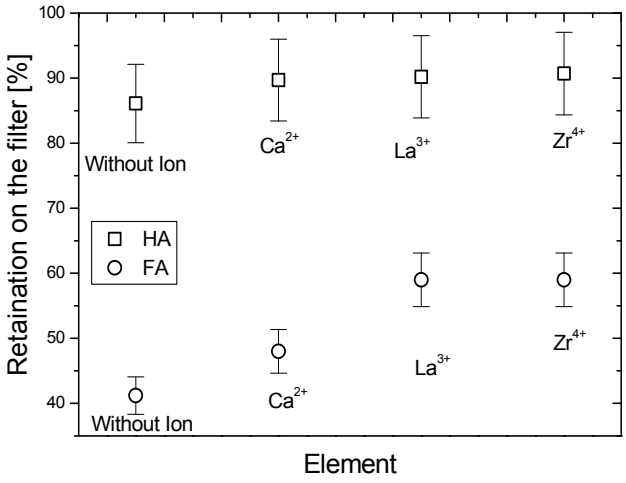

Figure 8: Percentage of humic (square dot) and fulvic acids (round dot) on the filter in the presence and absence of metal ions at pH 6, contact time of seven days, [Ca^{2+}, La^{3+}, Zr^{4+}] = 10^{-4} M and [FA, HA] = 20 mg/L.

To study the applicability of the ultrafiltration method for the determination of complextation constants of metal ions with HA and FA, different metal ions (Ca(II), La(III), Zr(IV)) have been chosen. FA and HA (20 and 50 mg/L) were brought into contact with the metal ions (Ca(II),

La(III), Zr(IV), 10^{-4} M) at pH 6 and the mixtures were shaken continuously. After a preselected time (168 h), aliquots of the solution were filtrated using ultrafiltration (1k Dalton pore size), and the concentration of the humic substances in the filtrate was determined by UV-vis spectroscopy. As can be seen in Fig. 8, 40 to 60% of FA passes through the filter depending on the complexed element.

In the case of HA, only 5 to 15% of HA pass through the filter. From this data it can be concluded that the ultrafiltration method is not suited for the determination of complexation constants with fulvic acid.

4.2 Reduction of plutonium in contact with fulvic acid

The reduction of Pu(VI) in contact with Gorleben FA has been investigated by on-line coupling CE-ICP-MS. Tab. 3 describes the experimental conditions and parameters for the redox experiments. The reduction rate of Pu(VI) is strongly influenced by the pH, ionic strength, concentration, and Eh of the solution. Fig. 9 shows the reduction of Pu(VI) by FA as a function of time. The reduction of Pu(VI) by FA shows a significant dependence on the pH value. The enhanced reduction of Pu(VI) by increasing the pH may be explained by the increased fraction of dissociated groups of FA. Therefore, the rate of reduction increases by increasing the pH [36]. In these redox experiments, Eh and temperature were not measured.

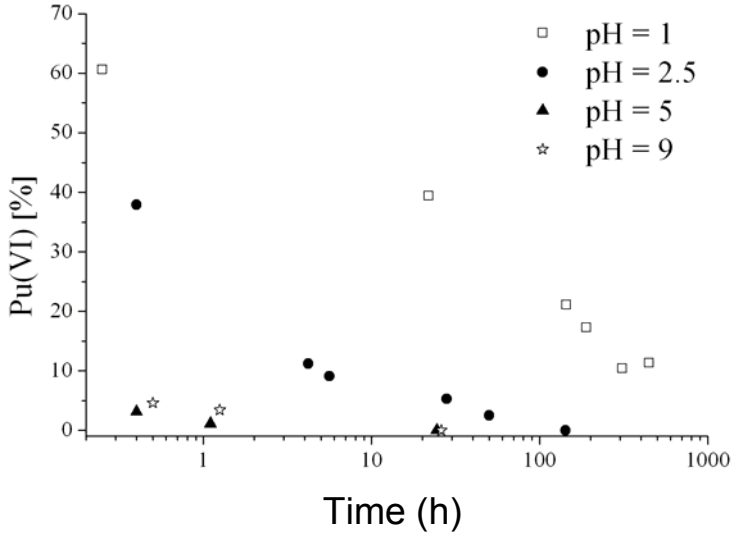

Figure 9: Reduction of Pu(VI) (2.5×10^{-6} M) in contact with Gorleben fulvic acid (Gohy-573, 0.5 mg/L) at ionic strength I ≈ 1 M $NaClO_4$ and different pH values as a function of time as determined by CE-ICP-MS (Tab. 3, Expt. 1).

The kinetics of the Pu(VI) reduction by FA is slower at acidic pH compared to neutral pH. At neutral pH, a complete reduction of Pu(VI) by FA within one day is observed. Consistently, a fast reduction of Pu(VI) by humic substances is reported by Choppin [37] and for humic-rich Gorleben groundwater by Marquardt et al. [38].

Redox kinetics of plutonium with Gorleben fulvic acid

For the investigation of the redox kinetics of the different oxidation states of Pu with Gorleben FA (pH about 1), the FA has been added stepwise. The composition of the different oxidation states was checked by CE-ICP-MS. Tab. 3 (Expt. 2) describes the experimental conditions.

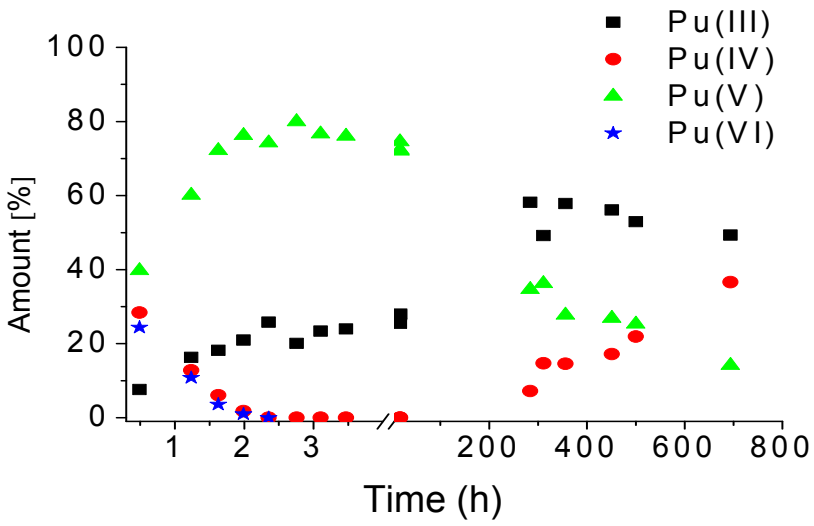

Figure 10: Interaction of a plutonium cocktail (6×10^{-5} M) with Gorleben fulvic acid (Gohy-573, 36 mg/L) at ionic strength I ≈ 1 M $NaClO_4$ and pH 1 as a function of time determined by CE-ICP-MS (Tab. 3, Expt. 2)

Fig. 10 presents the redox kinetics of a stable mixture of all four naturally occurring plutonium oxidation states (~5% Pu(III), ~39% Pu(IV), ~22% Pu(V), and ~34% Pu(VI)) brought stepwise in contact with Gorleben FA for a contact time up to one month. Within approx. two hours, Pu(IV) and Pu(VI) are disappeared and Pu(V) and Pu(III) are formed. The increase in the Pu(V) concentration is the result of both the reduction of Pu(VI) and the oxidation of Pu(IV) which is associated with the fact that the Gorleben FA was added stepwise under aerobic conditions. Only after the complete amount of Gorleben FA (36 mg/L) has been added and no additional oxygen was introduced into the solution, the reducing power of the FA appar-

ently becomes dominant, and the intermediately produced Pu(V) is reduced to Pu(IV), see Fig. 10, so that the majority of the plutonium is finally in the oxidation states III and IV. This is an important result as it indicates that the speciation of plutonium in the presence of humic substances needs not to be studied with Pu(VI) and Pu(V) because they are unstable under these conditions.

The experiments have shown that Pu(VI) is reduced by FA and HA to Pu(IV) and Pu(III) within a couple of weeks. Similar reduction behavior was found for humic rich Gorleben ground water [39]. The reduction of Pu(VI) with FA occurs faster with increasing pH values, and this was also found for HA [40]. The studies have shown that the reduction of Pu(VI) to Pu(V) is fast compared to the reduction of Pu(V) to Pu(IV) and Pu(III). The slow reduction of tetravalent plutonium to Pu(III) is due to the hydrolysis ($Pu(IV)(OH)_x^{(4-x)+}$), in particular at neutral pH ($Pu(OH)_4$), and the formation of eigen-colloids leading to a stabilization of Pu(IV) and thus decreasing the speed of reduction to the trivalent plutonium [32]. A further reduction of the pentavalent to tetravalent and trivalent plutonium occurs mainly at acidic pH, as discussed here for Gorleben FA and reported by several authors for HA [32, 36-39, 41].

Redox behavior of Pu(III)

A solution of freshly electrolyzed Pu(III) was analyzed with the focus on the redox behavior of Pu(III). It was found that the solution contained > 95% Pu(III) even after more than one month from the moment of preparation. This experiment was conducted at pH 0.1, under aerobic conditions, at room temperature. However, a pH 0.1 (1 M $HClO_4$) is not relevant for natural conditions. Therefore, a solution of freshly prepared Pu(III) with a concentration of 7.6 x 10^{-6} M in 0.1 M $NaClO_4$ at pH 5.5 was investigated by CE-ICP-MS over a period of about two weeks with respect to the redox behavior of plutonium. The experiment was conducted in an inert gas box (Ar, ~1–3 ppm O_2) at room temperature. It was observed that Pu(III) is rapidly oxidized.

In order to stabilize a solution of Pu(III), it was contacted with the following reagents. GoHy-573 FA, hydroxy-ammonium hydrochloride, ß-alanin, and ascorbic acid at various concentrations. It was found that the best suited reducing agent was NH_2OHHCl. A concentration of [NH_2OHHCl] = 0.025 M was necessary in order to achieve reliable results. However, it was only possible to maintain Pu(III) in the reduced form up to pH 6. All the following experiments with Pu(III) were conducted in the presence of 0.025 M NH_2OHHCl.

4.3 Complexation of plutonium with humic substances

The time dependence of the complexation of plutonium with HA has been investigated and the complexation constants of Pu(IV) at various pH values have been determined. Different concentrations of Pu(IV) (6.6 × 10^{-6} to 6.6 × 10^{-8} M), HA (0.01 to 25 mg/L) have been used. The experiments show that a period of about one week is necessary to reach equilibrium for the complexation of Pu(IV) with HA. The stability constants ($log ß_{LC}$) [34] were determined by means of ultrafiltration. For the LC [34], values of 3.3% at pH 1.8, 4.5% at pH 2.5, (see Fig.

11) and 9.2% at pH 3 for Pu(IV) were obtained. It has been observed that Pu(IV) exists as $[Pu(OH)_2]^{2+}$ at pH values 0.3 to 2.0 in aqueous solution [42], so Z = 2 was considered for the LC calculation [34]. The log$ß_{LC}$ values calculated are 6.5–7.9 at pH 1.8; 6.7-8.3 at pH 2.5; 6.4–8.4 at pH 3. The scattering of the log$ß_{LC}$ values may be due to co-precipitation effects with humic acid at the low pH values and colloid formation of Pu(IV).

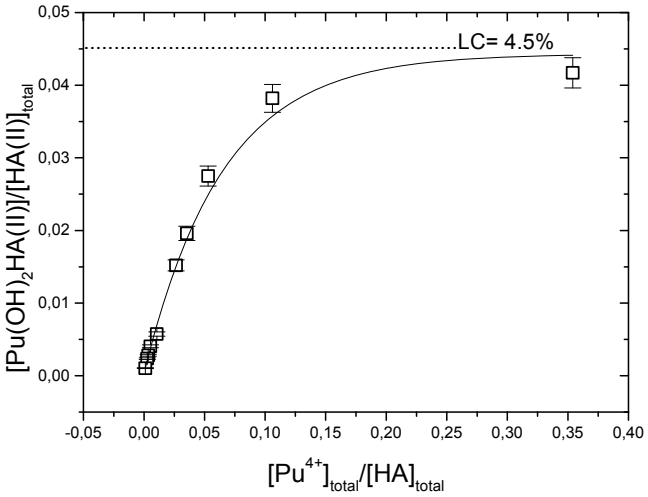

Figure 11: Determination of the loading capacity (LC) for the complexation of Pu(IV) with humic acid at pH 2.5, [Pu(IV)] = 6.6 $\times$ 10^{-7} M, [HA] = 0–25 mg/L, and ionic strength 0.1 M $NaClO_4$.

The complexation of the trivalent plutonium with Aldrich HA was investigated in a similar way. The kinetics of the complexation of Pu(III) with Aldrich HA was investigated in the presence of 0.025 M NH_2OHHCl under atmospheric and inert-gas conditions. Several solutions of freshly electrolyzed Pu(III) ([^{239}Pu(III)] = 1x10^{-6} M), were mixed with AHA at pH 3, 3.5, and 4. The concentrations of HA were also varied, ([AHA] = 0, 2.5, 10, 25 mg/L). The ultrafiltration technique was employed for these experiments. By simply observing the changes of the ratio free plutonium/complexed plutonium, it was determined that the complexation is fast, especially at higher concentrations of AHA. The complexation was completed in maximum one day as shown in Fig. 12 for pH 3.

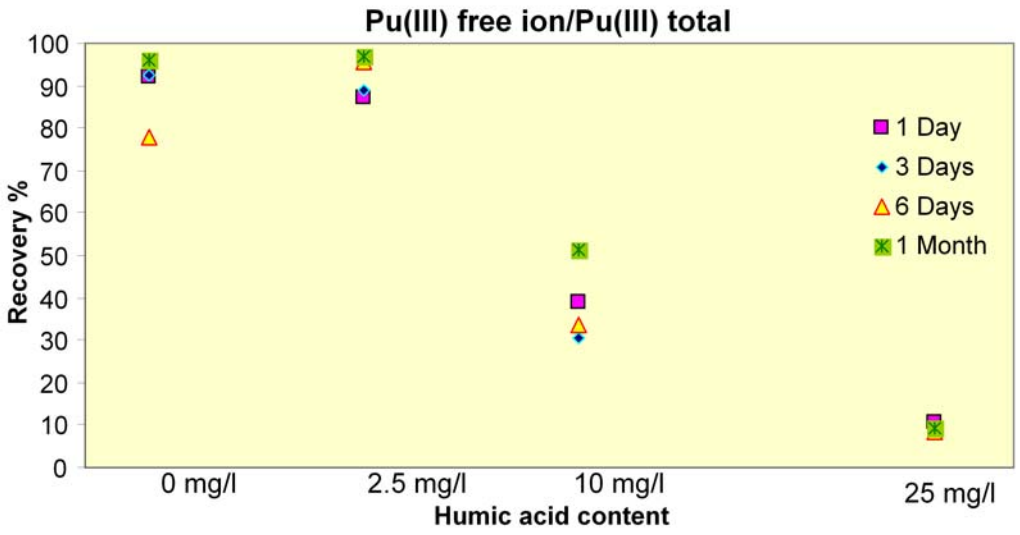

Figure 12: Time dependence of the complexation of Pu(III) with Aldrich humic acid at pH 3 in the presence of 0.025 M NH_2OHHCl under atmospheric conditions.

For the calculation of logß values, additional experiments were conducted. The experimental conditions are summarized in Tab. 4. For the PEC of the AHA, the value given by Kim and Czerwinski [34] (PEC_{AHA} = 5.43 ± 0.2 meq/g) was used yielding the complexation constants presented in Tab. 5.

Table 5: Complexation constants of Pu(III) with Aldrich humic acid.

pH	.C	logß (L/mol)
3	0.045 ± 0.005	6.21–6.86
4	0.11 ± 0.005	6.57–6.87

Following the same procedure, the complexation of Am(III) with AHA was investigated in parallel. The aim was to compare the data obtained for the experiments performed in our laboratory with the literature. No literature data were found for the complexation of Pu(III) with HA but on the other hand there is a large amount of studies on other trivalent actinides [34, 43]. A solution of ^{241}Am was contacted with HA as described in the experiments with plutonium. The advantage of working with $^{241}Am(III)$ is that it is always in the trivalent state in solution and that it is possible to work with lower amounts of metal ion due to the relatively short half-life (432.2 a). A loading capacity of LC ≈ 0.038 was used resulting in logß = 6.1–6.7.

5 Interaction of plutonium, neptunium, uranium, and humic substances with kaolinite

5.1 Experimental

Batch experiments with Np(V) and U(VI)

The sorption of Np(V) and U(VI) on kaolinite KGa-1b was investigated in batch experiments at room temperature and defined ionic strengths, typically 0.1 and 0.01 M $NaClO_4$, over a wide pH range under aerobic and anaerobic conditions. 50 mL polypropylene centrifuge tubes were used for the batch experiments. The total volume of the aqueous phase was 40 mL. For kaolinite the solid/solution ratio was 4 g/L. Experiments under anaerobic condition were carried out in a glove box under Ar atmosphere. All solutions used in the glove box were prepared with CO_2-free Milli-Q water (18 MΩ).

A suspension of kaolinite was prepared at the desired ionic strength and shaken for 72 h in an end-over-end rotator. After that the pH was adjusted to the appropriated pH using $HClO_4$ or NaOH. In air-equilibrated samples with a pH greater than 7.0, certain amounts of $NaHCO_3/Na_2CO_3$, calculated with the geochemical equilibrium speciation software Visual MINTEQ V. 2.5 [44], were added to accelerate equilibration with atmospheric CO_2. The pH adjustment was repeated for several days until the pH value was stable. Next, aliquots of the stock solution of the corresponding actinide element were added to each sample. The pH was readjusted to the desired value immediately after the addition of the actinide. Then, the samples were shaken for 60 h. During this time, the pH of the solutions was checked for two times more and, if necessary, was adjusted. After a contact time of 60 hours, the solid and liquid phases were separated by centrifugation at 4025 g for 7 min in a centrifuge SIGMA 3K30. The actinide concentration in the supernatant was determined by ICP-MS, γ spectroscopy, DNAA, or LSC, respectively, as described in Section 2. The percentage of actinide sorbed was calculated according to $\Gamma = \left(1 - {c_f}/{c_0}\right) \times 100\%$, where c_0 and c_f are the total actinide ion concentration in the clay suspension and its concentration in the supernatant after centrifugation, respectively. The effect of sorption on the wall of the centrifuge tubes was also determined and taken into account in the calculation of Γ.

Kinetic study of the sorption of Np(V) on kaolinite

Kinetics experiments were performed to determine the time required to establish equilibrium conditions. The time dependence of Np(V) sorption on kaolinite was examined at pH 9.0 in 0.1 M $NaClO_4$ solution in the presence of ambient CO_2 at 25 °C. 160 mg kaolinite were suspended in 40 mL 0.1 M $NaClO_4$ solution. Calculated amounts of $NaHCO_3/Na_2CO_3$ were added to accelerate equilibration with atmospheric CO_2. The pH was adjusted to 9.0 using

0.1 M NaOH solution. Aliquots of the Np(V) stock solutions were added to give a total concentration of 7 pM or 8 µM Np(V). Two control solutions containing no kaolinite were measured to determine the Np content in the 40 mL 0.1 M $NaClO_4$ solution. During a period of time between 1 to 6000 min, the suspensions were centrifuged at 4025 g for 7 min and 1 mL of the supernatant was taken for Np analysis. To study the sorption of 8 µM total Np concentration during the first 15 min, seven aliquots of 1 mL were taken from clay suspension after different time intervals and filtered with 0.2 µm pore size mini syringe membrane filter. The ^{237}Np concentration in the filtrates was measured by γ spectroscopy.

To study the kinetics of the desorption process, the kaolinite batch was re-suspended in 40 mL fresh 0.1 M $NaClO_4$ solution at pH 9.0. The percentage of Np desorbed from kaolinite was measured as a function of time.

Sorption isotherms

The isotherm of Np(V) sorption on kaolinite was determined at pH 9.0 in ambient air. After preconditioning and pH adjustment as described above, aliquots of Np(V) stock solutions were added to obtain the following total Np concentrations in the kaolinite suspensions: 4.8×10^{-12}, 5.7×10^{-12}, 1.5×10^{-11}, 1×10^{-9}, 1×10^{-7}, 1×10^{-6}, 1×10^{-5}, 2.5×10^{-5}, and 1×10^{-4} M.

At low Np concentrations, only ^{239}Np was used. At concentrations of 1 nM and higher, ^{237}Np was added. Immediately after the addition of Np, the pH was readjusted to 9.0. The pH was checked after 60 h and, if necessary, readjusted. The samples were shaken for about 60 h. Then, the final pH was measured, and the aqueous and solid phases were separated by centrifugation at 4025 g for 7 min. Subsequently, the supernatant was analyzed by γ spectroscopy. The isotherm for the sorption of 8 µM Np(V) at pH 9.0 in ambient air on varying amounts of kaolinite ranging from 0.5 to 25.0 g/L was determined in the same way as described in this paragraph.

Batch experiments with Pu(III) and Pu(IV)

The experimental conditions for the sorption of Pu(III), Pu(IV), Am(III), and Th(IV) are summarized in Tab. 6. The pH of the solutions was controlled regularly. The solid and liquid phases were separated by centrifugation (2500 rpm for 1 h).

The sorbed amount of Pu (air-dried kaolinite, solid phase) was also measured for some samples by DNAA. Using the LSC data for the liquid phase and the DNAA data for the solid phase, the amount of free and sorbed plutonium could be determined. From both measurements, the total amount of plutonium was controlled thus showing consistency. For all sorption experiments, < 10 % sorption on the centrifuge tube walls depending on pH values was found and a mathematical correction was applied.

Table 6: Experimental parameters and conditions for the sorption studies of Pu(III), Pu(IV), Am(III), and Th(IV) on kaolinite.

Parameter	Conditions
Kaolinite, [KGa-1b]	4 g/L
[^{239}Pu(III)]	1×10^{-6}–1×10^{-8} M
[^{241}Am(III)]	8×10^{-9} M
[^{239}Pu(IV)]	3.5×10^{-7}–6.9×10^{-9} M
[^{234}Th(IV)]	6.6×10^{-13} M
Ionic strength I	0.1 M $NaClO_4$
pH	1–11
Preconditioning time	48–64 h
Contact time of kaolinite with plutonium	48–120 h
p_{CO2}	$10^{-3.5}$ atm
Phase separation (centrifugation)	1 h (~ 2500 rpm)
Detection	LSC, DNAA, γ spectroscopy
Anaerobic conditions	~100% argon , < 4 ppm O_2

Desorption experiments

After performing the sorption studies, the supernatants were removed and fresh 0.1 M $NaClO_4$ was added to the solid phase at the desired pH value. The newly formed suspension was shaken continuously for five days, the same time that was applied for the sorption studies of Pu on kaolinite. Finally, the samples were centrifuged (2500 rpm for 1 h) and the plutonium concentration in the supernatant was determined by LSC.

5.2 Sorption of Pu(III) and Pu(IV) on kaolinite

Effect of contact time on the sorption of Pu(IV) on kaolinite

The sorption experiments were performed with different contact times (64 to 120 h) at pH 1–11. No significant time dependence was observed at all pH values. For the sorption experiments described in the following, 120 h have been chosen as contact time.

Effect of pH on the sorption of Pu(IV) on kaolinite

The sorption of tetravalent plutonium on kaolinite was investigated as a function of pH and the obtained results are shown in Fig. 13. A pH range of 0–11 was studied with Pu(IV) concentrations of 3.56×10^{-7}–6.91×10^{-9} M and a solid phase concentration of 4 g/L with ionic strength I = 0.1 M ($NaClO_4$). As can be seen from Fig. 13, the sorption behavior of plutonium on kaolinite is almost constant for varying concentrations of plutonium. The sorption of Pu(IV) in contact with kaolinite is strongly influenced by the pH. The sorption edge can be observed at pH ≈ 1.

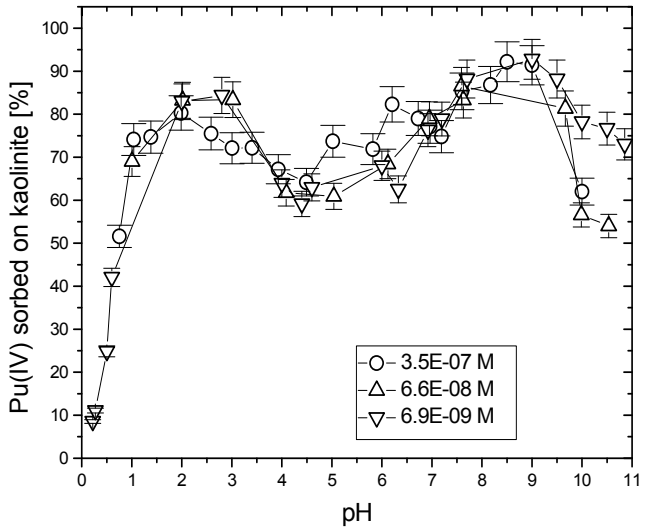

Figure 13: Sorption of tetravalent plutonium ions on kaolinite (4.0 g/L) as a function of pH at I = 0.1 M ($NaClO_4$) and 25 °C, after 120 h equilibration time with $p_{CO2} = 10^{-3.5}$ atm using varying plutonium concentrations.

The sorption increases with increasing pH up to 85 % at pH 2 and then decreases down to 55 % at pH 4. In order to shed light on the sorption behavior of Pu(IV) at pH 4–6, the oxidation state of the remaining Pu in the liquid phase after sorption on kaolinite was determined by liquid-liquid extraction [18, 45]. It has been found that at pH ≈ 4, Pu(V) is the dominant species in solution. It seems that the initially added Pu(IV) is partially oxidized in the liquid phase to Pu(V) in contact with kaolinite at pH values 4–6 under aerobic and anaerobic conditions, which might be an explanation for the lower sorption in this pH range. At pH > 8.5, the negatively charged plutonium carbonate species are predominant in the presence of CO_2, thus leading to a decrease of sorption of plutonium on the negatively charged kaolinite surface at that pH. In the absence of CO_2 at pH > 8.5, a stronger sorption of Pu(IV) on kaolinite has been found compared to the sorption in the presence of CO_2.

Desorption of Pu(IV) from kaolinite

Desorption experiments were also carried out at different pH values under the same experimental conditions used in the sorption experiments applying a fresh $NaClO_4$ solution of I = 0.1 M and buffered at the appropriate pH value. A desorption of 1–10% plutonium from kaolinite occurs depending on the pH. This indicates that the plutonium ions are bound strongly on kaolinite (chemisorption rather than physisorption) and that the sorption is only partially reversible.

Comparison of the sorption behavior of Pu(IV) and Th(IV)

For the tetravalent actinides Th(IV) and Pu(IV), a similar sorption behavior was found as a function of pH (Fig. 14). The sorption edges of Pu(IV) and Th(IV) for kaolinite are both at pH ≈ 1. It is supposed that at pH > 8.5 tetravalent Pu carbonate species are responsible for the decrease in sorption whereas no significant decrease was found for Th(IV).

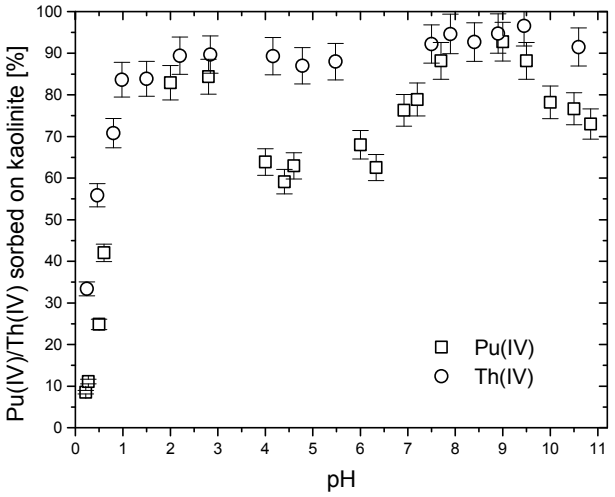

Figure 14: Comparison of the sorption of the tetravalent actinides Pu and Th on kaolinite as a function of pH; $p_{CO2} = 10^{-3.5}$ atm, [KGa-1b] = 4 g/L, contact time = 120 h.

At intermediate pH ranges (4–6), approx. 55–65% of the plutonium has been sorbed on the kaolinite, whereas in the case of thorium, 80–90% has been sorbed. As discussed earlier, at pH 4–6, the lower sorption for Pu(IV) may occur as a result of the (partial) oxidation of Pu(IV)

in the liquid phase to Pu(V). Pu(V) is expected to exhibit a lower sorption than Pu(IV). Thorium exists in aqueous solution only as Th(IV) and hence, no decrease in the sorption at pH 4–6 should occur.

Sorption of Pu(III) on kaolinite, time dependence

For the investigation of the sorption of Pu(III) on kaolinite the same procedure as the one described for Pu(IV) was applied. The experimental conditions are presented in Tab. 6. The influence of the contact time was investigated for the solutions with the highest concentration, in air as well as under inert atmosphere. There were found only slight changes between the sorption rates obtained from measurements performed 24 h and six days after the contact of kaolinite with plutonium (1–3% higher sorption after six days). Between the sorption rate after six days and one month there was no significant difference.

The influence of pH on the sorption of Pu(III) on kaolinite

The sorption of Pu(III) on kaolinite was investigated as a function of pH under atmospheric conditions and parallel under inert gas conditions in a glove box. Am(III) was used as a charge state analogue for comparison. The results obtained for the sorption of the two actinides under aerobic and anaerobic conditions are presented in Figs. 15 and 16. As can be seen there is no significant difference.

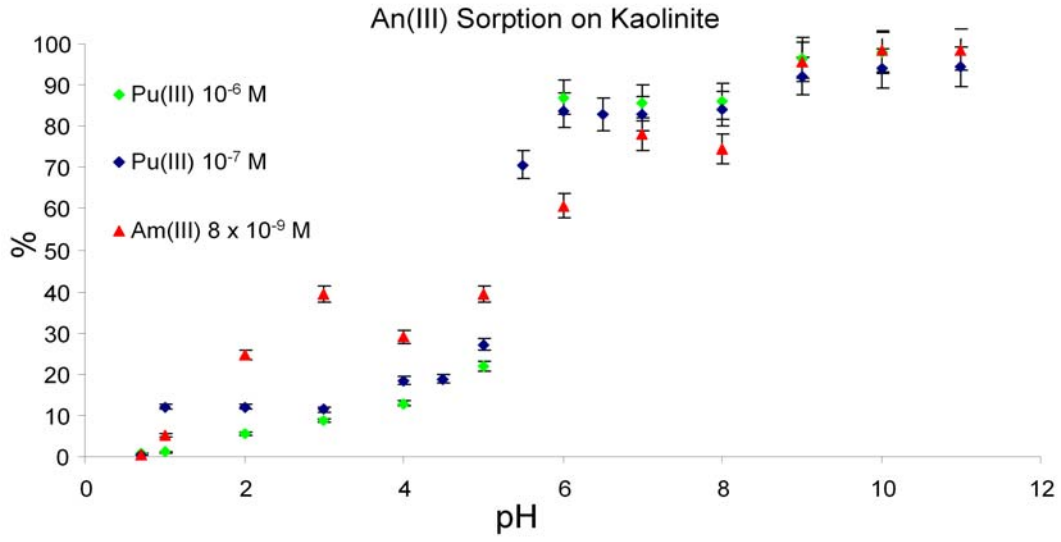

Figure 15: Sorption of Am(III) and Pu(III) on kaolinite under argon atmosphere as a function of pH (corrected for wall sorption).

The sorption edge at pH 5.5 is observed with low sorption below that value and high sorption above for both Am(III) and Pu(III). Also, it can be observed that the different concentrations of plutonium do not influence the sorption on kaolinite. Parallel to the sorption of plutonium on kaolinite, the walls of the vessels have also exhibited a tendency to sorb plutonium. Thus, not all plutonium that was not found in solution had to be necessarily sorbed on kaolinite. Therefore, the sorption on the walls of the vessels has been determined. For this, the vessels were emptied, and washed with Milli-Q water to remove the last traces of kaolinite. Then, they were dried and the plutonium was removed from the walls with 2 mL of a mixture of 0.36 M HCl/0.05 M HF. The activity of this solution was determined by LSC, and the amount of plutonium found on the walls was subtracted from the amount of metal considered to be sorbed on kaolinite. The wall sorption was also pH dependent. The oxidation state of plutonium desorbed from the walls of the vessels was determined by liquid-liquid extraction and it was found that > 95% was Pu(IV). It could not be detected whether the metal was sorbed from the beginning as Pu(IV). The fraction of Pu(IV) increased with the pH as NH_2OHHCl is only able to keep the solution safely reduced to Pu(III) up to pH ≈ 6.

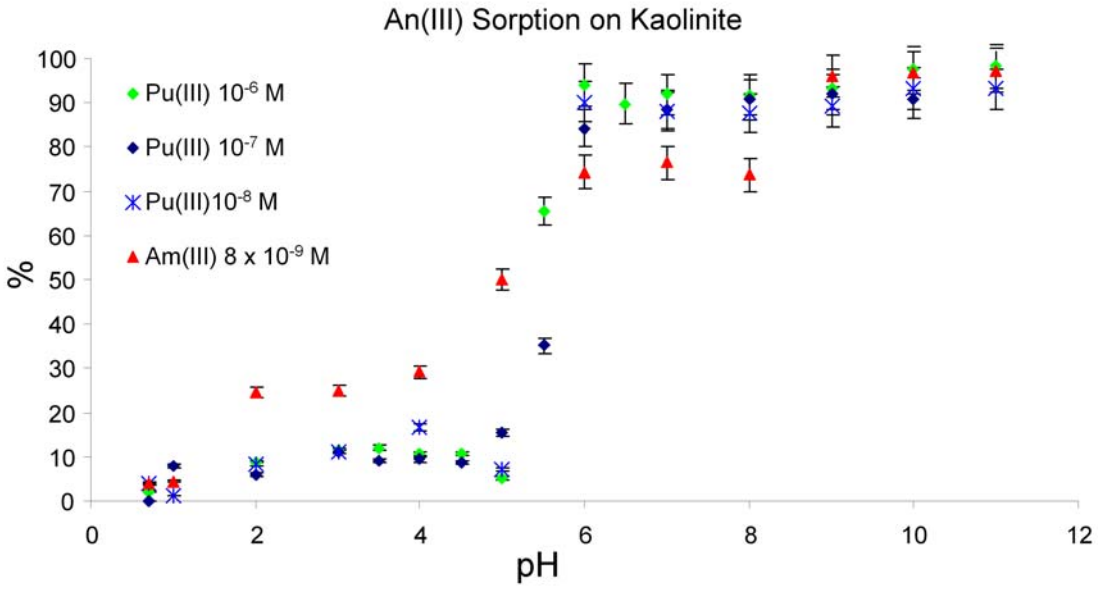

Figure 16: Sorption of Am(III) and Pu(III) on kaolinite under air as a function of pH (corrected for wall sorption).

Reversibility of the sorption of Pu(III)

The reversibility of the sorption was also investigated. For this, the samples were centrifuged and the supernatant was removed. The solid phase was afterwards re-suspended in a fresh solution of 0.1 M $NaClO_4$ with the same pH as the original solution. The suspension was then shaken for 48 hours. After a new centrifugation, the concentration of plutonium was deter-

mined measuring the activity of the supernatant by LSC. In all cases it was found that 3–10% of the plutonium sorbed on kaolinite in the earlier experiments, were desorbed and found in the solution. This could be an indication that the sorption on the surface of the kaolinite is not a physical but a chemical sorption and is mostly irreversible. The pH values of the solutions were next lowered to pH ≈ 1 with 0.1 M $HClO_4$, and after 48 h of shaking the samples, they were again centrifuged and the amount of plutonium measured. It was determined that > 90% of the sorbed plutonium was desorbed and found in the solution. These results will be used later in the section dealing with the ternary system Pu(III)–kaolinite–AHA.

In order to understand the processes that take place on the surface of the kaolinite, it is necessary to investigate also the speciation of the solid phase. Huertas et al. [46] give a detailed description for this. They found that the aluminium layer is positively charged below pH ≈ 5.5 and that the silicon sites contribute to the negative charge under neutral and basic pH (Fig. 17). The overall surface is neutral in a narrow range at pH ≈ 5.5 (point of zero charge, pH_{zpc}), as a result of the balance of positive and negative charges irrespective of the nature of the sites. The negative charge above pH 5.5 is produced by the deprotonation of the ≡SiOH groups and at pH > 9 of the AlOH groups. The sorption curves of the positively charged Pu(III) show a considerable increase of the sorption exactly from the point when the solid phase surface is negatively charged.

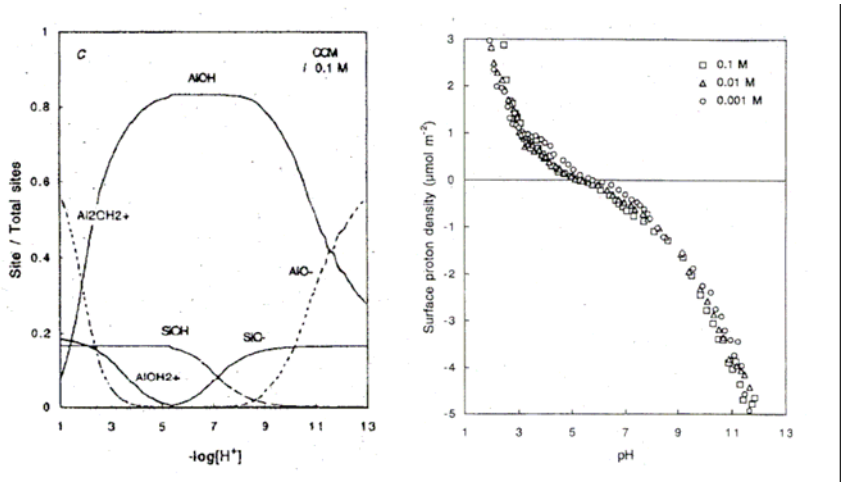

Figure 17: Speciation of the surface of KGa-1 kaolinite as a function of pH at I = 0.1 M, and the charge of the surface of kaolinite as a function of ionic strength and pH. The point of zero charge is also indicated in (b)[46].

It can be concluded that the charge of the solid phase surface plays an important role with respect to the sorption behavior of Pu(III) on kaolinite. Thus, at pH < 5, the Pu^{+3} ion can be repulsed by the positively charged surface, so the cation exchange with the kaolinite is hindered, explaining the low sorption. At higher pH values, the opposite effect is encountered and inner-sphere surface complexation to ≡$SiOAn^{2+}$, ≡$SiOAn(OH)^{+}$, and ≡$SiOAn(OH)_2°$ as well as ≡$AlOAn^{2+}$, ≡$AlOAn(OH)^{+}$, and ≡$AlOAn(OH)_2°$ is to be expected, with an increase of the sorption.

5.2.1 XAFS measurements

For a better understanding of the sorption process of plutonium species on the solid phase, several samples of Pu(III) and Pu(IV) sorbed on kaolinite were analyzed by X-ray absorption spectroscopy. This kind of measurements has been performed for the first time for plutonium sorbed on kaolinite. The samples were prepared in Mainz and the measurements were performed at the INE beamline at ANKA (Forschungszentrum Karlsruhe). Two beam times were allocated for the measurements at ANKA. The experimental conditions are summarized in Tab. 7. It was determined in all cases by XANES spectroscopy that the oxidation state of plutonium sorbed on kaolinite was Pu(IV). The results of the measurements performed in the year 2005 are shown in Tab. 8. From the experimental Pu L_{III}-edge k^3-weighted EXAFS data and fits it can be observed that sample B exhibits a different EXAFS pattern in particular in the *k* range 6–8 Å.

Table 7: Description of the samples examined by XAFS

Year	Sample	Description
2005	Pu(IV) A	pH 1, air, 94 ppm
2005	Pu(III) B	pH 6, argon, 243 ppm
2005	Pu(IV) C	pH 4, air, 370 ppm
2005	Pu(IV) D	pH 9, air, 412 ppm
2006	Pu(III) E	pH 6, argon, 359 ppm
2006	Pu(III) F	pH 8, argon, 404 ppm
2006	Pu(III) G	pH 10, argon, 426 ppm
2006	Pu(IV) H	pH 6, air, 282 ppm

While EXAFS indicates a Pu-Al/Si coordination shell at 3.62–3.66 Å for the samples A, C, and D which can be explained by an inner-sphere sorption of the polynuclear Pu(IV) species formed in solution to the kaolinite surface, the EXAFS spectrum of the sample B could not be modeled with a Pu-Al/Si shell. The best fit was obtained by including an additional Pu-O interaction at 3.25 Å. The data resulting from the experiments performed in the year 2006 are still being analyzed. It is so far clear from XANES and EXAFS analyses that plutonium is found in the tetravalent form on the surface of kaolinite. The finding of the Pu(IV)-Pu(IV) interaction on the surface of kaolinite is in good agreement with the published results of Neck et al. [47] according to which in neutral to alkaline solutions, at a constant level of log[Pu(IV)] = -8.3 ± 1.0, Pu(IV) colloids are present in solution. They have also proposed that $Pu(OH)_3(s)$

is unstable and undergoes a solid transformation into PuO_2(s) [47]. This is in line with the XANES/EXAFS observation in the present work, that the sorbed species on the solid phase is Pu(IV) when Pu(III) is brought into contact with kaolinite at pH > 6.

Table 8: Distances to Pu neighbors in Å measured by EXAFS.

	$8 \times O_1$	$2 \times O_2$	$2 \times$ Al/Si	$2 \times$ Pu
A	2.34	-	3.66	3.70
B	2.31	3.25	-	3.70
C	2.28	-	3.62	3.69
D	2.27	-	3.62	3.68

Further XAFS experiments are planned for investigating the ternary system Pu–kaolinite–HA.

Comparison of the sorption behavior of Pu(IV), Th(IV), Pu(III), Am(III)

The effect of pH on the sorption of tri- and tetravalent actinides (Pu(III), Am(III), and Pu(IV), Th(IV)) on kaolinite has been investigated in detail. As can be seen from Fig. 18, the sorption edge found for both trivalent actinides (Am, Pu) is at pH ≈ 5.5.

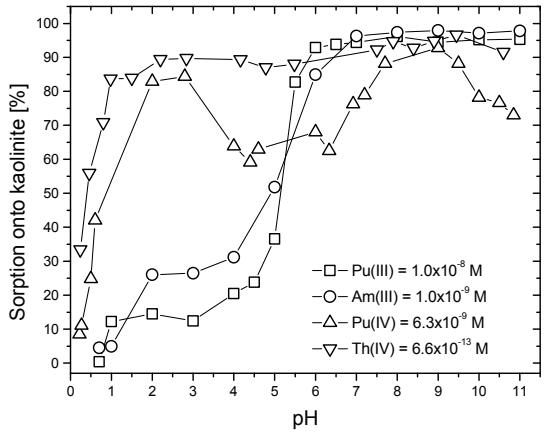

Figure 18: Sorption of trivalent (Pu, Am) and tetravalent (Pu, Th) actinides on kaolinite as a function of pH; pCO2 = $10^{-3.5}$ atm, [KGa-1b] = 4 g/L, contact time = 120 h.

For the trivalent actinides no significant effect was found in the presence of carbonate species in the solution, i.e., a decrease of the sorption of trivalent actinides on kaolinite at pH > 8 was not observed. A strong sorption of tetravalent actinides on kaolinite at lower pH values was found with the sorption edge at pH 1.5 and an influence of carbonate at pH > 8 in the case of plutonium.

5.3 Sorption of Np(V) on kaolinite

5.3.1 Batch experiments

Kinetics of sorption and desorption

As shown in Fig. 19, for total concentrations of 7 pM and 8 µM Np(V), the sorption and desorption processes at pH 9.0 are fast and equilibrium was reached in about two hours. At low Np(V) concentration, about 80% of Np(V) was sorbed in the first two hours, and only 20% of the Np(V) sorbed could be desorbed. In contrast, at higher Np(V) concentration about 60% of Np(V) was sorbed and 20% desorbed. As a conclusion, the sorption of Np(V) at kaolinite is fast, reversible at environmentally-relevant concentration, and not fully reversible at higher Np concentration.

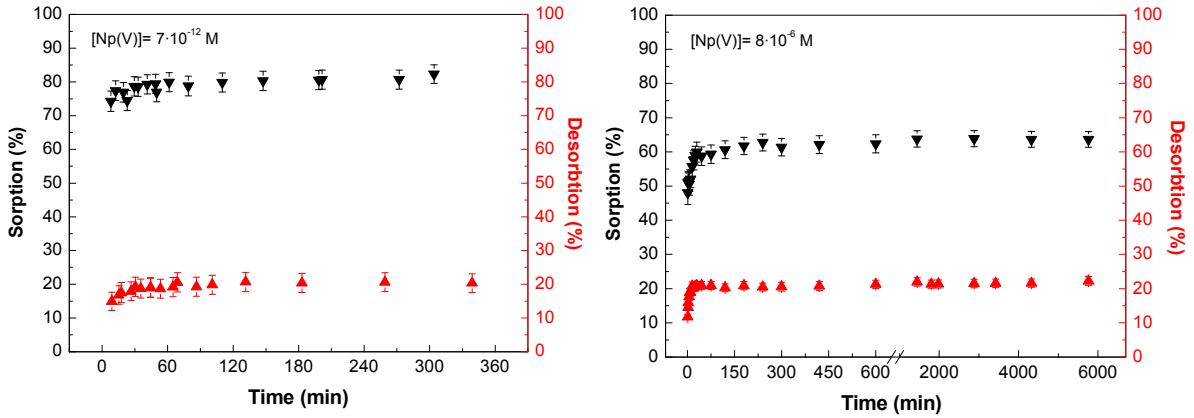

Figure 19: Percentage sorption/desorption of Np(V) on kaolinite as a function of time at pH 9.0 in 0.1 M $NaClO_4$, 4 g/L, 25 °C, $p_{CO2} = 10^{-3.5}$ atm.

Sorption isotherms

Fig. 20A shows a linear increase in the amount of Np(V) sorbed on kaolinite with increasing Np concentration in the range of 4.8×10^{-12} to 1×10^{-5} M. In this range, the sorption behavior could be fitted to a Freundlich-type isotherm with a slope of one. That means, the sorption mechanism of Np(V) on kaolinite in this concentration range is similar. At total concentrations of 1×10^{-5} and 1×10^{-4} M Np(V), precipitation was observed (Fig. 20A). The equilibrium concentration of 2×10^{-5} M Np(V) agrees with the Np concentration determined from the solubil-

ity of $NaNpO_2CO_3(s)$ in 0.1 M $NaClO_4$ at pH 9.0 [48]. Therefore, the following batch experiments and EXAFS measurements were performed at a total Np(V) concentration of 8 µM or less.

The dependence of the sorption of 8 µM Np(V) on the solid-to-liquid ratio (g/L) at pH 9.0 is shown in Fig. 20B. The percentage of Np sorbed increases with increasing amount of kaolinite form 0.5 to 10.0 g/L. This reflects the increase in surface sites available for Np sorption as more kaolinite is added. The percentage sorption remains constant above 10.0 g/L.

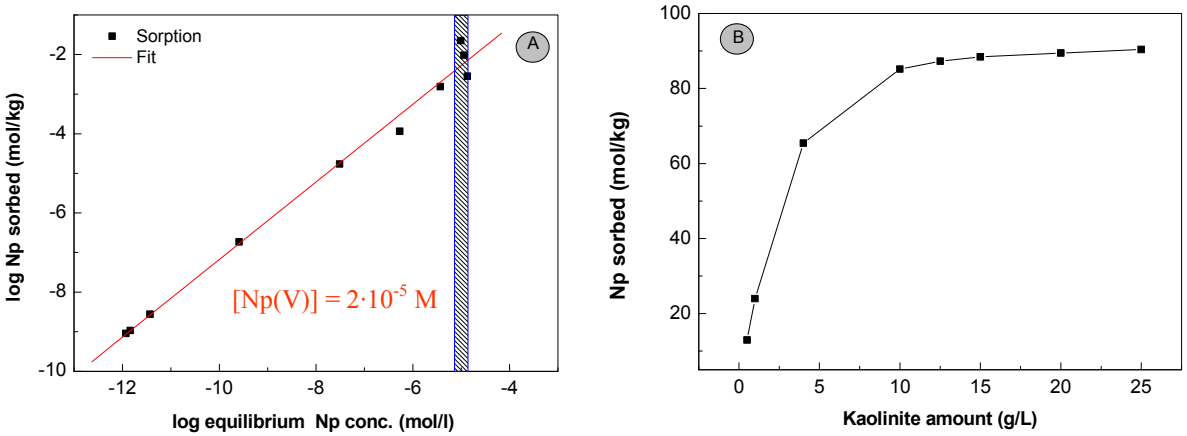

Figure 20: Sorption isotherms for Np(V) on kaolinite at pH 9.0 in 0.1 M $NaClO_4$ (p_{CO2} = $10^{-3.5}$ atm) at 25 °C. A – dependence on Np(V) concentration; B – dependence on kaolinite concentration.

Effect of pH and CO_2 presence

After studying the kinetics and isotherms of Np(V) sorption at pH 9, its dependence on pH and CO_2 was investigated in more detail since not much is known about it from the literature. Briefly, Niitsu et al. [49] studied the effect of humic acid on the sorption of Np(V) on kaolinite. They measured the sorption coefficient, K_d, at pH 6-11 and with humic acid concentrations of 0 to 40 mg/L at 0.1 M ionic strength and a Np(V) concentration of 7 µM under Ar atmosphere. Kohler et al. [50] investigated the sorption of Np(V) on kaolinite in the absence of ambient CO_2 at 0.1 M ionic strength. The concentration of Np(V) was 0.1 µM.

Figure 21 shows the sorption of Np(V) on kaolinite at the environmentally-relevant concentration of 7 pM as a function of the pH and in the presence and absence of CO_2. The curves show that the sorption edge occurs at pH 8.0. The uptake of Np(V) by kaolinite strongly increased above pH 7.0 and reached its sorption maximum (84%) at pH 9.0 in the presence of CO_2. Above pH 9.0, the amount of Np(V) sorbed on kaolinite decreased and reached 0% at pH 10.0 due to the formation of Np(V)-carbonato species in the aqueous solution. In the CO_2-

free system, the sorption of Np(V) increased continuously with pH until a sorption of 100% was reached at pH 10.0.

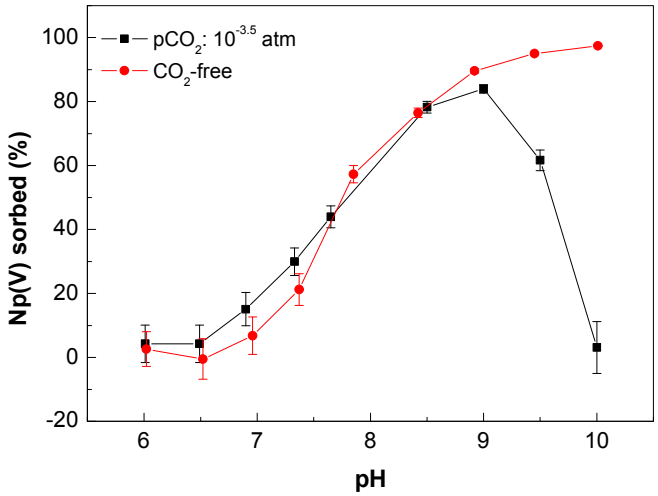

Figure 21: Sorption of 7 pM Np(V) on kaolinite (4 g/L) as a function of pH in 0.1 M $NaClO_4$ in the absence and presence of CO_2 ($p_{CO2} = 10^{-3.5}$ atm) at 25 °C.

A similar sorption behavior was found in batch experiments in the CO_2-equilibrated system with Np concentrations of 8 µM. Fig. 22 shows the sorption behavior of Np(V) on kaolinite at a total concentration of 8.0 µM Np. The uptake of Np(V) by kaolinite starts at pH 7.0 and the sorption edge occurs at approx. pH 8.0 in the presence and absence of CO_2. A sorption maximum is observed at pH 9 (70 % sorption) in the air-equlibrated system. In the CO_2-free system, the sorption of Np(V) increases with increasing the pH until 80 % at pH 10.0. In ambient CO_2 atmosphere, the sorption of Np(V) starts to decrease at pH 9.0, and no sorption is observed at pH 10.0. The decrease of Np(V) sorption with increasing pH can be explained by the formation of negatively charged Np(V)-carbonato species in solution and an increase in the negative surface charge of the mineral.

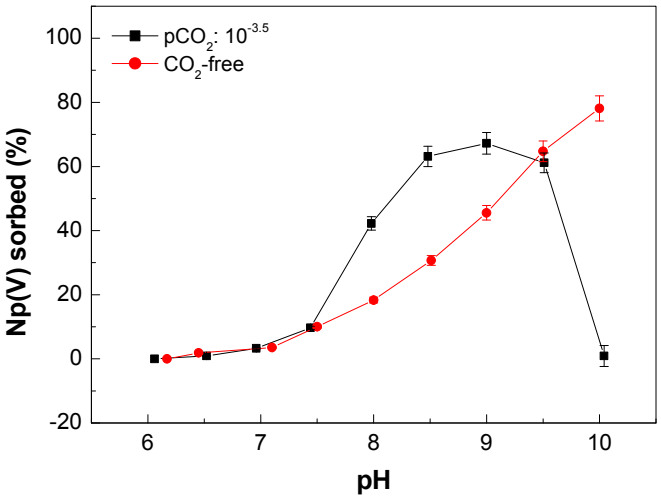

Figure 22: Sorption of 8 µM Np(V) on kaolinite (4 g/L) as a function of pH in 0.1 M $NaClO_4$ in the presence (p_{CO2} = $10^{-3.5}$ atm) and absence of CO_2 at 25 °C.

Effect of ionic strength

The sorption of Np(V) on kaolinite was investigated also as a function of ionic strength at total concentrations of 7 pM and 8 µM Np(V). Fig. 23 shows the sorption behavior at low concentration in the presence and absence of CO_2 in 0.01 and 0.1 M $NaClO_4$. In contrast to the experiments performed under Ar atmosphere, ionic strength affects the sorption of Np(V) when CO_2 is present (Fig. 23A). The sorption edge in 0.01 M $NaClO_4$ is shifted by 0.5 units toward higher pH, i.e., the sorption increases with increasing ionic strength (up to 10% at pH 9). A similar effect of ionic strength was observed for 8 µM Np(V) (Fig. 24A).

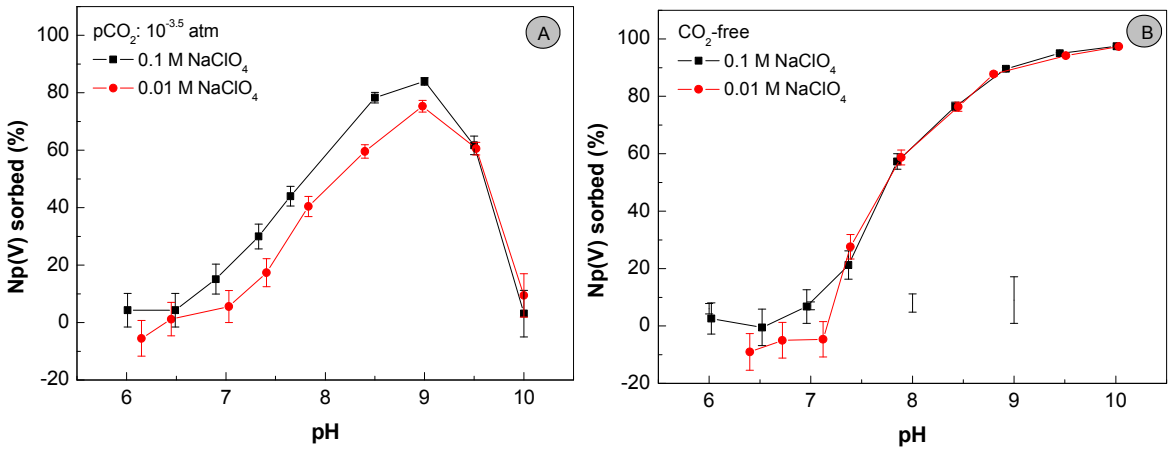

Figure 23: Sorption of 7 pM Np(V) on kaolinite (4 g/L) as a function of pH at 0.01 and 0.1 M $NaClO_4$ in the presence (A) (p_{CO2} = $10^{-3.5}$ atm)and absence (B) of CO_2 at 25 °C.

The CO_2-free experiments both at 7 pM and 8 µM Np(V) showed that the ionic strength (0.01 and 0.1 M $NaClO_4$) has no effect on the sorption (Figs. 23B and 24B), indicating inner-sphere sorption of Np(V) species at the kaolinite surface.

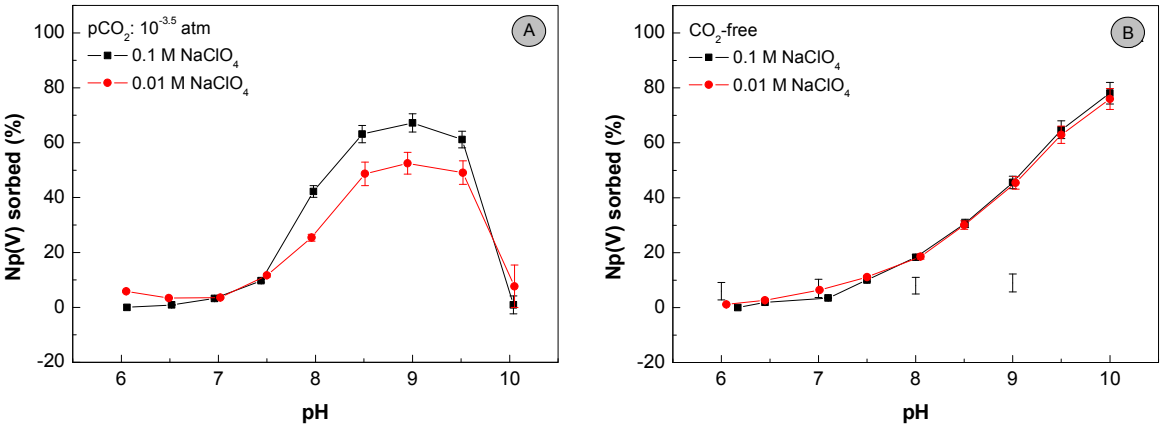

Figure 24: Sorption of 8.0 µM Np(V) on kaolinite (4 g/L) as a function of pH at 0.1 and 0.01 M $NaClO_4$ in presence (A) (p_{CO_2} =$10^{-3.5}$ atm) and absence (B) of CO_2 at 25 °C.

5.3.2 XAFS measurements

The use of EXAFS spectroscopy and related synchrotron radiation techniques for the molecular-level speciation of environmental contaminants including actinides such as Np leads to an improved understanding of the fundamental chemical processes determining their behavior in complex systems. From the available literature there is no information regarding XAFS studies of Np(V) sorption on kaolinite up to now. Therefore, our aim was to apply XAFS spectroscopy to study the sorption of Np(V) on kaolinite in aqueous solution in greater detail. XAFS investigations should deliver data on the speciation of Np(V) at the surface of kaolinite. Samples with different amounts of ^{237}Np(V) sorbed on kaolinite were prepared in suspensions of 200 mg kaolinite in 50 mL 0.1 M $NaClO_4$. Samples A, B, and C (Table 9) were prepared in the presence of ambient CO_2 at pH 8.0, 9.0, and 10.0, respectively. Samples D, E, F, and G (Tab. 9) were prepared in a glove box with Ar atmosphere at pH 8.0, 9.0, 10.0, and 10.5, respectively. These samples can be compared to samples A–C prepared in equilibrium with air. Except for sample B, which was measured at 25 K as dry powder, all samples were studied at room temperature as wet pastes. Tab. 9 summarizes the preparation conditions of samples A–G and the amount of Np sorbed in each sample.

Fig. 25 shows the raw Np L_{II}-edge k^3-weighted EXAFS oscillations for Np(V) samples and their corresponding Fourier transforms (FTs). The spectrum of sample D has not been included in Fig. 25 due to the low-signal-to-noise ratio. The FTs are not corrected for EXAFS phase shifts causing peaks to appear at shorter distances (R+Δ) relative to true distance R. As can be seen from Fig. 25, the spectra of samples A–C show comparable EXAFS oscillations.

Table 9: Summary of XAFS samples prepared at 8 µM Np(V), 4.0 g /L, 0.1 M $NaClO_4$.

Sample	Atmosphere	pH	T/K	Np loading / ppm
A	air	8.0	298	240
B	air	9.0	25	330
C	air	10.0	298	190
D	Ar	8.0	298	70
E	Ar	9.0	298	215
F	Ar	10.0	298	380
G	Ar	10.5	298	430

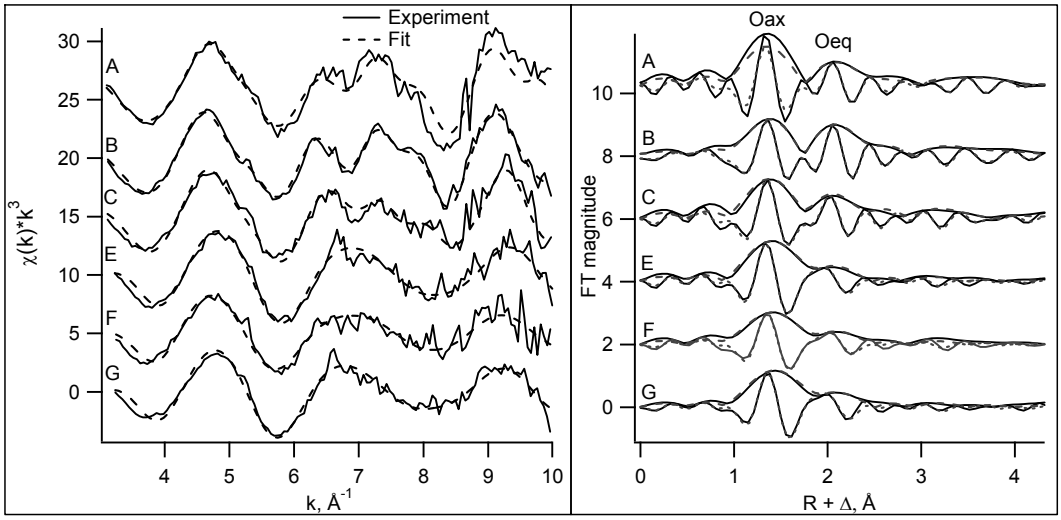

Figure 25: Np L_{II}-edge k^3-weighted EXAFS spectra (left) and the corresponding Fourier transform magnitudes and real parts (right) for Np(V) sorption on kaolinite. See Tab. 9 for sample description.

Samples A–C prepared in the presence of CO_2 show a different EXAFS pattern compared to samples E–G, which were prepared under Ar atmosphere. Five coordination shells are evident in the FTs of the samples A–C. A peak at about 1.3 Å dominates the FTs. This peak corresponds to the axial oxygen atom of the neptunyl unit (NpO_2^+). A smaller FT peak at about 2.0 Å represents four oxygen atoms that are coordinated to neptunium in equatorial

plane. A coordination shell at about 2.97 ± 0.02 Å corresponds to two carbon atoms (Tab. 10).

Table 10: EXAFS structure parameters of Np(V) sorbed on kaolinite (R ± 0.02 Å, σ^2 = ±0.001 Å^2).

Sample	Conditions	2 × O_{ax}		4 × O_{eq}		2 × C		2 × O_{dis}		1 × Np		ΔE_0
	pH/CO_2/T(K)	R	σ^2	R	σ^2	R	σ^2	R	σ^2	R	σ^2	eV
A	8.0, air, 298	1.84	0.003	2.56	0.008	3.00	0.004	4.25	0.006	4.90	0.003	0.7
B	9.0, air, 25	1.85	0.004	2.57	0.004	2.97	0.001	4.28	0.003	4.88	0.003	0.3
C	10.0, air, 298	1.86	0.003	2.52	0.006	2.90	0.003	4.23	0.010	4.88	0.003	0.8
E	8.0, Ar, 298	1.85	0.003	2.45	0.013	-	-	-	-	-	-	0.4
F	9.0, Ar, 298	1.86	0.005	2.50	0.017	-	-	-	-	-	-	0.4
G	10.0, Ar, 298	1.87	0.003	2.47	0.013	-	-	-	-	-	-	1.1
$NpO_2(H_2O)_4^+$ [51]	0, air, 298	1.82	0.002	2.49	0.006	-	-	-	-	-	-	-
$NpO_2(CO_3)_3^{5-}$ [52]	-, air, 295	1.86	0.001	2.53	0.013	2.98	0.0004	4.22	Na	-	-	-

The coordination shell at about 4.25 ± 0.03 Å results from the three-legged multiple scaring paths U–C–O_{dis} along the Np-carbonate moiety (see Tab. 10 and Fig. 26). The peak at about 4.88±0.02 Å represents one Np atom. Due to a poor signal-to-noise ratio in the spectra E–G, only two coordination shells were modeled at about 1.86±0.01 Å and 2.47±0.03 Å related to two axial and four equatorial oxygen atoms, respectively. In all samples the coordination numbers of all shells were held constant at the values determined during the previous fits.

Tab. 10 summarizes the metrical parameters derived from the EXAFS fits. The Np coordination shells and bond distances of samples A, B, and C are consistent with the formation of a Np(V)-carbonato species at the kaolinite surface. The average Np-O_{eq} bond distance (2.47±0.03 Å) of samples E and G is somewhat shorter than in the Np(V)-aquo ion (see Tab. 10). The EXAFS investigations of the air-equilibrated samples show that NpO_2^+ sorbed on the kaolinite surface is coordinated in a bidentate fashion by two carbonate groups (Fig. 27B, see also Tab. 10). This is based on the detection of Np-C and Np-O_{dis} interactions at about 3.0 and 4.2 Å, respectively. Based on the low signal-to-noise level of the data, a Np-Si/Al shell was not modeled. Therefore, these spectra do not allow concluding on the formation of

inner-sphere or outer-sphere sorption complexes. In the CO_2-free system, the Np-O_{eq} distance of 2.47 Å is similar to or shorter than for NpO_2^+(aq.) (Tab. 10), indicating inner-sphere sorption of NpO_2^+ on the kaolinite surface (Fig. 27A).

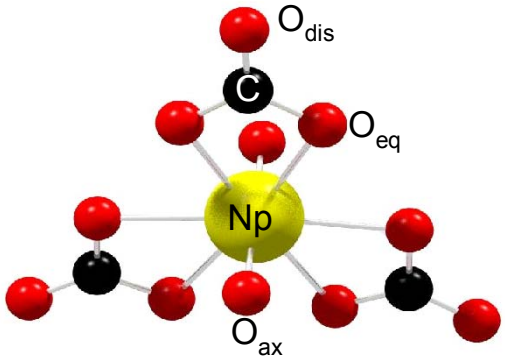

Figure 26: Structure model of $NpO_2(CO_3)_3^{5-}$(aq.).

This agrees with the conclusion drawn from the dependence of sorption of Np(V) on ionic strength.

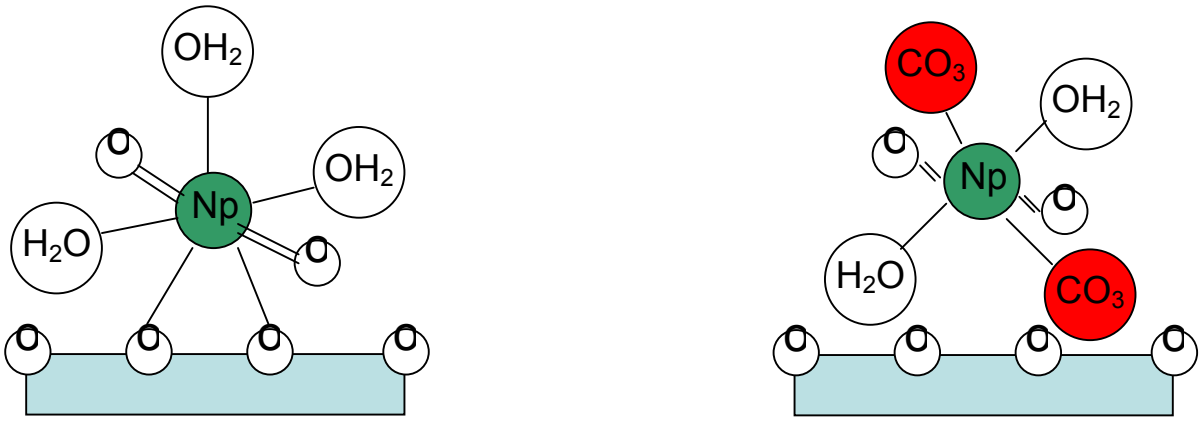

A: inner-sphere sorption of NpO_2^+

B: inner-/outer-sphere sorption of $NpO_2(CO_3)_2^{3-}$

Figure 27: Ball-and-stick representation of NpO_2^+ (A) and $NpO_2(CO_3)_2^{3-}$ (B) sorbed to the surface of kaolinite.

Conclusions

The sorption of Np(V) on kaolinite KGa-1b was investigated both by batch experiments and XAFS measurements. The sorption study showed that the Np(V) sorption on kaolinite is influenced by pH, Np concentration, ionic strength, partial pressure of CO_2, and the amount of sorbent. The batch experiments showed significant differences between systems with and without CO_2. In the presence of ambient CO_2, the sorption of Np(V) increased with increasing ionic strength, the curves of Np(V) are characterized by a maximum at pH 9.0 with 7 pM as well as with 8 µM Np(V) concentration followed by decreasing sorption with increasing pH (to 0% sorption at pH 10) due to formation of strong Np(V)-carbonato complex in the aqueous solution. In the CO_2-free system (Ar atmosphere), the sorption increases continuously with pH (to 100% at pH 10.0) and the batch experiments did not show any ionic strength dependence.

Kinetic studies showed that the sorption and desorption processes of Np(V) on kaolinite are fast and that equilibrium was reached in about 3 h. The desorption process was not fully reversible at 8 µM but reversible at 7 pM Np(V). The sorption isotherms were also determined and the data could be fitted to a Freundlich isotherm in the concentration range from 7×10^{-12} M to 1×10^{-5} M. Above 5×10^{-5} M Np(V), the solutions became oversaturated.

The Np(V) species sorbed on the kaolinite surface have been determined by EXAFS spectroscopy. Measurements in air-equilibrated system showed that the average distances of the Np-O_{ax} (1.84 Å), Np-O_{eq} (2.56 Å), Np-C (3.00 Å), and Np-O_{dis} (4.25 Å) coordination shells agree with those of the $[NpO_2(CO_3)_3]$ moiety. The bidentate coordination of two CO_3^{2-} groups to NpO_2^+ indicates inner- or outer-sphere sorption of $NpO_2(CO_3)_2^{3-}$ at the kaolinite surface. The precipitation of Np(V) carbonate at an initial concentration of 8 µM Np(V) can be ruled out based on the sorption isotherm measurements. The Np(V) surface complexes in the CO_2-free system showed two prominent coordination shells, i.e., Np-O_{ax} and Np-O_{eq} at 1.87 and 2.47 Å, respectively. The Np-O_{eq} distance is slightly shorter than the corresponding value for the Np(V) aquo ion of 2.49 Å, indicating inner-sphere sorption of NpO_2^+ on the kaolinite surface. This conclusion has been supported by our recent EXAFS in March 2007 measurement that showed clear evidence for Np-Al/Si interaction.

5.4 Sorption of U(VI) on kaolinite

5.4.1 Batch experiments

Figs. 28 and 29 show the sorption curves for 1 and 10 µM U(VI) obtained in the presence and absence of CO_2 for pH 3.0–10.0. For 1 µM total U(VI), the sorption edge occurs at pH 5. This observation agrees with the previous results of Sekine and Redden et al. [53, 54]. Maximum sorption occurs at pH ≥ 6. In the presence of CO_2, the uptake by kaolinite starts to decrease at pH 8.5. At 10 µM total U(VI), the sorption edge is shifted slightly higher to pH 6.

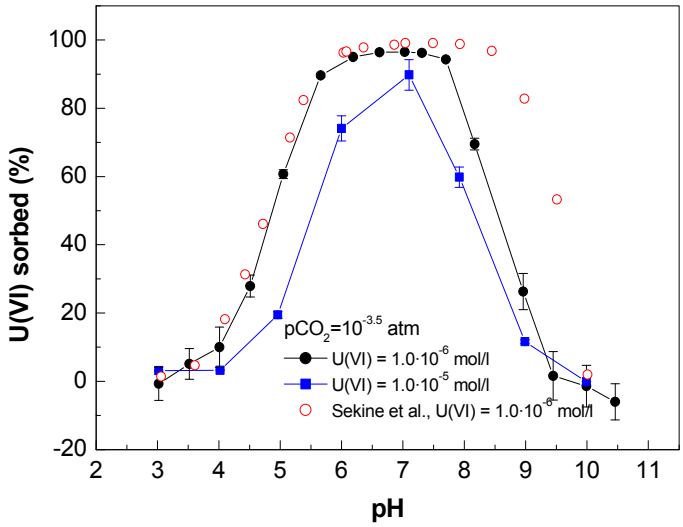

Figure 28: Sorption of 1and 10 µM U(VI) on kaolinite (4 g/L) as a function of pH in the presence of CO_2 (p_{CO2} = $10^{-3.5}$ atm).

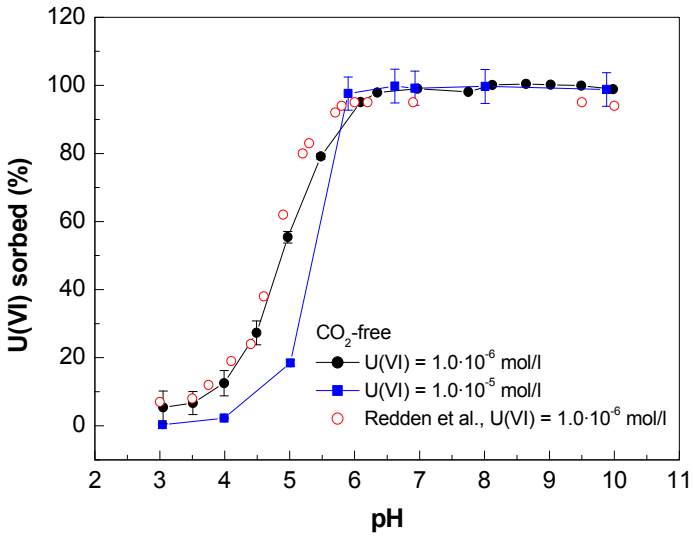

Figure 29: Sorption of 1and 10 µM U(VI) on kaolinite (4 g/L) as a function of pH in the absence of CO_2.

The uranium uptake decreases above pH 8 in the presence of CO_2 and remains at 100 % in the CO_2-free system (see Figs. 28 and 29). It can be concluded that the results of our batch experiments are in good agreement with previous studies.

The results of the chemical analysis of samples 1–8 used in the EXAFS measurements are summarized in Tab. 11. The sorption data for the majority of these samples can also be seen in the sorption curves for 10 µM U(VI) given in Figs. 28 and 29. The highest uranium loading of the EXAFS samples was 1200 ppm and the lowest loading was less than 100 ppm, i.e., significantly less than in the previous EXAFS study of Thompson at al. [55].

Table 11: Initial concentrations of U(VI) in the solutions and analytical results for the EXAFS samples. Samples 1–7 were prepared in air-equilibrated solutions.

Sample	[U(VI)] µmol/L	pH_{start}	pH_{final}	ppm sorbed	% sorbed
1	10	5.0	4.96	99	16.6
2	10	6.0	5.94	468	78.6
3	10	7.0	6.93	540	90.7
4	10	8.5	8.43	73	12.2
5	5	7.0	6.71	291	97.6
6	10	7.0	6.67	581	97.6
7	20	7.0	6.83	1161	97.6
8	10, no CO_2	8.5	8.52	591	99.3

5.4.2 XAFS measurements

The raw data of the U L_{III}-edge k^3-weighted EXAFS spectra of samples 1–8 together with the best theoretical fit to the data and the corresponding FTs are shown in Fig. 30. The metrical parameters derived from the least-square fits are summarized in Tab. 12. As expected for U(VI), the average distance between uranium and its two axial oxygen atoms, O_{ax}, is nearly constant for all samples and equals 1.79 ± 0.02 Å. The average coordination number for the equatorial oxygen atoms, O_{eq}, is five. As can be seen from Tab. 12, the average U-O_{eq} distance varies between 2.36–2.40 Å. Therefore, it is interesting to discuss these changes in more detail.

The U-O_{eq} distance increases from 2.37 to 2.40 Å with increasing pH from 5.0 to 8.5 in the presence of CO_2 (samples 1–4, Tab. 12). These distances are somewhat shorter than 2.41 ± 0.02 Å, the average U-O_{eq} distance of the U(VI) aquo ion [56]. This indicates inner-sphere sorption of U(VI) on the kaolinite surface. Sample 8, which was prepared at pH 8.5 without CO_2, can be compared to sample 4, which was prepared at the same pH but in the presence of CO_2. In contrast to sample 4, the average U-O_{eq} distance for sample 8 is 2.37 ± 0.02 Å. This is the same U-O_{eq} distance as observed at pH 5.0 (sample 1). It can be concluded that the presence of CO_2 leads to a lengthening of the average value of the U-O_{eq} bond distance. A change in pH from 5.0 to 8.5 does not have any influence on the average U-O_{eq} distance in the CO_2-free samples.

Table 12: EXAFS structure parameters of U(VI) sorbed on kaolinite; σ^2 for Si was fixed at 0.0030 $Å^2$. (N ±15 %, R ±0.02 Å, σ^2 ±0.001 $Å^2$).

Sample	Conditions	2 × O_{ax}		5 × O_{eq}		N × Si		N × Si		ΔE_0
	[U(VI)] (µM)/pH	R(Å)	$\sigma^2(Å^2)$	R(Å)	$\sigma^2(Å^2)$	R(Å)	N	R(Å)	N	eV
1	10/ 5.0, air	1.79	0.0029	2.37	0.014	3.10	1.1	3.30	0.9	2.69
2	10/ 6.0, air	1.78	0.0023	2.37	0.012	3.10	0.8	3.29	0.8	0.91
3	10/ 7.0, air	1.79	0.0020	2.38	0.012	3.09	1.1	3.29	0.9	1.65
4	10/ 8.5, air	1.80	0.0022	2.40	0.010	3.08	1.6	3.29	1.5	1.39
5	5/7.0, air	1.79	0.0026	2.38	0.011	3.09	1.3	3.30	1.2	1.86
6	10/7.0, air	1.79	0.0023	2.37	0.011	3.10	1.1	3.31	1.0	1.89
7	20/7.0, air	1.79	0.0020	2.36	0.014	3.11	0.7	3.32	0.5	1.80
8	10/ 8.5, no CO_2	1.80	0.0025	2.37	0.016	3.09	0.9	3.29	0.9	3.18

The average U-O_{eq} bond distances of the aqueous $[UO_2(CO_3)_3]^{4-}$ complex is 2.44 ± 0.02 Å [57]. Therefore, the observed lengthening of the U-O_{eq} bond distance with increasing concentration of CO_3^{2-}/HCO_3^- in solution could to some extend indicate the formation of ternary U(VI) surface complexes with carbonate on the kaolinite surface. Samples 5–7, which were prepared at pH 7 but different U(VI) concentrations, did not show any change in the average U-O_{eq} bond distance within the experimental uncertainties (see Tab. 12). This indicates that the speciation of the U(VI) surface complexes at pH 7 does not change in the range of 5 to 20

µM U(VI) in solution. Even at the highest uranium loading of 1200 ppm (sample 7), the EXAFS spectrum did not show any indication of a U-U interaction or formation of polymeric surface complexes.

The theoretical fits to the raw data improved significantly when the structural model includes two U-Si coordination shells at 3.1 and 3.3 Å. Since the scattering properties of Si and Al are similar, it is impossible to distinguish between these two backscattering atoms in EXAFS spectra. A U-Al distance of 3.1 Å could be rationalized by coordination of U(VI) to [AlO_6] octahedra of kaolinite. The U-Al distance expected for such a coordination would be in the

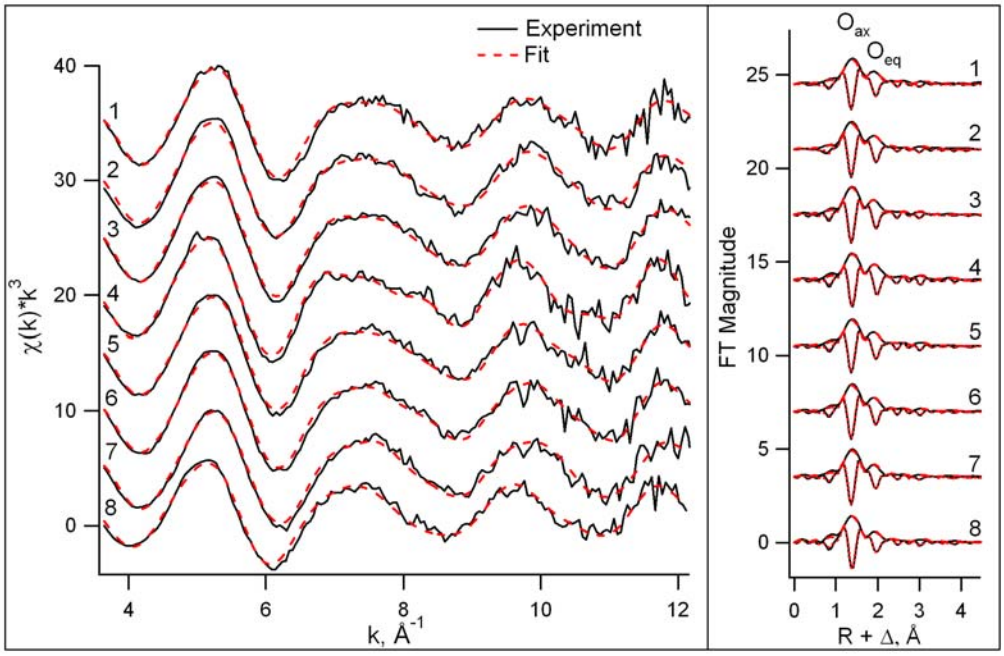

Figure 30: U L_{III}-edge k^3-weighted EXAFS spectra (left) and their corresponding Fourier transforms (right) for U(VI) sorbed on kaolinite. See Tab. 10 for sample description. Dashed lines are fits to the spectra.

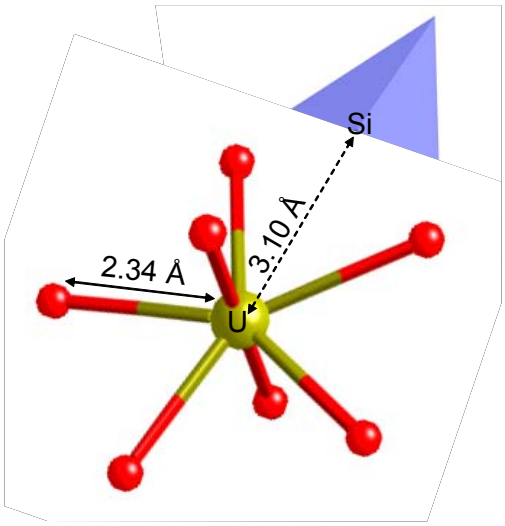

Figure 31: Ball-and-stick representation of UO_2^{2+} bonded to a [SiO_4] tetrahedron by edge sharing.

range of 3.2–4.2 Å [58]. The interaction of U(VI) with [SiO_4] tetrahedra can result in U-Si distances between 3.10–3.5 Å depending on the edge-sharing or corner-sharing geometries of the [UO_2O_5] pentagonal bipyramid and the [SiO_4] tetrahedron. These geometries can be found in the mineral soddyite, $(UO_2)_2SiO_4 \cdot 2H_2O$ [27]. According to the crystal structure of soddyite, the U-Si distances equal 3.16 and 3.80 Å for edge sharing and corner sharing with [SiO_4], respectively (see Fig. 31).

Conclusions

The batch experiments of U(VI) sorption on kaolinite showed significant differences between systems with and without CO_2. The strong decrease of the amount of U(VI) sorbed above pH 7 (10 µM U(VI), $p_{CO2} = 10^{-3.5}$ atm) can be rationalized by the formation of U(VI)-carbonato complexes in solution. The EXAFS experiments, where CO_2 was present, seem to indicate that the speciation of U(VI) at the kaolinite surface changes with increasing pH. A small lengthening of the average U-O_{eq} bond distance could be due to the formation of ternary surface complexes with carbonate. Such surface complexes have been detected in the case of U(VI) sorption on hematite [59, 60]. This conclusion is supported by the observation that the U-O_{eq} distance remains constant over the pH range 5.0–8.5 when CO_2 was absent.

The EXAFS experiment showed that U(VI) forms inner-sphere, monomeric surface complexes with kaolinite in the pH range of 5.0–8.5 and total U(VI) concentrations of 5–20 µM. A small peak in the FT of all samples at approximately 3 Å (see Fig. 30) could be fit best with two Al/Si coordination shells at an average U-Al/Si distance of 3.1 and 3.3 Å. These U-Al/Si distances evidence inner-sphere sorption of U(VI) on kaolinite.

5.5 Sorption of humic substances on kaolinite

5.5.1 Batch experiments

The time dependence of HA and FA sorption on kaolinite was investigated with contact times between 20 h and 120 h. The concentration of humic substances (HS) was determined by UV-vis spectroscopy. It is evident that the sorption equilibrium is reached quite fast, i.e., no strong effect of the contact time on the sorption equilibrium was found. For the sorption experiments of HS on kaolinite, contact time of 120 h was chosen. Tab. 13 summarizes the parameters and operating conditions for the experiments on the sorption of HS on kaolinite. The sorption of HA and FA on kaolinite as a function of pH at HS concentrations of 20, 50, and 100 mg/L has been investigated. HS is strongly sorbed on the kaolinite surface at low pH values. The sorption of HS decreases with increasing pH value and with the initial concentration of HA and FA. These results are in good agreement with literature data [61, 62]. The decreased sorption of HS with increasing pH might be explained by the repulsion between the negatively charged kaolinite surface and the negatively charged HA and FA molecules. The point of zero charge of kaolinite is reported to be at pH $\approx$ 5 [61, 62].

Table 13: Experimental parameters and operating conditions for the sorption of humic substances (HS) on kaolinite.

Parameter	Conditions
Kaolinite, [KGa-1b]	4 g/L
[HS]	10–150 mg/L
Ionic strength	0.1 M $NaClO_4$
pH	1, 5, 8
Preconditioning time	48 h
Contact time of kaolinite with HS	120 h
p_{CO2}	$10^{-3.5}$ atm
Phase separation	1 h (~2500 rpm)
Detection	UV-vis spectroscopy

The negative charge density of kaolinite increases with increasing pH. Furthermore, at higher pH values, the dissociation of functional groups of HA/FA is greater, which results in an increase in the negative charge density of the HA/FA molecules.

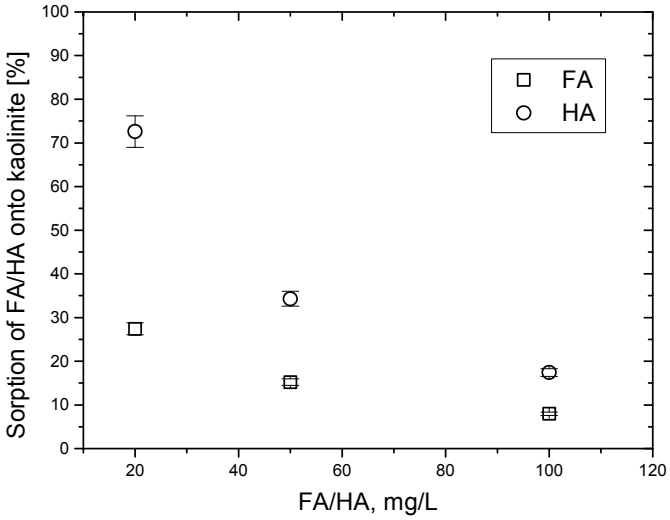

Figure 32: Sorption of humic acid (HA) and Gorleben fulvic acid (FA) on kaolinite as a function of HA/FA concentration; [KGa-1b] = 4 g/L, contact time = 120 h, pH 5, and ionic strength 0.1 M $NaClO_4$.

The electrostatic interaction between both negatively charged surfaces repels the HA/FA from the kaolinite surface and thus leads to a decrease in the sorbed fraction of HA/FA at higher pH. Křepelová et al. [61] investigated the sorption of synthetic HA (M42) on kaolinite as a function of pH at varying HA concentrations and ionic strengths and found that the sorption decreases with increasing pH and concentration of the synthetic HA. Fig. 32 displays the percentage of AHA/FA sorbed on kaolinite at pH 5 for the concentrations 20, 50, and 100 mg/L. The sorption of FA on kaolinite is lower in comparison to that of HA That might be explained by the lower molecular size of FA compared to HA and its less hydrophobic character.

5.5.2 XPS measurements

In collaboration with the Institute of Radiochemistry, Forschungszentrum Dresden-Rossendorf, the interaction of HA with kaolinite was studied by XPS. Previous studies had shown that the presence of HA influences the sorption of U(VI) on the clay mineral kaolinite [61]. XPS is a powerful technique for qualitative and quantitative surface analysis of solid samples, typically within a few nm of a surface layer [63].

Solutions of 10 mg/L synthetic HA of type M42 [64] in 0.1 M $NaClO_4$ were contacted with kaolinite KGa-1b at pH 4.0 and 7.5, respectively. 94 % of HA was sorbed at pH 4.0, corre-

sponding to 2.4 mg HA/g kaolinite (sample HA_4.0). At pH 7.5, the HA uptake by kaolinite was 45 %, corresponding to 1.2 mg/g (sample HA_7.5). An additional sample (R11/04KS) resulted from the synthesis of HA in the presence of kaolinite as described in [65]. The uptake of humic substances by kaolinite was 9 mg/g. Kaolinite powder without any treatment was measured as reference.

The elements C, O, Al, Si, and minor amounts of Na were detected in the overview spectra of all HA samples. The binding energies and relative intensities of the XPS lines of C, O, Al, and Si were determined from twenty sweeps of each line. Sample HA_7.5 was measured twice. The O1s, Si2s, Al2s, Si2p, and Al2p binding energies of the HA/kaolinite samples agree within the experimental uncertainty of ±0.1 eV with each other and with those of the untreated kaolinite sample (see Tab. 14).

Table 14: Binding energies E_b of O1s, Si2s, Al2s, Si2p, and Al2p XPS lines in eV. E_b(C1s) = 285.0 eV. Error ±0.1 eV.

Sample	O1s	Si2s	Al2s	Si2p	Al2p
HA_4.0	531.9	153.6	119.0	102.6	74.3
HA_7.5	532.0	153.8	119.1	102.7	74.4
HA_7.5	531.9	153.7	119.0	102.6	74.3
HA_7.5[a]	531.8	153.5	119.4	102.5	74.6
R11/04KS	532.0	153.7	119.0	102.7	74.3
KGa-1b[b]	532.2	153.9	119.3	102.9	74.6

a) after 10 min Ar^+ sputtering (4000 V, 10 – 15 μA), b) untreated kaolinite.

The following conclusions can be drawn from the relative intensities given in Tab. 15:

1) Relatively small amounts of sorbed hydrocarbons, i.e., approximately 1 atom % C, were detected at the untreated kaolinite surface. Although the HA uptake by kaolinite varied by a factor of eight (9–1.2 mg/g), the C1s/Al2p intensity ratio is nearly constant and does not show any correlation with the HA loading. The surface of the HA/kaolinite samples contains only approximately 5 atom % C. This leads to the important conclusion that the surface of the clay particles is not covered by a homogenous layer of HA. Part of the HA must be distributed between the clay particles. This implies that in the ternary system U/kaolinite/HA U(VI) can interact with significant parts of the kaolinite surface that are not covered by HA.

2) All HA/kaolinite samples show the same surface composition with respect to Si, Al, and O as the untreated kaolinite. The chemical composition of the kaolinite surface was not altered by HA adsorption or during HA synthesis.

3) The experimental intensity ratios Si2p/Al2p and O1s/Al2p agree with the theoretical values that were calculated according to the chemical composition of kaolinite, i.e., $Al_2[Si_2O_5(OH)_4]$.

4) After sputtering sample HA_7.5 10 min with Ar^+ ions, the C1s/Al2p intensity ratio decreased from 0.47 to 0.18 (Tab. 15). This means that a significant amount of carbon, i.e., approximately 60%, could be removed by Ar^+ sputtering from the surface of the clay particles. However, the C1s/Al2p intensity ratio after sputtering was nearly twice that of the untreated kaolinite surface. This indicates that the remaining HA may not be bound to the kaolinite surface but could be located between the clay particles (*cf* first conclusion).

Table 15: Relative XPS line intensities and uptake of humic substances by kaolinite.

Error ±5 %.

Sample	mg/g	C1s/Al2p	Si2p/Al2p	O1s/Al2p
HA_4.0	2.4	0.61	1.60	20.6
HA_7.5	1.2	0.45	1.55	20.0
HA_7.5	1.2	0.47	1.62	20.1
HA_7.5[a]	-	0.18	1.48	16.6
R11/04KS	9.0	0.52	1.59	20.0
KGa-1b[b]	-	0.10	1.54	19.6
Calculated[c]	-	0	1.52	22.7

a) and b) see Table 14; c) $Al_2[Si_2O_5(OH)_4]$.

6 Sorption of neptunium on hematite

6.1.1 Experimental

The hematite powder used in these experiments was synthesized from 0.2 M $Fe(ClO_4)_3$ solution at 98 °C for seven days following the method of Schwertmann and Cornell [66]. The synthesized hematite was purified by repeated intensive washing with Milli-Q water. Separation of the phases was achieved by centrifugation. With this procedure clean hematite was produced. XPS measurements in ultra-high vacuum (<10^{-9} mbar) showed only Fe, O, and trace

amount of adventitious carbon at the hematite surface (Fig. 33). The specific surface of the dried powder as measured by N_2 BET (single-point Brunauer-Emmett-Teller) adsorption isotherms was 41.1 ± 0.4 m^2/g. The powder X-ray diffraction pattern agreed with the structural data for crystalline α-Fe_2O_3 [67]. There was no evidence for goethite or other impurity phases. Sorption experiments of Np(V) on hematite were conducted at room temperature as a function of pH in the presence and absence of CO_2. Experiments under anaerobic condition were carried out in a glove box filled with Ar gas. All the solutions used under anaerobic condition were prepared with CO_2-free Milli-Q water (18 MΩ). The batch experiments with hematite were carried out following exactly the same procedure as for the sorption experiments with kaolinite.

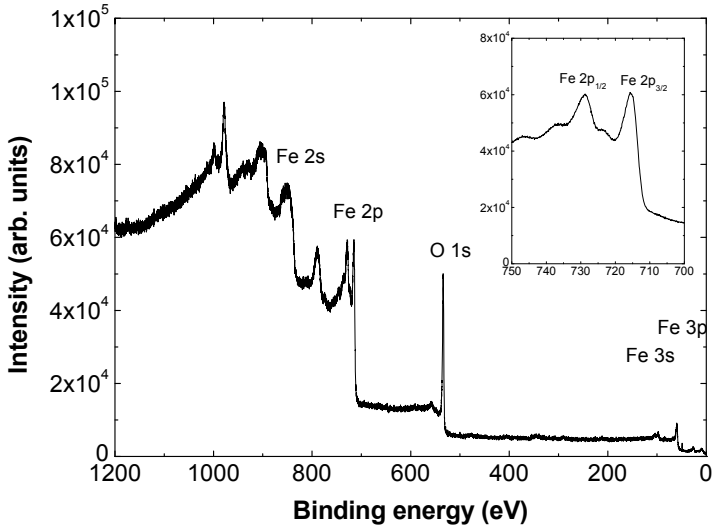

Figure 33: X-ray photoelectron spectra of synthetic hematite (α-Fe_2O_3). The spectra were corrected for Al Kα satellites due to non-monochromatic excitation.

The only difference was a smaller solid-to-liquid ratio of 0.5 g/L due to the larger surface area of hematite compared to kaolinite. Neptunium L_{III}-edge EXAFS spectra of Np(V) sorbed on hematite were collected at ROBL in fluorescence mode at room temperature and 13 K from wet pastes and dried powders, respectively.

6.1.2 Batch experiments

The results of sorption experiments on hematite are summarized in Fig. 34. In the air-equilibrated system, the uptake of Np(V) by hematite increased from pH 6.5 to 8.5 (84% sorption) and decreased above pH 8.5 due to the formation of Np(V)-carbonato complexes in aqueous solution. No decrease in Np uptake was observed when CO_2 was absent. The sorp-

tion maximum is ~100% in the pH range 9.5–10.5. The sorption edge occurs at pH 7.0 and 7.5 in both atmospheres, respectively. These observations agree with previous batch experiments of Kohler et al. [68]. They modeled their sorption data assuming inner-sphere sorption of Np(V) on hematite and formation of ternary Np-carbonato surface complexes. Since these and other surface complexes were postulated and have not been confirmed by spectroscopy, the XAFS experiments described below aimed at the speciation of Np(V) at the hematite surface.

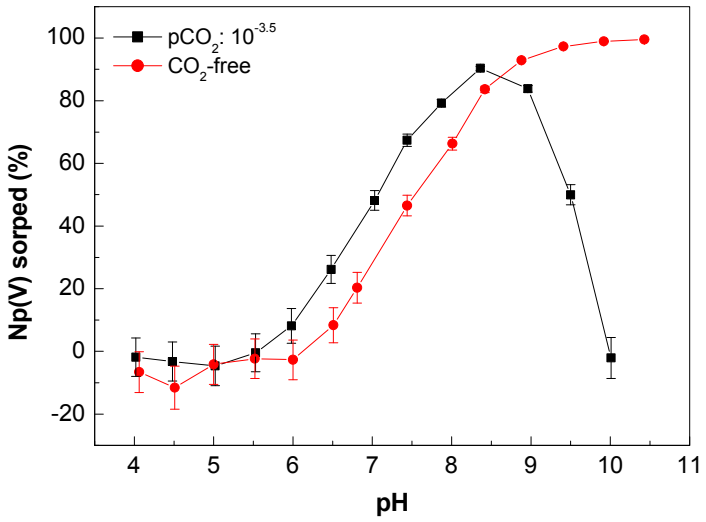

Figure 34: Sorption of 8 µM Np(V) on hematite (0.5 g/L) as a function of pH at 0.1 M $NaClO_4$ in the presence (p_{CO2} = $10^{-3.5}$ atm) and absence of CO_2.

6.1.3 XAFS measurements

Tab. 16 summarizes the preparation conditions of samples A–E and the amount of Np sorbed in each sample. Three XAFS samples, labeled A, B, and C, were prepared in the presence of ambient CO_2 at pH 7.0, 9.0, and 10.0, respectively. Samples D and E were prepared in a glove box with Ar atmosphere at pH 8.5 and 9.0, respectively. These samples can be compared with samples that were prepared in equilibrium with air. The total Np(V) concentration in each sample was 8 µM. The Np loading of the samples was approximately 500 ppm.

All Np L_{III}-edge XANES spectra of the samples show neither a shift in the absorption edge energy (at 17610 eV) nor a significant structure difference at the high energy side of XANES (data not shown). In all samples, Np was in the pentavalent oxidation state.

Table 16: Summary of XAFS samples prepared at 8 µM Np(V), 4.0 g /L, 0.1 M $NaClO_4$.

Sample	Atmosphere	T/K	pH	Np loading/ppm
A	CO_2	298	7.0	460
B	CO_2	13	9.0	469
C	CO_2	298	10.0	422
D	Ar	298	8.5	474
E	Ar	13	9.0	474

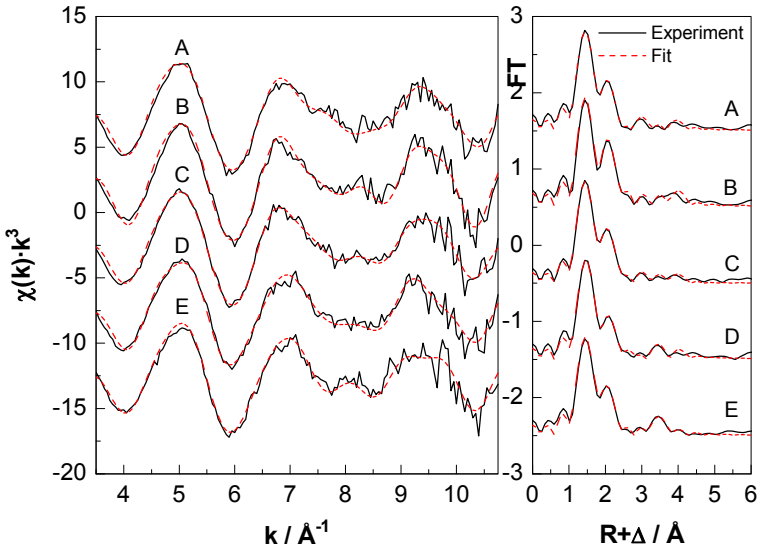

Figure 35: Np L_{III}-edge k^3-weighted EXAFS spectra (left) and their corresponding Fourier transform magnitudess (right) for Np(V) sorbed on hematite. See Tab. 16 for sample description.

The raw Np L_{III}-edge k^3-weighted EXAFS spectra of all samples together with the best fit to the data and their corresponding FTs are shown in Fig. 35. Note that the FTs are uncorrected for scattering phase shifts (R+Δ) causing peaks to appear at shorter distances. The EXAFS spectra of all samples show similar oscillations indicating similar Np near-neighbor

surroundings. The samples prepared in Ar atmosphere (D and E) show clearly a peak at ~3.5 Å in the FTs. (Fig. 35). The scattering interactions with Fe of the [FeO_6] octahedra of hematite are expected in this region.

The calculation of the best theoretical fit to the raw EXAFS data shown in Fig. 35 included two steps. In the first step, we assumed the NpO_2^+ cluster as a structural model (Fig. 36, lower left) and fitted the raw EXAFS data with the single scattering (SS) path Np–$O_{ax,}$ multiple scattering (MS) path Np–O_{ax}, SS path Np–O_{eq}, and SS path Np–$O_{(FeO6)}$. The distances of the Np-O_{ax}, Np-O_{eq}, and Np-$O_{(FeO6)}$ for all samples were 1.87 ± 0.01, 2.48 ± 0.02, and 2.86 ± 0.02, respectively, and agree with the formation of the NpO_2^+ cluster for the first two shells. The second step aimed at determining the structural parameters of possible Fe and Np shells. To be more sensitive in the fit to these minor components, we isolated the region of possible Fe and Np scattering contributions from the raw data according to the difference technique [69].

Briefly, the theoretical fit obtained in the first step was subtracted from the raw data followed by Fourier filtering of the residual in the R range of 3.0–4.5 Å. The residual EXAFS was modeled using the SS path Np-Fe and SS path Np-Np. For the final fit to the raw data, the coordination numbers of all shells were held constant at the values determined during the previous two modeling steps. The results are presented in Fig. 36, summarized and compared in Tab. 17 to the EXAFS data for $NpO_2(H_2O)_4^+$[51] and $NpO_2(CO_3)_3^{5-}$ [52].

An equally good fit to the EXAFS could be obtained by including a Np-Fe shell but without a Np-Np shell. The EXAFS measurements of samples D und E detected an Fe atom at a distance of 3.73 ± 0.01 Å. Samples A, B und C detected an Fe atom at a distance of 3.43 ± 0.02 Å. The Np-O_{eq} bond distances in all samples are comparable to or shorter than those for NpO_2^+ (aq.) [51] (see Tab. 17). All FTs contain a peak at 2.5 Å. This feature has been a structure part of the proposed sorption complex, because of its short distance. This peak at 2.5 Å is related to the Np-$O_{(FeO6)}$ shell. The obtained Np-O_{eq} distances in all samples are shorter than in $NpO_2(CO_3)_3^{5-}$(aq.) [52]. There is no significant difference in the Np-O_{eq} distances at pH 9.0 between samples B and E. In all samples there is also no evidence for the formation of Np(V) carbonato species at the hematite surface. At pH 9.0 and 10.0 the presence of HCO_3^-/CO_3^{2-} has no effect on the Np(V) species sorbed.

The EXAFS fits of all samples did not need any Np-Np interactions, which would indicate formation of polynuclear Np(V) species at the hematite surface.

According to the fit results, the structure model of possible Np(V) surface species on hematite is shown in Fig. 36 (upper left). One possible bidentate inner-sphere structural model implying an edge sharing between the Np(V) and Fe-octahedra was developed on the basis of structural parameters determined by EXAFS. Fig. 36 shows the coordination of Np(V) sorbed on hematite if the ∠(Np, Fe, $O_{(FeO6)}$) is ~ 60°. In this case the calculated Np-Fe and Np-$O_{(FeO6)}$ distances are in relative good agreement with fit results. In this model, a short distance of 2.0 Å is obtained between O_{ax} and $O_{(FeO6)}$. A more complicated model may be necessary to interpret the EXAFS results better.

As a conclusion, the EXAFS investigations indicate that Np(V) is coordinated directly to the surface [FeO_6] octahedra in a bidentate fashion. There is no spectroscopic evidence for the ternary carbonate complexes (e.g. ≡$FeONpO_2(O_2COH)_2^{2-}$) postulated by Kohler et al. [68]. In the system U(VI)/iron oxides, Waite et al. [8, 9] postulated the existence of (≡$FeO_2UO_2CO_3^{2-}$) ternary complexes to model U(VI) adsorption on ferrihydrite. They found that models not having this species underpredicted U(VI) uptake between pH 7 and 9.

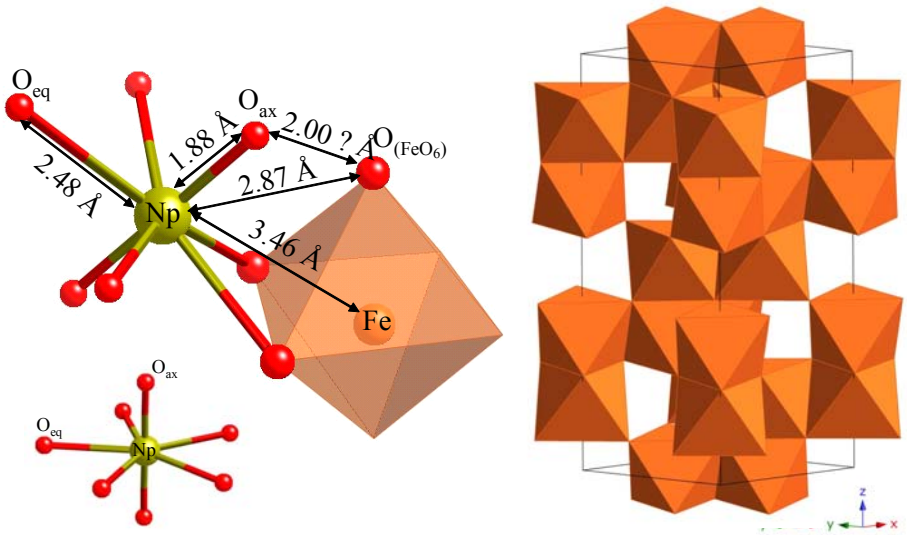

Figure 36: Schematic diagram illustrating a possible coordination environment of Np(V) on the hematite surface (upper left), the arrangement of the [FeO_6] octahedra in the hematite structure (right), and the neptunyl ion (NpO_2^+) used as a fit model (lower left).

They attributed this charge reversal to the presence of negatively charged U(VI)-carbonato-hematite complexes. Dent et al. [72] and Bargar et al. [59, 60] reported evidence form EXAFS for the existence of sorbed U(VI)-carbonato complexes on montmorillonite and hematite, respectively. The absence of Np(V)-carbonato complexes at the hematite surface observed in our EXAFS study agrees with several EXAFS measurements [8, 70, 73] of U(VI)/iron oxide systems.

Table 17: EXAFS structure parameters of Np(V) sorbed on hematite (R ±0.02 Å, σ^2 ±0.001 Å^2).

Sample	Description	2 × O_{ax}		4 × O_{eq}		2 × O		0.5 × Fe		ΔE_0
		R (Å)	σ^2 (Å^2)	R (Å)	σ^2 (Å^2)	R (Å)	σ^2 (Å^2)	R (Å)	σ^2 (Å^2)	(eV)
A	pH 7.0, air	1.87	0.003	2.48	0.010	2.86	0.016	3.43	0.006	5.7
B	pH 9.0, air, 13 K	1.88	0.002	2.48	0.006	2.84	0.010	3.44	0.011	7.0
C	pH 10.0, air	1.87	0.003	2.46	0.009	2.86	0.013	3.46	0.014	4.2
D	pH 8.5, Ar	1.88	0.003	2.49	0.013	2.87	0.010	3.74	0.003	7.2
E	pH 9.0, Ar, 13 K	1.87	0.003	2.46	0.010	2.84	0.015	3.73	0.002	5.1
[51]	$NpO_2(H_2O)_4^+$	1.82	0.002	2.49	0.006	-	-	-	-	-
[52]	$NpO_2(CO_3)_3^{5-}$	1.86	0.001	2.53	0.013	-	-	-	-	-

Manceau et al. [70] and Waite et al. [8] used EXAFS to study U(VI) sorption on ferrihydrite, but did not report any findings regarding carbonate ligands. Ho and Miller [71] observed that hematite particles, which were positively charged in near- and sub-neutral pH carbonate-bearing solutions (i.e., at pH 7.5), acquired net negative charges following adsorption of U(VI).

Conclusion

Batch sorption experiments at 8 µM Np(V), 0.5 g/L, and 0.1M $NaClO_4$ were conducted to determine the effects of varying pH and CO_2 on Np(V) sorption on hematite. The results show that sorption is strongly influenced by pH and ambient CO_2. In the absence of CO_2, Np(V) sorption increases continuously until 100 % sorption in pH range 9.5–10.5. For experiments open to atmospheric CO_2, Np(V) sorption increases up to pH 8.5 and decreases to zero at pH 10.0. A comparison of the pH dependence of Np(V) sorption with that of Np(V) aqueous speciation indicates a close correlation between Np(V) sorption and the intervals where Np(V)-carbonato and -hydroxo complexes are the dominating species in solution. In the presence of CO_2, sorption is inhibited at pH > 8 due to formation of aqueous Np(V)-carbonato complexes. The spectroscopic investigation shows that Np L_{III}-edge EXAFS spectroscopy is a valuable tool to determine the structure parameters for the Np near-neighbor environment at water-solid interfaces. The Np(V) species at the hematite surface have been identified as mononuclear, inner-sphere complexes. This is based on the absence of Np-Np interaction and the presence of a Np-Fe interaction near 3.5 Å. This distance is in accordance with an edge-sharing, bidentate surface complex, supporting the assumptions made Kohler et al. [68] regarding inner-sphere sorption. However, there was no evidence for the formation of ternary Np(V)-carbonato surface complexes. Therefore, our experiments do not support the existence of the ternary Np(V)-carbonato complexes (e.g. $\equiv FeONpO_2(O_2COH)_2^{2-}$) postulated by Kohler et al. [68].

7 Sorption of plutonium on kaolinite in the presence of humic substances

For the studies of the ternary system Pu(III)–Kaolinite–Humic substances (Pu(III)–K–HS) fixed concentrations of the reactants were used. Four different addition sequences of the components were chosen. The experimental conditions and the components addition sequences in the ternary system are summarized in Tab. 18.

The shortcuts are explained as follows: for example in case (A) K–Pu(III) –AHA means that the kaolinite was preconditioned, mixed first with Pu(III) and after a contact time of 48 h after verifying the sorption of Pu(III) on kaolinite, the AHA was added. The kaolinite was preconditioned for 48 h at the working pH before mixing it with the other components. The activity of the solutions was measured immediately after adding the freshly electrolyzed $^{239}Pu(III)$ by LSC. These were considered as the start concentrations before any sorption could take part, as the measurements were conducted immediately after the mixing of the phases. After mixing the first two fractions, the solutions were agitated by end-over-end rotation. After certain periods, in which the solutions were continuously agitated, aliquots were taken and centrifugation for 45 minutes at 2500 rpm was performed.

Table 18: Experimental conditions and the addition sequences of the components for the investigations of the ternary system.

Addition sequence	Concentration			pH	3rd component added after
	K	Pu	AHA		
(A) K- Pu(III)-AHA	4 g/L	$1x10^{-6}$M	25 mg/L	1 - 10	48 hours
(B) K-AHA-Pu(III)	4 g/L	$1x10^{-6}$M	25 mg/L	2, 4, 5, 6, 8, 10	48 hours
(C) AHA-Pu(III)-K	4 g/L	$1x10^{-6}$M	25 mg/L	2 – 10	28 days
(D) All together	4 g/L	$1x10^{-6}$M	25 mg/L	2, 4, 5, 6, 8, 10	all at the same time

Ionic Strength 0.1 M $NaClO_4$ K – kaolinite, AHA – Aldrich humic acid

Table 19: Experimental conditions and the addition sequence of the components for the investigations of the ternary system Pu(IV)-K-HS.

Addition sequence	Concentration			pH	3rd component added after
	K	Pu(IV)	HS		
(1) All together	4 g/L	$1x10^{-8}$M	10-100 mg/L	1, 3, 6, 9	all at the same time
(2) K-Pu(IV)-HS	4 g/L	$1x10^{-8}$M	10-100 mg/L	1, 3, 6, 9	48 hours
(3) HS- K-Pu(IV)	4 g/L	$1x10^{-8}$M	10-100 mg/L	1, 3, 6, 9	48 hours

Ionic Strength 0.1 M $NaClO_4$

The concentration of Pu and/or AHA in the supernatant was determined, and then this fraction was ultrafiltrated through filters with pore size 1 k Dalton. The amount of free plutonium in the filtrate was also measured. In this way it was possible to determine the amount of plutonium fixed on kaolinite, complexed with AHA, and the free plutonium. It was also possible to find out the percentage of sorption of AHA on kaolinite. In these experiments the influence of the addition sequence of the elements, reaction time, and pH on the sorption of Pu(III) on kaolinite in the presence of Aldrich humic acid could be observed.

The experimental conditions used for the studies of the ternary system Pu(IV)–K–HS are presented in Tab. 19. The experiments were performed similarly to the ones described for the ternary system Pu(III)–K–HA. For comparison, similar experiments were conducted with Th(IV) as a charge state analogue. The experimental conditions were similar with the exception that the concentration of Th(IV) was 10^{-13} M.

The influence of humic substances on the sorption of Pu(IV) and Th(IV) on kaolinite was investigated using three adding sequences of the reactants. The abbreviations are interpreted as follows: sequence 1 - all reactants are mixed at the same time; sequence 2 - a pre-equilibrium of metal ion and kaolinite was achieved and then the HS (HA or FA) were added; sequence 3 - a pre-equilibrium of kaolinite and HS was achieved; then the metal ion (Pu(IV) or (Th(IV)) was added. In the experiments, the influence of time, pH, and concentration of humic and fulvic acid on the sorption was observed.

Pu(IV)–K–HS; influence of the contact time

The kinetics of the sorption of Pu(IV) on kaolinite in the ternary systems (Pu(IV), HS, kaolinite) has been studied. The results indicate that the system reaches a sorption equilibrium within a few hours after addition of Pu(IV) and HS to the pre-equilibrated kaolinite suspension. Comparing the different sequences in which the reactants were added, no significant difference in the Pu(IV) sorption behavior as a function of time was found.

Pu(IV)–K–HS; influence of pH

The presence of HS influences significantly the sorption of Pu(IV) on kaolinite. This was studied at pH 1, 3, 6, and 9 in varying adding sequences (1, 2, 3) at a HS concentration range of 10–100 mg/L. While the sorption behavior of Pu(IV) on kaolinite in the ternary system is comparable to the case of the binary system (kaolinite-metal ion) at pH 3 and 6, an obvious decrease of the sorption of Pu(IV) is observed at pH 1 in all adding sequences in the ternary system.

Pu(IV)–K–HS; influence of HS concentration

Sorption experiments have been conducted at constant pH values (pH = 1, 3, 6, 9) and ionic strength (I = 0.1 M $NaClO_4$) as a function of the HS concentration between 10-100 mg/L. In general, Pu sorption on kaolinite decreases when the HS concentration increases regardless of the pH and adding sequence of the reactants. This might be explained by the increased number of binding sites of HS with increasing HS concentration in the solution.

Pu(IV)–K–HS; influence of the adding sequence

For the sorption of Pu(IV) on kaolinite in the presence of HS, a slight effect was observed on the adding sequences of the reactants (Pu(IV), kaolinite, HS). The results obtained when Pu(IV) is pre-equilibrated with kaolinite before addition of FA/HA (sequence 2) and when Pu(IV) is added to the pre-equilibration of kaolinite and FA/HA (sequence 3) do not show

strong deviations. The sorption of Pu(IV) is just slightly hindered when FA/HA and kaolinite are equilibrated before adding the metal (sequence 3).

Sorption of Pu(IV) on kaolinite in presence and absence of HS

The sorption of Pu(IV) on kaolinite is lower in the presence of HS compared to the system free of HS. This effect has been observed as a function of FA/HA concentration due to the competition reactions between kaolinite, sorbed fulvic and humic acid sites, free HS, and plutonium ions. For comparison, the influence of HS on the sorption of Th(IV) on kaolinite was also investigated and a good agreement with the results of Pu(IV) was obtained. Sachs et al. [74] reported recently a slightly lower sorption of Np(V) and U(VI) on kaolinite in the presence of HA compared to the HA-free system. Kautenburger et al. [75] showed a similar phenomenon for the sorption of Eu(III) and Gd(III) on kaolinite in the presence of HA compared with the system without HA in the alkaline pH range.

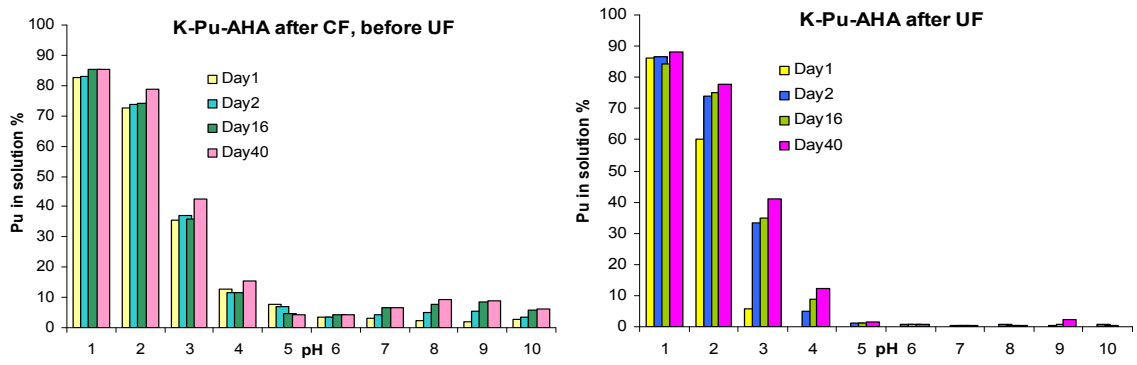

Figure 37: The influence of Aldrich humic acid on the sorption of Pu(III) on kaolinite as a function of pH and time; the measurements were performed 1, 2, 16, and 40 days after adding the AHA to the Pu(III)-K suspension.

Pu(III)–K–HA; influence of the contact time and pH

The amount of plutonium found in solution after various periods of time in the experiment (A) (see Tab. 18) after the separation from the solid phase through centrifugation (a CF) before (b UF) and after the ultrafiltration (a UF) as a function of pH can be seen in Fig. 37. At pH 1 and 2, no significant influences of the humic acid on the sorption of plutonium on kaolinite are observed as at this acidic pH the sorption is low, and the humic acid is precipitated. At pH 4, it was observed that the amount of plutonium found free in solution after the separation from AHA is slightly increasing with time. Most notable is the increase of plutonium found after the centrifugation in solution at pH 7–10 after longer periods of time. The data resulting from the subsequent ultrafiltration, presented in the right part of Fig. 37, show clearly that this part of plutonium is complexed with humic acid, as it is not found in solution after the ultrafiltration.

This is a clear indication that the humic acid found free in solution, is interacting with the plutonium sorbed on the surface of the kaolinite, and is able to transfer some parts of it into solution leading thus to a remobilization of it. A completely different sorption curve was found in the experiment (C) as presented in Fig. 38. It was found that at pH 3, the concentration of plutonium found free in solution after centrifugation, was lower compared to experiment (A).

The alteration of the sorption over the time was observed in all the experiments performed for the investigation of the K–Pu(III)–HA system. It can be observed that the time of contact has an opposite effect on the equilibria as in the two systems presented in Fig. 37 and Fig. 38.

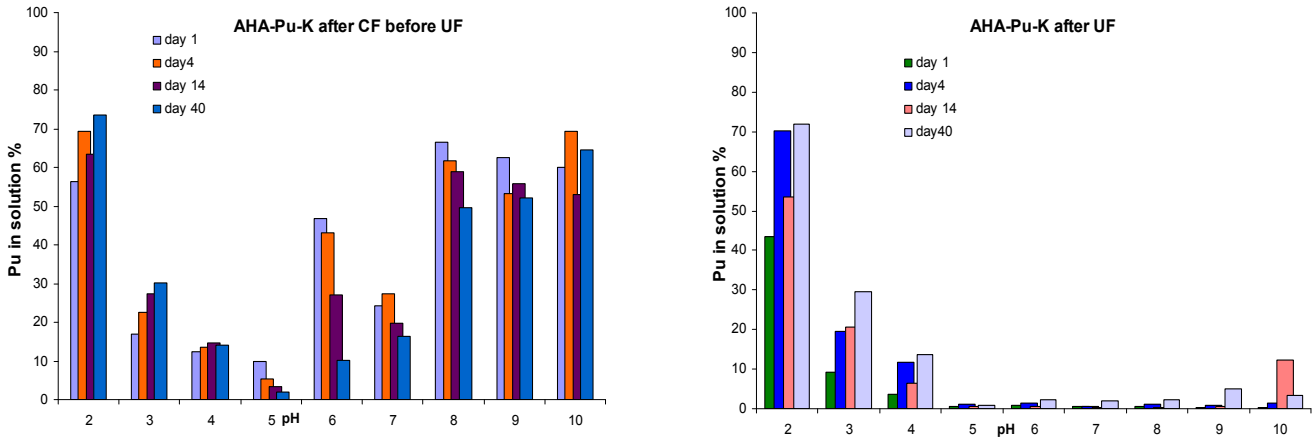

Figure 38: The sorption of plutonium complexed with Aldrich humic acid on kaolinite.

In case A, the concentration of plutonium is slowly increasing in solution with contact time at pH > 4 , while in the case C, the opposite tendency is observed. It was concluded that the 40 days in which the sorption was observed were not sufficient for attaining equilibrium.

Pu(III)–K–HA; influence of the pH and adding sequence

The influence of humic acid on the sorption coefficient K_d of plutonium on kaolinite was also investigated. The K_d values were calculated as presented in eq. (1) using the experimental data obtained after 40 days from the moment of contact of all three phases.

$$K_d = \frac{\Gamma}{C} \text{ (L/kg)} \qquad (1)$$

Γ - the adsorbed amount per unit mass of solid [mol/kg]

C – the equilibrium concentration of Pu(III) [mol/L]

Fig. 39 presents the K_d values obtained for the four adding sequences in comparison with the results obtained for the sorption of Pu(III) with the same concentration, under argon atmosphere, in the absence of humic acid.

It is observed that at pH < 6 the humic acid enhances the sorption of metal ion on kaolinite when the addition sequence is that from the experiments (A), (B), and (C). When the components come in contact all at the same time, the adsorption coefficient are almost not affected by the presence of AHA at pH < 6. It can also be observed that the humate-plutonium complexes are sorbed easier than the free plutonium on kaolinite, or on a HA coated kaolinite surface at pH < 6. Above pH 6, the sorption of Pu(III) on kaolinite is hindered by AHA depending strongly on the adding sequence of the components. In this pH range, the sorption of the humate-plutonium complexes is lower than the one corresponding to the sorption of uncomplexed plutonium.

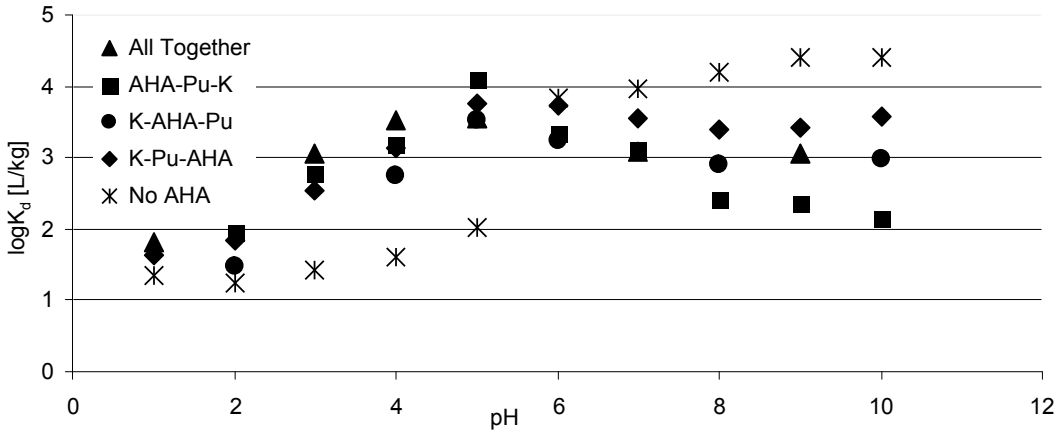

Figure 39: K_d values for the sorption of plutonium(III) on kaolinite as a function of pH. Comparison between different adding sequences of humic acid (AHA), kaolinite (K), and plutonium (Pu); I = 0.1 M $NaClO_4$, [K] = 4 g/L, [AHA] = 25 mg/L, and Pu(III)] = 1×10^{-6} M.

Pu(III)–K–HA; speciation of the sorbed species

The question whether the metal ion (M) is directly sorbed on kaolinite or a humate mediated sorption takes place is difficult to answer. The following hypotheses were considered:

the sorption of metal ion (M) and humic substances are independent of each other

- K-AHA-M bridge is formed
- K-M-AHA bridge is formed

Several authors have concluded that the metal complexation with humic substances sorbed on mineral surfaces is stronger than humate complexation in solution [76, 77], so the first hypothesis is less likely to happen.

Because of the relatively limited possibilities of speciation of the sorbed species, attempts to determine chemically the form of binding to the solid surface were performed. It was proven in previous experiments that at pH ~ 1 Pu(III) is almost completely desorbed from kaolinite, while at pH ~ 11 it remains strongly fixed. On the other hand, humic acid is strongly sorbed on kaolinite at low pH values, but desorbed at pH ~ 11. Assuming that no other interactions take part, if a K-AHA-M bridge is formed, the AHA-M complex should be desorbed from the kaolinite when the pH of the solution is ~ 11. On the contrary, when a K-M-AHA bridge is formed, M-AHA will remain fixed at pH ~ 11 and will only be desorbed when the pH is lowered.

The adding sequences (A) and (C) were used for these investigations. After determining the sorption of AHA and Pu(III) on kaolinite in batch experiments, the pH of the solutions was first increased to pH ~ 11 by adding NaOH. The reaction vials were agitated for 48 hours, centrifuged and the activity of the supernatant determined ("basic desorption"). Afterwards, the supernatant was removed and ultrafiltrated with the purpose to determine whether the desorbed plutonium is complexed by AHA or not. A fresh solution of 0.1 M $NaClO_4$ with pH ~ 1 was mixed with the separated solid phase from the earlier experiment. After another 48 hours of agitating, the suspension was again centrifuged, and the activity of the liquid phase was determined by LSC providing information on the desorption under acidic conditions ("acid desorption"). The supernatant was also ultrafiltrated and the free plutonium ion content was determined by LSC in the filtrate. It was found that the desorption takes place differently in the two cases, especially the "acid desorption" as can be see in Fig. 40.

The obtained data are not yet completely understood and further experiments are required. It could be assumed that the low amount of plutonium sorbed on kaolinite in experiment (C) (see Fig. 39) is not sorbed as a complex but as metal ion, thus it is readily desorbed at pH < 1 similar to the case when no humic acid is present. This assumption was also sustained by the fact that plutonium was found in the filtrate after ultrafiltration. The part of plutonium sorbed as a humate complex is only in smaller amounts desorbed at either basic or acidic pH. It could be concluded that, although the sorption of Pu(III) on kaolinite is impaired by the presence of humic acids, once sorbed, the plutonium-humate complexes are stronger desorbed over the entire pH range, than the metal alone.

So far, it was not possible to determine in which form plutonium and the humic acid are sorbed on kaolinite in the ternary system (over K-Pu-AHA bridges or K-AHA-Pu bridges).

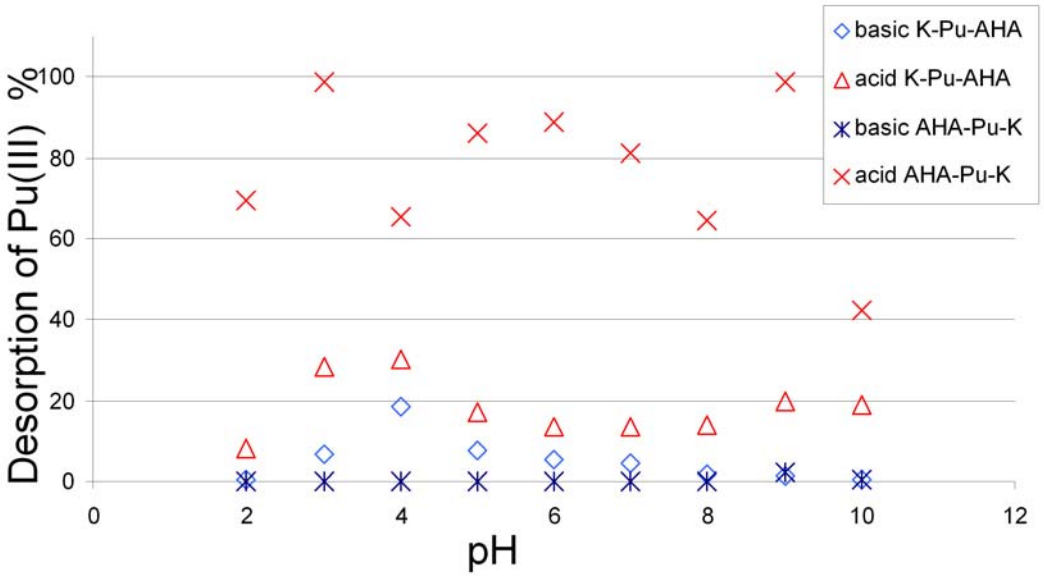

Figure 40: Influence of the pH and adding sequence of the components on the desorption of Pu(III) and Pu(III)-AHA complexes from kaolinite at pH ~ 11 (basic) and pH ~ 1 (acidic).

8 Summary and outlook

The purpose of this work was to accumulate data on the behavior of the light actinides with respect to their migration into the environment.

It was assumed that by complexation with humic substances (HS) the actinides are easier transported in the ground waters, while, on the other hand their sorption on the surrounding geological barriers leads to an immobilization. Therefore, these two contradictory processes were investigated in the binary systems HS-Pu, kaolinite (K), and hematite (HE)–An; HS-K, and in the ternary system and K–HS–Pu.

The redox chemistry of plutonium in contact with humic substances was studied. It was found that under natural relevant conditions plutonium is reduced to Pu(III) and Pu(IV) in the presence of HS. The focus was therefore put on the investigation of these two species in contact with humic substances and mineral phases.

The complexation constant of Pu(III) with Aldrich AHA was found to be $\log ß_{Pu(III)}$ = 6.2–6.9 and for Pu(IV) with the same humic acid $\log ß_{Pu(IV)}$ = 6.4–8.4. As comparison, the complexation of the charge state analogue Am(III) with AHA was investigated for Pu(III). The results were in good agreement between the two actinides, as well as with the literature data.

Furthermore, the sorption of Pu(III), Pu(IV), Np(V), and U(VI) on kaolinite was studied. Fig. 41 shows the individual sorption curves of the four species, as a function of pH in the presence of ambient CO_2.

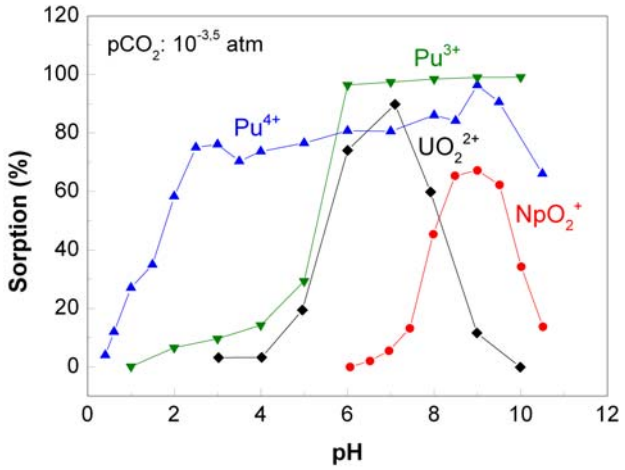

Figure 41: Sorption of Pu(III), Pu(IV), Np(V), and U(VI) on kaolinite as a function of pH in the presence of CO_2.

The sorption experiments were conducted under atmospheric conditions as well as under inert gas conditions. It was found that CO_2 has a distinct influence on the sorption of the actinides, depending strongly on the oxidation state.

For comparison, studies of the sorption of Am(III) and Th(IV) on kaolinite were performed. The sorption curves found were in good agreement with the ones found for Pu(III) and Pu(IV).

XAFS measurements were carried out for the sorbed species in order to determine their speciation on the surface of the mineral. Pu(IV) was determined on the surface of kaolinite, even when its oxidation state was Pu(III) before the sorption took place. Also, it was established that it undergoes an inner sphere sorption with Pu-O distances at 2.27 – 2.34 Å, Pu-Al/Si distances at 3.62 – 3.66 Å, and Pu-Pu distances at ~ 3.70 Å.

From the EXAFS investigations conducted for Np(V) on kaolinite, it was concluded that in air-equilibrated system the average distances of the Np-O_{ax} (1.84 Å), Np-O_{eq} (2.56 Å), Np-C (3.00 Å), and Np-O_{dis} (4.25 Å) coordination shells agree with those of the $[NpO_2(CO_3)_3]$ moiety. The bidentate coordination of two CO_3^{2-} groups to NpO_2^+ indicates inner- or outer-sphere sorption of $NpO_2(CO_3)_2^{3-}$ at the kaolinite surface. The precipitation of Np(V) carbonate at an initial concentration of 8 µM Np(V) can be ruled out based on the sorption isotherm measurements. The Np(V) surface complexes in the CO_2-free system showed two prominent co-

ordination shells, i.e., Np-O_{ax} and Np-O_{eq} at 1.87 and 2.47 Å, respectively. The Np-O_{eq} distance is slightly shorter than the corresponding value for the Np(V) aquo ion of 2.49 Å, indicating inner-sphere sorption of NpO_2^+ on the kaolinite surface.

For U(VI) the EXAFS experiments showed that inner-sphere monomeric surface complexes are formed with kaolinite in the pH range 5.0 -8.5. The data could be best fitted with two U-Al/Si interactions at 3.1 and 3.3 Å.

The sorption of humic substances on kaolinite was also investigated. It was found that at acidic pH the sorption is strong, while at higher pH value it decreases drastically. From XPS studies it was concluded that the surface of the clay particles is not covered by a homogenous layer of HA. Part of the HA must be distributed between the clay particles. All HA/kaolinite samples show the same surface composition with respect to Si, Al, and O as the untreated kaolinite. The chemical composition of the kaolinite surface was not altered by HA adsorption or during HA synthesis.

The experimental intensity ratios Si2p/Al2p and O1s/Al2p agree with the theoretical values that were calculated according to the chemical composition of kaolinite, i.e., $Al_2[Si_2O_5(OH)_4]$.

The experiments performed for the study of the sorption of Np(V) on hematite showed that the sorption is strongly influenced by pH and ambient CO_2. In the presence of CO_2 the sorption is inhibited at pH > 8. The EXAFS investigations showed that the Np(V) species identified at the surface of the hematite are mononuclear, inner-sphere complexes. There was no evidence found for the formation of ternary Np(V) carbonato surface complexes.

The ternary system Pu(III)/Pu(IV) – HS – K was also investigated. It could be proven that the immobilization of the actinides by sorption on mineral phase is dependent on pH, concentration of HS, nature of HS (humic or fulvic acid), and in the case of Pu(III) on the sequence in which the components are added to the system. While the sorption of plutonium is enhanced at pH < 6 by the presence of HS, the contrary happens at pH > 6 where the sorption is impeded by the presence of HS.

For a better understanding of the processes that take place in the ternary system Pu–K–HS, XAFS measurements are planned for the future.

Also, experiments concerning the sorption of Pu(III), Pu(IV), Np(V), and U(VI) on Opalinus Clay are in progress at our institute.

The speciation methods CE-RIMS and CE-DAD-ICP-MS will be applied for the speciation of ultra trace amounts of plutonium and for the determination of the complexation constants of actinides with HA and FA, respectively.

9 References

1. Bodansky, D., Nuclear Energy: Principles, Practices, and Prospects. Springer-Verlag: New York, 2004.

2. Gomper, K., Zur Abtrennung langlebiger Radionuklide. In Radioaktivität und Kernenergie, Hoffmann, J.; Kuczera, B., Eds. Forschungszentrum Karlsruhe: 2001; 153.

3. Kaszuba, J. P.; Runde, W. H., The aqueous geochemistry of neptunium: Dynamic control of soluble concentrations with applications to nuclear waste disposal. Environ. Sci. Technol. 1999, 33, 4427.

4. Chipera, S. J.; Bish, D. L., Baseline studies of the Clay Minerals Society source clays: Powder X-ray diffraction analyses. Clays Clay Minerals 2001, 49, 398.

5. Kogel, J. E.; Lewis, S. A., Baseline studies of the Clay Minerals Society source clays: Chemical analysis by inductively coupled plasma-mass spectroscopy (ICP-MS). Clays Clay Minerals 2001, 49, 387.

6. Mermut, A. R.; Cano, A. F., Basline studies of the Clay Minerals society source clays: Chemical analysis of major elements. Clays Clay Minerals 2001, 49, 381.

7. Moll Jr, W. F., Basline studies of the Clay Minerals Society source clays: Geological origin. Clays Clay Minerals 2001, 49, 374.

8. Waite, T. D.; Davis, J. A.; Payne, T. E.; Waychunas, G. A.; Xu, N., Uranium(VI) adsorption to ferrihydrite: Application of a surface complexation model. Geochim. Cosmochim. Acta 1994, 58, 5465.

9. Waite, T. D.; Payne, T. E.; Davis, J. A.; Sekine, K., Uranium sorption: Alligator Rivers analogue project; final report. Australian Nuclear Science and Technology Organization 1997, 13.

10. Kim, J. I.; Buckau, G. Characterization of reference and site specific humic acids; TU München, RCM-Report 02188: 1988.

11. Kim, J. I.; Buckau, G.; Li, G. H.; Duschner, H.; Psarros, N. Z., Characterization of humic acid and fulvic acids from Gorleben groundwater. Fresenius Z. Anal. Chem. 1990, 338, 245.

12. Payne, T. E.; Davis, J. A.; Lumpkin, G. R.; Chisari, R.; Waite, T. D., Surface complexation model of uranyl sorption on Georgia kaolinite. Appl. Clay Sci. 2004, 26, 151.

13. Pruett, R. J.; Webb, H. L., Sampling and analysis of KGa-1b well-crystallized kaolin source clay. Clays Clay Minerals 1993, 41, 514.

14. Albinsson, Y.; Ekberg, C.; Holgersson, S.; Jakbobsson, A. M.; Lendgren, A.; Skarnemark, G., A method for preparation and purification of ^{234}Th. Appl. Radiat. Isot. 2002, 56, 681.

15. Cohen, D., The absorption spectra of plutonium ion in perchloric acid solutions. J. Inorg. Nucl. Chem. 1961, 18, 211.

16. Cohen, D., Electrochemical studies of plutonium ions in percholoric acid solutions. J. Inorg. Nucl. Chem. 1961, 18, 207.

17. Rudolph, W.; Kratz, K. L.; Herrmann, G., Half-lives, fission yields and neutron emission probabilities of neutron-rich antimony isotopes. J. Inorg. Nucl. Chem. 1977, 39, 753.

18. Neu, M. P.; Hoffman, C. D., Comparison of chemical extractions and laser photoacustic spectroscopy for the determination of plutonium species in near-neutral carbonate solutions. Radiochim. Acta 1994, 66/67, 251.

19. Kuczewski, B.; Marquardt, C. M.; Seibert, A.; Geckeis, H.; Kratz, J. V.; Trautmann, N., Separation of plutonium and neptunium species by capillary electrophoresis-inductively coupled plasma-mass spectrometry and application to natural groundwater samples. J. Anal. Chem. 2003, 75, 6769.

20. Grüning, C.; Huber, G.; Klopp, P.; Kratz, J. V.; Kunz, P.; Passler, G.; Trautmann, N.; Waldek, A.; Wendt, K., Resonance ionization mass spectrometry for ultratrace analysis of plutonium with a new solid state laser system. Int. J. Mass Spectrom. 2004, 235, 171.

21. Matz, W.; Schell, N.; Bernhard, G.; Prokert, F.; Reich, T.; Claußner, J.; Oehme, W.; Schlenk, R.; Dienel, S.; Funke, H.; Eichhorn, F.; Betzl, M.; Pröhl, D.; Strauch, U.; Hüttig, G.; Krug, H.; Neumann, W.; Brendler, V.; Reichel, P.; Denecke, M. A.; Nitsche, H., ROBL-a CRG beamline for radiochemistry and materials research at the ESRF. J. Synchrotron Rad. 1999, 6, 1076.

22. Denecke, M. A.; Rothe, J.; Dardenne, K.; Blank, H.; Hormes, J., The INE-beamline for actinide reseach at ANKA. Physica Scripta 2005, 115, 1001.

23. Newville, M.; Livins, P.; Yacoby, Y.; Rehr, J. J.; Stern, E. A., Near edge X-ray-absorption fine structure of Pb: A comparison of theory and experiment. Phys. Rev. B 1993, 47, 14126.

24. George, G. N.; Pickering, I. J., EXAFSPAK: A suite of computer programs for analysis of x-ray absorption spectra. Stanford Synchrotron Radiation Laboratory, Stanford, CA, USA 2000.

25. Ankudinov, A. L.; Bouldin, C. E.; Rehr, J. J.; Sims, J.; Hung, H., Parallel calculation of electron multiple scattering using Lanczos algorithms. Phys. Rev. B 2002, 65, 104107/1.

26. Ankudinov, A. L.; Ravel, B.; Rehr, J. J.; Conradson, S. D., Real space multiple scattering calculation of XANES. Phys. Rev. B 1998, 58, 7565.

27. Demartin, F.; Gramaccioli, C. M.; Pilati, T., The importance of accurate crystal structure determination of uranium minerals. II. Soddyite $(UO_2)_2(SiO_4)\cdot 2H_2O$. Acta Crystallogr. C 1992, 48, 1.

28. Volkov, Y. F.; Tomilin, S. V.; Visyashcheva, G. I.; Kapshukov, I. I., Carbonate compounds of pentavalent actinides with alkali metal cations, X-ray structure analysis of $LiNpO_2CO_3$ and $NaNpO_2CO_3$. Radiokhimiya 1979, 21, 668.

29. Bacmann, M.; Bertaut, E. F., Structure du nouveau compose $UFeO_4$. Bull. Soc. Franc. Mineral. Crist. 1967, B90, 257.

30. Nunnemann, M.; Erdmann, N.; Hasse, H. U.; Huber, G.; Kratz, J. V.; Kunz, P.; Mansel, A.; Passler, G.; Trautmann, N.; Waldek, A., Trace analysis of plutonium in environmental samples by resonance ionization mass spectrometry (RIMS). J. Alloys Compd. 1998, 271, 45.

31. Trautmann, N.; Passler, G.; Wendt, K. D. A., Ultratrace analysis and isotope ratio measurements of long-lived radioisotopes by resonance ionization mass spectrometry (RIMS). Anal. Bioanal. Chem. 2004, 378, 348.

32. Bürger, S.; Banik, N. L.; Buda, R. A.; Kratz, J. V.; Kuczewski, B.; Trautmann, N., Speciation of the oxidation states of plutonium in aqueous solutions by UV-vis spectroscopy CE-ICP-MS and CE-RIMS. Radiochim. Acta 2007, 95, 1.

33. Seibert, A.; Mansel, A.; Marquardt, C. M.; Keller, H.; Kratz, J. V.; Trautmann, N., Complexation behaviour of neptunium with humic acid. Radiochim. Acta 2001, 89, 505.

34. Kim, J. I.; Czerwinski, K. R., Complexation of metal ions with humic acid: metal ion charge neutralization model. Radiochim. Acta 1996, 73, 5.

35. Ambard, C.; Delorme, A.; Baglan, N.; Aupiais, J.; Pointurier, F.; Madiac, C., Interfacing capillary electrophoresis with inductively coupled plasma mass spectrometry for redox speciation of plutonium. Radiochim. Acta 2005, 93, 665.

36. Jianxin, T.; Yaozhong, C.; Zhangji, L., A kinetic study of the reduction of plutonium with humic acid. Radiochim. Acta 1993, 61, 73.

37. Choppin, G. R., Actinide speciation in the environment. Radiochim. Acta 2003, 91, 645-650.

38. Marquardt, C. M.; Seibert, A.; Artinger, R.; Denecke, M. A.; Kuczewski, B.; Schild, D.; Fanghänel, T., The redox behaviour of plutonium in humic rich groundwater. Radiochim. Acta 2004, 92, (9-11), 617.

39. Kuczewski, B. Trennung der Oxidationsstufen des Plutoniums mit CE-ICP-MS und Untersuchung des Redoxverhaltens von Plutonium im Grundwasser. Johannes Gutenberg-Universität Mainz, PhD Thesis, 2004.

40. Andre, C.; Choppin, G. R., Reduction of Pu(VI) by humic acid. Radiochim. Acta 2000, 88, 613.

41. Choppin, G. R., Humics and radionuclide migration. Radiochim. Acta 1988, 44/45, 23.

42. Bitea, C.; Kim, J. I.; Kratz, J. V.; Marquardt, C.; Neck, V.; Seibert, A.; Walther, C.; Yun, J. I., A study of colloid generation and disproportionation of Pu(IV) in aquatic solutions by LIBD and LPAS. Institut für Kernchemie, Universität Mainz, Germany, Annual Report 2002, C4.

43. Mizera, J.; Mizerova, G.; Benes, P., Radiotracer study of europium interaction with humic acid using electrophoresis, ultrafiltration and dialysis. J. Radioanal. Nucl. Chem. 2005, 263, 75.

44. Gustafsson, J. P., Geochemical equilibrium speciation model Visual MINTEQ V. 2.5. Stockholm, Sweden, U.S. Environmental Protection Agency 2006.

45. Nitsche, H.; Lee, S. C.; Gatti, R. C., Determination of plutonium oxidation states at trace level pertinent to nuclear waste disposal. J. Radioanal. Nucl. Chem. 1988, 124, 171.

46. Huertas, J. F.; Chou, L.; Wollast, R., Mechanism of kaolinite dissolution at room temperature and pressure: Part 1. Surface speciation. Geochim. Cosmochim. Acta 1998, 62, 417.

47. Neck, V.; Altmaier, M.; Seibert, A.; Yun, J. I.; Marquardt, C. M.; Fanghänel, T., Solubility and redox reactions of Pu(IV) hydrious oxide: Evidence for the formation of PuO_{2+x}(s, hyd). Radiochim. Acta 2007, 95, 193.

48. Neck, V.; Runde, W.; Kim, J. I.; Kanellakopulos, B., Solid-liquid equilibrium reaction of neptunium(V) in carbonate solution at different ionic strength. Radiochim. Acta 1994, 65, 29.

49. Niitsu, Y.; Sato, S.; Ohashi, H.; Sakamoto, Y.; Nagao, S.; Ohnuki, T.; Muraoka, S., Effect of humic acid on the sorption of neptunium(V) on kaolinite. J. Nucl. Mater. 1997, 1997, 328.

50. Kohler, M.; Wieland, E.; Leckie, J. O. In Actinides and their daughter and fission products, geochemistry of important radionuclides in geological repository, 7th International Symposium on Water-Rock Interaction-WIR-7, 1992; Kharaka, Y. K.; Meast, A. S., Eds. Balkema, Rotterdam: 1992; 51.

51. Reich, T.; Bernhard, G.; Geipel, G.; Funke, H.; Hennig, C.; Rossberg, A.; Matz, W.; Schell, N.; Nitsche, H., The Rossendorf Beamline ROBL-A dedicated experimental station for XAFS measurements of actinides and other radionuclides. Radiochim. Acta 2000, 88, 633.

52. Clark, D. L.; Conradson, S. D.; Ekberg, S. A.; Hess, N. J.; Neu, M. P.; Palmer, P. D.; Runde, W.; Tait, C. D., EXAFS studies of pentavalent neptunium carbonato complexes. Structural elucidation of the principal constituents of neptunium in groundwater environments. J. Am. Chem. Soc. 1996, 118, 2089.

53. Sekine, K.; Payne, T. E.; Waite, T. D.; Davis, J. A., International Alligator Rivers analogue project (18): Experimental study of uranium adsorption on kaolinite-pH dependence in air-equilibrated system. JAERI Memo 03-036 1991.

54. Redden, G. D.; Li, J.; Leckie, J. O., Adsorption of U^{VI} and citric acid on goethite, gibbsite, and kaolinite. In Adsorption of Metals by Geomedia, Jenne, E. A., Ed. Academic Press: San Diego, 1998; 291.

55. Thompson, H. A.; Parks, G. A.; Brown Jr., G. E., Structure and composition of uranium^{VI} sorption complexes at the kaolinite-water interface. In Adsorption of Metals by Geomedia, Jenne, E. A., Ed. Academic Press: San Diego, 1998; 349.

56. Allen, P. G.; Bucher, J. J.; Shuh, D. K.; Edelstein, N. M.; Reich, T., Investigation of aquo and chloro complexes of UO_2^{2+}, NpO_2^{+}, Np^{4+}, and Pu^{3+} by X-ray absorption fine structure spectroscopy. Inorg. Chem. 1997, 36, 4676.

57. Bernhard, G.; Geipel, G.; Reich, T.; Brendler, V.; Amayri, S.; Nitsche, H., Uranyl(VI) carbonate complex formation: Validation of the $Ca_2UO_2(CO_3)_3$(aq.) species. Radiochim. Acta 2001, 89, 511.

58. Hennig, C.; Reich, T.; Dähn, R.; Scheidegger, A. M., Structure of uranium sorption complexes at montmorillonite edge sites. Radiochim. Acta 2002, 90, 653.

59. Bargar, J. R.; Reitmeyer, R.; Davis, J. A., Spectroscopic confirmation of uranium(VI)-carbonato adsorption complexes on hematite. Environ. Sci. Technol. 1999, 33, 2481.

60. Bargar, J. R.; Reitmeyer, R.; Lenhart, J. J.; Davis, J. A., Characterization of U(VI)-carbonato ternary complexes on hematite: EXAFS and electrophoretic mobility measurements. Geochim. Cosmochim. Acta 2000, 64, 2737.

61. Křepelová, A.; Sachs, S.; Bernhard, G., Uranium(VI) sorption on kaolinite in the presence and absence of humic acid. Radiochim. Acta 2007, 94, 825.

62. Samadfam, M.; Jintoki, T.; Sato, S.; Ohashi, H.; Mitugashira, T.; Hara, M.; Suzuki, Y., Effects of humic acid on the sorption of Am(III) and Cm(III) on kaolinite. Radiochim. Acta 2000, 88, 717.

63. Briggs, D.; Grant, J. T., Surface Analysis by Auger and X-ray Photoelectron Spectroscopy. IM Publications: West Sussex, 2003.

64. Sachs, S.; Schmeide, K.; Brendler, V.; Křepelová, A.; Mibus, J.; Geipel, G.; Heise, K. H.; Bernhard, G., Investigation of the complexation and migration of actinides and non-radioactive substances with humic acids under geogenic conditions: Complexation of humic acids with actinides in the oxidation state IV Th, U, Np. Wissenschaftliche Berichte, Forschungszentrum Rossendorf 2004, FZR-399, 4.

65. Sachs, S.; Bernhard, G., Study of the humic acid synthesis in the presence of kaolinite and of the U(VI) adsorption on a synthetic humic substance-kaolinite sorbate. Institut für Radiochemie, Forschungszentrum Rossendorf, Annual Report 2005, FZR-419, 49.

66. Schwertmann, U.; Cornell, R. M., Iron Oxides in the Laboratory: Preparation and Characterization. Wiley-VCH: Weinheim, 2000.

67. Maslen, E. N.; Streltsov, V. A.; Streltsova, N. R.; Ishizawa, N., Synchrotron x-ray study of the electron density in α-Fe_2O_3. Acta Crystallogr. B 1994, 50, 435.

68. Kohler, M.; Honeyman, B. D.; Leckie, J. O., Neptunium(V) sorption on hematite (α-Fe_2O_3) in aqueous suspension: The effect of CO_2. Radiochim. Acta 1999, 85, 33.

69. Teo, B. K., EXAFS: Basic Principles and Data Analysis. Springer-Verlag: Berlin, 1986.

70. Manceau, A.; Charlet, L.; Boisset, M. C.; Didier, B.; Spadini, L., Sorption and speciation of heavy metals on hydrous Fe and Mn oxides. From microscopic to macroscopic. Appl. Clay Sci. 1992, 7, 201.

71. Ho, C. H.; Miller, N. H., Adsorption of uranly species from bicarbonate solution on hematite particles. J. Colloid Interface Sci. 1986, 110, 165.

72. Dent, A. J.; Ramsay, J. D. F.; Swanton, S. W., An EXAFS study of uranyl ion in solution and sorbed on silica and montmorillonite clay colloids. J. Colloid Interface Sci. 1992, 150, 45.

73. Reich, T.; Moll, H.; Arnold, T.; Denecke, M. A.; Hennig, C.; Geipel, G.; Bernhard, G.; Nitsche, H.; Allen, P. G.; Bucher, J. J.; Edelstein, N. M.; Shuh, D. K., An EXAFS study of uranium(VI) sorption on silica gel and ferrihydrite. J. Electron Spectrosc. Related Phenom. 1998, 96, 237.

74. Sachs, S.; Křepelová, A.; Schmeide, K.; Koban, A.; Günther, A.; Mibus, J.; Brendler, V.; Geipel, G.; Bernhard, G., Migration behavior of actinides (uranium, neptunium) in clays: Characterization and quantification of the influence of humic substances. Wissenschaftliche Berichte, Forschungszentrum Dresden-Rossendorf 2007, FZD-460, 116.

75. Kautenburger, R.; Nowotka, K.; Beck, H. P., Online analysis of europium and gadolinium species complexed or uncomplexed with humic acid by capillary electrophoresis-

inductively coupled plasma mass spectrometry. Analytical and Bioanalytical Chemistry 2006, 384, 1416.

76. Tipping, E., Modelling the binding of europium and the actinides by humic substances. Radiochim. Acta 1993, 62, 141.

77. Laxen, D. P. H., Trace metal adsorption/coprecipitation on hydrous ferric oxide under realistic conditions : The role of humic substances. Water Research 1985, 19, 1229.

10 Acknowledgements

The authors thank S. Boulyga (Institute of Inorganic Chemistry and Analytical Chemistry, Universität Mainz) for ICP-MS measurements of uranium. XAFS measurements were performed at the INE and ROBL beamlines at ANKA and ESRF, respectively. We thank B. Brendebach, K. Dardenne, M. A. Denecke, J. Rothe (Institute of Nuclear Waste Management, Forschungszentrum Karlsruhe) and H. Funke, C. Hennig, A. Roßberg, , and A. Scheinost (Institute of Radiochemistry, Forschungszentrum Dresden-Rossendorf) for their support during the XAFS measurements. A. Bauer (Institute of Nuclear Waste Management, Forschungszentrum Karlsruhe) is gratefully acknowledged for the preparation of the kaolinite size fraction < 2 µm.

R. Buda and S. Bürger were financially supported by the DFG Interdisciplinary Research Training Group Program 826 “Trace Analysis of Elemental Species: Development of Methods and Applications”.

We would like to thank all colleagues who contributed to the success of this work.

Appendix C - Institut für Anorganische und Analytische Chemie und Radiochemie, Universität des Saarlandes

KINETIC INVESTIGATIONS IN THE SYSTEM HUMIC ACID - METAL - KAOLINITE

R. Kautenburger, K. Nowotka, H.P. Beck

Final Report

Support Contract Number
02 E 9683

Anorganische und Analytische und Radiochemie
Universität des Saarlandes
P.O.Box 151150
66041 Saarbruecken
Germany

Content

List of symbols

A Electrode surface
β Conditional stability constant (log β)
c molar concentration
CE Capillary Electrophoresis
CE-ICP-MS Capillary Electrophoresis- Inductively Coupled Plasma-Mass Spectrometry
HPLC High Performance Liquid Chromatography
HPLC-DAD High Performance Liquid Chromatography with Diode Array Detection
MICN Metal ion charge neutralization model
D Diffusion coefficient
DP Differential-Pulse
Eq. Equation
Fig. Figure
g Standard acceleration due to Earth's gravity (9.81m/s^2)
HA Humic acid
I Ionic strength
ICP Inductively Coupled Plasma
ICP-MS Inductively Coupled Plasma-Mass Spectrometry
IHA Iodinated humic acid
K Stability constant (logK)
K‘ Electrochemical constant
K_c Equilibrium constant
L Loading in % (compared to the maximum complexation)
LC Loading Capacity
M Molar
Me^{z+} Metal ion
MQ MilliQ(-Water)
n Number of electrons
PEC Proton Exchange Capacity
ppb Parts per Billion
ppm Parts per Million
s Rate of potential scan
Tab. Table
TOC Total Organic Carbon
UF Ultrafiltration
V Volt

Abstract

The project was mainly focused on the determination of lanthanide distribution, namely Eu and Gd, on kaolinite surfaces. The main components of the system under study are the metals europium and gadolinium (homologues of the actinides americium and curium), clay mineral (kaolinite KGa-1b) and humic acid (purified Aldrich HA). The HA was analysed in the frame of other projects by means of SEC, UF, CE, UV/Vis, IR. The kaolinite was characterized by EDXRF and XRD.

One aim of the project was to study the complexation behavior of metal ions with HA and to evaluate the stability constants of corresponding chemical reactions. These stability constants are required for geochemical modeling of metal-ion behavior in the environment after assembling them in a thermodynamic database. Among the different complexation models to describe the metal ion complexation by humic substances the metal ion charge neutralization (MICN) model was used within this work allowing for good transferability of the results.

To guarantee reliable results, two different analytical methods were used to determine stability constants by differentiating between free metal ions and metal ions which are bound to HA. The evaluation of complex stability constants was performed by applying ultrafiltration, thereby mechanically separating non HA complexed ions of Eu and Gd from the metal-humate complexes. Measurement of the separated ions from the filtrate was done by ICP-MS. As a powerful alternative technique, capillary electrophoresis (CE) was hyphenated with inductively coupled plasma-mass spectrometry (ICP-MS) to investigate in standardized laboratory experiments the complexation behavior of HA and its influence on the migration of the lanthanides Eu and Gd. With this method, both the free metal and metal humate can be detected in one analysis step which allows for improved precision over methods that rely on the determination of only one species, like ultrafiltration. Furthermore, it is possible to investigate the heterogeneity in HA complexation by evaluating the stability of humates during CE-separation. The kinetically labile lanthanide humates partially collapse because of the applied separation voltage and interactions of the sample with the electrolyte which leads to interesting behavior, especially with changing experimental conditions. In the binary system, the influence of different lanthanide concentrations, changing pH and competing cations was investigated.

One problem with the analysis of HA and its complexes is that they are not detectable by ICP-MS. To make HA visible, we used a simple chemical procedure to halogenate the aromatic hydrocarbon-rings in the HA with iodine as “ICP-MS” marker. This leads to a clear indication of ICP-MS metal signals, assigned to humates and those, that count for non HA complexed metal.

All obtained conditional stability constants β of the different methods are in good agreement with one another and with data from other sources. For europium we obtained a log β_{EuHS} with an over all average of all methods and test series of 6.44±0.15. Gadolinium was found to have a conditional stability constant with HA of log β_{GdHS}=6.33±0.14.

A wide range of geochemical parameters was investigated to reveal the relations between the single influences in the different binary systems and finally in the ternary system. The

lanthanide concentration was varied in a range that could be relevant for geological metal migration in all metal containing systems. Generally, a higher metal ratio is present in the liquid phase with higher lanthanide concentration besides in presence of HA. The influence of pH is rather low in terms of metal sorption on kaolinite surface except for extreme, unnatural values. HA suppresses sorption at higher pH-values and increases it through sorption of neutralized complexes at lower ones.

Besides adsorption isotherms and pH-edges, the influence of Ca and Mg as natural occurring competitors was investigated explicitly. Their presence resulted in a dramatically decreased kaolinite sorption of the lanthanides at naturally occurring alkaline earth concentrations. With HA present, sorption is stabilized with almost no influence of Ca and Mg. Lanthanides adsorb at the kaolinite surface as ions by ion exchange or as HA complexes through hydrophobic interactions. As alkaline earth concentration rises, HA gets neutralized without displacement of lanthanides from the complexes because the bivalent ions only occupy lower active sites of the HA, neutralising it.

The experiments give a close insight into the behaviour of heavy metals in the ternary system. Financial support was granted by the BMWA (grant number 02 E 9683).

1 Introduction

Safety assessment of waste disposal requires detailed information and understanding of the radionuclides in the heterogeneous environment. Their migration or sorption in the geosphere can be affected by a wide variety of chemical reactions; some of them involve humic substances. Humic material is a large and heterogeneous group of macromolecules of different molecular weight and charge density, with complex and difficultly identifiable structure [1]. According to new findings, humic substances can be classified as supramolecules which are collections of diverse, relatively low molecular mass components forming dynamic associations which are capable of organization into micellar structures in suitable aqueous environments [2]. The mechanism of complexation with metal ions is not well understood, especially with respect to the role of phenolic OH-groups. Additionally, the influence of metal ion and humic acid concentrations on the humate complexation, the role of metal ions on aggregation of humic molecules, and the kinetics of involved reactions are unsolved problems so far [3,4], which experiments performed within this project should help to solve.

One aim of the project was to study the complexation behavior of metal ions with HA and to evaluate the stability constants of corresponding chemical reactions. For example, these stability constants are required for geochemical modeling of metal-ion behavior in the environment after assembling them in a thermodynamic database [4]. Among the different complexation models to describe the metal ion complexation by humic substances the metal ion charge neutralization (MICN) model [5] was used within this project. The MICN model is relative simple and requires only a few parameters which can be determined by experiments. The parameters are the proton exchange capacity (PEC) and the loading capacity (LC) of the HA. Both parameters are necessary to estimate the actual free HA concentration in chemical terms. To guarantee reliable results two different analytical methods are used to determine the stability constants by differentiating between free metal ions and metal ions which are bound to humic substances.

Methods usually used combine chemical separation procedures, for example, extraction methods, ion exchange, ultrafiltration or precipitation steps, with sensitive detection techniques, such as nuclear spectroscopy, soft X-ray spectromicroscopy (NEXAFS) or mass spectrometry [6-11]. However, such methods have the adverse effect that the quantitative amount of the interesting species can not be detected or, that kinetic not stable complexes may be modified during chemical separation.

In our study, the determination of the complex stability constants was performed first by applying ultrafiltration separating non HA complexed ions of Eu and Gd (as homologues of the actinides americium and curium) from the metal-humate complexes. The measurement of the separated ions was done by ICP-MS. As an alternative technique, capillary electrophoresis (CE) was hyphenated with a homemade interface to inductively coupled plasma-mass spectrometry (ICP-MS) [12-16] to investigate in standardized laboratory experiments the complexation behaviour of HA and its influence on the migration of the lanthanides europium and gadolinium. In this project, Eu-HA and Gd-HA complexation data obtained by CE-ICP-MS and ultrafiltration have been compiled for a direct comparison of both methods under comparable experimental conditions.

Generally, HA are not detectable by ICP-MS. To make the HA visible, we used a simple chemical procedure to halogenate the aromatic hydrocarbon-rings in the HA with iodine as “ICP-MS” marker [17,18].

With these analytical techniques we investigate in standardized laboratory experiments the complexation behaviour of humic acid (purified Aldrich humic acid) and its influence on the migration (sorption and desorption experiments) of the lanthanides europium and gadolinium first in the three different binary systems and finally in the ternary system consisting of these heavy metals, humic acid and kaolinite (KGa-1b) under varying experimental conditions close to nature [19] together with the influence of geochemical parameters like pH-value, ionic strength or different competing metal cations on the complexation [20].

2 Experimental

One important part of the project is the measurement of stability constants of complexes of humic acids and the heavy metals Eu and Gd. There are two different strategies to determine log K or log β_{LnHS} values:

the uncomplexed metal is first separated from the complexed metal, for example by *ultrafiltration* (*UF*), and in a second step the uncomplexed metal ions in the filtrate are measured by *inductively coupled plasma-mass spectrometry* (*ICP-MS*).

the uncomplexed metal is separated from the metal humate complex and simultaneously measured in one step, for example by coupling *capillary electrophoresis* (*CE*) with *ICP-MS*

The methods given in *italics*, the iodination of the HA as well as the batch-experiments will be explained in short in the following sections.

2.1 Characterisation of the clay mineral kaolinite (KGa-1b)

Kaolinite KGa-1b was characterized by EDXRF to analyse its element composition. In addition a phase analysis with XRD and subsequent evaluation with the Topas software (version 2.1, Bruker AXS) was performed. Table 1 gives the main elemental composition expressed in the form of their binary oxides.

Table 1: Semi-quantitative EDXRF analysis of kaolinite KGa-1b

Components	***Mass%***
SiO_2	55,3
Al_2O_3	42,2
TiO_2	2,2
Fe_2O_3	0,3

According to XRD analysis, TiO_2 was found to exist as a separate phase in the form of anatase.

2.2 Batch experiments

Fig. 1 shows the general procedure of the batch experiments. The experiments were performed in scintillation vessels, which have low adsorption properties.

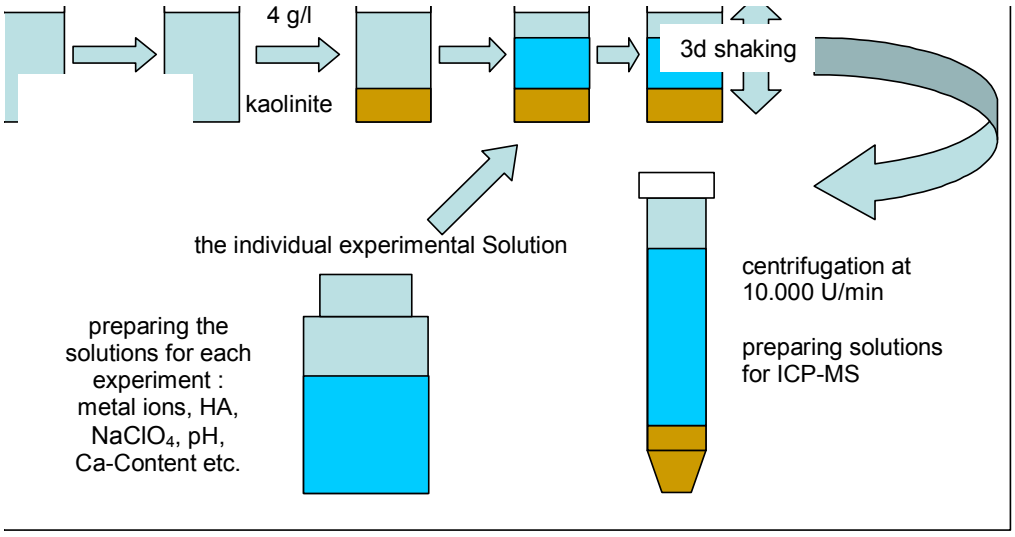

Fig. 1: General procedure of the batch experiments

In the first step the vessels were cleaned by MQ-Water. Cleaning with acid is not recommended, because pH-errors then may occur during the experiment. In test series with kaolinite an equivalent amount of 4g/l kaolinite was weighted into the cleaned vessels. After a 72h preconditioning with the corresponding solvent (10mM $NaClO_4$ in most cases), the remaining components were added and the pH adjusted.

Some experiments were performed with each metal separately and others with Eu and Gd together in one solution. The crucial parameter here is the total lanthanide concentration. In all cases an ion strength of 0.01M $NaClO_4$ was present in the solutions. The samples were equilibrated for 48h with all components present and during the shaking the temperature was kept at 23±2°C. Afterwards the vessels were centrifuged at 10.000 rotations per minute (12.800g). Samples were taken from the supernatant solutions. Diluted and acidified solutions were prepared to determine the remaining content of metal in the solution by ICP-MS. As the total concentration of the metal (before contacting it with the kaolinite) is known and the free metal is measured it is possible to calculate the amount of bound metal. All batch experiments containing kaolinite were performed in this way.

2.3 Capillary electrophoresis (CE)

Electrophoresis is the migration of charged molecules or ions in a solution under the influence of an electric field. In the case of Capillary Electrophoresis (CE) the sample migrates in thin fused-silica capillaries (50-100cm in length) with inner diameters ranging from 25 to 100µm filled with an appropriate CE electrolyte. The influence of the electric field on an ion causes a constant migration rate for every ion within the CE buffer. Cations with different electrophoretic mobility (different charge, radius, molar mass) are separated from other cations and from neutral or anionic molecules or ions. Electroosmotic Flow (EOF) is the result of electroneutrality constraints, which cause the formation of a charge double layer at the walls of the CE capillary. The walls of a fused silica capillary contain silanol groups which ionise in contact with a high pH electrolyte solution This dissociation produces a negatively charged wall. A layer of counter ions (e.g. metal ions) is then formed at the wall to preserve electroneutrality (see Fig. 2). When an electric field is applied these counter ions and their associated solvating water molecules migrate towards the cathode. This movement of ions and their associated water molecules results in a flow of solution towards the detector which is called electroosmotic flow (EOF). At low pH the silanol groups are not ionized and therefore the flow rate is much reduced or can become zero at very low pH values. The principal build-up of a CE is shown in Fig. 2: the capillary fits into two buffer vials and the high voltage is applied through the capillary. A detector and the data acquisition are placed at one end of the capillary.

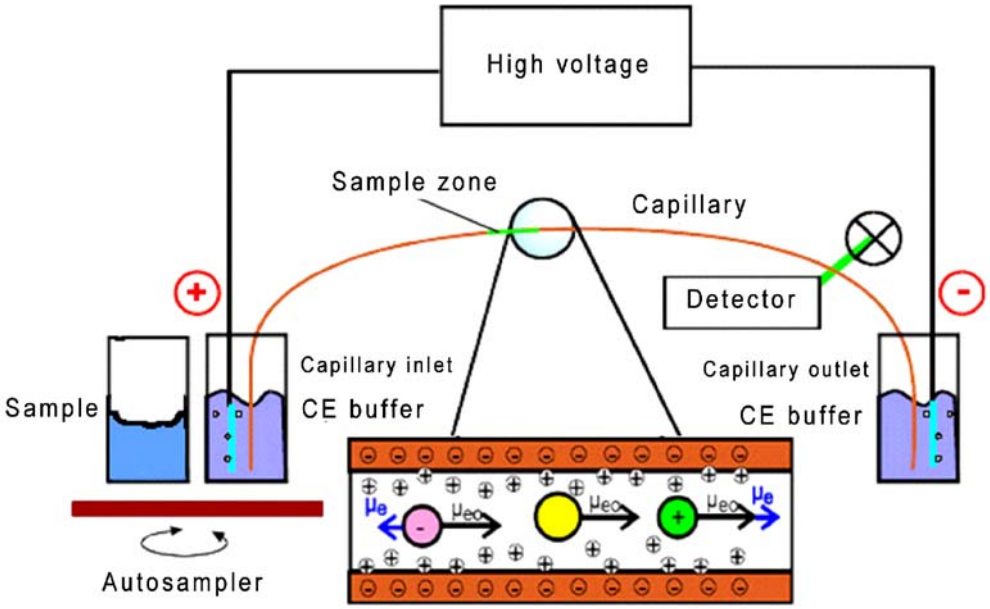

Fig. 2: Principal configuration of a capillary-electrophoresis system

The idea of using CE for the determination of stability constants for metals is sometimes described in the literature (especially in protein chemistry), but the direct separation of uncomplexed metal ions from their complexes is rarely used and - so far - even less in the case of humic acid complexes.

The CE experiments were carried out with a Beckmann P/ACE MDQ (Beckmann Instruments, USA). CZE separations were carried out in an uncoated fused silica capillary (Polymicro Technologies, USA). The samples were injected hydrodynamically at 30 psi×s (1.5psi for 20sec) which corresponds to a sample volume of 220nL. To precondition the capillary before each run, the capillary was rinsed with HCl (4.5M) for 30sec at 20psi, with NaOH (0.5M) for 30sec at 20psi, with Milli-Q deionized water for 20sec at 20psi, and additionally with CE electrolyte buffer for 30sec at 20psi. To prevent buffer depletion and to reduce background levels of europium and gadolinium, the buffer was changed completely every 10th run. The separations were performed under optimized conditions at 30kV/3psi and 25°C. In order to find out the best CE-conditions for the above mentioned separation of uncomplexed and HA complexed metal ions (Eu and Gd) several CE buffers and different concentrations of the buffers were tested.

2.4 ICP-MS

A VG Elemental PlasmaQuad 3 quadrupole-based ICP-MS was used for the isotopic measurements. Detailed analytical conditions are given in Table 2.

Table 2: Operating parameters and analytical conditions of the CE and the ICP-MS

CE	Beckman Coulter P/ACE® MDQ
Capillary	Non coated fused silica, self-made from a 50m tubing roll (TSP075375, Polymicro Technologies, Phoenix, AZ, USA)
Capillary parameters	74µm i.d., 362µm o.d., 80 or 85cm length, 25°C
CE electrolyte buffer	100mM acetic acid, 10mM Na-acetate, pH 3.7
Internal Standard CE buffer	1.50µmol/l Cs
CE injection	20sec at 1.5psi
CE separation (voltage/current/pressure/flow)	+ 30kV / 16-18µA / 3psi / 2.0µl/min
Spray-chamber	Jacketed cinnabar cyclonic, 20ml volume, chilled at 4°C
Nebulizer	MicroMist 50µl, Typ AR35-1-FM005E, 2.8bar Ar
Make-up fluid	2% HNO_3, 24nmol/l Ho (I.S.), sheath flow: 190µl/min

ICP-MS	VG Elemental Plasma Quad 3
RF-power	1400W
Cooling / auxiliary gas	12.5 / 1.25l/min
Dwell times	200ms (Eu, Gd, I), 50ms (Cs, Ho), 10ms (Br)
Sweeps	500 (1 channel per mass)
Samples	
Eu-, Gd-ICP-standards	CertiPUR® (Merck), diluted in 10mM $HClO_4$
Analyzed isotopes	^{81}Br, ^{127}I, ^{133}Cs, ^{153}Eu, ^{158}Gd, ^{165}Ho
Humic acid (HA)	Purified HA (Aldrich H1,675-2)
Iodinated HA	Homemade (see section 2.6)
Ion strength in HA samples:	10mM $NaClO_4$

2.5 CE-ICP-MS

Capillary electrophoresis (CE, Beckman Coulter P/ACE MDQ) was hyphenated by a homemade interface to inductively coupled plasma mass spectrometry (ICP-MS, VG Elemental PlasmaQuad 3) to obtain a high sensitivity for the determination of the rare earth element species of europium and gadolinium with HA [12]. To couple CE to ICP-MS a fused-silica CE-capillary was fitted into a MicroMist 50µl nebulizer with a Cinnabar cyclonic spray chamber (chilled to 4°C) in the external homemade interface. A make-up fluid including 4ppb Ho as an internal standard was combined with the flow from the capillary within the interface to obtain a fluid throughput high enough to maintain a continuous nebulization. Detailed analytical conditions are given in Table 2.

2.6 Iodination of the humic acid

To make the humic acid detectable in the ICP-MS we used a relatively simple chemical procedure to halogenate the cyclic- or polycyclic aromatic hydrocarbon-rings in the humic acid with iodine as “ICP-MS” marker [17,18].

A mixture of 100ml purified Aldrich humic acid solution (312.5ppm), 39.7mg I_2, 11.0mg HIO_3, 23.4mg NaI and 51.3µl HNO_3 (60%) was heated at 80°C for 24h.

$$5\,Ar-H + 2\,I_2 + HIO_3 \xrightarrow{80^\circ C,\ 24h} 5\,Ar-I + 3\,H_2O$$

The reaction product (iodinated humic acid) was precipitated by 500µl $HClO_4$ conc. (70%), separated from the supernatant and washed twice with saturated NaI solution (pH 1). The precipitate was dissolved in 2ml of 100mM NaOH and diluted with 30ml Milli-Q water. The iodinated humic acid was precipitated again by 300µl $HClO_4$ conc., separated from the supernatant, dissolved in 2ml of 100mM NaOH and diluted with 30ml Milli-Q water again. This precipitation procedure was repeated once again and finally, the iodinated humic acid was dissolved in 30ml of 10mM NaOH and 10mM $NaClO_4$.

The yield of iodinated humic acid in comparison to the humic acid as reactant before the iodination was determined by TOC (Total Organic Carbon; liquiTOC, Elementar Analysensyteme GmbH, Germany) measurements. The iodinated humic acid is used as stock solution for all further complexation experiments. This guarantees a constant and reproducible amount of halogenated humic acid in all experiments.

2.7 Ultrafiltration

As alternative separation techniques the determination of the uncomplexed metal ions were performed by ultrafiltration separating the humic acid and the humate complexes from the free metal ions. The ultrafilters of the type MicroSep™ 1K were obtained from Pall Life Sciences (Ann Arbor, USA). The pore size was 1 kDalton. With these filters, it was possible to

separate all humic acids and all metal ions bound to the humate while the free metal ions passed the membrane without any hindrance. In order not to disturb the complex formation equilibrium, only 3ml of a total sample volume of 10ml were separated by centrifugation at 7500g for 10min. To reach the complex formation equilibrium between humic acid and the lanthanides, a contact time of at least 48h was necessary.

2.8 Other methods

Besides the methods mentioned above, a wide range of other methods was used for the measurement of humic acids and metal concentrations. UV/Vis- and fluorescence- spectroscopy as well as HPLC-DAD were used as detection method for both the humic acid and iodinated humic acid concentration. Furthermore IR-measurements, CHN- Analyses, TOC-determinations, potentiometric titration and hyphenation of HPLC-DAD and ICP-MS have been performed.

3 Results and Discussion

3.1 The binary system humic acid/kaolinite

Humic acid has two ways to influence the metal transport in ternary systems consisting of heavy metal, humic acid and kaolinite. On the one hand HA binds metals and stabilizes them in the solution. On the other hand HA can be bound to the clay mineral. The bound HA can contain heavy metals too and in that way the metal concentration in the solution is decreased. HA is able to enhance the mobilisation of heavy metals as well as to diminish it, depending on its allocation. Information about the allocation of the HA in the ternary system is therefore essential to interpret sorption experiments and to estimate the mobility of heavy metals in the environment.

3.1.1 Kinetic aspects

Kinetic aspects are of great importance for all experiments with humic acids. The following experiments were performed to examine the influence of the preconditioning time on the sorption behaviour of humic acid on kaolinite. All experiments were carried out as described in section 2.2 varying one kinetic parameter. The influence of the preconditioning of humic acid and kaolinite was examined at different ion strengths (

Fig. **3**.).

In this case the contact time was varied from 0 to 72h. The sorption of the humic acid (25mg/l) on the kaolinite (4g/l) was found to be nearly constant at values of 70% (4.4mg HA/g

kaolinite) after 48h, particularly at ion strengths of 0.01 and 0.1M $NaClO_4$. Therefore, for all following experiments a preconditioning time of 48h and a $NaClO_4$ ion strength of 0.01M was selected.

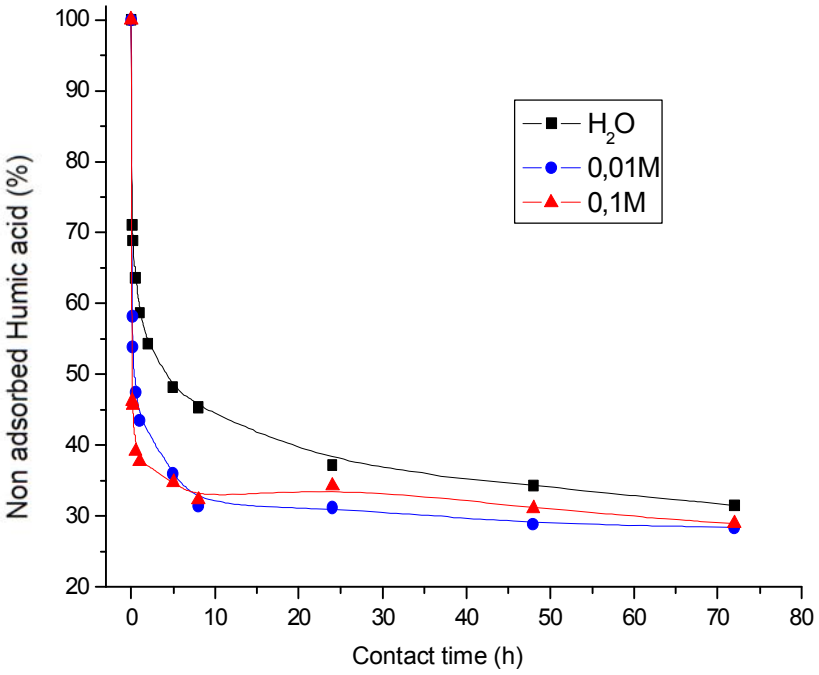

Fig. 3: Influence of the preconditioning time on the HA sorption on kaolinite

3.1.2 Determination of pH-edges

To reveal the influence of the pH-value on the sorption of humic acid on kaolinite, batch experiments were performed. A 25ppm solution of HA was used and the experiments were performed as described in section 2.2 (instead of plastic vessels glass vessels were used, to minimize the background pollution with carbon).

The humic acid sorption on kaolinite reaches its maximum for pH-values lower than 3 (Fig. 4). In this case 80-85% of the HA is bound and no remarkable influence of the ion strength is visible. This corresponds to a bound humic acid mass of 5mg/g kaolinite. At pH values over 3 the sorption decreases in a linear manner. The sorption decreases to only 25% of the used HA at pH 8 which corresponds to a sorption of 1.5mg/g kaolinite. Higher ion strengths lead to a higher sorption of the humic acid on the kaolinite particularly at higher pH-values.

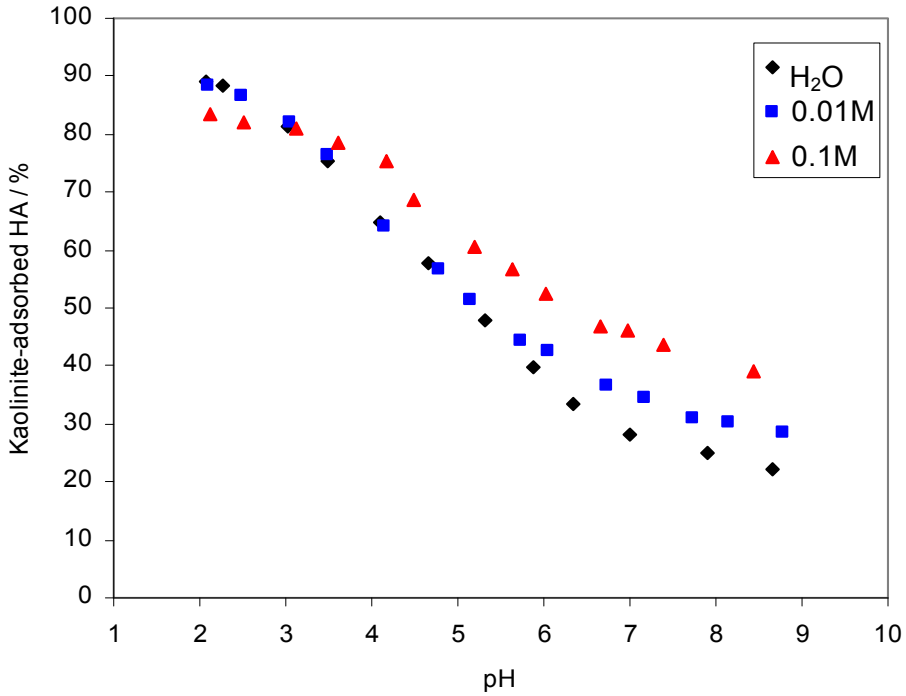

Fig. 4: Interaction of humic acid and kaolinite depending on pH and ion strength

In the pH-range between 3 and 8 the dependence of the sorption on pH is strong. This behaviour can be explained by the deprotonation of both, the humic acid and the kaolinite with increasing pH resulting in a negative charge for both.

With increasing surface charge, humic acid and kaolinite repel each other and the sorption decreases. The experiment demonstrates that the role of humic acid as a geocoating agent has well to be taken into consideration.

Additionally, the dissolving of the kaolinite at lower and higher pH-values must be considered so that the increasing amount of Al^{3+} in the solution has a negative effect on the radionuclide complexation by humic substances due to the competing complexation properties of the highly charged aluminium ions (Fig. 5).

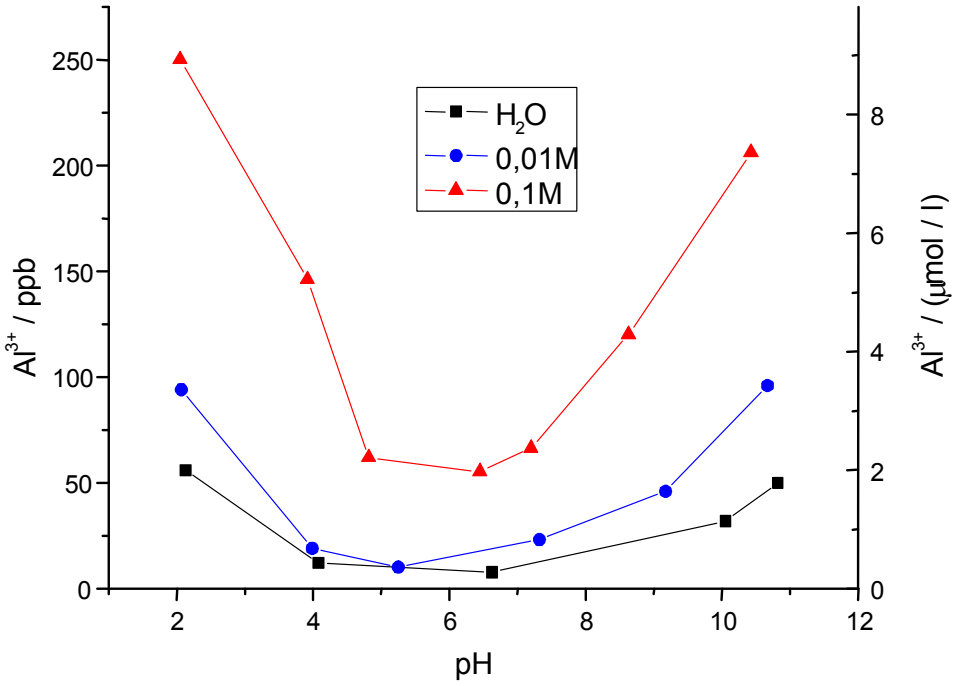

Fig. 5: Aluminium dissolving out of the kaolinite at different pH-values

3.2 The binary system humic acid/metal

3.2.1 Development of analytical tools for the metal-humate speciation

3.2.1.1 Optimisation of the CE-ICP-MS system

Two micro concentric nebulizers were tested for the CE-ICP-MS coupling, the Cetac MCN 100 and the MicroMist 50µl system. By comparing the signal sensitivity and the long-term stability of the two systems, the MicroMist 50µl exhibited good signal stability while the MCN 100 nebulizer was not satisfactory. The MicroMist nebulizer type was chosen for the experiments due to its high stability and good signal sensitivity. The coupling of the CE capillary and the MicroMist 50µl nebulizer was done by a homemade interface (Fig. 6) consisting of flexible PTFE tubing between the CE-outlet and the nebulizer [12].

As optimized CE parameters, we used a DC-voltage of 30kV and additionally, a pressure of 3psi as the best separation conditions for the HA-complexed and uncomplexed metal ions. The complementary separation pressure was necessary to transfer the negatively loaded metal/ humic acid complexes into the ICP-MS. Additionally; the jacketed cinnabar small-volume (20ml) cyclonic spray chamber was chilled at 4°C, which increases the signal sensitivity for Eu and Gd respectively (Fig. 7).

It was shown in test runs that the distance between the end of the CE capillary and the inlet into the nebulizer capillary was an important parameter responsible for chromatographic resolution.

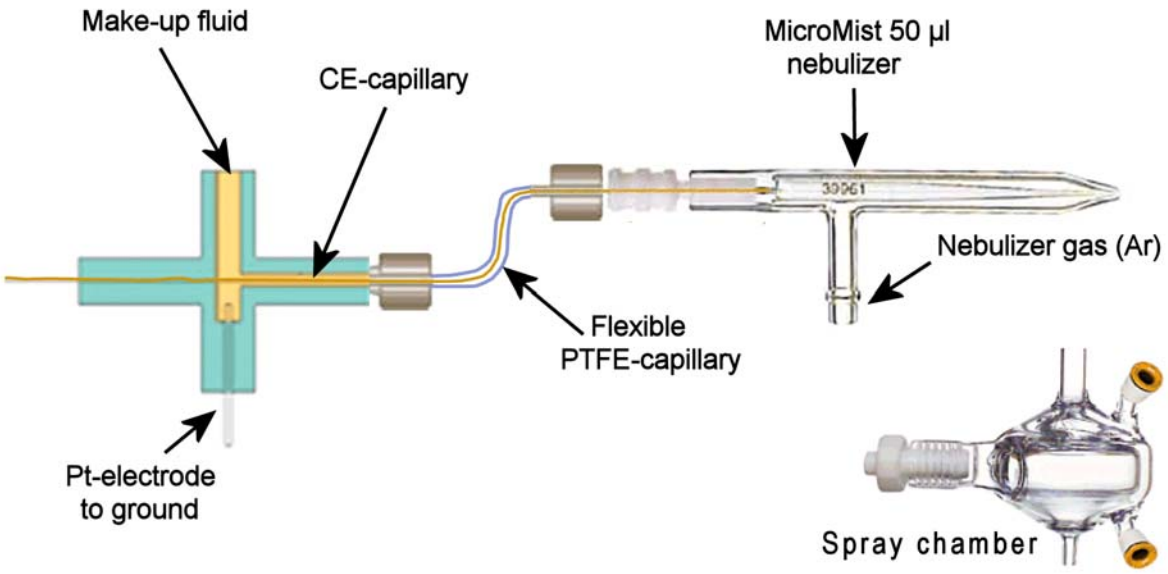

Fig. 6: Modified Interface: Flexibly fitted CE-capillary into a MicroMist 50µl nebulizer with a jacketed cinnabar cyclonic spray chamber

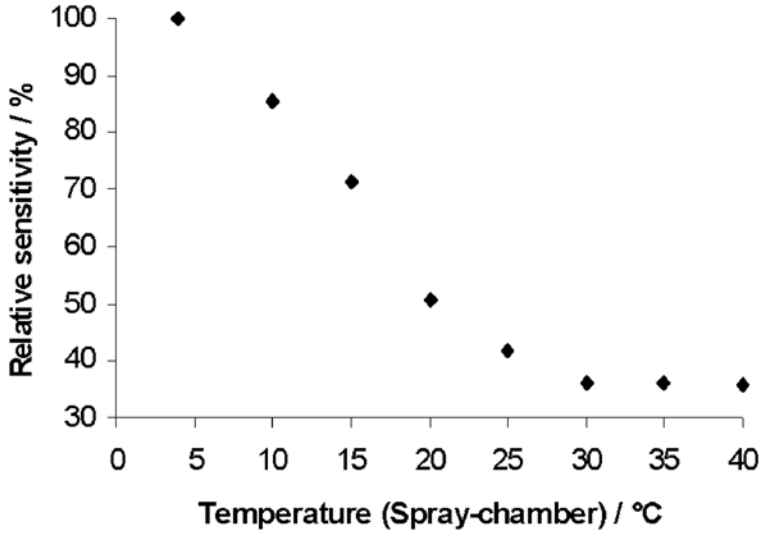

Fig. 7: Increase of the relative signal sensitivity of Eu (the measured counts of ^{153}Eu for 1ppb at 4°C are set to 100%) by chilling the spray chamber

Too small distances resulted in peaks with a sharp rise but with an extended tail, which might be explained by a suction effect in the CE capillary. Well-shaped peaks and the best separation resolution were obtained at a distance of 1-3mm. By increasing the distance above that length, which enlarges the mixing zone and leads to a dilution of the sample solution, the peaks became broader with an extended tail.

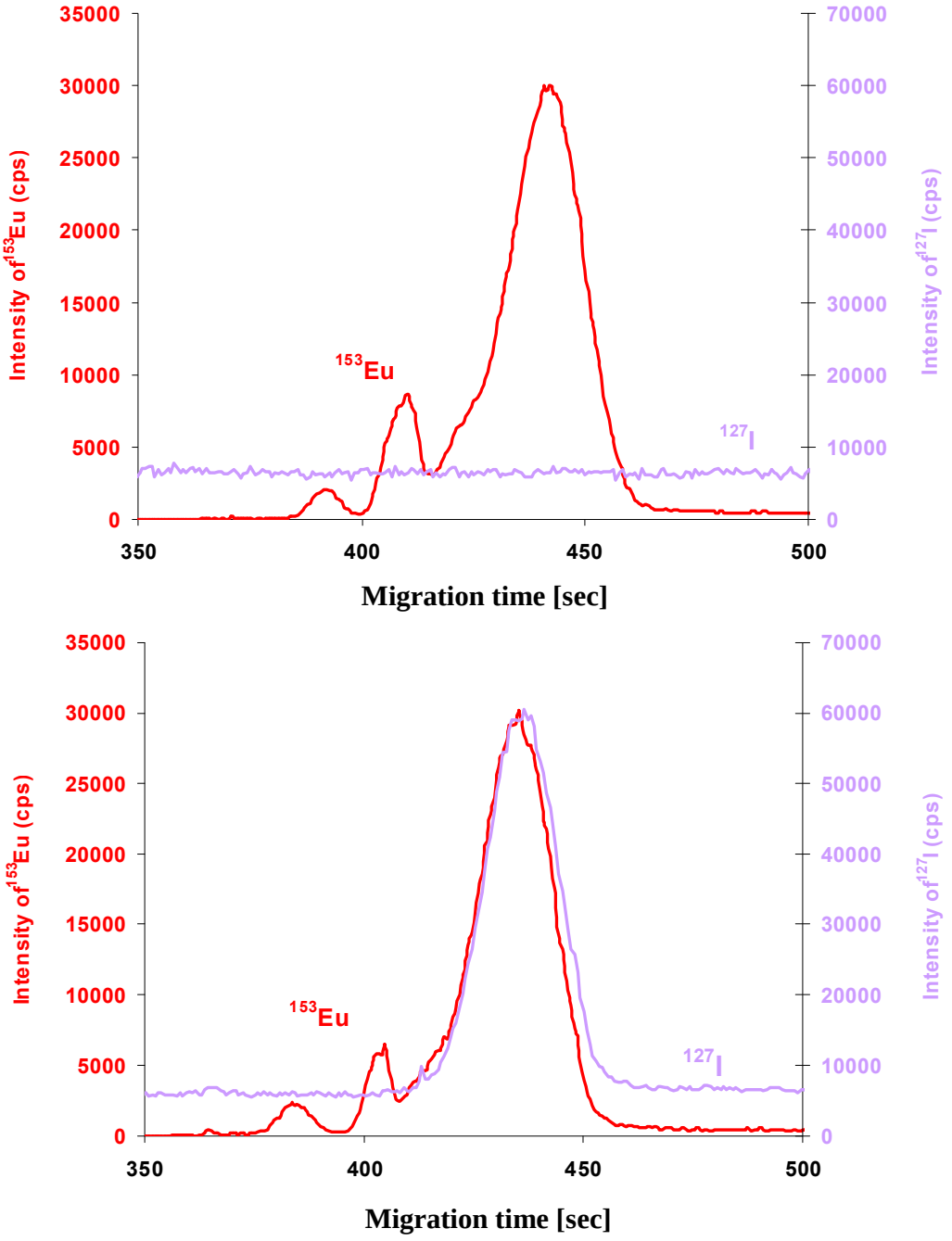

Fig. 8: Comparison of the Eu-complexation with non iodinated and iodinated humic acid

3.2.1.2 Results of the iodination of the Aldrich humic acid

To make the humic acid detectable in the ICP-MS, we have halogenated the cyclic- or polycyclic aromatic hydrocarbon-rings with iodine as “ICP-MS” marker (^{127}I) by a simple procedure which yields a high percentage of successfully halogenated humic acid [17,18].

The yield of iodinated humic acid was 10% after the halogenation and cleanup steps as determined by a TOC analyzer (liquiTOC, Elementar Analysensyteme GmbH, Germany). The comparison of the complexation behaviour of Eu and Gd with non iodinated and iodinated humic acid revealed no detectable differences (see Fig. 8).

3.2.1.3 The optimized CE-ICP-MS system

In the improved CE-ICP-MS-system we used a DC-voltage of 30kV and a continuous pressure of 3psi as mentioned above in section 3.2.3.1. and chilled the spray chamber for a better sensitivity at 4°C. The CE-ICP-MS method developed was checked by analyzing different standard solutions. The detection limits (125ppt for ^{153}Eu and 250ppt for ^{158}Gd) and correlation coefficients of the calibration curves for Eu (> 0.995) and Gd (> 0.999) were very satisfactory. After calibrating the system for the measured isotopes, standard solutions containing 0.66-98.7µmol/l Eu together with 25ppm iodinated HA and 0.64-95.4µmol/l Gd mixed with 25 ppm iodinated HA were injected as samples for the determination of the loading capacity (LC) and complex stability constants.

To stabilize the Eu species formed in the samples during the CE run, and to minimize the adsorption of the highly charged species on the silica wall of the capillary, we have checked many different carrier electrolyte compositions, concentrations and pH-values for the CE buffer. The finally used CE-buffer, consisting of 100mM acetic acid and 10mM sodium acetate, shows the best results for the CE-ICP-MS separation at the conditions given here. As a result, the electropherogram presented in Fig. 9 shows different Eu species complexed or uncomplexed with HA as analyzed by CE-ICP-MS and after iodination of the HA as ICP-MS marker (via the ^{127}I signal). To determine the charge (positive, neutral or negative) of the analyzed species we have used 1-bromopropane (shown as ^{81}Br signal) as neutral (EOF) marker. Additionally, we have added Cs (seen as ^{133}Cs) to the CE-buffer to control the carrier-flow from the CE.

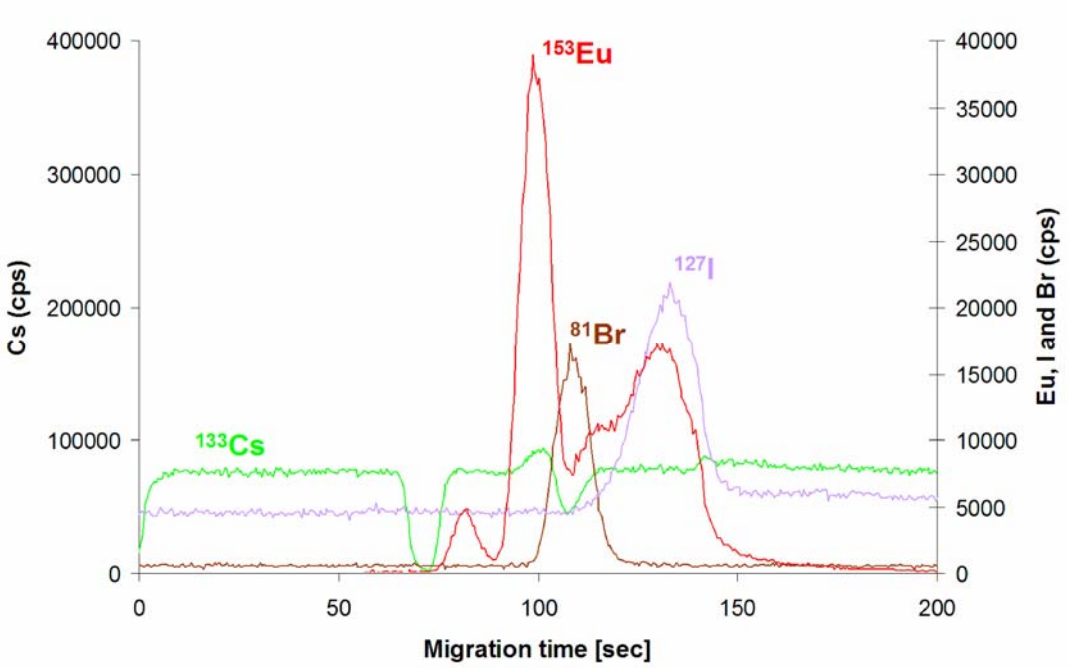

Fig. 9: Typical CE-ICP-MS electropherogram which shows Eu species (as ^{153}Eu) complexed or uncomplexd with iodinated HA (^{127}I), 1-bromopropane (^{81}Br) as EOF marker and Cs (^{133}Cs) as CE electrolyte flow marker; sample: 3.29µmol/l Eu, 25 ppm iodinated HA and 10mM $NaClO_4$ at pH 5

Three different ^{153}Eu signals can be detected in a typical CE-ICP-MS run. The first signal represents the non HA complexed Eu species. The second and third signal are caused by HA complexed Eu species. The splitting into two peaks occurs because of the acetate (AC) in the CE-buffer. Within the buffer solution Eu exists mainly as $Eu(AC)^{2+}$ in the concentration area used. The samples were prepared in an acetate free solution (10mM $NaClO_4$ at different pH-values is used for the experiments). During the CE separation Eu partly dissociates out of the HA-complex. For a short time this $Eu(aq)^{3+}$ migrates faster than the $Eu(AC)^{2+}$ until it moves out of the sample zone into the CE buffer zone which contains acetate at higher concentrations. However, this buffer effect is not relevant for the analysis because the non HA complexed Eu fraction (first ^{153}Eu signal) is clearly separated from the HA complexed fractions (the last two signals).

3.2.2 Determination of complex stability constants by the MICN-model

The complexation reaction of a metal ion (Ln^{z+}) with HA can be considered as a neutralization of the ion charge by the HA. At very low metal ion concentrations the formation of mononuclear complexes is assumed as the only existing species.

The free HA concentration $[HA]_{free}$ is calculated with the charge neutralization model [5, 19]. Within this model, it is assumed that in a metal ion charge neutralization process the metal ion occupies a number of proton exchange sites equal to its charge *z*+. Thereby, the group of

complexing sites needed to neutralize the metal ion is considered as one HA complexation unit.

The reaction is described as:

$$Ln^{z+} + HA_{(z)} \rightarrow LnHA_{(z)}.$$

Thus, the stability constant K is expressed as:

$$K = \frac{[LnHA_{(z)}]}{[Ln^{z+}]_{free} \times [HA_{(z)}]_{free}}.$$

The concentrations of $LnHA_{(z)}$ and Ln^{z+} can be measured with the different methods mentioned above. $[HA_{(z)}]_{free}$ is calculated by $[HA_{(z)}]_{total} - [LnHA_{(z)}]$ with:

$$[HA_{(z)}]_{total} = \frac{\{HA\} \times PEC \times LC}{z}.$$

In the above equation, {HA} is the HA content in g/l and PEC is the proton exchange capacity which is determined by potentiometric titration to be 5.0±0.1 meq/g [21]. The LC must be determined for each pH, metal ion Ln^{z+}, ionic strength and HA. This leads to β- or log β-values. With this model the conditional stability constants β for Eu and Gd at 10mM ionic strength ($NaClO_4$) for different metal ion concentrations and the stability constant β for different pH-values were determined by both CE-ICP-MS and ultrafiltration.

3.2.3 Determination of the Loading Capacity (LC)

The stability constant K depends on the pH, ionic strength, HA concentration. The use of the MICN model however provides a conditional stability constant β independent of the aforementioned parameters. The LC as a correction value is now a decisive parameter. The conditional stability constant β should now be constant and independent of the experimental conditions.

The LC is graphically determined as the slope of the F vs. $[Ln^{z+}]_{free}$ graph (see Fig. 10), in which F is taken from the definitions in the MICN model:

$$F = \frac{[Ln^{z+}]_{free} \times \frac{PEC}{z}}{[LnHA_{(z)}]}.$$

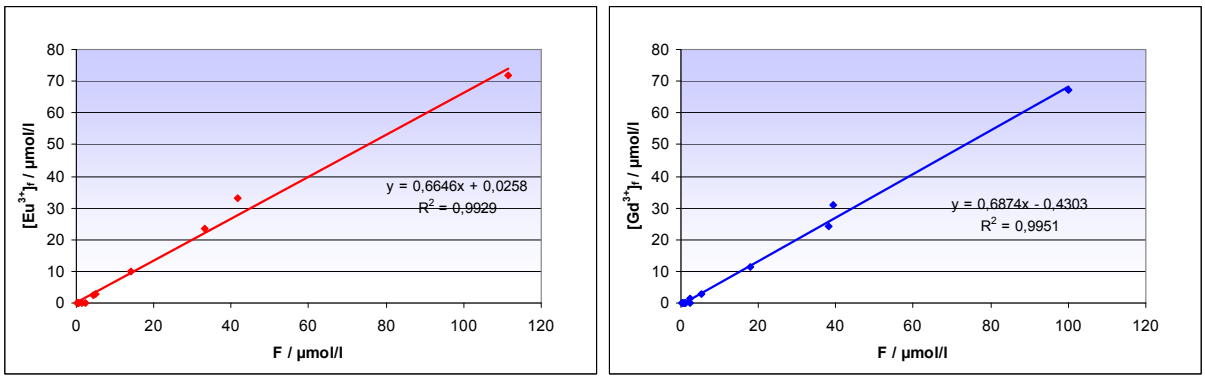

Fig. 10: Determination of the Loading capacity (LC) of Eu and Gd; c(HA)=25ppm, pH=5.0, 10mM $NaClO_4$. (F taken from the definitions in the MICN model, see equation above)

The LC-values for both lanthanides are shown in Table 3. The LC`s determined by CE-ICP-MS are lower than those measured by the combination of ultrafiltration and ICP-MS. To check the completeness of the HA separation by ultrafiltration we have used halogenated HA in the complexation experiments. After the ultrafiltration step we have analyzed the filtrate by CE-ICP-MS.

Table 3: Loading capacity (LC) of Eu and Gd; c(HA)=25ppm, pH=5.0, 10mM $NaClO_4$. (F taken from the definitions in the MICN model), different methods

	LC [%]	
Metal ion	Eu	Gd
CE-ICP-MS	43.5	44.0
UF / ICP-MS	66.5	68.7

The increase of the ^{127}I signal particularly at higher pH-values shows a breakthrough of the iodinated HA and Eu-HA complexes by ultrafiltration through the 1000 Dalton filter as shown in Fig. 11. This will result in an overestimation of the uncomplexed Eu concentration in the filtrate, as can also be seen by the appearance of an additional Eu signal belonging to the Eu-HA complex at higher migration times in the CE-ICP-MS separation. In contrast an underestimation due to the low recovery rate of 75.7±4.1% (n=5) caused by the adsorption of the non HA complexed metal ions on membrane and filter materials is found.

Since the latter effect is stronger a lower amount of non complexed Eu and Gd is determined by ultrafiltration as in comparison to CE-ICP-MS and therefore higher LC-values for the HA are determined. In contrast to ultrafiltration followed by ICP-MS detection of the filtrate where only the non HA complexed metal species are determined, the CE-ICP-MS method allows to determine non complexed as well as HA complexed metal species simultaneously in one detection step.

3.2.4 Comparison of log β determined by CE-ICP-MS or ultrafiltration/ICP-MS

At low metal ion concentrations the log β-values for Eu are similar for both methods at the same concentration range as seen in Table 4. The higher logβ-values detected by the ultrafiltration method are a result of the higher LC-value as described in section 3.3. For the ultrafiltration method as well for the CE-ICP-MS method the conditional stability constants of Eu show a little bit higher values than the LC-values for Gd at the same experimental conditions because of the lower electronegativity of Eu as also assumed in section 3.4. At higher metal ion concentrations the log β-values determined by the hyphenation of CE and ICP-MS show rather low conditional stability constants due to the fact that the metal ion concentrations exceed the complexation capacity of the HA and a high amount of non complexed metal is determined. Additionally, the limited CE-ICP-MS capacity at the used analytical conditions prevents the analysis of higher concentrations of metal ions and HA caused by the different electrolytic conductivity developed by the buffer and sample zone during the separation on the CE capillary.

Table 4: Comparison of conditional stability constants β for Eu- and Gd-humate complexes at pH 5, I=10mM $NaClO_4$ as a function of metal ion concentrations, ($C_{(HA)}$=25ppm)

C [ppm]	0,1		0,2		0,5		1		2	
Metal ion	Eu	Gd	Eu	Gd	Eu	Gd	Eu	Gd	Eu	Gd
CE-ICP-MS	6,17	nd[1]	6,28	nd	6,40	nd	6,30	nd	6,55	nd
UF / ICP-MS	6,37	5,62	6,59	6,16	6,64	6,33	6,63	6,43	6,71	6,55
C [ppm]	4		6		8		10		15	
Metal ion	Eu	Gd	Eu	Gd	Eu	Gd	Eu	Gd	Eu	Gd
CE-ICP-MS	5,27	nd	nd	nd	4,80	nd	nd	nd	nd	nd
UF / ICP-MS	6,26	6,11	nc[2]	6,10	nc	5,72	nc	nc	5,66	5,87

[1]nd = not determined; [2]nc = not calculable

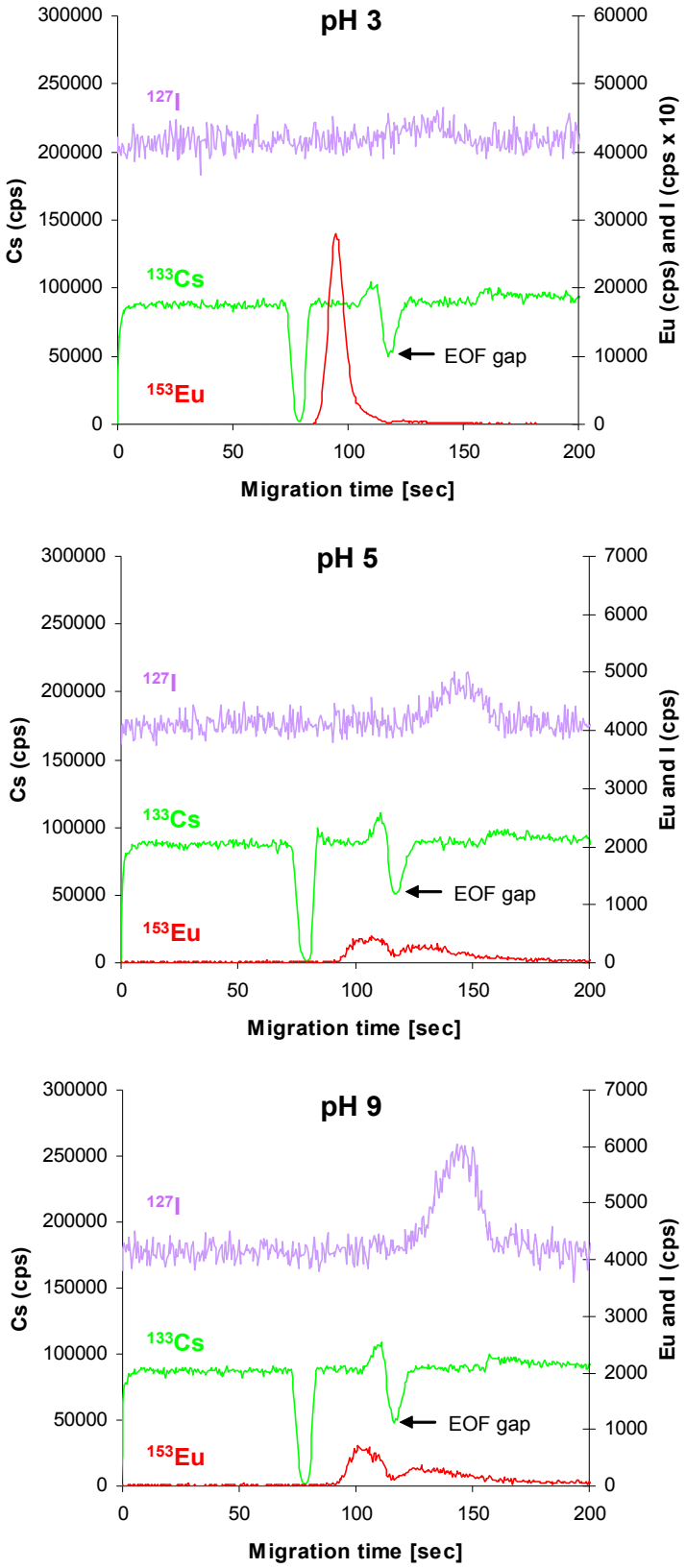

Fig. 11: Discharge of iodinated HA (^{127}I isotope as ICP-MS marker for the HA) through the 1kDalton filter in dependence of different pH-values.

3.2.5 Influence of geochemical parameters

Some (geo)chemical parameters have a significant influence on the complexation behaviour of humic acids with heavy metals, be it due to changes in the humic acid itself or an influence on the heavy metal sorption. These parameters include pH-value, ionic strength and competing cations. However, log β-values are more or less independent of pH or ionic strength and so far better comparable than log K‘-values.

3.2.5.1 The lanthanide concentration

Different concentrations of the lanthanides can cause different behaviour in humic acid complexation. CE-ICP-MS readings were taken at Eu- and Gd-concentrations between 0.317 and 19.7µmol/l at pH 5. By quantification of the CE-electropherograms, stability constants for Eu- and Gd-humates can be calculated.

At 250ppb the larger part of both lanthanides is HA-complexed, represented by the two rear signals. For low metal concentrations, mainly stronger binding sites of the HA are occupied with lanthanides. Thus, only little metal is extracted from the complex during the separation and the second signal is relatively small. At higher concentrations, e.g. 1.5ppm, as shown in Fig. 12, this signal gets significantly higher which means that less strong binding sites of the HA have been occupied with lanthanides that cannot “withstand” the separation voltage and acetic acid complexation competition. Those species migrate faster than the remaining complex after the separation from the HA in the sample zone. Consequently, one can state predications about the stability of HA-complexes by qualitative analysis of the second signal in our CE-separations. Quantification is difficult, because the reproducibility is not very good.

The first signal which represents the non HA-complexed lanthanides is important for the determination of stability constants. As seen in Fig. 12, this signal cannot be appraised at high lanthanide concentrations above approximately 500ppb, as the higher second signal interferes with the analysis. At lower concentrations the evaluation is possible without restrictions. Table 5 shows calculated conditional stability constants which are corrected with an LC that was determined by ultrafiltration experiments at pH 5.

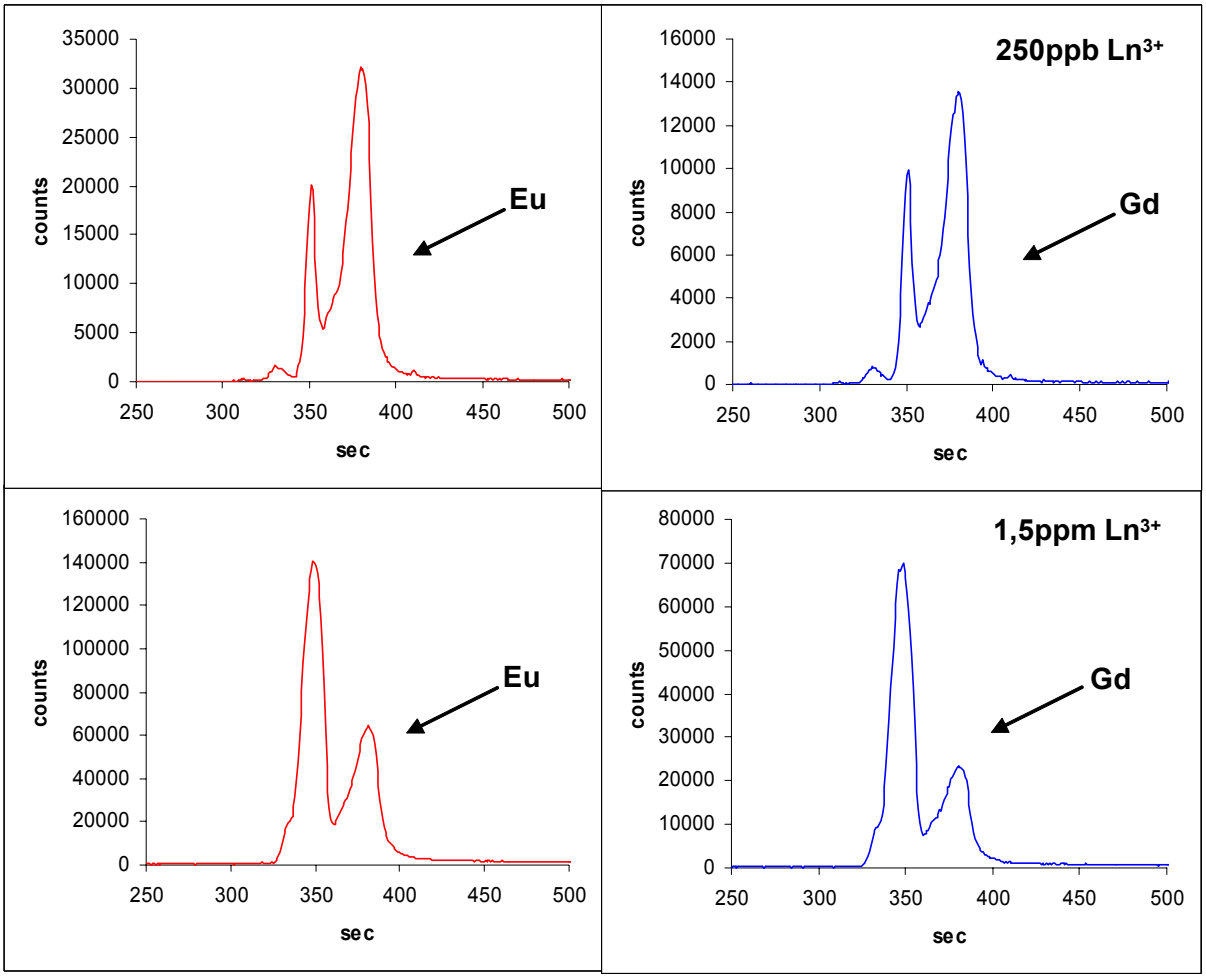

Fig. 12: CE-electropherograms of Eu (red signal) und Gd (blue signal), lanthanide concentrations 250ppb and 1.5ppm, pH=5, ionic strength ($NaClO_4$)=10mM

Table 5: Conditional stability constants for Eu and Gd with Aldrich HA at different concentrations, determined by quantitative CE-ICP-MS measurements, c(HA)=25ppm, pH=5, LC(Eu)=66.5%, LC(Gd)=68.7%, determined by ultrafiltration

Metal concentration	*log β (Eu)*	*log β (Gd)*
50ppb	6.53	6.59
125ppb	6.26	6.20
250ppb	6.16	6.12
350ppb	6.38	6.34
500ppb	6.34	6.32

Between 50ppb and 250ppb the amount of non HA-complexed lanthanides rises because of the favoured occupancy of highly active sites at lower metal concentrations. Above 250ppb, the stability constants begin to rise again. Assuming that this behaviour is not caused by measurement errors, a possible explanation is the formation of micelles by the HA at low metal concentrations in addition to a relatively low ionic strength. With those micelles, the non polar parts of the HA would be inside the aggregates, along with many potentially (weaker) negatively loaded complexation sites. As the metal concentration gets higher the micelles could break and those sites would be available for complexation which results in higher stability constants at 350 and 500ppb. Differences in the complexation behaviour of Eu and Gd are clearly visible in this experimental series as both metals were present in the same samples, thus directly competing for HA complexation sites. Eu always is complexed a little stronger than Gd because of its higher electropositivity. Furthermore, the amount of extracted metal during CE separation is significantly higher for Gd which is clearly visible on the electropherograms, shown in Fig. 12.

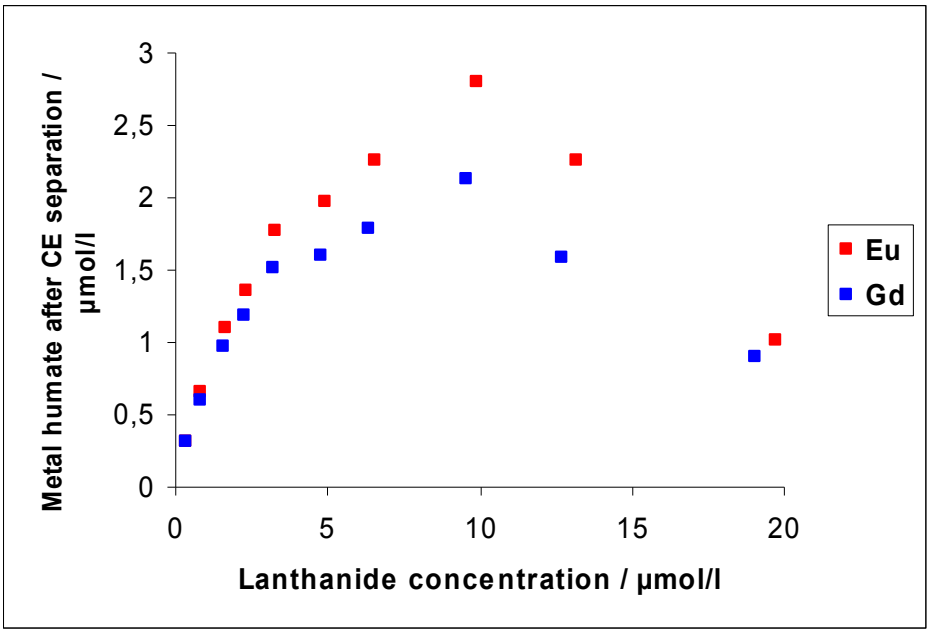

Fig. 13: Illustration of the complexation of Eu and Gd with HA depending on the lanthanide concentration, c(HA)=25ppm, ionic strength ($NaClO_4$)=10mM, pH=5

In order to determine the humate concentration after the CE separation as shown in Fig. 13, only the right signal of the electropherograms, which contains the stronger binding humate fractions, was evaluated. This cannot serve as quantification but highlights interesting trends in HA complexation. The plotted “adsorption isotherme” displays a linear increase at low lanthanide concentrations up to about 2µmol/l Ln^{3+}. Above that point the curve bends to the right with a maximum at 10µmol/l which means that between 2 and 10µmol/l metal concentration,

the complexation runs into saturation. At even higher Ln^{3+}-concentrations the HA starts to coagulate due to neutralisation of the organic molecule.

3.2.5.2 pH-edges

The HA complexation of Eu and Gd depends on the pH of the sample solution. Protons compete with the lanthanides and replace them from the humate. In addition, the complexation ability of the HA scales with pH-values. Particle size increases with lower pH, causing less complexation, and at pH <3 coagulation occurs which removes HA and complexed metal from solution.

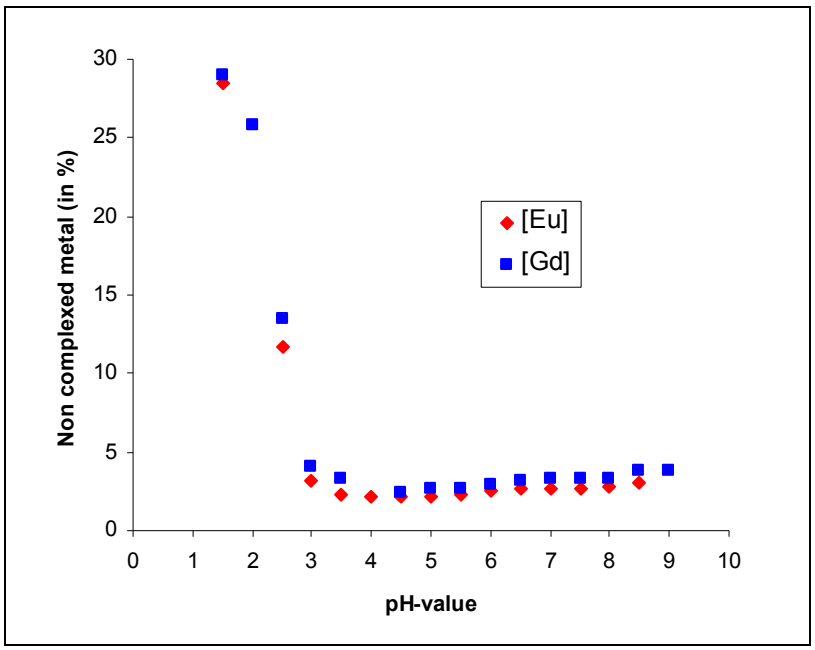

Fig. 14: Illustration of HA complexation with Eu (red dots) and Gd (blue dots) depending on pH, $c(Ln^{3+})$=, pH=1.5-9.0, c(HA)=25ppm, ionic strength ($NaClO_4$)=10mM, CE electrolyte: 100mM acetic acid + 10mM NaAc

Fig. 14 shows a comparison between Eu and Gd for the non complexed metal contingent. Consistent with the results in section 3.2.7.1, the amount of non complexed Gd is always a little higher than the amount of non complexed Eu. Numerical results are shown in Table 6.

Table 6: Stability constants for Eu and Gd complexes with HA, measured with CE-ICP-MS, c(Ln^{3+})=500ppb, pH=1.5-9.0, c(HA)=25ppm, ionic strength ($NaClO_4$)=10mM, LC not accounted for (LC=1)

pH-value	*log K (Eu)*	*log K (Gd)*
1.5	3.90	4.80
2	4.87	4.87
2.5	5.28	5.22
3	5.86	5.79
4	6.02	6.00
5	6.01	5.97
6	5.95	5.91
7	5.92	5.88
8	5.86	5.74
9	5.85	5.80

Between pH 3 and pH 9 there is only little variation in stability constants for Eu and Gd with HA. The expectation would be that the complexation should decline at lower pH-values because of the higher concentration of protons. However, as pH rises, carbonato- and hydroxo-species of the lanthanides are formed, which carry a lower positive charge than the Ln^{3+}-aquo ion. Therefore, the amount of non HA complexed lanthanides at high pH-values is even a little higher than at low values. At very low pH (<3), the HA coagulates because of neutralisation through protons (red numbers in Table 6) which causes a significantly lower lanthanide complexation. At those extreme conditions it can be assumed that besides the lanthanide which is still in solution as metal humate, there will also be metal in the precipitate.

3.2.5.3 Competing complexation with Ca, Mg and Al

Another aspect of geochemical parameters is the influence of naturally occurring metals on the complexation of humic acid with the pollutant heavy metals.

There are a lot of possible interferences here, i.e. alkaline and alkaline earth metals, aluminium, iron or manganese. Magnesium, calcium and aluminium are chosen here due to the relatively high amount in which they can be found in the environment. The influence on the complexation behaviour of europium and gadolinium with HA of alkaline metals is very weak because of the low charge and big size of alkaline ions.

Calcium and magnesium are usually found in groundwater and at higher concentrations the effect on the HA complexation is more distinct than for sodium and potassium because of their bivalency. Aluminium may be present in larger concentrations because of kaolinite decomposition at extreme experimental conditions.

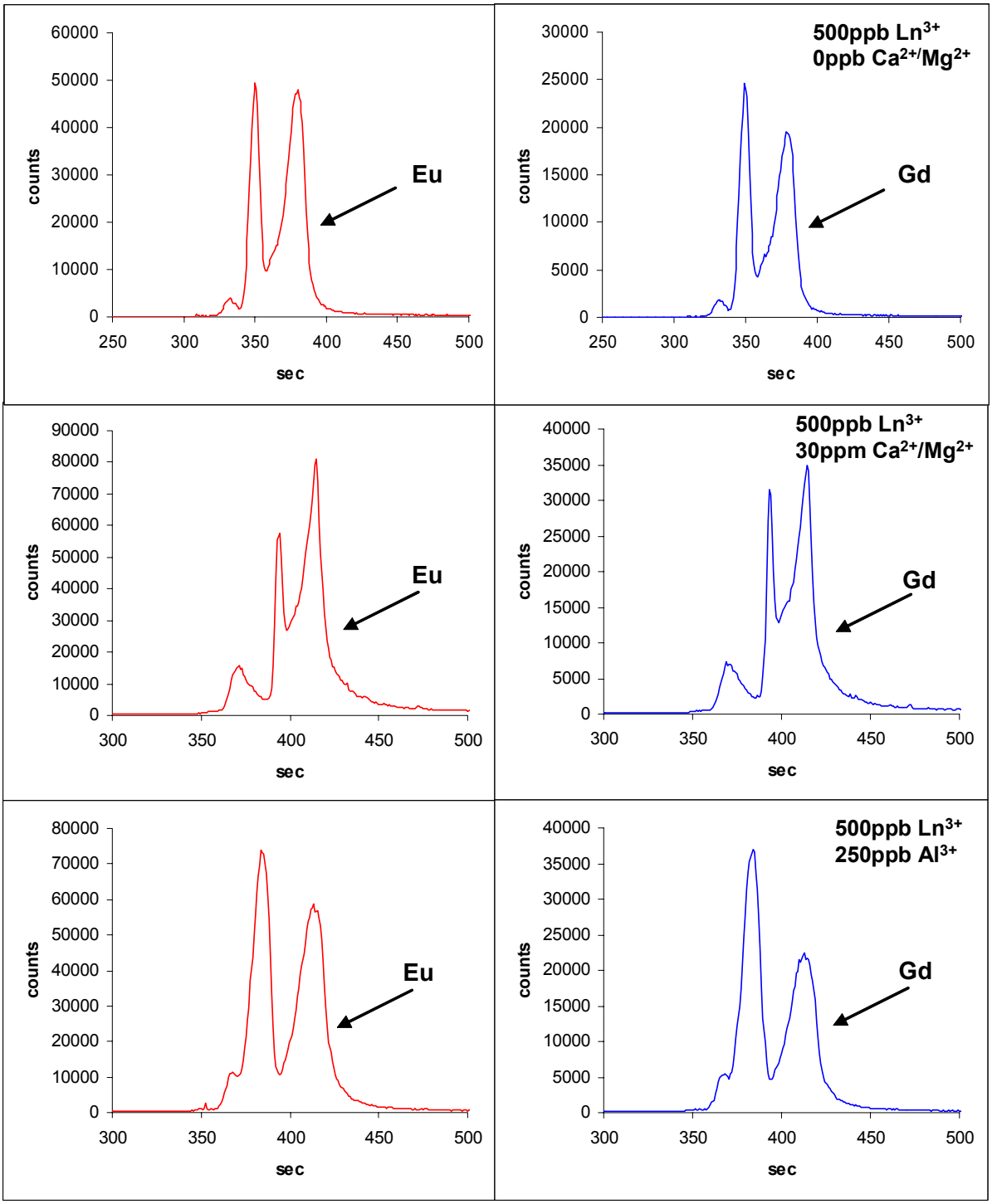

Fig. 15: CE-electropherograms of Eu (red signal) und Gd (blue signal) with different competing ion concentrations, c(Ln^{3+})=500ppb, pH=5, ionic strength ($NaClO_4$)=10mM, c(HA)=25ppm

Comparing electropherograms without the influence of competing cations and the ones with 30ppm Ca and Mg, a significant increase in the first signal can be observed (Fig. 15). The lanthanides are replaced by alkaline earth elements particularly in the less strong binding HA fractions. The second peak decreases for the benefit of the non HA complexed metal peak. This is because of the higher stability of the Ln^{3+}-complexes in comparison with Ca and Mg HA complexes. For the 250ppb aluminium sample the ratios are different. The first and the second peak increase at the cost of the third. This means that Al is able to displace the lanthanides from stronger binding HA sites to the less strong binding sites and to non complexed metal. However, the vast amount of the displaced lanthanides is found in the second peak, which shows that it is still HA complexed before CE separation.

With other analysis methods, such as ultrafiltration, the change in complexation behaviour could possibly not have been detected because these methods only distinguish between complexed and non complexed metal, no matter how stable the complexes really are in presence of competing ions. Unfortunately, in the Al samples the big second peak inhibits a reliable quantification of the non complexed lanthanides.

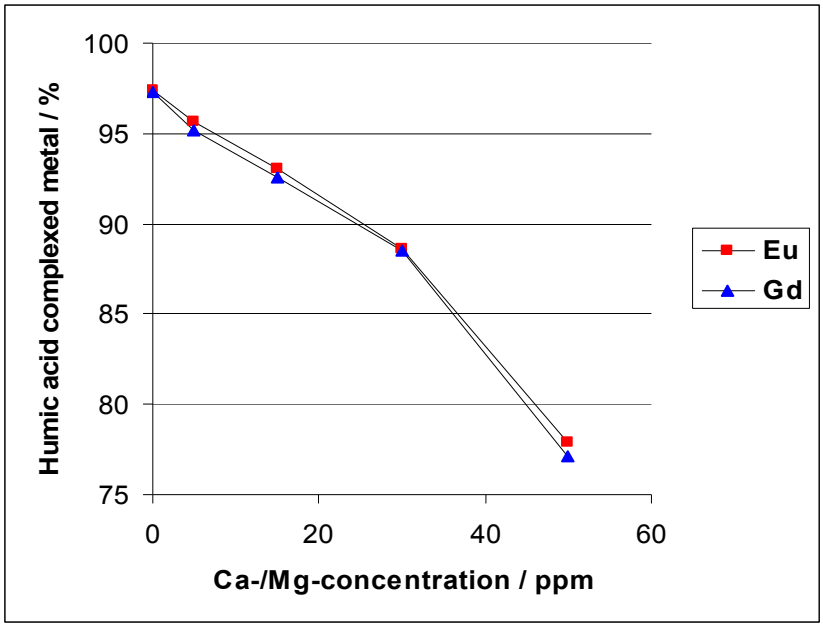

Fig. 16: Illustration of HA complexed lanthanides depending on Ca/Mg-conentration, measured by CE-ICP-MS, pH=5, $c(NaClO_4)$=10mM, c(Eu+Gd)=500ppb

The replacement of Eu and Gd from the HA complexes scales with the alkaline earth concentration as shown in Fig. 16. However, even at a 200fold excess concentration of Ca and

Mg the HA complexed amount of the lanthanides is still over 75% due to their higher affinity to the stronger binding sites of the HA.

Relatively high alkaline earth concentrations are needed to see a significant effect in this system. Aluminium as a small, trivalent cation presents a strong competition in HA complexation. At 250ppb Al, which is a concentration that can be estimated when working e.g. at low pH-values and 0.1M ionic strength, a large amount of the lanthanides gets displaced from the stronger binding HA complexation sites. Thus, it is advisable to work at preferably natural conditions when performing sorption and complexation experiments involving clay mineral.

3.3 The binary system metal/kaolinite

The system metal/kaolinite is perhaps the most important of the three binary systems. It represents the key for understanding lanthanide migration in clay formations. Humic acid can be understood as an additional research parameter in the ternary system. It is important to understand the influences of lanthanide concentration, pH and competing cations like calcium and magnesium. The performed desorption experiments are based on the corresponding sorption experiments and simulate metal migration at a multiple equilibration basis.

3.3.1 Adsorption isotherms

At a certain metal concentration an adsorption maximum is reached for clay minerals, dependent on metal charge and other experimental conditions. When this concentration is reached, additional metal could pass virtually without retention through a geological barrier.

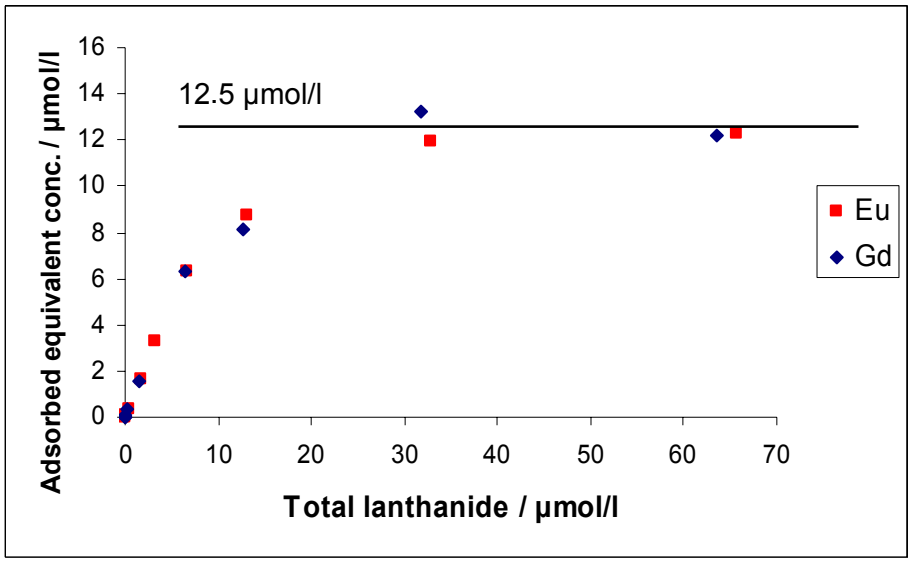

Fig. 17: Illustration of an adsorption isotherm for Eu and Gd on kaolinite, $c(Ln^{3+})$=500ppb, pH=5, $c(NaClO_4)$=10mM

At lower concentrations of europium and gadolinium the curve plotted in Fig. 17 has a linear positive slope. A vast amount of additional metal with raising concentration is adsorbed by kaolinite in this concentration area. Above about 8µmol/l the slope begins to decrease until the sorbed lanthanides reach a limit of 12.5µmol/l which is equivalent to an exchange capacity of 0.94meq/100g for the trivalent cations. This value is a little lower than the CEC, determined by NH_4Cl-exchange (1.24meq/100g), and suggests an incomplete covering of the clay mineral, possibly due to interference between the highly positive charged Ln^{3+}-ions. Consequently, the exchange capacity introduced here applies specifically for the system Ln^{3+}/kaolinite KGa-1b at the experimental conditions used. The curve progression clearly indicates the existence of highly active (binding-) sites on the kaolinite surface that are preferably occupied at low metal concentrations. At higher concentration the weaker binding sites are also used which results in a slightly higher amount of unsorbed metal remaining in the sample solution.

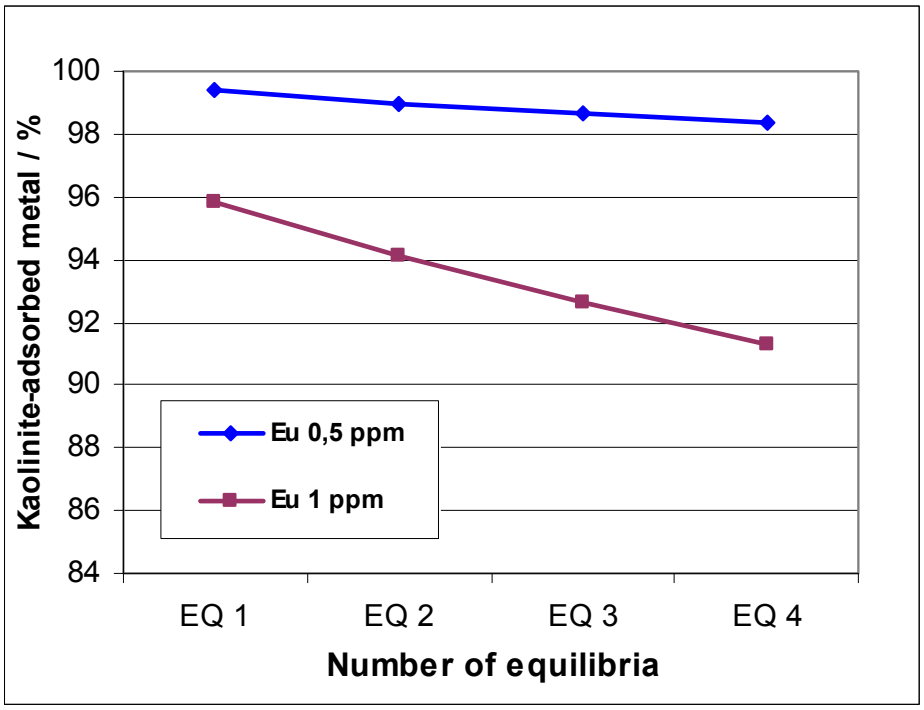

Fig. 18: Illustration of kaolinite-sorbed europium after repeated desorption with metal free 10mM $NaClO_4$-solution depending on the original europium concentration, pH=5

Desorption and consequently the migration speed of lanthanides is directly dependent on the number of equilibration steps, analysed in batch experiments. As seen in Fig. 18, desorption is increased at higher lanthanide concentrations. This is due to the preferred occupation of highly active sites on the kaolinite surface at lower metal concentrations. As the metal concentration rises, less active sites are occupied which results in a higher ratio of non sorbed

metal. After the fourth desorption step of a material originally treated with a solution containing 500ppb Eu, more than 98% of the originally deployed metal is still adsorbed at the kaolinite. For 1ppm Eu this value decreases to about 91% at the same experimental conditions. Such metal concentrations are still well below the maximum exchange capacity for Ln^{3+} on kaolinite. However, at the investigated concentrations the metal sorption in the system metal/kaolinite can be estimated as high, not considering of other experimental parameters like pH or competing ions.

3.3.2 pH-edges

Sorption of Eu and Gd is dependent on the surface charge of kaolinite. Changing pH-values have direct influence on the charge through protonation and deprotonation. Additionally the protons act as competing ions and are able to replace metal ions. Furthermore, carbonato- and hydroxo-species of the lanthanides can be formed at higher pH-values which can influence the lanthanide sorption.

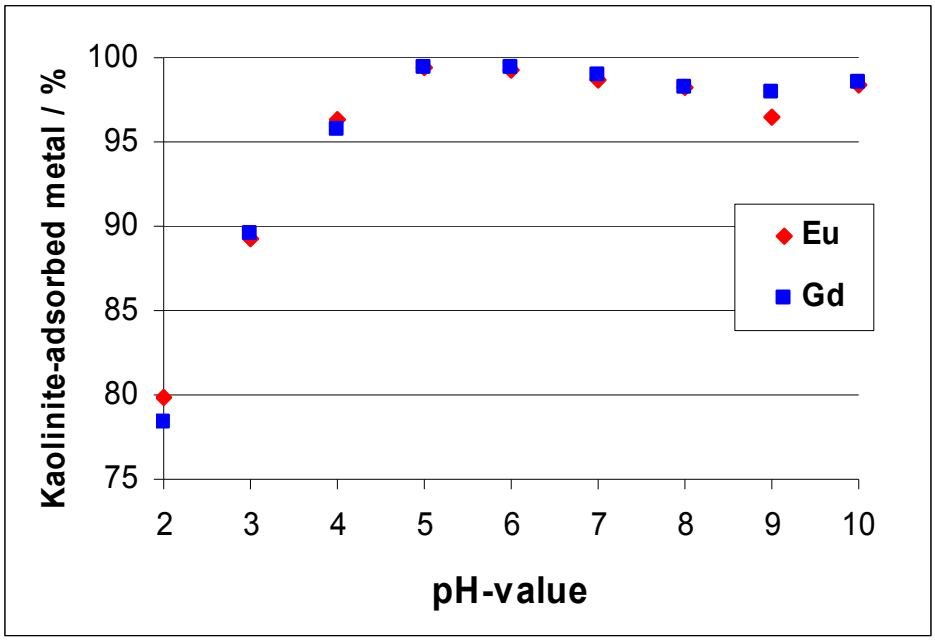

Fig. 19: Illustration of sorption behaviour of Eu and Gd on kaolinite depending on pH, $c(Ln^{3+})$=500ppb, $c(NaClO_4)$=10mM

The lanthanide sorption is quite high over the whole pH-area under investigation as seen in Fig. 19. The fraction of non sorbed metal never exceeds 20%. This means that kaolinite is generally able to retain trivalent lanthanide metals in geological formations. However, thing change with changing pH. At values below pH 5 the sorption is reduced because of competing protons, but such extreme pH-values are not expected to occur in nature. At higher val-

ues carbonato- and hydroxo-species of the lanthanides suppress surface sorption. However, this effect is rather small, the sorption never falls below about 97%.

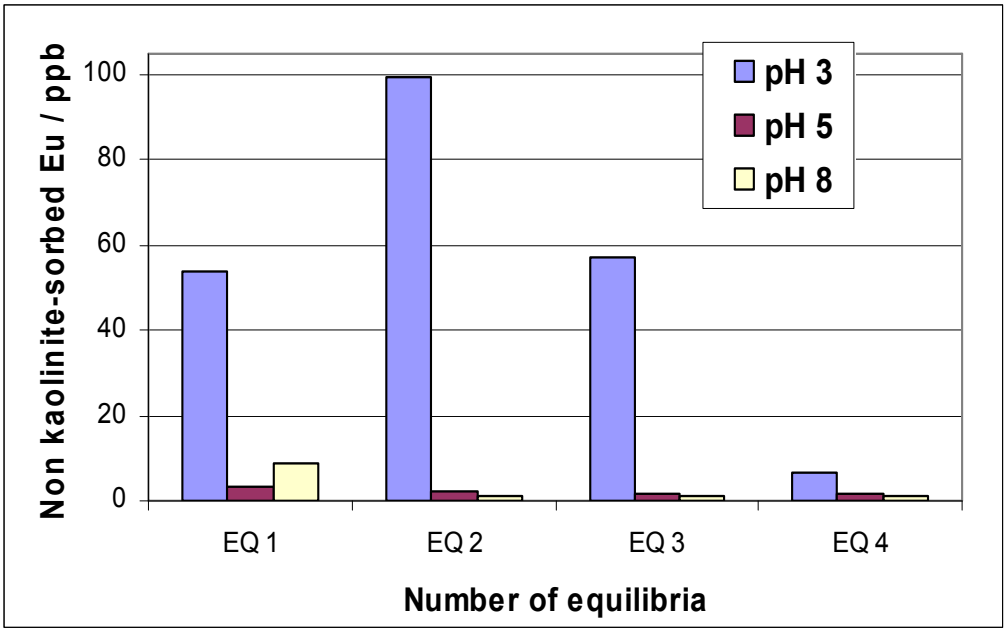

Fig. 20: Illustration of non kaolinite-sorbed europium after repeated desorption with metal free 10mM $NaClO_4$-solution depending on pH, c(Ln^{3+})=500ppb

The concentration of Eu, measured in the centrifugate of multiple desorption equilibria for different pH-values is shown in Fig. 20. At pH 3 the non sorbed fraction at EQ 2 is higher than the one at EQ 1. This is exceptional because the desorbed fraction should decrease gradually as the higher active sites of the kaolinite surface stay occupied. In this test series, samples from the sorption experiments were used which were covered with a residue of supernatant solution of different pH for a certain period of time. At pH 3 this could have caused a reduction of kaolinite particle size, thus preventing the sample from being separated completely by centrifugation. However, if this would occur in a natural environment, the smaller particles would possibly also be able to migrate through geological formations, similar to solutions.

At pH 5 and pH 8, the desorption decreases with each equilibrium step. But again, there is an unforeseen behaviour in comparison between those two pH-values. At EQ 1 there is more desorbed lanthanide at pH 8 compared to the situation at pH 5 because of the metal speciation. However, the ratios are inverted at EQ 2 to 4. When lanthanides are sorbed at pH 8, desorption is possibly kinetically suppressed because of the absence of competing ions such as protons.

3.3.3 Influence of competing metals

It is important to know how the possibly present water hardness (Ca, Mg) affects lanthanide sorption on kaolinite. In such an ion exchange reaction, the replacement of europium and gadolinium depends on the competing ion concentration. Aluminium, which could be present in sample solutions because of kaolinite decomposition, can also be of interest in this context.

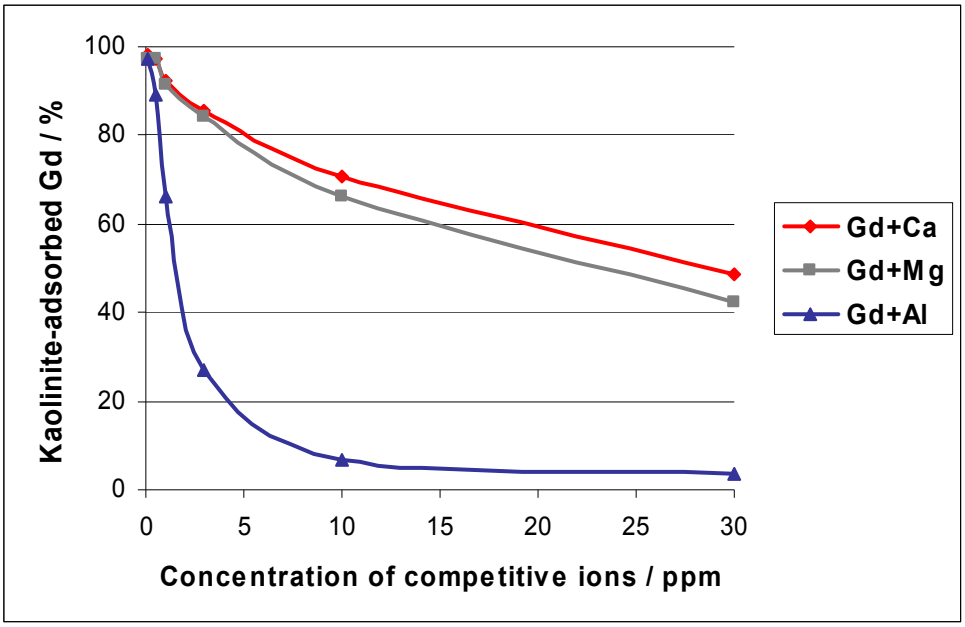

Fig. 21: Illustration of kaolinite-sorbed Gd depending on competing ion concentrations, c(Ln^{3+})=500ppb, c($NaClO_4$)=10mM, pH=5

The amount of kaolinite-sorbed lanthanides decreases with increasing competing ion concentrations as shown in Fig. 21 for gadolinium. Sorption is almost 100% without calcium, magnesium or aluminium and it is reduced significantly when competing metals are present. In presence of trivalent Al^{3+}, a vast amount of Gd remains in solution above a concentration of 10ppm Al. However, such Al concentrations are not expected to occur in nature. Ca^{2+} and Mg^{2+} represent less strong competitors, yet in excess concentrations they are able to suppress lanthanide sorption significantly. With 30ppm Ca/Mg about 50% of Gd remain soluted. Due to its higher electropositivity, Ca is a stronger competitor than Mg.

In comparison with lanthanide desorption from kaolinite without competing ions, desorption is significantly higher in the presence of Ca and Mg as seen in Fig. 22. While kaolinite sorption is still above 90% after the fourth equilibrium for both europium concentrations without alkaline earth elements, the value drops to near zero when 30ppm Ca or Mg are present. This would mean that there is a dramatically increased migration speed of trivalent lanthanides through geological formations under these conditions.

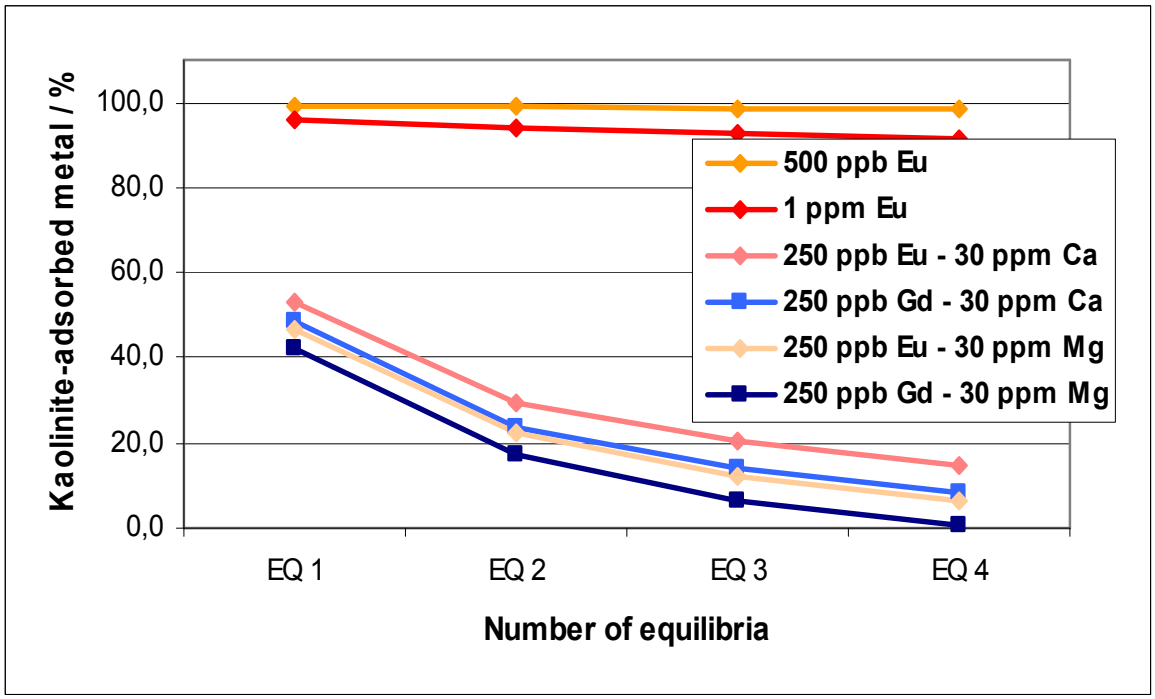

Fig. 22: Illustration of kaolinite sorption of Eu and Gd depending on different competing ion concentrations after desorption with metal free 10mM $NaClO_4$-solution containing different concentrations of Ca or Mg, pH=5

The differences between the several measuring points at EQ 4 may be overestimated due to adding measurement failures over the four sequenced tests. The relative offset of the desorption curves results from different affinities of the metal ions to the negatively charged kaolinite surface. The following ranking can be made, starting with high affinity:

Eu > Gd >> Ca > Mg

3.4 The ternary system humic acid/metal/kaolinite

The ternary system is most suitable for simulating metal migration under natural conditions. Research in the three binary systems can be seen as preliminary tests for understanding partial aspects of the complete system. With HA, there is the possibility that metal humates could adsorb on the kaolinite surface through hydrophobic interactions, thus increasing lanthanide retention. Negatively charged complexes could also inhibit lanthanide sorption and accelerate migration through clay minerals. Sorption behaviour is strongly dependent on experimental conditions as tests performed in the ternary system clearly show.

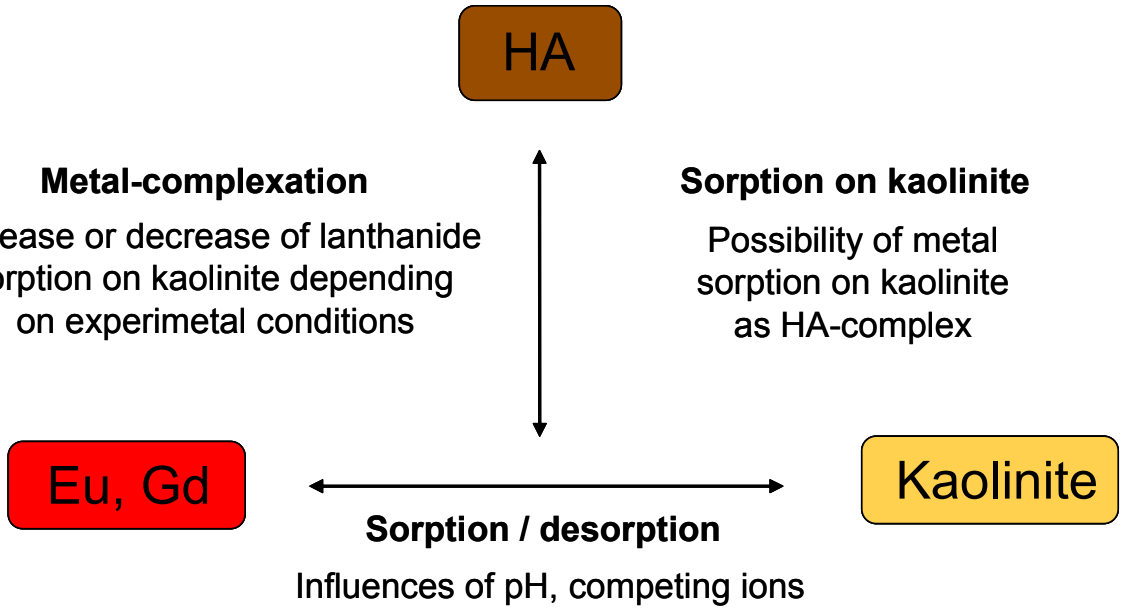

Fig. 23: Conception of the ternary system, consisting of lanthanides, humic acid and kaolinite and important influence factors

The experiments which were performed here are based on the test series of the system metal/kaolinite with HA as an additional influencing factor. Fig. 23 shows the most important test parameters which were examined here and relations to the binary systems.

3.4.1 Influence of lanthanide concentration

This experimental series was performed on the basis of the corresponding tests in the system metal/kaolinite (section 3.3.1). With HA present, lanthanide sorption on kaolinite is suppressed especially at low concentrations of europium and gadolinium (Fig. 24). As lanthanides are complexed by HA and since there are not enough positive charged ions present to neutralize the complexes at pH 5, a significant amount stays in solution. With rising lanthanide concentration, which also means a higher amount of metal complexed by HA, the HA partially loses its negative charge and is able to adsorb at the kaolinite surface through hydrophobic interactions including the complexed metal. From about 3µmol/l lanthanide concentration the sorbed absolute amount of metal is almost the same as without HA present. With HA, even a little more lanthanide seems to be removed from solution at higher concentrations of metal. This could indicate that the vast amount of HA complexed lanthanides is adsorbed at kaolinite under these circumstances. It should be pointed out that in presence of HA the adsorption ratios for different lanthanide concentrations can be opposite to the ones in absence of HA. It can be summarized:

Conditions with higher lanthanide migration:

- higher metal concentrations in absence of HA
- lower metal concentrations in presence of HA

Conditions with lower lanthanide migration:

- lower metal concentrations in absence of HA
- higher metal concentrations in presence of HA

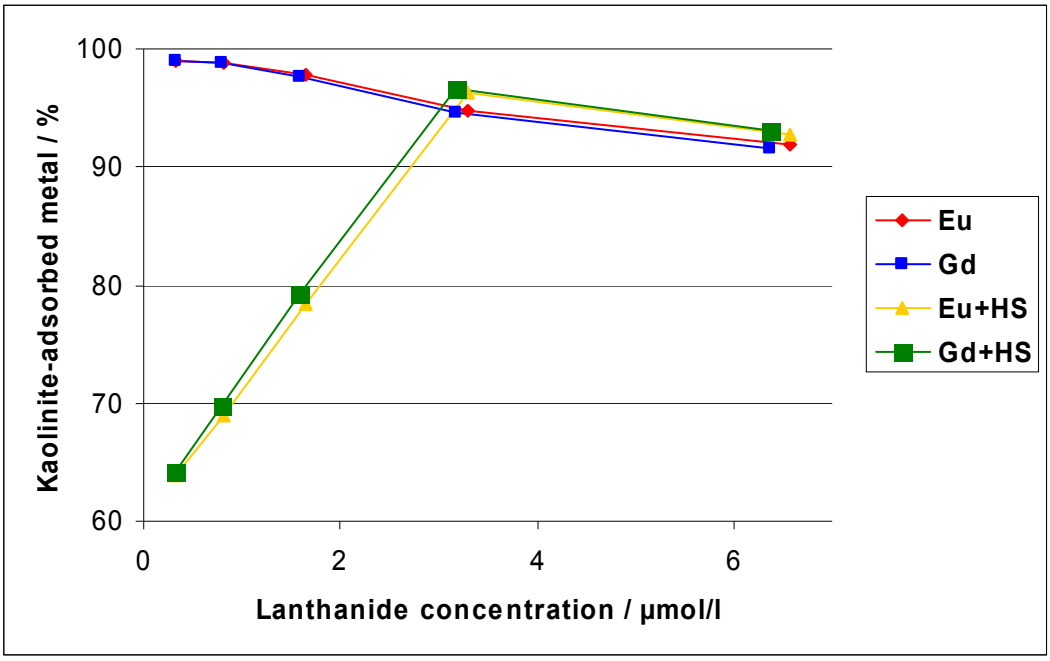

Fig. 24: Illustration of the influence of humic acid on the sorption of europium and gadolinium on kaolinite at different lanthanide concentrations, c(HA)=25ppm, pH=5, c($NaClO_4$)=10mM

3.4.2 pH-edges

The influence of HA on lanthanide sorption at kaolinite surfaces with different pH values is based on similar mechanisms as different lanthanide concentrations. Protons act analogously to metals and are able to neutralize the kaolinite surface as well as HA complexes. That leads to interesting results which are discussed below.

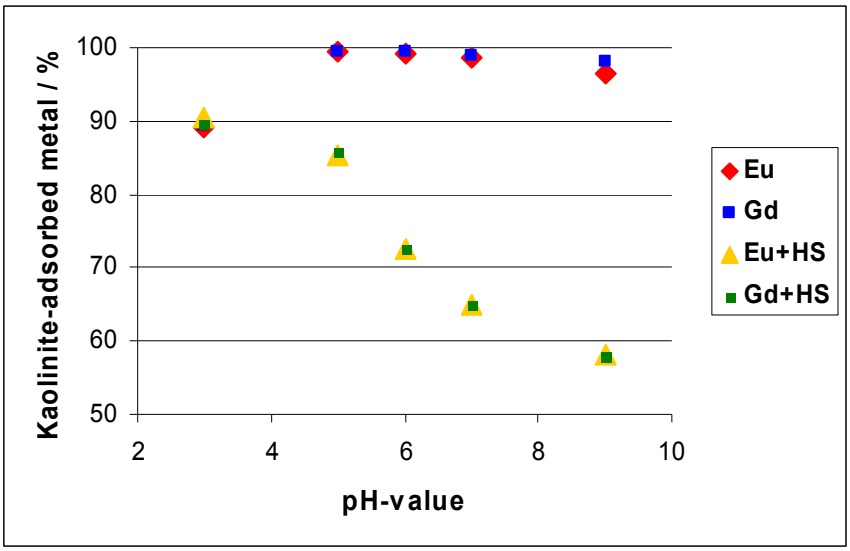

Fig. 25: Illustration of the influence of humic acid on the sorption of europium and gadolinium on kaolinite at different pH-values, c(Ln^{3+}): 500ppb, c(HA)=25ppm, c($NaClO_4$)=10mM

At pH 3, lanthanide sorption is about the same with or without the presence of HA, as seen in Fig. 25. HA and the kaolinite surface are covered with protons and lanthanides at different ratios, depending on pH. With increasing pH, the negative charges inhibit HA sorption and a higher amount of lanthanides stays in solution. While almost 100% of Eu and Gd are sorbed above pH 5 in absence of HA, the amount of dissolved lanthanides rises to over 40% at pH 9 if HA is present. The organic complexing agent suppresses lanthanide sorption over a wide pH area due to formation of overall negatively charged metal complexes that are unable to adsorb onto the kaolinite surface. The influence of different pH values is strongly dependent on the presence of HA and can be summarized as follows:

Conditions with higher lanthanide migration:

- lower pH-values (<pH 4) in absence of HA
- higher pH-values in presence of HA

Conditions with lower lanthanide migration:

- higher pH-values (>pH 4) in absence of HA
- lower pH-values in presence of HA

3.4.3 Ca and Mg as competing metals

As shown in Fig. 26, lanthanide sorption behaviour on kaolinite in presence of competing ions is strongly dependent on the presence of HA. Sorption at different concentrations of Ca and Mg is reversed through the influence of the humic substance. In absence of the alkaline earth metals, HA complexation leads to a decrease in kaolinite sorption of the lanthanides because the humate retains a negative total charge. Eu and Gd are being held in solution which would also mean an increased migration through geological formations. Ca and Mg occupy lesser active sites of the HA while the trivalent lanthanides stay strongly complexed.

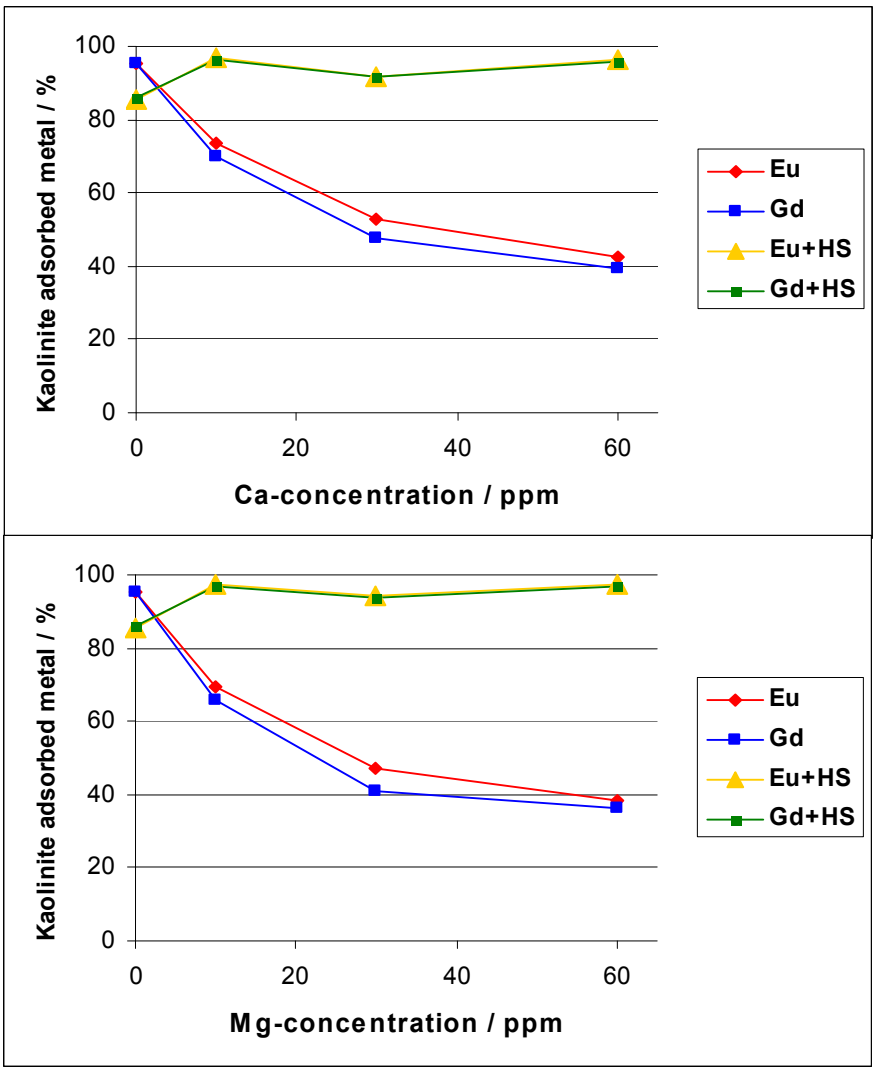

Fig. 26: Illustration of the influence of different Ca- and Mg-concentrations on the Eu- and Gd-sorption on kaolinite with and without the presence of humic acid, pH=5, c(Ln^{3+})=500ppb, c($NaClO_4$)=10mM

This reduces the negative humate charge with increasing alkaline earth concentration. Through this neutralisation the humates adsorb onto the clay surface, reducing the amount of

lanthanides in solution. Already at a relatively low Ca/Mg concentration (10ppm), lanthanide sorption is above 95% where it stays also at higher competing ion concentrations in presence of humic acid. This behaviour clearly shows that it is of paramount importance to know the exact geological conditions at a potential disposal site.

Conditions with higher lanthanide migration:

- higher alkaline earth concentrations (e.g. due to water hardness) in absence of HA
- lower alkaline earth concentrations in presence of HA

Conditions with lower lanthanide migration:

- lower alkaline earth concentrations in absence of HA
- higher alkaline earth concentrations in presence of HA

4 Conclusions and Outlook

To elucidate mechanisms during migration in aquifer systems in the presence of humic acid the different binary systems and the ternary system consisting of heavy metals (Eu and Gd), humic acid (Aldrich HA) and clay mineral (kaolinite KGa-1b) have been examined. First, the complex ternary system was divided into three binary subsystems: metal/humic acid, humic acid/kaolinite and metal/kaolinite. As there are interdependences between the subsystems, experiments with the ternary system were performed as well. One of the main topics was the determination of stability constants for the complexation of lanthanides with humic acid. Therefore different speciation methods like ultrafiltration and CE-ICP-MS were used. Especially CE-ICP-MS analysis was explored and improved for this purpose. To determine HA with ICP-MS, Aldrich humic acid was iodinated which allows a simultaneous detection of all metal species in one analysis step. The complexation constants were derived with the MICN model and are in good agreement with other values taken from literature. For europium we obtained a log β_{EuHS} of 6.44±0.15, and gadolinium was found to have a log β_{GdHS} of 6.33±0.14 (averaged over all pH-values, concentrations from 0.1 to 4.0ppm and using two different methods).

The analytic tools developed for speciation were further used to elucidate the influence of naturally occurring competing cations in the different binary and ternary systems examined. It could be shown that Ca, Mg and Al ions inhibit the binding of the lanthanides to the humic acid significantly and has a strong effect particularly with regard to the sorption and desorption behaviour on kaolinite. Additionally kinetic aspects of the sorption were examined. The influence of preconditioning time could be shown as well as the reversibility of the sorption. In the binary system metal/kaolinite, adsorption isotherms, pH-edges and the influence of the

water hardness were analyzed. With increasing lanthanide concentration, desorption of these metals from kaolinite rises even before the CEC of 0.94meq/100g is reached. This indicates that, in absence of HA, and with low pollutant metal concentrations there is lower metal migration. The pH-value has only a minor influence in natural occurring ranges. Significant changes in migration behaviour have to be considered only at high (above pH 8) or low (below pH 4) pH-values. The biggest influence factor without HA in solution are competing cations. While alkaline metals show no relevant competition to lanthanide sorption on kaolinite, alkaline earth metals like calcium and magnesium have a significant impact on the system metal/kaolinite. With competing ion concentrations close to nature, lanthanide sorption decreases dramatically. Desorption experiments show, that after four equilibrating steps, virtually all lanthanide has been extracted from kaolinite to the solution, meaning that there is very high metal migration in geological formations.

The HA seems to play the role of a mediator which makes the ternary system more stable against influences like the pH-value and competing cations. The tendencies obtained in the binary system metal/kaolinite are often reversed in presence of humic acid. With both low lanthanide concentrations and higher pH, lanthanide migration should be accelerated by HA. Under conditions which would normally suppress metal sorption, like high lanthanide concentrations and low pH, HA acts as a sorption agent between lanthanides and kaolinite. Neutralized lanthanide complexes are able to adsorb to kaolinite through hydrophobic interactions, lowering metal migration. The described behavior also applies for competing cations like calcium and magnesium which significantly increase lanthanide migration in the binary system metal/kaolinite. With HA present, alkaline earth cations occupy lower active sites of the HA, allowing the lanthanides to stay complexed and neutralising the humates which leads to enhanced kaolinite sorption.

In sum, the results of our studies clearly indicate the necessity to know the exact geological conditions at a potential disposal site. Many factors influence metal migration, metal concentration, pH and presence of competing cations as well as humic substances being the most important factors. A better study of metal migration than by the evaluation of batch experiments would be possible by using miniaturized clay columns as alternative to classical column setups. This would lead to fast and economical migration analysis of radionuclides and other heavy metals in clay formations under conditions close to nature.

Appendix

Chemicals

The used humic acid is commercially available from Aldrich (St Louis, USA; humic acid sodium salt), it was purified as described in the literature [7]. All other chemicals (see also Table 2) were of at least p.a. quality or better (suprapure) and were obtained from Merck (Darmstadt, Germany). Milli-Q deionized water (18MΩ) was used to prepare all solutions. The CE electrolyte buffer (100mM acetic acid / 10mM Na-acetate) was filtered (0.45µm syringe filter, Minisart, Sartorius, Germany) and degassed in a supersonic bath before use. The single-element standards of Cs, Eu, Gd and Ho (Certipur or Suprapur) were obtained from Merck. Argon 4.6 (99.996%, Messer Griesheim, Germany) was used as plasma gas. All standard dilutions and samples were prepared with 10mM $NaClO_4$ ionic strength. The 1kD ultrafiltration system (Microsep 1K Omega) was obtained from Pall Life Sciences (Ann Arbor, USA).

Instruments

pH-Measurements

pH-measurements were carried out with pH-electrodes from Metrohm (CH) and pH-meters from WTW, WTW pH521 and WTW pH91.

UV/Vis-Spectroscopy

Spectra and concentration measurements of humic acids were carried out with a UV/Vis-Spectrometer Lambda 25, Perkin Elmer with software for Windows 95. Detection in the CE was carried out with the built-in Diode Array Detector or the UV/Vis-Detector with four fixed wavelengths (210, 214, 254 and 280nm).

Capillary Electrophoresis

All CE-measurements were carried out on a CE MDQ from Beckman Coulter with the software P/ACE MDQ version 2.30, fitted with two detectors, a DAD and a UV/Vis at fixed wavelength. The quartz capillaries were fused-silica ones from Polymicro Technologies with inner diameters of 75µm.

ICP-MS

All ICP-MS measurements were carried out on a Plasma Quad 3 instrument from VG Elemental.

5 References

[1] Stevenson FJ (1994) Humus Chemistry. Wiley, New York.

[2] R. Sutton, G. Sposito, Environ. Sci. Technol. 39 (2005) 9009-9015.

[3] Marquardt CM (ed) (2000) Influence of humic acids on the migration behaviour of radioactive and non-radioactive substances under conditions close to nature: Final report, Wissenschaftliche Berichte, FZKA 6557, FZ Karlsruhe.

[4] Marquardt CM (ed) (2004) Investigations on the complexation behaviour of humic acids and their influence on the migration of radioactive and non-radioactive substances under conditions close to nature. Wissenschaftliche Berichte, FZKA-6999, FZ Karlsruhe.

[5] Kim JI, Czerwinski KR (1996) Radiochimica Acta 73: 5-10.

[6] Plaschke M, Rothe J, Denecke M, Fanghänel T (2004) J Electron Spectrosc 135: 53-62.

[7] Kim HJ, Baek K, Kim BK, Yang JW (2005) J Hazard Mater 122: 31-36.

[8] Wrobel K, Sadi BB, Wrobel K, Castillo JR, Caruso JA (2003) Anal Chem 75: 761-767.

[9] Gehmecker H, Trautmann N, Herrmann G (1986) Radiochim Acta 40: 81-88.

[10] Coates JT, Fjeld RA, Paulenova A, DeVol T (2001) J Radioanal Nucl Chem 248: 501-506.

[11] Röllin S, Eklund UB (2000) J Chromatogr A 884: 131-141.

[12] Kautenburger R, Nowotka K, Beck HP (2006) Anal Bioanal Chem 384: 1416-1422.

[13] Kautenburger R, Nowotka K, Beck HP (2005) Migration'05: 10th International Conference on Chemistry and Migration Behaviour of Actinides and Fission Products in the Geosphere, Avignon.

[14] Schaumlöffel D, Prange A, Marx G, Heumann KG, Bratter P (2002) Anal Bioanal Chem 372: 155-163.

[15] Kuczewski B, Marquardt CM, Seibert A, Geckeis H, Kratz JV, Trautmann N (2003) Anal Chem 75: 6769-6774.

[16] Pröfrock D, Leonhard P, Ruck W, Prange A (2005) Anal Bioanal Chem 381: 194-204

[17] Kautenburger R, Nowotka K, Beck HP (2006) Proceedings of the 13th Meeting of the International Humic Substances Society, Karlsruhe (Germany). 45-II: 937-940.

[18] Braun D, Wirth HO (1961) Patentschrift 1 088 227, Deutsches Patentamt.

[19] Kautenburger R, Beck HP (2007, in print) Journal of Chromatography A.

[20] Nowotka, K.: Untersuchungen zur Migration von Europium und Gadolinium in Kaolinit als Modellmineral für eine Endlagerstätte. Dissertation, Universität des Saarlandes (2007, in print).

[21] Zeitz, M.: Untersuchungen zur Verteilung von toxischen Schwermetallen im System: Schwermetall, Huminsäure und Seesand unter natürlichen Bedingungen. Dissertation, Universität des Saarlandes (2003).

Appendix D - Institut für Interdisziplinäre Isotopenforschung e.V., Leipzig

Development and application of radiotracers for investigations on formation and partitioning of colloidal species of mobilised heavy metals in geosystems

H. Lippold, K. Franke, M. Richter, H. Kupsch

Final Report

Support Contract Number
02 E 9663

Institut für Interdisziplinäre Isotopenforschung e. V. (IIF)
Permoserstr. 15
04318 Leipzig
Germany

Content

Abstract

Main objective of the research project under report was to study the influence of geochemical parameters on the humic-bound transport of actinides. Emphasis was also placed on an improvement of process understanding as a prerequisite for the development of migration models. For measurements at adequate concentration levels, as well as for the realisation of spatially resolving transport experiments by means of positron emission tomography, radiolabelling techniques for humic substances were developed, and radioisotopes of rare earth elements were employed as short-lived tracer analogues of trivalent actinides.

Metal adsorption onto kaolinite is strongly affected by the presence of humic acid. The pH dependence of co-adsorption in the ternary system can be qualitatively ascribed to the pH dependences of the elementary processes in binary subsystems. Generally, humic-bound mobilisation is counteracted by the acidic surface properties of kaolinite.

A major task of the project was to characterise the competitive effect of iron(III) on actinide-humate complexation. Displacement reactions gain in importance at micromolar concentrations. They are accompanied by flocculation processes, which were attributed to charge compensation at humic colloids. Kinetic effects were explained by a retarded degradation of polynuclear hydrolysis species bound to humic acid.

A significant influence of sulfate ions as competing ligands was not observed.

On the basis of changes in the hydrophilic / hydrophobic properties of humic colloids, different modes of interaction with low-molecular-weight DOC constituents could be identified. A micellar character of the aggregates is unlikely. Implications on adsorption and metal complexation were found to be of minor importance.

Referat

Im Mittelpunkt des Projektes stand die Erfassung des Einflusses maßgeblicher Randbedingungen des huminstoffgebundenen Transportes von Actiniden in geochemischen Systemen. Wesentliches Anliegen war auch die Erbringung von Beiträgen zum besseren Prozessverständnis als Grundlage für die Konzeption von Ausbreitungsmodellen. Zur Realisierung von Verteilungsmessungen unter adäquaten Konzentrationsverhältnissen, sowie zur erstmaligen Durchführung ortsauflösender Transportuntersuchungen mittels Positronen-Emissions-Tomographie, wurden Huminstoffe durch Entwicklung geeigneter Markierungsverfahren radioanalytisch zugänglich gemacht, und Radioisotope von Seltenerdmetallen wurden als kurzlebige Analogtracer dreiwertiger Actiniden eingesetzt.

Die Metalladsorption an Kaolinit wird durch die Komplexbildungs- und Adsorptionseigenschaften von Huminsäuren stark überprägt. Dabei ist die pH-Abhängigkeit der Koadsorption im ternären System qualitativ rückführbar auf die pH-Abhängigkeiten der mobilitätsbestimmenden Elementarprozesse in binären Randsystemen. Kaolinit wirkt einer huminstoffgebundenen Mobilisierung durch seine Oberflächenacidität prinzipiell entgegen.

Ein Schwerpunkt des Vorhabens lag auf der Charakterisierung des Konkurrenzeffektes von Eisen(III) bezüglich der Humatkomplexbildung von Actiniden. Verdrängungsreaktionen gewinnen im mikromolaren Bereich an Bedeutung und sind von Flockungsprozessen begleitet, die offenbar durch Ladungskompensation am Huminstoff herbeigeführt werden. Kinetische Effekte konnten durch einen verzögerten Abbau polynuklearer Hydrolysespezies im gebundenen Zustand begründet werden.

Ein signifikanter Einfluss von Sulfat-Ionen als Konkurrenzliganden wurde nicht festgestellt.

Anhand von Veränderungen der hydrophilen / hydrophoben Eigenschaften von Huminstoffkolloiden konnten verschiedene Prinzipien der Wechselwirkung mit niedermolekularen DOC-Bestandteilen identifiziert werden. Ein mizellarer Charakter der Aggregate ist dabei nicht wahrscheinlich. Auswirkungen auf Adsorptionsverhalten und Komplexierungsvermögen sind gering.

List of abbreviations

DBS	Sodium dodecylbenzenesulfonate
DGP	Dodecyl-β-D-glucopyranoside
DOC	Dissolved organic carbon
DTAB	Dodecyl trimethylammoniumbromide
HA	Humic acid
HPLC	High-performance liquid chromatography
HPSEC	High-performance size exclusion chromatography
HTAB	Hexadecyl trimethylammoniumbromide
PE	Polyethylene
PEC	Proton exchange capacity
PET	Positron emission tomography
PP	Polypropylene
SDS	Sodium dodecylsulfate
UV	Ultra-violet
VIS	Visible
XRF	X-ray fluorescence

List of symbols

c	Concentration
D	Solid-liquid distribution ratio
K_d	Distribution coefficient (solid-liquid distribution)
$\dot{m}$	Mass flow rate
M	Momentum
$P_{O/W}$	Partition ratio (octanol-water distribution)
t	Time
$T_{1/2}$	Half-life
v	Flow velocity
z	Coordination number
β	Complexation constant
Γ	Adsorbed amount

Square brackets denote concentrations.

1 Introduction

Assessments of the transport behaviour of actinides in case of release from subterranean radwaste repositories are an essential part of long-term safety analyses. In geochemical systems, adsorption onto mineral surfaces is the principal mechanism of immobilisation. This process is, however, negated by the presence of a dispersed phase of solid particles or colloids as part of the transport medium [1-3]. In particular, the complexing ability of humic and fulvic acids (HA, FA), as major constituents of the dissolved organic carbon (DOC), can dominate the speciation of multivalent metals [4, 5].

The risk of a facilitated migration is not sufficiently described by interaction constants since the carrier colloids themselves are also subject to a solid-liquid distribution. The underlying processes are dependent on the geochemical circumstances, which cannot be regarded as invariant in pertinent scenarios. For the development of site-specific transport models, the relevant mechanisms and their interaction must be fully understood in order to be able to identify the respective conditions of an enhancement or confinement of actinide migration by organic matter.

Furthermore, binding of actinides can be counteracted by other higher-valent metals which are present in natural waters. Thus, a mitigating effect on mobilisation is possible, and needs to be quantified. The influence of multivalent electrolyte constituents is not confined to competitive effects but is also characterised by flocculation processes, entailing complete immobilisation [6, 7]. For this reason, the stability of the colloidal system metal / humic substance must be regarded as well.

Binding of higher-valent metals is often accompanied by kinetic effects which result in an increasing inertness of the humate complexes [8, 9]. Accordingly, the applicability of equilibrium models must be considered carefully. The structural background of these time-dependent processes is far from being understood. Hence, an implementation in transport models is hardly possible at present.

The investigations presented in this report are oriented to clay rock as a potential host formation for a final repository. According to an agreement among the participants of the joint project, kaolinite was used as a model component. The pH-dependent influence of humic acid on metal adsorption was studied, and was related to the pH dependences of the elementary processes in binary subsystems, using a composite distribution approach.

Major emphasis was also placed on competitive effects of iron(III) and sulfate on humate complexation of actinides. Threshold concentrations of displacement reactions were determined for various humic and fulvic acids (GoHy-573 HA and FA, bog soil HA, Aldrich HA), and flocculation as a concomitant phenomenon was systematically investigated. Special attention was given to the elucidation of time-dependent processes in the interaction of iron(III) and HA.

Another topic was the influence of low-molecular-weight organic compounds on relevant processes of the humic colloid-borne transport. In natural systems, these DOC components

are likely to be associated with the colloids, but most studies are performed with isolated humic materials. Therefore, possible interferences were examined in this project.

Migration of radionuclides in real geological matrices is not only determined by partitioning equilibria but also by hydrodynamic transport phenomena depending on the inner structure of the barrier material. PET (positron emission tomography), as a non-destructive method for 3D imaging of radiotracer distributions, is a very promising tool for a direct observation and analysis of spreading processes in such systems. As part of the project, this technique was utilised for visualising colloidal transport in a closed matrix, which is a novelty in geochemical research.

Interaction of metals with humic substances has been found to be dependent on the concentration ratio [10, 11]. For this reason, partitioning of actinides in DOC-containing systems must be investigated at adequate concentration levels in order to generate reliable data. In general, conventional analytical methods are too insensitive for this purpose. In the studies presented, radioisotopes of rare earth elements (^{86}Y, ^{152}Eu, ^{160}Tb) were employed as short-lived tracer analogues of trivalent actinides, allowing experiments in the nanomolar range to simulate realistic settings. As a special tool, radiolabelling techniques for humic substances (using ^{18}F, $^{124/131}$I) were developed and applied to get analytical access to systems with low DOC content.

2 Experimental

2.1 Materials

2.1.1 Humic materials

Aquatic humic and fulvic acids isolated from an aquifer in the area of Gorleben (Lower Saxony, Germany), designated as GoHy-573 HA / FA, were supplied by Forschungszentrum Karlsruhe, Germany. Humic acid from Sigma-Aldrich (Taufkirchen, Germany), herein referred to as Aldrich HA, was purified by repeated precipitation and redissolution with 0.1 M HCl and 0.1 M NaOH / 0.01 M NaF, respectively. A further humic acid was extracted from soil which had been collected from the raised bog “Kleiner Kranichsee” (Saxony, Germany). The isolation was performed in accordance with the procedures adopted by the International Humic Substances Society [12]. Table 1 shows the elemental compositions of the purified materials, determined with a Vario EL III elemental analyser (Elementar, Hanau, Germany).

Table 1. Elemental compositions of HA and FA in wt% (normalised to dry weight, values of H and O corrected for H_2O content).

	Aldrich HA	**Bog soil HA**	**GoHy-573 HA**	**GoHy-573 FA**
C	53.2	53.2	58.3	51.7
H	4.2	4.4	4.3	4.2
O	38.0	34.1	33.4	41.6
N	0.8	2.4	1.9	1.1
S	3.7	0.5	2.0	1.3

2.1.2 Adsorbent material

Kaolinite KGa-1b standard material was obtained from the Clay Minerals Society of America (West Lafayette, USA), and was used as received. Some characteristics are given in Table 2. The loss on ignition was determined after heating at 1050°C for 1 h, pH_{eq} values were measured after equilibration of 15 mg kaolinite with 15 mL 0.1 M $NaClO_4$ for two weeks. Major element data were obtained by X-ray fluorescence analysis using a DX-95 energy-dispersive spectrometer (Edax, USA).

Table 2. Characteristics of kaolinite KGa-1b

Particle diameter	(µm)	0.8 [a]
Surface area	(m^2 g^{-1})	12.5 [a]
pH_{eq}		4.4
Loss on ignition	(wt%)	14.1
XRF data	(mg g^{-1})	
Al		227.4
Ca		n. d. [b]
Fe		1.8
K		n. d.
Mn		0.1
Si		202.0
Ti		22.5

[a] Taken from Ref. [13].
[b] n. d. = not detectable.

2.1.3 Radionuclides

[^{160}Tb]Tb ($T_{1/2}$ = 72.3 d) was produced by neutron activation of ^{159}Tb (1 mg mL^{-1}, as nitrate) at the TRIGA Mark II reactor of the University of Mainz. 50 h of irradiation at a neutron flux of 7×10^{-11} n cm^{-2} s^{-1} yielded a specific activity of 1.2 MBq mg^{-1}. [^{152}Eu]$EuCl_3$ ($T_{1/2}$ = 13.3 y) was purchased from Isotope Products Laboratories (USA), [^{59}Fe]$FeCl_3$ ($T_{1/2}$ = 44.5 d) was sup-

plied by Amersham Biosciences (UK). After transformation into perchlorate systems, stock solutions in 0.1 M $NaClO_4$ were prepared. For Eu and Fe, experimental concentrations were adjusted by adding $Eu(NO_3)_3$ or $Fe(NO_3)_3$ (analytical grade, Sigma-Aldrich) in 0.1 M $NaClO_4$ solution. N.c.a. [^{86}Y]YCl_3 ($T_{1/2}$ = 14.7 h) was supplied by QSA Global (Germany). [^{131}I]NaI ($T_{1/2}$ = 8.0 d) was purchased from Amersham (Germany), [^{124}I]NaI ($T_{1/2}$ = 4.1 d) was kindly provided by the University of Duisburg-Essen. N.c.a. [^{18}F]KF ($T_{1/2}$ = 1.8 h) was delivered by the University of Leipzig.

2.2 Methods

2.2.1 General remarks

All experiments were conducted at room temperature under aerobic conditions. Water was purified with an SG Ultra Clear system. Adjustment of pH values was accomplished by adding diluted $HClO_4$ or NaOH, using a Sentix 41 combination electrode (WTW, Weilheim, Germany) for measurement. Unless otherwise stated, usage of buffer systems was avoided. Stock solutions of HA or FA were discarded three weeks after preparation.

A 1480 Wallac WIZARD 3” gamma counter (Perkin Elmer, USA) was used for measurements of activity. All samples of a test series were made up to equal volumes to ensure a uniform measuring geometry.

UV-VIS spectrometry was conducted by means of a spectrophotometer Cadas 100 (Lange, Düsseldorf, Germany).

Size exclusion chromatography was performed with an HPLC equipment HP 1100 (Hewlett-Packard, USA), using a 300 × 7.8 mm TSKgel G3000 PWXL HPSEC column (Phenomenex, USA). 46 mM phosphate buffer (pH 7) was used as eluent at a flow rate of 0.6 mL min^{-1}.

2.2.2 Radiolabelling techniques for humic substances

Labelling with $^{124/131}$I. The Iodogen method for radioiodination of proteins [14] was adopted for radiolabelling humic acid with ^{124}I or ^{131}I. Halogenation is achieved by electrophilic substitution at activated positions of the aromatic backbone after oxidation of [$^{124/131}$I]I^- by Iodogen (1,3,4,6-tetrachloro-3a,6a-diphenylglycouril). The reaction was performed in 5 mL glass vials with 150 µg Iodogen, which was added in 200 µL chloroform to produce a coating on the surface after evaporation of the solvent. A mixed solution of [$^{124/131}$I]NaI and HA in borate buffer (pH 8) was prepared, and portions of 500 µL were dispensed into several vials containing Iodogen. After shaking for 10 min, the solutions were transferred into centrifuge tubes. For purification from excessive or loosely bound labelling material, the humic acid was precipitated by acidification to pH < 1 with concentrated $HClO_4$. After centrifugation (20 min at 8000 rpm), the supernatant was discarded, and the precipitate was redissoluted in 10^{-3} M NaOH. This procedure was repeated until the loss of activity was negligible (Fig. 1).

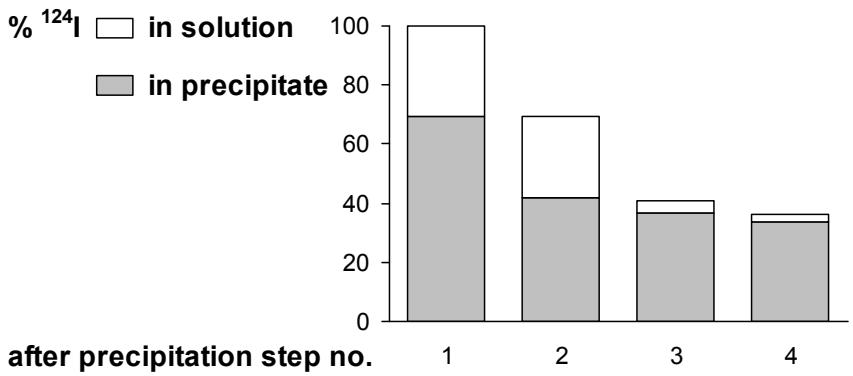

Figure 1. Purification of ^{124}I-labelled HA by repeated precipitation / re-dissolution (activities in precipitate and supernatant).

For batch experiments with ^{131}I-HA, input activities were suited to yield specific activities of about 10 MBq per mg HA after purification. For PET studies, comparatively high activities of the positron-emitting isotope ^{124}I were required. Labelling was performed starting with 175 MBq ^{124}I, yielding a specific activity of 625 MBq per mg HA.

Labelling with ^{18}F.

A new labelling technique was developed within the framework of the project, based on an azo coupling reaction with ^{18}F-labelled aniline as a precursor (Fig. 2). Since N=N bonds are known to be very stable, it was expected that this kind of labelling is more persistent than a direct iodination.

[^{18}F]fluoride (100 - 1000 MBq), K_2CO_3 (13 µmol) and Kryptofix 222 (26 µmol) in water or acetonitrile (1 mL) were mixed in a 5 mL reaction vial. The water was evaporated under a stream of N_2, using a heating block. Acetonitrile (1 mL) was added and re-evaporated three times. Then, a solution of 1,4-dinitrobenzene in acetonitrile (0.75 mg in 500 µL) was added. To assist the synthesis of 1-[^{18}F]fluoro-4-nitrobenzene, the mixture was enclosed in a PEEK capillary, and was treated with several intervals of microwave energy (30 s, followed by 30 s cooling time). Subsequently, the mixture was transferred with methanol (2 mL) into a reaction vessel containing 2 mg Pd/C catalyst (10% Pd). A stream of H_2 was passed through for 10 min to reduce the 1-[^{18}F]fluoro-4-nitrobenzene to 4-[^{18}F]fluoroaniline. The catalyst was then filtered off, the solvent was evaporated, and the residue was taken up in ethyl acetate / methanol (80/20 v/v). This mixture was separated by chromatography, using a semi-preparative HPLC column LiChrosorb Si 60 (250 × 10 mm), run with ethyl acetate / methanol at 4 mL min^{-1}. The product peak fractions were collected. After adding 100 µL of 1 M HCl, the eluent was evaporated.

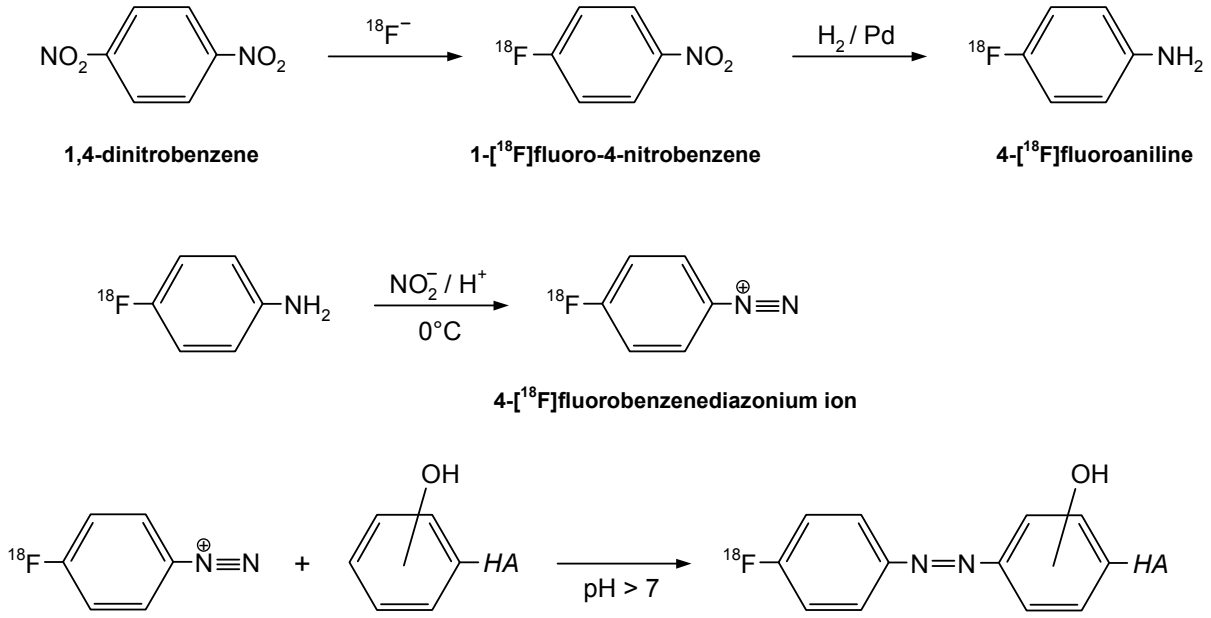

Figure 2. Reaction scheme for labelling humic acid with ^{18}F by azo coupling with ^{18}F-labelled aniline.

To produce the 4-[^{18}F]fluorobenzenediazonium ion, the residue was dissolved in 2 mL of 1 M HCl, and a 100 µL aliquot was treated with 10 µL of 1 M $NaNO_2$ at 0°C for 2 min. For labelling, 40 µL of this solution, together with 40 µL of 1 M NaOH and 170 µL of 0.05 M tris buffer, were added to 250 µL of HA solution (200 mg L^{-1}, in tris buffer). The components were allowed to react for 10 min at 0°C. Separation of unreacted labelling material was carried out as described for $^{124/131}$I. The purification process is illustrated in Fig. 3.

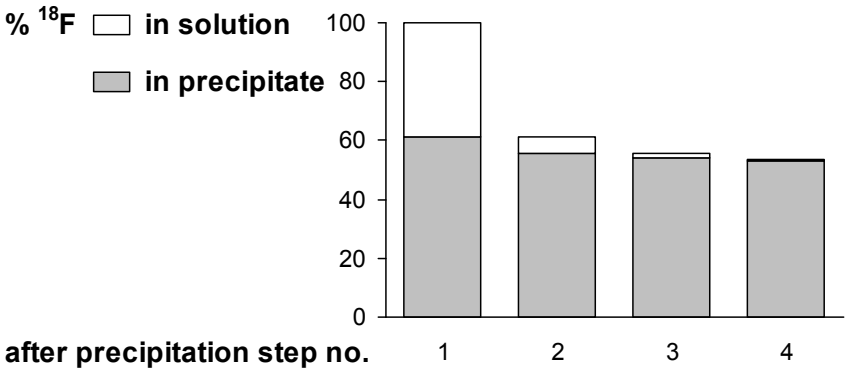

Figure 3. Purification of ^{18}F-labelled HA by repeated precipitation / re-dissolution (activities in precipitate and supernatant) [15].

Fig. 4 shows an HPSEC separation of the labelled product. Obviously, the ^{18}F radio signal, obtained with a gamma detector, is in good agreement with the UV signal, i.e., the humic acid is uniformly labelled, with no indications of selectivity towards particular size fractions [15].

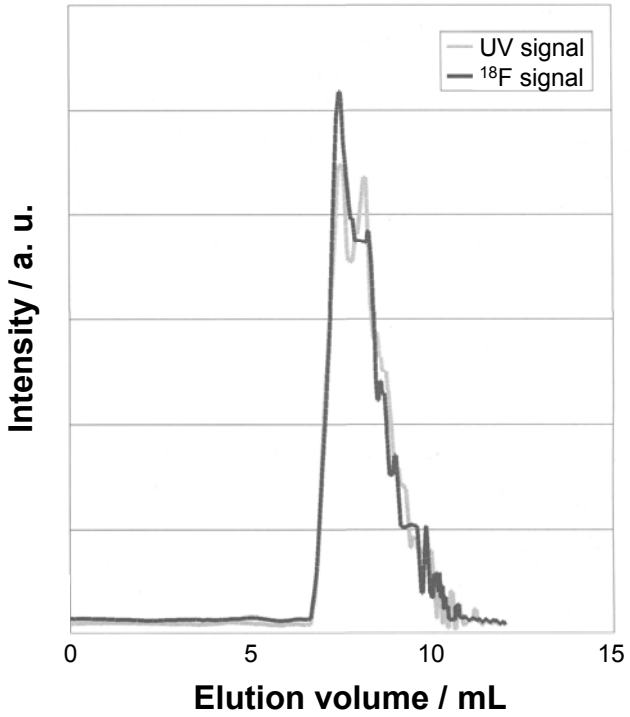

Figure 4. Size exclusion chromatogram of ^{18}F-labelled HA (UV absorption at 254 nm and ^{18}F radio signal) [15].

2.2.3 Adsorption experiments

For pH-dependent measurements of adsorption, suspensions of 50 mg kaolinite in 50 mL 0.1 M $NaClO_4$ were pre-conditioned to a series of pH values. Dispersing was facilitated by sonication. The samples were weighed, and the pH was adjusted to the desired value by addition of acidic or alkaline 0.1 M $NaClO_4$ until the buffering capacity of the adsorbent material was exhausted (typically 10 - 20 readjustments within a period of two weeks). Subsequently, the systems were weighed again, and an appropriate amount of solution was removed to attain a final solid/solution ratio of 1 g L^{-1}, allowing for the volumes of Tb and / or HA solutions to be added. The suspensions were then dispensed into 5 mL PP centrifuge tubes while stirring, and the solutes were added (small amounts of near-neutral solutions). The initial concentrations of Tb and HA were fixed at 10^{-7} M and 5 mg L^{-1}, respectively.

After rotating end-over-end at 10 rpm for 48 h, the systems were centrifuged at 8000 rpm for 10 min, and aliquots of the supernatant were taken for analysis. Depletion was determined radioanalytically in relation to reference solutions. The final pH was checked after analysis. Wall adsorption was found to be negligible.

2.2.4 Measurement of metal-humate complexation

Anion exchange method [16]*.* Metal/HA systems (8 mL), prepared with pH-adjusted stock solutions, were allowed to equilibrate for 48 h in PE vials. The anion exchange resin Sephadex DEAE A-25 (Sigma-Aldrich) was used as a separating agent. Prior to use, it was washed with methanol, rinsed with 0.1 M $NaClO_4$ and kept therein after pH adjustment. For measurements, it was introduced as a slurry of approx. 200 mg to 4 mL aliquots of the equilibrated solutions, which was verified to be sufficient to adsorb the humic material (including the bound metal fraction) quantitatively. Free cationic metal species are left in solution. After shaking for 1 min and sedimentation, 3 mL were taken for analysis. The decrease in metal concentration in relation to the starting solution was determined by radiotracer analysis (^{160}Tb). The difference, corrected for the water content of the slurry, is equal to the concentration of bound metal.

Cation exchange method [17]*.* Humic-bound metal fractions were also determined on the basis of a metal exchange equilibrium between HA / FA and an acidic adsorbent, Bio-Rad AG 50W-X2 cation exchange resin. In order to avoid changes in pH, the material was converted into the Na^+ form by treatment with 1 M NaOH. Solutions of HA / FA, Eu and Fe in 0.1 M $NaClO_4$ (pH 4) were prepared with pH-adjusted stock solutions, and were spiked with tracer amounts of ^{152}Eu or ^{59}Fe. Equilibration with the cation exchange resin was performed in PE vials at a solid-liquid ratio of 10 mg / 10 mL. After shaking for 48 h, 2 mL aliquots of the supernatant were taken for measurement of activity. The concentration of bound metal [M_{bound}] was calculated from the relationship

$$[M_{bound}] = [M_{total}]\left(1 - \frac{D}{D_0}\right) \quad (1)$$

with D and D_0 denoting the solid-liquid distribution ratios of the radiotracer in the presence and in the absence of humic material, respectively. To account for wall adsorption, analogous test series were performed without exchange resin.

2.2.5 Flocculation experiments

Flocculation of Fe/HA systems was investigated in jar tests using 20 mL clear glass vials. A total of ~ 300 pH-adjusted solutions with varying concentrations of Fe and HA were allowed to stand undisturbed over a period of two weeks. Sedimentation of flocculated HA was then examined by measuring the UV absorbance of the supernatant at 254 nm.

2.2.6 Measurement of octanol-water partitioning

Both solvents were mutually saturated by rotating end-over-end in 2 L bottles. Solutions of 5 mg L^{-1} ^{131}I-labelled humic acid and different amounts of surfactant in 0.1 M NaCl (pH 4.0) were prepared with pH-adjusted stock solutions. After standing for 15 h, portions of 2 mL were transferred into PP screw-cap tubes, and were overlaid with 2 mL of octanol. For equilibration, the tubes were slowly shaken horizontally along their longitudinal axes (50 motions per minute), preventing emulsification. After 24 h, samples of both phases were taken by means of an Eppendorf pipette (organic phase: 1000 µL, aqueous phase: 50 µL), and the partition coefficient was determined radioanalytically.

2.2.7 Positron emission tomography (PET)

In this spatially resolving radiotracer method, which is used in nuclear medical diagnostics, positron-emitting radionuclides are localised by means of the positron-electron annihilation radiation, a pair of gamma photons moving in opposite directions. Every coincident arrival of photons is registered by a circular array of scintillation detectors. Thus, the decay event can be assigned to the connecting line (line of response). Since the direction of photon emission varies, the source of radiation can be exactly localised at the crossing point of a multitude of connecting lines.

In this project, humic colloid-borne transport in a sand matrix was investigated with a commercial PET camera ECAT EXACT HR^+/CTI (Siemens, Germany) at the University of Leipzig. The distributions of tracer concentrations in stacks of cross sections were calculated by the image reconstruction algorithm of the PET device. The column experiment is described in Section 3.5.

3 Results and Discussions

3.1 Co-adsorption of Tb(III) and humic acid onto kaolinite depending on the solution pH

3.1.1 Tb(III) adsorption in the absence and presence of HA

In Fig. 5, the influence of Aldrich HA on Tb adsorption onto kaolinite is shown as a function of pH. The range is limited to pH values up to 6.4 due to the onset of Tb hydroxide precipitation. Adsorption data are represented as distribution coefficients K_d, which are defined by Eq. (2), where Γ is the adsorbed amount per unit mass of solid (in mol g^{-1}), and c is the equilibrium concentration in mol mL^{-1}.

$$K_d = \frac{\Gamma}{c} \qquad (2)$$

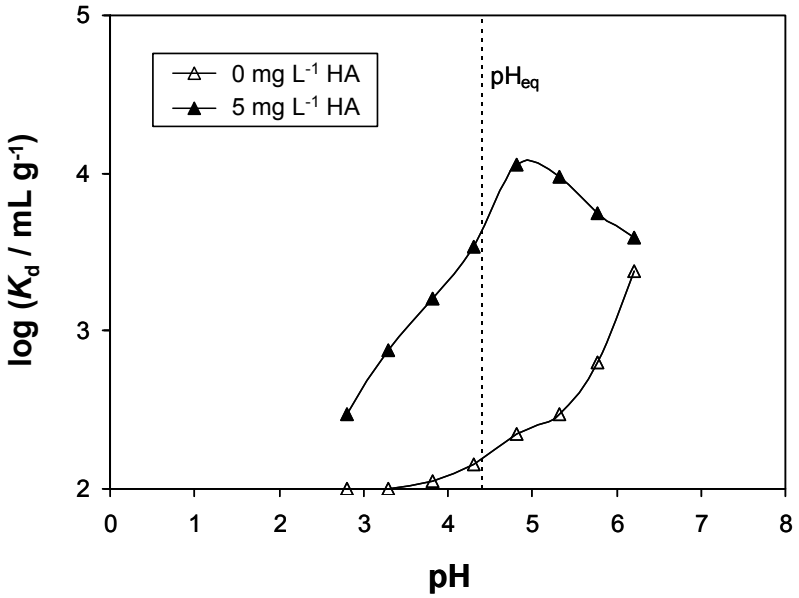

Figure 5. Adsorption of [^{160}Tb]Tb(III) (10^{-7} M) on kaolinite in 0.1 M $NaClO_4$, depending on the pH value, in the absence and presence of Aldrich HA. The dotted line indicates the pH value that would be present under the experimental conditions without pH adjustment.

In contrast to other geological materials [18], within the solubility limits of Tb and HA, adsorption of Tb onto kaolinite is always enhanced in the presence of HA. Only at higher pH values, there would be a changeover from demobilisation to mobilisation. The pH_{eq} value (dotted line) is, however, situated in the acidic region, i.e., the acid-base properties of the kaolinite surface ensure that a mobilisation of metal species by HA does not occur. Thus, kaolinite as a representative of clay minerals turns out to be an effective geochemical barrier in respect

of humic colloid-borne transport, aside from the hydrodynamic characteristics of clay materials.

3.1.2 Tb(III)-humate complexation and HA adsorption

In order to understand the relative trends of the pH functions in the absence and presence of HA, humate complexation of Tb and adsorption of HA were likewise investigated in pH-dependent experiments. As can be seen from Fig. 6, the extent of Tb-humate complexation decreases considerably on acidification since the binding sites (carboxyl and phenolic hydroxyl groups) are blocked by protonation. Whereas the metal is complexed almost completely at pH > 6, the organically bound fraction is reduced to just above 10% at pH 3.

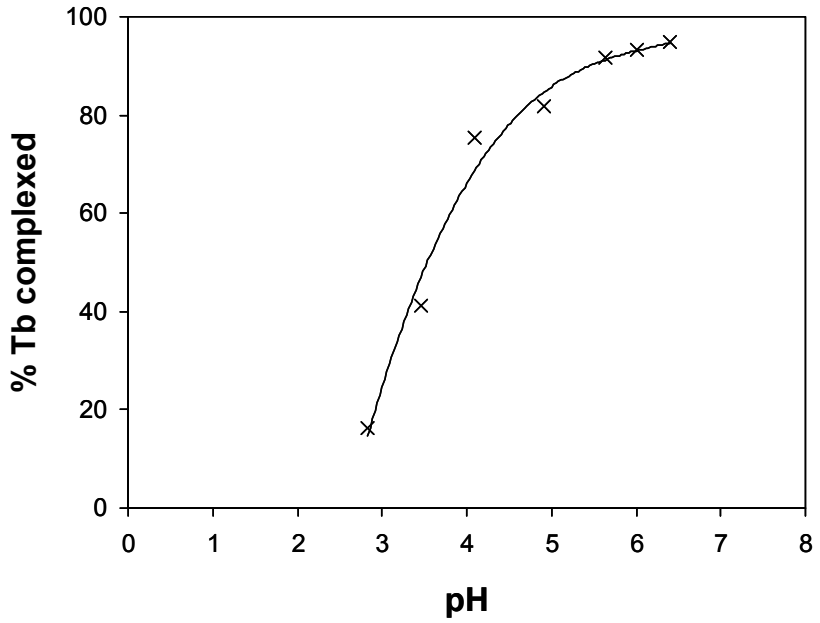

Figure 6. Humate complexation of [^{160}Tb]Tb(III) (10^{-7} M) with Aldrich HA (5 mg L^{-1}) in 0.1 M $NaClO_4$, depending on the pH value.

Figure 7 shows the results of time-dependent measurements of HA adsorption onto kaolinite. The adsorbed amount increases rapidly within the first hours of end-over-end rotation and exhibits an asymptotic trend on a timescale of about two days. Thus, an equilibration time of 48 h was adopted for all adsorption experiments in binary and ternary systems.

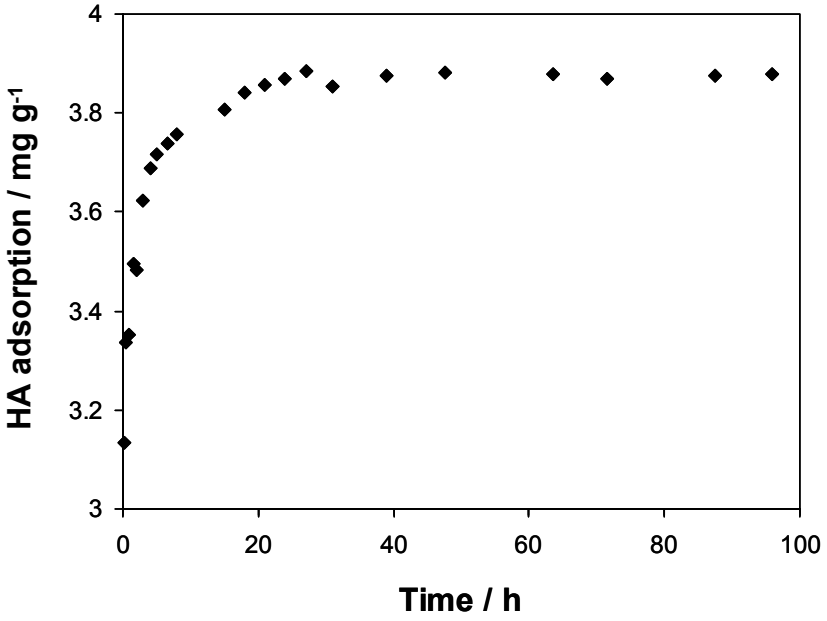

Figure 7. Time dependence of HA adsorption onto kaolinite (5 mg L^{-1} Aldrich HA, labelled with ^{131}I; 0.1 M $NaClO_4$; pH 5.0).

The pH dependence of HA adsorption is shown in Fig. 8. The adsorbed amount is increased on acidification because the negative charges of colloids and solid surface are reduced by protonation of acidic centres. In contrast to humate complexation where the pH dependence is most pronounced in the acidic range, the gradient of HA adsorption diminishes at lower pH, which is indicative of saturation behaviour with respect to protonation or HA adsorption.

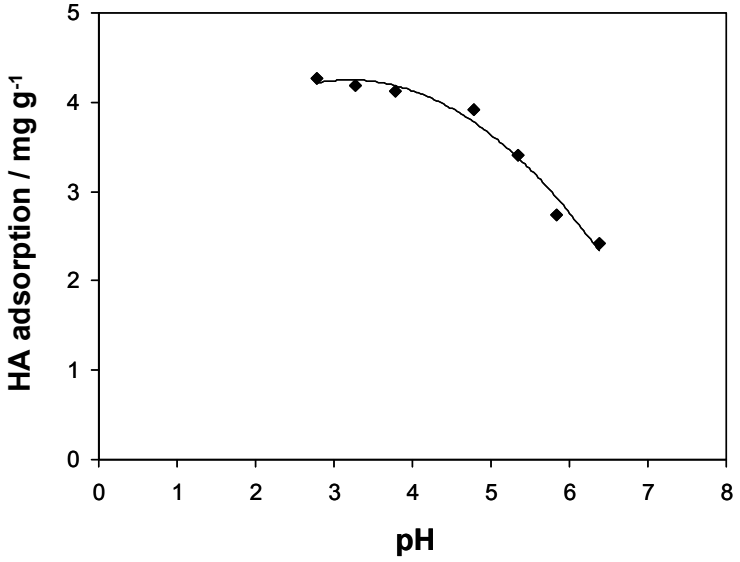

Figure 8. Adsorption of Aldrich HA (5 mg L^{-1}, labelled with ^{131}I) on kaolinite in 0.1 M $NaClO_4$, depending on the pH value.

3.1.3 Modelling co-adsorption of Tb(III) and HA on the basis of a composite distribution approach

Based on the observed pH dependences within the binary subsystems, it is possible to give a qualitative interpretation of the pH-dependent influence of HA in the ternary system. With increasing pH, dissociation of acidic groups leads to a corresponding gain in metal binding sites on the colloids, and also, to a hindrance of colloid-solid interactions due to the build-up of an electrostatic barrier. Consequently, a competitive situation arises between metal adsorption and humate complexation, which is the reason for the decreasing trend above pH 5 (Fig. 9). On lowering the pH, humic acid is increasingly adsorbed (Fig. 8), thereby adopting a mediating function in that Tb is co-adsorbed as a humate complex. Since, however, complexation declines more and more (Fig. 6), and the increase in HA adsorption levels off, the curve passes through a maximum and goes down again at more acidic pH.

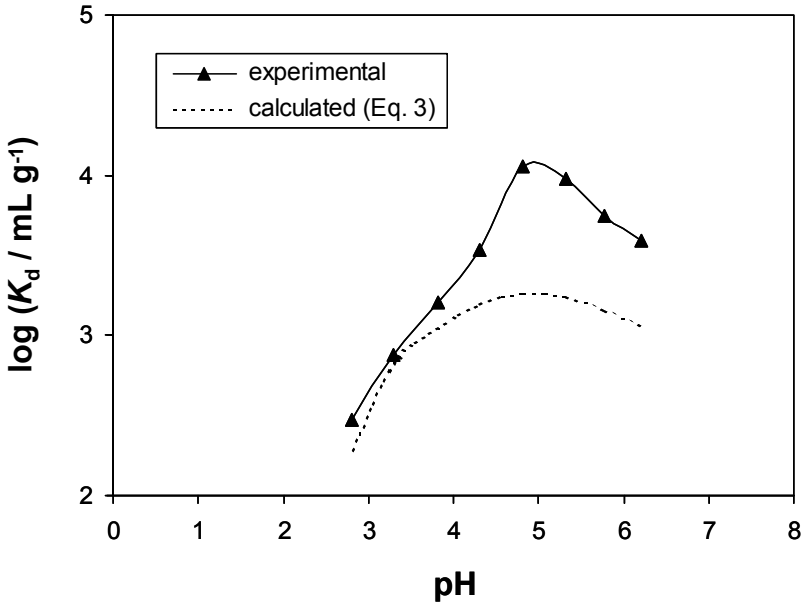

Figure 9. Calculation of Tb adsorption in the presence of HA from experimental data of the binary subsystems according to the composite distribution approach.

In Fig. 9, an attempt was made to reproduce the pH-dependent adsorption of Tb in the presence of HA quantitatively on the basis of experimental data on Tb adsorption (Fig. 5, binary system), Tb-humate complexation (Fig. 6), and HA adsorption (Fig. 8). In the Linear Additive Model [18-20], these constituent processes are considered as a system of interdependent partitioning equilibria. By combining the individual distribution coefficients, one obtains Eq. (3) for co-adsorption of metal (M) and humic-bound metal (M–HA) on the solid surface (S):

$$K_d^{(M+M\text{-}HA)/S} = \frac{K_d^{M/S} + K_d^{HA/S} K_d^{M/HA} c_{HA}}{1 + K_d^{M/HA} c_{HA}} \quad (3)$$

To reconstruct the pH dependence of Tb adsorption in the ternary system, the experimentally determined values of $K_d^{M/HA}$, $K_d^{HA/S}$ and c_{HA} as a function of pH were fitted by polynomials, and $K_d^{(M+M\text{-}HA)/S}$ was calculated for the measured $K_d^{M/S}$/pH data. As can be seen from Fig. 9, the model calculations do not fit the experimental results exactly, albeit the general trends are reproduced properly.

The following basic assumptions are implicit in Eq. (3): (a) The individual distribution processes are described by linear isotherms within the concentration range to be covered, (b) adsorption of the M–HA complex corresponds to HA adsorption, as measured in the absence of M, (c) the stability of the M–HA complex in solution is equal to its stability in the adsorbed state, and (d) adsorption of M and M–HA can be regarded as independent of each other. Whereas assumption (a) is applicable for the chosen concentration level, the other assumptions are not necessarily correct and have to be examined in detail. For the data management, it would be a considerable advantage if ternary systems could be constructed from binary systems. Further studies are intended in this respect.

3.2 Competitive effect of Fe(III) on complexation of Eu(III) with humic substances

3.2.1 Investigations on the binary system Eu(III) / HA

Eu binding by HA was first examined in the absence of Fe. Generally, the stability constant β is defined by Eq. (4) where $[ML_z]$ and [M] are the equilibrium concentrations of complexed and non-complexed metal species, respectively, [L] is the equilibrium concentration of free ligands, and z is the coordination number.

$$\beta = [ML_z] / [M] [L]^z \quad (4)$$

In the case of humic substances, β is an average value for a variety of ligands with different affinities to M. Usually, their total concentration is arbitrarily defined on the basis of the proton exchange capacity PEC, although the acidic groups are only partly available for complexation. For very low metal loads, the equilibrium concentration of L can be equated with the total concentration.

$$\beta \approx [ML_z] / [M] [L_{\text{total (PEC)}}]^z \quad (5)$$

Here, z is the average number of proton exchanging groups per bound metal atom. In the presence of a cation exchange resin, the complexed metal fraction is kept in solution, and non-complexed metal ions are in an adsorption equilibrium. The following relation holds, with

D_0 and D denoting the solid-liquid distribution ratios of the metal in the absence and in the presence of complexing ligands, respectively.

$$D_0/D - 1 = \beta\,[L_{\text{total (PEC)}}]^z \qquad (6)$$

From a logarithmic plot of $D_0/D - 1$ *vs.* $[L_{\text{total (PEC)}}]$, z and log β can be obtained from the slope and the intercept, respectively. In Fig. 1, such Schubert plots are shown for three different Eu concentrations, the HA concentration varying over two orders of magnitude. $[L_{\text{total}}]$ was calculated assuming a PEC of 5 meq g^{-1}.

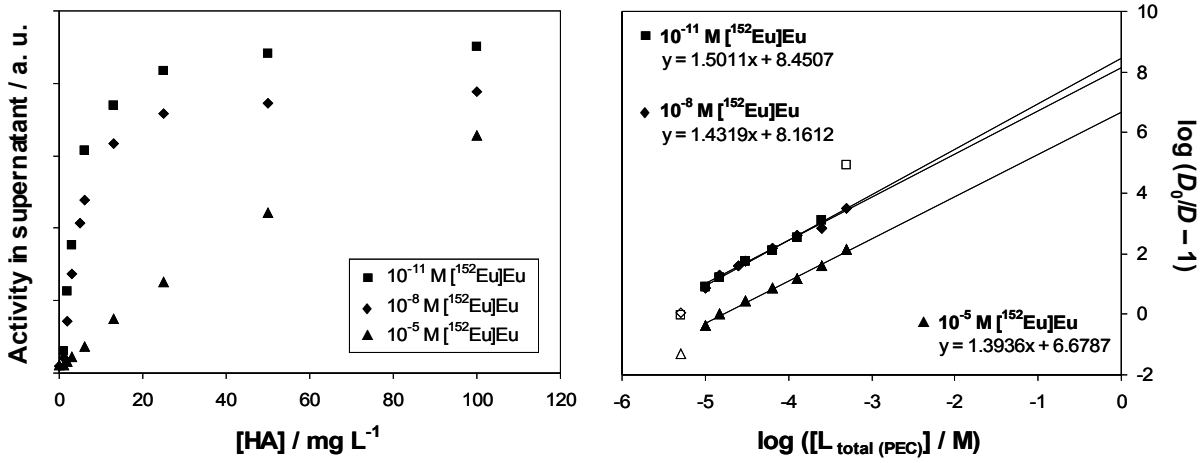

Figure 10. Complexation of Eu(III) with Aldrich HA depending on the metal/HA ratio (0.1 M $NaClO_4$; pH 4.0). Left: Raw data as obtained from cation exchange experiments, right: Schubert plots (see text for explanations).

For 10^{-5} M Eu, the Schubert plot is shifted to lower values. This is, however, not indicative of a concentration dependence of log β but is due to the fact that the basic assumption $[L] = [L_{\text{total}}]$ does not apply at high metal loads. Interestingly, the plots are almost identical for 10^{-8} M and 10^{-11} M Eu, i.e., there are not any indications of "hot sites" which are preferentially occupied at very low metal concentrations. This is contradictory to several studies which yielded evidence that the stability of metal-humate complexes increases with decreasing metal concentration [10, 11].

3.2.2 Confinement of Eu(III) binding to humic materials in the presence of Fe(III)

Complexation of Eu(III) in the presence of Fe(III), as the most abundant trivalent electrolyte constituent in terrestrial waters, was investigated for three humic acids and one fulvic acid. Figure 11 shows how the concentration of organically bound Eu depends on the total concentration of Fe. The bound fractions of Fe are shown in Fig. 12.

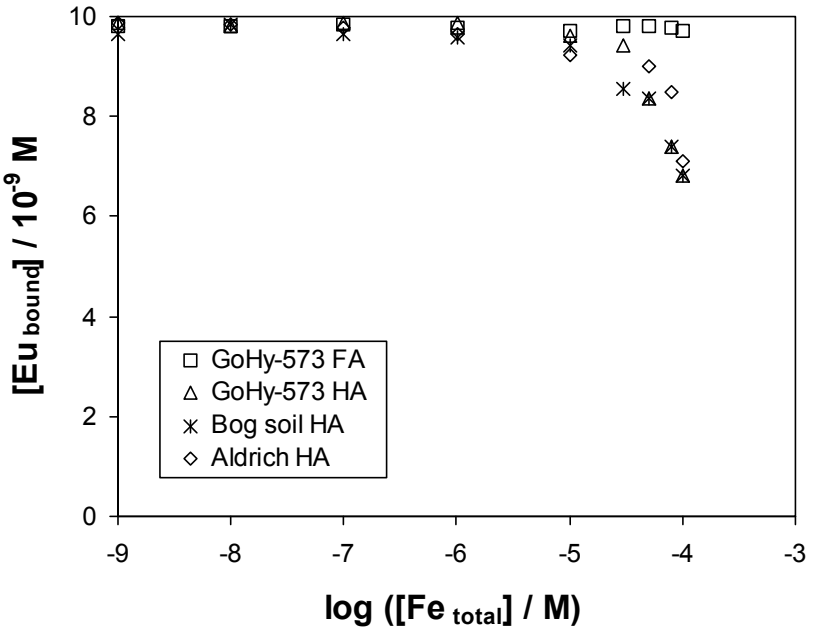

Figure 11. Competitive effect of Fe(III) on complexation of Eu(III) with different humic materials (10^{-8} M [^{152}Eu]Eu; 5 mg L^{-1} HA / FA; 0.1 M $NaClO_4$; pH 4.0; simultaneous addition of Fe and Eu).

Throughout the nanomolar range, a competitive influence is not discernible, but significant effects are observed at micromolar Fe concentrations. About one third of originally bound Eu is excluded from humate complexation in the presence of 10^{-4} M Fe. For the fulvic acid, however, there is no displacement in the concentration range studied. As can be seen in Fig. 12, Fe is bound to a lesser degree in this case, but the different behaviour is primarily explained by the higher content of acidic groups in FA compared to HA, providing more binding sites per unit mass. Accordingly, competition will gain in importance at higher Fe concentrations.

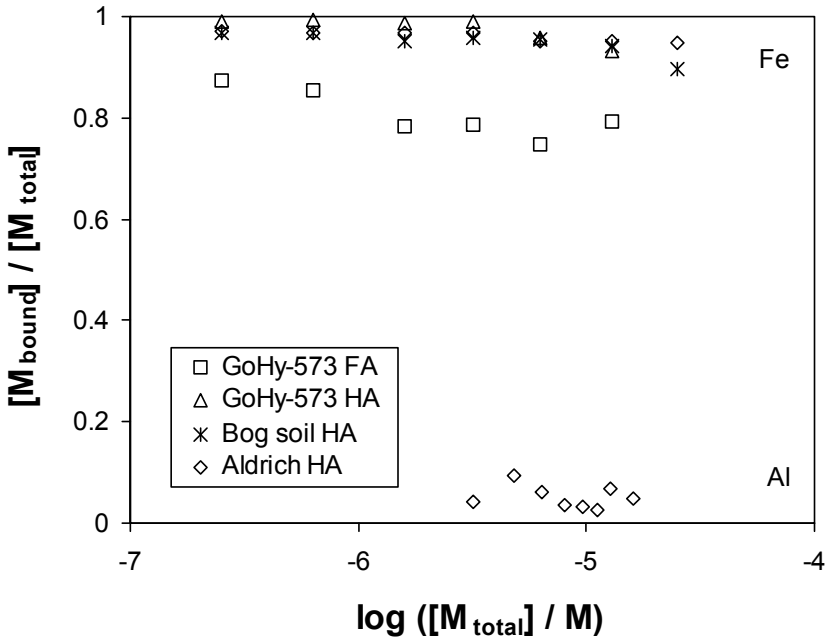

Figure 12.Binding of Fe(III) and Al(III) by humic materials (radiotracer experiments with ^{59}Fe, conditions as in Fig. 11).

3.2.3 Flocculation of humic acid on addition of Fe(III)

The experiments on competitive complexation were limited to Fe concentrations up to 10^{-4} M. If this value is exceeded, flocs of Fe/HA agglomerates are precipitated. This process may be even more important than displacement reactions since out-competed actinide species are not necessarily immobilised subsequent to detachment. For the example of Aldrich HA, flocculation on metal addition was systematically investigated at different HA concentrations and pH values (Fig. 13). As the colloids differ in size and chemical composition, precipitation proceeds gradually within a certain range of metal concentration, indicated by the bars.

The concentration of Fe required for flocculation depends linearly on the concentration of HA, i.e., the colloidal stability is determined by the Fe/HA ratio. It may be concluded that flocculation is induced by charge compensation of HA colloids. At pH 6, more Fe is needed than at pH 4 because deprotonation of acidic groups results in a higher colloid charge to be compensated. Furthermore, the effective charge of the Fe species is reduced due to hydrolysis.

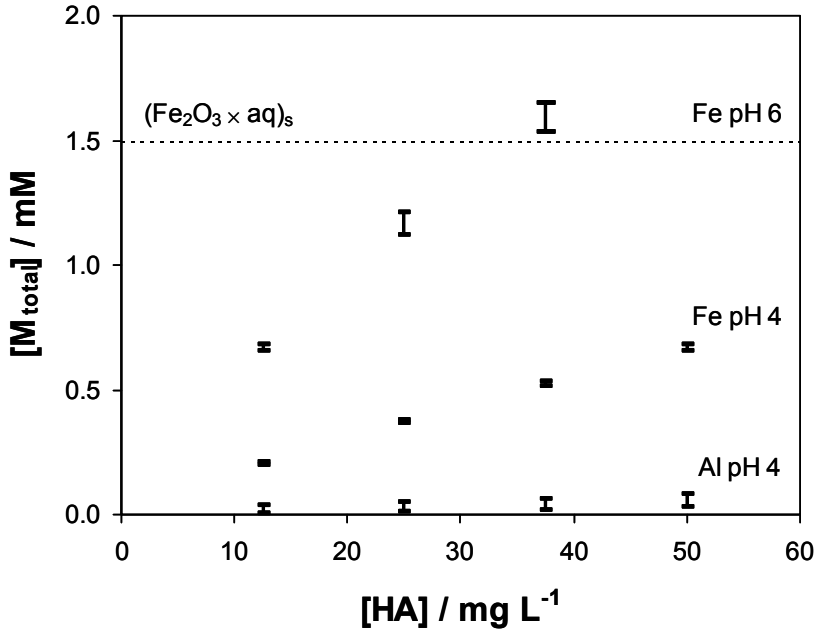

Figure 13. Flocculation of Aldrich HA on addition of Fe(III) and Al(III) at pH 4 and pH 6. The bars indicate the concentration ranges in which precipitation proceeds. The dotted line shows the stability limit of an Fe(III) solution at pH 6.

It is obvious that the iron colloids are not destabilised by interaction with HA since they are stable when HA is present in excess. Instead, precipitation is clearly attributable to the humic colloids, even at pH 6 where the Fe colloids are very susceptible to flocculation in the absence of HA (dotted line). Here, stability against precipitation is even enhanced by the presence of HA.

3.2.4 Characterisation of kinetic effects

In the experiments shown in Fig. 11, Fe and Eu were simultaneously contacted with the humic materials, which does not actually correspond to real situations to be considered since the contact with the competing ion will occur prior or subsequent to actinide-humate complexation. Figure 14 shows a time-dependent study where the metals were introduced in two steps. Mixed solutions of HA and Fe had been pre-equilibrated for different periods of time before Eu was added and the cation exchange experiment was accomplished. Two test series were performed, covering a time frame of one week and four months, respectively.

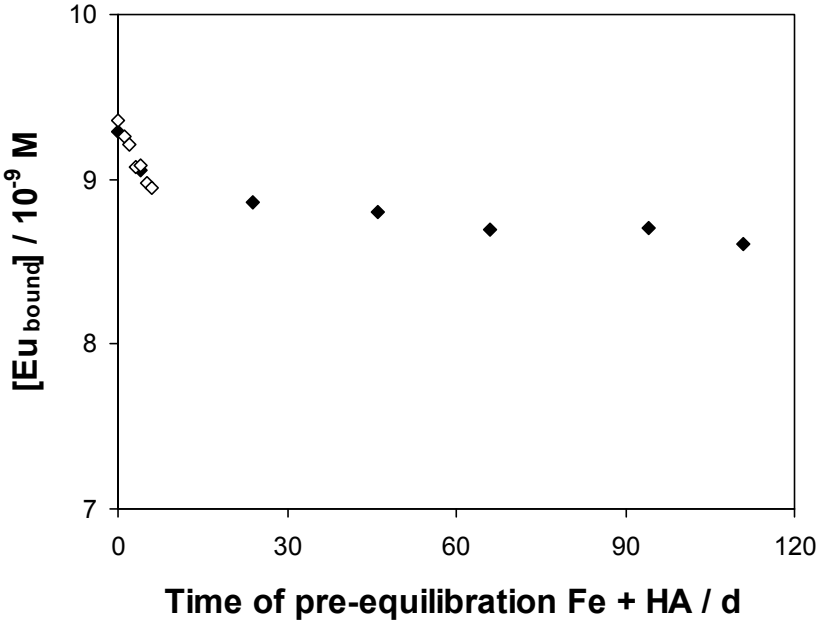

Figure 14. Complexation of Eu(III) with Aldrich HA after pre-equilibration of HA and Fe(III) (10^{-8} M [^{152}Eu]Eu; 5×10^{-5} M Fe; 5 mg L^{-1} HA; 0.1 M $NaClO_4$; pH 4.0). Full and open symbols refer to different test series.

It turned out that the degree of Eu-humate complexation is markedly influenced by the time of Fe/HA pre-equilibration; Eu binding decreased asymptotically over a period of several weeks. During that time, the amount of bound Fe (apparent complex stability) proved to be unchanged (data not shown). Consequently, the effect must be caused by structural alterations, impeding Eu/HA interaction. The possibility that these changes are due to ageing of HA or Fe as single components can be discounted since the same stock solutions were used throughout a test series, and data of short-term and long-term tests (conducted with different stock solutions) match each other.

These results are in accordance with time-dependent studies on dissociation of metal-humate complexes, showing that a detachment by competing ligands or cation exchangers becomes more difficult with increasing contact time [8, 9]. Such kinetic effects are often interpreted as slow diffusion processes within the humic colloids. Following a fast equilibration with weak binding sites on the surface, the metals are assumed to move to stronger sites inside, which are not directly accessible (Fig. 15a) [21-23]. However, this reasoning implies that the initial sites are vacated and should thus be available for competing metal ions. Consequently, the transfer model fails to explain the time-dependent effects observed in this study. Other kinetic approaches are based on different binding modes which do not necessarily refer to separate sites [24]. Instead, dissociation may be complicated by slow structural changes which are induced by the metal, for instance, intra- or intermolecular bridging (Fig. 15b).

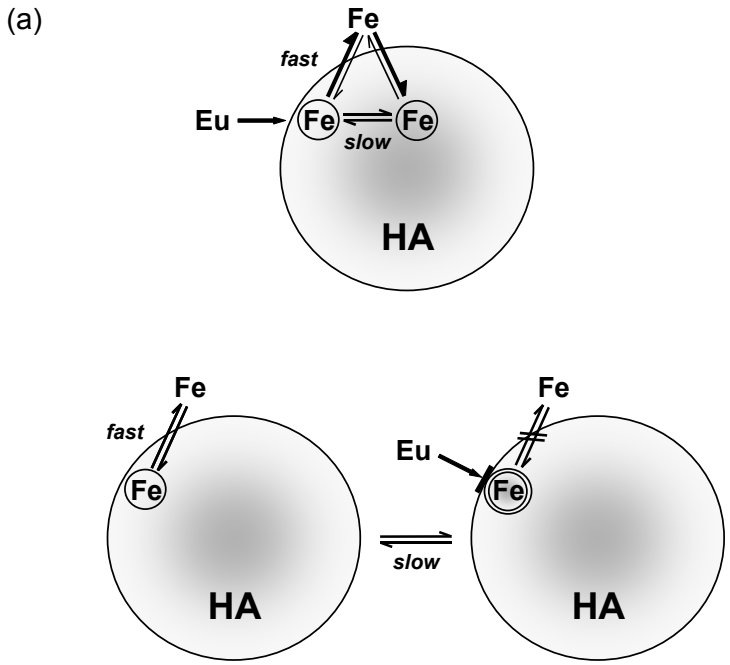

Figure 15. Interpretations of kinetic processes leading to an increased inertness of metal-humate complexes.

In the present case, an alternative explanation is conceivable, arising from the particular characteristics of aqueous Fe(III) species. In Figs. 12 and 13, data for Al(III) have been included for comparison. Interaction with HA is much weaker for Al(III) than for Fe(III), but on the other hand, less Al(III) is required to initiate flocculation. In weakly acidic solutions, as a consequence of hydrolysis, Fe is present in the form of isopolyoxo cations with an effective charge considerably lower than 3:

$$[Fe(H_2O)_6]^{3+} \xrightarrow[-H^+]{} [Fe(H_2O)_{6-x}(OH)_x]^{(3-x)+} \xrightarrow[-H_2O]{-H^+} \left[-O-\underset{\displaystyle O}{\overset{\displaystyle |}{\overset{\displaystyle |}{Fe(H_2O)_a(OH)_bO_c}}}-Fe(H_2O)_d(OH)_eO_f-O- \right]^{y+}$$

Apparently, this oligomeric structure is not eliminated when Fe(III) is bound to HA. The UV/VIS spectra shown in Fig. 16 corroborate this. Visible absorption of an Fe(III) solution at pH 4 is solely due to the formation of Fe polycations. In the presence of HA, the spectral enhancement is nearly additive, although most Fe is bound to the organic colloids. Consequently, it appears that the polynuclear Fe species are not decomposed in the interaction.

This would explain the large amount necessary for flocculation in spite of the high degree of binding.

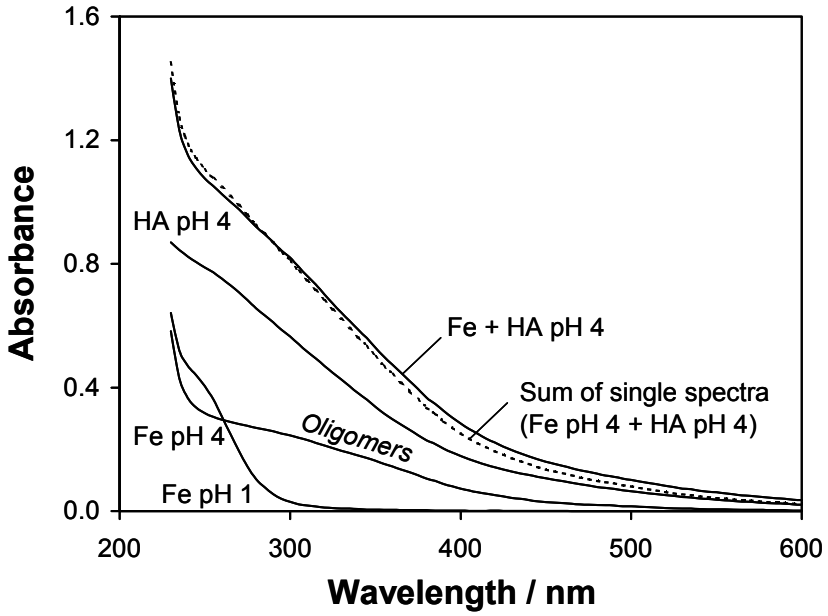

Figure 16. UV/VIS spectra of Aldrich HA (20 mg L^{-1}) and Fe(III) (10^{-4} M) in single and mixed systems (0.1 M $NaClO_4$; pH 4.0).

Thus, the increase in the competitive effect could also be explained by a slow degradation process which takes place when the Fe polycations are associated with the humic colloids. Figure 17a shows the results of a long-term observation of the pH value for an Fe/HA system which had initially been adjusted to pH 4.0, data for single-component systems also included.

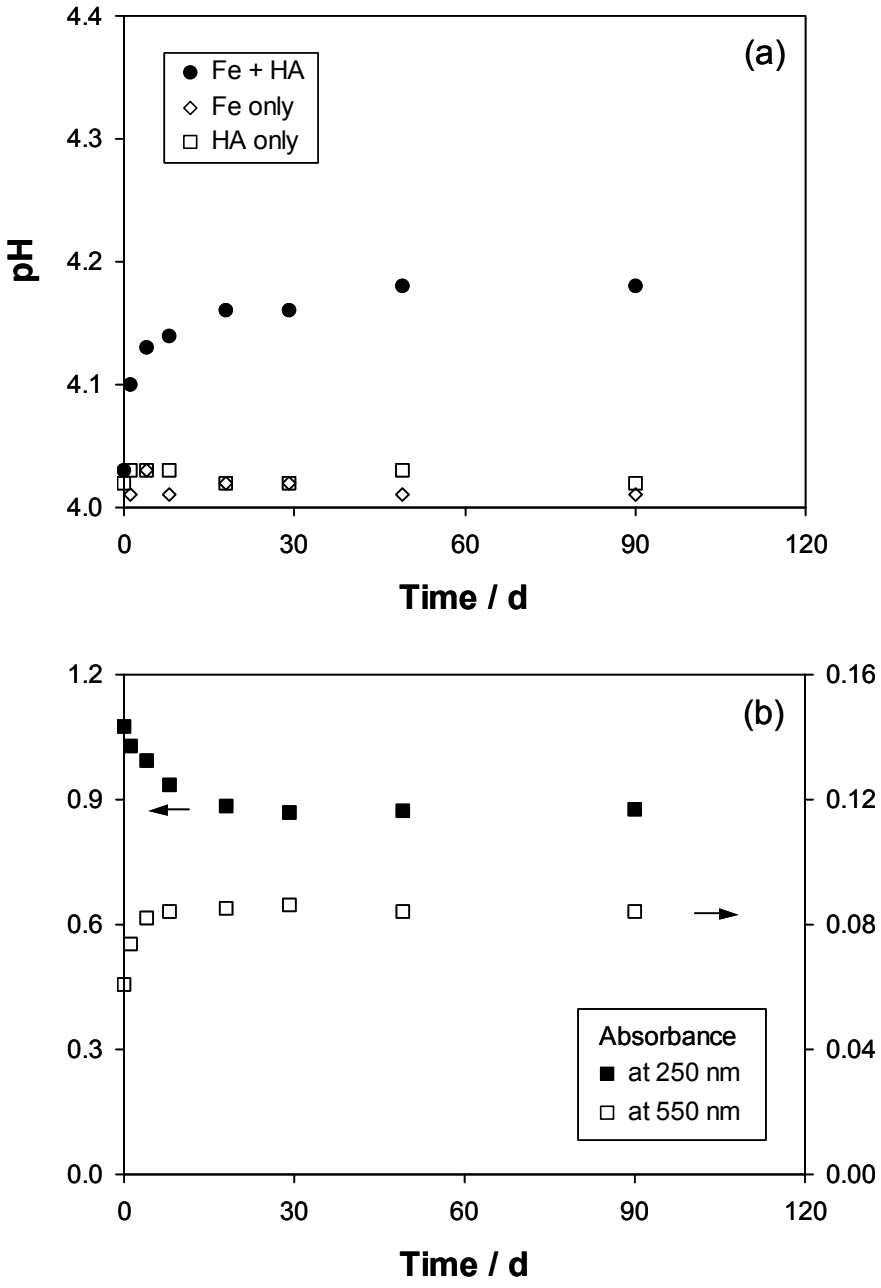

Figure 17. Changes in pH (a) and UV/VIS absorption (b) of a mixed HA/Fe(III) system depending on time (20 mg L^{-1} Aldrich HA; 10^{-4} M Fe; 0.1 M $NaClO_4$).

Normally, the pH of a HA solution decreases when metal salts are added since protons from the acidic binding sites are released in exchange for metal ions. In the present case, however, there is an increase in pH. This anomalous effect can only be attributed to the Fe component. For adjusting an Fe(III) salt solution to pH 4, large amounts of NaOH must be added because the formation of polynuclear hydrolysis species is associated with a release of protons which has to be compensated for. Apparently, this process is inverted in the presence of HA. Protons are consumed to degrade the oligomeric structure of hydrolysed Fe. Remarkably, the time profile of the increase in pH corresponds to the temporal change in the competi-

tive effect (Fig. 14). As depicted in Fig. 17b, the process is also accompanied by changes in the UV/VIS spectrum. These findings strongly suggest that the time dependence in Fe competition is due to the fact that polynuclear Fe is metastable when bound to HA. Decomposition into smaller units brings about an increase in stability. Thus, the number of available binding sites is reduced, and complexation of Eu is counteracted more effectively, as illustrated in Fig. 18.

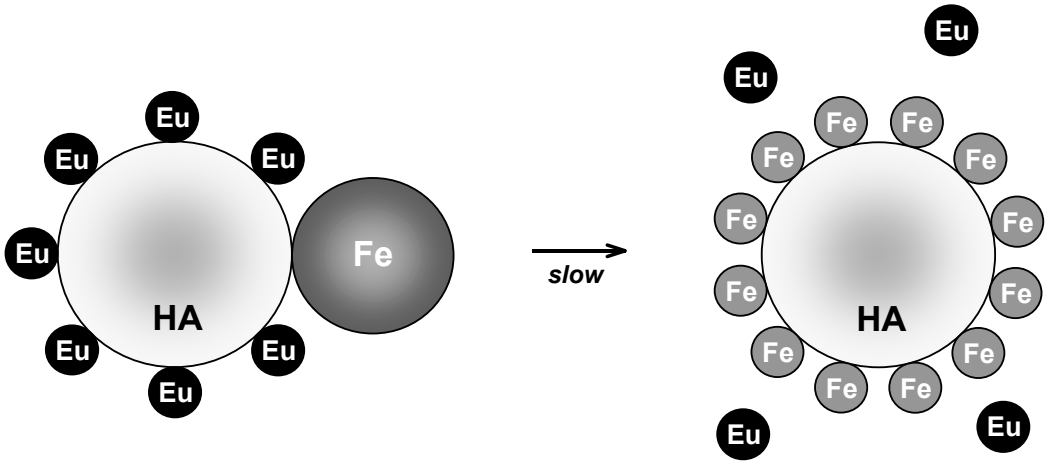

Figure 18. Explanation of the increase in the competitive effect of Fe(III) on humate complexation of Eu(III), based on the findings presented in Fig. 17.

Whether Fe oligomers are completely degraded to monomers cannot be ascertained definitely. In Fig. 19, the rise in pH is shown for systems with varying HA concentrations, measured after three weeks of standing. Up to a concentration of ~ 100 mg L^{-1} HA, the effect increases, i.e., the more binding sites are provided, the more Fe is degraded. At higher concentrations, however, this trend levels off. Obviously, further decomposition is not possible at this stage. One may assume that bound Fe is then present in a monomeric form. The total concentration of potential ligands would in fact be sufficient in this range; 100 mg L^{-1} of HA correspond to 0.5 mM of acidic groups, which is the fivefold amount compared to Fe.

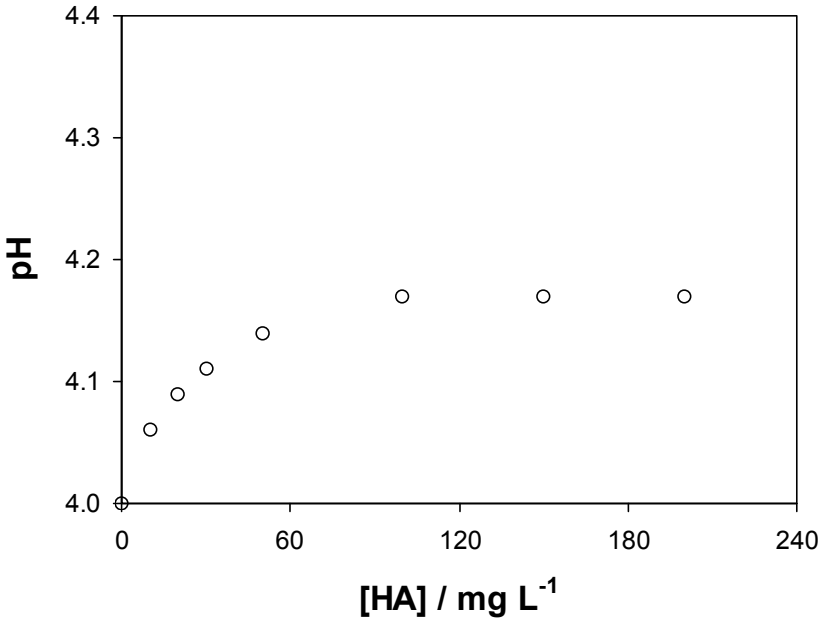

Figure 19. pH of mixed HA/Fe(III) systems, initially adjusted to pH 4.0, after 21 days of standing (10^{-4} M Fe; 0.1 M $NaClO_4$).

3.3 Influence of sulfate on humate complexation of Eu(III)

Figure 20 shows a calculation of the species distribution of Eu(III) as a function of sulfate concentration. The calculation was carried out by using the speciation programme JCHESS 2.0. It can be seen that Eu forms complexes with sulfate ions, dominating the speciation at millimolar concentrations. Thus, the question arises as to whether Eu-humate complexation can be counteracted by sulfate ions as potential competing ligands.

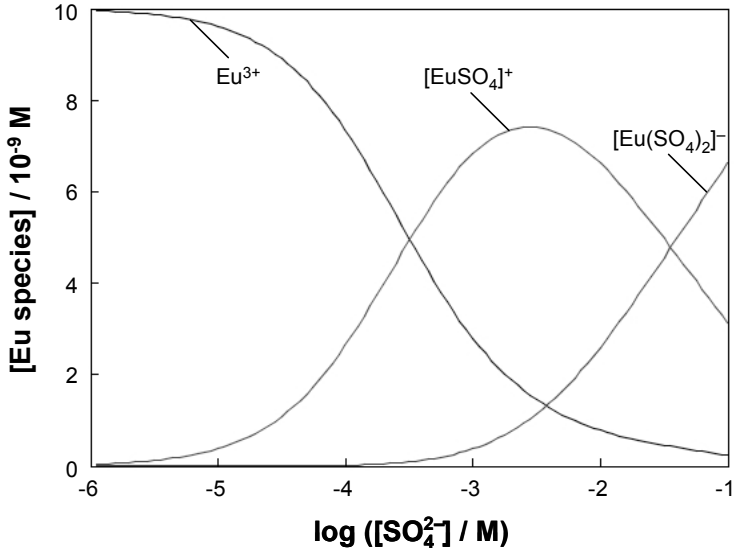

Figure 20. Species distribution of Eu(III) in the presence of sulfate at pH 4.0.

To investigate possible competitive effects, adsorption of Eu on cation exchange resin was measured in the presence of HA and / or Na_2SO_4. For comparison, analogous experiments were performed with $NaClO_4$ as an inert electrolyte, which does not form complexes. Figure 21 shows the concentration of non-adsorbed Eu depending on the concentrations of sulfate and perchlorate.

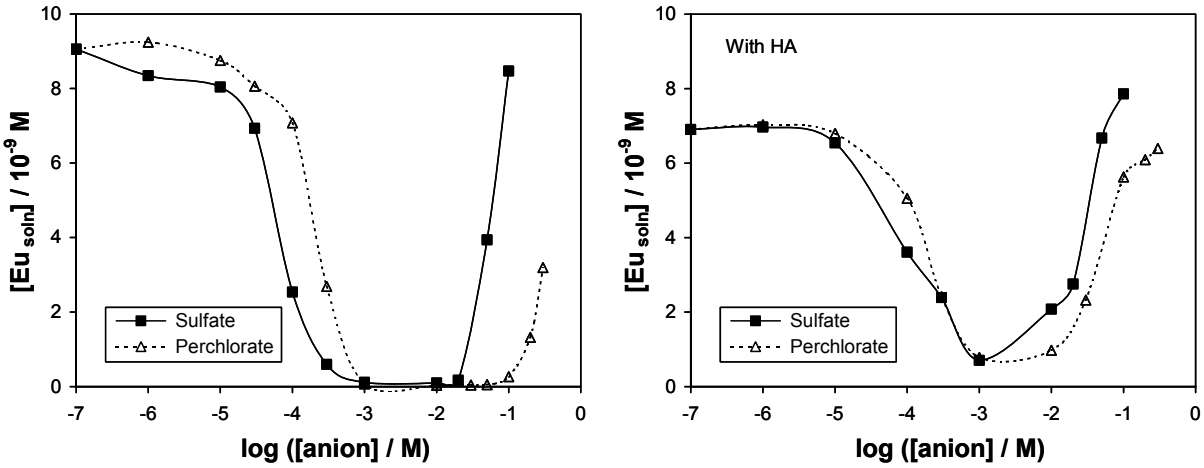

Figure 21. Effects of Na_2SO_4 and $NaClO_4$ on adsorption of Eu(III) onto Bio-Rad AG 50W-X2 cation exchange resin in the absence (left) and presence (right) of Aldrich HA (10^{-8} M [^{152}Eu]Eu; 5 mg L^{-1} HA; pH 4.0).

The interpretation of the results is not straightforward. Both in the presence and in the absence of HA, there is a decreasing trend at low salt concentrations and an increasing trend at high salt concentrations. In the systems without HA, Eu is almost entirely adsorbed in the concentration range between 10^{-3} M and 10^{-2} M. The u-shaped profile of the curves is thus not attributable to the humic material. Also, since this behaviour is observed for sulfate as well as for perchlorate, complexation cannot be a decisive factor. Instead, the course of the curves must be dominated by electrolyte effects. This becomes obvious if the data are plotted against the ionic strength (Fig. 22). Here, the graphs are nearly superimposed.

One may conclude that humate complexation of Eu is not significantly influenced by the presence of sulfate. Possibly, mixed-ligand complexes are formed, which is, however, not proven by these results.

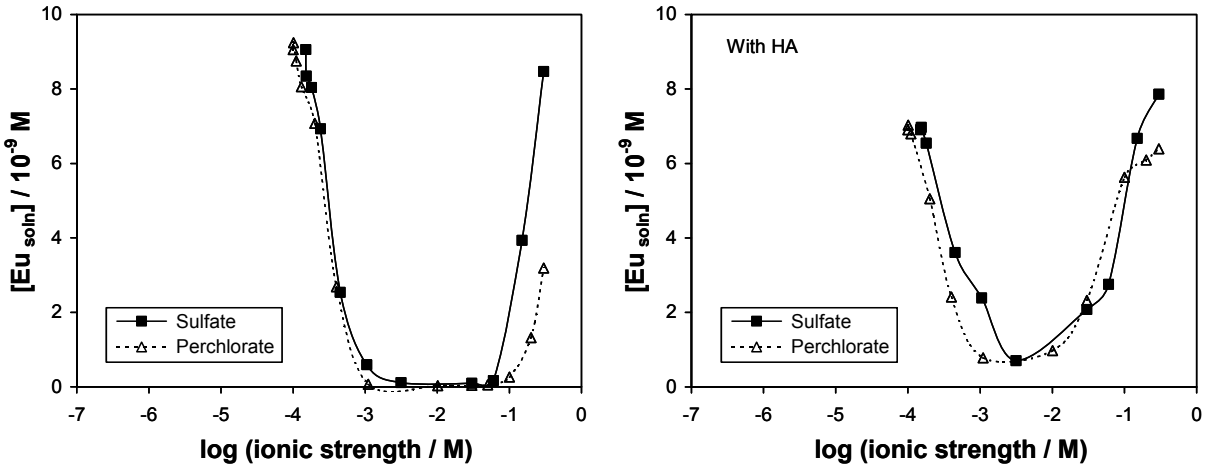

Figure 22. Data from Fig. 21 as a function of ionic strength.

3.4 Association of HA with low-molecular-weight organic compounds

In most studies on metal binding to natural organic colloids, humic and fulvic acids are used which have been isolated from soil or water samples. In these procedures, the humic materials are separated from low-molecular-weight organic compounds. It is, however, probable that – in the natural system – these compounds are associated with the humic colloids. Therefore, it is important to know how the transport properties are modified by possible interaction processes.

3.4.1 Different interaction modes as identified by octanol-water partitioning experiments

In this study, the octanol-water partition ratio $P_{O/W}$ was used as an indicator of changes in the hydrophilic / hydrophobic properties of humic colloids in contact with low-molecular-weight organic compounds. Since humic substances are multi-component mixtures, the partition ratio actually represents the sum of numberless partitioning equilibria for each individual component i:

$$P_{O/W} = \frac{\sum_i c_i^{oct}}{\sum_i c_i^{aq}} \qquad (7)$$

At first, time-dependent experiments were conducted in order to determine the time required for equilibration. Based on the results shown in Fig. 23, a shaking time of 24 h was chosen.

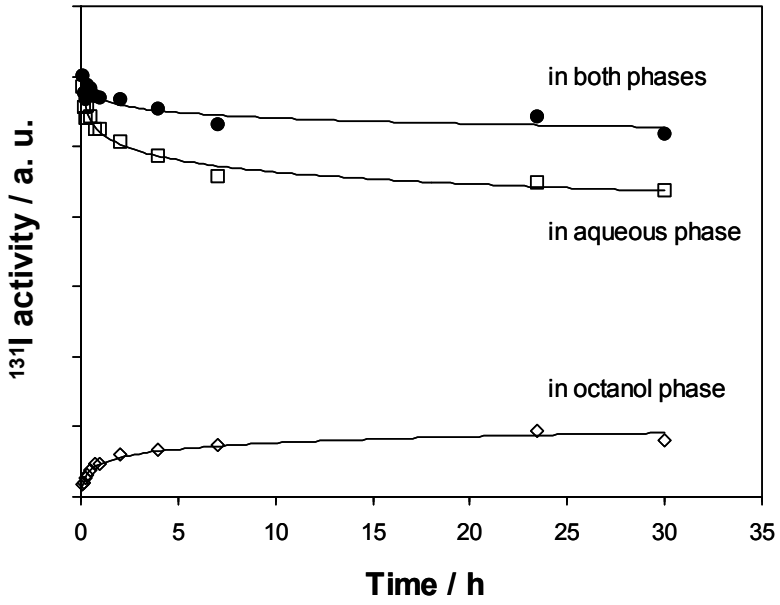

Figure 23. Octanol-water partitioning of HA, depending on the time of shaking (5 mg L^{-1} Aldrich HA, labelled with ^{131}I; 0.1 M NaCl; pH 4.0).

The sum of the total ^{131}I activities in both phases exhibits a time-dependent trend as well, indicating that the humic acid is partly adsorbed to the inner walls of the PP tube. Consequently, partition ratios cannot be determined indirectly *via* the mass balance, i.e., by analysing only one phase. Instead, both phases have to be analysed directly. In view of the asymmetric partitioning, conventional detection methods (e.g., UV photometry) would fail for lack of sensitivity. This analytical problem was overcome by the radiolabelling technique, providing a signal intensity that allows reliable measurements even at low HA concentrations as they are required in these experiments.

Surfactants were chosen as model components of low-molecular-weight organic material. These compounds consist of a hydrophobic moiety (mostly an alkyl chain) and a hydrophilic head group which can be cationic, anionic, or non-ionic. Thus, a variety of possible interaction mechanisms can be covered effectively.

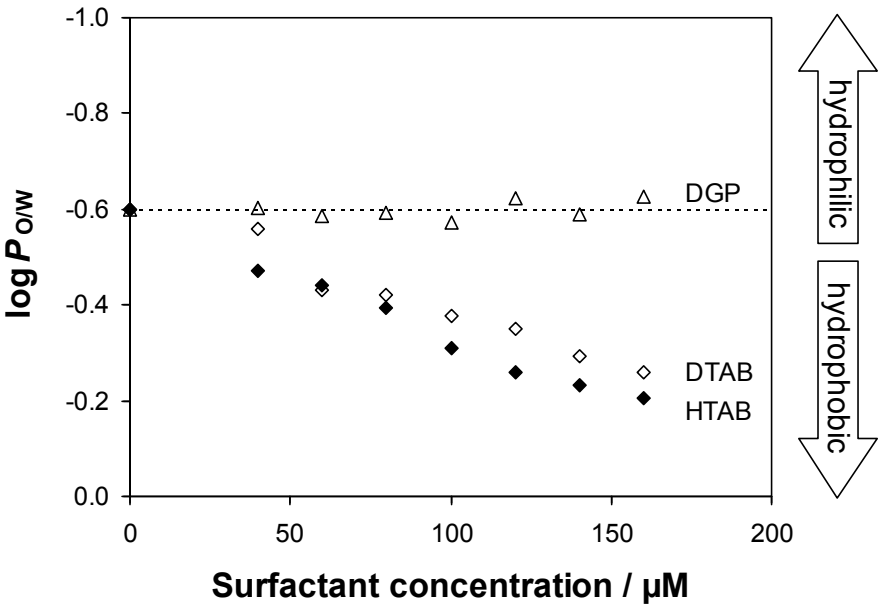

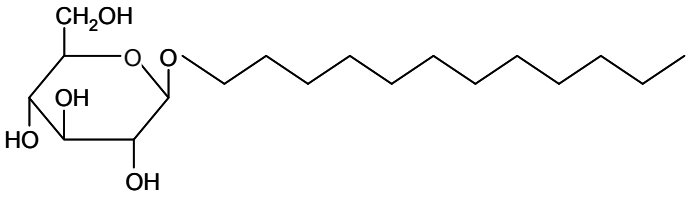

DGP: dodecyl-β-D-glucopyranoside

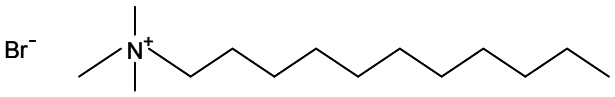

DTAB: dodecyltrimethylammonium bromide

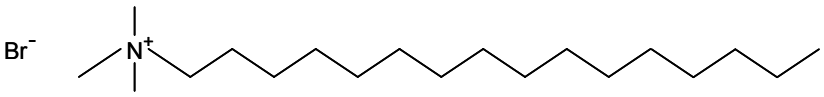

HTAB: hexadecyltrimethylammonium bromide

Figure 24. Effects of non-ionic (DGP) and cationic surfactants (DTAB, HTAB) on octanol-water partitioning of HA (5 mg L^{-1} Aldrich HA, labelled with ^{131}I; 0.1 M NaCl; pH 4.0).

Figure 24 shows the influence of cationic and non-ionic surfactants on octanol-water partitioning of Aldrich HA. Surfactant concentrations were below the critical micelle concentration in all cases, i.e., self-aggregation of surfactant molecules did not take place. There was no indication of emulsification, which would be recognisable from the appearance of turbidity.

Whereas the non-ionic surfactant does not exert any influence, the log $P_{O/W}$ values are shifted considerably in the presence of cationic surfactants. Obviously, the organo-cations

interact with dissociated acidic groups of the humic acid, and charge neutralisation renders the colloids more hydrophobic. The effect seems to be more pronounced for the C_{16}-alkyl homologue, suggesting that the alkyl chains of the surfactants contribute to the increase in hydrophobicity. Without shaking, flocculation occurs in these systems.

The effect of anionic surfactants is demonstrated in Fig. 25. In this case, the partitioning equilibria are shifted towards the aqueous phase, i.e., in the opposite direction as compared to the cationic surfactants. Consequently, the respective modes of interaction must be entirely different. An additional test series with NaCl clearly indicated that the changes in the partition ratios cannot be attributed to a salt effect but are in fact specific to the organo-anions.

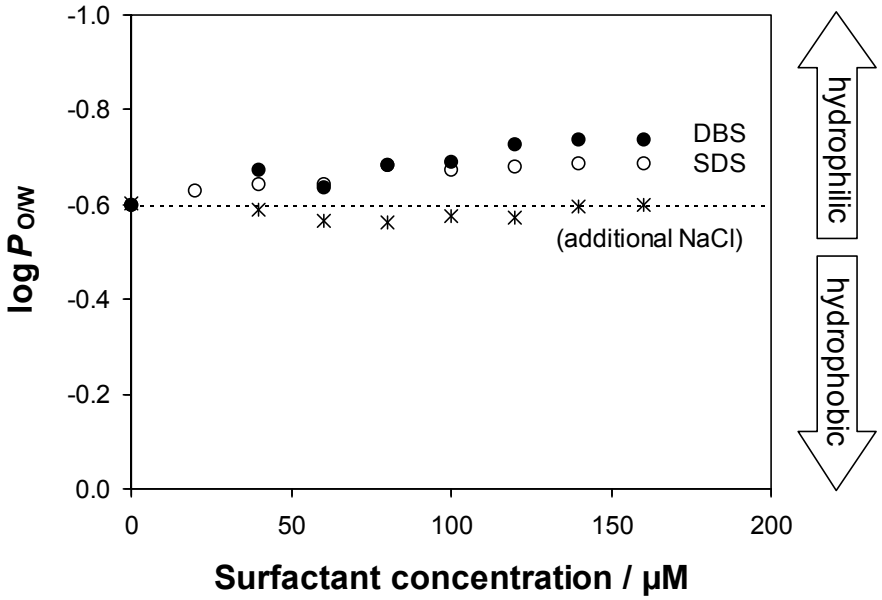

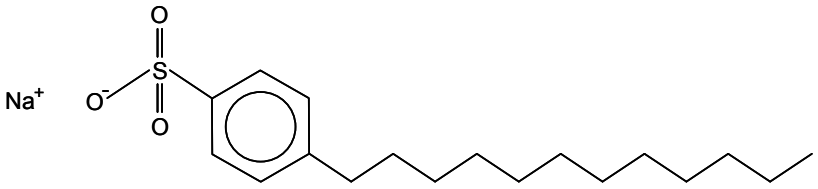

DBS: sodium dodecylbenzenesulfonate

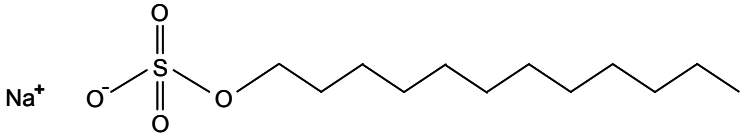

SDS: sodium dodecylsulfate

Figure 25. Effects of anionic surfactants on octanol-water partitioning of HA (5 mg L^{-1} Aldrich HA, labelled with ^{131}I; 0.1 M NaCl; pH 4.0).

Since humic acids are polyanions, binding of anionic surfactants can only be achieved by hydrophobic interaction with the alkyl groups. The ionic head groups of the surfactant molecules are free of interaction and keep the aggregates in the aqueous phase, that is, the colloids become more hydrophilic.

Considering the fact that anionic surfactants do interact with HA in spite of electrostatic repulsion, it is very unlikely that there is no interaction with the non-ionic surfactant. Instead, the absence of any effect may indicate that the hydrophilic-lipophilic balance is comparable to that of the humic material. The different interaction modes are illustrated schematically in Fig. 26.

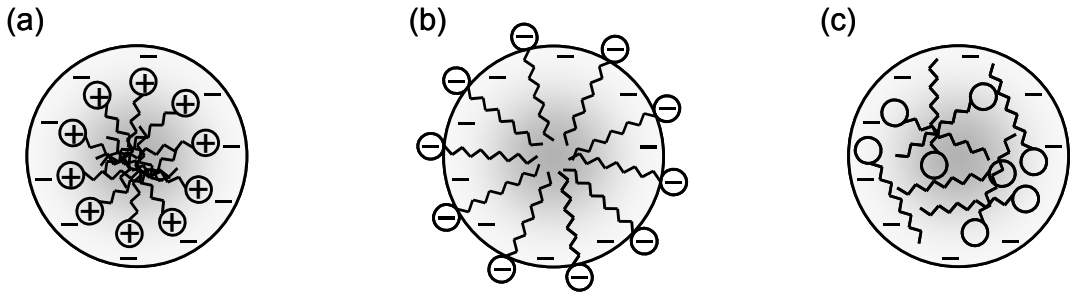

Figure 26. Schematic representation of possible modes of association between humic colloids and cationic (a), anionic (b) and non-ionic (c) surfactants as derived from the results shown in Figs. 24 and 25.

3.4.2 Implications on HA adsorption onto kaolinite

As in the partitioning experiments, systems of HA and surfactants (0.1 M NaCl, pH 4.0) were pre-equilibrated for 15 h. Then, 2 mL aliquots were added to 2 mL portions of a pH-adjusted kaolinite suspension (2 g L^{-1}, in 0.1 M NaCl) in PP centrifuge tubes (5 mL). Equilibration and analysis were performed as described in Section 2.2.3.

Figure 27 shows how adsorption of humic acid onto kaolinite is influenced in the presence of DTAB, SDS and DGP. Whereas adsorption is increased in the presence of the cationic surfactant, a decrease is observed for the anionic and non-ionic surfactants. The contrary effects of DTAB and SDS can be explained by the fact that adsorption is counteracted by a negative colloid charge since the mineral surface is likewise negatively charged [25]. Consequently, charge compensation by the organo-cations promotes HA adsorption while the additional input of negative charge by organo-anions entails a decrease in adsorption. Surprisingly, the same trend is obtained for the non-ionic surfactant although the colloid charge is not changed in this case. Most likely, the decrease is caused by competitive adsorption of DGP molecules which are not associated with HA. One might expect that a competitive effect of free surfactant molecules is more pronounced for the cationic DTAB. Apparently, its influence is dominated by the promoting charge neutralisation effect.

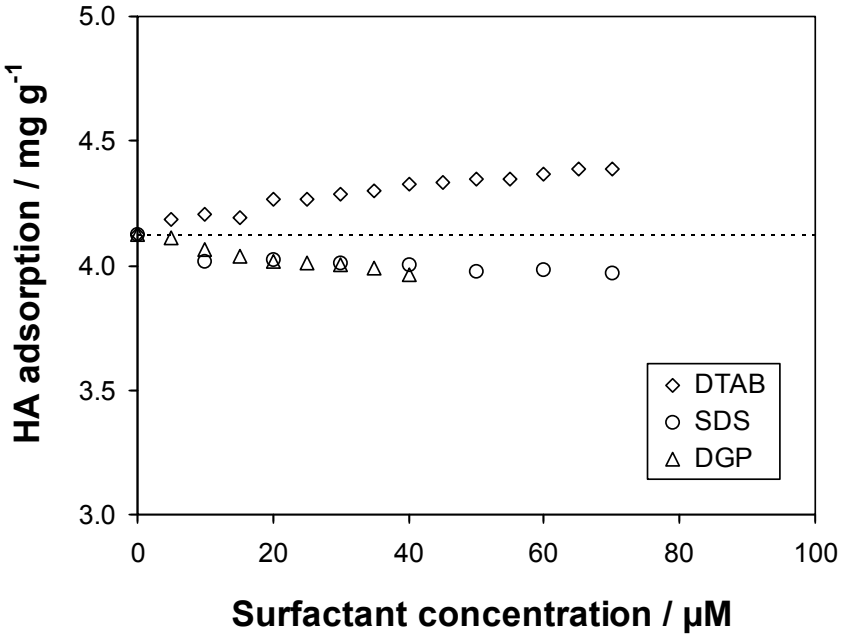

Figure 27. Effects of DTAB (cationic), SDS (anionic) and DGP (non-ionic) on adsorption of HA onto kaolinite (5 mg L^{-1} Aldrich HA, labelled with ^{131}I; 0.1 M NaCl; pH 4.0; 1 g L^{-1} kaolinite)

3.4.3 Implications on Tb(III)-humate complexation

In this study, the question was addressed whether metal binding to HA is affected by the interaction processes with low-molecular-weight organics. After pre-equilibration of HA/surfactant systems, $[^{160}Tb]Tb(NO_3)_3$ (10^{-7} M) was added, and the solutions were allowed to stand for 48 h. Subsequently, the concentration of humic-bound Tb was determined by the anion exchange method. The results are shown in Fig. 28.

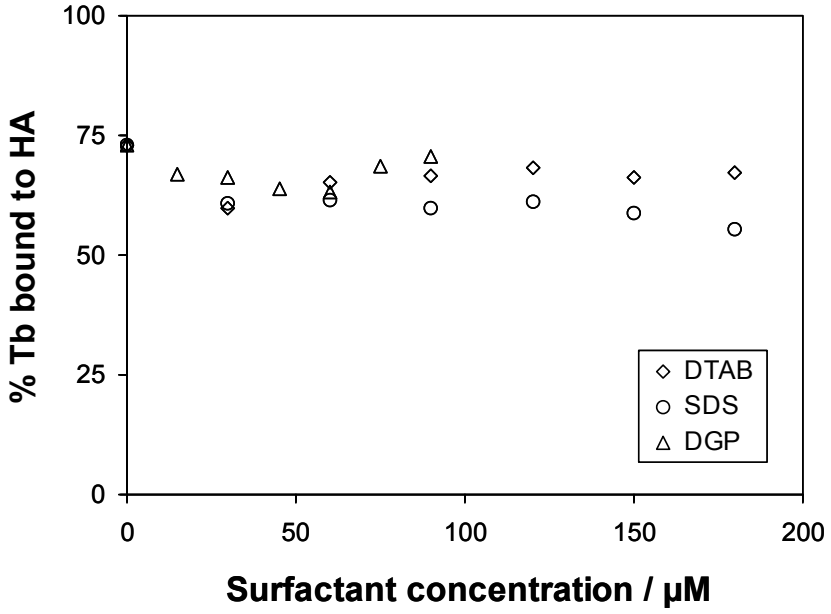

Figure 28. Effects of DTAB (cationic), SDS (anionic) and DGP (non-ionic) on complexation of HA with Tb(III) (10^{-7} M [^{160}Tb]Tb; 5 mg L^{-1} Aldrich HA; 0.1 M NaCl; pH 4.0).

Within the limits of accuracy, the complexed fraction appears to be unchanged in all cases. As regards the anionic and non-ionic surfactants, this result is not surprising since the binding sites are not directly affected by the interaction processes. The cationic surfactant, however, is bound to the acidic groups which are involved in Tb complexation, and a blocking effect might be expected. Obviously, the monovalent organo-cation is outcompeted by Tb(III) which is bound much more strongly.

3.4.4 Implications on size distribution

The character of humic substances in aqueous solution is not yet fully understood. There is a controversy about whether humic colloids are in fact macromolecules or aggregates of smaller entities. For instance, a micelle-like structure has been proposed, derived from certain similarities to the surface-active behaviour of detergents [26]. Furthermore, it has been reported that humic colloids are disrupted in the presence of carboxylic acids [27].

Considering these findings, it seems likely that the aggregation processes between humic acid and surfactants are accompanied by substantial changes in the size distribution of the colloids. Figure 29 shows HPSEC separations of Aldrich HA in the presence of DTAB and SDS, respectively. Since the humic acid is partially adsorbed on the stationary phase at acidic pH, these experiments were conducted at pH 7, using phosphate buffer as solvent and eluent. The buffer concentration was set to give an ionic strength of 0.1 M.

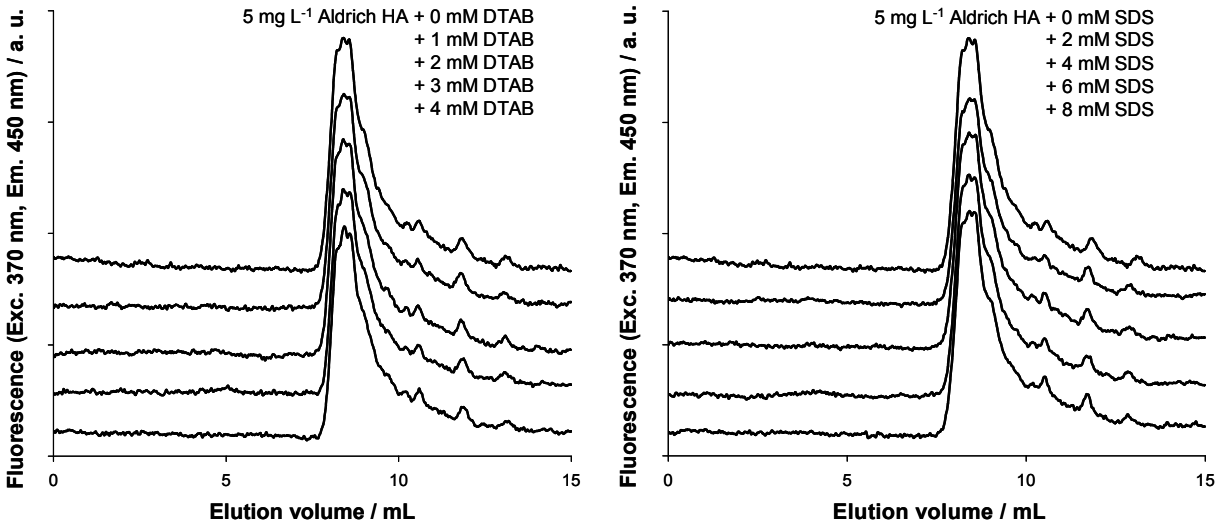

Figure 29. Size exclusion chromatograms of Aldrich HA in the presence of DTAB and SDS, respectively (46 mM phosphate buffer; 0.05% NaN_3; pH 7.0).

Unexpectedly, the size exclusion chromatograms of the humic acid in the absence and presence of DTAB or SDS are virtually unchanged, even though the surfactant concentrations are considerably higher than in the partitioning experiments. There is not any evidence of rearrangement processes among loose aggregates; a micellar character can be ruled out. Instead, this study supports the proposition that humic colloids are static entities.

3.5 Utilisation of PET for visualising humic colloid-borne transport

Within the framework of the project, some important steps were taken to utilise positron emission tomography (PET) for 3D imaging of colloidal transport processes in geological matrices, which represents a novel application of this technique.

For first experiments, a sand column (54 $cm^2 \times 50$ cm) was chosen as a simple system. The column was arranged in an upright position, and a constant water flow of 10 mL min^{-1} was supplied from the bottom up. Water inlet and outlet were protected by filters. After recycling water through the column for one week, 2 mL of the tracer solution were injected using a three-way valve. The effluent water was then collected in a waste container. The equilibrium pH was about 6. For PET measurements, the flow was stopped after certain time intervals, and the column was placed in the scanning device horizontally. The time required for a PET scan was 10 min.

3.5.1 Transport of humic acid in comparison with a conservative tracer

Figure 30 shows PET images of the distribution of humic acid in the column after different times of transport. The humic material was labelled with the positron-emitting nuclide ^{124}I (see Section 2.2.2.). After 60 min, two distinct domains could be observed. The upper one moved with a velocity that corresponded to the linear flow velocity of the transport medium. Hence, this transport zone was attributed to free [^{124}I]iodide which had been detached from the HA, possibly due to the cleavage of C-I bonds as a consequence of light exposure. Thus, albeit unintentionally, the iodide acted as a conservative (i.e., non-interacting) tracer, and a direct comparison with the transport behaviour of humic colloids was possible. The activity of free ^{124}I was less than 1% of the total activity. 20 minutes later, the colloidal transport domain had moved on into the scanned region of column.

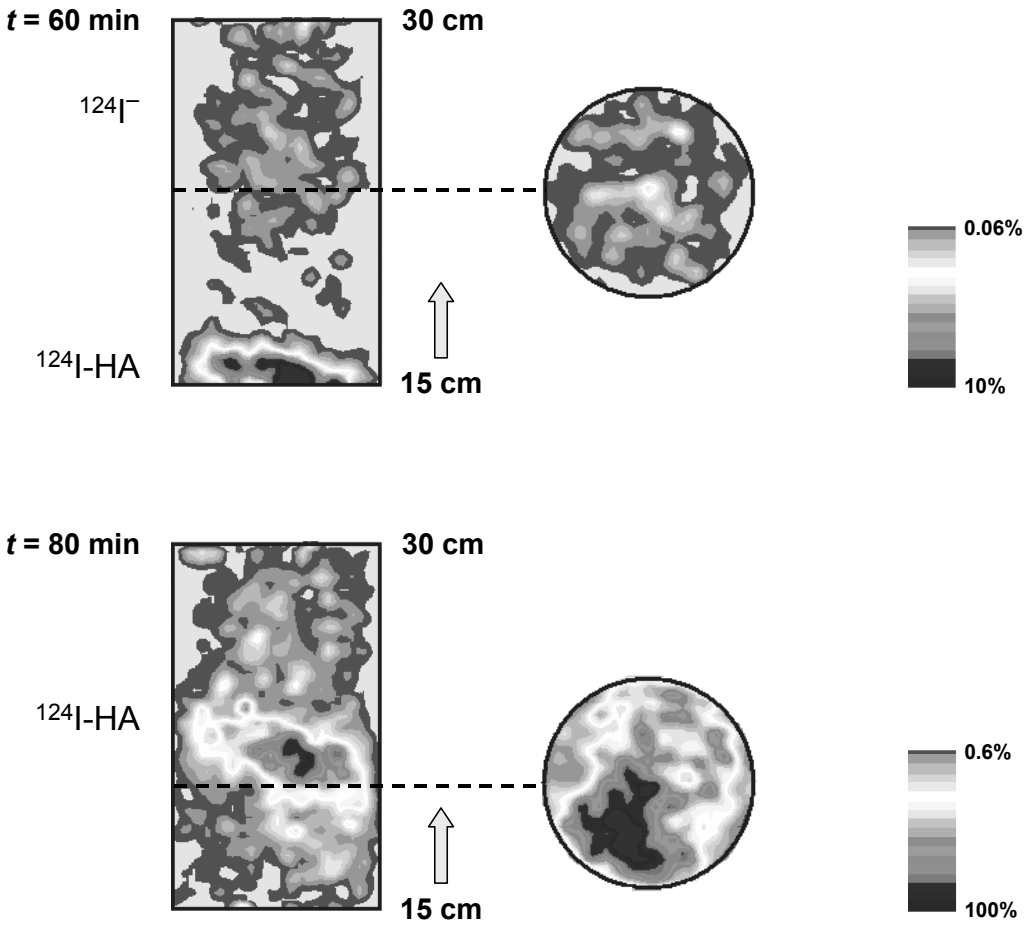

Figure 30. Transport of humic acid in a column (54 cm^2 × 50 cm) filled with synthetic quartz sand (grain size: 70 µm). PET images of axial and cross-sectional tracer distributions after 60 min and 80 min, respectively (water flow rate: 10 mL min^{-1}; injection: 2 mL of a solution of 40 mg L^{-1} Aldrich HA labelled with ^{124}I, ~ 50 MBq).

Comparing the cross-sectional images of the two domains, it can be seen that the labelled colloids are concentrated in certain regions, whereas the activity in the transport zone of [^{124}I]iodide is more evenly distributed. This phenomenon is known as “channelling”, and is often observed for large migrating particles, depending on the structure of the matrix.

By means of the activity data for the volume elements (d*x*d*y*d*z*), it is possible to calculate the distributions of transport velocity *v* and mass flow rate $\dot{m}$ for a selected cross-section:

$$v(x,y) = \frac{M_1}{M_0\, t} \tag{8}$$

$$\dot{m}(x,y) = M_0\, v(x,y) \tag{9}$$

with

$$M_0(x,y) = \int_0^\infty c(x,y,z)\,\mathrm{d}z$$

$$M_1(x,y) = \int_0^\infty c(x,y,z)\,z\,\mathrm{d}z$$

The results are shown in Fig. 31. As a first approach, a rather wide grid pattern was chosen for defining the volume elements. The major differences between both transport zones are, however, obvious. A nearly parabolic profile is obtained for the [^{124}I]iodide domain. In contrast, for the ^{124}I-HA domain, the velocities and mass flow rates are distributed very asymmetrically.

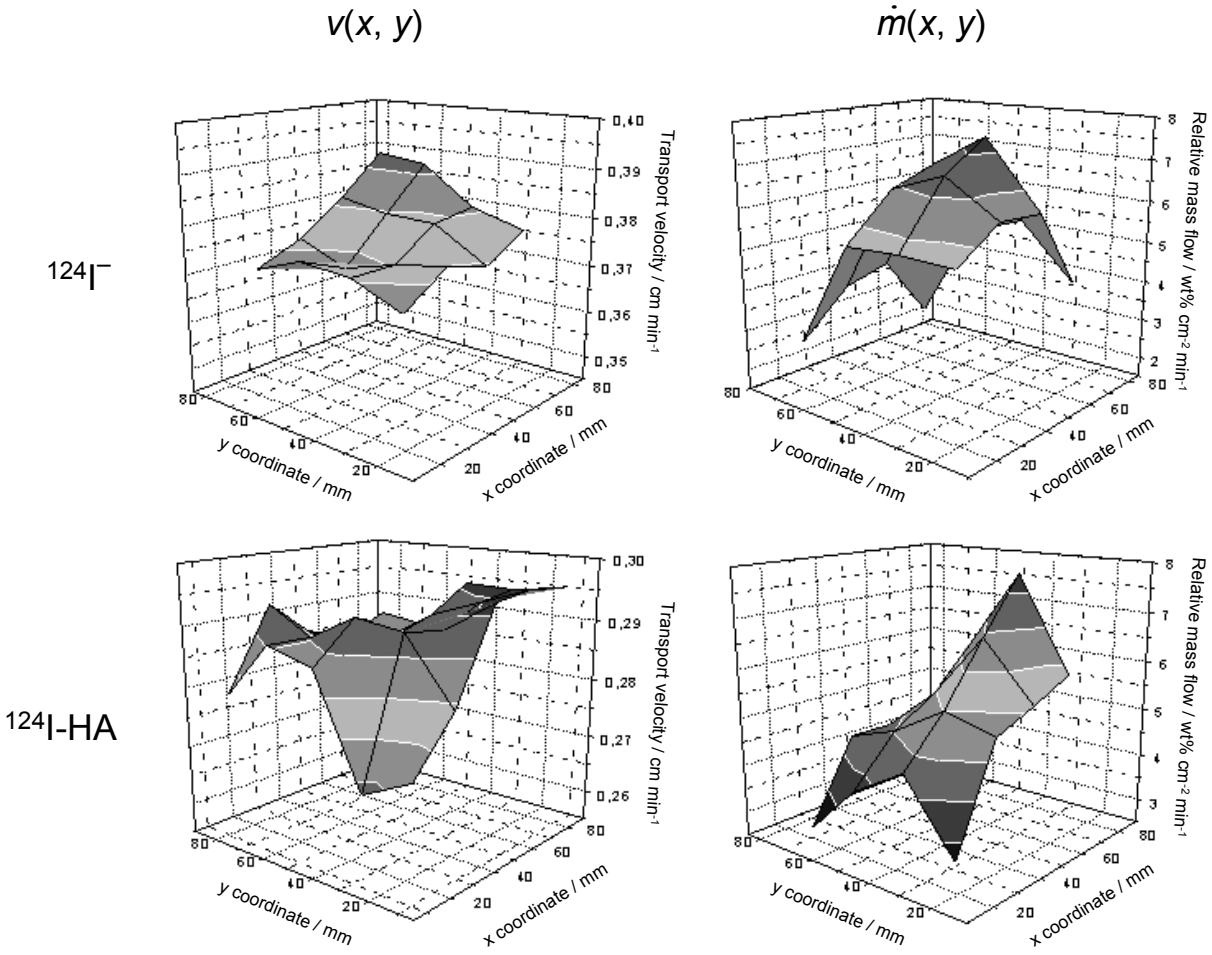

Figure 31. Distributions of transport velocities (left) and mass flow rates (right) over the cross-sectional area, calculated according to Eqs. (8) and (9), respectively, for both transport zones shown in Fig. 30.

As mentioned above, humic substances radiolabelled by iodination are susceptible to light irradiation because of the limited stability of C-I bonds. Binding of fluorine to carbon is known to be more persistent. Thus, labelling with the positron emitter ^{18}F instead of ^{124}I appeared to be a promising alternative. Since a direct fluorination by electrophilic substitution is not possible, an indirect labelling technique was developed, based on a coupling reaction with [^{18}F]aniline. The complete procedure is described in Section 2.2.2.

Although the ^{18}F-labelled product proved to be superior in stability, this technique turned out to be unsuitable for the PET experiments within this project. The principal drawback consists in the short half-live of ^{18}F (110 min) compared to ^{124}I (4.1 d). Unless very high input activities are applied (> 1 GBq), transport experiments on a longer time scale are hardly feasible since the labelling procedure itself is rather time-consuming as well.

3.5.2 Humic-bound transport of Y(III)

In another transport experiment, humic colloid-borne transport of Y(III), employed as a positron-emitting tracer analogue of trivalent actinides, could be visualised successfully (Fig. 32). The concentration of Y was adjusted by addition of inactive $Y(NO_3)_3$ to the ^{86}Y tracer solution, yielding 10^{-7} M after mixing with HA solution. The system was allowed to equilibrate for 3 h before the column experiment was started. The experimental conditions were the same as in the study with ^{124}I-HA.

In this case, only one transport zone was to be seen after 60 min. This was surprising since Y(III) was not expected to be bound to HA completely. Free metal species would be adsorbed on the sand matrix, and should thus be immobilised in the bottom range of the column. Apparently, there was only a minor fraction of non-bound Y, which was not detected in the PET scan.

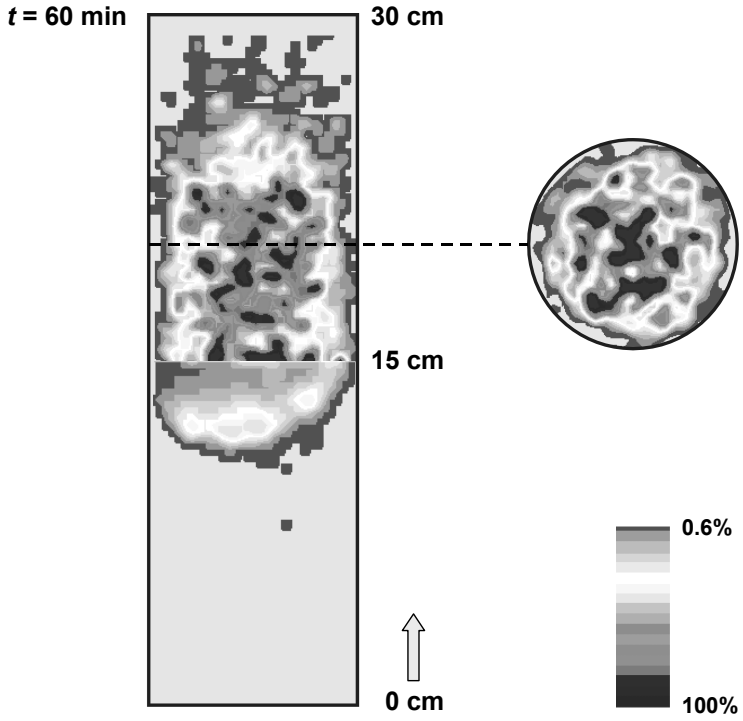

Figure 32. Humic colloid-borne transport of Y(III) in a column (54 cm^2 × 50 cm) filled with synthetic quartz sand (grain size: 70 µm). PET images of axial and cross-sectional tracer distributions after 60 min (water flow rate: 10 mL min^{-1}; injection: 2 mL of a solution of 40 mg L^{-1} Aldrich HA and 10^{-7} M [^{86}Y]Y, ~ 100 MBq).

4 Conclusions and outlook

Adsorption of actinides onto kaolinite is substantially influenced when colloidal organic matter is present even at low concentrations. This is a consequence of the strong affinity of humic substances towards higher-valent metals as well as to the mineral surface. Metal adsorption was found to be enhanced by humic acid within a comparatively wide range of pH, different from adsorption onto other geological materials. A mobilising effect may be expected in alkaline or circumneutral solutions, but the acidic surface properties of kaolinite will keep the pH outside this range. Thus, this material proved to be an effective geochemical barrier in respect of humic-bound transport. Since, however, kaolinite alone is not representative of clay rock, it is necessary to perform similar studies with other clay minerals as well as with natural clay samples containing organic material.

The pH-dependent influence of HA can be satisfactorily explained by the pH dependences of direct metal adsorption, metal-humate complexation and HA adsorption. Nonetheless, a quantitative recombination of the ternary system by a composite K_d calculation does not fit the experimental data exactly. Apparently, the constituent binaries cannot be treated independently of each other. In future work, the prerequisites of such an additive combination will be examined thoroughly by means of radiotracer studies. Questions to be answered will concern, for instance, the reversibility of HA adsorption as well as the equal treatment of dissolved and adsorbed metal-humate complexes.

Due to its valency and abundance, Fe(III) has a unique potential to counteract humic colloid-borne transport of contaminant metals. At micromolar concentrations, competitive effects proved to be significant. Displacement is limited by flocculation, leading to complete immobilisation. This process was shown to be induced by charge compensation at HA colloids on metal loading.

The competitive influence of Fe(III) was found to be kinetically controlled. Unlike dissociation kinetics, the observed time dependence can hardly be explained on the basis of transfer processes between different binding sites. Instead, the present results indicate that the effect arises from the polynuclear nature of hydrolysed Fe(III). When interacting with humic colloids, this structure is not disrupted immediately. Strictly, this first-stage association cannot be termed as humate complexation. In the bound state, however, the polycations are slowly decomposed, probably into monomeric Fe(III), and more binding sites are occupied at equal Fe load. Thus, regular complexation is merely preceded by a metastable state, and equilibrium thermodynamics remains applicable. The ageing process is not due to irreversible structural changes within humic molecules, as is often assumed. Similar studies with other higher-valent metals, such as Al(III), are needed to ascertain if these findings can be generalised.

Obviously, sulfate ions do not act as competing ligands with respect to humate complexation. In speciation models, they are to be considered as electrolyte constituents only.

By means of radioanalytical $P_{O/W}$ measurements, different modes of interaction between humic substances and low-molecular-weight organic compounds were identified on the basis of changes in the hydrophilic / hydrophobic properties of the colloids. Effects on adsorption and

metal binding turned out to be of minor importance. It can be concluded that the transport properties of organic colloids are not substantially affected by isolating them from the total inventory of organic matter. The absence of implications on size distribution suggests that humic colloids are macromolecules, rather than loose aggregates.

Based on suitable radiolabelling techniques, positron emission tomography was successfully utilised for 3D imaging of humic colloid-borne transport processes in geological matrices. As a result of first experiments with a sand column, a pronounced inhomogeneity in the mass flow distribution (channelling) was detected for a humic acid as compared with a conservative tracer. Studies on real geological barrier materials (clay rock, granite), planned in a follow-up project, are promising.

5 References

[1] Lieser, K. H., Ament, A., Hill, R., Singh, R. N., Stingl, U., Thybusch, B., *Radiochim. Acta* 49 (1990) 83-100.

[2] Dearlove, J. P. L., Longworth, G., Ivanovich, M., Kim, J. I., Delakowitz, B., Zeh, P., *Radiochim. Acta* 52/53 (1991) 83-89.

[3] Kim, J. I., Zeh, P., Delakowitz, B., *Radiochim. Acta* 58/59 (1992) 147-154.

[4] Buffle, J., "Complexation reactions in aquatic systems: an analytical approach", Ellis Horwood, Chichester 1988.

[5] Choppin, G. R., *Radiochim. Acta* 58/59 (1992) 113-120.

[6] Carlsen, L., Lassen, P., Warwick, P., Randall, A., *Chemosphere* 33 (1996) 659-670.

[7] Lippold, H., Mansel, A., Kupsch, H., *J. Contam. Hydrol.* 76 (2005) 337-352.

[8] Van den Bergh, J., Jakubowski, B., Burba, P., *Talanta* 55 (2001) 587-593.

[9] Geckeis, H., Rabung, T., Ngo Manh, T., Kim, J. I., Beck, H. P., *Environ. Sci. Technol.* 36 (2002) 2946-2952.

[10] Bidoglio, G., Grenthe, I., Qi., P., Robouch, P., Omenetto, N., *Talanta* 38 (1991) 999-1008.

[11] Seibert, A., Mansel, A., Marquardt, C. M., Keller, H., Kratz, J. V., Trautmann, N., *Radiochim. Acta* 89 (2001) 505-510.

[12] Swift, R. S., in: Sparks, D. L. (Ed.), "Methods of soil analysis. Part 3: chemical methods", Soil Sci. Soc. Am., Madison 1996, pp. 1018-1020.

[13] Bereznitski, Y., Jaroniec, M., Maurice, P., *J. Colloid Interface Sci.* 205 (1998) 528-530.

[14] Fraker, P. J., Speck., J. C., *Biochem. Biophys. Res. Commun.* 80 (1978) 849-857.

[15] Franke, K., Patt, J. T., Patt, M., Kupsch, H., Steinbach, J., *Radiochim. Acta* 92 (2004) 359-362.

[16] Hiraide, M., Tillekeratne, S. P., Otsuka, K., Mizuike, A., *Anal. Chim. Acta* 172 (1985) 215-221.

[17] Schubert, J., *J. Phys. Colloid. Chem.* 52 (1948) 340-350.

[18] Lippold, H., Müller, N., Kupsch, H., *Appl. Geochem.* 20 (2005) 1209-1217.

[19] Zachara, J. M., Resch, C. T., Smith, S. C., *Geochim. Cosmochim. Acta* 58 (1994) 553-566.

[20] Samadfam, M., Sato, S., Ohashi, H., *Radiochim. Acta* 82 (1998) 361-365.

[21] Cacheris, W. P., Choppin, G. R., *Radiochim. Acta* 42 (1987) 185-190.

[22] Rao, L., Choppin, G. R., Clark, S. B., *Radiochim. Acta* 66/67 (1994) 141-147.

[23] King, S. J., Warwick, P., Hall, A., Bryan, N. D., *Phys. Chem. Chem. Phys.* 3 (2001) 2080-2085.

[24] Schüßler, W., Artinger, R., Kienzler, B., Kim, J. I., *Environ. Sci. Technol.* 34 (2000) 2608-2611.

[25] Yukselen, Y., Kaya, A., *Water, Air, and Soil Pollution* 145 (2003) 155-168.

[26] Guetzloff, T. F., Rice, J. A., *Sci. Total Environ.* 152 (1994) 31-35.

[27] Piccolo, A., Nardi, S., Concheri, G., *Chemosphere* 33 (1996) 595-602.

Appendix E - Institut für Theoretische Chemie, Technische Universität Münnchen

Quantum Mechanical Modeling of the Complexation of Actinides by Humic Substances

Notker Rösch und Sven Krüger

Final Report

Support Contract Number
02E9693

Department Chemie, Theoretische Chemie
Technische Universität München
85747 Garching
Germany

Content

1 Introduction

The versatile complexation chemistry of actinide elements strongly affects their distribution and their transport in the environment [1-3]; ; other important factors are colloid formation and the large variety of solid phases [4,5].The behavior of actinides under natural conditions is determined not only by their solubility and complexation in aqueous solution, but also by the interaction of aqueous species with soils, minerals, and natural organic matter [6,7]. Sorption and colloid formation strongly influence the chemical state as well as the transport behavior of actinide ions. In turn, migration of actinides is a central issue in safety analysis and long-term storage modeling for predicting the distribution and the behavior of actinides in the environment, especially with regard to radioactive waste management as well as remediation of contaminated sites of uranium mining and former nuclear weapon production. Whereas the aquatic chemistry of the more common oxidation states of actinides is now fairly well understood [1,3,8], much less is known regarding sorption at mineral surfaces and interaction with natural organic matter. These two topics form the subject of the research organized by the consortium “Migration von Actinoiden im System Ton, Huminstoff, Aquifer”. Modeling of the interaction of humic materials with actinides by quantum chemistry methods was the central topic of one of the involved projects, the results of which will be discussed in the following.

Humic substances form an important class of natural organic matter [9], which is ubiquitous in the lower geosphere, besides other organic molecules, like carboxylic acids. They originate from the metabolism of organisms or the degradation of biological materials. Humic substances are an essential component of soils, but they also are present in surface and ground waters [9]. They complexate metal ions and are redox active and thus noticeably affect the speciation and the distribution of metals in the environment [6,7,9]. Their more solubale fraction, humic and fulvic acids [9], is formed by very variable larger organic molecules, that exhibit a variety of functional groups. Among them, carboxyl groups are considered to be most important for metal and, specifically, actinide complexation [10-15]. Only recently several studies began to inspect possible contributions of other functional groups to actinide complexation of humic substances [16-18]. Thus far, the structure of actinide carboxylate and humate complexes is accessible mainly indirectly from EXAFS experiments [19] via analogy with definite data from crystal structures. Also the interpretation of the results of other spectroscopic approaches to actinide complexes of humic acids rely on analogies [18,20,21]. There are quite a number of experimental studies on the interaction of actinides with humic acids [12,13,15,19-23] and also on the effect of humic substances on actinide sorption and colloid formation [11,24,25]. However, a comprehensive understanding of these processes on the atomic scale is still lacking, also due to experimental difficulties that result from the heterogeneity of humic substances.

The main goal of the present project was to complement current knowledge on actinide interaction with humic substances, which largely originates from experiments, by means of quantum chemical calculations. Modeling of actinide complexation by relevant organic functional groups provides new insights at the atomic level. Modern quantum chemistry methods, e.g. those derived from relativistic density functional theory, were applied to provide accurate geometric, spectroscopic as well as energy data [26-28], which are directly related to rele-

vant and well-defined species. Thus, these data are useful for interpreting spectroscopic results, especially when geometric models are involved as in the interpretation of EXAFS measurement. The results of this project also provide insight into bonding mechanisms, solvation effects, and other detailed chemical and physical features that will foster an understanding of similarities and differences of actinide complexes.

2 Tasks of the Project and Prerequisites

The project was mainly concerned with modeling the complexation of actinyl ions by humic substances with the help of quantum chemical methods. The basic modeling strategy relied on replacing functional groups of humic substances by analogous small organic molecules that represent a single and isolated active site. The same approach to studying simple species as model compounds and to understanding actinide complexation at the atomic level has earlier been put forward in experimental studies [29-31]. An accurate relativistic density functional method [32,33] was employed to calculate electronic and geometric structures of actinide complexes in solution as well as their energetic parameters. For this purpose, the high-performance software PARAGAUSS [34] was employed. In addition, a polarizable continuum model [35] was used to account for long-range (electrostatic) solvation effects. The latter method had been implemented in the software package PARAGAUSS during the preceding project 02E9450. Short-range chemical interactions with the solvent were modeled by means of aqua ligands, explicitly included in the quantum chemical models [35].

The central topic of the project was the characterization of complexes of actinyls, mainly of uranyl(VI), with organic ligands. In this way the variability of properties of functional groups was characterized by varying model ligands that mimic different chemical surroundings present in larger molecules like humic acids. The results were then compared to experimental data, assisting their interpretation at the atomic level. The overall picture emerging may also be compared to empirical speciation and complexation models for actinide interaction with humic substances [36,37]. Here, energetic parameters as well as the qualitative compareson of different functional groups are of particular interest. Besides these goals, also other issues, e.g., the determination of fundamental thermochemical parameters of uranyl or the sorption of uranyl on mineral surfaces were addressed, as inspired by the work of partner projects in this cooperative initiative.

The project was divided into the following tasks:

- **Complexes of simple aliphatic carboxylates**
  The most simple aliphatic carboxylic acids were treated as model ligands to study various complexation modes, geometries, and energetics as well as the variation of these properties with increasing aliphatic chain length. This class of ligands served as central reference and as benchmarks to verify methods and modeling strategies.
- **Complexes of derivatives of carboxylates and aromatic carboxylates**
  A broad investigation of various carboxylic ligands was carried out to explore the varia-

bility of properties of possible carboxylic sites in humic substances. By comparison to experimental findings these results were intended to yield information about the atomistic structure and the thermochemical properties of actinide humate complexes.

- **Complexes with alternative functional groups**
  Focusing on alcoholic groups, alternative functional groups of humic acids were investigated and compared to carboxylic groups. Previously, carboxylic functionalities were taken almost exclusively into account in experimental studies. This task supported experimental activities of the project partner Institute of Radiochemistry at the Forschungszentrum Dresden-Rossendorf which inspected the role of phenolic OH groups in actinide complexation.
- **Models of humic acids**
  While starting with small organic molecules as models (see above), it was necessary to explore their adequacy as models and the potential need to account for a wider chemical environment when aiming at the proper representation of active centers of humic substances. Results of earlier tasks would then have to be compared to larger carboxylic acids and to enhanced models which relied on a combined quantum mechanical and molecular mechanical approach (QM/MM), where the distant environment of a complexation site would approximately be described by a classical force field.
- **Method development**
  For the treatment of actinide complexes in solution appropriate parameters for the polarizable continuum model had to be determined and verified. Implementation of a QM/MM method for larger models of humic acids was intended if results of previous tasks indicated the need. In addition, a discrete solvation model of QM/MM type had to be implemented which allows an efficient treatment of a larger number of solvent molecules around the model complexes. For this purpose, a commonly applied force field for water was combined with the polarizable continuum treatment for long-range solvation effects. In this way an accurate representation of the discrete nature of the solvent environment was achieved. In addition, the relativisitic density functional methods applied had to be supported and extended as required by the other tasks of the project.

A prerequisite for the large number of demanding electronic structure calculations and geometry optimizations performed in this project was the application of an efficient high-performance software for computers with parallel architecture. These requirements are satisfied by the density functional package ParaGauss [34], which is available on various hardware platforms. The Linux cluster of the group executing the project, currently comprising about 100 CPUs, was essential for the success of the project. In the framework of this project, four dedicated two-processor nodes had been granted, which had been put into operation for the second half of the project.

3 Development of the State of the Art

Computational modeling of actinide complexes in solution as the central topic of the project represents a challenge for quantum chemistry because several complications have to be

faced simultaneously. Actinides are very heavy elements; therefore, a relativistic treatment is indispensable. Actinide ions exhibit several open valence shells which requires a careful treatment of electron correlation. For very accurate calculations on open-shell complexes also spin-orbit interaction may have to be considered. In addition to these aspects related to the electronic structure, solvent effects have to be taken into account. In the following, we will briefly discuss the state of the art and recent developments of pertinent computational techniques and their application to actinide complexes, focusing on solution chemistry. For more detailed presentations of the field, the reader is referred to recent reviews [26-28].

The most popular strategy to account for relativistic effects in heavy atoms relies on effective core potentials (ECPs, “pseudopotentials”) [38,39]. Thereby, one represents the effect of core electrons of a heavy atom by a relativistically determined pseudopotential; this allows a conventional nonrelativistic treatment of the valence electronic structure. Explicitly relativistic methods, with which one is able to describe larger actinide complexes, invoke a quasi- (or scalar) relativistic approximation to the Dirac-Kohn-Sham method that may include spin polarization. Of practical importance in actinide chemistry are the ZORA approach [40,41] and the Douglas-Kroll-Hess method [32,33]. The latter was used in this project. Fully relativistic four-component methods or self-consistent two-component approaches including spin-orbit interaction are still restricted to small molecules, without any environmental modeling. For the example of PuN_2 it was recently demonstrated by means of an accurate CASPT2 calculation and a subsequent treatment of spin-orbit interaction that spin-orbit effects are small for actinide compounds with only few electrons in the open f shell ($5f^2$) [42]; this is a consequence of the localization of the f-electrons on the actinide center. Also for electron transfer reactions in mixed valent complexes of Np(VI) and Np(V) it was shown that spin-orbit effects hardly affect activation energies [43].

Long-range solvation effects on molecules are commonly modeled by means of polarizable continuum models (PCM) where the molecule is placed in a cavity inside a dielectric continuum that is constructed mainly as superposition of atom-centered spheres [44]. This modeling approach may be complemented by empirical corrections for some short-range interactions (e.g. cavity formation). However, this modeling approach does not account for short-range chemical interactions of solvent molecules; rather, they have to be accounted for by including water molecules in the model treated quantum mechanically. This has been shown to be necessary for an accurate description of charged solutes like actinyls; in recent years, this combination approach of an explicitly treated first solvation shell supplemented by a PCM has been established as standard for describing actinide complexes in solution [27,45]. We had developed and applied this modeling strategy even earlier [35,46,47] and used it throughout this project.

Recent studies showed that the successful application of the PCM approach rests on a careful design of the physical model and a judicious choice of the cavity type and pertinent parameters [48,49]. The limitations of the explicit first shell model recently were explored for the solvated uranyl ion as test system where, in some models, also the second solvation shell was represented in a restricted fashion. Changes of bond lengths of uranyl up to 0.01 Å and stronger effects on the bonds with the aqua ligands were observed as well as a nonnegligible charge transfer from the second shell [48,50]. Explicit inclusion of the second shell only marginally affected the solvation energy; also, the second solvation shell alone accounted for all

essential effects when an aqua ligand is removed from the first ligand shell [48]. To avoid the rather demanding quantum mechanical treatment of a larger solvation environment, a QM/MM approach has been invoked [51,52]. In this way the discrete nature of the solvent can be represented more realistically. For $[UO_2(OH)_4(H_2O)_n]^{2-}$ it was shown that an accurate description of structures and charge distribution is possible by restricting the quantum mechanical system to the first solvation shell, but energies were corrected by single-point quantum chemistry calculations using a larger cluster model [51]. For $[UO_2F_4(H_2O)_n]^{2-}$ it was shown that only by means of an explicit quantum mechanical model of the first solvation shell of 11 aqua molecules the experimentally determined fivefold coordination of uranyl could be reproduced [52]. Recently, Car-Parinello "first principles" molecular dynamics (CPMD) was applied for the first time to solvated actinide complexes [53]. The exchange of an aqua ligand [54] as well as the acidity of solvated uranyl [55] were explored, reproducing experimental values within about 10 kJ/mol. For mixed uranyl nitrate hydroxide and nitrate tetramethylmalonamide complexes solvation effects of the much more demanding CPMD method and the ZORA/PCM approach were shown to agree well [56].

From these examples one may conclude that a solvation treatment exceeding the explicit inclusion of a first solvation shell, combined with a PCM treatment, will be only necessary when properties are examined that crucially depend on the discrete nature of the molecule-solvent interaction. In view of this result, we elaborated a combined QM/MM-PCM procedure in ParaGauss (Section 4.6).

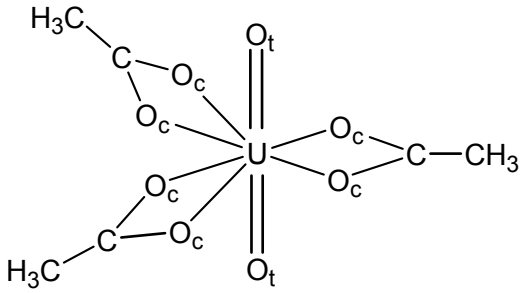

Figure 1. Sketch of the structure of uranyl(VI) triacetate.

In recent years, only few computational studies were devoted to uranyl carboxylate complexes, the main topic of this project. Ion trap experiments for the hydration of uranyl monoacetate in the gas phase showed that up to three aqua ligands are attached to this complex, leading to a four- or five-fold coordination of uranyl by equatorial ligands which may vary with the coordination mode of the ligands [57]. Accompanying density functional calculations on $UO_2(CH_3COO)(H_2O)_3$ determined the energy difference between these two coordination modes to be by only 2 kJ/mol [57]. Uranyl acetate complexes with one to three ligands were studied with ECP density functional calculations [58], but this study did not include explicit aqua ligands or long-range solvation effects. As a result, much stronger variations of uranyl vibrational frequencies than inferred from crystalline probes were calculated. Although oxalate can not be regarded as a model for complexation by humic acids, it is of interest as

ligand exchange mechanisms as well as the chelate effect have been studied in detail for this carboxylic acid [3]. To the best of our knowledge, the interaction of uranyl with alcoholic groups has not been treated computationally until now. Thus, the results provided in this project fill a gap, especially with respect to data which may be helpful for interpreting experimental studies on actinyl humate complexation and the construction of empirical complexation models.

4 Results

Here, we will review the main results of the project following the project plan. First we will present computational results for actinyl complexation by organic ligands and their impact on the current view on actinyl humate complexes. Then we will describe studies on the thermochemistry of actinyls. Finally we will review methodological work on relativistic density functional methods and solvation models. Where publications are already available, the presentation will be more concise. Project-related publications are listed in Section 6 and also included among the references.

4.1 Complexes with aliphatic carboxyl ligands

4.1.1 Uranyl triacetate

Uranyl(VI) triacetate (Figure 1) represents a well characterized reference system for the validation of methods and models. In solution the three acetate ligands coordinate in bidentate fashion in the equatorial plane of uranyl, excluding aqua ligands from the first ligand shell. To inspect solvation effects and validate different models of solvation, gas phase as well as PCM [35] calculations have been performed, with and without explicitly modeled water ligands of the second solvation shell [59,60]. We modeled the effect of explicit aqua ligands of the second coordination shell in a qualitative way as we assumed them to bridge oxygen atoms of different carboxyl groups. The structure from a scalar relativistic density functional approach [33] in the form of a local density approximation (LDA) for the exchange correlation (XC) potential agrees very well with available experimental results in solution [67,70].

The best agreement is achieved for the model with PCM embedding and additional aqua ligands. Available distances in solution agree within 0.02 Å and the symmetric uranyl stretching frequency is reproduced within 10 cm^{-1}. This has to be regarded as a good agreement for accurate density functional calculations. As LDA XC functionals are known to overestimate binding energies, single-point calculations at the level of a gradient-corrected functional (generalized gradient approximation – GGA) were carried out to obtain better estimates of energetics. As shown here for the example of uranyl triacetate, structures from GGA calculations tend to overestimate interatomic distances (Table 1, BP and PW91 functionals) [59,60].

Table 1. Geometric parameters (in Å) und symmetric stretching frequency of uranyl (ν_s, in cm^{-1}) of uranyl(VI) triacetate $[UO_2(OOCCH_3)_3]^- \cdot (H_2O)_n$ for bidentate ligand coordination. Results obtained with LDA (VWN) and GGA (BP, PW91) exchange-correlation potentials are compared with experimental results form aqueous solution (Sol.) and crystal structures (Cryst.). Gas phase (GP) and solvated (PCM) model results without and with n additional explicit aqua ligands are compared. For the designations of atoms, see Figure 1.

	n	XC	U=O_t	U-O_c	U-C	U-CH_3	ν_s
Exp.							
Sol.[a]			1.78(2)	2.44(2)	–	4.34	823
Cryst.[b]			1.78(1)	2.48(2)	2.88(3)	–	–
LDA							
GP	0	VWN	1.792	2.449	2.816	4.315	837
GP	3	VWN	1.783	2.459	2.848	4.337	857
PCM	0	VWN	1.803	2.424	2.817	4.299	811
PCM	3	VWN	1.792	2.438	2.849	4.323	831
GGA							
GP [c]	0	PW91	1.81	2.51	–	4.38	–
GP	0	BP	1.81	2.52	2.89	4.41	810
GP	3	BP	1.80	2.53	2.92	4.43	825
PCM[c]	0	PW91	1.81	2.50	–	4.38	–
PCM	0	BP	1.82	2.49	2.89	4.39	785
PCM	3	BP	1.81	2.50	2.91	4.41	799

[a] Refs.67,70. [b] Average, Refs. [15, 30,61,62,71]. [c] Ref. [63].

4.1.2 Monocarboxylates $[UO_2OOCR]^+$ in the gas phase

The effect of ligand size and type has been examined for bidentate complexes in the gas phase with a single aliphatic carboxylate (Figure 2). The omission of solvent effects in this approximate model study should increase the sensitivity of the model since the damping effect of a polarization field and the concurrence to aqua ligands is missing. To study the influence of ligand size, the aliphatic chain length was increased. Cα substitution of acetic acid models was used as a model for the varying chemical environment of a carboxylic group in a humic acid molecule. In this way uranyl monocarboxylate complexes were constructed which are useful models for inspecting variations in the chemical properties of carboxylic groups of humic substances [60].

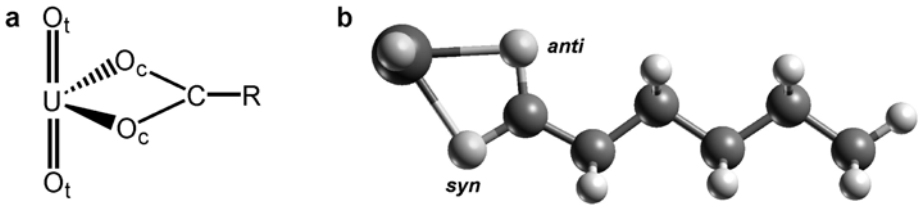

Figure 2. (a) Sketch of bidentate aliphatic uranyl monocarboxylates $[UO_2(OOCR)]^+$, R = C_nH_{2n+1}, (b) Optimized structure for n = 5 in C_s symmetry. The oxygen atoms of the carboxyl group are distinguished as *syn* ($O_{c,s}$) and *anti* ($O_{c,a}$) with respect to the C_α-H moiety of the hydrocarbon chain.

Table 2. Geometric parameters (distances in Å, angles in degree), Mulliken charges q of uranyl (in e) and symmetric stretching frequency of uranyl ν_s (in cm^{-1}) of bidentate uranyl monocarboxylates $[UO_2(OOCR)]^+$, R = C_nH_{2n+1}, for n = 0–5 in the gas phase.

n	U=O_t	O_t=U=O_t	U-$O_{c,s}$	U-$O_{c,a}$	U-C	q(UO_2)	ν_s
0	1.745	172.6	2.242	2.242	2.628	0.96	946
1	1.749	172.0	2.224	2.224	2.640	0.91	936
2	1.750	171.8	2.213	2.227	2.635	0.90	933
3	1.751	171.8	2.205	2.234	2.635	0.89	932
4	1.751	171.8	2.206	2.234	2.635	0.88	930
5	1.752	171.8	2.206	2.236	2.634	0.87	927

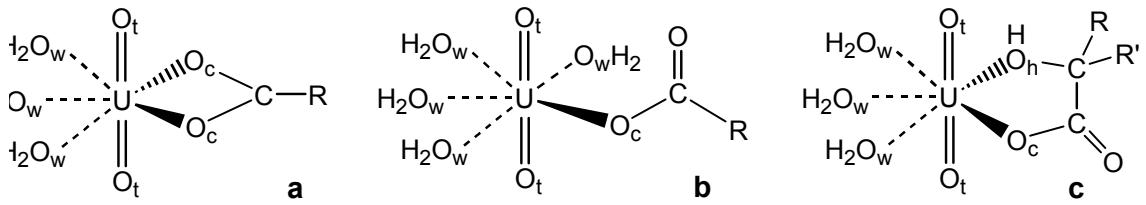

Figure 3. Schematic structure of different coordination modes of uranyl monocarboxylate complexes $[UO_2(OOCR)(H_2O)_n]^+$: a) bidentate, b) monodentate, c) chelate.

The effect of the length of the aliphatic chain on uranyl monocarboxylate complexes was studied in the gas phase for bidentate complexes, applying Cs symmetry constraints. The results for the complexes [UO2(OOCCnH2n+1)]+ (n = 0–5) are collected in Table 2. With the exception of the formiate complex, a rather uniform picture arises, as expected. Interatomic distances, charge, and symmetric stretching frequency of uranyl for longer aliphatic carboxyls are very similar to the results for the acetate species. Only the difference of 0.03 Å between the two uranyl carboxylate U-Oc bonds converges later, namely for propionic acid. With increasing chain length, one notes very weak trends of decreasing uranyl charge, increasing uranyl bond length, and decreasing uranyl stretching frequency from the data of Table 2. The inspected properties converge very well for propionic acid (n = 3). This can be taken as a hint that effects of the chemical environment also in humic substances should be mainly restricted to the range of about three carbon-carbon bonds.

We modeled bidentate monocarboxylate complexes of acrylate, glycolate, and glycin in the same way and found only small differences to the acetate complex, the largest ones for glycin. Compared to other carboxylate ligands, the uranyl bond length is elongated by 0.005 Å in line with a reduced symmetric uranyl stretching frequency of the glycin complex, by 16 cm─1. The corresponding U-C distance is 0.02 Å longer. Thus, also variations due to substitution close to the carboxylate group are small. Hence, one expects rather small variations of properties of aliphatically connected carboxyl functional groups in humic substances.

4.1.3 Monocarboxylates [UO2OOCR(H2O)n]+ in aqueous solution

We examined monocarboxylates of uranyl(VI) in solution as models of uranyl complexes with humic substances. However, monocarboxylates are also of interest by themselves, as they occur as a first stage of uranyl complexation by carboxylic acids or at low carboxylate concentrations. Monodentate, bidentate, and chelate complexation modes have been discussed (Figure 3). Chelate complexes require an appropriate second group besides carboxyl. Coordination n = 5 in the equatorial plane of the uranyl moiety was chosen as it is most common [29,64]. Thus, to complete the first ligand shell of uranyl, the models of monocarboxylate

complexes are complemented by four aqua ligands for monodentate carboxylate coordination and by three in case of bidentate and chelate complexes. As a first approximation, we studied C_s symmetric models. The equatorial plane of the uranyl was chosen as mirror plane, leading to more stable structures than a perpendicular mirror plane [59,60]. We also applied a PCM treatment to model long-range solvation effects.

Table 3. Geometric parameters (in Å) and symmetric uranyl stretching frequency ν_s (in cm^{-1}) for uranyl(VI) monocarboxylates $[UO_2(OOCR)(H_2O)_n]^+$ in bidentate (bi, n = 3), monodentate (mono, n = 4), and chelate coordination (chel, n = 3) of the carboxylate ligand in comparison to experimental data for acetate as well as averaged data for various carboxylates in solution (Sol.) and from crystal structures (Cryst.). The model results were obtained with C_s symmetry constraints and a PCM treatment of long-range solvation effects. For the designations of atoms, see Figure 3.

	R	U=O_t	U-O_c	U-O_h	U-C	U-O_w	U-O_{eq}	ν_s
bi	H	1.783	2.394		2.770	2.356	2.371	860
	CH_3	1.787	2.371		2.769	2.360	2.364	858
	CH_2CH_3	1.786	2.369		2.768	2.369	2.369	853
	CH_2OH	1.783	2.393		2.771	2.353	2.369	862
Exp.	CH_3 Solv.[a]	1.78(1)	2.50(2)		2.91(2)	2.38(2)	2.43(2)	861
	Sol.[b]	1.78(1)	2.46(4)		2.87(4)	2.40(4)	2.42(4)	–
	Cryst.[c]	1.76(3)	2.48(5)		2.86(5)	2.36(4)	2.42(6)	–
mono	H	1.788	2.221		3.400	2.415	2.376	850
	CH_3	1.790	2.201		3.401	2.421	2.377	846
	CH_2CH_3	1.790	2.201		3.401	2.421	2.377	849
	CH_2OH	1.786	2.247		3.400	2.408	2.375	852
Exp.	Sol.[b]	1.78(1)	–		–	–	2.38(4)	–
	Cryst.[c]	1.76(3)	2.39(5)		3.5(1)	2.42(6)	2.36(2)	–
chel	CH_2OH	1.790	2.229	2.423	3.272	2.380	2.359	846
Exp.	Sol.[d]	1.79(1)	–	–	3.25(3)	–	2.37(1)	–
	Cryst.[e]	1.75(1)	2.37	2.50	3.3	–	2.36(2)	–

[a] Refs. 30,69, 70, [b] Average over data from Refs. 29,30, 31, [c] Average over data from Refs. 10, 30, 71 [d] Average over data from Ref. 29 [e], Ref. 72.

The calculated results [59,60,65] for geometries and symmetric uranyl stretching frequencies, obtained with a LDA (VWN) XC functional, for formiate, acetate, propionate, and glycolate are collected in Table 3 and compared to available experimental data. As definite ex-

perimental data for monocarboxylates are not available, we compared the calculated results to experimental findings in solution [29-31,69,70], which normally contain a mixture of species with different numbers of ligands. Also given in Table 3 are averaged data for various carboxylates in solution [29-31] as well as geometric parameters from crystal structures [10,30,71,72], which are also used to interpret the experimental findings in solutions [29,66]. Referring to crystal structures, EXAFS results for complexes in solution have been interpreted as bidentate when the average distance between uranium and the oxygen atoms of the equatorial ligand shell, U-O_{eq}, amounts to about 2.42 Å [29-31]. For monodentate and chelate coordinated complexes, a value of about 2.36 Å has been inferred from crystal structures. As a second criterion for assigning structures, measured U-C distances can be employed: they are about 3.40 Å for monodentate complexes, notably shorter for chelate coordination (3.25), but only 2.80–2.90 Å for bidentate complexes (Table 3).

For all four ligands inspected, we compared monodentate and bidentate coordination, for glycolate also chelate coordination (Table 3). The calculated uranyl bonds of 1.78 to 1.79 Å were found to agree well with experimental results in solution; its weak variation points to similar bond strength in the complexes, independent of the coordination mode. Consequently, also the uranyl stretching frequency varies only slightly. A weak trend to softer vibrations (by ~10 cm^{-1}) was obtained for monodentate compared to bidentate complexes, but this is too small a variation to be indicative for the coordination mode of the carboxyl ligands. The bond length U-O_c depends on the coordination mode. We calculated 2.20–2.25 Å for monodentate and chelate complexes, while we obtained almost 2.40 Å for the bidentate coordination mode. This trend agrees with experiment, but the calculated bond lengths are 0.1–0.2 Å shorter than experimental values. Calculated U-C distances deviate similarly from experiment: they are ~0.1 Å too short for mono- and bidentate complexes. Yet, the value of 3.27 Å for the chelate structure agrees with the experimental result of 3.25 Å [29]. As in experimental, shorter U-C distances (2.77 Å) were calculated for bidentate and longer ones (3.40 Å) for monodentate complexes. Thus, the *differences* of the calculated carboxyl bonds between the two coordination modes agree qualitatively with the experimental differrences. The bond lengths of aqua ligands to uranyl, U-O_w, were calculated in agreement with EXAFS results (Table 3). However, with EXAFS, it is difficult to resolve differences in interatomic distances of less then 0.1 Å; therefore, most often, one determines only the average U-O distance to equatorial ligands, U-O_{eq}. For this quantity, our calculation yielded values of 2.37±0.01 Å, irrespective of the coordination mode. This is at variance with experiment, where comparable distances, ~2.38 Å, have been assigned for monodentate and chelate complexes, but a longer value, ~2.42 Å, for bidentate coordination (Table 3). Thus, while qualitatively the characteristic differences of carboxylate bonding for various complexation modes were reproduced, the variation of U-O_{eq} was not found in the computational results [59,60].

To study further these remarkable deviations between quantum chemistry calculations and EXAFS results, we examined the effect of various model assumptions, i.e. of the assumed mirror symmetry of the structures and the five-fold coordination of uranyl. We also explored hydrolysis as a further possible rationalization for the deviation from experiment. Finally, we scrutinized the comparability of experimental and theoretical systems.

Table 4. Geometric parameters (in Å) of uranyl(VI) monocarboxylates $[UO_2(OOCR)\cdot(H_2O)_4]^+$ with monodentate ligand coordination. Comparison of calculated results without symmetry constraints in solution (PCM) and experimental data (Exp.) from solution (Sol.) and cyrstal structures (Cryst.). ΔC_s is the averaged difference to model calculations employing C_s symmetry (Table 3). For the designations of the atoms, see Figure 3.

	R	U=O_t	U-O_c	U-C	U-O_w	U-O_{eq}	ΔE
	H	1.786	2.290	3.341	2.394	2.373	-31
	CH_3	1.789	2.291	3.352	2.382	2.364	-28
	CH_2CH_3	1.790	2.287	3.333	2.383	2.364	-30
	ΔC_s	<0.01	0.08	-0.06	-0.03	-0.01	-30
Exp.	Sol.[a]	1.78(1)	–	–	–	2.38(4)	
	Cryst.[b]	1.76(3)	2.39(5)	3.5(1)	2.42(6)	2.36(2)	

[a] Average of data from Refs. 29-31. [b] Average of data from Refs. 10, 30, and 71.

Release of the symmetry constraints of the model complexes only insignificantly changes the geometries of bidentate complexes (Table 4, Figure 4a). All relevant distances relax less than 0.01 Å [60]. For monodentate complexes, an aqua ligand rotates around the coordination direction and forms a hydrogen bond with the uncoordinated oxygen atom of the carboxyl group (Figure 4b); in consequence, this complex stabilizes by about 30 kJ/mol. For the various carboxylates examined, this rearrangement resulted in longer U-O_c bonds, by 0.08 Å longer on average, and shorter U-C distances, by about 0.06 Å (Table 4). Overall this improvement of the models does not lead to better agreement with experiment. U-carboxylate distances are still ~0.1 Å too short and the average U-O_{eq} changes at most ~0.01 Å (Table 4) [59,60].

We examined the effect of hydrolysis on uranyl monocarboxylate complexes for the bidentate complexes $[UO_2(OOCR)(OH)(H_2O)_2]$ of formiate, acetate, and propionate [60]. Due to the strong binding of the hydroxyl ligand, the U-O_t distance elongates to 1.80–1.81 Å. Bond competition also results in an elongation of the U-O_c bonds, by ~0.07 Å, which brings them close to the experimental findings (Table 3). Also the aqua ligand bonds are weakened. For the hydroxo-carboxylates, they are about 0.04 Å longer than typical EXAFS results (Table 3). Still, the deviation between experiment and computational results for U-O_{eq} remains. The calculated value, 2.38 Å, of U-O_{eq} in all species examined is nearly the same as for all other complexes inspected (Table 3). In summary, in the hydroxide complexes, the agreement with experiment improves for the parameters of the uranyl carboxylate bonds, but all other parameters agree less well with experiment. Especially the longer uranyl bond is noteworthy.

Thus, we excluded hydrolysis as reason for the observed disagreement with experiment. As most experiments were performed at rather low pH, the presence of a ternary hydroxo carboxylate complexes has to be regarded anyhow as improbable [29-30].

Table 5. Geometric parameters (in Å) and symmetric uranyl stretching frequency ν_s (in cm^{-1}) of uranyl(VI) monoacetat $[UO_2(OOCCH_3)(H_2O)_n]^+$ in solution (PCM) with bi- and monodentate acetate coordination for the equatorial coordination numbers N = 5 and 6. Comparison with experimental results (Exp.) from solution (Sol.) and cyrstal structures (Cryst.). For the designations of the atoms, see Figure 3.

	n	N		U=O_t	U-O_c	U-C	U-O_w	U-O_{eq}	ν_s
bi	3	5		1.787	2.371	2.772	2.365	2.367	854
	4	6		1.787	2.400	2.783	2.462	2.441	846
	Exp.	CH_3 Solv.[a]		1.78(1)	2.50(2)	2.91(2)	2.38(2)	2.43(2)	861
		Sol.[b]		1.78(1)	2.46(4)	2.87(4)	2.40(4)	2.42(4)	–
		Cryst.[c]		1.76(3)	2.48(5)	2.86(5)	2.36(4)	2.42(6)	–
mono	4	5		1.789	2.291	3.401	2.382	2.364	824
	5	6		1.790	2.363	3.389	2.465	2.448	838
	Exp.	Sol.[b]		1.78(1)	–	–	–	2.38(4)	–
		Cryst.[c]		1.76(3)	2.39(5)	3.5(1)	2.42(6)	2.36(2)	–

[a] Refs. 30,69,70. [b] Average of data from Refs. 29-31. [c] Average of data from Refs. 10, 30, 71.

The most common equatorial coordination number of uranyl complexes is N = 5 [29,64]. As coordination numbers are determined in EXAFS with an uncertainty of up to 20% [29,30,67], neighboring coordination numbers N of 4 or 6 can not be excluded. Therefore, we also investigated the effect of coordination number N = 6 of equatorial ligands for the example of uranyl monoacetate [60,68] (Table 5, Figure 4). Due to bond competition with an additional aqua ligand, all equatorial bonds elongate. While uranyl-carboxylate distances are closer to the experimental data for N = 6 than for N = 5, the aqua ligand bond is slightly overestimated for N = 6. The weaker bonds of aqua ligands leads to a network of hydrogen bonds between them (Figure 4c,d). Interestingly, with the coordination number also the average equatorial uranyl-oxygen distance U-O_{eq} increases to ~2.44 Å for mono- and bidentate coordinated complexes. This value is close to the experimental result of ~2.42 Å (Table 5), which is regarded as indicative for bidentate coordination. According to our studies, the equatorial coordination number N is the only parameter which appreciably affects the value of U-O_{eq}. Therefore, we suggested a re-interpretation of the EXAFS results [59,60,68].

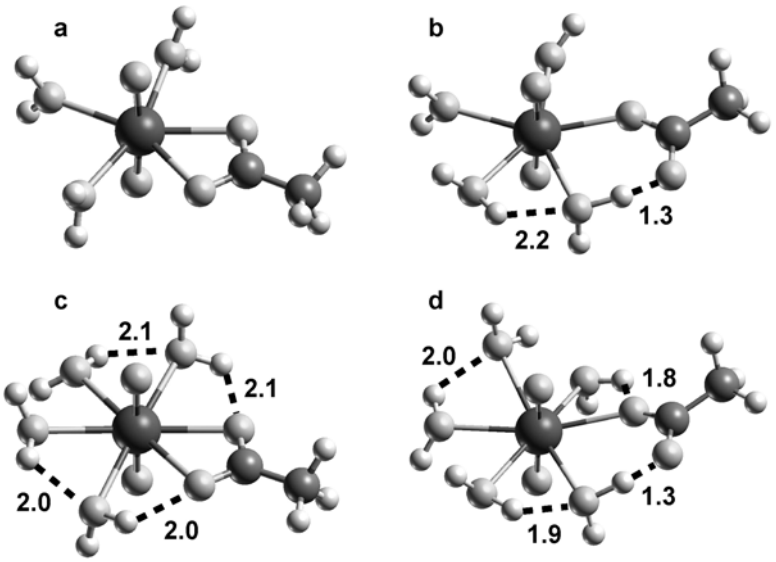

Figure 4. Structures of uranyl(VI) monoacetate $[UO_2(OOCCH_3)(H_2O)_n]^+$, optimized without symmetry constraints, with different acetate coordination modes and equatorial coordination numbers N of uranyl : (a) N = 5, bidentate, (b) N = 5, monodentate, (c) N = 6, bidentate, (d) N = 6, monodentate. Dashed lines indicate hydrogen bonds, lengths in Å.

Accordingly, changes in the average equatorial uranyl-oxygen distance should be interpreted as a change of the coordination number, where values of ~2.37 Å are typical for N = 5, whereas U-O_{eq} values of ~2.44 Å indicate N = 6. This interpretation is supported by data from crystal structures, which formed the basis of the earlier interpretation which yielded an average U-O value of 2.38±0.05 Å for monodentate carboxylate groups and 2.48±0.05 Å for groups bound in bidentate fashion [10]. A re-evaluation of the *same* data according to the coordination numbers of the uranyl centers furnished U-O_{eq} values of 2.39 ±0.04 Å for N = 5 and 2.48±0.03 Å for N = 6, in line with our new interpretation. An average equatorial U-O distance which essentially only depends on the coordination number was also found for other complexes (Sections 4.2, 4.3). This finding is also important for the interpretation of EXAFS results on actinyl humate complexes (Section 4.4).

In the course of optimization of the various complexes discussed above, we also obtained thermodynamic parameters (Table 6). We characterized the stability of the complexes by a reaction where one (monodenate) or two (bidentate) aqua ligands are substituted by a carboxylate. For C_s symmetric model complexes, we calculated the same ligand exchange energy for both monodentate and bidentate forms of the monocarboxylates.

Table 6. Calculated thermodynamic quantities of uranyl complexation by carboxylate due to a ligand exchange reaction:[a] energies ΔE_{sub}, enthalpies ΔH_{sub}, and free energies ΔG_{sub} (in kJ mol^{-1}) for complexes $[UO_2(OOCR)(H_2O)_n]^+$ with bi- (bi, n = 3) and monodentate (mono, n = 4) coordination. Calculations without symmetry constraints in the gas phase (GP) and in aqueous solution (PCM) .

	R	ΔE_{sub}		ΔH_{sub}		ΔG_{sub}	
		GP	PCM	GP	PCM	GP	PCM
bi	H	-832	-72	-839	-79	-867	-107
	CH_3	-861	-91	-868	-98	-902	-132
	CH_2CH_3	-859	-91	-861	-93	-901	-133
mono	H	-901	-110	-905	-114	-896	-104
	CH_3	-926	-121	-930	-125	-916	-111
	CH_2CH_3	-921	-122	-921	-123	-910	-112

[a] Reaction $[UO_2(H_2O)_5]^{2+} + [RCOO]^- \rightarrow [UO_2(OOCR)(H_2O)_n]^+ + (5–n)\ H_2O$

Thus, the second uranyl carboxylate bond in bidentate complexes stabilizes the complex by about the same amount as an aqua ligand; for $UO_2(H_2O)_5^{2+}$, that energy is 80 kJ/mol on average [60]. Full geometry optimization revealed that monodentate complexes are about 30 kJ/mol more stable than bidentate complexes. We traced this back to a bridging hydrogen bond between an aqua ligand and the carboxyl group (see above). The trend of enthalpies is similar (Table 6). In contrast, when free energies are considered, bidentate complexation in solution is preferred by ~20 kJ/mol. This entropy effect reflects the release of two aqua ligands when a bidentate complex of the solvated uranyl is formed, while in the case of monodentate ligation only one aqua ligand is replaced. Comparison with corresponding free energies for models in the gas phase shows that only in solution this entropy effect is strong enough to reverse the stability of mono- and bidentate complexes (Table 6). Thus, the preference for bidentate complexation is the combined effect of solvation and entropy, in agreement with experimental findings for many crystal structures and the structure of uranyl triacetate.

4.1.4 Neptunyl monocarboxylates

We examined monocarboxylates of the most stable oxidation state V of neptunyl and of NpO22+ and we compared them to analogous complexes of uranyl(VI) [60]. We employed the same model approach as for uranyl (see above). As expected, we obtained rather similar results for neptunyl(VI) while for neptunyl(V), due to the lower charge, we obtained less stable complexes. For neptunyl(VI), the neptunyl bond and the bonds to the ligands were determined 0.02 Å shorter than for their uranium congeners (Table 7). This reflects the smaller radius of the neptunyl ion for the same oxidation state (actinide contraction [64]).The addi-

tional f electron of neptunyl(VI) is only marginally involved in ligand bonding. Thus, uranyl and neptunyl(VI) complexes yield also rather similar ligand exchange energies. For all complexes and coordination modes examined (Table 7), the reaction energies differ less than 5 kJ/mol.

Table 7. Geometric parameters (in Å) and symmetric neptunyl stretching frequency ν_s in cm^{-1} for neptunyl(V) monocarboxylates $[NpO_2(OOCR)(H_2O)_n]$ in solution (PCM) with bi- (bi, n = 3) and monodentate (mono, n = 4) carboxylate coordination in comparison to experimental data from cyrstal structures (Cryst.) Comparison of average values (Av.) of for Np(V), Np(VI), and U(VI) complexes for different residues R. Np(VI) = values of Np(V) minus values of Np(VI). Designation of the atoms in analogy to Figure 3.

	R	Np=O_t	Np-O_c	Np-C	Np-O_w	Np-O_{eq}	ν_s
bi	H	1.818	2.470	2.822	2.408	2.433	771
	CH_3	1.821	2.445	2.819	2.417	2.428	770
	CH_2CH_3	1.830	2.441	2.815	2.449	2.446	778
Exp.	Np(V) Cryst.[a]	1.85(3)	2.59(8)	2.94(4)	2.47(7)	2.55(2)	–
	Np(V) Av.	1.82	2.45	2.82	2.42	2.42	773
	Np(VI) Av.	1.77	2.36	2.75	2.34	2.35	888
	U(VI) Av.	1.79	2.38	2.77	2.36	2.37	857
	ΔNp(VI)	0.05	0.09	0.07	0.08	0.07	-115
	CH_3	1.822	2.310	3.446	2.457	2.428	769
	CH_2CH_3	1.822	2.316	3.451	2.459	2.430	769
Exp.	Np(V) Cryst.[a]	1.84(2)	2.45(2)	–	2.47(7)	2.47(2)	–
	Np(V) Av.	1.82	2.32	3.45	2.46	2.43	770
	Np(VI) Av.	1.77	2.18	3.38	2.40	2.36	850
	U(VI) Av.	1.79	2.21	3.40	2.42	2.38	848
	ΔNp(VI)	0.05	0.14	0.07	0.06	0.07	-80

[a] Ref. 13.

For monocarboxylate complexes of neptunyl(V), we calculated considerably longer bond distances (Table 7). Compared to oxidation state VI, the neptunyl bond is 0.05 Å longer and the bonds to the carboxyl oxygen atoms increase by ~0.1 Å for bidentate and ~0.15 Å for monodentate carboxylates. As for uranyl, the average equatorial Np(V)-O distance is independent of the coordination mode and amounts to 2.43 Å for five-fold neptunyl coordination. Evaluation of crystal structures again suggested a longer Np-O_{eq} distance for bidentate compared to monodentate carboxylate binding [13]. As for uranyl, we suggested also for neptunyl complexes in solution that the value of Np-O_{eq} should mainly be determined by the coordination number [60].

Exchange energies of aqua ligands by a carboxylate ligand are ~60 kJ/mol smaller for neptunyl(V) than for neptunyl(VI). For neptunyl(V), in contrast to uranyl(VI), bidentate coordination of the carboxyl group was calculated to be already energetically slightly favored. The two f electrons of neptunyl(V) are not strongly involved in the ligand interaction and remain mainly localized on the Np center. Correspondingly, triplet states were calculated to be more stable than singlet states, by ~40 kJ/mol for bidentate complexes and ~20 kJ/mol for monodentate complexes [60].

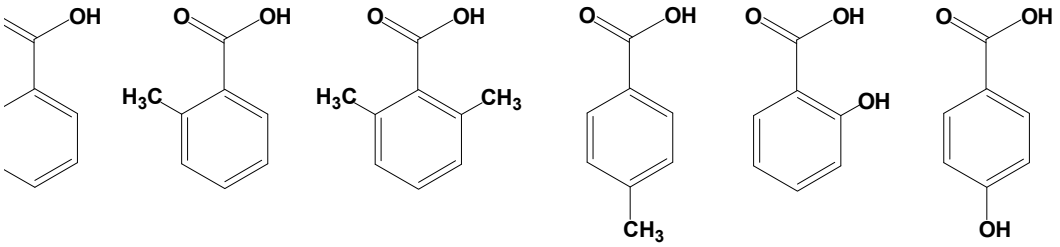

Figure 6. Sketches of aromatic carboxylic acids inspected as ligands in uranyl monocarboxylate: Benzoic acid, methyl and hydroxyl substituents.

4.2 Complexes with aromatic carboxyl ligands

We examined aromatic carboxylic acids as ligands of uranyl by means of five-coordinate monocarboxylate model complexes [73] – in the same way as complexes of aliphatic ligands (see above). Benzoic acid as well as methyl and hydroxyl substituents (Figure 6) served as models of carboxylic groups attached to aromatic rings in humic substances and thus helped to complement the results for their aliphatic congeners. Para substituents of benzoic acid may be viewed as models of aromatic rings that are connected to a larger organic framework. Ortho substituents may be taken to represent steric and electrostatic effects of different chemical environments of carboxylic groups at aromatic rings.

Table 8 collects the calculated results for interatomic distances, energies and free energies of the exchange of aqua ligands by carboxyl. Uranyl monobenzoate yielded very similar results as acetate. As an effect of the polarizability of the aromatic ring, we noted slightly lower

Table 8. Uranyl monocarboxylates $[UO_2OOCR(H_2O)_n]^{2+}$ of benzoic acid and substituents (Figure 6) in solution (PCM) with bidentate (bi, n =3) and monodentate (mono, n = 4) coordination of the carboxyl group. Comparison of geometric parameters (in Å), ligand substitution energies and free energies[a] (in kJ/mol).

	R	U=O_t	U-O_c	U-C	U-O_w	U-O_{eq}	ΔE	ΔG
bi	C_6H_5	1.785	2.37	2.77	2.36	2.37	-83	-125
	C_6H_4(p-CH_3)	1.786	2.37	2.76	2.37	2.37	-86	-128
	C_6H_4(p-OH)	1.787	2.37	2.77	2.37	2.37	-90	-133
	C_6H_4(o-CH_3)	1.787	2.36	2.77	2.37	2.37	-88	-125
	C_6H_4(o-CH_3)$_2$	1.788	2.36	2.77	2.37	2.37	-75	-115
	C_6H_4(o-OH)	1.783	2.39	2.80	2.35	2.37	-36	-100
	CH_3	1.786	2.37	2.77	2.37	2.37	-91	-132
mono	C_6H_5	1.788	2.27	3.31	2.39	2.37	-111	-99
	C_6H_4(p-CH_3)	1.788	2.29	3.29	2.39	2.37	-115	-105
	C_6H_4(p-OH)	1.789	2.27	3.34	2.39	2.37	-118	-103
	C_6H_4(o-CH_3) syn	1.789	2.30	3.34	2.38	2.36	-112	-96
	C_6H_4(o-CH_3) anti	1.790	2.26	3.35	2.39	2.37	-112	-100
	C_6H_4(o-CH_3)$_2$	1.788	2.29	3.34	2.38	2.37	-95	-77
	C_6H_4(o-OH) syn	1.786	2.32	3.38	2.38	2.37	-74	-52
	C_6H_4(o-OH) anti	1.788	2.27	3.38	2.39	2.36	-81	-66
	CH_3	1.789	2.29	3.35	2.38	2.36	-121	-111

[a] Reaction $[UO_2(H_2O)_5]^{2+} + [RCOO]^- \rightarrow [UO_2(OOCR)(H_2O)_n]^+ + (5–n)\ H_2O$

complexation energies (by ~10 kJ/mol), in line with the trend to lower pK_a values of aromatic acids compared to small aliphatic ones.

Substitution in para position had a very small effect on geometric parameters; they changed by less than 0.02 Å. Also energies were comparable; they increased by a few kJ/mol (Table 8). Interestingly, there again is no difference in U-O_{eq} values between mono- and bidentate complexes, irrespective of the systems considered. This nicely corroborates our previous conclusion that this geometric parameter is independent of the coordination mode. The results for para-substituted benzoic acids also confirmed that small molecular models of the size inspected seem to be sufficient for representing carboxylic sites of larger organic molecules. A carboxylic group connected to a polyaromatic framework is an interesting case, yet to be examined, which may furnish larger changes.

For monodentate carboxylate coordination, we determined stronger variations with the type of the substitutent. For ortho hydroxyl species, we noted distinct effects of the position of the hydroxyl group – syn or anti with respect to the uranyl carboxylate bond. Structures of “anti” configurations are very similar to that of the simple monodentate benzoate complex. For syn

position of the hydroxyl group, the value of U-O_c is 0.05 Å larger and the binding of the ligand to uranyl is weaker. A methyl substituent has a similar, but weaker effect. As for the bidentate coordination mode, we noted a destabilization of the monodentate complex for di-ortho methyl benzoate. Due to the emerging sixfold ring, chelate complexes by ortho hydroxyl benzoate were less favorable than the examples discussed thus far.

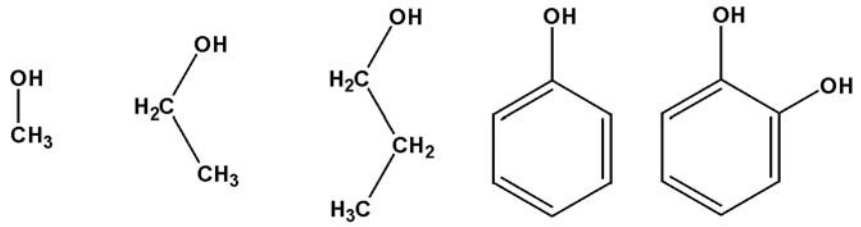

Figure 7. Alcohol ligands examined in uranyl mono-alcohol and -alcoholate complexes: methanol, ethanol, propanol, phenol, and catechol.

Overall, carboxyl groups attached to aromatic rings are slightly weaker bound than aliphatic carboxylates. The corresponding ligand substitution energies varied more. Therefore, analogous functional groups of humic substances are expected to provide a range of weaker complexation sites compared to aliphatic carboxyl groups.

4.3 Complexes with alcohol ligands

Experiments at pH 4, where phenolic hydroxyl groups were blocked by methylation, revealed that the loading capacity of humic acids in uranyl complexation decreases [74]; this finding was taken to indicate a contribution of these groups in uranyl complexation. A similar result was obtained for Np(V) [75]. In contrast, EXAFS experiments at pH 2 did not reveal any change compared to unmodified humic acids [76]. These experiments of the project partner Institute of Radiochemistry at the Forschungszentrum Dresden-Rossendorf represent a very rare case where functional groups of humic substances other than carboxyl have been studied with regard to actinide complexation. They stimulated our related computational model study [77]. This comparison of carboxylic and alcoholic mono-ligand complexes also broadened the range of functional sites examined in the present project

We modeled complexes of uranyl(VI) with single methanol, ethanol, propanol, phenol, and catechol ligands (Figure 7), following the strategy as for carboxylic acids [77]. We considered protonated as well as deprotonated alcohol ligands to inspect the interaction of uranyl in different pH regimes (Table 9). For deprotonated alcohol ligands, referring to a high pH regime, we noted a strong interaction between uranyl and the alcoholat ligand in uranyl(VI) monoalcoholates. The uranyl bond of 1.80–1.81 Å is up to 0.02 Å longer than that of carboxylates, e.g. acetate (Table 9). Correspondingly, we determined rather short U-O_c bonds of 2.1–2.2 Å, which are comparable to U-O bonds of hydroxide or monodentate carboxylates. For pro-

tonated alcohol ligands, which are to be expected at low pH, a shorter uranyl bond of 1.78 Å was calculated and the U-O_c bonds were typically between 2.3 and 2.4 Å (Table 9). The U-C distance, often determined by EXAFS experiment as a helpful quantity to distinguish different complexation modes, turned out to be less characteristic. Typical values were around 3.4 Å, with a tendency to lower values for deprotonated and higher values for protonated alcohols. As for the carboxylate ligands, we did not observe any effect of the type of complex on the average U-O_{eq} distance. The calculated values, all close to 2.37 Å, compare very well with the results for carboxylates (Tables 3 and 8) and reflect the same coordination number of 5, chosen for these model complexes. The close similarity of geometric parameters U=O_t and U-O_{eq} for alcoholate ligands and carboxyl groups nicely rationalizes the agreement of EXAFS results for uranyl complexation with unmodified and blocked humic acids at pH 2 [76]. Thus, these parameters are not suited for discriminating between hydroxyl or carboxyl sites; alcoholic groups have to be expected to contribute to uranyl complexation.

Table 9. Calculated structural parameters, (distances in Å, angles in degrees) for complexes $UO_2(H_2O)_4OR]^+$ and $[UO_2(H_2O)_4HOR]^{2+}$ of uranyl with alcohols, optimized without symmetry constraints in solution (PCM). Complexes with H_2O and OH^- ligands (R = H) as well acetate are also shown.

	R	U=O	U-O_c	U-C	U-O_{eq}	ν_s
OR^-	H	1.795	2.20		2.37	834
	CH_3	1.807	2.09	3.24	2.37	795
	CH_2CH_3	1.807	2.08	3.45	2.37	800
	$CH_2CH_2CH_3$	1.807	2.08	3.46	2.37	814
	C_6H_5	1.798	2.17	3.33	2.37	826
	2-OH-C_6H_4 anti[a]	1.798	2.14	3.45	2.37	867
	2-OH-C_6H_4 syn[a]	1.800	2.13	3.45	2.38	
CH_3COO^-		1.790	2.20	3.40	2.38	846
HOR	H	1.781			2.36	869
	CH_3	1.778	2.34	3.41	2.36	854
	CH_2CH_3	1.782	2.34	3.40	2.36	835
	$CH_2CH_2CH_3$	1.778	2.32	3.45	2.38	
	C_6H_5	1.777	2.46	3.53	2.38	853
	2-OH-C_6H_4 anti[a]	1.777	2.50	3.77	2.39	
CH_3COOH		1.790	2.20	3.40	2.38	846
Exp. Sol.[b]		1.78(2)			2.39(2)	

[a] H of second hydroxyl group oriented syn or anti with respect to first hydroxyl group
[b] Ref. [17].

We calculated the energy of complexation of uranyl by alcohols and used protonated alcohols and alcoholate complexes as references as this corresponds to typically low pH at which uranyl complexation by humic acids is experimentally examined (Table 10) [74,76]. To gain a

better understanding, the reaction is divided into two steps, deprotonation and complexation (Figure 8). Two pathways to uranyl alcoholates can be envisaged. First the alcohol may deprotonate, depending on pH, and then replace an aqua ligand at the uranyl ion (Path 1).

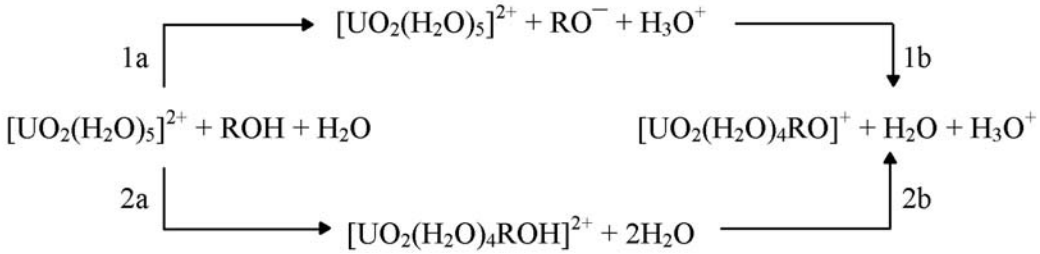

Figure 8. Reaction scheme for the complexation of solvated uranyl by an alcohol ligand. Path 1: deportonation of the alcohol with subsequent uranyl complexation. Path 2: uranyl complexation with subsequent deprotonation of the alcohol.

Alternatively, first the alcohol may complexate with uranyl and deprotonate in a second step in the field of the uranyl ion (Path 2).

Inspection of Table 10 shows that deprotonation of aliphatic and phenolic alcohols is strongly endothermic (1a). The deprotonation energy qualitatively correlates with the pK_a values; this includes even complexation by an aqua ligand or acetic acid. We determined the same approximate correlation for the exothermic step of complexation of uranyl by the alcoholate (1b), where phenol and catechol yield rather small free energies, comparable to acetate (Table 10).

Table 10. Total free energy ΔG_{tot} (in kJ/mol) and free energies of partial steps 1a, 1b, 2a, and 2b of the reaction of uranyl(VI) with an alcohol ligand to form $[UO_2(H_2O)_4OR]^+$ in solution according to the reaction scheme of Figure 8. Analogous values for the complexation of uranyl by acetate and hydroxide (R = H) are shown for comparison.

R	1a	1b	2a	2b	ΔG_{tot}
H	317	-271	0	46	46
CH_3	264	-234	-17	47	30
CH_2CH_3	260	-215	-7	52	45
$CH_2CH_2CH_3$	258	-198			60
C_6H_5	172	-114	47	11	58
(2-OH)C_6H_4 anti	180	-125	32	23	55
CH_3COOH	150	-117	10	23	33

In summary, one notes a trend where aromatic alcohols show similar total reaction energies than aliphatic ones. Path 2 starts with the attachment of the alcohol to uranyl, which is slightly exothermic for aliphatic, but endothermic for aromatic alcohols. The deprotonation energy of alcohols in the field of uranyl is considerably reduced compared to free alcohols. Overall, Path 2 avoids the high barrier of alcohol deprotonation and thus can be regarded as the preferred route of uranyl complexation by alcohols.

4.4 Remarks on actinyl complexation by humic acids

Actinyl complexation by humic acids at low pH is expected to take place mainly via carboxylic groups [3,6,7,10,13,15] with some contribution of phenolic groups [74,75], especially at higher pH values. Consequently, EXAFS data on the structure of actinyl humate complexes have been interpreted using carboxylate crystal structures as reference [12,13,15]. From short U-O_{eq} values of ~2.38 Å for uranyl(VI) and ~2.48 Å for neptunyl(VI) as well as missing signals of U-C distances, a monodentate uranyl humate complex structure was inferred [12,13], whereas longer values, by ~0.05 Å, would have been expected for bidentate coordination [10,13,30,71]. EXAFS experiments on Np(IV) arrived at similar results [22]. This interpretation is mainly based on An-O_c distances from crystal structures (Table 11), assuming that U bonds to aqua ligands are rather independent of the coordination mode of the carboxyl group [12].

Table 11. EXAFS data (distances in Å) for the complexation of uranyl(VI) and neptunyl(V) by natural and synthetic humic acids (HA), compared with averaged data from crystal structures of actinyl carboxylates. The crystal structure data provide distances An-O_{eq} averaged over complexes with a given equatorial coordination number N = 5 or N = 6) and An-O_c for a given coordination mode of the carboxylate ligand (monodentate and bidentate). For the designations of the atoms, see Figure 3.

		An=O_t	An-O_{eq}	An-O_c
U(VI)-HA[a]		1.77–1.78	2.37–2.39	–
Cryst.[b]	N = 5	1.76±0.03	2.39±0.02	
	N = 6	1.74±0.04	2.48±0.02	
	mono	1.76±0.03		2.39±0.05
	bi	1.76±0.03		2.48±0.05
Np(V)-HA[c]		1.84–1.85	2.48–2.49	–
Cryst.[d]	N = 5	1.85±0.03	2.45±0.03	
	N = 6	1.85±0.03	2.55±0.03	
	mono	1.85±0.03		2.46±0.04
	bi	1.85±0.03		2.59±0.08

[a] EXAFS data from solution, Refs. 10,15. [b] Averaged values from crystal structures,
Ref. 10. [c] EXAFS data from solution, Ref. 13. [d] Averaged values from crystal structures, Ref. 13.

As discussed in the previous sections, we examined computationally complexes of uranyl and neptunyl with one carboxylate ligand and we took them to represent carboxylate groups of humic substances. As a most remarkable result, we noted that the average bond length between uranyl and oxygen donor ligands does not depend on the coordination mode for monocarboxylates, in contrast to experimental results inferred from crystal structures (Table 11). Assuming coordination number N = 5 for uranyl, the value most often encountered, we calculated an almost constant value for U-O_{eq} of about 2.37±0.02 Å for various carboxylic acids and different complexation modes (Tables 3 and 8). We also obtained very similar values for monoligated complexes with alcohols and alcoholates (Table 9).

Table 12. Comparison of calculated geometrical parameters (in Å) of uranyl(VI) complexes $UO_2X(H_2O)_n$, where X are carboxylates, alcohols, alcoholates, or hydroxides, for coordination numbers N = 4–6 in the equatorial plane of uranyl as well as for various coordination modes (Coord.). Except in the pseudo-bridging structure of acetate, models with C_s symmetry constraints were examined. For the designations of the atoms, see Figure 3.

X	Coord.	n	N	U=O_t	U-O_x	U-O_w	U-O_{eq}
$(OH)_2^{2-}$	–	2	4	1.82	2.14	2.47	2.31
–	–	4	4	1.77	–	2.31	2.31
OH^-	–	4	5	1.80	2.10	2.44	2.37
CH_3COO^-	bi	3	5	1.79	2.37	2.36	2.36
	mono	4	5	1.79	2.20	2.42	2.38
	pseudo	4	5	1.79	2.29	2.38	2.36
$CH_2(OH)COO^-$	chelate	3	5	1.79	2.33	2.38	2.36
$(CH_3COO)_2^{2-}$	bi	1	5	1.79	2.38	2.35	2.37
$OH(CH_3COO)^{2-}$	bi	2	5	1.81	2.12/2.44[a]	2.44	2.38
$OH(C_2H_5COO)^{2-}$	bi	2	5	1.81	2.12/2.44[a]	2.44	2.38
CH_3O^-	–	4	5	1.81	2.07	2.45	2.38
$C_6H_5O^-$	–	4	5	1.80	2.13	2.44	2.38
CH_3OH	–	4	5	1.78	2.41	2.37	2.38
C_6H_5OH	–	4	5	1.78	2.42	2.36	2.37
–	–	5	5	1.78	–	2.36	2.36
$(CH_3COO)^-$	bi	4	6	1.79	2.39	2.46	2.44
$(CH_3COO)_2^{2-}$	bi	2	6	1.79	2.42	2.49	2.45
$(CH_3COO)_3^{3-}$	bi	0	6	1.80	2.42	–	2.42
–	–	6	6	1.79	–	2.41	2.41

[a] Short bonds refer to hydroxide, longer ones to carboxylate.

Extending the discussion for the exemplary case of acetate (Section 4.1), we collected in Table 12 calculated structural characteristics of typical carboxyl and alcohol complexes, also with different coordination numbers N, and compared them to results for solvated uranyl (aqua ligands only) and hydroxides as well as ternary complexes (hydroxo-carboxylates). All these data were determined with the same computational procedure. Inspection of Table 12 confirms that the values of U-O_{eq} are mainly determined by the coordination number N of the complexes, but are essentially independent of the type of ligand and its coordination mode. This interpretation is also in line with crystal structure data as an evaluation of crystal structures with respect to the coordination number of the actinyl ion demonstrates: coordination number N = 5 yields shorter An-O_{eq} values then N = 6 (Table 11).

On the basis of these findings, we suggest a reinterpretation of pertinent EXAFS results to indicate five-fold coordination of uranyl humate complexes instead of monodentate complex structures. Unfortunately, the complexation mode as well as the number of functional groups involved can not be inferred from the indicator U-O_{eq} only. Thus, a separation of different bond distances in the first ligand shell, an identification of the U-C distance or help from other spectroscopies is needed to gain more detailed insight in the nature of actinyl humate complexes.

As carboxylates in general prefer bidentate coordination [78], one can also expect a bidentate coordination mode for actinyl humates. Our calculations support this expectation: bidentate coordination is preferred as an entropy effect (Sections 4.1, 4.2). An open issue is the role of chelate complexes. In this project, we studied only a few examples, invoking models with C_s symmetry constraints. For glycolate, salicylic acid, as well as catechol, these estimates did not yield any energetic preference compared to bidentate carboxylate complexes [73,77]. Yet, one can not exclude that particular combinations of functional groups exist, which form strong coordination bonds via a chelate ring. On the other hand, due to specific structural requirements, these sites should be rare and thus should not be of determining influence on actinyl complexation by humic acids.

Given our results for aliphatic carboxylates of increasing chain length as well as the small calculated substituent effects for aliphatic and aromatic carboxylic acids, we refrained from inspecting larger models of humic acid sites because only small corrections of our model results had to be expected. Instead, in view of the experience gained in this project, we regarded the treatment of solvation as a more important issue, worth further studies which should aim at improving and confirming the present results (see Section 4.6).

4.5 Thermochemistry of actinyl ions

In this project we also showed that modern quantum chemistry methods are very useful for determining fundamental thermochemical data for actinide compounds, for which in some cases only experimental data of limited accuracy exist [79]. In a showcase fashion, we demonstrated this for the enthalpy of formation of uranyl(VI) [79] and plutonyl(VI) [80]. For this purpose, we selected a series of formal reactions which transform actinyls into species for which the enthalpies of formation are known with good accuracy. The enthalpies of formation were obtained via calculated reaction enthalpies and known (experimental) formation enthalpies of all other species involved. Using the BP XC functional, we determined $\Delta_f H^\circ_0$ at 1527±42 kJ/mol for uranyl(VI); with the PW91 XC functional, the result was 1548±50 kJ/mol [79]. These values are in very good agreement with a new experimental determination, carried out simultaneously, which yielded $\Delta_f H^\circ_0$ = 1523±63 kJ/mol [81]. Thus, previous estimates of 1300 kJ/mol ≤ $\Delta_f H^\circ_0$ ≤ 1800 kJ/mol [82] and other earlier estimates were significantly improved, in line with this recent, more accurate experiment [81]. In the same way, the enthalpy of formation for PuO_2^{2+} was calculated at $\Delta_f H^\circ_0$ = 1749±63 kJ/mol via model reactions involving plutonium fluorides [80]. Also this result agreed very well with a very recent experimental result, $\Delta_f H^\circ_0$ = 1728±67 kJ/mol [81] which relied on new measurements of the ionization potentials of PuO_2 und PuO_2^+. To reach such accurate computational results, both these com-

putational studies employed relativistic density functional methods that included a new self-consistent treatment of the spin-orbit interaction developed in our group (see below) [83,84].

4.6 Methodological topics

4.6.1 Relativistic treatment of the Coulomb interaction of electrons

As stated earlier, all electronic structure calculations of this project were carried out with the Douglas-Kroll-Hess approach [38] to relativistic density functional theory [32,33]. The parallel density functional software PARAGAUSS [34], developed in our group, affords a very efficient scalar relativistic method to solve the Kohn-Sham-Dirac problem at the all-electron level as well as several variants that permit a self-consistent treatment of spin-orbit interaction [32,33]. The more accurate variants, which include spin-orbit interaction, are mainly important for treating open-shell complexes as well as for spectroscopic studies, but are also very useful for the accurate determination of thermodynamic parameters of actinide complexes (see above) [79,80].

For most applications, also of this project, the more economic scalar relativistic approximation suffices where only two terms of the electronic Hamiltonian, the kinetic energy and the Coulomb potential of the nuclei, are subject to a relativistic transformation [32,38]. The terms of electron-electron interaction are kept in their non-relativistic form.
The nuclear potential of the electrons accounts for the largest part of the spin-orbit interaction; we had suggested such a method some years ago [85]. In a preceding project (BMWi 02E9450), we developed a self-consistent relativistic treatment of spin-orbit interaction that, in addition, takes the Hartree part of the electron-electron interaction into account. It relies on a matrix representation of the relevant operator products in momentum space [86]. This numerical approach requires very flexible basis sets and entails a considerable computational effort. During this project, we introduced a new algorithm, which is more accurate, numerically more stable, and more efficient. This new approach relies on a direct, analytic evaluation of the matrix representation of the relativistic Hartree term [84]. In addition, basis sets of normal size suffice and thus result in an improved computational efficiency [84]. For dimer molecules with heavy elements, we demonstrated these advantages of the new approach. This methodological advance considerably facilitates inclusion of spin-orbit interaction in accurate calculations. This new method will be very valuable for applications in actinide chemistry, e.g. when low oxidation states of actinides have to be treated [79,80], as envisaged in a subsequent project.

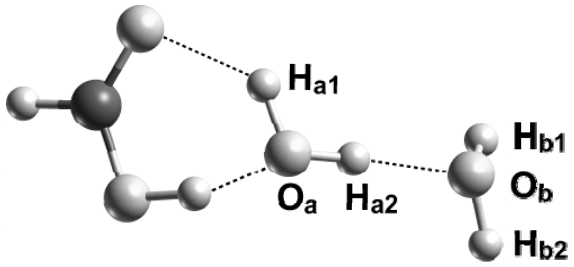

Figure 10. Model system $HCOOH(H_2O)_2$ to probe the interaction of a carboxylic acid with the solvent molecules. One aqua ligand H_2O_a positioned in the first solvation shell, the other, H_2O_b, in the second solvation shell.

4.6.2 A discrete QM/MM solvation model

In this project, solvation of complexes in an aqueous solution was described with a two-step procedure. The first solvation shell of actinyl complexes was explicitly included in that part of the model that was treated at the quantum mechanical level. In addition, long-range solvation effects of the remaining solvent environment were accounted for via a polarizable continuum model (PCM, Section 3). Thus, beyond the first solvation shell, the discrete nature of the solvent was neglected. Recently, calculations which included explicit water molecules of the second shell showed that chemical effects like charge transfer may occur in this part of a system, which are not represented by a PCM treatment [48-50] (Section 3). Especially for highly charged ions and in situations where the orientation of aqua ligands in a complex plays a key role, e.g. in pseudo-bridging structures of actinyl monocarboxylate complexes (Section 4.1), explicit modeling of the second solvation shell may lead to more accurate results.

Quantum mechanical modeling of actinide complexes that includes an extended shell of solvent molecules requires notably larger computational resources, especially during a geometry optimization. Therefore, we developed a QM/MM approach that combines quantum mechanical and molecular mechanical methods for different parts of a system [51,52,87,88], to achieve an improved representation of the solvation environment. To account for the discrete nature of the solvent environment in an efficient way, the actinide complex itself and a limited number of solvent molecules are treated with a quantum mechanical method (QM region), while a shell of more distant solvent molecules is represented by a "classical" force field (MM region). We chose the well established family of TIPnP water models [89,90] to describe solvent molecules in the MM region. In these models, water molecules are considered as rigid with a fixed charge distribution [89,90]. Inclusion of polarization and charge transfer effects need more elaborate force fields, which will be added at a later stage of development. The QM/MM approach implemented in the software PARAGAUSS [34] relies on the additive Hamiltonian $H_{tot} = H_{QM} + H_{MM} + H_{int}$, where the coupling term H_{int} includes electrostatic and van der Waals interactions between the QM and MM regions of the system under study. A three-step procedure was also realized; in addition to the QM/MM partitions, it also includes a PCM representation of the farther environment. While the QM/MM method describes a solvated complex as a molecule in a water cluster, the extended QM/MM/PCM procedure also accounts for long-range electrostatic effects.

Table 13. Interaction of formic acid with aqua ligands: $HCOOH \cdot H_2O$ and $HCOOH \cdot (H_2O)_2$ with one aqua ligand positioned in the second shell (Figure 10). Quantum mechanical results for $HCOOH \cdot H_2O$ (n=1) and effect Δ of the second-shell aqua ligand (n = 2) from quantum mechanical (ΔQM) and QM/MM calculations with TIPnP force fields (ΔTIP3P und ΔTIP4P) representing the water molecule in the second solvation shell. Distances in Å, angles in degree. For the designation of the atoms, see Figure 10.

$HCOOH \cdot (H_2O)_n$	n=1	n=2		
	QM	ΔQM	ΔTIP3P	ΔTIP4P
C=O	1.232	0.000	0.000	0.000
C-O	1.335	-0.002	-0.003	-0.003
O-H	1.022	0.016	0.016	0.014
$O \cdots HO_a$	1.895	0.173	0.128	0.075
$H \cdots O_a$	1.658	0.083	0.074	0.063
O_a- H_{a1}	0.994	-0.008	-0.006	-0.005
O_a- H_{a2}	0.975	0.018	0.028	0.020
COH	107	0.7	-0.3	-0.3
OCO	126	0.1	0.3	0.3
$H_{a1}O_aH_{a2}$	107	-0.2	-1.8	-0.7
OHO_a	157	5.7	4.7	3.7
OH_aO_a	140	-7.2	5.0	3.5

The method was validated and its performance was demonstrated by comparison with full density functional calculations for a series of test systems. Results for $(H_2O)_2$ and $(H_2O)_3$ showed that, in comparison to density functional calculations, a TIP4P model yields more accurate geometries than a TIP3P description. In QM/MM calculations of $(H_2O)_2$ where one of the water molecules is treated by the force field, more accurate results are expected if the donating molecule is assigned to the QM partition. In this case, the resulting length of the hydrogen bond deviates only 0.01 Å from the result of a full density functional optimization; a MM description of the donating molecule leads to a deviation of 0.08 Å. The binding energy of $(H_2O)_2$, 31 kJ/mol, and the solvation energy, 49 kJ/mol, as obtained in a density functional reference calculation, are slightly underestimated with a QM/MM treatment. In the model with the donating water in the MM region, these deviations are 2 and 9 kJ/mol, respectively, whereas in the reversed model (accepting water molecule in the MM region) these deviations are

are less than 1 and 6 kJ/mol, respectively. To probe the effect of a solvent molecule of the second shell, we also studied a simple model of formic acid and two aqua ligands (Figure 10); there, one of the water molecules coordinates directly to formic acid, while the second one is only in contact with the first aqua ligand.

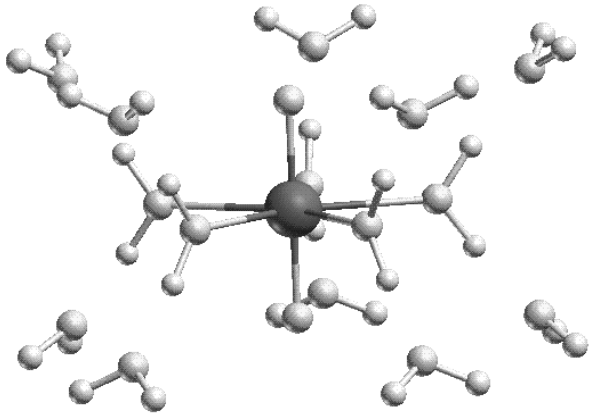

Figure 11. Model of the solvated uranyl ion in D_{5h} symmetry

From a full density functional optimization of this model complex, one identifies an elongation of the two hydrogen bonds between the acid and the solvent molecule of the first shell, by 0.17 and 0.08 Å (ΔQM, Table 13), as main effect of the second water molecule on $HCOOH \cdot H_2O$. In a QM/MM treatment, where the aqua ligand of the second shell is assigned to the MM part, these effects as well as smaller changes of the molecule are qualitatively well reproduced. With a single exception, also effects on bond angles are rather accurately modeled by the QM/MM procedure (Table 13). As a trend, the MM treatment of the outer solvent molecule results in a minor underestimation of second-shell effects; on average, the TIP3P model performs slightly better than the TIP4P force field.

To illustrate the three-step modeling of an extended solvation shell including embedding in a PCM model (QM/MM/PCM), we present results for a solvated uranyl(VI) ion where D_{5h} symmetry constraints have been invoked (Figure 11, Table 14). At the QM/MM level, when only the first solvation shell is explicitly treated in the model compound $UO_2^{2+}(H_2O)_5$, one notes strong structure relaxations from the full density functional result. The uranyl bond, 1.75 Å, is calculated 0.03 Å too short and the U-O_w bonds to the aqua ligands are underestimated by ~0.3 Å (Table 14). Addition of a second explicit solvation shell in the model complex $UO_2^{2+}(H_2O)_{15}$ has only small effects on the solvated uranyl ion; the uranyl bond U=O and the U-O_w bonds increase by ~0.01 Å. A QM/MM calculation with the second solvation shell represented by a force field yields very good agreement with the results from the full density functional calculation (Table 14), even though the second-shell solvent molecules are attached in donating configurations via hydrogen bonds to the first shell of aqua ligands. The uranyl bond U=O is underestimated by 0.02 Å, while the U-O_w bonds are well reproduced with deviations of only 0.01 Å. The hydrogen bonds H···O_b between the first and the second solvation shells reproduce the full quantum mechanical result within 0.03 Å (Table 14).

Table 14. Model of the solvated uranyl(VI) ion with D_{5h} symmetry constraints. Comparison of geometric parameters (distances in Å, angles in degree) from quantum mechanical (QM) and QM/MM calculations, including embedding in a PCM model. Uranyl bond U=O, uranyl water bond U-O_a, hydrogen bond H···O_b between first and second solvation shell, angle OUO_b between uranyl oxygen, uranium, and an oxygen center of an aqua ligand of the second shell. Aqua ligands of the first solvation shell are denoted as H_2O_a, of the second as H_2O_b. In QM/MM calculations, the outermost solvation shell of the complexes is represented by the TIP4P force field.

		U=O	U-O_a	H···O_b	OUO_b
$UO_2^{2+}\cdot(H_2O)_5$	QM	1.78	2.37		
	QM/MM	1.75	2.04		
$UO_2^{2+}\cdot(H_2O)_{15}$	QM	1.79	2.38	1.59	63.1
	QM/MM	1.77	2.39	1.62	63.2

These results demonstrate that the QM/MM approach implemented is well suited for describing an extended explicit solvation environment of an actinide complex in a sufficiently accurate and efficient manner.

5 Summary and Outlook

Quantum mechanical modeling of actinyl complexation by humic substances was the central topic of the project. Humic substances, especially their soluble fraction, which comprises fulvic and humic acids, considerably affect the chemical state and the migration of actinide elements in the environment due to their complexating and redox abilities. In addition, their sorption on minerals and coagulation to immobile phases plays a role. Understanding the interaction of actinides with these very variable substances, together with the complex chemical processes they are involved in, is a necessary prerequisite for predicting the chemistry and the migration behavior of acintides in natural and technical systems. This, in turn, forms the basis of safety analysis of radioactive waste repositories and contaminated sites. Therefore, a mechanistic understanding of the interaction of actinide and humics is crucial as a basis for the design of accurate, higher-level models of actinide chemistry and transport in the environment as well as for interpreting pertinent experiments and designing new ones.

Humic acids are considered to interact with actinide ions mainly via carboxylic groups, and experimental results, especially from EXAFS, suggest monodentate complexation of actinyls and other actinide ions by these groups. There are indications that phenolic OH groups also contribute to the complexation ability of humic substances. With reference to these concepts, we mainly explored actinyl interactions with carboxylic and alcoholic groups with the help of

relativistic density functional calculations, that also modeled solvent effects. Small carboxylic acids and alcohols were used as models of pertinent complexation sites of humic substances. We showed that already rather small organic molecules can be regarded as reasonable models, as the properties of the complexes did not change appreciably with the size of the model or their substituents. These results justified the omission of intended studies on larger models of humic substances. On the other hand, experience gained in this project strongly suggested a shift of focus on building more elaborate models of solvation, which turned out to be more involved than expected.

Our studies concentrated on the interaction of actinyls with a single organic molecule, mimicking an isolated complexation site of a humate molecule. We examined mainly uranyl(VI), but also neptunyl in the oxidation states (VI) and (V). Results on monocarboxylate complexes of uranyl with aliphatic and aromatic acids indicated somewhat stronger complexation interaction for aliphatic than for aromatic ligands. Monodentate structures turned out to be energetically preferred due to a strong hydrogen bond between an aqua ligand of the uranyl solvation shell and the carboxyl group (pseudo-bridging geometry), but the bidentate complexation mode turned out to be favored at the free energy level, due to stabilizing entropy effects. The latter findings are in line with crystal structures and common knowledge for carboxylate complexes, but are at variance with the prevailing interpretation of EXAFS results on actinyl humate complexes. The average length An-O_{eq} of actinyl oxygen bonds in the equatorial plane is regarded as important indicator. It is found at ~2.37 Å for the well studied case of uranyl; average distances of bidentate complexes are expected to be ~0.05 Å longer. At variance with this interpretation, our calculations yielded almost constant values for An-O_{eq} of about 2.37 Å, irrespective of the coordination mode and even of the chemical nature of the oxygen donor ligand (carboxylate, alcohol, alcoholate, hydroxide, water, ternary complexes). According to our model calculations, the only factor affecting the value of An-O_{eq} of solvated complexes is the coordination number of the complexes. Therefore, we suggested a reinterpretation of the EXAFS results as indicative for five-fold coordinated complexes. Unfortunately, the value of An-O_{eq} as the geometric parameter most commonly determined in experiment does not seem to be sensitive to the detailed structure and the chemical nature of an oxygen donor site. Therefore, a resolution of different An-O distances or measurement of other distances, e.g. An-C, is necessary for a further differentiation of the coordination modes. These findings also explain why blocking of phenolic OH groups of humic acids, which results in a change in the complexation behavior, is not reflected in the lengths of the actinyl bonds and the An-O_{eq} data determined experimentally. After all, carboxylic and alcoholic ligands were calculated to yield the same values for commonly used structural parameters.

As expected, our calculations showed that complexation of protonated alcoholic groups proceed with lower barriers when the alcoholic group is deprotonated in the field of the actinyl ion. This mechanism may allow actinide complexation by alcoholic groups even at moderate pH values, especially for multiply charged species.

Complexation energies of the species studied were determined mainly via exchange reactions involving aqua ligands. While experimentally accessible geometric parameters gave a rather uniform picture of bonding, ligand exchange energies vary stronger, hence are more sensitive. These results support empirical models of actinide humate complexation which

assume a broad range of bond strengths of complexation sites. Summarizing the consequences of the results of this project on the interpretation of the atomistic structure and the energetics of actinyl humate complexation, we propose that these complexes, with a preferential coordination number of 5 for uranyl and neptunyl, should be regarded as bidentate, mainly involving carboxylic groups, but likely also other oxygen donor sites, e.g. hydroxyl groups.

In addition to the tasks laid out in the project proposal, we carried out accurate calculations of the heat of formation of uranyl(VI) and plutonyl(VI), fundamental quantities in actinide chemistry. Our results, 1527±42 kJ/mol for uranyl(VI) and 1749±63 kJ/mol for plutonyl(VI), improved earlier determinations and agree very well with recent experiments. As a side issue, not covered by this project, but inspired by the work of partners in the project consortium, we started to examine uranyl sorption at mineral surfaces using quantum mechanical methods. To the best of our knowledge, our study on uranyl sorption on alumina was the first accurate quantum mechanical modeling in this field [91]; the model results indicated outer sphere complexes to be preferred on the defect free (0001) surface of Al_2O_3.

As a support for the calculations in this project and also future work in actinide chemistry, the Douglas-Kroll-Hess approach to relativistic density functional chemistry was extended by an accurate and efficient method for a self-consistent relativistic treatment of the Coulomb interaction between electrons, which is modeled only at the nonrelativistic level in most other computational approaches. For an explicit and efficient modeling of extended solvation shells of solvated complexes, we developed a QM/MM/PCM procedure which currently employs a TIPnP force field for the water molecules. Test calculations on simplified model systems and the solvated uranyl ion demonstrated the quality and the efficiency of the approach, which should prove very useful in future projects.

This project brought unexpected insights into the atomic structure and energetics of actinyl complexes with organic functional groups. Our computational results turned out to be useful for interpreting currently available data on actinyl humate complexes. Thus we are confident that further work along these lines will be very worthwhile. Further studies are expected to focus primarily on issues that were only briefly treated in this project. To complement the current project, a more thorough inspection of chelate complexation as well as complexation by more than a single functional group are suggested. Preliminary results of this project already showed that for carboxylic and alcoholic groups chelate structures do not necessarily result in complexes which are more stable than other complexation modes. Of particular interest will be studies of actinide ions in lower oxidation states, as the corresponding data base from experiments is incomplete. Results of the present project also suggest that further efforts directed at more detailed modeling of solvation will be beneficial for constructing more accurate models of actinide complexes in aqueous solution. Such method-oriented research is also a prerequisite for a more reliable determination of thermochemical parameters of these complexes – a major challenge to current quantum chemistry.

6 Publications Resulting from This Project

1) F. Schlosser; A Relativistic Density Functional Study of Actinide Complexation in Aqueous Solution, Dissertation, Technische Universität München, 2006.

2) L. V. Moskaleva, A. V. Matveev, J.Dengler, N. Rösch: The Heat of Formation of Gaseous PuO_2^{2+} from Relativistic Density Functional Calculations, Phys. Chem. Chem. Phys. 8, 3767-3773 (2006).

3) L. V. Moskaleva, V. A. Nasluzov, N. Rösch: Modeling Adsorption of the Uranyl Dication on the Hydroxylated α-Al_2O_3 (0001) Surface in an Aqueous Medium. Density Functional Study, Langmuir 22, 2141-2145 (2006).

4) F. Schlosser, S. Krüger, N. Rösch: A Density Functional Study of Uranyl Monocarboxylates, Inorg. Chem. 45, 1480-1490 (2006).

5) M. García-Hernández, C. Willnauer S. Krüger, L. V. Moskaleva, N. Rösch: Systematic DFT Study of Gas Phase and Solvated Uranyl and Neptunyl Complexes $[AnO_2X_4]^n$ (An = U, Np; X = F, Cl, OH, n = 2-; X = H_2O, n = 2+), Inorg. Chem. 45, 1356-1366 (2006).

6) L. V. Moskaleva, A. V. Matveev, S. Krüger, N. Rösch: The Heat of Formation of the Uranyl Dication: Theoretical Evaluation Based on Relativistic Density Functional Calculations, Chem. Eur. J. 12, 629-634 (2006).

7) S. Krüger, F. Schlosser, S. R. Ray, N. Rösch: Uranyl Complexation by Carboxylic Acids: A Relativistic Density Functional Model Study for Actinide Complexation by Humic Acids, Lecture Series on Computer and Computational Sciences 7, 904-907 (2006).

8) S. Krüger, F. Schlosser, N. Rösch: Monocarboxylate Complexes of Uranyl: A Relativistic Density Functional Study, in: Recent Advances in Actinide Science, R. Alvarez, N. D. Bryan, I. May (Eds.), Proceedings of the Conference Actinides 2005, Manchester, 2005, The Royal Society of Chemistry, Cambridge, 2006, p. 252-254.

9) V. Matveev, S. Majumder, N. Rösch: Efficient Treatment of the Hartree Interaction in the Relativistic Kohn-Sham Problem, J. Chem. Phys. 123, 164104, 1-8 (2005).

Further publications on results of this project and follow-up studies are in preparation.

7 References

[1] J. J. Katz, G. T. Seaborg, L.R. Morss (Eds.), The Chemistry of the Actinide Elements, 2. ed., Chapman and Hall, New York, 1986.

[2] L. R. Morss, N. M. Edelstein, J. Fuger (Eds.), Actinide and Transactinide Elements, 3. ed., Springer, Dordrecht, 2006.

[3] Z. Szabo, T. Toraishi, V. Vallet, I. Grenthe, Coord. Chem. Rev. 250 (2006) 784.

[4] Ref. 2, vol. 4, chap. 22.

[5] D. L. Clark, D. E. Hobart, M. P. Neu, Chem. Rev. 95 (1995) 25.

[6] K. H. Lieser, Radiochim. Acta 70/71 (1995) 355.

[7] R. J. Silva, H. Nitsche, Radiochim. Acta 70/71 (1995) 377.

[8] Ref. 2, vol. 4, chap. 23.

[9] F. J. Stevenson, Humus Chemistry, 2. Aufl., Wiley, New York, 1994.

[10] K. L. Nash, J. M. Cleveland, T. F. Rees, J. Environ. Radioact. 7 (1988) 131.

[11] G. R. Choppin, Radiochim. Acta 44/45 (1988) 23.

[12] M. A. Denecke, S. Pompe, T. Reich, H. Moll, M. Bubner, K. H. Heise, R. Nicolai, H. Nitsche, Radiochim. Acta, 79 (1997) 151.

[13] S. Sachs, K. Schmeide, T. Reich, V. Brendler, K. H. Heise, G. Bernhard, Radiochim. Acta, 93 (2005) 17.

[14] K. Schmeide, T. Reich, S. Sachs, V. Brendler, K. H. Heise, G. Bernhard, Radiochim. Acta, 93 (2005) 187.

[15] M. A. Denecke, T. Reich, S. Pompe, M. Bubner, K. H. Heise, H. Nitsche, P. G. Allen, J. J. Bucher, N. M. Edelstein, D. K. Shuh, J. Phys. IV 7, C2 (1997) 637.

[16] S. Pompe, K. Schmiede, M. Bubner, G. Geipel, K. H. Hiese, G. Bernhard, H. Nitsche, Radiochim. Acta 88 (2000) 553.

[17] K. Schmiede, S. Sachs, M. Bubner, T. Reich, K. H. Hiese, G. Bernhard, Inorg. Chim. Acta 351 (2003) 133.

[18] S. Sachs, G. Bernhard, Radiochim. Acta 93 (2005) 141.

[19] M. A. Denecke, Coord. Chem. Rev. 250 (2006) 730.

[20] P. Lubal, D. Fetsch, D Siroky, M. Lubalova, J. Senkyr, J. Havel, Talanta 51 (2000) 977.

[21] D. Schild, C. M. Marquardt, Radiochim. Acta 88 (2000) 587.

[22] K. Schmeide, T. Reich, S. Sachs, V. Brendler, K. H. Heise, G. Bernhard, Radiochim. Acta 93 (2005) 187.

[23] S. Pompe, A. Brachmann, M. Bubner, G. Geipel, K. H. Heise, G. Bernhard, H. Nitsche, Radiochim. Acta 82 (1998) 89.

[24] J. I. Kim in: Handbook of the Physics and Chemistry of the Actinides; A. J. Freeman, C. Keller (Eds.), Elsevier, Amsterdam, 1986, Chapter 8.

[25] A. Krepelova, S. Sachs, G. Bernhard, Radiochim. Acta 94 (2006) 825.

[26] V. Vallet, Z. Szabó, I. Grenthe, Dalton Trans. (2004) 3799.

[27] V. Vallet, P. Macak, U. Wahlgren, I. Grenthe, Theor. Chem. Acc. 115 (2006) 145.

[28] N. Kaltsoyannis, P. J. Hay, J. Li, J.-P. Blaudeau, B. E. Bursten, in Ref. 2, vol. 3, chap. 17.

[29] Moll, H.; Geipel, G.; Reich, T.; Bernhard, G.; Fanghänel, T.; Grenthe, I. Radiochim. Acta 91 (2003) 11.

[30] J. Jiang, L. Rao, P. Di Bernardo, P. L. Zanonato, A. Bismondo, J. Chem. Soc., Dalton Trans. 8(2002) 1832.

[31] P. G. Allen, J. J. Bucher, D. K. Shuh, N. M. Edelstein, T. Reich, Inorg. Chem., 36 (1997) 4676.

[32] N. Rösch, S. Krüger, M. Mayer, V. A. Nasluzov The Douglas-Kroll-Hess Approach to Relativistic Density Functional Theory: Methodological Aspects and Applications to Metal Complexes and Clusters, in: Recent Developments and Applications of Modern Density Functional Theory, J. M. Seminario (Eds.), Theoretical and Computational Chemistry Series, Bd. 4, Elsevier, Amster¬dam, 1996, S. 497.

[33] N. Rösch, A. V. Matveev, V. A. Nasluzov, K. M. Neyman, L. Moskaleva, S. Krüger Quantum Chemistry with the Douglas-Kroll-Hess Approach to Relativistic Density Functional Theory: Efficient Methods for Molecules and Materials, in: Relativistic Electronic Structure Theory-Applications, P. Schwerdtfeger (Eds.) Theoretical and Computational Chemistry Series, Elsevier, Amsterdam, 2004, S. 656.

[34] T. Belling, T. Grauschopf, S. Krüger, F. Nörtemann, M. Staufer, M. Mayer, V. A. Nasluzov, U. Birkenheuer, A. Hu, A. V. Matveev, A. M. Shor, M. Fuchs-Rohr, K. Neyman, D. I. Ganyushin, T. Kerdcharoen, A. Woiterski, A. Gordienko, S. Majumder, N. Rösch, ParaGauss, Version 3.0, Technische Universität München, 2004.

[35] M. S. K. Fuchs, A. M. Shor, N. Rösch, Int. J. Quantum Chem. 86 (2002) 487.

[36] Y. Dudal, F. Gerard, Earth-Science Revs. 66 (2004) 199.

[37] L. K. Koopal, T. Saito, J. P. Pinheiro, W. H. Riemsdijk, Colloids Surf. A 265 (205) 40.

[38] B. A. Hess (Hrsg.), Relativistic Effects in Heavy Element Physics and Chemistry, Wiely, Chichester, 2003, Kap. 3.

[39] X. Cao, M. Dolg, Coord. Chem. Rev. 250 (2006) 900.

[40] L. Belkhiri, R. Lissillour, A. Boucekkine, J. Mol. Struct. Theochem 757 (2005) 155.

[41] G. A. Shamov, G. Schreckenbach, J. Phys. Chem. A 109 (2005) 10961.

[42] C. Clavaguéra-Sarrio, V. Vallet, D. Maynau, C. J. Marsden, J. Chem. Phys. 121 (2004) 5312.

[43] E. Fromager, V. Vallet, B. Schimmelpfennig, P. Macak, T. Privalov, U. Wahlgren, J. Phys. Chem. A 109 (2005) 4957.

[44] J. Tomasi, Theor. Chem. Acc. 112 (2004) 184.

[45] Z. Cao, K. Balasubramanian, J. Chem. Phys. 123 (2005) 114309.

[46] L. V. Moskaleva, S. Krüger, A. Spörl, N. Rösch, Inorg. Chem. 43 (2004) 4080.

[47] F. Schlosser, Dichtefunktionaluntersuchungen an zweikernigen Uranylkomplexen, Diplomarbeit, Technische Universität München, 2001

[48] K. E. Gutkowski, D. A. Dixon, J. Phys. Chem. A 110 (2006) 8840.

[49] V. Vallet, U. Wahlgren, B. Schimmelpfennig, H. Moll, Y. Szabó, I. Grenthe, Inorg. Chem. 40 (2001) 3516.

[50] B. Siboulet, C. J. Marsden, P. Vitorge, Chem. Phys. 326 (2006) 289.

[51] I. Infante, B. van Stralen, L. Vischer, J. Comp. Chem. 27 (2006) 1156.

[52] I. Infante, L. Vischer, J. Comp. Chem. 25 (2004) 386.

[53] M. Bühl, R. Diss, G. Wipff, J. Am. Chem. Soc. 127 (2005) 13506.

[54] M. Bühl, H. Kabrede, Inorg. Chem. 45 (2006) 3836.

[55] M. Bühl, H. Kabrede, Chem. Phys. Chem. 7 (2006) 2290.

[56] M. Bühl, H. Kabrede, R. Diss, G. Wipff, J. Am. Chem. Soc. 128 (2006) 6357.

[57] W. Chien, V. Anbalagan, M. Zandler, M. Van Stipdonk, D. Hanna, G. Gresham, G. Goenewold, J. Am. Soc. Mass. Spectrom. 15 (2004) 777.

[58] W. A. de Jong, E. Aprà, T. L. Windus, J. A. Nichols, R. J. Harrison, K. E. Gutowski, D. A. Dixon, J. Phys. Chem. A 109 (2005) 11568.

[59] F. Schlosser, S. Krüger, N. Rösch, Inorg. Chem. 45 (2006) 1480.

[60] F. Schlosser, Dissertation, Technische Universität München, 2006.

[61] J. Leciejewicz, N. W. Alcock, T. J. Kemp, Struct. Bonding 82 (1996) 43.

[62] D. H. Templeton, A. Zalkin, H. Ruben, L. L. Templeton, Acta Cryst. C41 (1985) 1439.

[63] J. Vázquez, C. Bo, J. M. Poblet, J. de Pablo, J. Bruno, Inorg Chem. 42 (2003) 6136.

[64] F. A. Cotton, G. Wilkinson, Advanced Inorganic Chemistry, 5th ed., Wiley, New York, 1988, p. 980-993.

[65] S. Krüger, F. Schlosser, N. Rösch in: Recent Advances in Actinide Science, R. Alvarez, N. D. Bryan, I. May (Eds.), Proceedings of the Conference Actinides 2005, Manchester, 2005, The Royal Society of Chemistry, Cambridge, 2006, p. 252.

[66] L. Rao, J. Jiang, P. Zanonato, P. Di Bernardo, A. Bistondo, a. Y. Garnov, Radiochim. Acta 90 (2002) 581.

[67] H. Nitsche, R. J. Silva, V. Brendler, T. Geipel, T. Reich, Y. A. Teterin, M. Thieme, L. Baraniak, G. Bernhard, G. in: Actinide Speciation in High Ionic Strength Media; Ed. D. T. Reed, S. B. Clark, L. Rao, Kluwer Academic/Plenum Publishers: New York, 1999, S. 11.

[68] S. Krüger, F. Schlosser, S. R. Ray, N. Rösch Lecture Series on Computer and Computational Sciences 7 (2006) 904.

[69] F. Quilès, A. Burneau, Vibr. Spectros., 18 (1998) 61.

[70] C. Nguyen-Trung, G. M. Begun, D. A. Palmer, Inorg. Chem. 31 (1992) 5280.

[71] M. A. Denecke, T. Reich, M. Bubner, S. Pompe, K. H. Heise, K. H. Nitsche, P. G. Allen, J. J. Bucher, N. M. Edelstein, D. K. Shuh, J. All. Comp., 271 (1998) 123.

[72] B. F. Mentzen, H. Sautereau, Acta Cryst, B36 (1980) 2051.

[73] S. R. Ray, S. Krüger, N. Rösch, in preparation.

[74] S. Pompe, K. Schmeide, M. Bubner, G. Geipel, K. H. Heise, G. Bernhard, H. Nitsche, Radiochim. Acta 88 (2000) 553.

[75] S. Sachs, G. Bernhard. Radiochim. Acta 93 (2005) 141.

[76] K. Schmeide, S. Sachs, M. Bubner, T. Reich, K. H. Heise, G. Bernhard. Inorg. Chim. Acta 351 (2003) 133.

[77] A. Kremleva, S. Krüger, N. Rösch, in preparation.

[78] C. J. Carrell, H. L. Carrell, J. Erlebacher, J. P. Glusker, J. Am. Chem. Soc. 110 (1988) 8651.

[79] L. V. Moskaleva, A. V. Matveev, S. Krüger, N. Rösch, Chem. Eur. J. 12 (2006) 629.

[80] L. V. Moskaleva, A. V. Matveev, J.Dengler, N. Rösch, Phys. Chem. Chem. Phys. 8 (2006) 3767.

[81] J. K. Gibson, R. G. Haire, M. Santos, J. Marçalo, A. P. de Matos, J. Phys. Chem. A 109 (2005) 2768.

[82] H. H. Cornehl, C. Heinemann, J. Marçalo, A. P. de Matos, H. Schwarz, Angew. Chemie 35 (1996) 650; Angew. Chemie Int. Ed. Engl. 35 (1996) 891.

[83] A. V. Matveev, N. Rösch, J. Chem. Phys. 118 (2003) 3997.

[84] A. V. Matveev, S. Majumder, N. Rösch, J. Chem. Phys. 123 (2005) 164104.

[85] M. Mayer, S. Krüger, N. Rösch, J. Chem. Phys. 115 (2001) 4411.

[86] A. V. Matveev, N. Rösch, J. Chem. Phys. 118 (2003) 3997.

[87] H. Lin, G. T. Truhlar, Theor. Chem. Acc. 117 (2007) 185

[88] T. Kerdcharoen, U. Birkenheuer, S. Krüger, A. Woiterski, N. Rösch, Theor. Chem. Acc. 109 (2003) 285.

[89] W. L. Jorgensen, J. Chandrasekhar, J. D. Madura, R. W. Impey, M. Klein, J. Chem. Phys. 79 (1983) 926.

[90] J. Zielkiewicz, J. Chem. Phys. 123 (2005) 104501.

[91] L. V. Moskaleva, V. A. Nasluzov, N. Rösch, Langmuir 22 (2006) 2141.

Appendix F - Institut für Chemie und Physikalische Chemie, Universität Potsdam

Spectroscopical determination of thermodynamic and kinetic parameters to describe complexation between humic substances and metal ions

Sascha Eidner, Michael U. Kumke

Final Report

Support Contract Number
02 E 9924

University of Potsdam, Institute of Chemistry, Physical Chemistry
Karl-Liebknecht-Str. 24-25
14476 Potsdam-Golm
Germany

Content

LIST OF TABLES

LIST OF FIGURES

Abstract

Different time-resolved and steady-state luminescence spectroscopy techniques were applied to have a closer look on the interactions between lanthanide ions (Ln^{3+}) and humic substances (HS). In a first step, the intrinsic HS fluorescence as well as the sensitized Ln^{3+} luminescence was used to describe and to quantify the complex formation. Upon addition of Ln^{3+} to humic acids (HA) a blue shift of the intrinsic HA fluorescence was found in addition to the overall decrease of the intrinsic fluorescence intensity. In contrast, in experiments with fulvic acids (FA) no spectral shift of the intrinsic fluorescence was detectable, but the intrinsic fluorescence intensity also decreases. From the quenching of the HS fluorescence and the increase of the Tb^{3+} luminescence upon addition of Ln^{3+} (Tb^{3+}) ions to a HS solution, complex formation constants were derived. The measurements showed in case of FA a close picture. Here, the value of the complex formation constant resulting from the quenching of the intrinsic FA fluorescence was always lower than for the constant originating from the increase in the sensitized luminescence intensity of the Ln^{3+} (Tb^{3+}) ion. In case of HA, the picture was not that clear and in some cases no sensitized luminescence signal of the Ln^{3+} could be observed at all.

The different behavior of HA and FA fractions can also be observed in stopped-flow experiments. For FA a fast quenching of the intrinsic FA fluorescence was found, which was within the dead time of the instrument. In measurements with HA in addition to the fast quenching, a second quenching process, much slower than the first one, was observable. The findings of the steady-state and stopped-flow measurements give raise to the assumption, that FA and HA differ in size and/or association due to metal complexation. Time-resolved fluorescence anisotropy measurements additionally support this assumption. In these experiments the rotational correlation time becomes accessible. Increasing of the Ln^{3+} concentration in a HA solution yields a decrease of the correlation time, which can be directly connected to a decrease of the volume of the molecule under investigation.

The luminescence decay behavior of luminescent Ln^{3+} (Eu^{3+}, Tb^{3+}) was used to get additional insight in the Ln^{3+}-HS complexes. In case of Tb^{3+} HS complexes a different approach to analyze the luminescence kinetic was applied. Here, the possibility of an energy transfer back from the Tb^{3+} to the HS was implemented. As a consequence, only one decay time was derived. In addition, parameters reflecting the inhomogeneity of the complexes were calculated from the model applied.

In an additional set of experiments, the luminescence properties of Eu^{3+} at ultra-low temperatures (5 K) was taken as advantage to have a closer look on the molecular surrounding of Eu^{3+} complexed to HS. For a better interpretation of the data, measurements with model compounds (salicylic and other hydroxy benzoic acids) where performed as well. The measurements showed a preferential monodentate binding of the Eu^{3+} to HS, mainly via carboxylic acids.

Spektroskopische Bestimmung von thermodynamischen und kinetischen Kenngrößen zur Beschreibung der Huminstoff-Metall-Komplexierung

Zeitaufgelöste und stationäre Lumineszenzspektroskopie wurden eingesetzt, um ein verbessertes Verständnis in die Wechselwirkung zwischen Lanthanoidionen (Ln^{3+}) und Huminstoffe (HS) zu gewinnen. Zunächst wurden die intrinsische HS-Fluoreszenz und die sensibilisierte Ln^{3+}-Lumineszenz genutzt, um die Bildung von Ln^{3+}-HS-Komplexen zu untersuchen. Dabei wurde festgestellt, dass es bei der Zugabe von Ln^{3+} zu Huminsäuren (HA) neben der Abnahme der intrinsischen Fluoreszenzintensität zusätzlich zu einer Blauverschiebung der intrinsischen Fluoreszenz kommt. In Experimenten mit Fulvinsäuren (FA) hingegen, wurde keine spektrale Verschiebung der intrinsischen Fluoreszenz beobachtet, lediglich die Abnahme der intrinsischen Fluoreszenzintensität wurde gefunden. Aus der Löschung der HS-Fluoreszenz und der Zunahme der (sensibilisierten) Tb^{3+}-Lumineszenz wurden Komplexbildungskonstanten bestimmt. Die Messungen zeigten für FA ein einheitliches Bild. Die Werte der Komplexbildungskonstanten, die aus der Löschung der intrinsischen HS-Fluoreszenz gewonnen wurden, waren jeweils kleiner, als die entsprechenden Werte, die sich aus der Zunahme der sensibilisierten Ln^{3+}- (Tb^{3+}-) Lumineszenz ergeben haben. Im Fall der HA war das Bild nicht so eindeutig. In Abhängigkeit vom Ursprungsort der HA konnten teilweise überhaupt keine sensibilisierte Tb^{3+}-Lumineszenz gemessen werden.

Das unterschiedliche Verhalten der HA- und FA-Fraktionen findet sich auch als Ergebnis von stopped-flow-Untersuchungen. Für FA zeigt sich eine sehr schnelle Abnahme der Fluoreszenzintensität innerhalb der Totzeit des Instruments. Für HA wird zusätzlich zu dem sehr schnellen ersten Schritt ein zweiter, wesentlich langsamerer Schritt gefunden. Die Ursache für dieses unterschiedliche Verhalten in Kombination mit den Ergebnissen der stationären Lumineszenzspektroskopie deutet auf unterschiedliche Größe bzw. Assoziation der Moleküle in FA und HA hin. Zeitaufgelöste Anisotropieexperimente unterstützen diese Annahme. Mit diesen Experimenten wird die Rotationskorrelationszeit zugänglich, die direkt mit dem Rotationsvolumen verknüpft ist. Eine Zugabe von Ln^{3+} zu einer HA-Lösung führt zur Abnahme der Rotationskorrelationszeit.

Das Zeitverhalten der Lumineszenz von Tb^{3+} bzw. Eu^{3+} wurde bestimmt. Für Tb^{3+} wurde ein neuer, modifizierter Ansatz zur Beschreibung der Lumineszenzkinetik gewählt. Bei diesem wird die Möglichkeit eines Rücktransfers der Energie vom Tb^{3+} auf HS berücksichtigt. Es wird im Vergleich zu multiexponentiellen Ansätzen nur eine Lumineszenzabklingzeit erhalten und zusätzlich Parameter, die die Inhomogenität der gebildeten Komplexe wiedergeben.

Zusätzlich zu diesen Experimenten wurden spezielle Eigenschaften der Eu^{3+}-Lumineszenz bei ultratiefen Temperaturen (5 K) untersucht, um Einblick in die molekulare Umgebung des Eu^{3+} in HS-Komplexen zu bekommen. Um die erhaltenen Ergebnisse besser verstehen zu können, wurden ebenfalls Messungen mit Modellverbindungen (Salicylsäure und andere Hydroxybenzoesäuren) durchgeführt. Die Ergebnisse zeigten ein bevorzugt mondentate Bindung des Eu^{3+} an den HS, hauptsächlich über Carboxylgruppen.

1 Introduction

For the design and performance assessment of a radioactive waste repository detailed studies concerning migration and accumulation of (long-lived) radionuclides in the near and far field of the repository is mandatory. To elucidate a suitable host rock formation the migration of radionuclide ions in the host rock as well as – after a possible release – in an aquifer must be fully understood with respect to the fundamental processes and mechanisms involved. In order to achieve this goal, the thermodynamic database of actinoid ions including the influence of chemical environmental parameters on the mobilization and immobilization of the radionuclides including kinetic aspects of such processes has to be validated and expanded. The behavior of metal ions (especially actinoid ions) in aquifer systems is mainly governed by humic substances (HS) and colloids. Due to the complexation and redoxing abilities of HS, the impact on retardation or transport of actinoid ions has to be further evaluated. Upon improving the thermodynamic and kinetic database a better description of the fundamental physical and chemical processes in the near and in the far field can be achieved. The deeper understanding of the processes involved on a molecular level will lead to new and improved models to describe the behavior of a repository over a very long time period (hundreds of thousand years) and finally, to provide expertises on long-time safety of such repositories.

Humic substances (HS) as well as their operationally defined fractions *fulvic acids* (FA) and *humic acids* (HA) show an intrinsic fluorescence, which is dependent on the excitation wavelength as well as the solvent conditions (e.g., pH, ionic strength) [1-5]. Based on the assumption of genesis, i.e., degradation of lignin, the intrinsic HS fluorescence was connected to different structural elements [4, 6-8]. As major fluorescing structures substituted benzoic acids were proposed. The photophysical properties of some substituted benzoic acid, like salicylic acid, are well known. However, there is a lack of knowledge for other substituted benzoic acids like cinnamic acid and how the photophysics of such compounds depends on parameters like pH or ionic strength [9].

Due to complexation of metal ions the intrinsic fluorescence of HS is generally quenched [10]. Based on this fluorescence quenching a conditional complexation constant becomes accessible by simple Stern-Volmer analysis or by models like the one proposed by Ryan and Weber [11].

On the other hand the metal complexation can also be monitored by using lanthanide ions (Ln^{3+}, e.g.,Eu^{3+} and Tb^{3+}) as luminescence probes. Using Ln^{3+} as luminescence probes is a common tool in biological and biochemical applications [12]. In that case the Ln^{3+} luminescence is evaluated and used for the determination of conditional binding constants. In such experiments the luminescence can be either excited directly by excitation into an absorption band of the Ln^{3+} ion or via indirect excitation by sensitization over the ligand (here: HS). The energy transfer from the ligand to the Ln^{3+} ion can be very efficient and thus, a strong Ln^{3+} luminescence can be observed. This so-called antenna effect is successfully used in analytical applications based on Ln^{3+} ions to circumvent the very low absorption coefficients of the Ln^{3+} ions to increase the observable luminescence signal. Up to now, this method was only applied in investigations of metal-HS complexation at room temperature. From these experi-

ments complexation constants were derived, but structural information were, if any. only extracted to a limited extend [13-16].

The aim of the present study was to investigate the intra- and intermolecular interactions between metal ions, especially lanthanoid ions, and humic substances in solution in order to increase the understanding of the fundamental processes involved. The combined application of steady-state and time-resolved luminescence methods yielded information on thermodynamic as well as on kinetic parameters. In order to reduce the influence of complexity of HS materials on the experimental data, model compounds with better defined properties (e.g., known structure) were investigated as well. Using model compounds reduces the complexity of the system and helps to understand the fundamental interactions, like the influence of proton transfer reactions or changes in HS conformation on the observed spectroscopic properties. As humic substances Aldrich HA and Gohy573 HA and Gohy573 FA have been used as internal reference HS, in addition reference HS supplied by the *International Humic Substance Society (IHSS)* were examined in the spectroscopic experiments. Because HS represent an extremely complex matrix experiments have been carried out with a synthetic humic material (M42 supplied by the Institute of Radiochemistry from the Research Center Rossendorf[4]) and simple organic model compounds (different substituted benzoic acids, assumed to be precursor compounds or subunits for HS).

The study was divided into four main work packages.

I) Conditional complexation constants

The conditional complexation constants of reactions of lanthanoid ions, like Terbium (Tb^{3+}) and Europium (Eu^{3+}) with HS are deduced from fluorescence experiments. On the one hand, the quenching of the intrinsic HS fluorescence was used to calculate the complexation constant. On the other hand, due to an intramolecular energy transfer from HS to the lanthanoid ions (Tb^{3+} and Eu^{3+}) the sensitized lanthanoid ion's luminescence was analyzed.. For the calculation of the complexation constant, the model proposed by Ryan and Weber was applied [11]. Following the idea of Ryan and Weber, the amount of bound lanthanoid ions is related to a decrease of the intrinsic HS fluorescence or to an increase in the sensitized lanthanoid luminescence in case an effective intramolecular energy transfer is operative. Thereby, the changes in luminescence intensity can be described by the following two equations,

$$I_{HS} = \frac{(I_M - 1)}{2K_{HS}c_L}\left[(K_{HS}c_L + K_{HS}c_M + 1) - \sqrt{(K_{HS}c_L + K_{HS}c_M + 1) - 4K_{HS}^2 c_L c_M}\right] + 1 \qquad (1a)$$

$$I_{Ln} = \frac{I_{Ln,\infty}}{2K_{Ln}c_L}\left[(K_{Ln}c_L + K_{Ln}c_M + 1) - \sqrt{(K_{Ln}c_L + K_{Ln}c_M + 1) - 4K_{Ln}^2 c_L c_M}\right] \qquad (1b)$$

[4]now Research Center Dresden-Rossendorf

where equation (1a) describes the evaluation using the decrease of the intrinsic HS fluorescence and equation (1b) uses the sensitized luminescence of the lanthanoide ion. In these equations I_{HS} denotes the relative intrinsic fluorescence intensity referring the unquenched situation (no lanthanoid ion present), I_M accounts for the remaining fluorescence intensity at a very high metal loading. In similarity I_{Ln} is the luminescence of the lanthanoid ion and $I_{Ln,\infty}$ is the maximum of the luminescence intensity, when all accessible binding site in HS are saturated. The concentration c_L is directly related to the concentration of available binding sites and c_M reflects the concentration of the added lanthanoid ion.

II) Intramolecular energy transfer, distance distributions and properties of metal binding sites in humic substances

Based on the well characterized luminescence of Tb^{3+} and Eu^{3+} fundamental properties of lanthanoid complexes such as the number of water molecules in the first coordination sphere and the average distance of binding sites in HS were investigated, The luminescence decay time is a function of the number of the OH-groups in the first coordination sphere. Working in aquatic solutions it is attractive to attribute the number of OH-groups directly to the number of coordinated water molecules. This property can be used to study changes in the complexation upon addition of lanthanoid (Ln^{3+}) ions. In the case of Eu^{3+} the intensities of some of the f-f transitions (especially, of the $^5D_0$- $^7F_1$ transition as the most prominent) are dependent on the complex properties because of the electronic character, while the intensities more magnetic transitions are not affected by properties such as polarity. A comparison of the behavior of the two types of transitions give additional information on changes (stoichiometry, geometry) in the complexes formed. The Ln^{3+} ion can be excited directly via an Ln^{3+} ion's absorption band or by an indirect excitation via energy transfer from HS. While in the first case both, the free and the complexed Ln^{3+} ion are excited, in the second case only the complexed species is monitored. As a consequence, by indirect excitation the complexed species can be specifically investigated, on the other hand direct excitation allows a more complete look on Eu^{3+} species distribution in solution.

To extract structural information and reduce the influence of the complex HS structure, it is promising to make use of the intra-lanthanoid energy transfer. The principle of *Förster resonance energy transfer* (FRET) is applied and this approach works like a "spectroscopic ruler" yielding information on the average distance between donor and acceptor. Possible pairs of donor and acceptor for the investigation of binding sites in HS are Tb^{3+} and Nd^{3+} as well as Eu^{3+} and Nd^{3+}, respectively. An important parameter for this energy transfer to be effective is the critical Förster radius R_0. This number gives the distance between donor and acceptor at which the probability for energy transfer 50 %. As shown in Table 7 the particular Förster radii for the Ln^{3+}/Ln^{3+} pairs are 0.912 nm for the pair Tb^{3+}/Nd^{3+} and 0.853 nm for the pair Eu^{3+}/Nd^{3+}, respectively.

Table 7:Förster radii of selected lanthanoid ions for an inter-lanthanoid energy transfer [17]

donor	acceptor	R_0 / nm
Eu^{3+}	Nd^{3+}	0.85
Eu^{3+}	Pr^{3+}	0.82
Tb^{3+}	Nd^{3+}	0.91
Tb^{3+}	Pr^{3+}	0.78
Tb^{3+}	Ho^{3+}	0.93
Tb^{3+}	Er^{3+}	0.81

In case energy is transferred from donor D to acceptor A, the donor's luminescence decay time is shortened and its luminescence intensity decreases as well. The efficiency *E* of the transfer corresponds to changes in decay time τ and intensity decrease *I*. It is given by the following equation (2a - 2c)

$$E = 1 - \frac{I_D}{I_{DA}} \tag{2a}$$

$$E = 1 - \frac{\tau_D}{\tau_{DA}} \tag{2b}$$

$$E = \frac{1}{1 + \left(\frac{r}{R_0}\right)^6} \tag{2c}$$

The index D indicates the donor's photophysical properties (intensity *I* or decay time τ) in absence of a suitable acceptor A, DA denotes the changed properties in presence of an acceptor, R_0 is the Förster radius and *r* the distance between donor and acceptor. Rearranging equation (2c) and equation (2b) to substitute *E* yields the distance *r* between D and A

$$r = R_0 \cdot \sqrt[6]{\frac{1}{E} - 1} = R_0 \cdot \sqrt[6]{\frac{\tau_D}{\tau_D - \tau_{DA}} - 1} \tag{3}$$

Eq. (3) shows the relation between the changes in the luminescence decay times τ_{DA} and the average distance *r* between donor and acceptor. From measuring the donor's luminescence decay time an average distance *r* between donor and acceptor can derived.

III) Association kinetics and conformational dynamics of HS and HS-metal complexes

Stopped-flow

In the literature is an ongoing discussion about the "size" (molecular mass) of HS. In older literature molecular masses of more than 10000 g/mol are discussed. In recent publications, HS molecules are understood as agglomerates of smaller molecules, each having molar masses below 1000 g/mol, which form more complex structures due to hydrogen bonds and metal ions as "bridging elements". The complex formation of HS with metal ions is a known

fact, but only little is known about the kinetic of these complex formation. To close this gap, a *stopped-flow*-technique is applied. In these experiments a solution containing HS and a second solution containing metal ions are rapidly mixed and the quenching of the intrinsic HS fluorescence upon complexation is recorded on a microsecond to second time scale. From the fluorescence intensity changes with time, the kinetics of the complex formation is analyzed.

Anisotropy

In the anisotropy experiments changes in the apparent molecular size are analyzed and used to come to detailed understanding of HS-metal complex formation. As HS can be understood as polyelectrolyte (polyanion), a change in size is expected upon complexation. By adding positive charges (metal ions) to a negatively charged polyelectrolyte some negative charges are saturated and the intramolecular repulsion of the polyanion should decrease and by this, the polyelectrolyte can switch from a stretched form to a more contracted. By decreasing the apparent molecular volume and effective charge of the whole macromolecules, the rotation and diffusion of the macromolecules should increase. By fluorescence anisotropy measurements the rotational diffusion time ϕ of molecules can be measured. Changes in ϕ indicated an alteration of the molecular size.

The anisotropy of a fluorophore can be calculated from its fluorescence intensity horizontal, $I(t)_h$, and perpendicular, $I(t)_v$, to the plane of the excitation light [26]

$$r = \frac{I(t)_v - I(t)_h}{I(t)_v + 2 \cdot I(t)_h} \tag{4}$$

Assuming a fluorophore in a highly viscose medium, in which diffusion or rotation are impossible, the resulting anisotropy is only a function of the angle between the excitation and emission transition dipole moment of the fluorophore, respectively. In this case, the anisotropy, so called fundamental anisotropy r_0, is given by

$$r_0 = \frac{2}{5}\left(\frac{3\cos^2\alpha - 1}{2}\right) \tag{5}$$

where α is the angle between the excitation and emission transition dipole momenta of the fluorophore. As the angle between these transition dipoles momenta can have values between $0 \le \alpha \le \pi/2$ the anisotropy has values ranging from $r = 0.4$ to $r = -0.2$, respectively. If rotation of the fluorophores is possible, the anisotropy is decreased due to rotational diffusion of the molecule. In this case, the time dependent anisotropy $r(t)$ is a function of the rotational correlation time ϕ. In the simplest approach, one can understand a molecule as spherical rotator. Here, the rotational diffusion can be described using the Perrin equation

$$\frac{r_0}{r} = 1 + \frac{\tau}{\phi} \tag{6}$$

with r as measured anisotropy and r_0 as fundamental anisotropy, the fluorescence decay time τ, and the rotational correlation time ϕ, respectively. In case the rotational correlation decay

time of the molecule is much larger than the fluorescence decay time, the measured anisotropy is equal to the fundamental anisotropy r_0. In contrary, in case ϕ is much shorter than the fluorescence decay time, the anisotropy becomes zero.

Generally, the time-dependent anisotropy *r(t)* of a rigid molecule decreases multiexponentially

$$r(t) = \sum_{j=1}^{5} r_{0,j} \exp\left(-\frac{t}{\phi_j}\right) \tag{7}$$

the parameter $r_{0,j}$ and ϕ_j resulting from the rotation along the axes of rotation and the relative orientation of absorption and emission dipoles to the axes of rotation. A sum of five exponentials is a border case for an asymmetric body, which can rotate along all of the three principal axis of inertia. Molecules can often be described by an ellipsoid of rotation with two equal axes and one unique axis. In this case, the complexity decreases and the time dependence of the anisotropy is a sum of three exponential terms. A rigid spherical rotor reflects the simplest case. Here, the anisotropy can be described by a monoexponential function resulting in only one rotation correlation time ϕ. In this case, equation (7) simplifies to

$$r(t) = r_0 \exp\left(-\frac{t}{\phi}\right) \tag{8}$$

To derive the rotational correlation time ϕ, the anisotropy can be calculated following equation (4). Applying a rigid spherical rotor, ϕ becomes available by fitting the calculated anisotropy using equation (8). The rotational correlation time is connected to the volume of the rotating object and some solvent properties.

$$\phi = \frac{\eta V}{RT} \tag{9}$$

Where η is the viscosity, *T* the absolute Temperature, *R* the universal gas constant and *V* the volume of the rotor.

IV) High spectral resolution spectroscopy of Eu^{3+}-complexes

As mentioned above, especially Eu^{3+} is well-suited as a speciation probe for metal complexation by macromolecules, because the luminescence properties strongly depend on the molecular environment (e.g., coordinated water molecules, charge density of ligands coordinated, complex symmetry). The spectroscopic parameters to be measured in order to extract the desired information on speciation are the luminescence decay time, the position of the $^5D_0$-$^7F_0$ transition as well as the splitting and number of peaks of the $^7F_1$ and $^7F_2$ multiplets.

The major experimental challenge is the determination of small changes in the Eu^{3+} luminescence spectra and in the luminescence decay characteristics. In particular, the expected

spectral variations such as position of the $^5D_0$-$^7F_0$ transition and splitting pattern, induced by complexation are very small since the f-electrons are well-shielded from coordination effects by outer s- and p-shells. At room temperature spectral broadening effects (inhomogeneous spectral broadening due to e.g., ligand exchange reactions, vibrations of moieties of the complex or collisions with solvent molecules) will render the measurement of very small spectral alteration extremely difficult. The situation becomes different at ultra-low temperatures (here: 4 K), where molecular motion, diffusion controlled interactions or ligand exchange reactions are stopped or at least minimized. At cryogenic temperatures the inhomogeneous line broadening processes are drastically reduced and highly resolved luminescence spectra can be recorded, which allow to analyze very small spectral difference. Compared to room temperature emission spectra (in which the $^5D_0 \rightarrow {}^7F_1$ transition appears as a single broad band of ca. 10 nm FWHM, not shown), the FLN spectra recorded at 4.7 K show much sharper luminescence peaks, in which the Stark levels of the ^7F_J transitions are well-resolved. The Stark levels are a result of the crystal field, which removes the degeneracy of the $^{(2S+1)}L_J$ levels (see Figure 2).

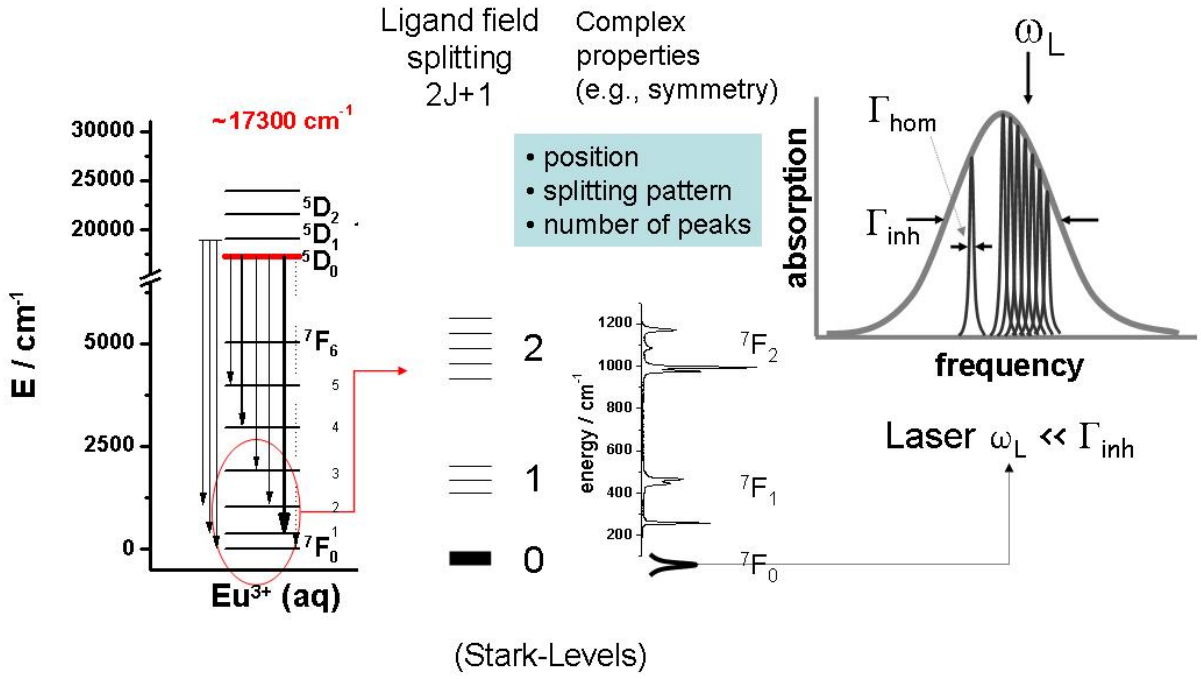

Figure 1: Basic principle of ultra-low temperature luminescence – (left) energy levels (^5D_x and ^7F_x multiplets only) of Eu^{3+} before and after ligand splitting. Due to the ligand field the degeneracy of the energy levels is removed and (2J+1) Stark levels can be observed under high spectral resolution conditions. (right) At room temperature inhomogeneous line broadening processes as well as the possible inter-exchange of different complexes (with respect to stoichiometry or symmetry) renders the measurement of high-resolutions spectra impossible. By cooling the sample to 4K those processes are no longer effective and the sample composition is fixed. With a narrow banded laser different species can now be selectively excited and detected (see spectrum in the middle).

In Figure 1 the basic idea of ultra-low temperature measurements of Eu^{3+} complexes is summarized. Because for Eu^{3+} complexes the $^5D_0$-$^7F_0$ transition is non-degenerated, its spectral position is specific for a formed complex and subsequently, the presence of different $^5D_0$-$^7F_0$ transitions indicates multiple complexes in the sample. Using a very narrow-banded laser, it is possible to selectively excited the different complexes in the sample and record the related emission spectra. Subsequently, the symmetry of the complex can be deduced from the observed pattern of the $^7F_1$ and $^7F_2$ multiplets in the luminescence spectra.

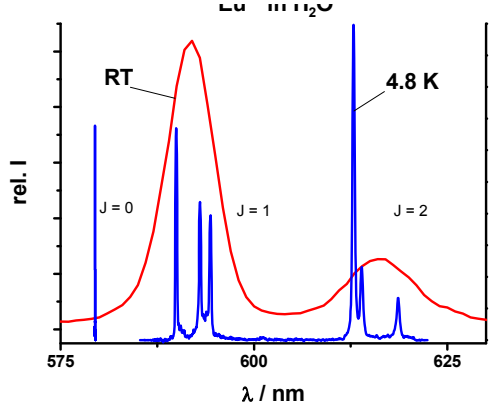

Figure 2: Comparison of Eu^{3+} luminescence spectrum (Eu^{3+}-salicylic acid complex) measured at room and ultra-low temperature.

2 Materials and methods

For all experiments stock solutions (10^{-2} mol/L) of different Ln^{3+} ions (Eu^{3+}, Tb^{3+}, Nd^{3+}) were prepared and stored in the dark. As humic substances FA and HA fractions of ground and surface waters (Gohy573 HA, Gohy573 FA, FG1 FA, HO14 FA, HO13 HA, BS1 HA, SR FA, and SR HA), synthetic HS (M1, M42) as well as a commercial HA (Aldrich HA) were used. A detailed description of the HS used can be found elsewhere [18]. In general, the HS concentration was set to 10 mg/L, the ionic strength to $I = 10^{-2}$ using $NaClO_4$ and pH = 5 was adjusted using HCl and NaOH, respectively. After addition of metal ions the HS solutions were left for equilibration for at least five minutes (up to several days). Prepared HS stock solutions were stored at 4°C and in the dark until use.

Because humic substances (HS) represent an extremely heterogeneous mixture of plant and tissue degradation products, model compounds such as hydroxy substituted benzoic acid derivatives were investigated as well and the results were compared with those obtained for HS.

Stationary fluorescence spectra were recorded at room temperature using a Fluoromax3 (Jobin Yvon) spectrofluorometer with a typical bandwidth of 2 nm in excitation and emission. In the fluorescence quenching experiments the samples were excited at λ_{ex} = 325 nm and 337 nm. The fluorescence spectra were recorded in the spectral range of 335 nm < λ_{em} < 640 nm. The quenching of the intrinsic HS fluorescence was analyzed in the spectral region 400 nm < λ_{em} < 460 nm. The changes in luminescence intensity of Tb^{3+} and Eu^{3+} were observed at λ_{em} = 545 nm and λ_{em} = 593 nm (615 nm), respectively.

In time-resolved luminescence measurements a nitrogen laser with a repetition rate of 10 Hz operating at 337 nm (LTB) was employed (for some of the time-resolved luminescence an OPO system (GWU) pumped with a Nd:YAG laser (Spectra Physics) was used). The luminescence of the lanthanoid ions was recorded in the spectra region 450 nm < λ_{em} < 650 nm using an iCCD camera Andor DH720-18H-13, Andor) equipped with a spectrograph (MS257, Oriel Instruments). The luminescence intensity at a certain time shift was recorded for a period of 10 μs, this detection window was shifted in 10 μs steps. Hence, a total detection window of 3.0 ms in the Tb^{3+} and 1.5 ms in the Eu^{3+} measurements was achieved.

A *stopped-flow* reaction analyzer SX.18MV-R (Applied Photophysics) equipped with a 150 W Xe arc lamp was used to monitor the kinetics of the complexation formation of Ln^{3+} and HS. The rapid mixing occurs in a 20 μL mixing cell. In experiments applying Nd^{3+} as metal ion the intrinsic HS fluorescence was recorded over the whole spectral range of the HS emission using an interference filter (IF 585). In experiment with Tb^{3+} a spectral bandpass filter (380 nm to 430 nm) was applied. In all experiments the samples were excited at 325 nm. The dead time of the instrument is 1.2 ms. The system allows two channel measurements. Within in one mixing event, two different signals can be detected. When two channel measurements were carried out, two emission signals were recorded. In the first channel the intrinsic HS fluorescence and in the second channel the Tb^{3+} luminescence around 545 nm were recorded.

The fluorescence anisotropy measurements were carried out using a Ti:Sapphire-Laser (Tsunmai, Spectra Physics) as excitation source (THG@266 nm). The HS fluorescence signal at λ_{em} = 465 nm was detected with a multi channel plate detector (Europhoton). The fluorescence decay curves were recorded on a FL920 spectrometer (Edinburgh Instruments), which is equipped with Glenn-Thompson polarizers in front of the emission monochromator. The instrument was operated in the single photon counting mode with the polarizer oriented at 0°, at 90° and at the magic angle (approx. 54.74°), respectively. The anisotropy was calculated following equation (4). In the experiments the fluorescence anisotropy of a 10 mg/L Gohy573 HA solution with an ionic strength of I = 0.1 using $NaClO_4$ was measured as function of metal loading (without and with 16 μmol/L Eu^{3+}). Moreover, the time-resolved measurements were carried out at different temperatures (20 °C up to 60 °C in steps of 10 °C) in order to investigate the influence of solvent viscosity (see eq. 9).

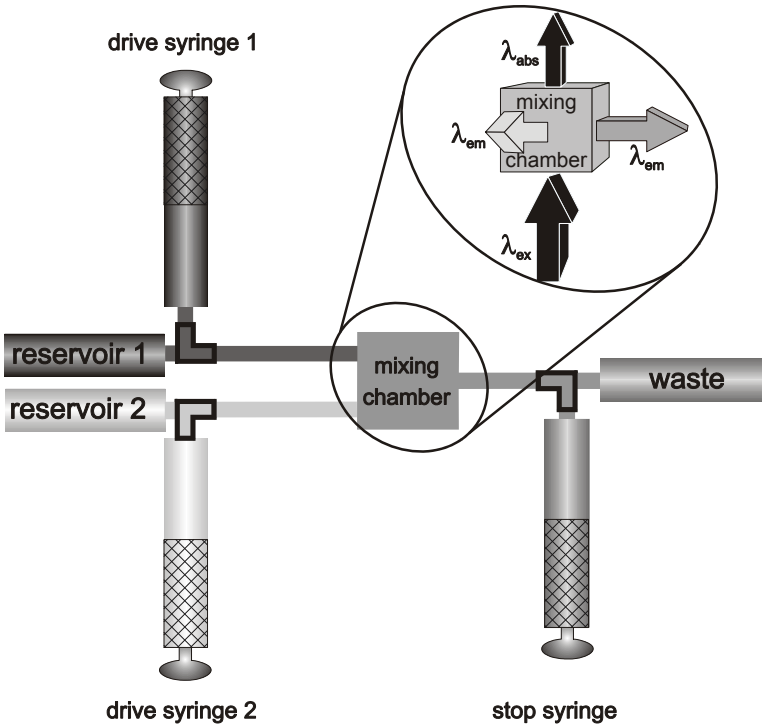

Figure 3: In a *stopped-flow* experiment two reactant solutions are mixed together very rapidly in a mixing chamber. The final solution in the mixing chamber can be observed by absorption and emission spectroscopy. In one mixing event, the hardware allows to measure the traces of two different emission wavelength using suitable band path filters. It is also possible, to observe changes in the absorption at the excitation wavelength in one channel and the change of emission in the second channel.

3 Results and discussion

3.1 Conditional complexation constants

Adding lanthanoide ions to HS solutions and monitoring the changes in the intrinsic fluorescence intensity shows always a similar trend. The intrinsic fluorescence intensity decreases (c.f. Figure 4). In case of HA often a blue shift of the intrinsic HS fluorescence was found (left hand side in Figure 4), whereas, no spectral shift (e.g., of the fluorescence maximum) was found for FA (Figure 4, right hand side). Changes in spectral shape give hints to a selective quenching of several fluorophores, the formation of new fluorescing species, differences in quenching efficiencies for different fluorescing subunits or alterations in the intramolecular deactivation pathways, e.g., due to changes in conformation of the HS. These effects limit the usability of quenching data in calculating conditional binding constants.

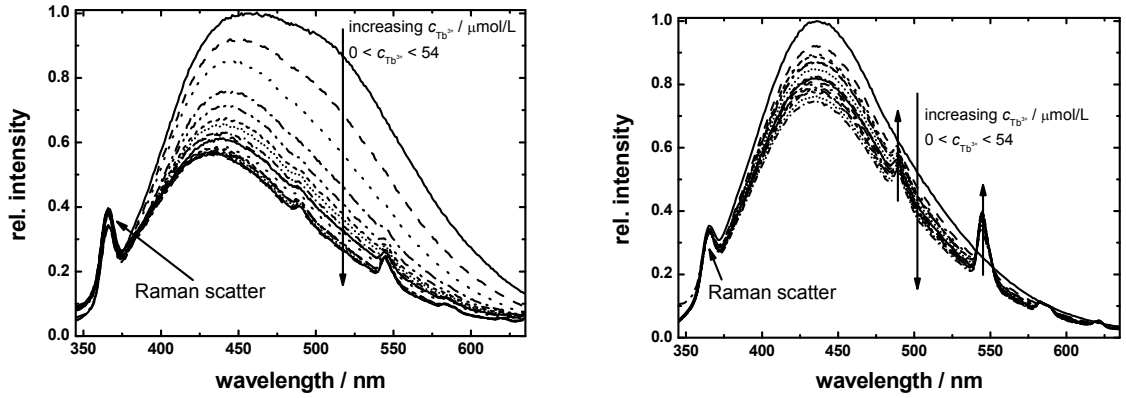

Figure 4: Fluorescence spectra of Aldrich HA (left) and FG1 FA (right) upon subsequent addition of Tb^{3+} after excitation at λ_{ex} = 325 nm.

The amount of intrinsic fluorescence quenching was dependent on the nature of the HS as well as on the lanthanoid ion added. The quenching of the intrinsic fluorescence was found for all lanthanoid ions used. Only Eu^{3+} and Tb^{3+} show intrinsic luminescence in aqueous solution in the visible spectral region. In all sensitization experiments (indirect excitation of the Ln^{3+}-ion) carried out, Tb^{3+} showed a stronger sensitization efficiency than Eu^{3+}. An explanation for the lower sensitization efficiency in case of Eu^{3+} maybe the presence of additional deactivation processes. It is well known that Eu^{3+} can be (photo)reduced to Eu^{2+} in presence of organic ligands like HS [19,20,21]. For such charge-transfer complex the deactivation could efficiently occur radiationless.

To deduce the conditional complexation constants, the relative intrinsic fluorescence and the Tb^{3+} luminescence intensity were plotted as function of the added Tb^{3+} concentration (see Figure 5a), respectively, followed by a fitting procedure using the ligand concentration c_L as global parameter.

From the mathematical analysis conditional complexation constants β were derived. In the two different approaches differences in the conditional complexation constants β as shown in Figure 5(b) were found. For all FA investigated a sensitization of the Tb^{3+} luminescence was observed. In contrary, only for HA derived from aquatic environments a sensitized luminescence signal could be observed. For soil-derived HA no sensitization of the Tb^{3+} luminescence was detected. For FA the β values calculated by the two approaches show very similar tendencies. Here, the conditional complexation constant deduced from the quenching of the HS K_{HS} is always smaller than the constant K_{Ln} derived from data based on the Tb^{3+}-sensitisation. In contrast, for HA showing sensitization, an opposite picture was observed, in which no clear connection between the two approaches could be drawn. The results for synthetic HA (M1 and M42) show also a very heterogeneous picture comparable to HA.

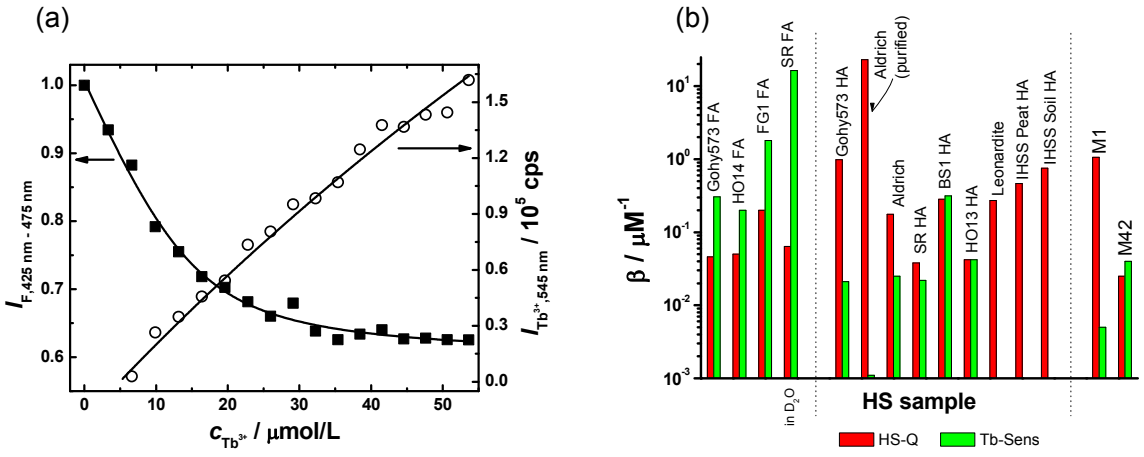

Figure 5: (a) Decrease of the relative intrinsic HS fluorescence intensity (black squares;) Aldrich HA) and increase of Tb^{3+} luminescence intensity (black open circles). The solid lines represents the result of the nonlinear fitting according equations (1a) and (1b), respectively. (b) The conditional complexation constants β for HS of different origin. The red bars reflect the conditional complexation constants β resulting from fitting following equation (1a), green bars give the findings from the measurements via the sensitized Tb^{3+} luminescence

3.2 Distance distribution and properties of metal binding sites

The photophysical properties of the lanthanoid ions (Ln^{3+}) Tb^{3+} and Eu^{3+} are changed upon complexation. In aqueous solution the luminescence decay time of both ions is monoexponential with values of $\tau(Tb^{3+})$ = (395 ± 10) µs and $\tau(Eu^{3+})$ = (100 ± 8) µs. In complexes with HS, the luminescence decay behavior is significantly altered. The luminescence decay for Tb^{3+} (at λ_{em} = 545 nm) becomes non-monoexponential, and for Eu^{3+} (at λ_{em} = 593 nm) the luminescence decay time decreases upon complexation with HS.

Different fundamental processes can contribute to the observed alteration and complexity in the photophysical properties of Tb^{3+} and Eu^{3+}, respectively. The first idea is to attribute this behavior to different complex species, in each, the lanthanoide ion has a different chemical environment, and consequently a different luminescence decay is found. For Tb^{3+}, even at low Tb^{3+} concentration a highly complex luminescence decay was observed. (The luminescence decays of Eu^{3+} (λ_{em} = 593 nm) in the presence of HS can often be described fairly well by a monoexponential rate law. However, at high Eu^{3+} loadings the decays become complex and at least a two-exponential rate law has to be applied for a good description of the experimental data with respect to the quality of the fitting.) In case this complex decay behavior was the result of different species formed, at low metal loadings only the strongest binding

sites should be involved in the complexation. Therefore, the heterogeneity should decrease and consequently, the luminescence decays would becomes (nearly) monoexponential with decreasing metal loading, which, at least for Tb^{3+}, is not the case. Hence, a different process has to be considered.

Upon decreasing the temperature of the sample, the luminescence decays of Tb^{3+} in the presence of HS become (almost) monoexponential below a certain temperature (140 K). There was only a small contribution from the intrinsic phosphorescence of the HS itself, which can only be seen at low temperatures and which is responsible for the observed deviation.

Based on the results, discussed above, it is attractive to attribute the nonexponential sensitized luminescence decay of Tb^{3+}, as shown in Figure 6, to an intramolecular energy back transfer. This means, that part of the energy transferred from HS to Tb^{3+} is funneled back to HS. This energy back transfer can occur, because the $^5D_4$ energy level of Tb^{3+} is relatively close to (possible) triplet energy levels of HS, which are assumed to be related to the triplet energies found in substituted benzoic acids like salicylic acid, which are suggested as structural building blocks of HS [30,31,32,33]. An energy back transfer is well described for various organic ligands [19,20]. Consequently, in the mathematical treatment of the luminescence decays, the energy back transfer has to be taken into account. Instead of a simple exponential equation, a stretched-exponential was applied.

$$I(t) = A + B_1 \exp\left[-\left(\frac{t}{\tau_1}\right) - C\left(\frac{t}{\tau_1}\right)^{\gamma}\right] + B_2 \exp\left(-\frac{t}{\tau_1}\right) \tag{10}$$

with

$$C = \frac{c_A}{c_A^0} \tag{11}$$

Here, c_A^0 reflects the acceptor concentration at which the energy back transfer has a probability of 50 %, the actual acceptor concentration is given by c_A. The heterogeneity of the HS is expressed by the exponent γ, with possible values between zero and one accounting for the dimensionality of the matrix. If free three-dimensional diffusion is possible, γ is expected to be 0.5. From the fitting procedure at different Tb^{3+} concentrations only one decay time τ_1 can be deduced, reflecting the situation were no acceptor is available and an energy back transfer is impossible. The second exponential term in equation (10) accounts for Tb^{3+} HS species, where a back transfer of energy is not possible because of a lack of suitable energy acceptors in HS.

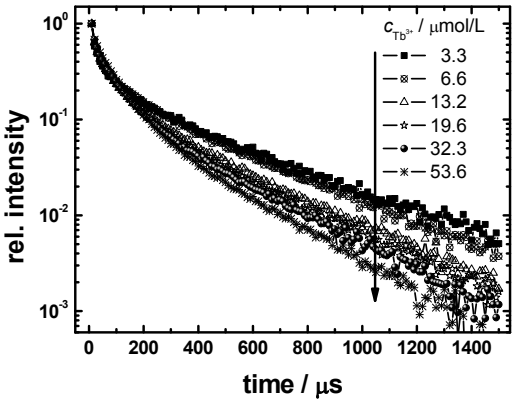

Figure 6: Luminescence decays of Tb^{3+} in Tb-HS complexes at different Tb^{3+} concentrations (λ_{ex} = 337 nm, λ_{em} = 545 nm).

The results of analyzing the luminescence decay data of Tb-HS complexes using equation (10) showed differences between FA and HA. As already found in steady-state quenching experiments, complexed to FA, the results of the time-resolved measurements gave a nicely homogeneous picture. For the heterogeneity parameter γ (see. eq. 10) values of $0.3 < \gamma < 0.4$ and for the luminescence decay times τ_{Tb} values of 300 μs < τ_{Tb} < 360 μs were found. In contrast to FA, for HA and synthetic HS, the luminescence decay time were scattered over a much broader time window of 100 μs < τ < 360 μs, respectively. For the parameter γ no trend at all could be observed. As Tb^{3+} and the complexing units in HS are fixed through the back bone of HS no free three-dimensional diffusion of donor (Tb^{3+}) and acceptor (HS) was expected and thus, γ = 0.5 should be an upper limit for the heterogeneity parameter. As already seen in the steady-state experiments, the binding situation for Tb^{3+} seems to be relatively similar among FA. In contrast, the differences in τ_{Tb} and γ in Tb-HA complexes points to a significantly higher variation in the binding environment for metals in HA, which is can be attributed to the average size and the possible stronger intra-molecular association reactions of HA compared to the related FA.

Additional deactivation pathways in Ln-HS complexes might be operative as well, which can be seen in HS complexes with Eu^{3+}. Due to a higher energy gap between the emitting $^5D_0$ level and the (assumed) triplet levels in HS an energy back transfer is not favorable.

Upon excitation the energy in Eu^{3+} is finally transferred to the $^5D_1$ and $^5D_0$ level. Both levels are luminescent, however the luminescence of the $^5D_1$ level decays very fast compared to the $^5D_0$ level. Here, only on emission from the excited $^5D_0$ level into the F-Multiplet was monitored (see Figure 1). These transitions can be of a more magnetic or more electric character. Whereas, the electric transitions are affected by the chemical environment of the Eu^{3+} ion, the magnetic transitions are not. Thus, when comparing the ratio of the intensities of a magnetic and an electric transition, changes in the chemical environment appear as changes in these intensity ratio κ.

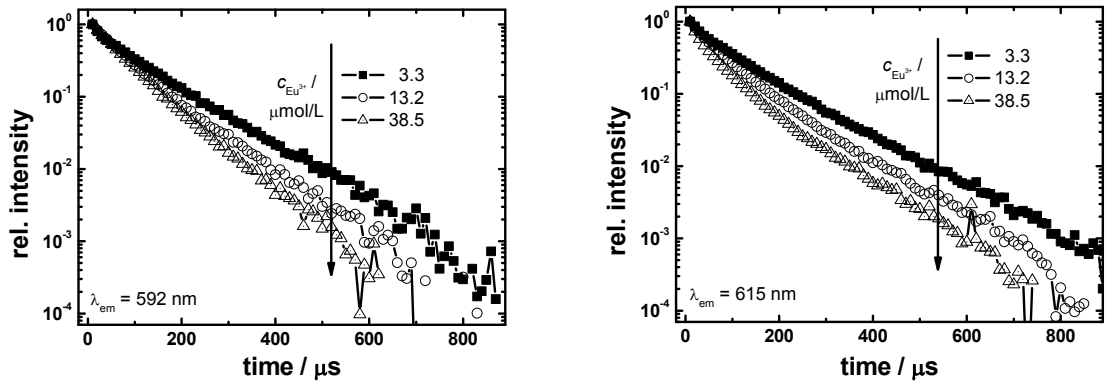

Figure 7: Luminescence decays for Eu^{3+} in Gohy573 FA complexes at different Eu^{3+} concentrations. On the left, luminescence decay at λ_{em} = 592 nm, the right, the luminescence decay measured at λ_{em} = 615 nm. λ_{ex} = 337 nm.

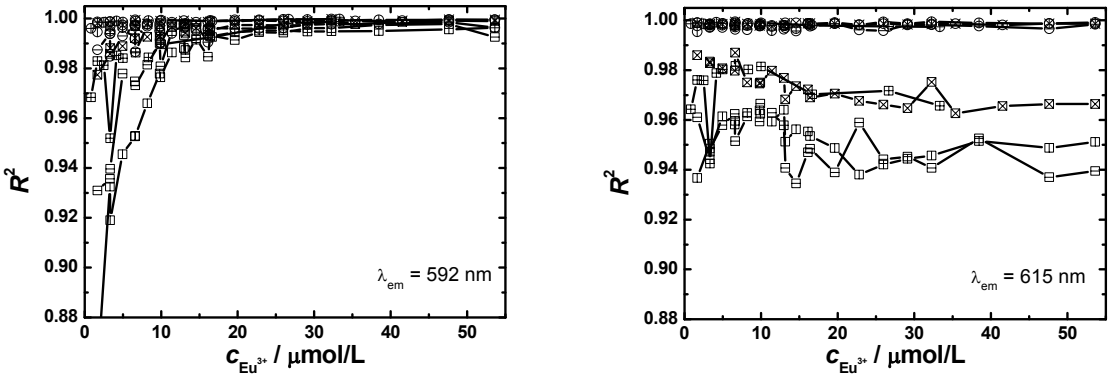

Figure 8: Coefficient of determination (R^2) for fitting Eu^{3+} luminescence decays using a monoexponential or a biexponential rate law: on the left for the magnetic transition at λ_{em} = 592 nm and on the right for the electric transition at λ_{em} = 615 nm. Here, data for different HS ([+] HO14 FA, [×] FG1 FA, [–] Gohy573 HA and [|] Aldrich HA) are shown. Open circles represents R^2 for biexponential and open squares for monoexponential fitting.

The transitions of main interest for this comparison are the $^7F_1 \leftarrow {}^5D_0$ (a magnetic transition) and the $^7F_2 \leftarrow {}^5D_0$ (an electric transition). Luminescence decays of the Eu^{3+} bound to HS

after indirect excitation via HS were recorded at two different emission wavelengths. The magnetic $^7F_1 \leftarrow {}^5D_0$ transition can be observed, e.g. for Gohy573 FA, at λ_{em} = 592 nm, the electric $^7F_2 \leftarrow {}^5D_0$ transition at λ_{em} = 615 nm. Interestingly, the time dependence of the two transitions show differences when the Eu^{3+} loading is increased.

Whereas, the luminescence decay via the magnetic transition at high Eu^{3+} concentration can be described by a monoexponential rate law for the luminescence decay following the electric transition a biexponential description is still necessary. This behavior was found for HS of different origin (see Figure 7). In all measurements of Eu-HS complexes, at Eu^{3+} concentrations > 25 μmol/L, its luminescence decay at λ_{em} = 592 nm can be described by a monoexponential rate law. The coefficient of determination (R^2) is not improved in the biexponential fit. In contrast, for the electric transition at λ_{em} = 615 nm over the whole concentration range a biexponential rate law has to be applied.

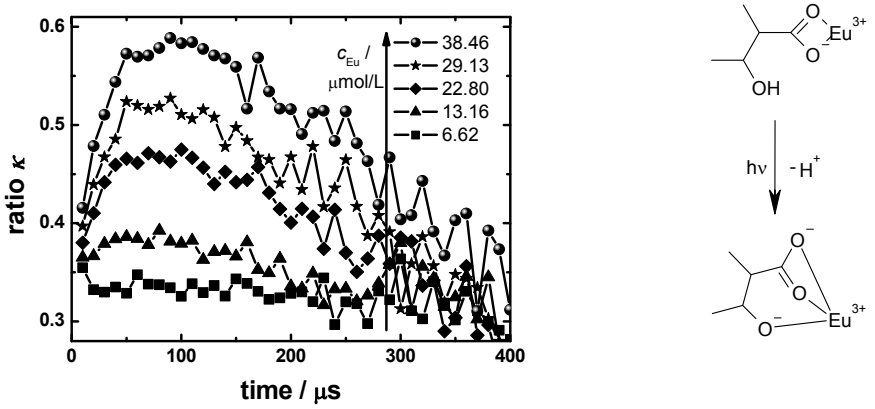

Figure 9: On the left, time-dependent intensity ratios κ for the $^7F_1 \leftarrow {}^5D_0$ and $^7F_2 \leftarrow {}^5D_0$ in Eu-Gohy573 FA complexes. At lower Eu^{3+} loadings, the ratio remains constant over the whole time interval, but at higher Eu^{3+} loading differences in the decays are remarkably and κ changes. On the right, as mentioned in the text a hypothetical photochemical reaction due to reorganization of HS upon excited state reaction is suggested.

The time-resolved intensity ratio $\kappa(t)$ was calculated from the luminescence decay measurements at λ_{em} = 592 nm and λ_{em} = 615 nm, respectively. It is attractive to attribute the changes in $\kappa(t)$ to changes in the conformation of the HS matrix during the excited state lifetime of the bound Eu^{3+} ion. After excitation different photophysical reactions become possible in the HS. A very important excited state reaction is proton transfer. It is known, that upon excitation phenolic hydrogens become highly acid. For example, in β-Naphthol the acidity constant decreases over seven orders (!) of magnitude. With respect to HS-Eu complex new (however, time-dependent) complexation sites might become accessible. Phenolic groups in neighborhood of carboxylic groups can participate in the complexation reactions in the excited state

more easily. Due to the presence and the temporal interaction with Eu^{3+} the electric transitions in HS as well as the conformation of HS might be affected. Because of the changed electronic situation in the HS-Eu-complexes, additional reactions like CT-formation might come into play, too.

In order to circumvent the drawbacks resulting from the complexity and heterogeneity of HS, resonance energy transfer (RET) between Tb^{3+} (or Eu^{3+}, donor) and Nd^{3+} (acceptor) was investigated and the concept of the "spectroscopic ruler" was applied. In the experiments a fixed concentration of Eu^{3+} was added to a HS solution and the concentration of Nd^{3+} was successively increased. The alteration of the Tb^{3+} luminescence intensity as well as of the Tb^{3+} decay upon addition of Nd^{3+} was investigated and an average distance between Tb^{3+} and Nd^{3+} bound to HS was calculated based on the RET concept. In order to prove the presence of RET control experiments with La^{3+}, which is not capable to participate in RET processes, were carried out. In these experiments the influence of competition for HS binding sites between Eu^{3+} and Nd^{3+} (La^{3+}) was tested and quantified. Figure 10 shows the results of steady state experiments, in which Nd^{3+} was added to Tb-HS and Eu-HS solutions, respectively.

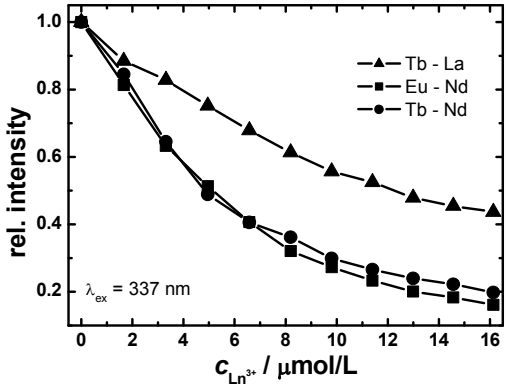

Figure 10: Changes in relative luminescence intensity of Tb^{3+} upon addition of La^{3+} (-▲-) or Nd^{3+} (-♦-) and of Eu^{3+} (-■-) upon addition of Nd^{3+} in solutions containing 10 mg/L Gohy573 FA.

As can be seen in Figure 10, the Tb^{3+} luminescence is quenched by La^{3+} as well as by Nd^{3+}. The quenching in case of La^{3+} is a result of the replacement of Tb^{3+} by La^{3+}. In case of Nd^{3+} the Tb^{3+} luminescence is quenched to a larger extent because of the contributions from the inter-lanthanoid energy transfer. As a result, the Tb^{3+} luminescence is additionally decreased. The same is found for Eu^{3+}. Simply applying equation (2a) without correction for metal competition will overestimate the efficiency of the inter-lanthanoid energy transfer.

The constraints from the steady state luminescence measurements can be overcome by time-resolved luminescence measurements. Here, the luminescence decay time of Tb^{3+} (or

Eu^{3+}) should be only affected by the inter-lanthanoid energy transfer. However, the complex luminescence decay behavior of the luminescence probes Tb^{3+} and Eu^{3+} due to energy back transfer or other excited state reactions complicates the data analysis of the measurements. Due to the energy back transfer operative in the case of Tb^{3+} a calculation of average distance between metal ions bound to HS is not straight forward. Because of the lack of intramolecular energy back transfer between Eu^{3+} and HS, Eu^{3+} and Nd^{3+} were used as FRET pair for probing the inter-lanthanoid energy transfer. To handle the biexponential behavior of the Eu^{3+} luminescence decay, all measured luminescence decays for the magnetic and electric transition were fitted according a biexponential rate law.

$$I = A_0 + A_1 \exp\left(-\frac{t}{\tau_1}\right) + A_2 \exp\left(-\frac{t}{\tau_2}\right) \tag{12}$$

Subsequently, the two decay times τ_1 and τ_2 were weighted by their relative contribution to the mean decay time τ (see eq. 13).

$$\tau = \frac{A_1\tau_1^2 + A_2\tau_2^2}{A_1\tau_1 + A_2\tau_2} \tag{13}$$

After equilibration, the luminescence decay curves of the Eu^{3+} were measured. The changes in the mean luminescence decay time are directly related to an transfer from Eu^{3+} to Nd^{3+} following equation (2b). From the experimental data average distances between metal binding sites could be derived. As the luminescence decay time of the Eu^{3+} itself is a function of metal ion loading (presumably, due to macromolecular effects such as conformation changes, coiling and/or inter- and intramolecular association), the impact was tested using La^{3+}. Under the assumption that La^{3+} will react in complex formation like other lanthanoid ions (Eu^{3+}, Tb^{3+} and Nd^{3+}), from these measurements the Eu^{3+} luminescence decay times, also referred to as τ_D, in absence of any energy acceptor was determined. Comparing Eu^{3+}/Nd^{3+} measurements with Eu^{3+}/La^{3+} measurements and applying equation (2b) gives direct access to the energy transfer efficiencies in HS with Eu^{3+} as donor and Nd^{3+} as acceptor.

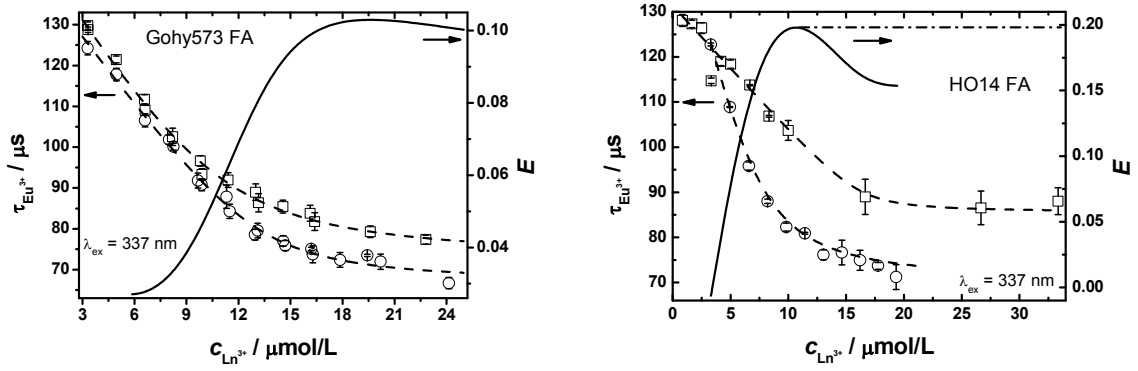

Figure 11: Determination of the average distance of metal binding sites in HS based on the concept of the "spectroscopic ruler". The open squares represents the changes in Eu^{3+} luminescence decay time by increasing the amount of Eu^{3+}. The changes of the Eu^{3+} luminescence decay time upon addition of Nd^{3+} to a solution of HS (c_{Eu} = 3.3 µmol/L) are marked by open circles. This figures show the results for two FA, Gohy573 FA (left) and HO14 FA (right). The energy transfer efficiencies resulting from the changes in the decay times are shown as well (solid lines). In the diagrams the metal content is corrected for total Ln^{3+} concentration.

For Gohy573 FA the energy transfer efficiency increases up to ten percent (c_{Nd} = 16 µmol/L). In the measurements using HO14 FA, the energy transfer efficiency seems to decrease at higher metal loadings, what is surprising, because especially at high metal concentrations most of the binding sites should be occupied and the shortest possible distance between the metal ions should be present. This finding is traced back to experimental uncertainties for the measurements of the Eu^{3+} luminescence decay time. For the FRET pair Eu^{3+}/Nd^{3+} an upper limit of the energy transfer efficiency of twenty percent was found. Applying equation (3) and using a Förster radius R_0 = 0.853 nm gives the distances of the two Ln^{3+} ions when bound to Hs.

From Figure 12 it can be seen, that the binding sites in HO14 FA are closer than in Gohy573 FA. The resulting distances between bound metal ions depends on the loading and covers the range of 1.6 nm > r > 1.1 nm, which is about ten to thirteen times the ionic radius of the Eu^{3+} ion ($r(Eu^{3+}_{(aq)})$ = 0.095 nm).

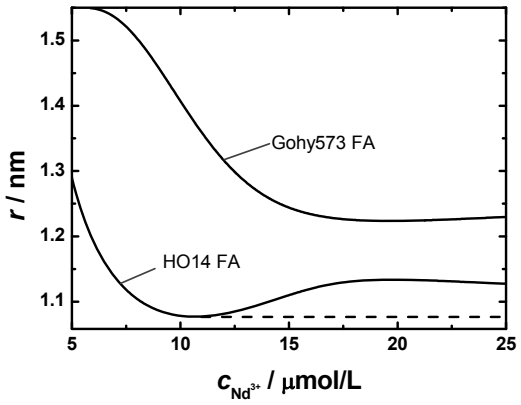

Figure 12: Distances of Eu^{3+} and Nd^{3+} in Gohy573 FA and HO14FA. The Förster radius R_0 = 0.853 nm was applied to calculate the distances between the metal ions bound to HS.

3.3 Association kinetics and conformational dynamics of HS and HS-metal complexes

To get insight in the complex formation kinetics between HS and lanthanoid ions, measurements with a *stopped-flow* reaction analyzer were performed. In these measurements the quenching of the intrinsic HS fluorescence was monitored. As Nd^{3+} does not show any luminescence in aqueous media, it is a excellent quencher (and metal probe) in *stopped-flow* measurements.

As shown in Figure 13, the whole spectral range of the intrinsic HS fluorescence can be measured using an interference filter. In contrast, when using Tb^{3+} as a quencher, the spectral region has to be selected properly to separate the intrinsic fluorescence of HS, which is quenched, from the sensitized luminescence of the Tb^{3+}, which is enhanced due to complexation. For this reason, different filters were used. In the first case, to cover nearly the whole spectral range, an interference filter (IF 585) was used. In the second case, band path filters were applied, which are transparent only in a certain spectral region. Here, a filter (BP 400 ± 40) transparent between 380 nm and 430 nm as well as a filter (FL 545.3) transparent between 536 nm and 554 nm were selected.

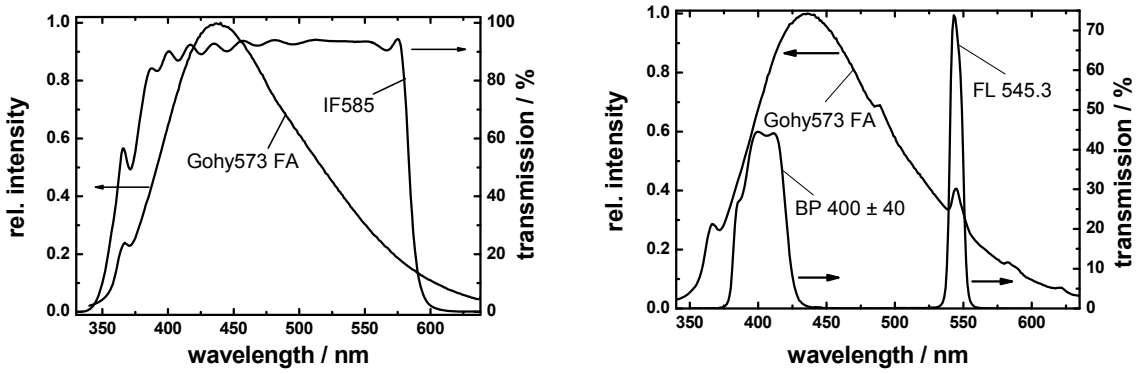

Figure 13: Comparison of the intrinsic Gohy573 FA fluorescence with the filters used in the *stopped-flow* experiments. Left: the transmission of the interference filter IF 585 is compared to the intrinsic fluorescence of the Gohy573 FA. Due to the optical properties of the filter nearly the whole spectral range of the intrinsic fluorescence can be detected. Right: the transmission spectra for the BP 400 ± 40 and the FL 545.3 filter as well as the intrinsic fluorescence spectrum of a Gohy573 FA solution containing 9.9 μmol/L Tb^{3+} are shown.

The *stopped-flow* measurements of the complexation of lanthanoid ions with HS showed differences in the complexation kinetics of lanthanoid ions with HA and FA.

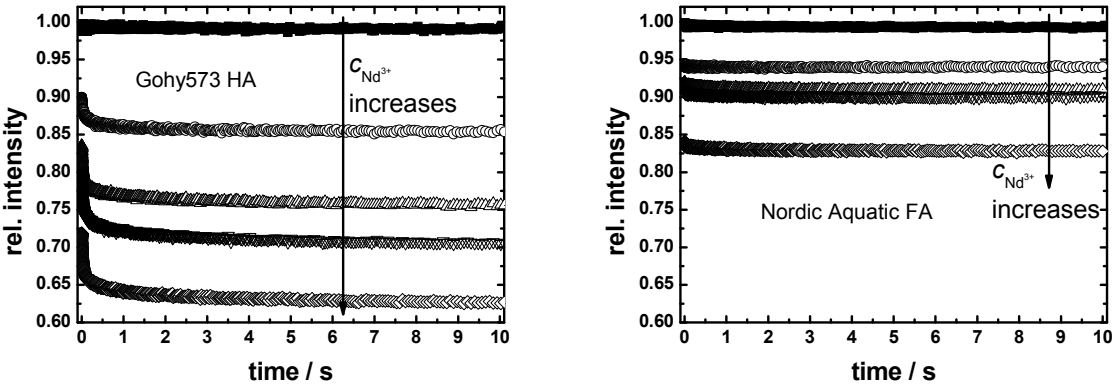

Figure 14: *Stopped-flow* time traces of a HA (right: Gohy573 HA) and a FA (Nordic Aquatic FA) intrinsic fluorescence quenching experiments at different Nd^{3+} concentrations. $c(Nd^{3+})$: ■ 0 μmol/L, ○ 5 μmol/L, △ 10 μmol/L, ▽ 15 μmol/L, ◊ 30 μmol/L

As can be easily seen form Figure 14, major differences between FA and HA were observed in the *stopped-flow* intrinsic fluorescence quenching measurements. It is tempting to attribute these discrepancies to differences in the complex formation. For both, HA as well as FA, a fast quenching process (sub-second time scale) can be found. In measurements with FA, the fast quenching is already finished within the dead time of the instrument (about 1.2 ms) and can only be seen as a decrease in signal intensity. In experiments with HA, a fast quenching process can be still resolved. In addition to the fast process, a slower quenching process can is found as well. Evaluation of the intrinsic fluorescence quenching of FA and HA at different times after mixing according to a Stern-Volmer analysis, the differences between FA and HA are striking. As shown in Figure 15, the relative quenching at the very beginning of the reaction (around 2 ms after mixing) is compared to the observed quenching at the end of the observation period (around 10 s after mixing).

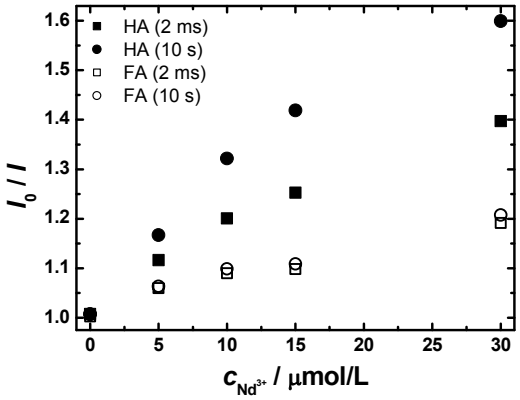

Figure 15: Comparison of intrinsic fluorescence quenching of HS different times after mixing for a FA (Nordic Aquatic FA) and a HA (Gohy573 HA) for different Nd^{3+} concentrations. In contrary to HA, the fluorescence quenching for FA is independent on the time after mixing.

The results obtained for fluorescence quenching at long times (seconds after mixing) are comparable to those found in regular steady state fluorescence quenching experiments. Bidoglio et al. found a slow exchange reaction, on a time scale of seconds to minutes, in experiments with Tb^{3+} competing with Ca^{2+} and Al^{3+} [22]. This finding was attributed to different types of binding sites present in HS. In other experiments, two different complexation processes with different reaction rates on a second time scale were found [23]. This was attributed to different binding sites as well as to conformational changes of the HS upon metal complexation. In these investigations the complexation was completed after 30 s [23,24,25].

Due to the macromolecular appearance of HS it is attempting to attribute the differences between FA and HA to properties resulting from their respective macromolecular structure. In contrast to low molecular weight compounds, in a macromolecule changes in structure and

conformation may occur upon complex formation (e.g. due to bridging or charge neutralization). Understanding HS as polyanion, the effective charge of a HS structure decreases upon complexation of cations. As a result, the intra-molecular repulsion forces of the macromolecular chain will decrease and subsequently this will alter the conformation of the macromolecule.

The discussed effects on conformation of HS molecules upon addition of metal ions should strongly influence the HS fluorescence anisotropy. According to equation (9), the capability of molecular rotation is dependent on the effective volume of the molecule and on solvent properties (e.g., viscosity). In case the dimension of a macromolecule is decrease upon complexation, the rotational correlation time should decrease correspondingly.

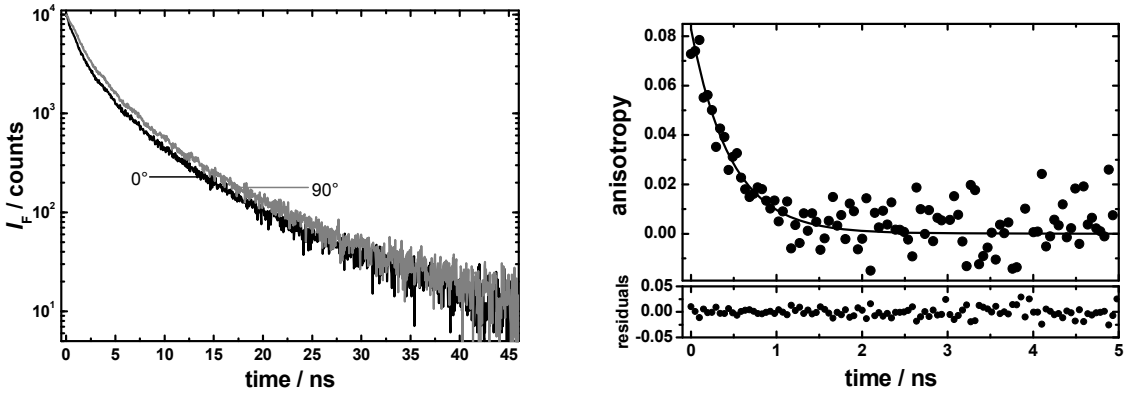

Figure 16: Left: Fluorescence decays vertical (black) and perpendicular (grey) to the plane of excitation light (λ_{ex} = 266 nm) of a solution containing 10 mg/L Gohy573 HA at 20°C. Right: Resulting anisotropy curve applying equation (4). The solid line reflects the best fit of equation (8) to the data points. Below the residuals are shown as well. A rotational correlation time of ϕ = 0.46 ns was calculated from the experimental data.

In Figure 16, the intrinsic fluorescence decay curves of a 10 mg/L Gohy573 HA solution at 20°C horizontal and perpendicular to the plane of excitation light (vertically polarization) are shown. From these curves using equation (4) the time dependent anisotropy can be calculated. Although, the intrinsic fluorescence decays of HS are highly complex [28,29], the anisotropy could be described using a monoexponential rate law. As can bee seen in Figure 16 (right hand side), after approximately 2 ns the anisotropy decreases down to zero. The decay can be described using a monoexponential rate law. For five different temperatures ranging from 20°C to 60°C fluorescence anisotropy decays were measured for a 10 mg/L Goyh573 HA solution in presence and absence of 16 μmol/L Eu^{3+}. In each case, the resulting anisotropy curves were fitted according equation (8) using an global fit approach. By this procedure only the rotational correlation times were treated as a fitting parameter. As a general tendency a decrease of the rotational correlation time with increasing temperature was found.

Assuming an rigid spherical rotor as simplest model for a molecule in solution, the calculated rotational correlation times can be used in combination with equation (9) to deduce the volume of the rotating unit. Accepting that the volume of the rotator is not affected by the temperature, the changes in the rotational correlation time are governed by the temperature dependence of the solvent viscosity. Because a lower viscosity will enhance the rotational motion, a decrease in the rotational correlation time is expected. Using literature data for the viscosity of water [27], the apparent volumes of the rotating units in Gohy573 HA in presence and absence of Eu^{3+} can be fitted globally for all measurements at different temperatures.

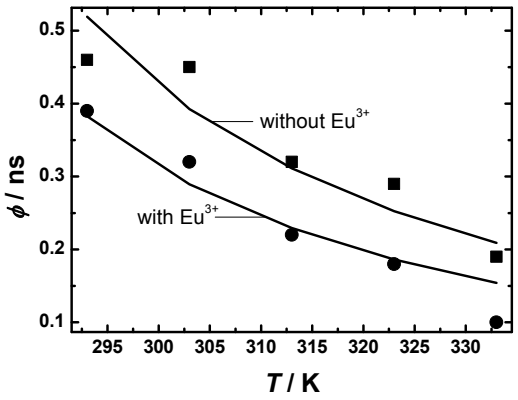

Figure 17: Calculated rotational correlation times of Gohy573 HA in absence (black squares) and presence (black circles) of Eu^{3+} following a global fit procedure according equation (8). The solid lines reflects the expected values for a fitting according equation (9). As a result, volumes of $V = 2.06$ nm^3 Gohy573 HA without Eu^{3+} and $V = 1.52$ nm^3 Gohy573 HA with Eu^{3+} were found.

At all temperatures the rotational correlation time for Goyh573 HA decreases upon addition of Eu^{3+}. The good agreement between calculation and experiment displayed in Figure 17 keeping in mind the assumption, that the changes in the rotational correlation time ϕ are only caused by the increasing solvent viscosity. Using the apparent rotational correlation times, volumes for the rotating units can be derived. At all temperatures the volume of the apparent unit is decreasing (from $V = 2.06$ nm^3 down to $V = 1.52$ nm^3) upon addition of Eu^{3+}, which is in good agreement with the model suggested.

3.4 High spectral resolution spectroscopy of Eu^{3+}-complexes

In general, the excitation wavelength was scanned over the range of 577 nm < λ_{exc} < 581 nm and the Eu^{3+} luminescence was observed in the spectral range between 585 nm < λ_{em} < 621 nm, covering the emission of the $^5D_0 \rightarrow {}^7F_1$ and the $^5D_0 \rightarrow {}^7F_2$ transitions. As an example, in

Figure 18 the luminescence of a Eu^{3+}-salicylic acid sample excited at different wavelengths are shown.

For these experiments a major challenge was the extremely low extinction coefficient of the $^5D_0 \leftarrow ^7F_0$ transition, due to parity forbiddance of the f-f transitions. This forbiddance is relaxed partially if the symmetry of the Eu^{3+} complex is lowered, e.g., due to the formation of non-centrosymmetric complexes or due to vibrational motion of the ligands.

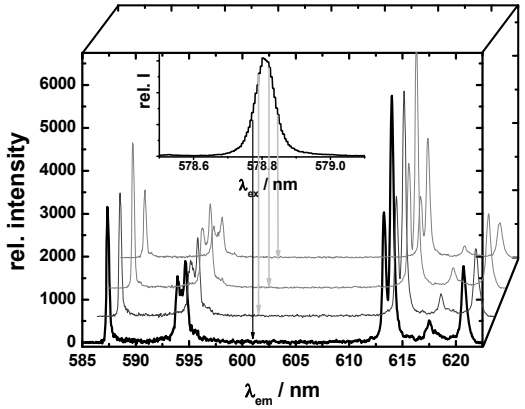

Figure 18: 4K luminescence of Eu^{3+}-salicylic acid complex at different excitation wavelengths.

As reference systems the TLS of $EuCl_3 \cdot 6H_2O$ crystals and of an aqueous $EuCl_3$ sample were also investigated at 4.7 K. For the $EuCl_3 \cdot 6H_2O$ crystals a single $^5D_0 \leftarrow ^7F_0$ transition was observed with a FWHM of 0.2 cm^{-1}. For the complexes with organic ligands the $^5D_0 \leftarrow ^7F_0$ transition was found to be broader: in the range of 2 cm^{-1} < FWHM < 23 cm^{-1} depending on the ligand.

Based on the observation of a very narrow and symmetric $^5D_0 \leftarrow ^7F_0$ transition in the reference system of $EuCl_3 \cdot 6H_2O$ it was concluded that only a single, well-defined Eu^{3+} complex was present. On the other hand, for the Eu^{3+} samples with organic ligands, the broader and often asymmetric $^5D_0 \leftarrow ^7F_0$ transition already point to the presence of more than one species. This is further supported by the observed dependence of the energy of the Stark levels of the $^5D_0 \rightarrow ^7F_1$ and $^5D_0 \rightarrow ^7F_2$ transitions on the excitation wavelength.

The first Stark peak of the $^5D_0 \rightarrow ^7F_1$ transition shifted upon scanning the excitation wavelength when organic ligands were present. In order to visualize the dependence on the excitation wavelength, the energy difference ΔE (in cm^{-1}) between the $^5D_0 \leftarrow ^7F_0$ excitation and the maxima of the $^5D_0 \rightarrow ^7F_{1\text{-}x}$ (x = 1, 2, 3) emission bands was calculated. It should be noted that in contrast to conventional molecular fluorescence line narrowing (FLN) spectroscopy, in

which vibronic excitation/emission takes place within the same electronic transition and ΔE is constant for a specific vibration, for these systems ΔE was found to depend on E_{exc} and to be different for the various $^7F_1$ levels; the variation in slopes is clearly shown in Figure 19.

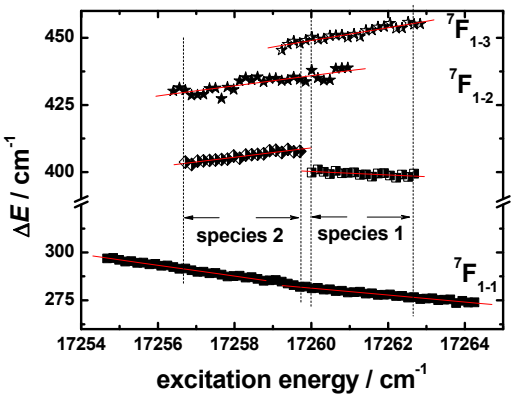

Figure 19: Dependence of the energy difference ΔE (between the $^5D_0 \leftarrow {}^7F_0$ excitation and the maxima of the $^5D_0 \rightarrow {}^7F_{1\text{-}x}$ (x = 1, 2, 3) emission bands) on the excitation wavelength for 3-methoxy benzoic acid (3MB).

A similar dependence has been reported before for the luminescence of Eu^{3+} in glassy matrices [24, 27]. The slight, continuous changes in ΔE can be attributed to small differences in the further environment of the complexes, e.g. in the second coordination sphere, whereas abrupt discontinuities in the slope point towards larger differences in the first coordination sphere of the Eu^{3+} ions. Therefore, these spectral regions were attributed to different "species" [21]. In Figure 19 two different species for Eu^{3+} and 3-methoxy benzoic acid (3MB) can be identified. Depending on the ligand and on the sample composition, different numbers of such species were found.

In order to connect the observed splitting pattern of the ultra-low temperature luminescence spectra with specific complex parameters crystal field strength parameter $N_v(B_{2q})$ was calculated. For weak crystal fields equation (1) connects ΔE_{MAX}, the energy difference between $^7F_{1\text{-}1}$ and $^7F_{1\text{-}3}$ for the lowest and the highest excitation energy of a species, to the crystal field strength parameter $N_v(B_{2q})$, according to [28]:

$$N_v(B_{2q}) = \sqrt{\frac{\pi(2+\alpha^2)}{0.3}}\Delta E_{MAX} \qquad (13)$$

with

$$\alpha = \frac{E_b - E_C}{\Delta E_{MAX} / 2} \tag{14}$$

E_b is the barycentre of the $^7F_1$ multiplet (mean energy) and E_C is the energy of the central level. Since ΔE_{MAX} is dependent on the excitation wavelength, $N_v(B_{2q})$ does as well.

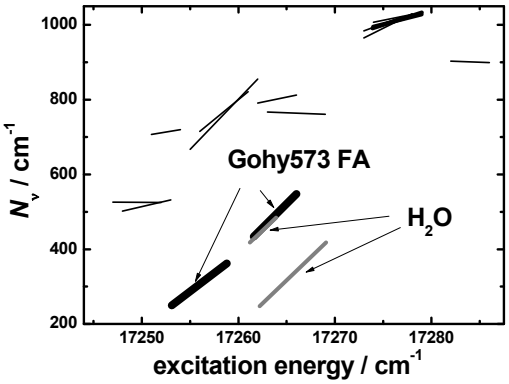

Figure 20: Crystal field strength parameters $N_v(B_{2q})$ of Eu^{3+}-salicylic acid complexes (2HB) at different excitation wavelengths. Shown are also the corresponding $N_v(B_{2q})$ for Eu^{3+} in water and in the presence of fulvic acid (Gohy573 FA).

In Figure 20 the crystal field strength parameter $N_v(B_{2q})$ vs. excitation energy is shown for salicylic acid (2HB) at different 2HB : Eu^{3+} ratios. Compared to other HB complexes investigated, 2HB shows a larger $N_v(B_{2q})$, which was found to be in the range of 500 cm^{-1} < $N_v(B_{2q})$ < 1000 cm^{-1} and also a slightly higher excitation energy, which was found to be in the range 17250 cm^{-1} < E_{exc} < 17285 cm^{-1}. For the Eu^{3+} complexes with meta- and para-hydroxybenzoic acid smaller crystal field strength parameters of 200 cm^{-1} < $N_v(B_{2q})$ < 500 cm^{-1} were found. The large $N_v(B_{2q})$ was attributed to the formation of chelate complexes between 2HB and Eu^{3+}. For comparison also $N_v(B_{2q})$ found for $EuCl_3$ in water and in the presence of fulvic acid (Gohy573 FA) are shown in Figure 20.

For HS it is tempting to conclude that the formation of chelates is small, the major binding is achieved via interactions comparable to complexes formed with carboxylic acids meta- and para- substituted benzoic acids. Those ligands are not capable to form chelate complexes. Complexes of the Gohy573 FA seem to be more similar to 3- or 4-hydroxybenzoic acid or 3,5-dihydroxybenzoic acid, which is in contrast to often assumed salicylate-type complexes [20]. From the data binding of Eu^{3+} to fulvate seems to be accomplished via deprotonated carboxylate groups. In addition, a considerable fraction of the Eu^{3+} ions don't seem to be tightly complexed since the observed $N_v(B_{2q})$ is very similar to the aqueous reference sam-

ple. This could be either explained by an excess of Eu^{3+} in this sample or by the assumption that FA forms a significant portion of outer sphere complexes. Although the samples were equilibrated for 24h it is possible that the formation of inner sphere complexes needs more time. This is a subject of work in progress.

Depending on the symmetry, different pattern of Stark levels can be observed for the $^5D_0 \rightarrow ^7F_1$ and the $^5D_0 \rightarrow ^7F_2$ transitions. In case the $^5D_0 \rightarrow ^7F_1$ transition is split into three lines, the possible point groups are D_2, C_{2v} (orthorhombic), C_2, C_s (monoclinic) or C_1(triclinic). Further discrimination is carried out based to the splitting of the $^5D_0 \rightarrow ^7F_2$ transition: three lines → D_2; four lines → C_{2v}; five lines → C_s, C_1 or C_2. The latter case can only be further distinguished by polarization measurements [29]. The luminescence spectra of the $^5D_0 \rightarrow ^7F_1$ and the $^5D_0 \rightarrow ^7F_2$ transitions of the different species for each model ligand and for HS were evaluated with respect to the number of Stark levels visible in the spectrum. For 2HB a C_x symmetry (x = s, 1 or 2) was assigned to the different formed in solution. In general, for the model ligands and for HS the complexes showed a C_y symmetry (y =2v, s, 1 or 2), while Eu^{3+} in water (reference sample) showed a higher symmetry, D_2.

It is interesting to note that the crystal field strength parameter $N_v(B_{2q})$ and the excitation energy are not directly correlated. In this case it would have been expected that the excitation energy would increase linearly with $N_v(B_{2q})$ By comparing the spectra of all investigated samples, it turns out that not only electrostatic repulsion forces influence the Stark splitting, but also the symmetry of the coordination polyhedron. Therefore, complexes of different symmetries may have the same crystal field strength parameter but different excitation energies ($^5D_0$-$^7F_0$ energy difference) [29]. Due to the formation of complexes with different symmetries the contribution of the spherical part of the crystal field, and subsequently the $^5D_0$ -$^7F_0$ energy is altered. The change of the induced crystal field splitting, however, is not necessarily pointing in the same direction. This depends on the individual influence of each ligand on the f-orbitals in that distinct symmetry.

4 Summary

Steady-state and time-resolved luminescence techniques were used for the investigation of interactions between HS and metal ions. In the experiments the intrinsic fluorescence properties of HS as well as the luminescence of Ln^{3+} ions, which were used as natural analogs for An^{3+}, were monitored. Data of time-resolved fluorescence anisotropy, stopped-flow analysis and high resolution ultra-low temperature luminescence excitation spectra were evaluated in the investigations in order to get specific information on effects of the metal complexation on the structure (conformation, aggregation) of HS.

The quenching of the intrinsic HS fluorescence and the sensitization of Ln^{3+} luminescence (Ln^{3+} = Eu^{3+}, Tb^{3+}) were investigated and compared. With respect to the FA fractions a consistent picture was obtained, in contrast to the HA fractions investigated. On close inspections of the steady-state fluorescence spectra of HA, a hypsochromic shift upon metal addition was observed. This spectral change points already to an induced alteration of the HA

structural properties due to the binding of metal ions. This fact is further supported by results from stopped-flow experiments, in which the complexation kinetics for FA and HA of different origins was measured. For the FA as well as for the HA fractions investigated a consistent picture was obtained. i) The complexation kinetics of the FA is very fast (beyond the time-resolution of the stopped-flow apparatus used) and is finished within the first millisecond after metal addition – this can be concluded from the instantaneous decrease of the intrinsic FA fluorescence. ii) for HA, in addition to the very fast process, a second, much slower kinetic was observed. This supports the idea of induced structural alterations in HA upon metal complexation. This view is further supported by time-resolved anisotropy measurements of the intrinsic HA fluorescence in the absence and presence of Eu^{3+} at different temperatures. It was found that the rotational correlation time are shortened after addition of Eu^{3+} indicating a decrease in effective size of the HS upon addition of Eu^{3+}. However, it is important to stress that the measured rotational correlation times are in the sub-nanosecond time regime, which means that either not the complete molecular rotation is monitored – in case of “large” molecules rather the rotation of a subunit – or the molecules are indeed small compared the “historic picture of HS”.

For the evaluation of the time-resolved measurements of the Tb^{3+} luminescence an intramolecular energy back-transfer was introduced in the data analysis. With this new approach a global analysis of the experimental data was feasible yielding for a particular sample set only one decay time. It has to be stressed that i) this decay time could be still an average value of a distribution of closely space decay times and ii) in contrast to former data analysis the assumption of discrete and completely different Tb-HS species is redundant. It is interesting to note that from such an analysis for the FA samples a very similar results for the decay time were obtained, which seems to be reasonable with in the newly established view of FA as mixture of “small” molecules with very similar binding sites. Again, for the HA fractions larger differences were derived in the analysis underlining the idea of HA being larger in size.

In order to get information on the distribution of metal ion bound to HS without a bias due to missing knowledge of HS structure, interlanthanoide energy transfer between Eu^{3+} (Tb^{3+}) and Nd^{3+} was investigated and the mean distance between metal ions was calculated. Depending on the origin of HS and on the loading with metal ions distance in the range of ten ionic radii were found.

In order to access further structural detail of metal-HS complexes high-resolution ultra-low temperature luminescence excitation spectra of Eu^{3+} complexes with model compounds and HS were recorded. From the excitation and emission spectra crystal field strength parameters and complex symmetries were derived. As expected significant difference were found between salicylic acid and other benzoic carboxylic acids, probably reflecting the formation of chelate complexes. A first comparison of the results for model ligands and of HS revealed that the major part of binding seems to be to carboxylic acid type of ligands with no significant contribution from chelates. However, this is work to be continued in the future.

Acknowledgement

The authors are grateful to the Bundesministerium für Wirtschaft und Technologie (BMWi) for the financial support. Furthermore, the authors greatly appreciate the contributions of Bettina Marmodée in the field of ultra-low temperature experiments and of Stefanie Zilm-Gramckow, Katlen Brennenstuhl, Melanie Hans, Tobias Krüger as well as Philipp Primus for their experimental support.

5 References

[1] J.C.G.E. Da Silva, A.A.S.C. Machado, and C.S.P.C.O. Silva. *Anal. Chim. Acta*, 318:365–372, 1996.

[2] U. Schmiedel and F.H. Frimmel. *Vom Wasser*, 77:333–348, 1991.

[3] M. Schnitzer and K. Gosh. Fluorescence excitation spectra of humic substances. *Can. J. Soil Sci.*, 60:373–379, 1980.

[4] N. Senesi, T.M. Miano, M.R. Provenzano, and G. Brunetti. *Sci. Tot. Environ.*, 81/82:143–156, 1989.

[5] S.A. Visser. *Aquatic and terrestrial humic materials*, pages 183–202. Ann Arbor Science, 1983.

[6] S.R. Ahmad and D.M. Reynolds. *Wat. Res.*, 29:1599–1602, 1995.

[7] N. Senesi, T.M. Miano, and M.R. Provenzano. *Lecture Notes in Earth Sciences*, 33:63–73, 1991.

[8] J. Chen, E.J. LeBoef, S. Dai, and B.H. Gu. *Chemosphere*, 50:639–647, 2003.

[9] H.C. Joshi, H. Mishra, and H.B. Tripathi. *J. Photochem. Photobiol. A*, 105:15–20, 1997.

[10] C.F. Scheck, F.H. Frimmel, and A.M. Braun. *Z. Naturforsch.*, 47b:399–405, 1992.

[11] D.K. Ryan and J.H. Weber. Fluorescence quenching titration for determination of complexing capacities and stability constants of fulvic acid. *Anal. Chem.*, 54:986–990, 1982.

[12] P.R. Selvin. *Annu. Rev. Biophys. Biomol. Struct.*, 31:275–302, 2002.

[13] G. Bidoglio, I. Grenthe, P. Qi, P. Robouch, and N. Omenetto. *Talanta*, 52:57–63, 1991.

[14] G. Bidoglio, I. Grenthe, P. Qi, P. Robouch, and N. Omenetto. *Talanta*, 9:999–1008, 1991.

[15] A. Dierckx, A. Maes, and J. Vancluysen. *Radiochim. Acta*, 66:149–156, 1994.

[16] G. Plancque, V. Moulin, P. Toulhoat, and C. Moulin. Eu^{3+} speciation by time-resolved laser-induced fluorescence. *Anal. Chim. Acta*, 478(1):11–22, February 2003.

[17] Jr. William DeW. Horrocks and Daniel R. Sudnick. Lanthanide ion luminescence probes of the structure of biological macromolecules. *Accounts of Chemical Research*, 14:384–392, 1981.

[18] F. H. Frimmel, G. Abbt-Braun, K. G. Heumann, B. Hock, H.-D. Lüdemann, and M. Spiteller, editors. *Refractory Organic Substances in the Environment*. Wiley-VCH, Weinheim, Germany, 2002.

[19] N. Sabbatini, M. Guardigi, J.-M. Lehn. Luminescent lanthanide complexes as photochemical supramolecular devices. *Coord. Chem. Rev.*, 123:201–228, 1993.

[20] B. Alpha, R. Ballardini, V. Balzani, J.-M. Lehn, S. Perathoner, N. Sabbatini. Antenna effect in luminescent lantanide cryptates: a photophysical study. *Photochem. Photobiol.*, 52:299–306, 1990.

[21] J.-M. Monsalier, F. Scherbaum, G. Buckau, J.I. Kim, M.U. Kumke, C.H. Specht, F.H. Frimmel. Influence of photochemical reactions on the complexation of humic acid with Eu^{3+3+}. *J. Photochem. Photobiol. A.*, 138:55–63, 2001.

[22] G. Bidoglio, N. Omenetto, P. Robouch. Kinetic studies of lanthanide interactions with humic substances by time resolved laser induced fluorescence, *Radiochim. Acta*, **52/53**:57-63, 1991.

[23] F.C. Wu, R.B. Mills, R.D. Evans, P.J. Dillon. Kinetics of metal-fulvic acid complexation using a stopped-flow technique and three-dimensional excitation emission fluorescence spectrophotometer, *Anal. Chem.*, **76**:110-113, 2004.

[24] R.A. Saar, J.H. Weber. Comparison of spectrofluorometry and ion-selective electrode potentiometry for determination of complexes between fulvic acid and heavy-metal ions, *Anal. Chem.*, **52**:2095-2100, 1980.

[25] S.E. Cabaniss. Synchronous fluorescence spectra of metal-fulvic acid complexes, *Environ. Science & Technol.*, **26**:1133-1139, 1992.

[26] J.R. Lakowicz. Principles of fluorescence spectroscopy. Springer 2006.

[27] Handbook of Chemistry and Physics, 84th edition 2003-2004, David R. Lide (editor in chief), CRC press, 2004

[28] M.U. Kumke, G. Abbt-Braun, F.H. Frimmel. Time-Resolved Fluorescence Measurements of Aquatic Natural Organic Matter, *Acta Hydrochimica et Hydrobiologica*, **26**:73-81,1998

[29] M.U. Kumke, C. Tiseanu, G. Abbt-Braun, F.H. Frimmel. Fluorescence Decay of Natural Organic Matter (NOM) – Influence of Fractionation, Oxidation, and Metal Ion Complexation, *Journal of Fluorescence*, **8**:309-318, 1998

[30] T.H. Yoon, H. Moon, Y.J. Park, K.K. Park. Investigation of metal binding sites on soil fulvic acid using Eu(III) luminescence spectroscopy. *Environmental Science and Technology*, **28**:2139-2146, 1994

[31] F.J. Stevenson. Humus Chemistry – Genesis, Composition, Reactions, Wiley: New York, 1982.

[32] A.C. Stenson, A.G. Marshall, W.T. Cooper. Exact masses and chemical formulas of individual suwannee river fulvic acids from ultrahigh-resolution electrospray ionization Fourier transform ion cyclotron resonance mass spectra. *Analytical Chemistry*, **75**:1275-1284, 2003.

[33] G. Davies, E.A. Ghabbour, C. Steelink.Humic acids: Marvelous products of soil chemistry. *Journal of Chemical Education*, **78**:1609-1614, 2001.